Polymer *grafted* Nanomaterials: Synthesis via RAFT Polymerization and the Applications

A Thesis Submitted for the degree of

DOCTOR OF PHILOSOPHY

BY

Nilanjan Mukherjee

School of Chemistry
University of Hyderabad
Hyderabad-500 046
INDIA

January 2024

Dedicated to

My Thesis Supervisor,

My Wife,

My Family and Friends

UNIVERSITY OF HYDERABAD

Central University (P.O.), Hyderabad-500046, INDIA

Declaration

I hereby declare that the thesis entitled as "**Polymer *grafted* Nanomaterials: Synthesis via RAFT Polymerization and the Applications**" submitted to School of Chemistry, University of Hyderabad, Hyderabad, India is a record of a bona fide research carried out by me under the guidance of **Prof. Tushar Jana**. This result has not been submitted elsewhere for the award of any diploma or membership or degree to any other University or Institution.

In harmony with the usual practice of reporting scientific methodology due acknowledgements have been mentioned wherever the work reported on the findings of other researchers. Any exclusion or omission that might have taken place is highly regretted.

Nilanjan Mukherjee

January, 2024

Nilanjan Mukherjee

Regd. No. 16CHPH18

UNIVERSITY OF HYDERABAD
Central University (P.O.), Hyderabad-500046, INDIA

Professor Tushar Jana
School of Chemistry

Web: http://chemistry.uohyd.ac.in/~tj/

Tel: 91-40-23134808 (Office)
91-9440127016 (Mobile)
Fax: 91-40-23012460
E-mail: tusharjana@uohyd.ac.in
tjscuoh@gmail.com

Certificate

This is to certify that the Thesis work entitled as "**Polymer *grafted* Nanomaterials: Synthesis via RAFT Polymerization and the Applications**" has been carried out by **Nilanjan Mukherjee** bearing registration number **16CHPH18** for the award of Doctor of Philosophy in the School of Chemistry is an authentic and genuine work carried out by him under my guidance and supervision and the same has not been submitted elsewhere. I consider that the thesis has reached the standards and fulfils all the requirements of the rules and regulations relating to the nature of the degree. This thesis is free from any plagiarism and has not been submitted previously for the award of any diploma or degree of this or any other University or Institution.

Parts of this thesis has been published in the following publications:

1. **Mukherjee, N.**; Das, A.; Dhara, M.; Jana, T.* *Polymer.* **2021**, *236*, 124315. (Chapter 3)
2. **Mukherjee, N.**; Das, A.; Mukhopadhyay, S.; Das, S. K.;* Jana, T.* *ACS Appl. Polym. Mater*. **2024,** *6,* 846-858. (Chapter 4)
3. **Mukherjee, N.**; Das, A.; Jana, T. *ACS Appl. Nano Mater.* **2023,** *6,* 544-557. (Chapter 6)

The student has made presentation in the following conferences:

1. 15th International Conference on Polymer Science and Technology (SPSI MACRO 2018) (**Poster presentation**).
2. 16th annual in-house symposium (ChemFest 2019) (**Poster presentation**).
3. 18th annual in-house symposium of (ChemFest 2021) (**Oral presentation**).
4. 13th International e-Conference of Advancements in Polymer Materials (APM 2022) (**Oral presentation**).
5. 16th International Conference on Polymer Science and Technology (SPSI MACRO 2022) (**Poster presentation**) (**Received best poster award**).

Further, the student has passed the following courses towards the fulfilment of course work:

Course Code	Course Name	No. of Credits	Grade
CY801	**Research Proposal**	**3**	**Pass**
CY802	**Chemistry Pedagogy**	**3**	**Pass**
CY805	**Instrumental Methods-A**	**3**	**Pass**
CY806	**Instrumental Methods-B**	**3**	**Pass**

24/01/2024

Dean
School of Chemistry (UoH-IoE)

Dean
School of Chemistry
University of Hyderabad
Hyderabad-500 046.

Prof. Tushar Jana
(Thesis Supervisor)

PROF. TUSHAR JANA
School of Chemistry
University of Hyderabad
HYDERABAD-500 046, INDIA.

PREFACE

This current thesis entitled "**Polymer *grafted* Nanomaterials: Synthesis via RAFT Polymerization and the Applications**" has been divided into eight chapters. ***Chapter 1*** as the introductory chapter, demonstrates the elementary idea and the aim of the thesis. Also contains a detailed discussion on the basics of controlled radical polymerization technique, RAFT technique along with the SI-RAFT approach on different nanomaterial surface to grow homo polymer and block copolymer chains of predeterminant architecture. Furthermore, different blending techniques to prepare mixed matrix membranes and their application in fuel cell is discussed elaborately with the benefits and use of heterocyclic nano catalyst in organic catalysis. ***Chapter 2*** explains the details of chemicals and materials used in this thesis work. ***Chapter 3*** demonstrates the synthesis of SiNP and the use of SI-RAFT polymerization technique to grow block copolymer chains containing imidazole and 1,2,4-triazole pendants on the SiNP surface along with the preparation of polymer-*g*-SiNP@OPBI nanocomposite membrane with OPBI polymer and tested their physical properties and application towards proton conductivity. ***Chapter 4*** demonstrates the synthesis of polymer brushes consisting of neutral, quaternary ammonium and zwitterionic units on the nano MOF surface (PGM) using aqueous SI-RAFT technique. The material was characterized and further used to prepare OPBI@PGM Mixed matrix membranes and utilized for proton conductivity application. ***Chapter 5*** illustrates the grafting of poly vinyl phosphonic acid chains on the UiO-66 NH_2 (PVPA-*g*-MOF) surface via aqueous SI-RAFT technique and thoroughly checked their proton conducting ability upon preparing pellets from the powdered nanomaterials. ***Chapter 6*** validates the grafting of block copolymer chains on the MWCNT surface (PGNT) upon chemical modification and utilized to prepare PGNT@OPBI MMMs which were then tested extensively for proton conduction abilities upon H_3PO_4 doping. ***Chapter 7*** utilized RAFT modified MWCNT to grow pNVI chains on the MWCNT surface and further utilized then to grow Pd nanoparticle on the polymer modified surface of MWCNT (Pd@PGNT). The material was extensively tested as heterogeneous catalyst in Suzuki-Miyaura coupling reaction. ***Chapter 8*** comprises of all the summaries of the importance of this current thesis which concludes all the remarks and demonstrates the future scopes of numerous scientific findings associated with this work.

January, 2024 Nilanjan Mukherjee

Acknowledgement

This PhD journey of discovering knowledge has been a real roller coaster ride for me. Multiple attempts of success and failures were what which makes this journey so exciting. Through this journey I learned to never give up on myself which helped to increase my inner strength. This journey was not an easy one but with hard work and persistence it made it on my way. Throughout this whole journey I met many inspiring persons, came to know about their struggles and as well as made many friends who helped me to grow as a person not only from outside but also from inside. This thesis has become a reality with the help and support of many individuals. It's been several years since when my interest and love for Chemistry has started. I would like to extend my sincere thanks to each one of them who has helped me directly or indirectly to come this far and successfully completing this thesis today.

First and foremost, I would like to thank and give my prayers to Loknath Baba, the almighty for his showers of blessings throughout my doctoral work and to complete it successfully.

I would like to express my sincere and deep gratitude to my supervisor Prof. Tushar Jana without whom I would never have made this research work successfully possible. His constant guidance and invaluable advice carried me through all the stages starting with the designing of the projects to writing to completing my doctoral work successfully. His sincerity, dynamism, vision and motivation have deeply inspired me throughout my research life. He has taught me about how to carry out the research work methodically and also how to present the research works systematically and beautifully. It was a great honour and privilege to continue with the research and work under his guidance. I am extremely grateful for his help. I would like to thank him for his empathy, friendship and great sense of humour. I would also like to extend my thanks to Mrs. Sutapa Sinha Mam for her patience and acceptance during this whole research period when I discussed with sir about my research work even on holidays. I also give my best wishes to Buchan and Babli for their amazing carrier ahead.

I would also like to thank my Doctoral Committee members headed by Prof. P.K. Panda and Prof. D. Barik for their brilliant suggestions, comments and exemplary recognition throughout my doctoral work. Yours meticulous scrutiny, timely and scholarly advice and scientific approach towards my each and every projects have helped me a lot to a great extent to accomplish this doctoral work successfully.

I would like to show my gratitude to all the esteemed Deans and Faculty members of the School of Chemistry, University of Hyderabad Dr. Goverdhan Mehta (Univ. Distinguished Professor), Dr. M. Durga Prasad (Emeritus Professor), Dr. Kalidas Sen (Emeritus Professor), Dr. M.Periasamy (Emeritus Professor), Dr. D. Basavaiah (IOE Chair Professor), Dr. Abani K. Bhuyan (Senior Professor), Dr. Ashwini Nangia (Senior Professor), Dr. Samudranil Pal (Senior Professor), Dr. Susanta Mahapatra (Senior Professor), Dr. K.C. Kumara Swamy (Senior Professor), Dr. T.P. Radhakrishnan (Senior Professor), Dr. Musti. J. Swamy (Senior Professor), Dr. Anunay Samanta (Senior Professor), Dr. Lalitha Guruprasad (Professor), Dr. M. Sathiyendiran (Professor), Dr. Perali Ramu Sridhar (Professor), Dr. R Chandrasekar (Professor), Dr. Akhila Kumar Sahoo (Professor), Dr. D.B. Ramachary (Professor), Dr.Pradeepta K. Panda (Professor), Dr. R. Nagarajan (Professor), Dr. Viswanathan Baskar (Professor), Dr. Samar Kumar Das (Professor), Dr. K. Muralidharan (Professor), Dr. S.G. Ramkumar (Associate Professor), Prof. Debashis Barik (Professor), Dr. Srinivasarao Yaragorla (Associate Professor), Dr. K.V. Jovan Jose (Assistant Professor), Dr. Manju Sharma (Assistant Professor), Dr. Murali Banavoth (Assistant Professor) and Dr. T Saravanan (Assistant Professor).

Next, I would like to heartily thank my University (University of Hyderabad) and my Department (School of Chemistry) for providing me the opportunity for doing my research and also providing us the facilities like TEM, FESEM, PXRD, AFM, NMR, HRMS, BET, DVS, Zeta Potential, FT-IR, RAMAN. Due to these facilities of our School, we can complete our research work so smoothly without any worries. I would like to convey my sincere acknowledgement to Dr. Durgaprasad for helping me with the TEM, AFM, RAMAN facilities and provide me with the data acquiring. I would also like to give my heartfelt thanks to Mr. Sunil (for FESEM), Mr. Pankaj (for TEM), Dr. Uday (for PXRD) and lastly Chaitanya Anna (for DVS).

I am grateful to my school Jhargram Kumud Kumari Institution (JKKI). A special thanks to all the teachers especially Subrata Barik, Nanda Dulal Pramanik, Mangalashish Jana for inspiring me and helping me to become what I am today. I would also like to appreciate my teachers Mr. Ujjwal Sinha, Dilip Dandapat, Suphal Chakraborty, Pradip Mallick and Ajit Nayak sir for helping me out at the time when I faced difficulties with any lessons even at the odd hours. I am also obliged to my mentors and teachers during my BSc from Jhargram Raj College Shirshnu Kumar Kundu, Sumana Sengupta, Rajarshi Chatterjee, Biplab Biswas, Partha Sarathi Singha and also my another teachers who encouraged me and also triggered the interest inside me to purse higher studies in chemistry Dr. Anup Das

Mahapatra, Dr. Nirmal Hazra and Dr. Tridip Tripathi. I am also much obliged to my faculties of MSc from National Institute of Technology, Durgapur Dr. Apurba Kumar Patra, Dr. Dipankar Sukul, Dr. Utpal Adhikari and Dr. Sankar Chandra Moi for their immense support and guidance.

I am thankful to the senior members of my Lab especially Dr. Arindam Sannigrahi, Dr. Sudhangshu Maity and Dr. Sandip Ghosh for giving me emotional and mental support throughout my research life not only professionally but also personally all the time over the phone except of your busy schedules. A special gratitude to Dr. Niranjan Yeole for making me understand so well about the basics of RAFT polymerization during the early days of my research life. I am also thankful to Dr. Bikash Kumar for helping me using the Centrifuge facilities and UTM. Thanks to Dr. Konda Reddy Kunduru for always taking care of uplifting our moods with his jokes when I used to feel low. I would also like to praise Dr. Mutyala Naidu for helping me finding a shelter in Hyderabad also amidst Covid. I owe my gratitude to Dr. Moumita Dhara and Nitai Da for their immense help. A long memory of enjoying cricket matches during the world cup, going for late night Bengali movies or even Moumita di cooking tasty Bengali cuisines for me and Anupam is what worth remembering of. Our innumerable laughters and discussions over various topics makes me happy till today. I would also like to thank my other lab seniors Dr. Dhamodaran Arunbabu, Dr. Shuvra Singha, Dr. Kuruma Malkappa, Dr. Mousumi Hazarika, Dr. Bala Kondareddy, Dr. Rambabu Koyilapu, Dr. K.S.N Raju, Dr. Harilal, Dr. Kalyan Ramesh, Dr. Krishna Kumar, Dr. P. Jaya Prakash Yadav, Dr. Mithun Chakraborty, Dr. Amaranadh Jhasti, Mr. Murali Sankar and Dr. Satheesh Mulkapuri.

A big thanks to other junior and senior colleagues of TJ Family Suchismita Subhadarshini, B. Prasannatha, Somdatta Rudra, Akhil Gorre, Ritu Saraswat, Sourav Jana, Dr. Mutyala Naidu and Dr. Satheesh Mulkapuri. A special mention to my favourite junior Arunava Dutta for always being a friend and small brother to me. I wish you all the best for your upcoming research life and will always pray for your health and success. I owe my sincere gratitude to all my project students namely, Soudipta Manna, Saikat Bera, Sahla Latheef, Dr. SuryaKala D. (Assistant Professor, Chemistry, GSS, VSP). I wish them all the best for their future endeavours.

I would like to acknowledge my gratitude towards Dr. Subhabrata Mukhopadhyay and Dr. Sneha Paul Di for giving me the best time of my research life. I really cherish the memories of going for photography sessions early in the morning, having the best Hyderabadi

biriyanis, going out for innumerable tea breaks and laughter. Planning mid-night outings to Sneha di's Murimakha to making fish fry and barbeque in the white rock are what uplifted our moods. I heard research life is tiring and boring but, because of you both, Anupam, Olivia and Chandni Di it was not. Each and every moment with Subho da is special for me. Starting from his inspiration towards higher studies to teaching photography skills to showing the opportunities ahead of us through his eyes to helping me in the research are what which adds the brownie points to our special bonding. Finally, I would like to congratulate you for completing your post doctorates successfully and for the upcoming success in your career. I would also like to thank Dr. Kallol Mukherjee, Dr. Arijit Mukherjee, Dr. Suman Ghosh, Dr. Sabari Ghosh, Dr. Koushik Ghosh, Dr. Rudraditya Sarkar, Dr. Sudipta Seth, Dr. Navendu Mondal, Dr. Tasnim Ahmed, Dr. Anil Kumar Gunnam, Dr. Mou Mandal, Dr. Apurba De, Dr. Tanmaya Kumar, Dr. Sk Saddam Hossain, Dr. Kuntal Bhattacharyya and Dr. Sugata Goswami for always standing behind me and supporting as a senior friend whenever and wherever I needed.

I would like to praise Dr. Shubham Debnath for his unconditional friendship starting even before my research life. Being your roommate is one of the best things which happened to me. I remember when you used to suddenly wake up from your sleep in the middle of the night and flow our room with your jokes and innumerable laughter. I will always remember our small weekend trip of going to visit the old streets of Hyderabad, visiting the Golconda Fort, going for having the spiciest biriyani and so on. Kudos to Dr. Soutrick Das, Dr. Somnath Das, Dr. Suman Mondal, Dr. Sumanta Paul, Dr. Saradamoni Mondal and Dr. Shubham Dutta for our friendship. Our unplanned picnics on the roof of our hostel, our unplanned getaways, our small gossips along with our excitement for small parties are what which I will cherish all throughout my life. I owe my thanks to Dr. Jyotsna Bania, Dr. Pritam Roy, Dr. Olivia Basu and Dr. Hema Kumari for sharing a beautiful friendship throughout my research period.

I would like to convey my gratitude towards Dr. Anupam Das for sharing such a good friendship with me. Starting from late night bike rides to early morning outings to sharing food to several tea breaks in the late nights I cherish them all. Without you my research life would not have turned so beautiful. We have completed several projects together successfully but, never we have doubted each other's skills. You are my best bud till date and will continue to do so.

I would also like to thank my amazing juniors Debojyoti Chatterjee, Arghadip Ghosh, Soumik Paul, Arka Patra, Somratan Sau, Debu Jana, 'Mohunbagani' Sourav, Md Alamgir and Sagnik Ghosh. I wish you all the best for your future and all of you be happy and healthy wherever you are.

My special mention to my best friend Dr. Ayan Chatterjee and thank him for gifting me each and every sweet memory. I appreciate my childhood friends Sayantan, Soumitra, Sourabh, Sourabh da, Arijit, Archita, Somnath, Tridib, Suman, Debashish, Rajib, Subhajit, Gabbar, Saroj, Arabinda, Aninda, Pathik, Subarna for their help. I really appreciate you all!

I would like to mention Mr. Lakshmi Kanta Mukherjee (Baba) and Mrs. Putul Mukherjee (Maa). I express my gratitude towards my parents for their immense support and always reminding me to believe in myself. Thank you for never giving up on me. You two always deserve the best from me. The sacrifices that you both have done and are still doing for me is beyond any description. I can never explain that how thankful I am to the almighty for making you both as my parents. I love you both in my own way and I hope to make you proud someday. I would like to give my prayers and gratitude towards Fakir Chandra Mukherjee (thakurda), Gita Rani Mukherjee (thakuma), Jyotish Chandra Chakraborty (dadu) and Aparna Chakraborty (dida). I would also like to profess my thank to my uncles and aunts Pinaki Bhusan Chakraborty, Kamalendu Chakraborty, Bishuneb Chakraborty, Dipak Mukherjee, Debdas Mukherjee, Shyamali Chakraborty, Lipi Chakraborty, Ratna Mukherjee, Sikha Mukherjee and Maitri Chakraborty. I appreciate your kindness and also thankful to have such amazing persons in my life. Thank you for always pampering me as your child. Lastly, I would like to owe my gratitude towards Krishna Gopal Mukherjee (Jethu), Mita Mukherjee (Boroma) and Amit Mukherjee (dada) for always being such kind towards me and always loving me. Without you people my childhood would not have been so beautiful. I would also like to thank here my cousins Tush didi, Rik dada, Piku, Doyel and Dodo.

Sri Ramakrishna Sarada Peeth (Kanya Gurukul), Jhargram has always been a very important part of my life since my birth. I would like to thank Paribrajika Veda Hridaya, Paribrajika Atma Hridaya, Paribrajika Amrita Hridaya, Sumita Sengupta, Dora Chaudhuri and Ila Pattanayak for always standing by me and my family.

A big thank you and respect to my other grandparents Fakir Chandra Sinha (dadu), Gobindo Saran Sarkar (dadu), Juthika Sarkar (dida), Pratibha Sinha (thakuma). I have never seen you all in person but I thank you all from the core of my heart for giving me such a

wonderful family (in-laws). My love for Rabindranath Sinha (Baba) and Samapti Sinha (Mamoni) has no bounds. I thank you both for encouraging me always and supporting me in your own ways whenever and wherever I needed. I would also love to mention here, Atrayee Sinha (Dishali). We both have come a very long way but, today I can say that we have become best of friends. I always consider you as my own sister and have never thought otherwise. Our small fights with each other are what made our bonding so special. I cannot thank you enough for being in my life. Lastly, I would love to thank Arup Sarkar (Dadabhai) and Madhumita Sarkar (Boumoni) for being such an important part of our life and I wish Abhi all the best for his future and hope that you will turn out to be a very good as a person just like your father.

This acknowledgement is never complete without mentioning the constant support and encouragement from my better half Maitrayee Sinha who has supported all my dreams and made me realize my inner strength since the day we first met. The journey with you started just after my PhD journey and I should also mention this PhD journey would not have been this smooth or achievable without your constant backing me up. I cannot mention less about the starting days when I faced low and struggled to establish my research failure due to a number of failed attempts and failed reactions but, you made me realised that that's not it and one day I will definitely taste success in my research life. You were there beside me in every single step of my life when I was facing struggle with my health and also said yes when I proposed you for marrying me during the Covid pandemic of 2020. Even though you tried to teach me German in every way possible but, due to lack of time I could not keep your request but, I promise that as soon as I complete, I will start learning the language just like you want me to. I also promise to fulfil all your dreams throughout my whole life. Though, you are the best thing which happed to me and I may not be the perfect husband you deserved but, I want to let you know that in my way Ich liebe dich auch viel and will always do.

My genuine appreciations and thanks go to each of my teachers, supervisor, colleagues, family and friends who have helped me out with their great abilities. I would like to convey my sincere apologies if I have forgot to mention any person but, I would love to thank and give my regards to each and every one who were there with me throughout my journey so far.

Nilanjan Mukherjee

Nilanjan Mukherjee

January, 2024

[Contents]

Chapter 1

Introduction

Introduction

This thesis documenters the synthesis along with the development of different functional polymer, block copolymer chains (N-heterocyclic polymers, acidic polymers) and polymer brushes (neutral, quaternized, zwitterionic) *grafted* on different solid and porous nanomaterial surface (silica, MOF, MWCNT) with better control over polymer architecture, molecular weight and narrow polydispersity (Đ). The surface chemistry of different nanomaterial was explored upon the *grafting* of polymer and block copolymer chains using surface initiated reversable addition fragmentation chain transfer (SI-RAFT) technique. The thesis also aims to provide deep insight towards the alteration of different physical properties of the polymer *grafted* inorganic organic super hybrid materials when compared with the pristine one. Furthermore, the challenges regarding the processability of the nanomaterials were also addressed and mixed matrix membranes (MMMs) were synthesized from the polybenzimidazole type oxypolybenzimidazole polymer using the polymer *grafted* nanomaterials and utilized them as high temperature proton exchange membranes (HT-PEM). Polymer *grafted* MWCNTs were further utilized to grow Pd nanoparticles without the need for an external reducing agent and examined their catalytic activity in C-C coupling reaction.

Living radical polymerization

'Living or controlled radical polymerization' (CRP) or in different words 'reversible-deactivation radial polymerization' (RDRP) as suggested by IUPAC is considered to be one of the frequently reconnoitring area in polymer chemistry and material science.[1–5] The dynamic equilibria in RDRP achieved in two different traditions such as (i) formation of a dormant species by reversable deactivation of the propagating radicals which then can immediately reactivated by a catalyst (in 'atom transfer radical polymerization' or ATRP) (ii) spontaneously in the existence of an organometallic species or aminoxyl radicals (in 'stable radical mediated polymerization' or SRMP). Degenerative transfer between the dormant species and the propagating radicals occur for 'degenerative transfer radical polymerization' or DTRP which includes 'reversible addition-fragmentation chain transfer' (RAFT) polymerization technique. RAFT polymerization kinetics is comparable to conventional radical polymerization technique where the external source of radicals are essential however, the presence of a chain transfer agent (commonly known as CTA or RAFT agent) is needed to perform RAFT polymerization technique. On the other hand, ATRP requires the presence of Cu-based catalyst and NMP (Nitroxide mediated polymerization) which requires the presence of both nitroxide and a free radical initiator or alkoxyamine which can serve the requirement for both. A huge number of

publications are available to date on CRP technique but a few drawbacks are associated with ATRP, NMP and RAFT techniques. Requirement of transition metal catalyst which can affect the purification process of the synthesized polymer and limits the usability in pharmaceuticals. Although the purification step is not prominent for NMP the limitation in the range of the monomers can be effectively controlled makes it less versatile. However, RAFT polymerization provides a vast scope towards the synthesis of homo polymer, block copolymer and polymeric architectures with excellent control. The process can be useful for a variety of monomer types and the control towards the polymerization process can further be enhanced by designing a more suitable RAFT agent according to the monomer type.

RAFT polymerization

The RAFT polymerization technique, first reported by the 'Commonwealth Scientific and Industrial Research Organization' (CSIRO) in 1998 and in a decade, it became the most suitable and multipurpose method for the synthesis of living polymer materials with predetermined molecular weight and low polydispersity (Đ). A RAFT polymerization process involves the presence of a RAFT agent in very tiny amount (tenth to several mole percentage in order to reduce the termination process[6,7]) in a free radical polymerization process. RAFT polymerization technique is suitable for bulk, solutions (organic or aqueous), emulsions, mini-microemulsions, suspensions and also in ionic liquids, even it can be employed at room temperature or even lower temperatures.[8] A typical RAFT polymerization process involves five steps where the first step corresponds to the initiation step (**a**) where, the radical initiator generates radicals in the reaction mixture and initiates a small amount of the monomers present in the system to create a few growing polymer chains. Then, the initial growing polymer chains with the active radical species reacts with the RAFT agents present in the system to produce intermediate RAFT adduct or the intermediate radical species which further undergo S-R bond cleavage to regenerate raft agent active structure attached with a growing polymer chain ($\mathbf{P_n}$) and produces R• (active radical). This process is well known as RAFT pre-equilibrium step. R• (active radical) then initiates new polymer chains which is called re-initiation step. The initial initiator concentration is intentionally kept low in order to generate most of the polymer chains by re-initiation step. The most important step in the RAFT polymerization step is the RAFT main equilibrium step where the growing polymer chains detach and reattach from the RAFT agent reversibly and this step is considered to be the rate determining step. When the active polymer chain is detached from the RAFT agent is free to undergo further polymerization with the monomer units present in the reaction mixture. Upon recombination with the RAFT agent,

it generates an active intermediate radical species (**3**) with two dormant polymer chains attached on the RAFT agent. Here the attached Z group of the RAFT agent plays a crucial part for the stabilization of the intermediate radical species. The other dormant polymer chain can however detach from **3** to undergo further polymerization. This particular step influences the equal distribution of the radicals amongst the active polymer chains and helps to attain better control over the polydispersity (Đ) of the growing polymer chains and avoids premature termination of the active polymer chains. However, the termination of the active radicals are possible upon combination of two radical species such as $\mathbf{P_n\bullet}$, $\mathbf{P_m\bullet}$, **I•** or **R•**. (Described schematically in **Scheme 1.1.**)

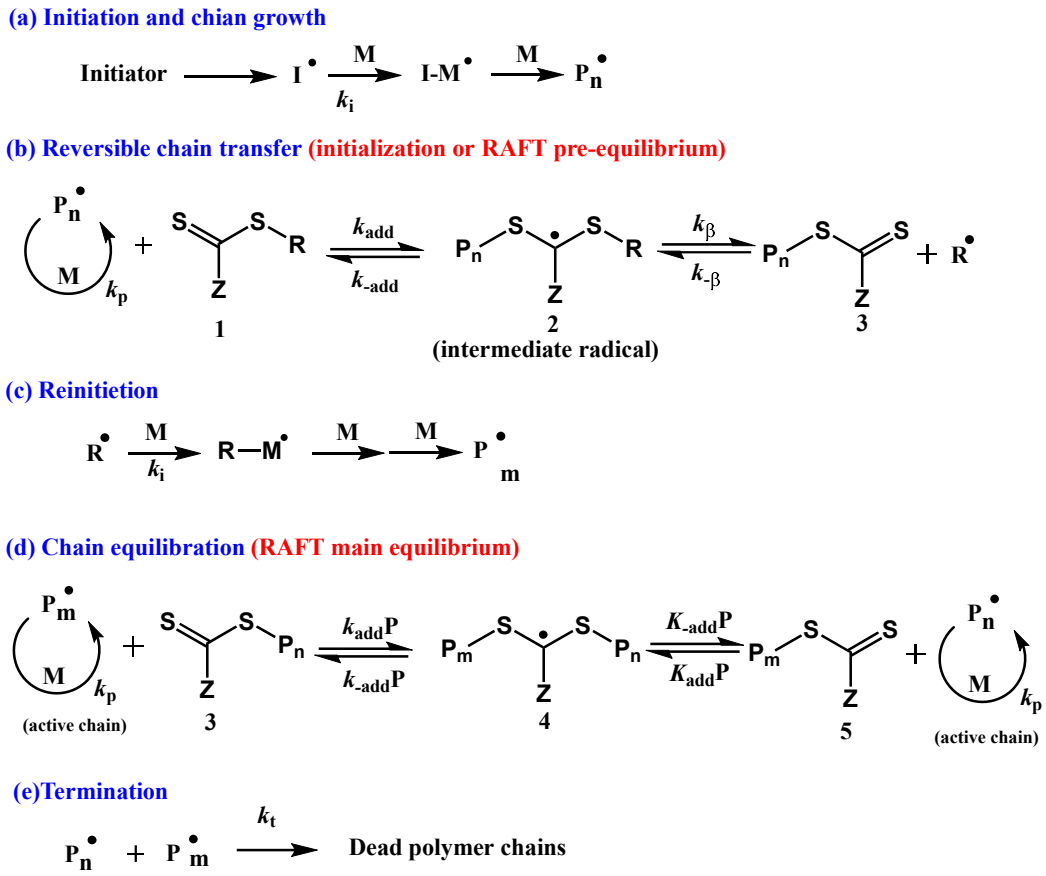

Scheme 1.1. Mechanism of RAFT polymerization showing initiation, propagation, reversible chain transfer, re-initiation, chain equilibration and termination steps.[6,7]

RAFT agents

The alteration of Z as well as R group on the RAFT agent controls the activity thus provides a huge possibility in order to design specific RAFT agents for the polymerization of specific monomer units. Roughly, four types of RAFT agents are of particularly interesting namely dithioesters, trithiocarbonates, xanthates and dithiocarbamates (see **Figure 1.1**).

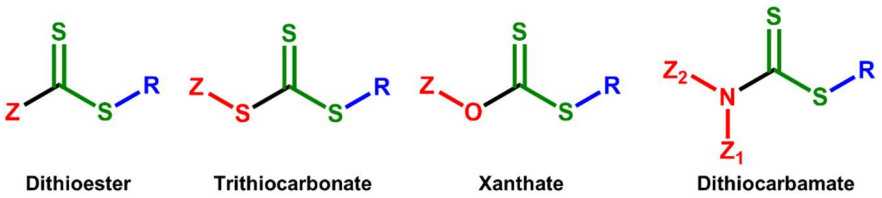

Figure 1.1. Representation of different types of RAFT agents.

The effect of different Z and R groups towards the responsiveness of the RAFT agents have extensively been studied by numerous groups (**Scheme 1.2**). The acuteness of the C=S bond is affected by Z group and the responsiveness decreases as Z= aryl> alkyl> S-alkyl> O-alkyl> N, N-di alkyl. Dithioester and trithiocarbonate type RAFT agents are among the most reported class of CTA or RAFT agents and are highly effective towards the polymerization reaction involving styrene, acrylate and methacrylate type monomers but inhibit vinyl acetate polymerization.[9,10] Chiefari et al. reported the value for chain transfer coefficients of RAFT agents with varrying Z group where the R group differs between benzyl moiety and cyanoisopropyl moiety. The chain-transfer rate declines in the order from dithiobenzoate to trithiocarbonate to xanthate and further to dithiocarbamate type.[11] The presence of two stable canonical forms in the case of O-alkyl xanthate and N, N-dialkyl dithiocarbamate type RAFT agents makes them less reactive (**Scheme 1.4.**). Furthermore, the interaction between the lone pairs of e^- of the oxygen atom and the nitrogen atom, respectively, and the double bond of thiocarbonyl group. Electron-withdrawing moiety present on the Z group strongly upsurges the double bond character of C=S and decreases interaction between the oxygen or nitrogen lone pairs with the C=S bond.

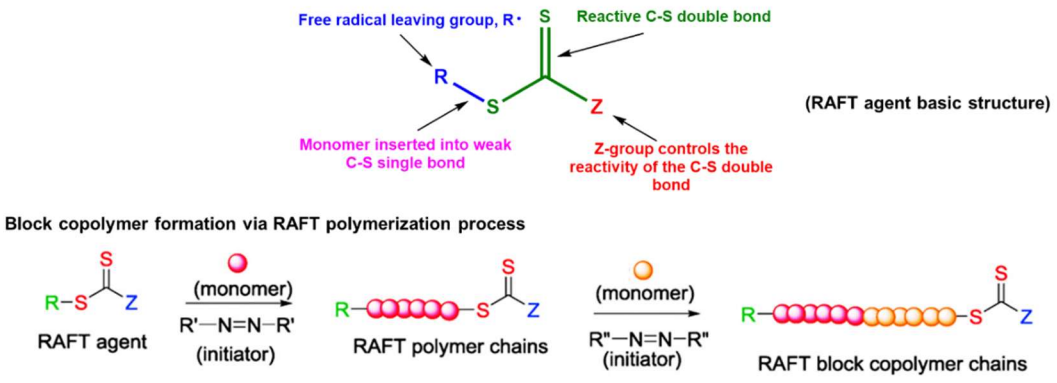

Scheme 1.2. Representation of the basic raft structure for the synthesis of homo polymer and block copolymer structure.

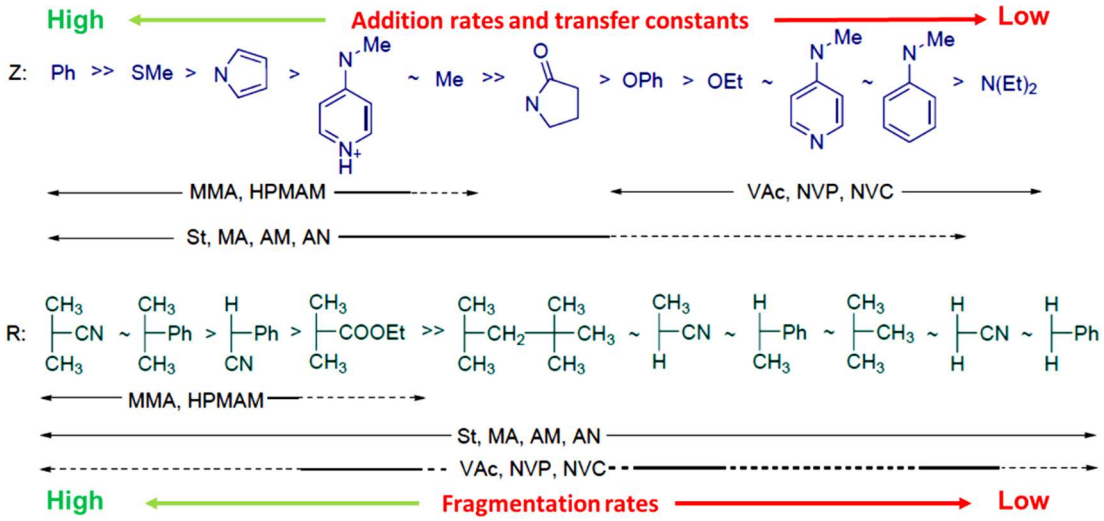

Scheme 1.3. representation for the selecting appropriate Z and R group in order to polymerize the most commonly used monomers. The fragmentation rate reduces from left to right for the R group. The fragmentation rate increases and also the addition rate drops from left to right for the Z group. Dashed line here designates a partial control over the polymerization process (i.e., less control over Đ). Here MMA is for methyl methacrylate, St is for styrene, MA is for methyl acrylate, AM represents acrylamide and VAc represents vinyl acetate.[9]

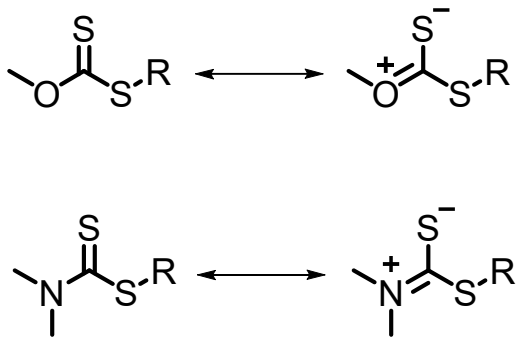

Scheme 1.4. Zwitterionic canonical forms of xanthates and dithiocarbamates.

Being a versatile technique, a wide range of monomer type can be efficiently polymerized using RAFT technique. From the **Scheme 1.3.** we can optimize the R and Z substituent of a RAFT agent in order to polymerize the concerned monomer as the rule of thumb suggests that, the more activated monomers (MAM) require a more activated RAFT agent (with high transfer constant) and less activated monomers (LAM) require less activated RAFT agent (with less transfer constant) in order to satisfy the compatibility between the monomer and the RAFT agent. However, the problem arises during the formation of block copolymer structure formation with a MAM and LAM units.[12] The problem can easily be addressed by using a switchable raft agent (a class of dithiocarbamate RAFT agent) where the

Z group can act as an electron rich or electron deficient unit which helps towards the double bond character of C=S bond can subsequently the transfer constant varies.[13] This provides us better control over the polymerization reaction while synthesizing a block copolymer chain using both the MAM and LAMs.[14,15]

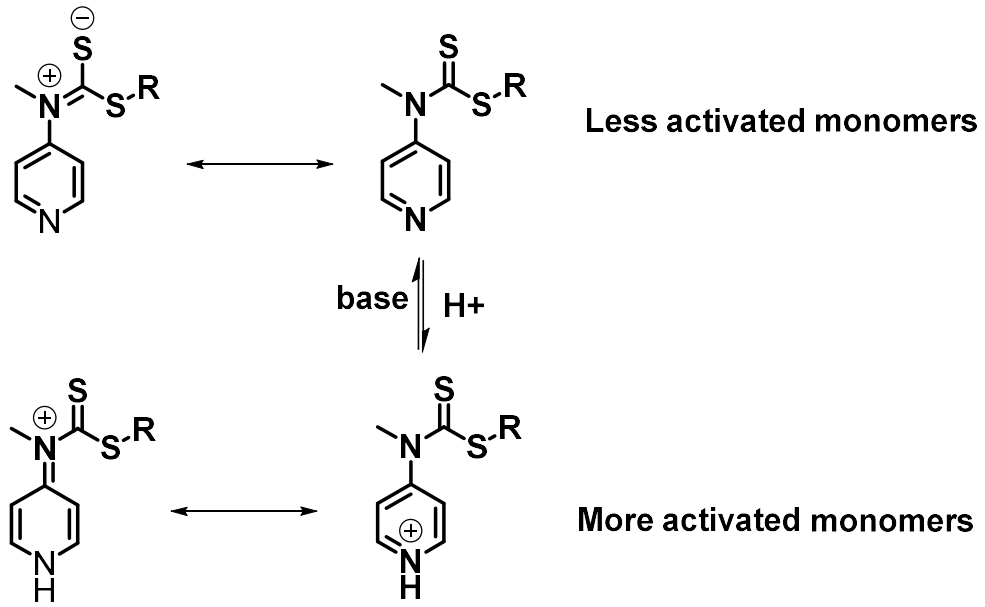

Scheme 1.5. Representative switchable RAFT agent structure under acidic and basic conditions.

Engineering the nano surface

Nanomaterials are identified as a particular class of compounds where the material must have at least one dimension in the range of 1-100nm scale.[16] Nanomaterials can be synthesized and tuned in a number of possible ways in order to obtain particular shape, size, defects etc. which effects the desired properties of the nanomaterial vastly. Nanomaterials exhibit outstanding improvement in the physical and chemical properties when compared with the bulk counterpart and this inherent characteristic nature makes nanomaterials particularly interesting.[17] In terms of chemical composition nanomaterials can be classified broadly into 4 category (i) purely inorganic, (ii) organic based, (iii) carbon based and (iv) composite based or hybrid nanomaterials.[18] Although nanomaterials can also be branded depending on of different shape and sizes (i) spherical (silica nanoparticle, TiO_2, spherical gold nanoparticle, etc.), (ii) sheet like (graphene, clay, MoS_2, etc.) and tube or rod like (carbon nanotube, cellulose nanotube, gold nano rod, palladium nano wire, etc.) which can be porous or nonporous in nature and can affect the properties tremendously.[19–24]

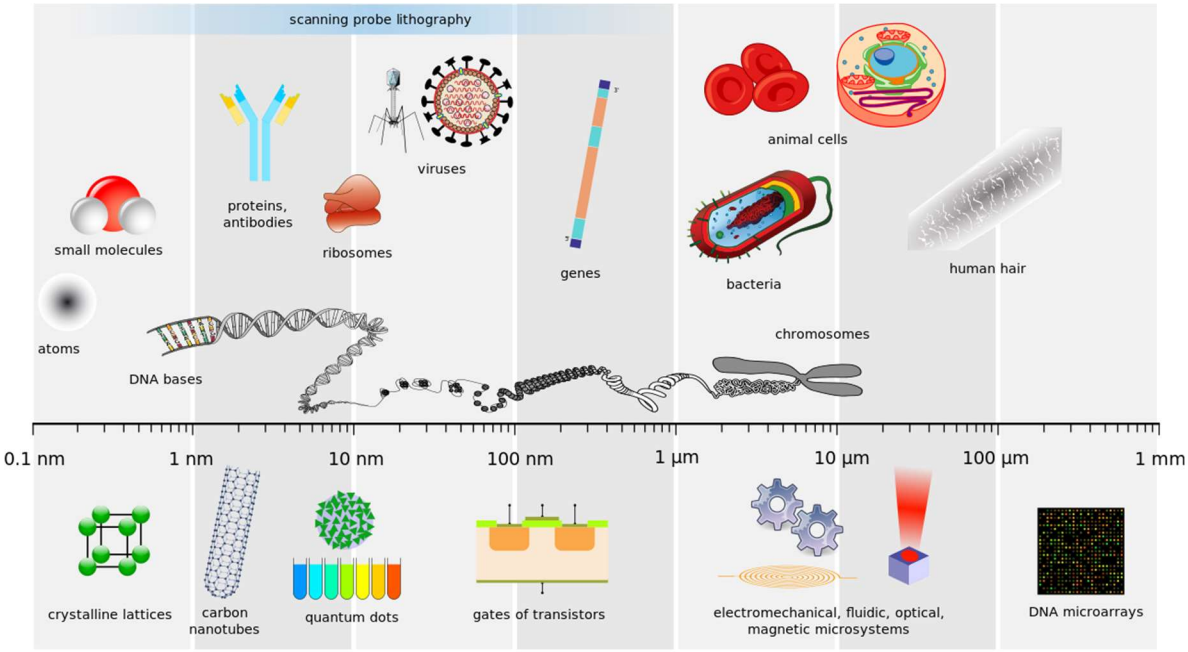

Figure 1.2. Representative image of different nano and macro material and their size range. (image source: Wikipedia)

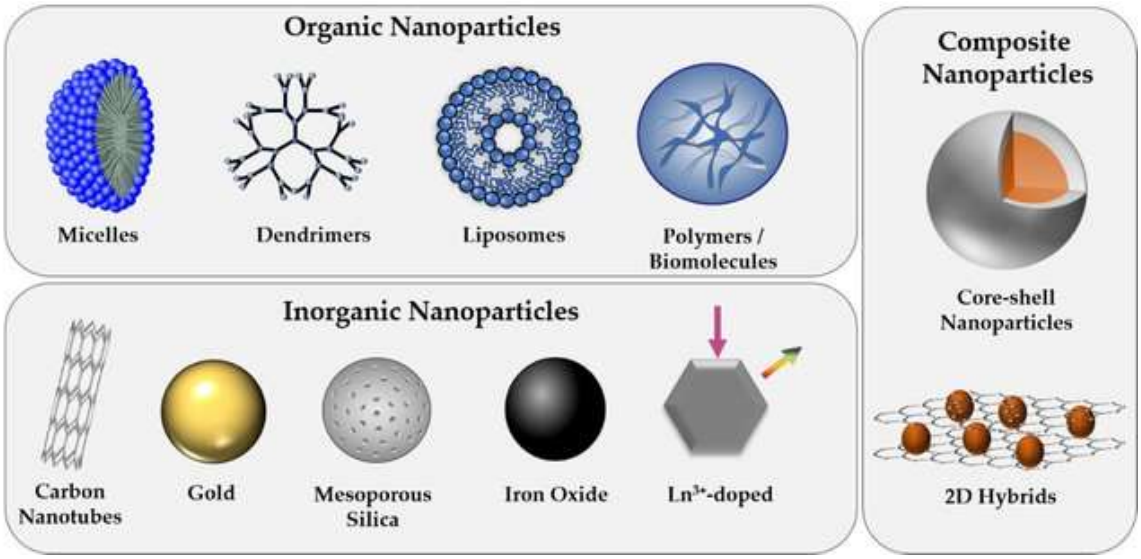

Figure 1.3. Representation of inorganic, organic, metal nanoparticles and hybrid materials.[25]

However, the properties can be enhanced tremendously by combining the nano world with the versatility of the polymer materials. A number of reports are present in the literature providing direct proof towards the improvement of the properties of both the materials when the nano materials were combined with the polymer material upon physical mixing. However, there are a few drawbacks regarding the physical mixing (less uniformity, stability issue due to the absence of covalent linkage etc.). The issue can be addressed upon synthesizing a covalent bond between the nano surface and the polymer chains. A number of approaches are present to

synthesize polymer chains covalently bound on the nano surface otherwise known as *grafting* of polymer chains. Surface *grafting* can be achieved using *grafting to*, *grafting from* or *grafting* through techniques (**Scheme 1.6.**). A previously synthesized polymer chain is attached covalently on the nano surface using the end groups in '*grafting to'* approach but the problem associated with this approach is to achieve high polymer *grafting* density by means of steric hindrance making the covalent bond formation less susceptible for longer polymer chains. In the case of '*grafting through*' approach the nano surface was modified with characteristically vinyl groups in order to utilize the nano surface as macromonomer unit which then further reacts with the growing polymer chains in the system upon initiation to create polymer *grafted* nano surface. However, during '*grafting from'* approach the polymerization process carries out using specific small molecules (RAFT agents, ATRP agents) upon initiation (photo initiated, thermally initiated, enzyme initiated). '*Grafting from'* approach is beneficial to achieve high '*grafting* density', better uniformity and ease of polymerization and purification of the polymer *grafted* nano surface. '*Grafting from'* approach is considered to be supreme in order to achieve tailor made architectures on the nano surface.[26]

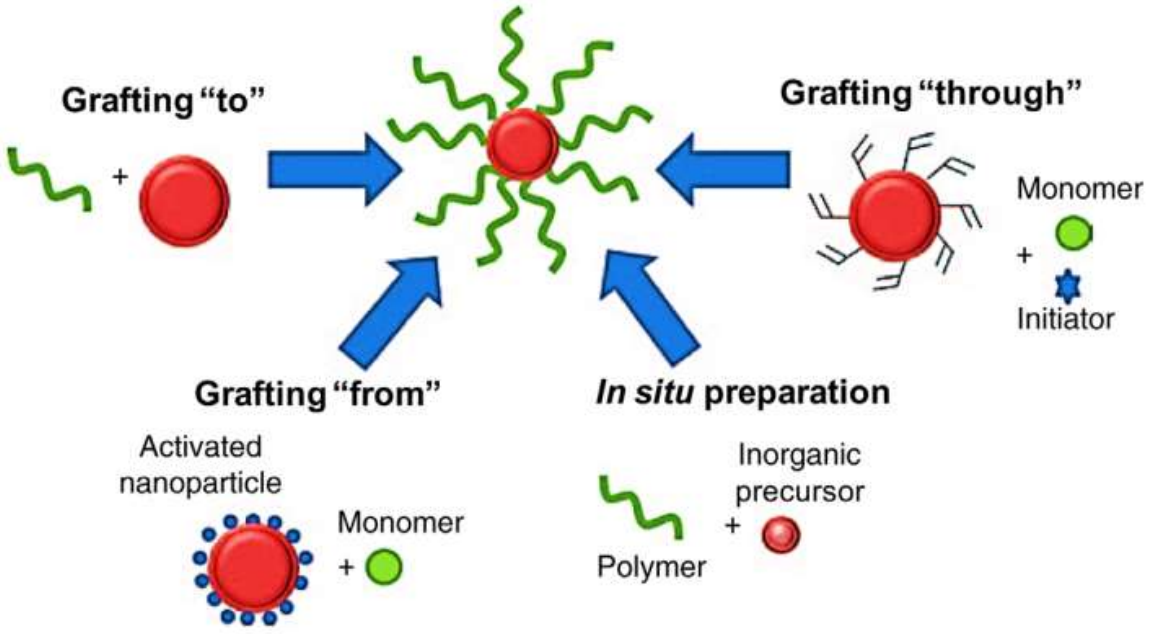

Scheme 1.6. Schematic representation of '*grafting to*', '*grafting from*' and '*grafting through*' approach.[27]

Smart nanomaterials

Smart nanomaterials or intelligent materials are considered to be those particular materials which provides a distinctive response upon stimulation with temperature, pH,

moisture, electric or magnetic fields, reduction, oxidation, stress or chemical environment etc.[28] Smart nanomaterials are considerably expanding market all over the world considering their potential in medicinal and health care sector, pharmaceutical industries, aerospace, defence, electronic industries, automobile and shipping industries, paints and coating industries, protective equipment manufacturing industries and many more. Further application includes self-healing polymers,[29] thermo-responsive materials,[30] invisible inks,[31] photo responsive and switchable surface[32,33] etc. The implementation of such smart materials in different applicative fields are wide spread. Among many different nanomaterials the utilization of silica nanoparticle (SiNP)[34–38], metal organic framework (MOF)[39,39–43], carbon nanotube (CNT)[44,44–48,48–51], graphene (GO)[52–55] and metal nanoparticles are worth mentioning. In this thesis further improvement of nanoparticle properties of SiNP, MOF and multi walled carbon nanotube (MWCNT) are explored upon *grafting from* approach using RAFT polymerization technique in organic as well as aqueous medium.

Surface functionalization of SiNP

Monodispersed silica nanoparticle is one of the fascinating nanomaterials which gained enormous interest among the material scientists since the discovery by Werner Stöber and the team in 1968.[56] The synthesis method is simple and can be modified in order to alter the nanoparticle size. SiNP is well known for its biocompatibility, chemical as well as mechanical stability and compatibility in different polymer media.[57–63]Although, there are issues regarding the dispersibility of SiNP in polymer matrix without polymer *grafting*. Unmodified SiNP do not interact much with the matrix polymer.[64] Thus, the *grafting* of polymer chains with homo polymer and block copolymer chains can provide better interaction with the matrix polymer and results in better homogeneity and better mechanical properties. Hyper branched and miktoarm polymer chain *grafting* further addresses specific processability and stimuli responsiveness and can be utilized in serving medicinal and pharmaceutical purposes (**Figure 1.4.**).[65] Also fluorinated polymer *grafted* silica nanoparticles and silica supported super hydrophobic membranes are reported with a high contact angle to be used as hydrophobic coating material and can be used in surface coating purposes (**Figure 1.5.**).[57,66,67]

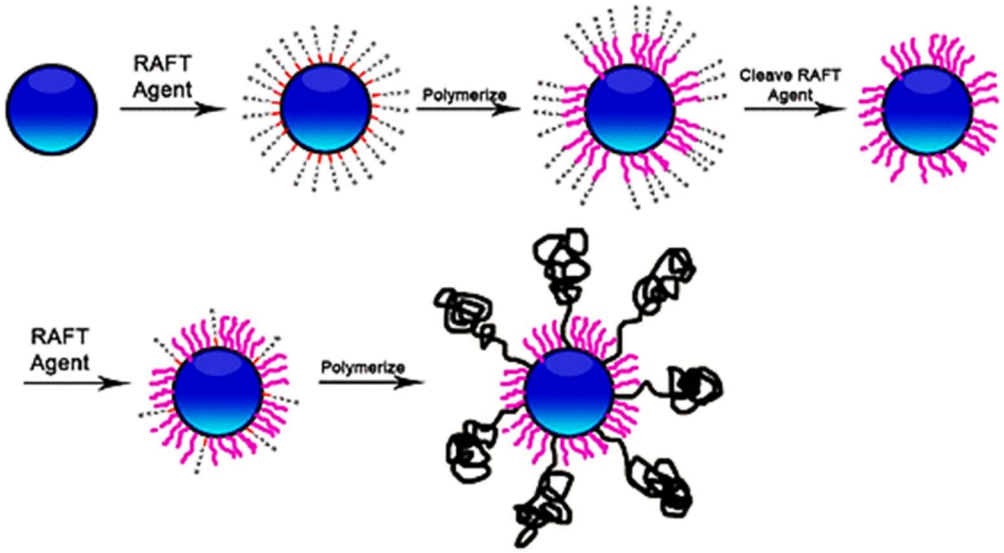

Figure 1.4. Schematic representation of mikto arm polymer chain modified SiNP surface.[65]

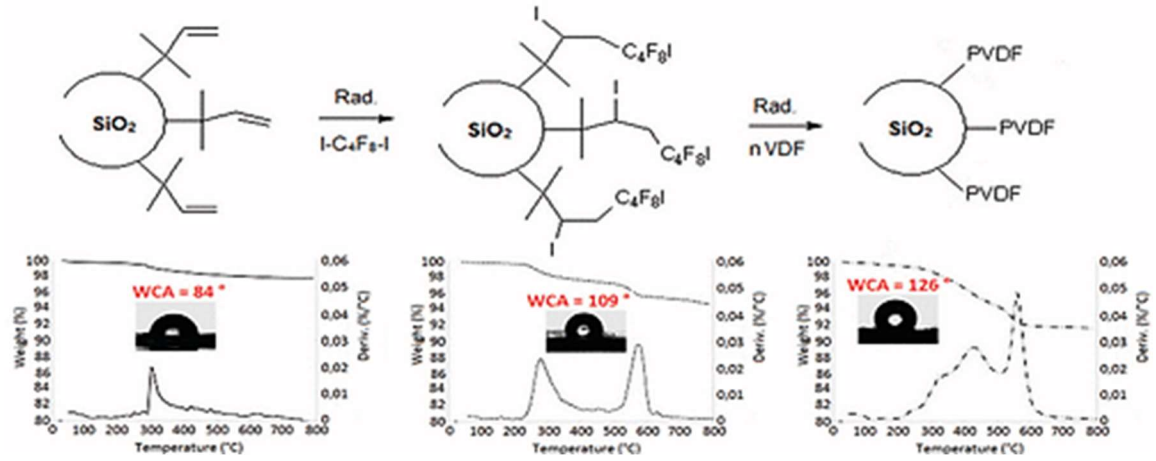

Figure 1.5. Schematic representation of super hydrophobic SiNP surface.[66]

Surface functionalization of MOF

Metal organic framework (MOF) is an unique type of material which consists of metal cluster or ions coordinated by organic ligands in order to form 1D, 2D or 3D structures.[68,69] The inherent and permanent porosity with large internal surface area and well defined crystal structure makes this material particularly interesting.[70,71] Although the possibility of amorphous or MOF glasses were recently published.[72] Specific MOF structures can be designed by tuning the particular metal cluster and organic linker molecules in order to incorporate specific properties in the MOF system and to alter the porosity and crystal structure depending on the application such as UiO type, ZIF type, MOF-74 type, MIL type etc.[68,73] Also, there are substructures of each type of MOFs by functionalizing the active functional groups of the MOF which is well known as post synthetic modification (PSM).[43,74–76] The

tuning ability of the pores, linker molecules, surface area as well as available functional groups make MOF materials an model candidate for the application in gas adsorption, gas separation, chiral molecule separation, guest molecule hosting, drug delivery, sensing, heterogeneous catalysis, dye separation, light emission, data storage, lasing, proton conduction etc (**Figure 1.6.**).[77–85]

However, this thesis focuses on particularly UiO-66 NH_2 type MOF structure and tries to improve different physical and chemical aspects upon polymer *grafting* in order to synthesize MOF-polymer super hybrid material.

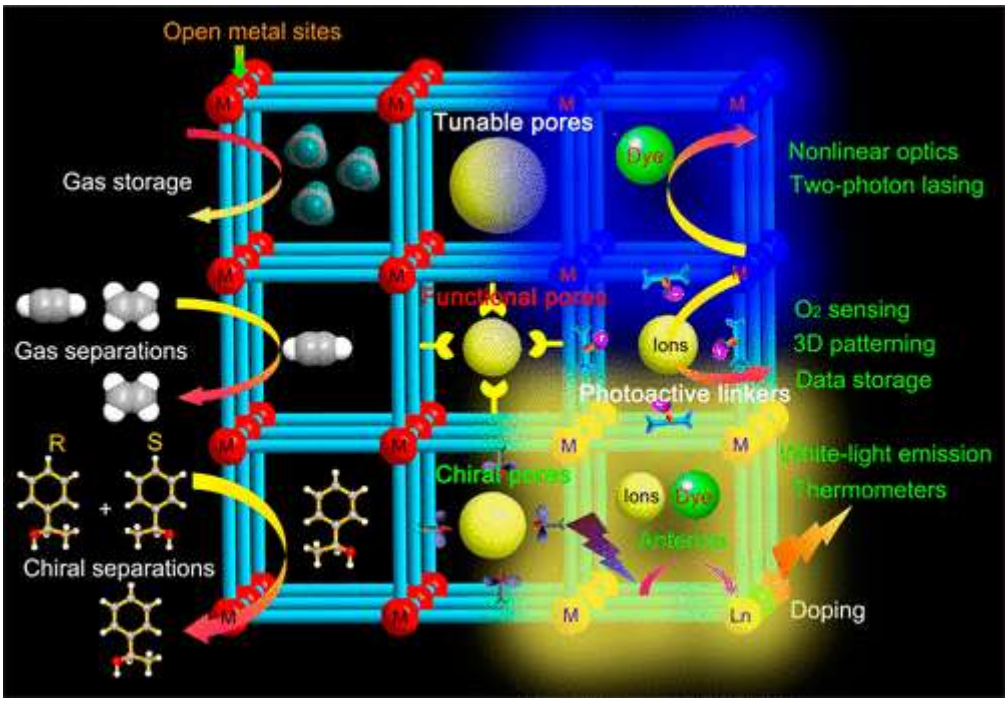

Figure 1.6. Graphic illustration on engineering the pores and functional groups for the development of MOF materials for different applicative fields.[86]

Surface functionalization of CNT

Carbon nanotubes (CNTs) attracted immense curiosity of material chemists due to its specific physical properties and versatile chemical characteristics. Since the discovery by Sumio Iijima in 1991,[46] CNTs have proven their potential in many applicative fields such as catalysis[87,88], gas adsorption[47], water purification[89,90], electrical and thermal conductivity[91–93] and high mechanical stability,[94,95]. This characteristic behaviour of CNT material comes from a number of unique physical and chemical structure such as high aspect ratio, hollow tube structure, concentric nanotube structure which arises in case of MWCNTs, strong Sp^2 hybridisation present in the core structure like graphene.[96,97] Combination of such distinct

properties has already been proven MWCNT as a special material, though several scientists are trying to further improve the properties by chemical treatment, surface modification, uniformly creating defects in the material and so on.[44,45,98–100] Conversely, there is a significant limitation on the usage and processability of CNTs because of the presence of strong van der Waals interaction acting upon the concentric nanotubes CNTs which makes it insoluble in almost all the solvents and are held together tightly to form bundles and rope like aggregation in solution and also in the polymer matrix.[48,49,51,101–103] Hydrophobicity of the core material along with the limitation to design the methodology of precisely *grafting* of polymer chains significantly limits their processability as composite materials. Although, few approaches are reported in literature to chemically modify the CNT surface for biological and other specific applications.[104–111]

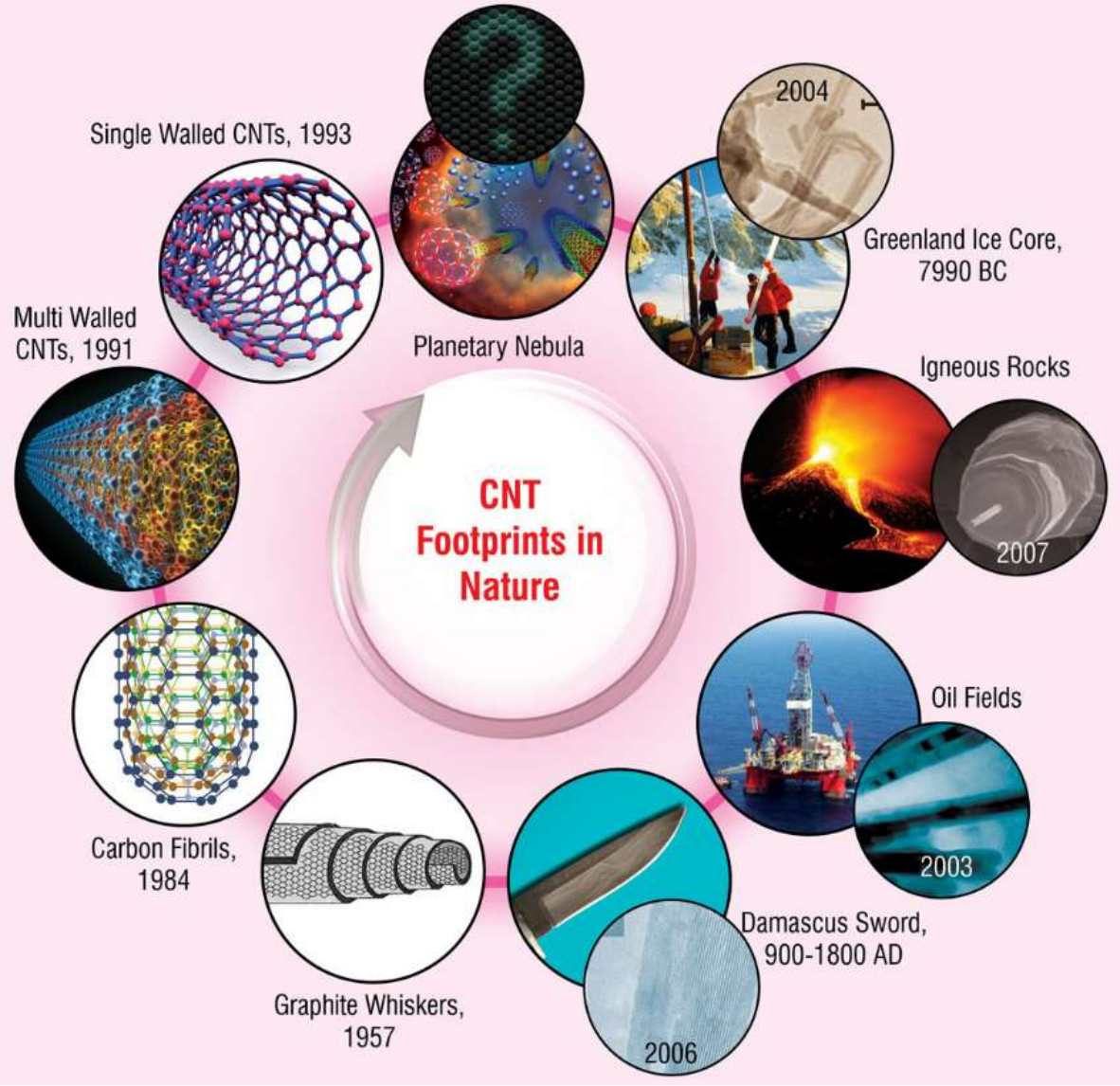

Figure 1.7. Graphical representation of CNT footprints. (image source: nanowerk.com)

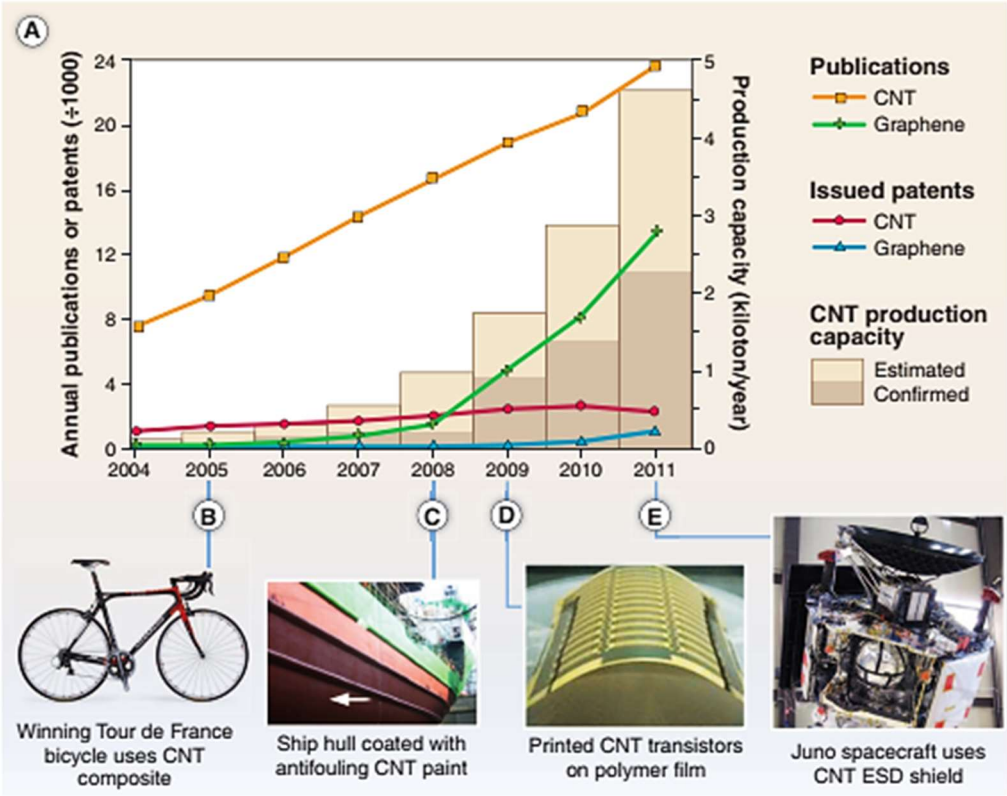

Figure 1.8. Graphical representation of the CNT research and commercialization. (**A**) research articles published worldwide, (**B-E**) selected CNT based equipment and products.[108]

Surface initiated RAFT (SI-RAFT) polymerization on different nano surface

In order to *graft* polymer chains on nano material surface via RAFT polymerization technique, the nano surface needs to be modified with CTAs (RAFT agents) covalently which can be obtained utilizing the available functional groups (by using -NH_2, -COOH groups of UiO-66 NH_2) and in some cases the nano surface needs chemical treatment to modify the surface accordingly (SiNP and MWCNT needs chemical modification to synthesize -NH_2 groups on the surface). However, a RAFT agent can be attached on the nano surface either by R substituent (R-group approach) where the propagating R-group is attached on the nano surface and the Z-group is free detach or by Z substituent (Z-group approach) where the stabilizing Z-group is attached on the surface. Although, there are a few advantages and shortcomings associated with both the approaches (**Figure 1.9.**). The situation becomes complicated in the case of trithiocarbonate type RAFT agents as there is a possibility of C-S bond cleavage at both the ends. However, upon strategical designing the RAFT agent it is possible to force the cleavage of C-S bond at a particular side and hence can be applied the consequences of both the approaches.

The propagating radicals, found at the terminal of *grafted* chains for the R-group method, and the solid support is still a member of the departing R group. In this instance, greater molecular weights of *grafted* polymers with high *grafting* densities can be obtained, albeit probable chain coupling may cause the molecular weight distribution to be more widely distributed.[112] The polymeric radical is constantly propagating in solution before it attaches to the surface bounded functionality in the Z-group approach, which is more akin to "*grafting to*" technique. In contrast, the surface *grafted* backbone stays a component of the Z-group. As a result, these methods entail the production of linear radical chains on functional solid supports and produce relatively monomodal molecular weight distribution with well-defined *grafted* polymer chains. Because of the shielding effect, the *grafting* density is likely to decrease in Z-group approach.[113] However, the advantage of this strategy is that it produces exact living polymer chains, easily separable among the dead materials generated in the medium by filtration and washing, leading to the creation of clean block copolymer synthesis as opposed to alternate CRP techniques.

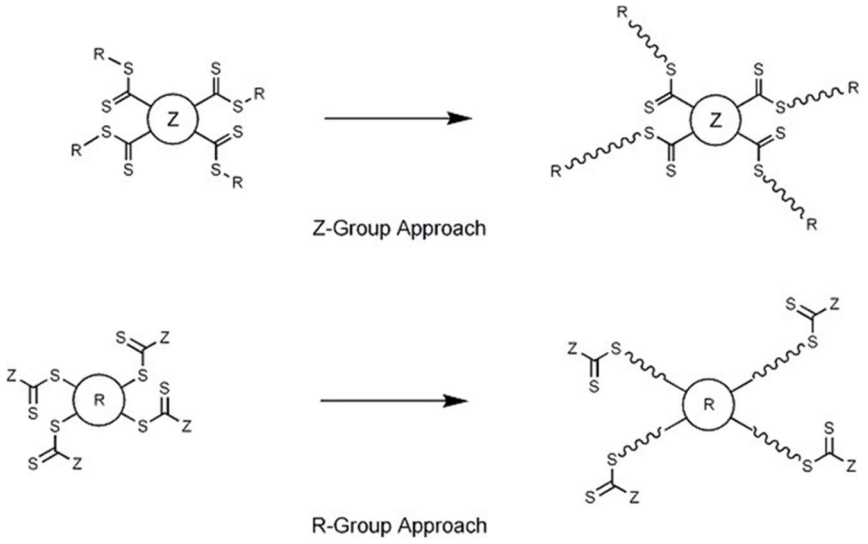

Figure 1.9. R-group and Z-group approach of SI-RAFT polymerization technique.[114]

Fuel cell

Utilizing energy effectively is the most important component in determining how sustainably a contemporary industrialized civilization will grow. Energy is a necessary resource when human power is insufficient to operate in areas like transportation, communication, agriculture, and industry. For a nation to grow, consolidate, advance, and retain its culture, it needs energy. At the moment, all nations rely heavily on the generation of energy from fossil fuels, which are not renewable energy sources.[115,116] It is crucial to transition

to alternative, clean, and sustainable energy sources that do not have long-term detrimental effects on the environment in order to satisfy the energy requirements of the people, which is expanding quickly.[117,118] Additionally, rising energy prices and growing energy use are significant. A quick literature search of the Fuel cells (FCs) history reveals that these devices have been developed around 160 years ago.[119–121] The essential electrochemical mechanism of fuel cells was discovered by Swiss scientists who segregated positive and negative ions on the anode. However, fuel cells can be classified in different types depending on their structure and the method of operation.[122] Different kinds of Fuel cells -

- ✓ Polymer electrolyte membrane fuel cells.
- ✓ Direct methanol fuel cells.
- ✓ Phosphoric acid fuel cells.
- ✓ Alkaline fuel cells.
- ✓ Molten carbonate fuel cells.
- ✓ Reversible fuel cells.
- ✓ Solid oxide fuel cells.

Proton exchange membrane fuel cell (PEMFC)

In the case of PEMFC an intermediate membrane electrolyte acts as an insulator for the passage of electrons while allowing positive ions, frequently protons, to go to the cathode. These electrons participate in an anodic reaction on the opposite side of the membrane after travelling through the cathode side of an electrical circuit, which produces electric current that powers an electrochemical device. At the cathode, an exothermic reaction between the hydrogen ion, electron, and oxygen atom results in formation of water molecules. On the anode, hydrogen is divided into positive ions and electrons. The in-between membrane electrolyte acts as an electron insulator while permitting the transmission of positive ions, frequently protons, to the cathode. These electrons participate in an anode semi reaction on the opposite side of the membrane after passing through the cathode side of an electrical circuit, which produces electric current that powers an electrochemical device. At the cathode, an exothermic reaction between the hydrogen ions, electrons, and O_2 atoms produces water molecules. Continuous fuel supply will result in continuous power output. shows a schematic for an operating flowchart for a polymer electrolyte fuel cell (PEMFC).[123,124] Described in **Figure 1.10.** and **Figure 1.11.**

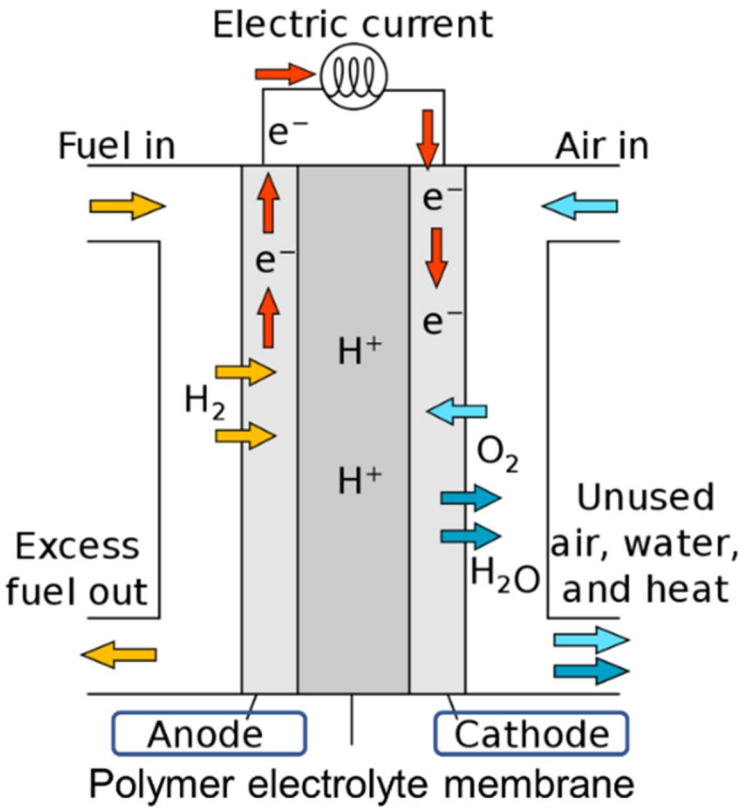

Figure 1.10. Representative diagram of PEMFC operations. (Image source: stanford.edu)

$$\textit{At the anode reaction}: 2H_2 \rightarrow 4H^+ + 4e \qquad (1)$$

$$\textit{At the cathode reaction}: O_2 + 4H^+ + 4e^- \rightarrow 2H_2O \qquad (2)$$

$$\textit{Overall cell reaction}: 2H_2 + O_2 \rightarrow 2H_2O + \text{electrical energy} + \text{heat}$$

Figure 1.11. Representation of anode and cathode reactions of PEMFC.

Polymer electrolyte membrane fuel cell

Because a polymeric membrane is employed as the electrolyte in these cells, they are known as PEMFCs. There are numerous designations in the literature published for this kind of fuel cells, including PMFC (polymeric membrane fuel cell) and PEFC (polymer electrolyte fuel cell). PEMFC's polymer electrolyte membrane (PEM) is a crucial component.[125] It is essential for assessing a PEMFC's efficiency since it transports protons from the anode to the cathode in a selective manner. In an FC, a PEM was originally used as supplementary source of power during the 'Gemini' space missions in the 1960s.[119] Because of its advantages, such as (i) high energy and power densities (ii) zero or very low emissions (iii) noiseless process (iv) wide variety of claims vacillating from everyday devices (v) automobiles (vi) power grids and (vii) ability to produce heat and energy at remote places, PEMFCs are now viewed as a

viable energy source in order to develop clean and effective energy conversion technologies in this century.[126] Also, several automakers have started selling green FC vehicles at competitive pricing in an effort to appeal to the middle-class population as the global fuel cell market is now growing quickly. As a result, tremendous efforts are being made to design and upgrade potential polyelectrolyte materials to be used as a proton conducting polymer membrane in PEMFCs.

H_3PO_4 doped PBI polymer as proton exchange membrane

In general, perfluorinated[127] molecules like 'Nafion' are employed as proton transporting membranes because they have greater thermal and chemical stability under fuel cell operation conditions and may be used safely for extended periods of time as proton exchange membranes. However, perfluorinated polymers exhibited a low glass transition temperature of roughly 120 °C[128], resulting in limited mechanical stability at higher temperatures. Other disadvantages include a decrease in proton conductivity at higher temperatures and, also very expensive. All of these disadvantages made it difficult to obtain a steady and highly effective membrane in fuel cells. In order to address these difficulties with 'Nafion', substantial research is being conducted to replace perfluorinated polymers with different membranes for fuel cells. H_3PO_4 doped PEMs has developed as the effective alternate PEM for HT-PEMFC (high temperature PEM) applications. Prof. Marvel and researchers from the University of Illinois pioneered the synthesis of polybenzimidazole, very stable at high temperatures, has greater chemical steadiness. These polymers have a highly stable linear structure with aromatic heterocyclic backbone (containing nitrogen or oxygen). Polybenzimidazoles were previously employed by the United States Air Force due to their exceptional qualities such as mechanical, thermal, and oxidative steadiness.[129,130]

Polybenzimidazoles[131] are a type of amorphous polymers with high glass transition temperatures ranges between 290 - 350 °C. The majority of polybenzimidazole polymers resemble strong threads with good film forming characteristics. To enhance the characteristics of PEM, Savinell et al originally added acid doped PBI. This study has resulted in a low-cost, high-efficiency fuel cell that is being actively investigated by various scientists in order to attain high performance in PEMFC. Also, H_3PO_4 doped PBI polymers are reported by several authors to have excellent proton conduction, low gas penetrability, oxidative as well as high temperature durability, and a low water drag coefficient.[132] Because of the creation of 3D network of H_3PO_4, the membranes are amphoteric, high temperature stable, and provide low vapour pressure at both temperature range low and high. In general, the literature proposes two

types of proton transport systems associated which are (i) Grotthuss' proton transport mechanism or proton hopping and (ii) Vehicular mechanism or dispersed mechanism.[133–140]

Polybenzimidazole synthesis

Polybenzimidazole synthesis with higher molecular weights and solubility features (in high polar mediums such as DMAC, DMF, DMSO, etc.) remains a concern for scientists. Many research groups produced polybenzimidazoles for various application in the late twentieth century, beginning in 1961. Marvel et al. created a variety of PBI structures with great thermal and chemical resistance.[141] Several techniques for the synthesis of PBIs with various chemical structural backbones have been devised. Polycondensation of tetraamine (TAB) and diacids can be used to produce polybenzimidazoles.[142–145] There are different types of polycondensation reaction techniques reported in literature such as (i) melt condensation polymerization, (ii) solution condensation polymerization and (iii) catalytic condensation polymerization.

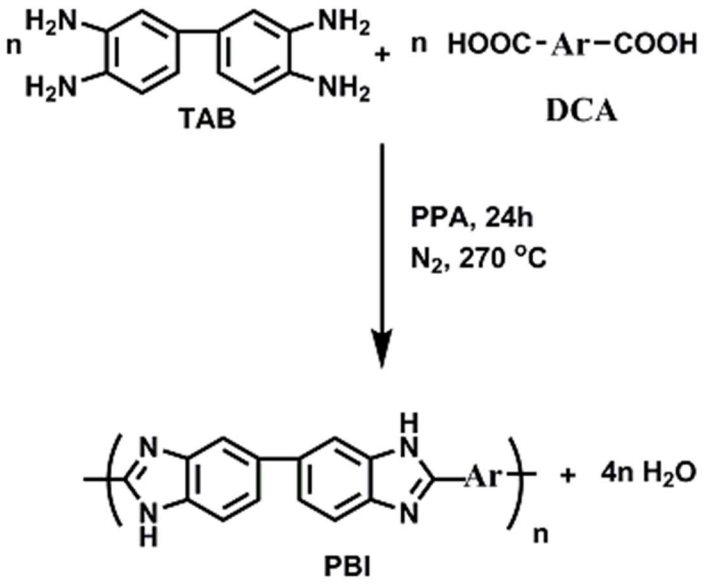

Scheme 1.7. Schematic representation of the synthesis procedure of PBI type polymer.[142]

PBI membrane casting technique

By studying the nature of the PBI polymers and their solubility, various methods for membrane casting were established. To create proton exchange membranes, three basic casting processes were employed. Benicewiz et al. described a sol-gel technique in the manufacturing process of PBI membranes.[146] After polymerization in the polyphosphoric acid (PPA) medium is complete, the viscous solution is immediately casted onto a glass plate. By collecting ambient

moisture, the membranes were able to pass through a sol-gel transition. These membranes demonstrated strong proton conductivities, thermal and mechanical stability.

Mixed matrix membrane preparation

The nanofiller material is dispersed in the appropriate solvent and then combined with pure PBI polymer solution. After agitating the nanofiller-PBI polymer solution for 24-36 hours, it is placed onto the Petri dish to dry the solvent. Since 1970s, the physical blending method has been used to fabricate mixed matrix membranes (MMMs). The procedure of membrane casting is identical to that of pure PBI membrane casting.[147] The homogeneous mixing of the solution is critical for this membrane production procedure. In general, high surface area fillers are the most effective for the synthesis of better MMMs to be used as PEM.[148] Strong and complex interaction patterns between the nanofiller and the membrane matrix plays a significant role in the production of homogeneous MMMs (**Scheme 1.8.**).[149–151] The problem arises if the interaction between the nanofiller material is stronger than the interaction between nanofiller and membrane polymer which results in formation of agglomeration of nanofiller in the composite membrane.[152] However, the problem can be addressed by the *grafting* of appropriate polymer chains on the nano surface of the nanomaterial.[153] The alternative method is to modify the polymer matrix with specific chemical functionality but this may alter/hamper the polymer properties. Upon mixing the nanofiller and the polymer material in solution state helps to create better interaction between the nanofiller and the swollen polymer chains thus creating interconnected network morphology to obtain improved physical properties of the MMM. The interconnected network further helps to create proton conducting nano channels which helps in effective proton hopping (**Figure 1.12.**).[154]

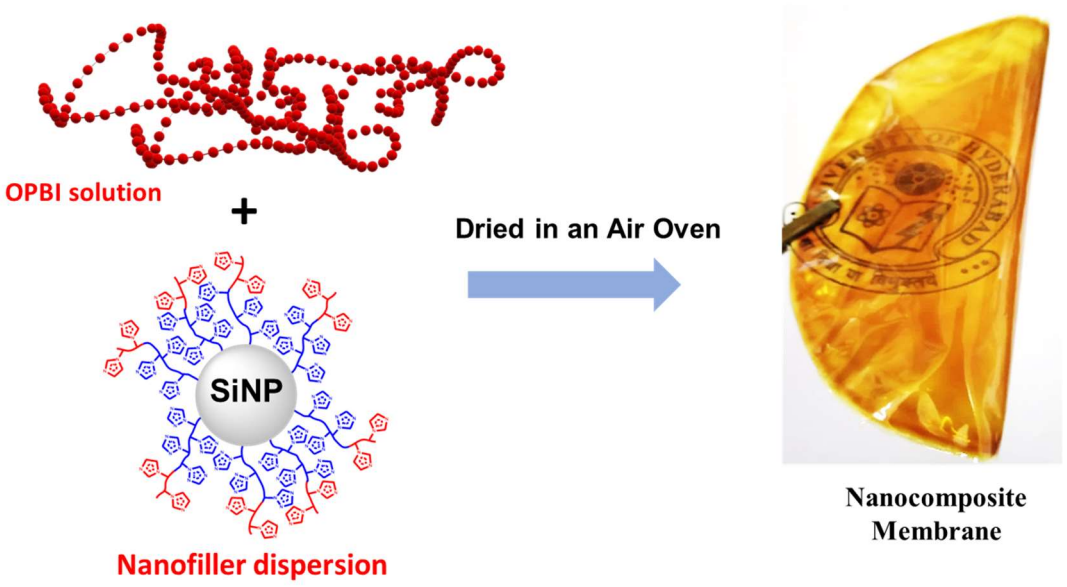

Scheme 1.8. Schematic representation of the solvent casting blending method to prepare nanocomposite membrane.

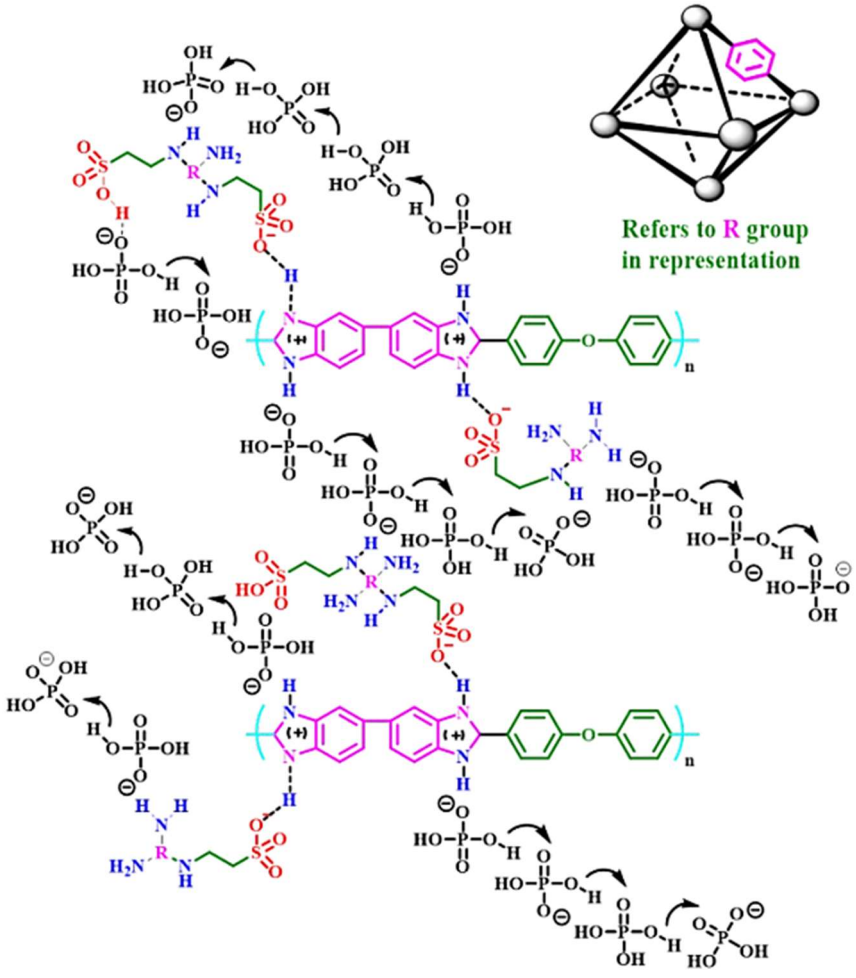

Figure 1.12. Representative diagram of proton transport hopping mechanism in MMM.[154]

Catalyst

Catalyst is a substance which can change the rate of a chemical reaction without being consumed in the process. It does this by providing a different mechanism for the reactants to follow, that has a lower energy barrier to overcome.[155] As a result, catalysts can enhance the efficiency of chemical reactions and make them more cost-effective. They are used in various industrial applications including production of drugs, fertilizers, fuels and plastics. Catalysts can be either homogeneous, in the same phase as the reactants or heterogeneous, in a different phase such as solid or gas.[156] Heterogeneous catalysts (solid) have unique properties which make them ideal for different industrial applications.[157,158] One of their main benefits is their high surface area-to-volume ratio, which allows for more access to the active sites of the catalyst by the reactants, thus increasing reaction rates and improving product selectivity.[159–162] Additionally, these catalysts can be easily removed after the reaction, making them easy to handle and recover. They can also be reused multiple times, making them more environmentally friendly and cost-effective. The ability to control and modify the reaction condition easily makes heterogeneous catalyst ideal for fine-tuning chemical processes and achieving desired products properties. They also contribute significantly to the development of new catalytic materials and understanding of chemical reaction mechanisms. They are used in various type of chemical reactions like hydrogenation, oxidation, dehydrogenation and many more.

Suzuki-Miyaura coupling reaction

The Suzuki-Miyaura coupling is a widely used method to create carbon-carbon bonds between organoboron compounds and aryl or alkyl halides.[163] It's one of the most versatile and efficient techniques for complex organic molecule synthesis. The reaction is often executed under mild conditions, which allows a wide range of substrate compatibility and functional group formation. It uses low temperature and a palladium catalyst that provides high selectivity and yield. Additionally, it is compatible with a variety of halides, such as aryl and alkyl, and has the ability to form biaryls which are present in many natural products and biologically active compounds. This makes it widely used in the synthesis of drugs, agrochemicals, and natural products.[164,165] Additionally, there has been an effort to make this reaction more environmentally friendly by developing more efficient, selective, active and recyclable catalysts. In summary, the Suzuki-Miyaura coupling is a powerful and versatile method for the synthesis of complex organic molecules, especially bioactive compounds, through the formation of carbon-carbon bonds. The Suzuki-Miyaura coupling reaction mechanism

generally comprises the following steps: (i) Initial step is the formation of a complex between the palladium catalyst and the organoboron compound through oxidative addition of the palladium atom to the boron atom. (ii) Nucleophilic attack of the aryl or alkyl halide on the palladium-boron complex forms a palladium-halide bond and the liberation of a boron byproduct. (iii) The next step is the reductive elimination of halide ligand from the palladium atom, resulting in the formation of a carbon-carbon bond between the aryl or alkyl group and the boron compound. (iv) The final step is the reductive elimination or the release of the palladium catalyst. A number of attempts were made in order to design efficient catalyst for Suzuki-Miyaura reaction such as Pd salts coordinated in nitrogen rich polymer matrix, Pd deposition on several nano surface.[166] However, there are scopes for the proper designing of Pd catalyst using nanomaterial and polymer chemistry techniques in order to result high catalytic activity without compromising on substrate scope and reusability of the catalyst.

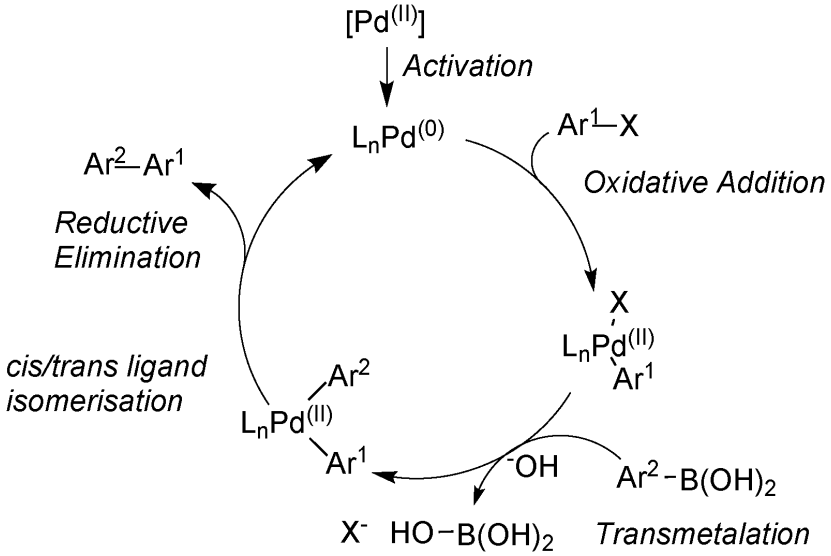

Figure 1.13. Schematic representation of Suzuki-Miyaura coupling reaction mechanism.[167]

Aim and objective of this thesis

In this **Chapter *1*** we have discussed the general idea of CRP along with the detailed understanding of RAFT polymerization. Also, different aspects of nanomaterials and the surface engineering technique of different nano surface to synthesize smart nanomaterials are explained. The idea and the detailed application of procedure of SI-RAFT technique on the nano surface are explained to synthesize polymer *grafted* nano materials which can be useful for a number of applicative fields. The strategy of synthesizing PBI based polymers and the nanomaterial blending and casting techniques and also the benefits of mixed matrix membranes towards the real-life applications have been demonstrated. The need for alternative energy

source and different ways of energy harvesting with zero emission is unavoidable in the present time. In order to, provide a better understanding of the future necessities and supply of energy to meet the requirements fuel cell can be a perfect alternative to the conventional fuel. The details of fuel cell application and different types of fuel cells are explained in details. Furthermore, properly designed nanomaterials and the choice of polymer matrix can result in the production of stable, proton conducting, robust MMMs which can be considered as an ideal candidate to be used in PEMFC. The efficiency can further be enhanced by engineering the nano surface and the *grafting* techniques.

In ***Chapter 2***, the synthesis process of OPBI and the list of materials which were used throughout this thesis work are mentioned. This chapter also includes different spectroscopic, microscopic and other techniques which were used in order to thoroughly characterize the synthesized nanomaterials which provide better understanding of the homo and block copolymer *grafted* nano surface. The techniques were also used in terms of proper characterization of the synthesized MMMs. The stability and the different physical aspects are described in the corresponding chapters. This said chapter as a whole provides the insight of different instrumentation techniques used throughout this thesis work.

Chapter 3 involves the synthesis of highly monodispersed silica nanoparticles (SiNPs) and the synthesis of CPDB RAFT agent. This chapter also deals with the *grafting* of RAFT agent on the SiNP nano surface and the methodology to synthesize block copolymer chains consisting of N-heterocyclic polymer units *grafted* on the SiNP surface with better control over the molecular weight and Đ in one-pot *grafting from* technique. The modified nanoparticles were thoroughly characterized and nanocomposite membranes were prepared. The nanocomposite membranes were characterized and tested for proton conducting abilities upon H_3PO_4 doping.

In ***chapter 4*** the synthesis of UiO-66 NH_2 MOF, synthesis of BSIPA RAFT gent and surface *grafting* of MOF surface with the BSIPA RAFT agent (MOF-BSIPA) are explained. MOF-BSIPA was further utilized to grow three different sets of polymer brushes consisting of neutral, quaternary ammonium and zwitterionic units *grafted* MOF materials with varying molecular weight of the *grafted* polymer brushes. Here, we have used aqueous SI-RAFT *grafting* process to grow the polymer brushes. We have further used detachment techniques to isolate bare polymer brushed which was detached from the MOF surface and analyzed them. The polymer *grafted* MOF (PGM) samples were thoroughly characterized using different

techniques as described in ***Chapter 2*** and were utilized further to prepare MMMs with OPBI polymer. The loading of PGMs were also varied to check the influence of the nanofiller material in the membrane matrix. The MMMs were further characterized and tested for proton conducting abilities and mechanical properties upon H_3PO_4 doping.

In ***Chapter 5*** we have utilized the BSIPA RAFT agent *grafted* MOF (MOF-BSIPA) material to grow polymer chains of vinyl phosphonic acid on the nano MOF surface using SI-RAFT technique in aqueous medium. The *grafted* polymer chains were detached to analyze by using GPC technique and to have a proper understanding of the molecular weight distribution upon the utilization polymerization technique. The thorough characterization demonstrated the presence of moisture holding capacity and nano proton conducting channel formation ability without the need for external acid doping. The material was checked for stability under different harsh conditions and was also utilized to check the proton conducting properties under varying humidity conditions. This study can provide answers towards the inherent properties and inherent proton conducting ability of the PGM sample without the support of the membrane matrix.

Chapter 6 deals with the chemical modification of the MWCNT surface to hinder the e^- flow and thus, can be useful for the proton conductivity applications. The MWCNT surface was attached covalently with the synthesized BEPA RAFT agent (MWCNT-BEPA). MWCNT-BEPA was then utilized to grow the block copolymer chains consisting of N-vinyl imidazole (NVI) and N-vinyl-1,2,4-triazole (NVT) units with varying molecular weights of the *grafted* block copolymer chains on the MWCNT surface. Here, different techniques were utilized in order to detach the block copolymer chain from the stable MWCNT surface and were characterized using different instrumental techniques available. The *grafting* of block copolymer chains consisting of NVI and NVT units creates a gradient of different pKa values around the block copolymer *grafted* MWCNTs (PGNTs) which proposes unique potential as a nanofiller for PEM synthesis. The PGNT samples were utilized to prepare composite membranes with OPBI polymer with varying nanofiller loading and were tested for mechanical and proton conducting properties upon phosphoric acid doping. This approach can provide better understanding of using the surface *grafted* hollow nanotubes towards the development of nanofiller material for efficient proton conducting membranes to be used in PEMFC.

In ***Chapter 7*** the MWCNT-BEPA was utilized to grow the polymer chains consisting of NVI units via SI-RAFT technique and was characterized using the available instrumental

procedures. The polymer *grafted* MWCNT material was further utilized to grow Pd nanoparticles on the polymer modified MWCNT surface without the need for an external reducing agent. The synthesized Pd nanoparticle modified polymer *grafted* MWCNT (Pd@PGNT) sample were characterized thoroughly and were tested for the catalytic activity of the synthesized Pd nanoparticles. The PGNT support can extensively increase the catalytic properties of heterogeneous catalyst with the ability to use the catalyst repeatedly with excellent yields. The stability of the Pd@PGNT sample was checked upon utilizing the catalyst in Suzuki-Miyaura coupling reaction.

References

(1) Matyjaszewski, K.; Davis, T. P. *Handbook of Radical Polymerization*; Matyjaszewski, K., Davis, T. P., Eds.; John Wiley & Sons, Inc.: Hoboken, NJ, USA, 2002.

(2) Goto, A.; Fukuda, T. Kinetics of Living Radical Polymerization. *Prog. Polym. Sci.* **2004**, *29*, 329–385.

(3) Braunecker, W. A.; Matyjaszewski, K. Controlled/Living Radical Polymerization: Features, Developments, and Perspectives. *Prog. Polym. Sci.* **2007**, *32*, 93–146.

(4) Destarac, M. Controlled Radical Polymerization: Industrial Stakes, Obstacles and Achievements. *Macromol. React. Eng.* **2010**, *4*, 165–179.

(5) Moad, G.; Rizzardo, E.; Thang, S. H. Toward Living Radical Polymerization. *Acc. Chem. Res.* **2008**, *41*, 1133–1142.

(6) Hardy, C. G.; Ren, L.; Zhang, J.; Tang, C. Side-Chain Metallocene-Containing Polymers by Living and Controlled Polymerizations. *Isr. J. Chem.* **2012**, *52*, 230–245.

(7) Destarac, M. On the Critical Role of RAFT Agent Design in Reversible Addition-Fragmentation Chain Transfer (RAFT) Polymerization. *Polym. Rev.* **2011**, *51*, 163–187.

(8) Moad, G.; Rizzardo, E.; Thang, S. H. Radical Addition–Fragmentation Chemistry in Polymer Synthesis. *Polymer.* **2008**, *49*, 1079–1131.

(9) Moad, G.; Rizzardo, E.; Thang, S. H. Living Radical Polymerization by the RAFT Process – A Third Update. *Aust. J. Chem.* **2012**, *65*, 985.

(10) Geagea, R.; Ladeira, S.; Mazières, S.; Destarac, M. Chromium and Molybdenum Pentacarbonyl Complexes of Phosphinocarbodithioates: Synthesis, Molecular Structure and Behaviour in RAFT Polymerisation. *Chem. – A Eur. J.* **2011**, *17*, 3718–3725.

(11) Chong, Y. K.; Krstina, J.; Le, T. P. T.; Moad, G.; Postma, A.; Rizzardo, E.; Thang, S. H. Thiocarbonylthio Compounds [SC(Ph)S−R] in Free Radical Polymerization with Reversible Addition-Fragmentation Chain Transfer (RAFT Polymerization). Role of the Free-Radical Leaving Group (R). *Macromolecules* **2003**, *36*, 2256–2272.

(12) Benaglia, M.; Chen, M.; Chong, Y. K.; Moad, G.; Rizzardo, E.; Thang, S. H. Polystyrene- Block -Poly(Vinyl Acetate) through the Use of a Switchable RAFT Agent. *Macromolecules* **2009**, *42*, 9384–9386.

(13) Benaglia, M.; Chiefari, J.; Chong, Y. K.; Moad, G.; Rizzardo, E.; Thang, S. H. Universal (Switchable) RAFT Agents. *J. Am. Chem. Soc.* **2009**, *131*, 6914–6915.

(14) Moad, G.; Keddie, D.; Guerrero-Sanchez, C.; Rizzardo, E.; Thang, S. H. Advances in Switchable RAFT Polymerization. *Macromol. Symp.* **2015**, *350*, 34–42.

(15) Harrisson, S.; Liu, X.; Ollagnier, J.-N.; Coutelier, O.; Marty, J.-D.; Destarac, M. RAFT Polymerization of Vinyl Esters: Synthesis and Applications. *Polymers (Basel).* **2014**, *6*, 1437–1488.

(16) Baig, N.; Kammakakam, I.; Falath, W. Nanomaterials: A Review of Synthesis Methods, Properties, Recent Progress, and Challenges. *Mater. Adv.* **2021**, *2*, 1821–1871.

(17) Roduner, E. Size Matters: Why Nanomaterials Are Different. *Chem. Soc. Rev.* **2006**, *35*, 583.

(18) Majhi, K. C.; Yadav, M. Synthesis of Inorganic Nanomaterials Using Carbohydrates. In *Green Sustainable Process for Chemical and Environmental Engineering and Science*; Elsevier, 2021; pp 109–135.

(19) Meen, T.-H.; Tsai, J.-K.; Chao, S.-M.; Lin, Y.-C.; Wu, T.-C.; Chang, T.-Y.; Ji, L.-W.; Water, W.; Chen, W.-R.; Tang, I.-T.; Huang, C.-J. Surface Plasma Resonant Effect of Gold Nanoparticles on the Photoelectrodes of Dye-Sensitized Solar Cells. *Nanoscale Res. Lett.* **2013**, *8*, 450.

(20) He, H.; Pham-Huy, L. A.; Dramou, P.; Xiao, D.; Zuo, P.; Pham-Huy, C. Carbon Nanotubes: Applications in Pharmacy and Medicine. *Biomed Res. Int.* **2013**, *2013*, 1–12.

(21) Jimenez-Ruiz, A.; Perez-Tejeda, P.; Grueso, E.; Castillo, P. M.; Prado-Gotor, R. Nonfunctionalized Gold Nanoparticles: Synthetic Routes and Synthesis Condition Dependence. *Chem. - A Eur. J.* **2015**, *21*, 9596–9609.

(22) Shah, M. Gold Nanoparticles: Various Methods of Synthesis and Antibacterial Applications. *Front. Biosci.* **2014**, *19*, 1320.

(23) Zhao, Y.; Wang, Y.; Ran, F.; Cui, Y.; Liu, C.; Zhao, Q.; Gao, Y.; Wang, D.; Wang, S. A Comparison between Sphere and Rod Nanoparticles Regarding Their in Vivo Biological Behavior and Pharmacokinetics. *Sci. Rep.* **2017**, *7*, 4131.

(24) Kokila, G. N.; Mallikarjunaswamy, C.; Ranganatha, V. L. A Review on Synthesis and Applications of Versatile Nanomaterials. *Inorg. Nano-Metal Chem.* **2022**, 1–30.

(25) Gessner, I.; Neundorf, I. Nanoparticles Modified with Cell-Penetrating Peptides: Conjugation Mechanisms, Physicochemical Properties, and Application in Cancer Diagnosis and Therapy. *Int. J. Mol. Sci.* **2020**, *21*, 2536.

(26) Barbey, R.; Lavanant, L.; Paripovic, D.; Schüwer, N.; Sugnaux, C.; Tugulu, S.; Klok, H.-A. Polymer Brushes via Surface-Initiated Controlled Radical Polymerization: Synthesis, Characterization, Properties, and Applications. *Chem. Rev.* **2009**, *109*, 5437–5527.

(27) Hussain, C. M.; Mishra, A. K. *Nanotechnology in Environmental Science*; Hussain, C. M., Mishra, A. K., Eds.; Wiley, 2018.

(28) Yoshida, M.; Lahann, J. Smart Nanomaterials. *ACS Nano* **2008**, *2*, 1101–1107.

(29) White, S. R.; Sottos, N. R.; Geubelle, P. H.; Moore, J. S.; Kessler, M. R.; Sriram, S. R.; Brown, E. N.; Viswanathan, S. Autonomic Healing of Polymer Composites. *Nature* **2001**, *409*, 794–797.

(30) Yang, J.; Yamato, M.; Kohno, C.; Nishimoto, A.; Sekine, H.; Fukai, F.; Okano, T. Cell Sheet Engineering: Recreating Tissues without Biodegradable Scaffolds. *Biomaterials* **2005**, *26*, 6415–6422.

(31) Schurig, D.; Mock, J. J.; Justice, B. J.; Cummer, S. A.; Pendry, J. B.; Starr, A. F.; Smith, D. R. Metamaterial Electromagnetic Cloak at Microwave Frequencies. *Science (80-.).* **2006**, *314*, 977–980.

(32) Lendlein, A.; Jiang, H.; Jünger, O.; Langer, R. Light-Induced Shape-Memory Polymers. *Nature* **2005**, *434*, 879–882.

(33) Lahann, J.; Langer, R. Smart Materials with Dynamically Controllable Surfaces. *MRS Bull.* **2005**, *30*, 185–188.

(34) Kutcherlapati, S. R.; Koyilapu, R.; Jana, T. Poly(N -Vinyl Imidazole) *Grafted* Silica Nanofillers: Synthesis by RAFT Polymerization and Nanocomposites with Polybenzimidazole. *J. Polym. Sci. Part A Polym. Chem.* **2018**, *56*, 365–375.

(35) Ghosh, S.; Maity, S.; Jana, T. Polybenzimidazole/Silica Nanocomposites: Organic-Inorganic Hybrid Membranes for PEM Fuel Cell. *J. Mater. Chem.* **2011**, *21*, 14897.

(36) Stöber, W.; Fink, A.; Bohn, E. Controlled Growth of Monodisperse Silica Spheres in the Micron Size Range. *J. Colloid Interface Sci.* **1968**, *26*, 62–69.

(37) Tian, X.; Wang, S.; Li, J.; Liu, F.; Wang, X.; Chen, H.; Ni, H.; Wang, Z. Composite Membranes Based on Polybenzimidazole and Ionic Liquid Functional Si–O–Si Network for HT-PEMFC Applications. *Int. J. Hydrogen Energy* **2017**, *42*, 21913–21921.

(38) Nohara, T.; Koseki, K.; Tabata, K.; Shimada, R.; Suzuki, Y.; Umemoto, K.; Takeda, M.; Sato, R.; Rodbuntum, S.; Arita, T.; Masuhara, A. Core-Size Dependent Proton Conductivity of Silica Filler Functionalized Polymer Electrolyte Membrane. *ACS Sustain. Chem. Eng.* **2020**, *8*, 14674-14678.

(39) Winarta, J.; Shan, B.; Mcintyre, S. M.; Ye, L.; Wang, C.; Liu, J.; Mu, B. A Decade of UiO-66 Research: A Historic Review of Dynamic Structure, Synthesis Mechanisms, and Characterization Techniques of an Archetypal Metal–Organic Framework. *Cryst.*

Growth Des. **2020**, *20*, 1347–1362.

(40) Saleem, H.; Rafique, U.; Davies, R. P. Investigations on Post-Synthetically Modified UiO-66-NH 2 for the Adsorptive Removal of Heavy Metal Ions from Aqueous Solution. *Microporous Mesoporous Mater.* **2016**, *221*, 238–244.

(41) Kalaj, M.; Cohen, S. M. Postsynthetic Modification: An Enabling Technology for the Advancement of Metal–Organic Frameworks. *ACS Cent. Sci.* **2020**, *6*, 1046–1057.

(42) Shanahan, J.; Kissel, D. S.; Sullivan, E. PANI@UiO-66 and PANI@UiO-66-NH 2 Polymer-MOF Hybrid Composites as Tunable Semiconducting Materials. *ACS Omega* **2020**, *5*, 6395–6404.

(43) Cohen, S. M. Postsynthetic Methods for the Functionalization of Metal–Organic Frameworks. *Chem. Rev.* **2012**, *112*, 970–1000.

(44) Khabashesku, V. N.; Billups, W. E.; Margrave, J. L. Fluorination of Single-Wall Carbon Nanotubes and Subsequent Derivatization Reactions. *Acc. Chem. Res.* **2002**, *35*, 1087–1095.

(45) Requardt, H.; Braun, A.; Steinberg, P.; Hampel, S.; Hansen, T. Surface Defects Reduce Carbon Nanotube Toxicity in Vitro. *Toxicol. Vitr.* **2019**, *60*, 12–18.

(46) Iijima, S. Helical Microtubules of Graphitic Carbon. *Nature* **1991**, *354*, 56–58.

(47) Yang, Y.; Narayanan Nair, A. K.; Sun, S. Adsorption and Diffusion of Carbon Dioxide, Methane, and Their Mixture in Carbon Nanotubes in the Presence of Water. *J. Phys. Chem. C* **2020**, *124*, 16478–16487.

(48) He, G.; Zhao, J.; Hu, S.; Li, L.; Li, Z.; Li, Y.; Li, Z.; Wu, H.; Yang, X.; Jiang, Z. Functionalized Carbon Nanotube via Distillation Precipitation Polymerization and Its Application in Nafion-Based Composite Membranes. *ACS Appl. Mater. Interfaces* **2014**, *6*, 15291–15301.

(49) Gorityala, B. K.; Ma, J.; Wang, X.; Chen, P.; Liu, X.-W. Carbohydrate Functionalized Carbon Nanotubes and Their Applications. *Chem. Soc. Rev.* **2010**, *39*, 2925.

(50) Hazra, B.; Wood, D. A.; Mani, D.; Singh, P. K.; Singh, A. K. Organic and Inorganic Porosity, and Controls of Hydrocarbon Storage in Shales; 2019; pp 107–138.

(51) Karousis, N.; Tagmatarchis, N.; Tasis, D. Current Progress on the Chemical Modification of Carbon Nanotubes. *Chem. Rev.* **2010**, *110*, 5366–5397.

(52) Yaragalla, S.; Bhavitha, K. B.; Athanassiou, A. A Review on Graphene Based Materials and Their Antimicrobial Properties. *Coatings* **2021**, *11*, 1197.

(53) Kumar, S.; Chatterjee, K. Comprehensive Review on the Use of Graphene-Based Substrates for Regenerative Medicine and Biomedical Devices. *ACS Appl. Mater. Interfaces* **2016**, *8*, 26431–26457.

(54) Menaa, F.; Abdelghani, A.; Menaa, B. Graphene Nanomaterials as Biocompatible and

Conductive Scaffolds for Stem Cells: Impact for Tissue Engineering and Regenerative Medicine. *J. Tissue Eng. Regen. Med.* **2015**, *9*, 1321–1338.

(55) Dasari Shareena, T. P.; McShan, D.; Dasmahapatra, A. K.; Tchounwou, P. B. A Review on Graphene-Based Nanomaterials in Biomedical Applications and Risks in Environment and Health. *Nano-Micro Lett.* **2018**, *10*, 53.

(56) Stöber, W.; Fink, A.; Bohn, E. Controlled Growth of Monodisperse Silica Spheres in the Micron Size Range. *J. Colloid Interface Sci.* **1968**, *26*, 62–69.

(57) Liao, Y.; Loh, C.-H.; Wang, R.; Fane, A. G. Electrospun Superhydrophobic Membranes with Unique Structures for Membrane Distillation. *ACS Appl. Mater. Interfaces* **2014**, *6*, 16035–16048.

(58) Graf, C.; Gao, Q.; Schütz, I.; Noufele, C. N.; Ruan, W.; Posselt, U.; Korotianskiy, E.; Nordmeyer, D.; Rancan, F.; Hadam, S.; Vogt, A.; Lademann, J.; Haucke, V.; Rühl, E. Surface Functionalization of Silica Nanoparticles Supports Colloidal Stability in Physiological Media and Facilitates Internalization in Cells. *Langmuir* **2012**, *28*, 7598–7613.

(59) Stark, W. J. Nanoparticles in Biological Systems. *Angew. Chemie Int. Ed.* **2011**, *50*, 1242–1258.

(60) Di Paola, M.; Quarta, A.; Conversano, F.; Sbenaglia, E. A.; Bettini, S.; Valli, L.; Gigli, G.; Casciaro, S. Human Hepatocarcinoma Cell Targeting by Glypican-3 Ligand Peptide Functionalized Silica Nanoparticles: Implications for Ultrasound Molecular Imaging. *Langmuir* **2017**, *33*, 4490–4499.

(61) Wang, X.; Masse, S.; Laurent, G.; Hélary, C.; Coradin, T. Impact of Polyethylenimine Conjugation Mode on the Cell Transfection Efficiency of Silica Nanovectors. *Langmuir* **2015**, *31*, 11078–11085.

(62) Wu, J.; Silvent, J.; Coradin, T.; Aimé, C. Biochemical Investigation of the Formation of Three-Dimensional Networks from DNA-*Grafted* Large Silica Particles. *Langmuir* **2012**, *28*, 2156–2165.

(63) Knowles, B. R.; Yang, D.; Wagner, P.; Maclaughlin, S.; Higgins, M. J.; Molino, P. J. Zwitterion Functionalized Silica Nanoparticle Coatings: The Effect of Particle Size on Protein, Bacteria, and Fungal Spore Adhesion. *Langmuir* **2019**, *35*, 1335–1345.

(64) Lizundia, E.; Meaurio, E.; Vilas, J. L. *Grafting* of Cellulose Nanocrystals. In *Multifunctional Polymeric Nanocomposites Based on Cellulosic Reinforcements*; Elsevier, 2016; pp 61–113.

(65) Rungta, A.; Natarajan, B.; Neely, T.; Dukes, D.; Schadler, L. S.; Benicewicz, B. C. *Grafting* Bimodal Polymer Brushes on Nanoparticles Using Controlled Radical Polymerization. *Macromolecules* **2012**, *45*, 9303–9311.

(66) Durand, N.; Boutevin, B.; Silly, G.; Améduri, B. "*Grafting from*" Polymerization of Vinylidene Fluoride (VDF) from Silica to Achieve Original Silica–PVDF Core–Shells.

Macromolecules **2011**, *44*, 8487–8493.

(67) Park, J.-W.; Seo, Y.-A.; Kim, I.; Ha, C.-S.; Aimi, K.; Ando, S. Investigating the Crystalline Structure of Poly(Vinylidene Fluoride) (PVDF) in PVDF/Silica Binary and PVDF/Poly(Methyl Methacrylate)/Silica Ternary Hybrid Composites Using FTIR and Solid-State 19 F MAS NMR Spectroscopy. *Macromolecules* **2004**, *37*, 429–436.

(68) Karimi, M.; Mehrabadi, Z.; Farsadrooh, M.; Bafkary, R.; Derikvandi, H.; Hayati, P.; Mohammadi, K. Metal–Organic Framework; 2021; pp 279–387.

(69) Yaghi, O. M.; Kalmutzki, M. J.; Diercks, C. S. *Introduction to Reticular Chemistry*; Wiley, 2019.

(70) Wang, S.; McGuirk, C. M.; D'Aquino, A.; Mason, J. A.; Mirkin, C. A. Metal–Organic Framework Nanoparticles. *Adv. Mater.* **2018**, *30*, 1800202.

(71) Öhrström, L.; Amombo Noa, F. M. *Metal-Organic Frameworks*; ACS In Focus; American Chemical Society: Washington, DC, USA, 2021.

(72) Fonseca, J.; Gong, T.; Jiao, L.; Jiang, H.-L. Metal–Organic Frameworks (MOFs) beyond Crystallinity: Amorphous MOFs, MOF Liquids and MOF Glasses. *J. Mater. Chem. A* **2021**, *9*, 10562–10611.

(73) García, H.; Navalón, S. *Metal-Organic Frameworks: Applications in Separations and Catalysis*; Wiley, 2008.

(74) Qian, Q.; Chi, W. S.; Han, G.; Smith, Z. P. Impact of Post-Synthetic Modification Routes on Filler Structure and Performance in Metal–Organic Framework-Based Mixed-Matrix Membranes. *Ind. Eng. Chem. Res.* **2020**, *59*, 5432–5438.

(75) Su, X.; Bromberg, L.; Martis, V.; Simeon, F.; Huq, A.; Hatton, T. A. Postsynthetic Functionalization of Mg-MOF-74 with Tetraethylenepentamine: Structural Characterization and Enhanced CO 2 Adsorption. *ACS Appl. Mater. Interfaces* **2017**, *9*, 11299–11306.

(76) Zhang, B.; Bai, X.; Wang, S.; Li, L.; Li, X.; Fan, F.; Wang, T.; Zhang, L.; Zhang, X.; Li, Y.; Liu, Y.; Chen, J.; Meng, F.; Fu, Y. Preparation of Superhydrophobic Metal–Organic Framework/Polymer Composites as Stable and Efficient Catalysts. *ACS Appl. Mater. Interfaces* **2021**, *13*, 32175–32183.

(77) Wang, C.; Liu, D.; Lin, W. Metal–Organic Frameworks as A Tunable Platform for Designing Functional Molecular Materials. *J. Am. Chem. Soc.* **2013**, *135*, 13222–13234.

(78) Czaja, A. U.; Trukhan, N.; Müller, U. Industrial Applications of Metal–Organic Frameworks. *Chem. Soc. Rev.* **2009**, *38*, 1284.

(79) Sun, C.-Y.; Wang, X.-L.; Zhang, X.; Qin, C.; Li, P.; Su, Z.-M.; Zhu, D.-X.; Shan, G.-G.; Shao, K.-Z.; Wu, H.; Li, J. Efficient and Tunable White-Light Emission of Metal–Organic Frameworks by Iridium-Complex Encapsulation. *Nat. Commun.* **2013**, *4*, 2717.

(80) Sierra-Serrano, B.; García-García, A.; Hidalgo, T.; Ruiz-Camino, D.; Rodríguez-

Diéguez, A.; Amariei, G.; Rosal, R.; Horcajada, P.; Rojas, S. Copper Glufosinate-Based Metal–Organic Framework as a Novel Multifunctional Agrochemical. *ACS Appl. Mater. Interfaces* **2022**, *14*, 34955–34962.

(81) Escobar-Hernandez, H. U.; Pérez, L. M.; Hu, P.; Soto, F. A.; Papadaki, M. I.; Zhou, H.-C.; Wang, Q. Thermal Stability of Metal–Organic Frameworks (MOFs): Concept, Determination, and Model Prediction Using Computational Chemistry and Machine Learning. *Ind. Eng. Chem. Res.* **2022**, *61*, 5853–5862.

(82) Park, J.; Yuan, D.; Pham, K. T.; Li, J.-R.; Yakovenko, A.; Zhou, H.-C. Reversible Alteration of CO 2 Adsorption upon Photochemical or Thermal Treatment in a Metal–Organic Framework. *J. Am. Chem. Soc.* **2012**, *134*, 99–102.

(83) Chen, C.-X.; Wei, Z.-W.; Jiang, J.-J.; Zheng, S.-P.; Wang, H.-P.; Qiu, Q.-F.; Cao, C.-C.; Fenske, D.; Su, C.-Y. Dynamic Spacer Installation for Multirole Metal–Organic Frameworks: A New Direction toward Multifunctional MOFs Achieving Ultrahigh Methane Storage Working Capacity. *J. Am. Chem. Soc.* **2017**, *139*, 6034–6037.

(84) Usman, M.; Ali, M.; Al-Maythalony, B. A.; Ghanem, A. S.; Saadi, O. W.; Ali, M.; Jafar Mazumder, M. A.; Abdel-Azeim, S.; Habib, M. A.; Yamani, Z. H.; Ensinger, W. Highly Efficient Permeation and Separation of Gases with Metal–Organic Frameworks Confined in Polymeric Nanochannels. *ACS Appl. Mater. Interfaces* **2020**, *12*, 49992–50001.

(85) Wales, J.; Hughes, D.; Marshall, E.; Chambers, P. A Review on the Application of Metal–Organic Frameworks (MOFs) in Pressure Swing Adsorption (PSA) Nitrogen Gas Generation. *Ind. Eng. Chem. Res.* **2022**, *61*, 9529–9543.

(86) Cui, Y.; Li, B.; He, H.; Zhou, W.; Chen, B.; Qian, G. Metal–Organic Frameworks as Platforms for Functional Materials. *Acc. Chem. Res.* **2016**, *49*, 483–493.

(87) Kang, S.; Jeong, Y. K.; Mhin, S.; Ryu, J. H.; Ali, G.; Lee, K.; Akbar, M.; Chung, K. Y.; Han, H.; Kim, K. M. Pulsed Laser Confinement of Single Atomic Catalysts on Carbon Nanotube Matrix for Enhanced Oxygen Evolution Reaction. *ACS Nano* **2021**, *15*, 4416–4428.

(88) Yan, Y.; Miao, J.; Yang, Z.; Xiao, F.-X.; Yang, H. Bin; Liu, B.; Yang, Y. Carbon Nanotube Catalysts: Recent Advances in Synthesis, Characterization and Applications. *Chem. Soc. Rev.* **2015**, *44*, 3295–3346.

(89) Lee, B.; Baek, Y.; Lee, M.; Jeong, D. H.; Lee, H. H.; Yoon, J.; Kim, Y. H. A Carbon Nanotube Wall Membrane for Water Treatment. *Nat. Commun.* **2015**, *6*, 7109.

(90) Ihsanullah. Carbon Nanotube Membranes for Water Purification: Developments, Challenges, and Prospects for the Future. *Sep. Purif. Technol.* **2019**, *209*, 307–337.

(91) Wang, Q.; Dai, J.; Li, W.; Wei, Z.; Jiang, J. The Effects of CNT Alignment on Electrical Conductivity and Mechanical Properties of SWNT/Epoxy Nanocomposites. *Compos. Sci. Technol.* **2008**, *68*, 1644–1648.

(92) Mora, A.; Verma, P.; Kumar, S. Electrical Conductivity of CNT/Polymer Composites: 3D Printing, Measurements and Modeling. *Compos. Part B Eng.* **2020**, *183*, 107600.

(93) Wang, Y.; Yang, C.; Xin, Z.; Luo, Y.; Wang, B.; Feng, X.; Mao, Z.; Sui, X. Poly(Lactic Acid)/Carbon Nanotube Composites with Enhanced Electrical Conductivity via a Two-Step Dispersion Strategy. *Compos. Commun.* **2022**, 101087.

(94) Zhan, H.; Chen, Y. W.; Shi, Q. Q.; Zhang, Y.; Mo, R. W.; Wang, J. N. Highly Aligned and Densified Carbon Nanotube Films with Superior Thermal Conductivity and Mechanical Strength. *Carbon N. Y.* **2022**, *186*, 205–214.

(95) Li, Y.; Li, M.; Pang, M.; Feng, S.; Zhang, J.; Zhang, C. Effects of Multi-Walled Carbon Nanotube Structures on the Electrical and Mechanical Properties of Silicone Rubber Filled with Multi-Walled Carbon Nanotubes. *J. Mater. Chem. C* **2015**, *3*, 5573–5579.

(96) Ruoff, R. S.; Lorents, D. C. Mechanical and Thermal Properties of Carbon Nanotubes. *Carbon N. Y.* **1995**, *33*, 925–930.

(97) Mu, M.; Composto, R. J.; Clarke, N.; Winey, K. I. Minimum in Diffusion Coefficient with Increasing MWCNT Concentration Requires Tracer Molecules To Be Larger than Nanotubes. *Macromolecules* **2009**, *42*, 8365–8369.

(98) Tromm Steffen, T.; César Fontana, L.; Hammer, P.; Becker, D. Amine Functionalization of Carbon Nanotubes with Solid Urea Using Different Plasma Treatments. *Appl. Surf. Sci.* **2022**, *583*, 152493.

(99) Maciejewska, B. M.; Jasiurkowska-Delaporte, M.; Vasylenko, A. I.; Kozioł, K. K.; Jurga, S. Experimental and Theoretical Studies on the Mechanism for Chemical Oxidation of Multiwalled Carbon Nanotubes. *RSC Adv.* **2014**, *4*, 28826–28831.

(100) Choi, E. Y.; Roh, S. C.; Kim, C. K. Noncovalent Functionalization of Multi-Walled Carbon Nanotubes with Pyrene-Linked Nylon66 for High Performance Nylon66/Multi-Walled Carbon Nanotube Composites. *Carbon N. Y.* **2014**, *72*, 160–168.

(101) Sakellariou, G.; Priftis, D.; Baskaran, D. Surface-Initiated Polymerization from Carbon Nanotubes: Strategies and Perspectives. *Chem. Soc. Rev.* **2013**, *42*, 677–704.

(102) Pramanik, C.; Gissinger, J. R.; Kumar, S.; Heinz, H. Carbon Nanotube Dispersion in Solvents and Polymer Solutions: Mechanisms, Assembly, and Preferences. *ACS Nano* **2017**, *11*, 12805–12816.

(103) Rao, R.; Pint, C. L.; Islam, A. E.; Weatherup, R. S.; Hofmann, S.; Meshot, E. R.; Wu, F.; Zhou, C.; Dee, N.; Amama, P. B.; Carpena-Nuñez, J.; Shi, W.; Plata, D. L.; Penev, E. S.; Yakobson, B. I.; Balbuena, P. B.; Bichara, C.; Futaba, D. N.; Noda, S.; Shin, H.; Kim, K. S.; Simard, B.; Mirri, F.; Pasquali, M.; Fornasiero, F.; Kauppinen, E. I.; Arnold, M.; Cola, B. A.; Nikolaev, P.; Arepalli, S.; Cheng, H.-M.; Zakharov, D. N.; Stach, E. A.; Zhang, J.; Wei, F.; Terrones, M.; Geohegan, D. B.; Maruyama, B.; Maruyama, S.; Li, Y.; Adams, W. W.; Hart, A. J. Carbon Nanotubes and Related Nanomaterials: Critical Advances and Challenges for Synthesis toward Mainstream Commercial

Applications. *ACS Nano* **2018**, *12*, 11756–11784.

(104) Datsyuk, V.; Kalyva, M.; Papagelis, K.; Parthenios, J.; Tasis, D.; Siokou, A.; Kallitsis, I.; Galiotis, C. Chemical Oxidation of Multiwalled Carbon Nanotubes. *Carbon N. Y.* **2008**, *46*, 833–840.

(105) Zhao, C.; Wang, X.; Chen, X.; Liu, Y.; Xie, Y.; Xu, H. Covalent Interactions between Carbon Nanotubes and P3HT by Thiol–Ene Click Chemistry towards Improved Thermoelectric Performance. *Mater. Chem. Front.* **2020**, *4*, 1174–1181.

(106) Ebbesen, T. W.; Lezec, H. J.; Hiura, H.; Bennett, J. W.; Ghaemi, H. F.; Thio, T. Electrical Conductivity of Individual Carbon Nanotubes. *Nature* **1996**, *382*, 54–56.

(107) Wu, Z.; Chen, Z.; Du, X.; Logan, J. M.; Sippel, J.; Nikolou, M.; Kamaras, K.; Reynolds, J. R.; Tanner, D. B.; Hebard, A. F.; Rinzler, A. G. Transparent, Conductive Carbon Nanotube Films. *Science.* **2004**, *305*, 1273–1276.

(108) De Volder, M. F. L.; Tawfick, S. H.; Baughman, R. H.; Hart, A. J. Carbon Nanotubes: Present and Future Commercial Applications. *Science.* **2013**, *339*, 535–539.

(109) Rastogi, S. K.; Kalmykov, A.; Johnson, N.; Cohen-Karni, T. Bioelectronics with Nanocarbons. *J. Mater. Chem. B* **2018**, *6*, 7159–7178.

(110) Wu, Y.; Zhao, X.; Shang, Y.; Chang, S.; Dai, L.; Cao, A. Application-Driven Carbon Nanotube Functional Materials. *ACS Nano* **2021**, *15*, 7946–7974.

(111) Schnorr, J. M.; Swager, T. M. Emerging Applications of Carbon Nanotubes. *Chem. Mater.* **2011**, *23*, 646–657.

(112) Li, C.; Han, J.; Ryu, C. Y.; Benicewicz, B. C. A Versatile Method To Prepare RAFT Agent Anchored Substrates and the Preparation of PMMA *Grafted* Nanoparticles. *Macromolecules* **2006**, *39*, 3175–3183.

(113) Hao, X.; Nilsson, C.; Jesberger, M.; Stenzel, M. H.; Malmström, E.; Davis, T. P.; Östmark, E.; Barner-Kowollik, C. Dendrimers as Scaffolds for Multifunctional Reversible Addition-Fragmentation Chain Transfer Agents: Syntheses and Polymerization. *J. Polym. Sci. Part A Polym. Chem.* **2004**, *42*, 5877–5890.

(114) Stenzel, M. H.; Davis, T. P. Star Polymer Synthesis Using Trithiocarbonate Functional ?-Cyclodextrin Cores (Reversible Addition-Fragmentation Chain-Transfer Polymerization). *J. Polym. Sci. Part A Polym. Chem.* **2002**, *40*, 4498–4512.

(115) Staffell, I.; Scamman, D.; Velazquez Abad, A.; Balcombe, P.; Dodds, P. E.; Ekins, P.; Shah, N.; Ward, K. R. The Role of Hydrogen and Fuel Cells in the Global Energy System. *Energy Environ. Sci.* **2019**, *12*, 463–491.

(116) Zhu, Y.; Romain, C.; Williams, C. K. Sustainable Polymers from Renewable Resources. *Nature* **2016**, *540*, 354–362.

(117) van Ruijven, B. J.; De Cian, E.; Sue Wing, I. Amplification of Future Energy Demand Growth Due to Climate Change. *Nat. Commun.* **2019**, *10*, 2762.

(118) Sorrell, S. Reducing Energy Demand: A Review of Issues, Challenges and Approaches. *Renew. Sustain. Energy Rev.* **2015**, *47*, 74–82.

(119) Litster, S.; McLean, G. PEM Fuel Cell Electrodes. *J. Power Sources* **2004**, *130*, 61–76.

(120) Lovering, D. G. Fuel Cell Systems. *J. Power Sources* **1994**, *52*, 155–156.

(121) Srinivasan, S.; Davé, B. B.; Murugesamoorthi, K. A.; Parthasarathy, A.; Appleby, A. J. Overview of Fuel Cell Technology. In *Fuel Cell Systems*; Springer US: Boston, MA, 1993; pp 37–72.

(122) Fang, J.; Qiao, J.; Wilkinson, D. P.; Zhang, J. *Electrochemical Polymer Electrolyte Membranes*; Fang, J., Qiao, J., Wilkinson, D. P., Zhang, J., Eds.; CRC Press, 2015.

(123) Parekh, A. Recent Developments of Proton Exchange Membranes for PEMFC: A Review. *Front. Energy Res.* **2022**, *10*, 956132.

(124) Wang, Y.; Pang, Y.; Xu, H.; Martinez, A.; Chen, K. S. PEM Fuel Cell and Electrolysis Cell Technologies and Hydrogen Infrastructure Development – a Review. *Energy Environ. Sci.* **2022**, *15*, 2288–2328.

(125) Zhang, H.; Shen, P. K. Advances in the High Performance Polymer Electrolyte Membranes for Fuel Cells. *Chem. Soc. Rev.* **2012**, *41*, 2382.

(126) Qin, C.; Wang, J.; Yang, D.; Li, B.; Zhang, C. Proton Exchange Membrane Fuel Cell Reversal: A Review. *Catalysts* **2016**, *6*, 197.

(127) Osborn, S. J.; Hassan, M. K.; Divoux, G. M.; Rhoades, D. W.; Mauritz, K. A.; Moore, R. B. Glass Transition Temperature of Perfluorosulfonic Acid Ionomers. *Macromolecules* **2007**, *40*, 3886–3890.

(128) Satterfield, M. B.; Majsztrik, P. W.; Ota, H.; Benziger, J. B.; Bocarsly, A. B. Mechanical Properties of Nafion and Titania/Nafion Composite Membranes for Polymer Electrolyte Membrane Fuel Cells. *J. Polym. Sci. Part B Polym. Phys.* **2006**, *44*, 2327–2345.

(129) Chen, D.; Yan, C.; Li, X.; Liu, L.; Wu, D.; Li, X. A Highly Stable PBI Solvent Resistant Nanofiltration Membrane Prepared via Versatile and Simple Crosslinking Process. *Sep. Purif. Technol.* **2019**, *224*, 15–22.

(130) Zhao, T. S. *Micro Fuel Cells*; Elsevier, 2009.

(131) Vogel, H.; Marvel, C. S. Polybenzimidazoles, New Thermally Stable Polymers. *J. Polym. Sci.* **1961**, *50*, 511–539.

(132) Mamlouk, M.; Scott, K. The Effect of Electrode Parameters on Performance of a Phosphoric Acid-Doped PBI Membrane Fuel Cell. *Int. J. Hydrogen Energy* **2010**, *35*, 784–793.

(133) Tuckerman, M. E.; Marx, D.; Parrinello, M. The Nature and Transport Mechanism of Hydrated Hydroxide Ions in Aqueous Solution. *Nature* **2002**, *417*, 925–929.

(134) Thisuwan, J.; Promma, P.; Sagarik, K. The Grotthuss Mechanism for Bifunctional

Proton Transfer in Poly(Benzimidazole). *R. Soc. Open Sci.* **2021**, *8*, 211168.

(135) Zuo, Z.; Fu, Y.; Manthiram, A. Novel Blend Membranes Based on Acid-Base Interactions for Fuel Cells. *Polymers (Basel).* **2012**, *4*, 1627–1644.

(136) Ogawa, T.; Kamiguchi, K.; Tamaki, T.; Imai, H.; Yamaguchi, T. Differentiating Grotthuss Proton Conduction Mechanisms by Nuclear Magnetic Resonance Spectroscopic Analysis of Frozen Samples. *Anal. Chem.* **2014**, *86*, 9362–9366.

(137) Ludueña, G. A.; Kühne, T. D.; Sebastiani, D. Mixed Grotthuss and Vehicle Transport Mechanism in Proton Conducting Polymers from Ab Initio Molecular Dynamics Simulations. *Chem. Mater.* **2011**, *23*, 1424–1429.

(138) Lim, D. W.; Sadakiyo, M.; Kitagawa, H. Proton Transfer in Hydrogen-Bonded Degenerate Systems of Water and Ammonia in Metal–Organic Frameworks. *Chem. Sci.* **2019**, *10*, 16–33.

(139) Suarez, S. N.; Jayakody, J. R. P.; Greenbaum, S. G.; Zawodzinski, T.; Fontanella, J. J. A Fundamental Study of the Transport Properties of Aqueous Superacid Solutions. *J. Phys. Chem. B* **2010**, *114*, 8941–8947.

(140) Asensio, J. A.; Sánchez, E. M.; Gómez-Romero, P. Proton-Conducting Membranes Based on Benzimidazole Polymers for High-Temperature PEM Fuel Cells. A Chemical Quest. *Chem. Soc. Rev.* **2010**, *39*, 3210.

(141) Plummer, L.; Marvel, C. S. Polybenzimidazoles. III. *J. Polym. Sci. Part A Gen. Pap.* **1964**, *2*, 2559–2569.

(142) Maity, S.; Jana, T. Polybenzimidazole Block Copolymers for Fuel Cell: Synthesis and Studies of Block Length Effects on Nanophase Separation, Mechanical Properties, and Proton Conductivity of PEM. *ACS Appl. Mater. Interfaces* **2014**, *6*, 6851–6864.

(143) Maity, S.; Jana, T. Soluble Polybenzimidazoles for PEM: Synthesized from Efficient, Inexpensive, Readily Accessible Alternative Tetraamine Monomer. *Macromolecules* **2013**, *46*, 6814–6823.

(144) Sana, B.; Jana, T. Polymer Electrolyte Membrane from Polybenzimidazoles: Influence of Tetraamine Monomer Structure. *Polymer.* **2018**, *137*, 312–323.

(145) Sana, B.; Das, A.; Jana, T. Polybenzimidazole as Alkaline Anion Exchange Membrane with Twin Hydroxide Ion Conducting Sites. *Polymer.* **2019**, *172*, 213–220.

(146) Xiao, L.; Zhang, H.; Scanlon, E.; Ramanathan, L. S.; Choe, E. W.; Rogers, D.; Apple, T.; Benicewicz, B. C. High-Temperature Polybenzimidazole Fuel Cell Membranes via a Sol-Gel Process. *Chem. Mater.* **2005**, *17*, 5328–5333.

(147) Yu, S.; Benicewicz, B. C. Synthesis and Properties of Functionalized Polybenzimidazoles for High-Temperature PEMFCs. *Macromolecules* **2009**, *42*, 8640–8648.

(148) Vinh-Thang, H.; Kaliaguine, S. Predictive Models for Mixed-Matrix Membrane

Performance: A Review. *Chem. Rev.* **2013**, *113*, 4980–5028.

(149) Dechnik, J.; Gascon, J.; Doonan, C. J.; Janiak, C.; Sumby, C. J. Mixed-Matrix Membranes. *Angew. Chemie Int. Ed.* **2017**, *56*, 9292–9310.

(150) Noble, R. D. Perspectives on Mixed Matrix Membranes. *J. Memb. Sci.* **2011**, *378*, 393–397.

(151) Nasir, R.; Mukhtar, H.; Man, Z.; Mohshim, D. F. Material Advancements in Fabrication of Mixed-Matrix Membranes. *Chem. Eng. Technol.* **2013**, *36*, 717–727.

(152) Ismail, A. F.; Goh, P. S.; Sanip, S. M.; Aziz, M. Transport and Separation Properties of Carbon Nanotube-Mixed Matrix Membrane. *Sep. Purif. Technol.* **2009**, *70*, 12–26.

(153) Basu, O.; Das, A.; Jana, T.; Das, S. K. Design of Flexible Metal–Organic Framework-Based Superprotonic Conductors and Their Fabrication with a Polymer into Proton Exchange Membranes. *ACS Appl. Energy Mater.* **2022**. https://doi.org/10.1021/acsaem.2c02972.

(154) Mukhopadhyay, S.; Das, A.; Jana, T.; Das, S. K. Fabricating a MOF Material with Polybenzimidazole into an Efficient Proton Exchange Membrane. *ACS Appl. Energy Mater.* **2020**, *3*, 7964–7977.

(155) Catalyst. In *The IUPAC Compendium of Chemical Terminology*; International Union of Pure and Applied Chemistry (IUPAC): Research Triangle Park, NC, 2011.

(156) Sharma, N.; Ojha, H.; Bharadwaj, A.; Pathak, D. P.; Sharma, R. K. Preparation and Catalytic Applications of Nanomaterials: A Review. *RSC Adv.* **2015**, *5*, 53381–53403.

(157) Melián-Cabrera, I. Catalytic Materials: Concepts to Understand the Pathway to Implementation. *Ind. Eng. Chem. Res.* **2021**, *60*, 18545–18559.

(158) Ahorsu, R.; Constanti, M.; Medina, F. Recent Impacts of Heterogeneous Catalysis in Biorefineries. *Ind. Eng. Chem. Res.* **2021**, *60*, 18612–18626.

(159) Ghosh, S.; Saha, S.; Sengupta, D.; Chattopadhyay, S.; De, G.; Basu, B. Stabilized Cu 2 O Nanoparticles on Macroporous Polystyrene Resins [Cu 2 O@ARF]: Improved and Reusable Heterogeneous Catalyst for On-Water Synthesis of Triazoles via Click Reaction. *Ind. Eng. Chem. Res.* **2017**, *56*, 11726–11733.

(160) Khalilzadeh, M. A.; Sadeghifar, H.; Venditti, R. Natural Clinoptilolite/KOH: An Efficient Heterogeneous Catalyst for Carboxymethylation of Hemicellulose. *Ind. Eng. Chem. Res.* **2019**, *58*, 11680–11688.

(161) Bai, H. Manufacturing of Platinum- and Color-Free Organosilicon Products Using Heterogeneous Platinum Catalysts. *Ind. Eng. Chem. Res.* **2014**, *53*, 1588–1597.

(162) Zhang, L.; Wang, Y.; Zhang, L.; Chi, Z.; Yang, Y.; Zhang, Z.; Zhang, B.; Lin, J.; Wan, S. Hydrogenolysis of Aryl Ether Bond over Heterogeneous Cobalt-Based Catalyst. *Ind. Eng. Chem. Res.* **2020**, *59*, 17357–17364.

(163) Miyaura, N.; Yamada, K.; Suzuki, A. A New Stereospecific Cross-Coupling by the Palladium-Catalyzed Reaction of 1-Alkenylboranes with 1-Alkenyl or 1-Alkynyl Halides. *Tetrahedron Lett.* **1979**, *20*, 3437–3440.

(164) Taheri Kal Koshvandi, A.; Heravi, M. M.; Momeni, T. Current Applications of Suzuki–Miyaura Coupling Reaction in The Total Synthesis of Natural Products: An Update. *Appl. Organomet. Chem.* **2018**, *32*, 4210.

(165) Suzuki, A. Synthetic Studies via the Cross-Coupling Reaction of Organoboron Derivatives with Organic Halides. *Pure Appl. Chem.* **1991**, *63*, 419–422.

(166) Bhattacherjee, D.; Rahman, M.; Ghosh, S.; Bagdi, A. K.; Zyryanov, G. V.; Chupakhin, O. N.; Das, P.; Hajra, A. Advances in Transition-Metal Catalyzed Carbonylative Suzuki-Miyaura Coupling Reaction: An Update. *Adv. Synth. Catal.* **2021**, *363*, 1597–1624.

(167) Lennox, A. J. J.; Lloyd-Jones, G. C. Selection of Boron Reagents for Suzuki–Miyaura Coupling. *Chem. Soc. Rev.* **2014**, *43*, 412–443.

Chapter 2

Materials, Synthesis and Methods

This chapter describes the detailed experimental as well as synthesis procedures, all the characterization techniques and the details of the instruments used in the working Chapters 3 to 7

Source of materials

Benzyl bromide (97%), 2-mercaptopropionic acid (2-MPA) (≥99%), α-methylbenzyl bromide (97%), 3-mercaptopropionic acid (3-MPA) (≥99%) and Carbon disulfide (CS_2) (≥99%) were purchased from Sigma-Aldrich India. Tetraethylorthosilicate (TEOS, 99%), (3-aminopropyl) triethoxysilane (APTES, 99%), 4-dimethylamino pyridine (DMAP), N-vinyl imidazole (NVI) (99.9%), N-vinyl-1,2,4-triazole (NVT) (≥97%), 4-dimethylamino pyridine (DMAP), 2-(dimethylamino)ethyl methacrylate (DMAEMA) (98%), 2-trimethylammonioethyl methacrylate chloride (METAC) (75 wt. % in H_2O), 3-((2-(methacryloyloxy)ethyl)dimethylammonio)propane-1-sulfonate (DMAPS) (95%), vinyl phosphonic acid (VPA) (97%) and 1,3-dicyclohexyl carbodiimide (DCC) were purchased from Sigma-Aldrich and used as received without any further purification except for the monomers. Zirconium chloride ($ZrCl_4$), 2-aminoterephthalic acid (99%) were purchased from TCI chemicals and used as received. Ammonium hydroxide (NH_4OH, 28%), ethyl alcohol (EtOH, 99%), sodium bicarbonate ($NaHCO_3$ 99%), sodium hydroxide (NaOH), potassium hydroxide (KOH), sodium carbonate (Na_2CO_3), potassium carbonate (K_2CO_3), dry toluene (AR grade) were purchased from Finar chemicals Ltd, India. MWCNT (type 4) purchased from Sisco research laboratories Pvt. Ltd. N-hydroxysuccinimide (NHS) (99.8%) and N, N'-dimethylformamide (HPLC grade) were purchased from Merck, India. 2,2′-azobis(2-methylpropionitrile) (AIBN, 98%) and 4,4′-azobis(4-cyanopentanoic acid) (ACP, 98%) from Sigma-Aldrich was freshly recrystallized from distilled methanol and was kept under nitrogen for its further use. 2-bromotoluene, 3-bromotoluene, 4-bromotoluene, phenylboronic acid, 1-naphthylboronic acid, 2-naphthylboronic acid, iodobenzene, 9-bromophenenthrene, 2-iodobenzoic acid were purchased from Avra Scientific and used as received. 3,3',4,4'-tetraaminobiphenyl (TAB), 4,4'-oxybis (benzoic acid) (OBA) polyphosphoric acid (115%) (PPA), formic acid (99%) and ortho phosphoric acid (85%) were purchased from Merck India. Sulphuric acid (98%), hydrochloric acid (HCl), N, N-dimethylformamide (DMF) (AR Dry), dichloromethane (DCM), acetone and ethanol were purchased from Finar Chemicals. DDI water was used throughout the projects.

Synthesis

Synthesis of CPDB RAFT agent and activation of RAFT agent

The synthesis of 4-cyanopentanoicacid dithiobenzoate (CPDB) was carried out according to the methods in literature.[1,2] The activation of CPDB was carried out by using NHS

as described elsewhere.[3] Briefly, CPDB (2.04 g, 7.3 mmol), N-hydroxysuccinimide (0.84 g, 7.3 mmol) were dissolved in dry dichloromethane (15 mL) and then N,N'-dicyclohexylcarbodiimide (DCC, 1.51 g, 7.3 mmol) was added to the above reaction mixture under nitrogen atmosphere, stirred at room temperature for 18 h in dark condition. The insoluble byproduct was filtered, the remaining solution was concentrated and was purified by using silica column chromatography in 4:1 (v/v) n-hexane/ethyl acetate giving crystalline red solid (2.28 g, 83% yield).

Synthesis of BSIPA RAFT agent

BSIPA [2-(((benzylthio)carbonothioyl)thio)propanoic acid], a RAFT agent, was synthesized using the modified literature reported synthetic procedure.[4] 9.42 mmol of 2-MPA, 9.42 mmol of K_3PO_4 and 10.4 mmol of CS_2 were taken in a round bottom flask having 15 mL of dry acetone under nitrogen atmosphere. The reaction mixture was stirred under ice bath condition for 30 min and 9.42 mmol of benzyl bromide was added slowly in the solution with the help of a syringe. The reaction was further stirred for an hour and quenched with water. The compound was extracted with ethyl acetate and the yellow liquid was dried under reduced pressure. The compound was further purified using column chromatography and yellow crystalline compound was obtained. The compound was also subjected to ^{1}H-NMR and ^{13}C-NMR for structural characterization (**Figure 2.1**).

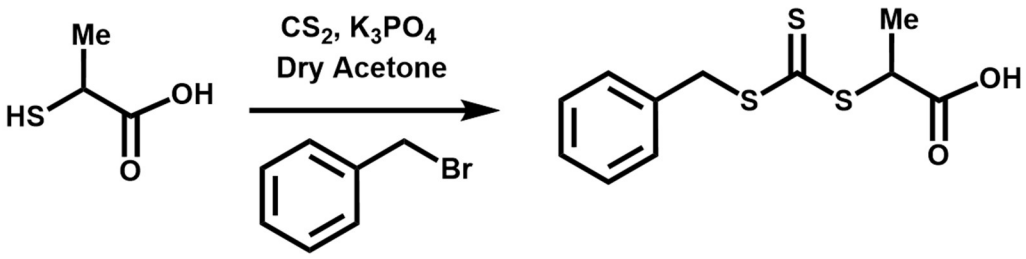

Scheme 2.1. Synthetic scheme for the synthesis of BSIPA RAFT agent.

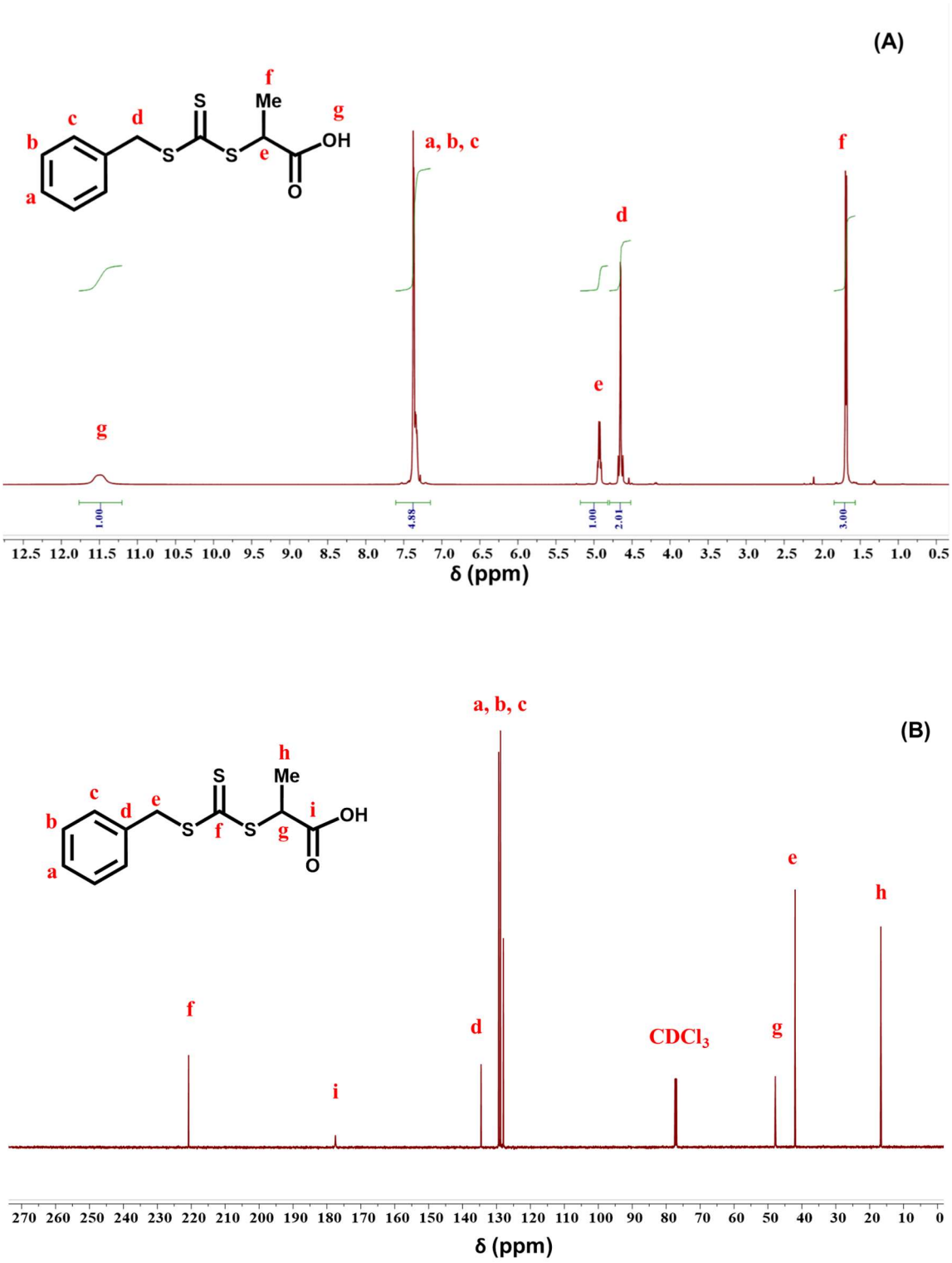

Figure 2.1. ^{1}H NMR **(A)** and ^{13}C NMR **(B)** spectra of BSIPA RAFT agent.

Activation of BSIPA RAFT agent (activated BSIPA)

According to literature reported procedure to activate the carboxylic acid group of RAFT agents, 0.122 mmol of BSIPA, 0.183 mmol of DCC along with 0.012 mmol of DMAP

were taken in a round bottomed flask filled with 20 mL dry DCC under N_2 atmosphere. The reaction was kept at 0 °C for 15 minutes and then slowly added 0.159 mmol NHS dissolved in 5 mL dry THF. The reaction was continued at 0 °C for 18 h and then the reaction mixture was kept in refrigerator for overnight which helps to precipitate out excess DCC from the solution. The reaction mixture was filtered out in cold condition to remove solids from the reaction mixture and purified using column chromatography. The purified activated BSIPA was then used for further reaction.

Synthesis of BEPA RAFT agent

BEPA [3-((((1-phenylethyl)thio)carbonothioyl)thio)propanoic acid] RAFT agent was synthesized (**Scheme 2.2**) using the modified literature reported synthetic procedure.[4] 9.42 mmol of 3-MPA, 9.42 mmol of K_3PO_4 and 10.4 mmol of CS_2 were taken in a round bottom flask having 15 mL of dry acetone under nitrogen atmosphere. The reaction mixture was stirred under ice bath condition for 30 min and 9.42 mmol of α-Methylbenzyl bromide was added slowly into the solution with the help of a syringe. The reaction was further stirred for an hour and quenched with water. The compound was extracted with ethyl acetate and the yellow liquid was dried under reduced pressure. The compound was further purified using column chromatography and the yellow crystalline compound was obtained. The compound was also subjected to ^{1}H-NMR, ^{13}C-NMR, HRMS (**Figure 2.2**) and FT-IR (**Figure 2.3**) studies for structural characterization.

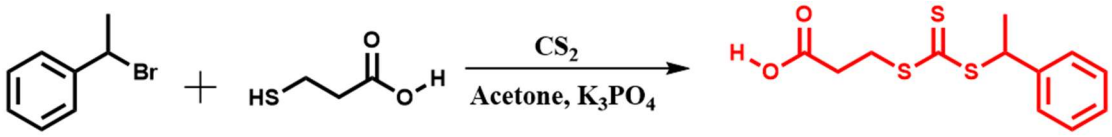

Scheme 2.2. The synthetic scheme for the synthesis of BEPA RAFT agent.

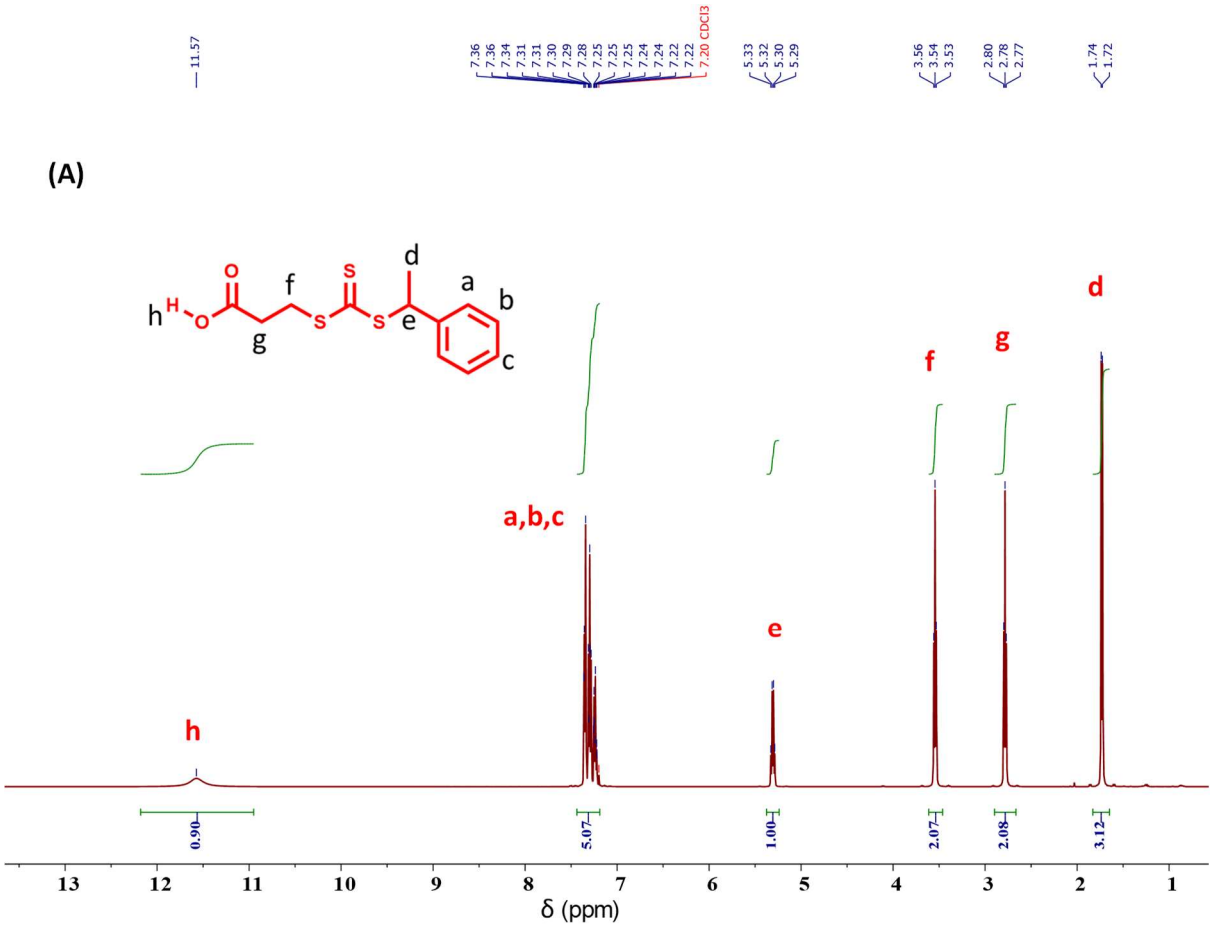
(A)
δ (ppm)
(B)
δ (ppm)

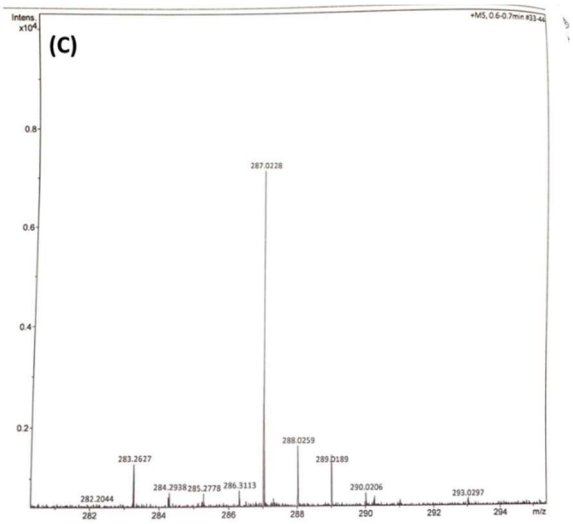

Figure 2.2. ^{1}H NMR **(A),** ^{13}C NMR **(B)** spectra and HRMS data **(C)** of BEPA RAFT agent are represented.

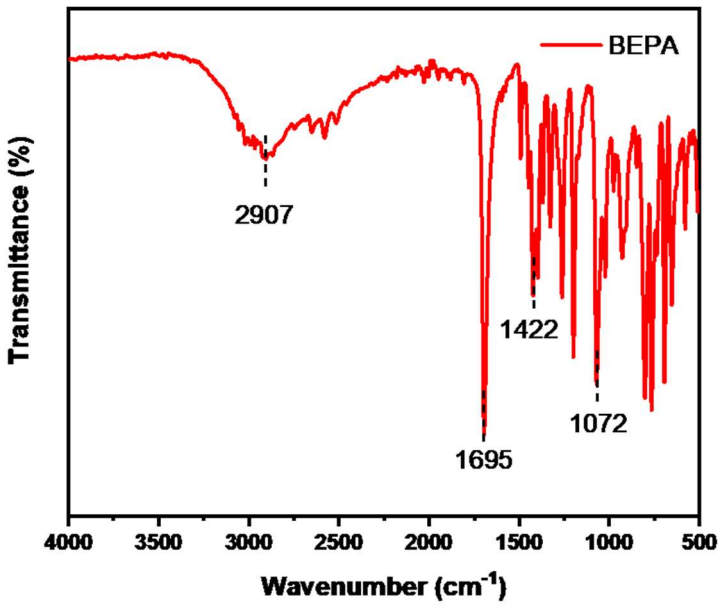

Figure 2.3. FT-IR spectrum of BEPA.

Synthesis of activated RAFT agent (BEPA-NHS)

To activate the carboxylic acid group of RAFT agents, 0.122 mmol of BEPA, 0.183 mmol of DCC along with 0.012 mmol of DMAP was taken in a round bottom flask filled with 20 mL dry DCC under N_2 atmosphere. The reaction was kept at 0 °C for 15 minutes and then slowly added 0.159 mmol NHS dissolved in 5 mL dry THF. The reaction was continued at 0 °C for 18 h and then the reaction mixture was kept in the refrigerator overnight which helped

to precipitate out the excess DCC from the solution. The reaction mixture was filtered out in cold condition to remove solids from the reaction mixture and was purified using column chromatography (**Scheme 2.3**). The purified activated BEPA (BEPA-NHS) was then used for further reaction.

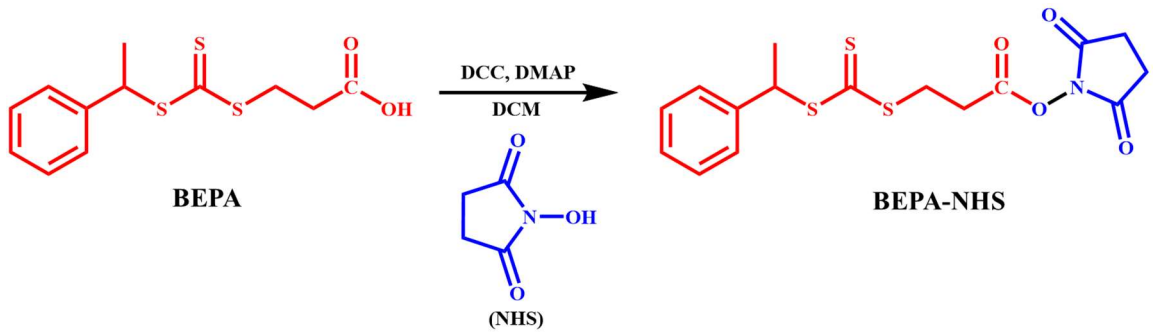

Scheme 2.3. The synthetic scheme to synthesize activated BEPA RAFT (BEPA-NHS) agent.

Synthesis of nanoparticles

Synthesis of silica nanoparticle (SiNP)

The widely adopted Stöber method was used to prepare SiNPs from TEOS by way of a hydrolysis and condensation reaction.[5] Briefly, the method is as follows: ammonium hydroxide (28 wt% in water, 10 mL) and ethanol (400 mL) were added to a 1000 mL round bottomed flask at room temperature. To this tetraethylorthosilicate (TEOS, 10 mL) and HPLC water (10 mL) were added dropwise under vigorous stirring. After stirring for 24 h at room temperature, the formed SiNPs were isolated by using centrifugation method at 10,000 rpm for 30 min. The sediments were then re-dispersed in ethanol (one time) and water (3 times) followed by centrifugation at a rate of 10,000 rpm for 30 min, respectively. The obtained SiNPs were dried under vacuum at 50 °C for 48 h. The yield obtained was 3.2 g.

Synthesis of amine modified SiNP (SiNP-NH_2)

The above synthesized SiNPs (3 g) were transferred into a round bottom flask containing dry toluene (70 mL) and was dispersed by using ultrasonication for 45 min, followed by the dropwise addition of (3-aminopropyl) triethoxysilane (APTES, 0.4 mL, 1.7 mmol) under vigorous stirring in presence of N_2 atmosphere and the reaction is continued for 24 h at 90°C. After the reaction, the reaction mixture was cooled down to room temperature and the reaction mixture was precipitated in hexane (300 mL). The amine functionalized SiNPs were then isolated by using centrifugation at 5000 rpm for 30 min. The sediments were re-dispersed in acetone and isolated by centrifugation at 5000 rpm for 15 min. This purification cycle was

repeatedly done for three times. The obtained amine modified SiNPs (SiNP-NH_2) were dried under vacuum at 70 °C for 48 h and the mass obtained was 2.85 g (95% yield) (**Scheme 2.4**).

Modification of SiNP surface with RAFT agents

The surface modified SiNP-NH_2 (SiNP-NH_2, 2.75 g) were dispersed in 50 mL dry THF and subjected to ultra-sonication for 30 min followed by nitrogen bubbling for 20 min while stirring. To this activated CPDB (CPDB-NHS, 0.5 g, 1.3 mmol) was added under stirring and the mixture was stirred for 24 h at room temperature by closing the reaction vessel with aluminum foil. After the reaction, the reaction mixture was precipitated from 4:1 mixture of cyclohexane and diethyl ether (400 mL) and isolated by using centrifugation (7000 rpm) for 20 minutes. The sediments were redispersed in THF followed by the precipitation from 4:1 mixture of cyclohexane and diethyl ether (400 mL) and isolated by using centrifugation (7000) rpm for 20 minutes for purification. This purification cycle was repeated four times and the obtained RAFT functionalized SiNPs were dried under vacuum at 50 °C for 24 h, and 2.45 g (89% yield, called as SiNP-CPDB) sample was collected (**Scheme 2.4**). The relative grafting amount of RAFT (CPDB) agent which is covalently attached on the SiNPs was estimated by using TGA analysis and is discussed in the results and discussion section of ***Chapter 3***.

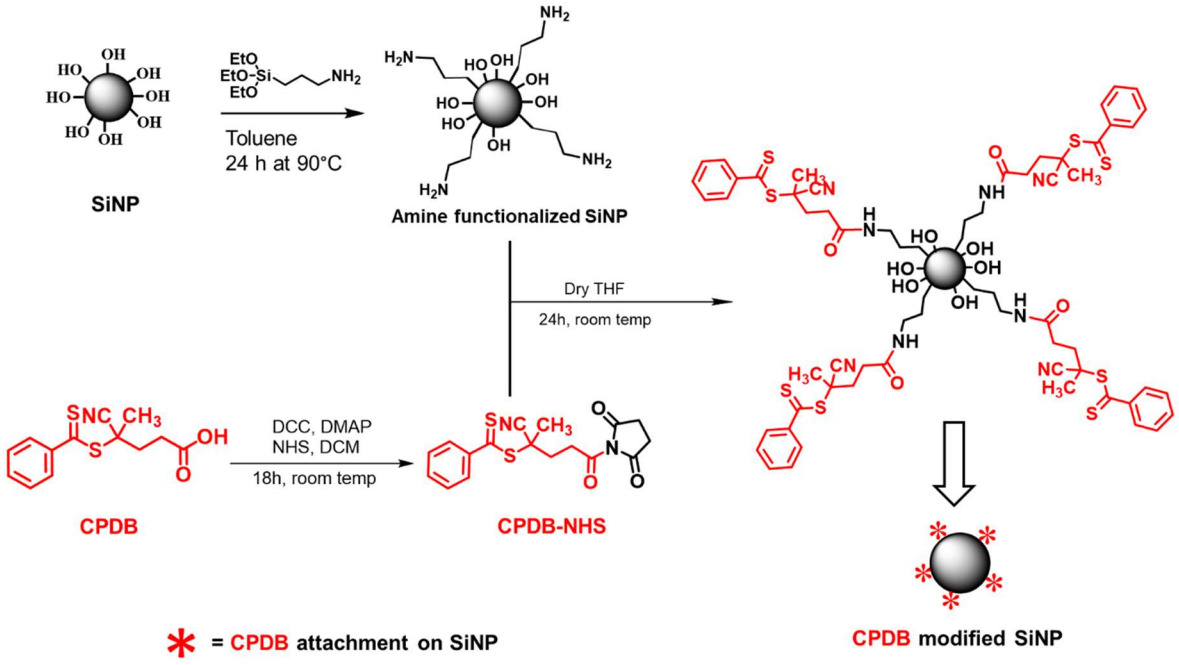

Scheme 2.4. Schematical representation of SiNP synthesis, amine modification of SiNP, CPDB RAFT activation and attachment of RAFT agent on SiNP surface.

Synthesis of UiO-66 NH_2 MOF

Synthesis of UiO-66 NH_2 MOF was adapted from the works of Farha and co-workers.[6] UiO-66 NH_2 MOF was prepared using 5.4 mmol of $ZrCl_4$ which was dissolved in 50 mL DMF in the presence of 10 mL concentrated HCl by sonication. Then 7.5 mmol of 2-aminoterephthalic acid (BDC-NH_2) was added along with 100 mL of DMF. The reaction mixture was then kept at 80 °C temperature for 24 hours in a sealed Teflon capped container. After slow cooling of the reaction vessel over a period of 6 hours, the reaction mixture was filtered and washed thoroughly. Then, the crude UiO-66 NH_2 MOF was stirred in dry ethanol for 72 hours to remove absorbed DMF molecules and dried prior to further characterizations (**Scheme 2.5**).

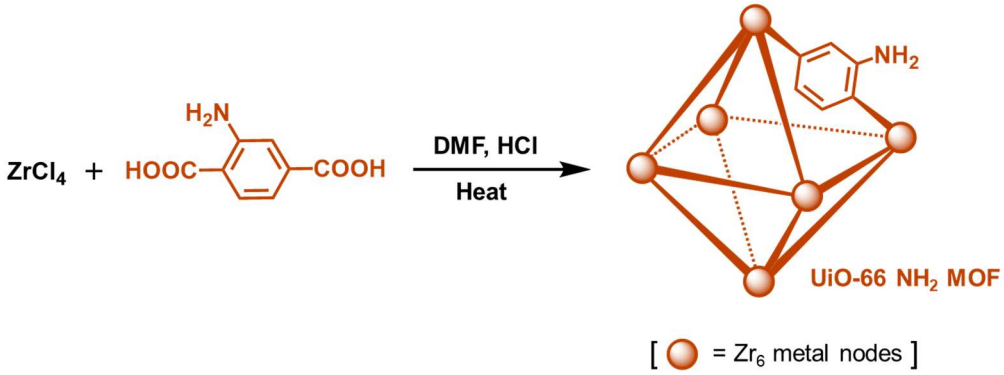

Scheme 2.5. Schematic representation of the synthesis of UiO-66 NH_2 MOF.

Attachment of activated BSIPA on UiO-66 NH_2 MOF surface (BSIPA-MOF)

Attachment of activated BSIPA RAFT agent on the surface of UiO-66 NH_2 was achieved by utilizing the free amine functionality present on the MOF surface arising from the BDC-NH_2 linker. UiO-66 NH_2 (300 mg) in 200 mL dry THF under N_2 atmosphere and activated BSIPA (30 mg, 0.081 mmol) in dry THF were added in the dispersion slowly and was allowed to stir under dark condition for 18 hours at room temperature. After completion of 18 hours, covalently attached BSIPA RAFT agent on the surface of UiO-66 NH_2 (MOF-BSIPA) was separated from the reaction mixture using centrifugation at 13000 rpm for 10 minutes. Followed by re-dispersion of the collected material in dry THF and centrifuged again to separate from the dispersion. The step was repeated thrice with a final re-dispersion and washing with dry acetone to separate all the unbound RAFT agents from the MOF. The MOF-BSIPA was dried under vacuum at 50°C for 24 hours before any further characterization.

Synthesis of MWCNT-COOH and MWCNT-NH_2

To obtain synthetically modified polymer grafted MWCNT (PGNT1, PGNT2, PGNT3) compounds first, carboxylic acid group modified MWCNT (MWCNT-COOH) was prepared from MWCNT using Hammer's method.[7] In a typical synthesis procedure 0.4 g of MWCNT was dispersed in 500 mL mixture of H_2SO_4 / HNO_3 (3:1, v/v) at 50 °C for 24 hours. The black solid which was obtained upon filtration was washed several times with distilled water until the traces of H_2SO_4 and HNO_3 were removed from the black solid and dried under vacuum for 24 hours at 80 °C. Acid functionalized MWCNTs (MWCNT-COOH) were further functionalized with amine functionality (MWCNT-NH_2) using ethylene diamine (EDA) in presence of DCC-DMAP as described by Yuen et. al.[7]

Attachment of BEPA-NHS on MWCNT-NH_2 surface to make MWCNT-BEPA

Attachment of BEPA-NHS RAFT agent on the surface of amine modified MWCNT (MWCNT-NH_2) was achieved by dispersing MWCNT-NH_2 (300 mg) in 200 ml dry THF under N_2 atmosphere and the BEPA-NHS (50mg) in dry THF was added drop wise in the dispersion and was allowed to stir under dark condition at room temperature for 18 hours. After the completion of 18 hours, the MWCNT with covalently attached BEPA RAFT agent (MWCNT-BEPA) was separated from the reaction mixture using centrifugation at 13000 rpm for 10 minutes. Then, the collected black coloured MWCNT-BEPA was re-dispersed in dry THF and was then centrifuged to separate from the dispersion. This step was repeated thrice to separate the unbound RAFT agents. The MWCNT- BEPA was dried under vacuum at 50°C for 24 hours. The characterization of this newly developed material MWCNT-BEPA has been discussed in result and discussion section of the **chapter 6**.

Detachment of grafted polymer chains from polymer grafted nanoparticles

Removal of SiNP core from BC-*g*-SiNP to analyse the bare polymers

Cleavage of the polymer chains from the polymer grafted SiNP was carried out according to the similar procedure as described elsewhere.[8,9] In a polyethylene tube, the pNVI-*b*-pNVT-*g*-SiNP (50 mg) was dispersed into 6 ml of methanol. In this solution, aqueous HF (48 wt%, 1.5 mL) was added, and the reaction mixture was stirred at room temperature for 12 hours as shown in the **Scheme 2.6** below. After completion of the reaction, the excess HF was neutralized with $NaHCO_3$ solution and the polymer was extracted with methanol. The polymer was precipitated by adding the polymer solution in an excess of dry acetone and then the

precipitate was recovered by filtration. The bare polymer chain obtained through precipitation was dried inside a vacuum oven at 80°C for 24 hours. The recovered bare polymer chains were then subjected to gel permeation chromatography (GPC) analysis for molecular weight determination.

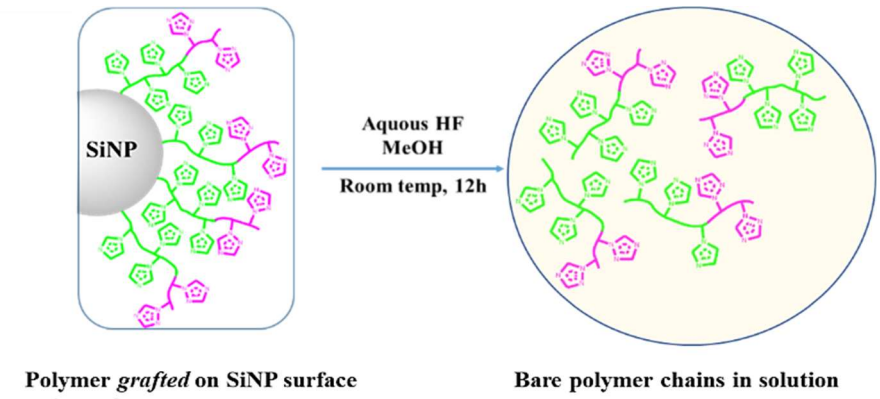

Scheme 2.6. Removal of silica core by treating polymer grafted SiNPs with aqueous HF.

Removal of grafted polymer chains from MOF core

Detachment of the polymer brushes from the MOF core was achieved by using aqueous HF acid solution which helps to break down the framework structure. The polymer grafted MOF (PGM) samples were subjected to dilute HF solution in PTFE vials. Upon digestion the solid residue was removed using centrifugation technique and the supernatant was further purified to obtain bare polymer chains. The bare polymer chains which were detached from the MOF surface were dissolved in HPLC water and the molecular weight was determined by gel permeation chromatography (GPC) technique using PEG/ PEO as standards and eluted in HPLC water at a flow rate of 0.5 mL/min at 30 °C on a GPC (Waters 515 HPLC) fitted with Waters 2414 refractive index detector and using Ultrahydrogel 250 Water column.

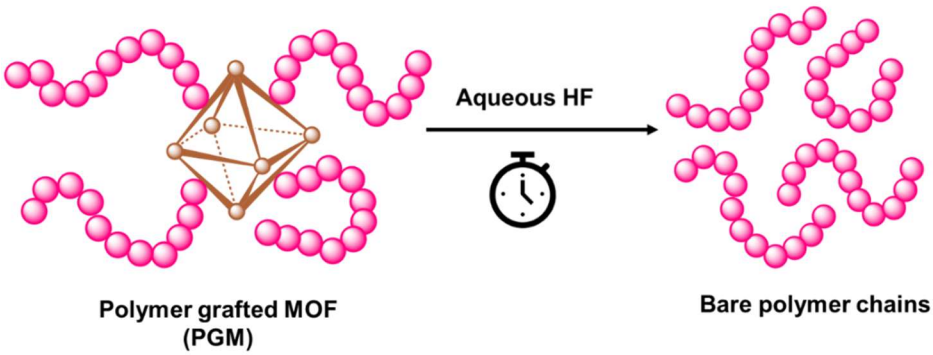

Scheme 2.7. The schematic representation for the detachment of grafted polymer brush from the surface of MOF.

Detailed procedure for the removal of the polymer chains from polymer grafted MWCNT samples are discussed in detail in the respective **Chapter 6**, **Chapter 7** and the respective **Appendix sections**.

Synthesis of OPBI polymer

According to the literature reported procedure[10–12], equimolar amounts of 3,3'diaminobenzidine and 4,4'-oxybis(benzoic acid) (OBA) along with the required amount of polyphosphoric acid (PPA) were placed in a three-necked round bottom flask. Then the reaction mixture was subjected to mechanical stirring with an overhead stirrer at 60 rpm in the presence of nitrogen gas purging to maintain inert atmosphere. The polymerization reaction was carried out at 190–220 °C for about 24-26 h. Thereafter, the reaction mixture was poured into the distilled water where the polymer melt gets isolated as brown fibrous mass. Then, the fibrous mass was neutralized with sodium bicarbonate, washed thoroughly with DDI water and then finally dried in a vacuum oven at 100 °C for 24 h to obtain dry OPBI powder. The inherent viscosity (I.V.) of the poly (4,4'-diphenyl-5,5'-bibenzimidazole) (OPBI) polymer was measured at 30 °C. The obtained I.V. value of the synthesised OPBI is 2.12 dL/g.

Synthesis procedures for all the other materials used and nanocomposite preparation procedures are described in details in the respective **Chapters** and its **Appendix section**.

Experimental methods

FT-IR study

FT-IR spectra of the samples were recorded on an iD7 ATR Thermo Fisher Scientific-Nicolet iS5 instrument. The sample was directly put on the sample holder without any modification and collected data for 32 scans.

^{1}H-NMR, ^{13}C-NMR, ^{31}P-NMR study

The samples were dissolved in $CDCl_3$, DMSO-D_6 or D_2O in order to analyze using Brucker 500 and 400 MHz Spectro meter. The collected data was analyzed using MestReNova software and fitted in order to isolate the compound peaks and solvent peaks.

X-ray studies (PXRD)

All the membranes and the powder samples were subjected to PXRD studies and the data were collected in a Bruker D_8 Advance powder diffraction apparatus. The samples were placed on a glass slide and the diffractograms were recorded with Cu Kα radiation (λ = 1.5406

Å) operated at 40 kV and 30 mA current in the angular range (2θ) of 5 to 60° at a scanning rate of 1°/1.2 minutes.

Field emission scanning electron microscope (FESEM) study

The morphology, mapping and the EDX data of all the powder samples and composite membranes along with the pellets were evaluated by using a field emission scanning electron microscope (FESEM) (Model: Zeiss Merlin Compact). The powder samples were dispersed in dry ethanol by using sonication and drop casted on a clean piece of glass slide. The slides were dried at 70 °C overnight to remove the solvent traces from the sample cavity and were gold coated before analysis. The FESEM cross section morphology of the membrane samples were done by breaking the membranes in liquid nitrogen medium. Samples were gold coated before imaging in FESEM.

Transition electron microscopy (TEM) study

Transmission electron microscopy (TEM), EDX and mapping studies were conducted on JEOL (JEM Model No. F200) TEM machine at an accelerating voltage of 200 kV. The nanoparticles, polymer modified nanoparticles, composite membrane samples were prepared by placing a drop of the sample dispersed in ethanol or DMAC on the carbon coated side of the copper grid (200 mesh) and were dried overnight in an oven. The composite samples were prepared by placing a drop of formic acid dispersed polymer grafted nanoparticle@OPBI solution on carbon coated side of the copper grids (200 mesh).

Atomic force microscopy (AFM) study

Atomic force microscope (AFM) images of the samples were acquired from Oxford Asylum Research AFM instrument model MFP-3D Origin. 1 cm x 1 cm piece of completely dried membrane samples were cut and was glued on a glass substrate by using a double-sided carbon tape and was mounted on the AFM instrument. These samples were scanned in AC air topography mode with a microcantilever spring at a constant scan rate of 0.30 Hz and 256 points per line with a scan size of 5 µm. The collected data was analyzed using Asylum Research Igor pro version 6.3 software.

RAMAN study

Raman spectral analysis of the samples were performed on a WITec model Alpha 300 R. 405 nm laser was used as the excitation source in Raman microscope. The laser intensity was maintained constant for all the samples

Thermogravimetric study analysis (TGA)

Thermogravimetric analysis of all the oven dried powder samples, nanocomposite and phosphoric acid doped membranes were carried out on Q500 TA Instruments, USA from 30 to 700 °C with a scanning rate of 10 °C/min in the presence of nitrogen flow. All the membrane samples were kept in isothermal condition at 100 °C for 30 minutes under N_2 atmosphere in order to get rid of surface adsorbed moisture molecules. The samples were then cooled to room temperature under N_2 atmosphere and recorded TGA data.

Dynamic mechanical analyzer (DMA) study

The mechanical properties of all the membranes were studied by using a dynamic mechanical analyser (DMA model Q-800). The loaded membranes dimensions were around 30 mm × 7 mm × 0.02 mm (L × W × T) and clamped on the films tension clamp of the pre-calibrated instrument. The samples were annealed at 400 °C for 15 minutes and were then scanned from 100 °C to 400 °C with the heating rate of 4 °C/min. The storage modulus (E'), loss modulus (E") and tan δ values were measured at a constant linear frequency 10 Hz with constant preloaded force of 0.01N.

Tensile stress-strain studies (UTM analysis)

The tensile strength measurement (stress-strain profile) of all the doped OPBI and nanocomposite membranes were obtained from the universal testing machine (UTM, INSTRON5965). 100 mm × 10 mm × 0.1 mm size PA doped films were used for this experiment. For each sample, at least for three times the measurements were carried out to check the reproducibility. Tensile stress and elongation at break values of the PA loaded nanocomposite membranes were obtained from the stress-strain plot.

Gel permeable chromatography (GPC)

Molecular weights (M.W.) and polydispersity index (Đ) of detached polymers, which were obtained after detaching the polymer chains from the SiNP, MOF or MWCNT core was achieved by using aqueous HF treatment or Aminolysis treatment in appropriate solvent

(discussed in the respective **Chapters** and the **Appendix section**). The solid residue was removed using centrifugation technique and the supernatant was further purified to obtain bare polymer chains. The water-soluble bare polymer chains were dissolved in HPLC water and the molecular weight was determined by Gel permeation chromatography (GPC) technique using PEG/ PEO as standards and eluted in HPLC water at a flow rate of 0.5 mL/min at 30 °C on a GPC (Waters 515 HPLC) fitted with Waters 2414 refractive index detector and using Ultrahydrogel 250 Water column. The N-heterocyclic polymer chains were dissolved in DMF/LiBr, were injected in gel permeation chromatography (GPC) and molecular weight was measured by using polystyrene standards and eluted in DMF/LiBr as an eluent at a flow rate of 0.4 mL/min at 30 °C on a GPC (Waters 515 HPLC) fitted with Waters 2414 refractive index detector and using Styragel HR 4 DMF column.

Column chromatography

The products obtained upon Suzuki-Miyaura catalysis reaction were purified by column chromatography technique using hexane and ethyl acetate mixture as eluent. The polarity of the eluent was increased gradually to isolate the product molecules from the reaction mixture.

Dynamic light scattering (DLS) study

Particle size measurements of water dispersed nano material samples were performed using a Zetasizer Nano S90 (Malvern Instruments, Germany) operating at 4mW He-Ne laser with 633nm wavelength at 25°C.

Zeta potential measurements

Zeta potential for all the samples were measured using a Horiba Scientific nano partica nano particle analyzer SZ-100 instrument. All the nanoparticles were dispersed in two different solvents namely milliQ water and 98 % formic acid solution and were sonicated for 5 minutes and the measurements were taken.

Dynamic vapor sorption (DVS) study

The dynamic vapor sorption (DVS) was measured for the nano materials (dry powder samples) were taken using TA instrument model Q5000 SA.

Brunauer–Emmett–Teller (BET) study

BET experiments of the nano material and polymer *grafted* samples were conducted in Autosorb iQ (Quantachrome ADIQC0000-4) using nitrogen as the adsorbing gas. Samples were activated and degassed at 100 °C under vacuum for 24 h prior to N_2 sorption analysis. The temperature for adsorption measurements (77 K) was controlled by using the refrigerated bath of liquid nitrogen.

Viscosity measurement

The inherent viscosity (I.V.) of the poly (4,4'-diphenyl-5,5'-bibenzimidazole) (OPBI) polymer was measured at 30 °C in water bath with the help of Cannon (model F725) Ubbelohde capillary dilution viscometer and the I.V. values were calculated from the flow time data. A solution of OPBI in H_2SO_4 was used for the viscosity measurement. The concentration of the OPBI solution in H_2SO_4 is 0.2 g/dL. The obtained I.V. value of the synthesised OPBI is 2.1 dL/g.

PA doping level, swelling ratio, water uptake

Three similar size pieces of the OPBI and PGNT-@OPBI membranes were made from the formic acid and were immersed in the phosphoric acid for 5 days. After that the doped membranes were wiped with the filter paper and transferred to 50 mL water and then were titrated against 0.1N sodium hydroxide (NaOH) by using an Autotitrator (Model Metrohm702). The phosphoric acid content was calculated as the number of PA moles per PBI repeat unit.[13]

Swelling ratio of the membranes were calculated from the following equation.

$$\%\text{Swelling Ratio} = \frac{L_w - L_d}{L_d} \times 100\% \quad (1)$$

Where, L_w, and L_d are the length of the wet membranes and dry membranes, respectively.

Swelling ratio of the membranes were calculated from the following equation.

$$\%\text{Water uptake} = \frac{W_w - W_d}{W_d} \times 100\% \quad (2)$$

Where, W_w, and W_d are the weight of the wet membranes and dry membranes, respectively.

Phosphoric acid leaching studies

Phosphoric acid leaching or in other terms phosphoric acid retention studies were performed using a setup where the phosphoric acid doped membranes were hung under a inverted funnel, over a boiling water bath. The boiling water vapour mimics the harsh humid and high temperature conditions and the inverted funnel allows more water vapour retension around the membrane and to form water droplets which may further enhance the leaching of doped acid molecules as shown in the **Figure 2.1**.

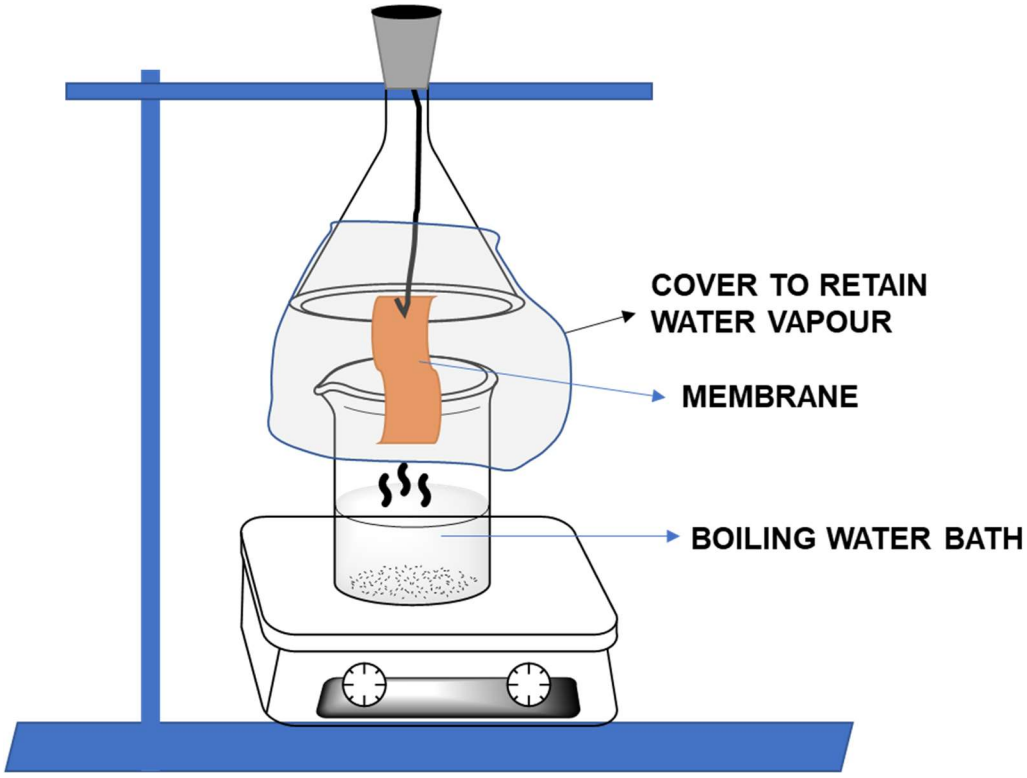

Figure 2.4. Schematic representation of the setup for the phosphoric acid leaching study.

Proton conductivity studies

Proton conductivity was carried out by four probe impedance analysis by using Autolab Impedance analyser (PGSTAT302N) over a frequency range from 1 Hz to 100 KHz. The phosphoric acid doped composite membranes were cut in rectangular shape and were then, kept sandwiched between the two Teflon plates with four platinum electrodes. Two outer electrodes (1.5 cm apart) supply current to the cell while, the two inner electrodes 0.5 cm apart on opposite sides of the membrane measure the potential drop. At first, the surface PA of the membranes were wiped out carefully and fitted into the conductivity cell. Then, the whole conductivity cell set up was kept in a vacuum oven to measure the temperature dependence of

the proton conduction. The conductivity cell was placed in a vacuum oven at 100 °C for 2h to avoid the conduction due to the presence of water molecules. The conductivities of the membranes were measured from room temperature to 180 °C at an interval of 20 °C. At every temperature jump, the sample was kept for 30 minutes to attain isothermal equilibrium and then the measurements were recorded. The conductivities of the membranes were calculated from the following equation:

$$\sigma = \frac{D}{RBL} \qquad (3)$$

Where, D is the distance between the electrodes (here it is 0.5 cm), B is the thickness of the membrane, L is the width of the membrane and R is the bulk resistance obtained from the Nyquist plot.

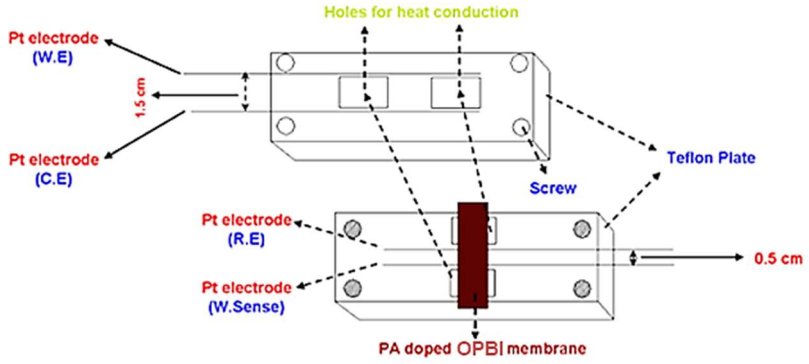

Figure 2.5. Schematic representation of the four electrode set up which was used for al the proton conductivity measurements of the membranes.[14]

Proton conductivity measurements for pellets

Electrochemical impedance spectroscopy (EIS) was conducted using an Ametek (PARSTAT MC) electrochemical workstation operated with VersaStudio software.

Electrochemical impedance measurements were performed using a 2-electrode setup in parallel plate mode. A similar protocol for sample preparation and experimental setup were followed for all the samples as reported earlier.

The MOF (approximately 400 mg) was powdered and pelletized as a sandwich between two carbon wafers, using a custom-made pellet maker die, using a hydraulic pressure of 2 tons for 2 minutes. After the pellets were prepared, they were checked for any cracks or breakage (**Figure 2.6**). The thickness of the pellets was then measured carefully using a screw

gauze. To determine the thickness of each pellet, three readings from screw gauze were averaged to minimize the manual error. The use of pellet maker die ensures that all the pellets have identical diameter. As the same pellet-maker die and same electrodes were used for all the samples, thus equal surface area of contact between the sample and the electrodes should be achieved.

The pellet was then placed between the two electrodes such that, the carbon wafers of the pellet were in contact with each of the stainless-steel plates of the two electrodes (**Figure 2.7**). This electrode setup was then placed in a double-walled incubating chamber maintaining the required humidity and temperature. The inner chamber of the incubator maintains the required temperature by circulating hot air. And the humidity is maintained by a separate flow of water vapor inside this chamber (**Figure 2.8**).

The impedance spectra were recorded at the open circuit potential for each sample, using a sinusoidal signal of amplitude 5 mV. The frequency was swept from 1 MHz to 1 Hz. Before any measurement at a given temperature and relative humidity (RH), the sample pellet was kept for two hours to equilibrate.

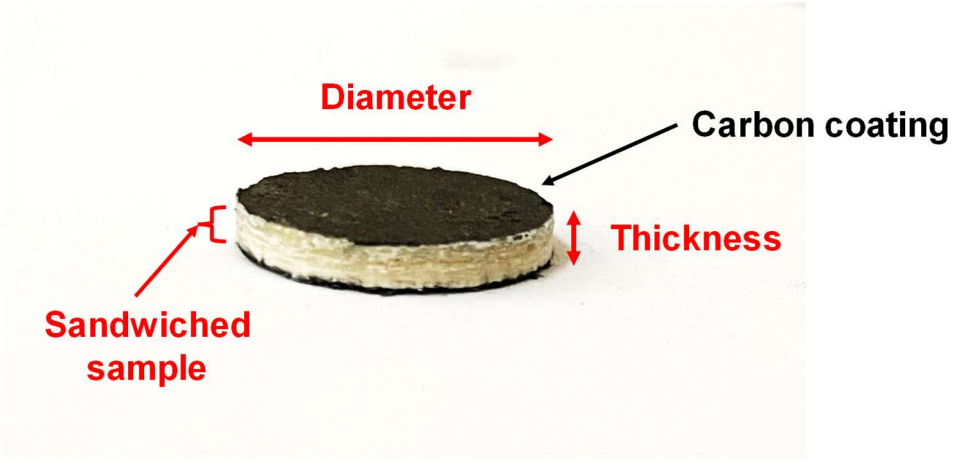

Figure 2.6. Representative image of the pellets prepared.

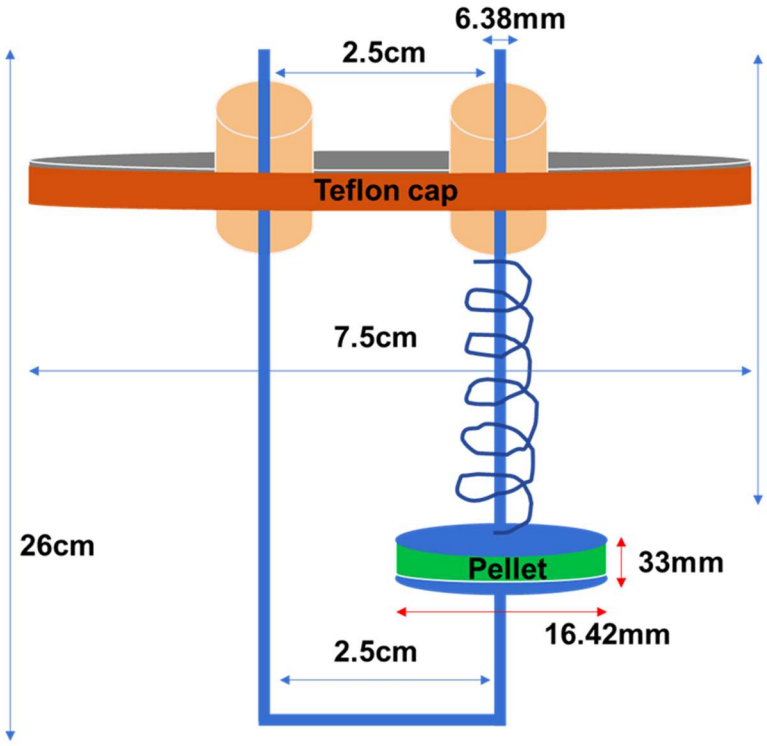

Figure 2.7. Schematic diagram of the two-electrode setup used for the proton conductivity experiment.

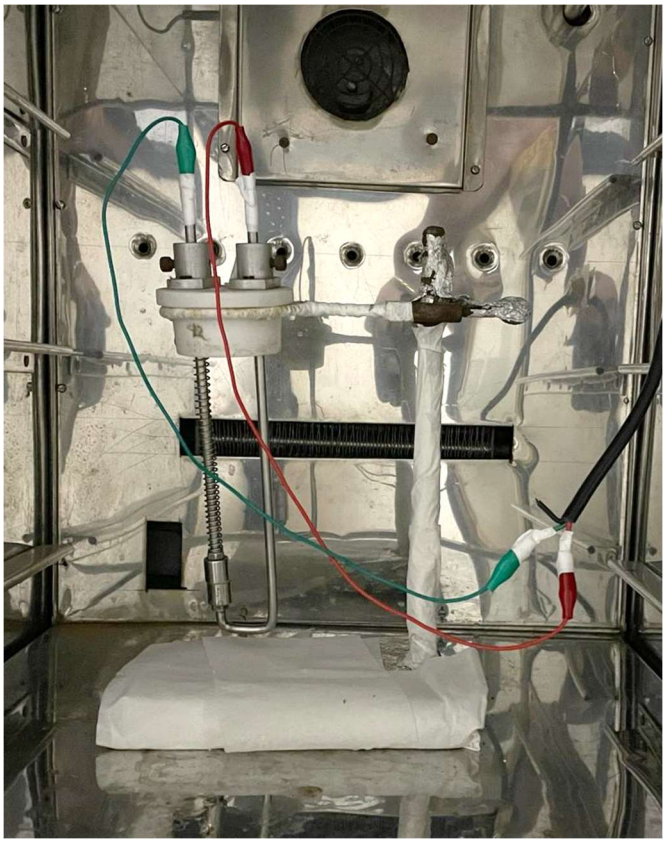

Figure 2.8. picture of the two-electrode setup inside humidity chamber.

References

(1) McCormick, C. L.; Lowe, A. B. Aqueous RAFT Polymerization: Recent Developments in Synthesis of Functional Water-Soluble (Co)Polymers with Controlled Structures. *Acc. Chem. Res.* **2004**, *37*, 312–325.

(2) Mitsukami, Y.; Donovan, M. S.; Lowe, A. B.; McCormick, C. L. Water-Soluble Polymers. 81. Direct Synthesis of Hydrophilic Styrenic-Based Homopolymers and Block Copolymers in Aqueous Solution via RAFT. *Macromolecules* **2001**, *34*, 2248–2256.

(3) Warren, N. J.; Mykhaylyk, O. O.; Mahmood, D.; Ryan, A. J.; Armes, S. P. RAFT Aqueous Dispersion Polymerization Yields Poly(Ethylene Glycol)-Based Diblock Copolymer Nano-Objects with Predictable Single Phase Morphologies. *J. Am. Chem. Soc.* **2014**, *136*, 1023–1033.

(4) Davis, T. P.; Barner-Kowollik, C.; Nguyen, T. L. U.; Stenzel, M. H.; Quinn, J. F.; Vana, P. Influences of the Structural Design of RAFT Agents on Living Radical Polymerization Kinetics; 2003; pp 551–569.

(5) Stöber, W.; Fink, A.; Bohn, E. Controlled Growth of Monodisperse Silica Spheres in the Micron Size Range. *J. Colloid Interface Sci.* **1968**, *26*, 62–69.

(6) Katz, M. J.; Brown, Z. J.; Colón, Y. J.; Siu, P. W.; Scheidt, K. A.; Snurr, R. Q.; Hupp, J. T.; Farha, O. K. A Facile Synthesis of UiO-66, UiO-67 and Their Derivatives. *Chem. Commun.* **2013**, *49*, 9449.

(7) Yuen, S.-M.; Ma, C.-C. M.; Lin, Y.-Y.; Kuan, H.-C. Preparation, Morphology and Properties of Acid and Amine Modified Multiwalled Carbon Nanotube/Polyimide Composite. *Compos. Sci. Technol.* **2007**, *67*, 2564–2573.

(8) Li, C.; Benicewicz, B. C. Synthesis of Well-Defined Polymer Brushes Grafted onto Silica Nanoparticles via Surface Reversible Addition−Fragmentation Chain Transfer Polymerization. *Macromolecules* **2005**, *38*, 5929–5936.

(9) Kutcherlapati, S. N. R.; Koyilapu, R.; Boddu, U. M. R.; Datta, D.; Perali, R. S.; Swamy, M. J.; Jana, T. Glycopolymer-Grafted Nanoparticles: Synthesis Using RAFT Polymerization and Binding Study with Lectin. *Macromolecules* **2017**, *50*, 7309–7320.

(10) Singha, S.; Jana, T. Structure and Properties of Polybenzimidazole/Silica Nanocomposite Electrolyte Membrane: Influence of Organic/Inorganic Interface. *ACS Appl. Mater. Interfaces* **2014**, *6*, 21286–21296.

(11) Singha, S.; Jana, T. Influence of Interfacial Interactions on the Properties of Polybenzimidazole/Clay Nanocomposite Electrolyte Membrane. *Polymer.* **2016**, *98*, 20–31.

(12) Ghosh, S.; Sannigrahi, A.; Maity, S.; Jana, T. Role of Clays Structures on the Polybenzimidazole Nanocomposites: Potential Membranes for the Use in Polymer

Electrolyte Membrane Fuel Cell. *J. Phys. Chem. C* **2011**, *115*, 11474–11483.

(13) Sana, B.; Jana, T. Polybenzimidazole Composite with Acidic Surfactant like Molecules: A Unique Approach to Develop PEM for Fuel Cell. *Eur. Polym. J.* **2016**, *84*, 421–434.

(14) Sannigrahi, A. Copolymerization, Aggregation and Thermoreversible Gelation of Polybenzimidazoles, University of Hyderabad, 2010.

Chapter 3

Block Copolymer *Grafted* Silica Nanoparticles: Designer Nanofiller for Improving Proton Exchange Membrane Properties

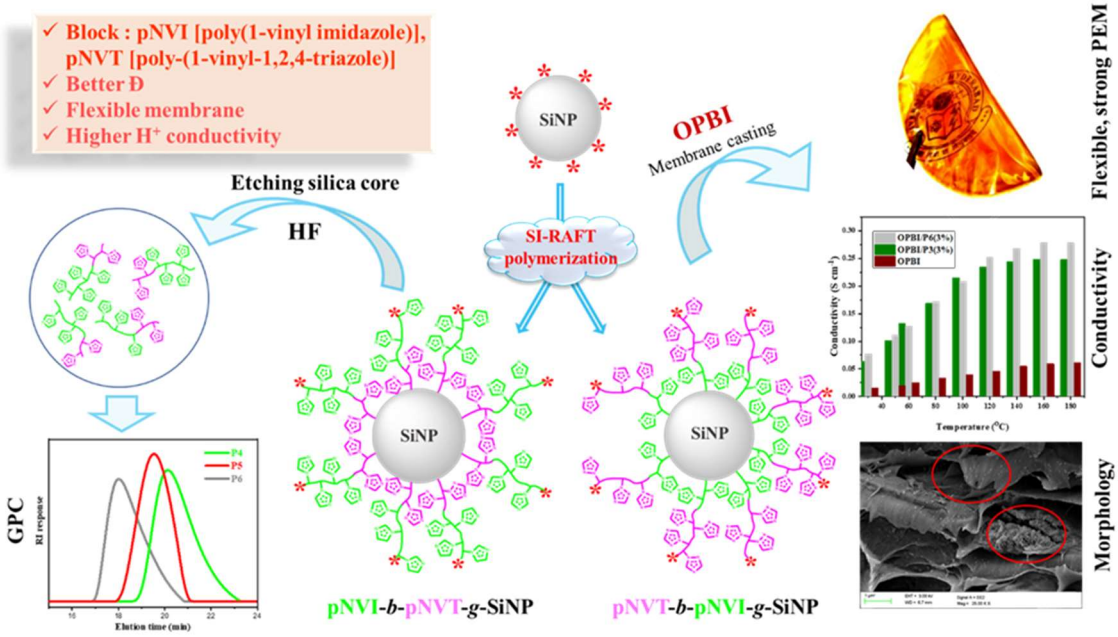

Nilanjan Mukherjee, Anupam Das, Moumita Dhara and Tushar Jana*. Surface Initiated RAFT Polymerization to Synthesize N-Heterocyclic Block Copolymer *Grafted* Silica Nanofillers for Improving PEM Properties. *Polymer*. **2021**, *236*, 124315.

Abstract

Though surface functionalized silica nanoparticles (SiNP) have gained immense attention as an efficient nanofiller in improving proton exchange membrane (PEM) properties but there are lot more which can be done on the SiNP surface to prepare smart nanofiller for further improvement in the PEM performance. SiNP surface functionalized with the suitable polymers consisting of similar chemical functionalities of the pristine polymer with which nanocomposite is to be made, can create a drastic enhancement in the properties of the nanocomposite PEM. Herein we report, the development of the block copolymer *grafted* SiNP (BC-*g*-SiNP) as functional nanofiller which was further solution blended with oxypolybenzimidazole (OPBI) to prepare nanocomposite based PEM. Block copolymer chains comprising of poly (N-Vinyl imidazole) (pNVI) and poly (N-Vinyl-1,2,4-triazole) (pNVT) were grown on the polymerizable SiNP surface using *grafting-from* RAFT polymerization in one pot process. Two series of BC-*g*-SiNP namely pNVI-*b*-pNVT-*g*-SiNP and pNVT-*b*-pNVI-*g*-SiNP were synthesized by altering the polymer chain grafting sequence. In addition, the chain length of each block was altered to obtain series of BC-*g*-SiNP so as to understand the effect of chain sequence and chain length on the properties of nanofiller and their influence in altering the PEM properties. The block copolymer structure, chain sequence and chain length were confirmed by means of NMR and GPC analysis of the cleaved copolymer chains. The BC-*g*-SiNP displayed core-shell morphology, where the thickness of the shell alters as the chain length and sequence of the *grafted* chain vary. OPBI/BC-*g*-SiNP hydrid nanocomposite membranes having different wt% of nanofillers were loaded with phosphoric acid (PA) to produce PEM. The nanocomposite PEM displayed very high thermal, mechanical and chemical stabilities along with proton conductivity as high as 0.278 S cm^{-1} at 180°C in case where OPBI was blended with 3wt% of **P6** [$pNVT_{95}$-*b*-$pNVI_{286}$-*g*-SiNP]. A very clear-cut dependence of PEM properties was observed on the architecture such as chain length, chain sequence etc. of the *grafted* block copolymers.

Introduction

In order to meet the increasing demand of the non-conventional energy sources over conventional resources, development of efficient polymer electrolyte membrane (PEM) for the use in fuel cell has become subject of immense interests among polymer chemists.[1–3] Majority of the well-researched PEMs encounter a number of serious problems which includes decrease in conductivity at higher temperature, low mechanical strength, weaker thermal and chemical

stabilities, low phosphoric acid (PA) loading and high leaching of PA in case of polybenzimidazole (PBI) based PEM.[4–7] Several studies showed that nitrogen containing heterocyclic compounds can play an effective role in alleviating the concerns raised above owing to stable basic heterocyclic rings and ability to form strong interactions with PEM forming polymers.[8–11] It has also been reported widely that polymers consisting of N-heterocycles can efficiently execute the acid-base complexes with the complementary molecules / polymers and hence, resulted efficient materials for the use in various fields.[12–16]

Polymers containing imidazole and triazole rings are being mostly used to prepare blend materials[17–19] but it has been also observed that polymerization of imidazole and triazole ring containing monomers are tricky. Controlling the polymerization of N-vinylic monomers which contains heterocyclic rings such as N-vinyl imidazole, N-vinyl triazole are challenging as propagating N-vinyl radicals present in the polymerization are highly reactive and unstable owing to the absence of resonance stabilization and thereby propagating radicals are responsible not only for chain transfer but also for chain termination event.[20] Therefore, it is an important task to get control over the polymerization of these N-vinylic monomers.

In the last few years, the combination of the surface initiated polymerization and the controlled polymerization techniques has become a very useful tool to design the surface functionality with the desired properties.[21–26] Among such approaches, the surface initiated reversible addition-fragmentation chain-transfer (SI-RAFT) polymerization has become a promising one because of its ability to polymerize a wide range of vinyl monomers containing different functionality, high precision over *grafted* polymers and easy functionalization of the end group of polymer chains.[27–33] Despite many useful functional characteristics and properties of N-vinyl-1,2,4-triazole (NVT) units, the research on NVT based monomers through RAFT polymerization technique are very limited. Fouillet et al. has used NVT to prepare protic ionic liquid monomers and synthesized polyampholytic copolymers via RAFT polymerization.[34] Mori et al. has presented the controlled synthesis of the four-arm pNVT stars and amphiphilic star block copolymers by RAFT polymerization using the xanthate-type tetrafunctional chain transfer agent (CTA).[35] K. Nakabayashi et al. has introduced RAFT polymerization of a new family of triazolium based monomers and successfully exploited in the preparation of novel 1,2,4-triazolium salt-based polymers and block copolymers having well-defined self-assembled structures.[36] Unfortunately, no reports were found where SI-RAFT polymerization techniques were used to prepare NVT based polymer over SiNP surface.

There are substantial number of reports where, NVT monomer has been polymerized in several different ways and has also been extensively used as potential candidate in a number of electro chemical and energy applications.[37–44] Vestergaard et al. reported that the molten mixture of 1,2,4-triazolium chloride-aluminium chloride can be used as secondary battery electrolyte which produced conductivity values between 4.02×10^{-5} and 7.78×10^{-2} S cm^{-1} for a wide range of temperature (-31℃ to 123℃).[41] Luo et al. has demonstrated that, the use of 1,2,4-triazolium methane sulfonate results in high ionic conductivity of 0.149 and 0.128 S cm^{-1} at 200 ℃.[45] Sen et al. has used pNVT blended with Nafion to produce PEM with temperature stability up to 220 ℃.[17] It has also been suggested by Zhou et al. that the presence of several proton-carrying isomers in case of triazole ring containing systems, the proton conductivity largely differs than imidazole ring containing systems.[46] Therefore, triazole ring containing membranes are of special interest for the enhancement of PEM performance.[47]

A quite good amount of research articles have been appeared in the recent past in which imidazole and triazole based compounds / polymers are blended with polybenzimidazole (PBI) to develop high temperature PEM. Meanwhile, many research groups have also tried to improve the PBI based PEM properties by incorporation of MOF, clay, silica and other nanofillers.[48–54] Among various nanofillers, surface functionalized SiNP appeared to be the most suitable in improving PBI based PEM performance.[20,54–58]

In this work, our idea is to combine the properties of both imidazole and triazole based polymers *grafted* on to the surface of SiNP to yield a better hybrid nanofiller for developing PEM from PBI based nanocomposites. To do so, we have *grafted* a series of block copolymer consisting of pNVT and pNVI on the SiNP by using SI-RAFT *grafting from* approach with varying block sequence and molecular weights. After that these nanofillers were mixed with OPBI polymer through the solution blending method in different weight % to produce nanocomposite membranes. All the synthesized BC-*g*-SiNP were thoroughly characterized using NMR, GPC, TEM, SEM and DLS. Nanocomposite membranes were tested for their proton conductivity at different temperatures in anhydrous condition, acid holding capacity, mechanical strength, thermal and chemical stabilities.

Experimental Section

Source of the materials, synthesis of the SiNP, preparation of amine modified SiNP, RAFT agent synthesis, activation of RAFT agent, attachment of it on the surface of SiNP were reported by our group previously[33] and are described briefly in **Chapter 2** and **Appendix I**.

We have used 4-cyanopentanoicacid dithiobenzoate (CPDB) as the RAFT agent for this work. Grafting density of the RAFT agent (CPDB) on the SiNP surface was kept constant for all the particles and grafting density of CPDB attached on SiNP (SiNP-CPDB) was calculated by means of thermal gravimetric analysis and found to be 0.97 number of CPDB/nm^2 of SiNP surface. We have followed our previously reported procedure [50,59] for the synthesis of (4,4'-diphenyl ether-5,5'-bibenzimidazole) (OPBI) polymer (also described in detail in **Chapter 2**).

Synthesis of block copolymer *grafted* SiNP (BC-*g*-SiNP)

We have carried out the reactions in two different sets. In the first set (**P1**-**P3**), we have grown poly-N-vinyl imidazole (pNVI) chains on the surface of SiNP followed by chain extension with poly-N-vinyl-1,2,4-triazole (pNVT) to form block copolymer *grafted* SiNP abbreviated as pNVT-*b*-pNVI-*g*-SiNP. In the second set, we have grown pNVT chains on the surface of SiNP first and then extended the polymer chains with pNVI to form the block co-polymer *grafted* SiNPs (**P4**-**P6**) which are abbreviated as pNVI-*b*-pNVT-*g*-SiNP. In both these cases, we have varied the monomers amount to alter the chains length in such a way that the mole ratio of the first block monomer: second block monomer remains as 3:1 in all of the six cases. However, the chain length of each block was altered in both the series to obtain different size polymers though keeping the mole ratio of monomers constant to 3:1.

Into a series of Schlenk tubes containing dry DMF (5 mL), SiNP-CPDB (0.3 g, 22.71 µmol of RAFT agent), NVI (calculated amount, we have varied the amount to prepare different chain lengths of pNVI first block), CPDB (6.34 mg, 22.71 µmol), 4,4'-azobis (4-cyanopentanoic acid) (ACP) (1.27 mg, 4.54 µmol) were added. The ratio of [SiNP-CPDB]: [CPDB]: [ACP] = 1:1:0.2 was kept constant throughout all the reaction procedure. The reaction flasks were then sealed with septum and subjected to three freeze-pump-thaw cycles and backfilled with nitrogen at the end of the third cycle and were sealed properly. The Schlenk tubes were sonicated for 10 minutes and stirred for 16 hours in a pre-heated oil bath at 70 °C. After completion of 16 hours, second monomer N-vinyl-1,2,4-triazole, NVT (calculated amount, we have varied the amount of monomer in order to obtain different chain lengths of pNVT, second block) and ACP (1.27 mg, 4.54 µmol) in degassed DMF was added via cannula transfer method and then sealed properly. The reaction tubes were then heated with continuous stirring at 75 °C for another 16 hours. The [RAFT agent]: [ACP] ratio kept 1:0.2 throughout the reaction constantly. After completion of 32 hours, the reaction mixtures were quenched using liquid N_2 and exposed to air. The block copolymer *grafted* SiNP (pNVT-*b*-pNVI-*g*-SiNP)

were precipitated from large excess of THF: hexane (80:20) mixture and isolated by using the centrifugation technique. The obtained precipitate was then re-dispersed into methanol (40 mL) and centrifuged at a rate of 7000 rpm for 30 min to separate the polymer modified SiNP from the dispersion. This step was repeated thrice, and the obtained block copolymer *grafted* SiNP (BC-*g*-SiNP) were dried under vacuum at 90°C for 48 hours.

The BC-*g*-SiNP with reverse block sequence (pNVI-*b*-pNVT-*g*-SiNP) were also prepared by altering the first and second monomer sequence keeping rest of the reaction procedure and amount of reactants constant to obtain 3:1 chain length ratio of the first block: second block for all the BC-*g*-SiNP samples. We have also varied the amount of NVI and NVT monomers to prepare a series of pNVI-*b*-pNVT-*g*-SiNPs with varying chain lengths of each block. The complete procedure for the synthesis of these particles are illustrated in the **Scheme 3.1** with all detailed conditions, the polymer structure and the pictorial presentation of the block copolymer *grafted* particles.

To obtain the chain length of the first block of the copolymer attached on SiNP surface, parallel reaction sets were kept with the same compositions and quenched after completion of the first phase i.e. 16 hours. The nanoparticles were then precipitated, washed and dried under vacuum following the procedures as mentioned above. The obtained polymer modified SiNP samples were subjected to characterization along with the BC-*g*-SiNP samples. The mono-block *grafted* intermediate forms of **P1**-**P6** nanoparticles are mentioned in this article as **P1(i)**, **P2 (i)**, **P3 (i)** and so on.

P1 to **P6** samples were also utilized as nanofillers to prepare nanocomposite membranes with varying nanofiller loading amount. All the experimental procedure used for characterization of pNVI-*b*-pNVT-*g*-SiNP, pNVT-*b*-pNVI-*g*-SiNP, the intermediate compounds and the composites prepared with the OPBI are discussed in details in **Chapter 2** and **Appendix I**.

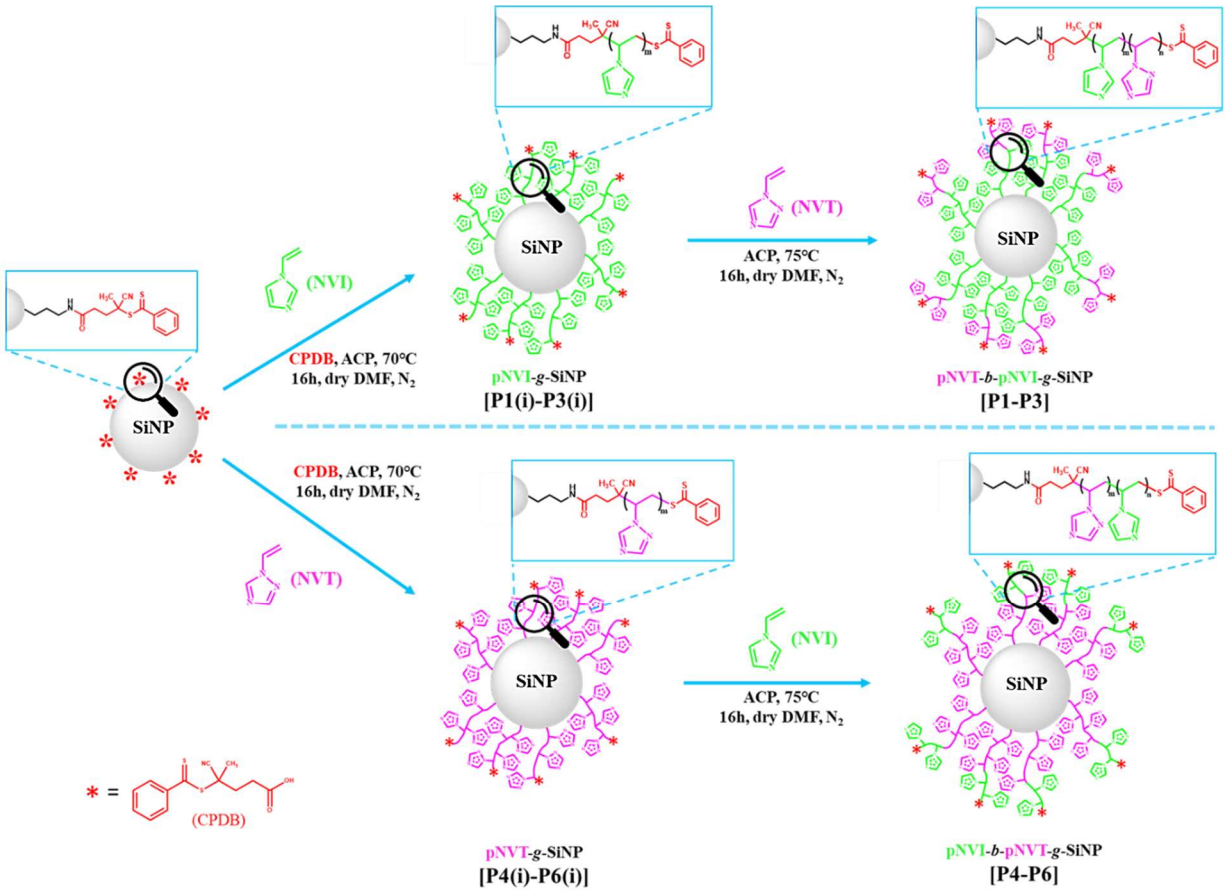

Scheme 3.1. One-pot RAFT polymerization method for the synthesis of pNVT-*b*-pNVI-*g*-SiNP (**P1-P3**) and pNVI-*b*-pNVT-*g*-SiNP (**P4-P6**). All the samples (**P1-P6**) were obtained in a one pot method by adding monomers one after another without separating the intermediate products [**P1(i)-P6(i)**]. In a separate controlled experiment **P1(i)-P6(i)** were separated and characterized.

Preparation of OPBI/ BC-*g*-SiNP Nanocomposite Membranes

Homogeneous nanocomposite membranes were prepared using solution blending technique by adding 1 wt % and 3 wt % (with respect to OPBI polymer concentration) of pNVT-*b*-pNVI-*g*- SiNP and pNVI-*b*-pNVT-*g*-SiNP which were dispersed individually in formic acid and then added into 2 wt % OPBI solution in formic acid separately. The final OPBI concentration of the solution was 1 wt %. The solution was then stirred vigorously at room temperature for 24 hours, poured into a glass petri dish and then the solution was slowly evaporated at 60 °C. The formed membrane was then peeled from the petri dish and then dried inside a vacuum oven at 100 °C to remove every little trace of the solvent molecules.

Results and Discussion

Synthesis of Block Copolymer-*g*-SiNP

Surface functionalization of SiNP is necessary to grow polymer chains on its surface via RAFT polymerization technique. Therefore, first we have covalently attached RAFT agent CPDB on the SiNP surface via a multistep process following our earlier method and a detailed description of this is presented in the **Appendix I**.[20,33] The amount of covalently bound CPDB on SiNP surface was measured by TGA analysis (**Appendix I-Figure 3.1**) and the grafting density (number of CPDB molecules/ nm^2 of SiNP surface) is found to be 0.97. We kept grafting density constant for all the samples developed in this work. The particle size of the bare SiNP was measured and found to be 47 (±3) nm in diameter by FESEM and TEM analysis and 50 nm from DLS measurement. The size of SiNP-CPDB shows increase in size: 48 (±2) nm from microscopic studies and 58 nm from DLS study (**Appendix I-Figure 3.1**). Size of the nanoparticles are measured by microscopic means showing monodisperse morphology. The particle size measured by light scattering experiment displays very low PDI (<0.1) and comparatively higher size than FESEM and TEM measurements because of the attached amine and CPDB on the particle surface which forms a hydration cell on the nanoparticle surface and we get hydrodynamic diameter of the particle in the light scattering experiments instead of the diameter of the particle in dry state.

After the attachment of RAFT agent on the SiNP surface, the block copolymer chains were grown on the SiNP surface using the procedure as depicted in **Scheme 3.1** and described in the experimental section. SI-RAFT technique was utilized on RAFT modified SiNP (SiNP-CPDB) by keeping the amount of the nanoparticle (SiNP-CPDB) constant in each case with varying the amount of monomer feed to grow polymer chains on to the nano-surface. Monomer ratio (NVI: NVT) in the feed was controlled and sequence of monomer addition was altered to obtain two different sets of BC-*g*-SiNP separately in one-pot *grafting from* approach. The amount of polymer *grafted* on the SiNP surface is obtained from the weight loss of the samples in the TGA scan (**Figure 3.1**) which were performed for all the samples of pNVT-*b*-pNVI-*g*-SiNP (**P1-P3**) and pNVI-*b*-pNVT-*g*-SiNP (**P4-P6)**. Weight loss in the temperature range up to 150 °C implies to bound and unbound moisture loss as both the block copolymer forming units are highly hydroscopic in nature. A second degradation in the temperature range 350°C-400°C for all the polymer *grafted* SiNP samples is observed. To understand this degradation, we have also cleaved the polymer chains from the **P6** polymer *grafted* SiNP and scanned in TGA

following similar experimental condition. The cleaved polymer sample shows degradation at around 350°C-400°C which indicates that the degradation at around 350°C-400°C range is due to degradation of the attached polymer chain. We have also observed that pNVI-*b*-pNVT-*g*-SiNP (**P4-P6**) samples show more weight loss compared to pNVT-*b*-pNVI-*g*-SiNP (**P1-P3**) though the attached polymer chains are of comparable length. (See the later section and **Table 1** for the molecular weight and chain length). A comparison of TGA plots of **P1** vs **P4**, **P2** vs **P5** and **P3** vs **P6** in **Figure 3.1** gives us a clear picture about their relative stability. This results also attribute to the significance of the chain sequence on the thermal stability of the block copolymer *grafted* SiNP (BC-*g*-SiNP). The TGA data of SiNP-CPDB are also compared with the weight loss of the BC-*g*-SiNP samples to calculate the amount of block copolymer *grafted* on the SiNP (in wt %) and the values are given in **Table 3.1**. We have also calculated the polymer grafting density using these data and considering the SiNP density as 2.4gm/cm^3. These values (grafting amount and grafting density) increases with the increasing chain length and also found to be marginally higher in case of **P4- P6** samples than **P1-P3** which signifies the influence of the chain sequence. It is also to be noted that for all the samples, polymer grafting density and amount of polymer in wt % much smaller that the grafting density of SiNP-CPDB (0.97, **Table 3.1**) and the amount of CPDB *grafted*. This means that all the polymerization sites on the surface of SiNP did not take part in the polymerization process.

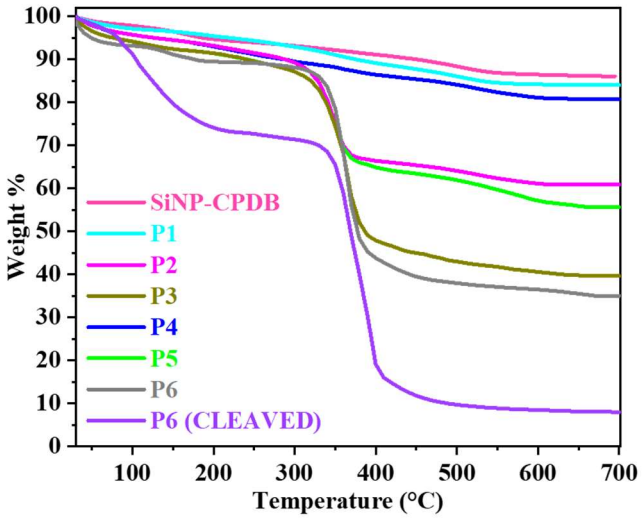

Figure 3.1. TGA plots of the block copolymer *grafted* SiNP (**P1-P6**) along with block co-polymer chain cleaved from **P6** and SiNP-CPDB.

In order to measure the molecular weight of the polymer chains *grafted* on the SiNP surface, the silica core was dissolved by HF treatment to obtain bare polymer chains for GPC

analysis as reported elsewhere [20,27,33] and schematically described in **Appendix I-Scheme 1**. The obtained GPC traces of the bare polymer chains are shown in **Figure 3.2** and the molecular weights and polydispersity (Đ) values are summarised in **Table 3.1**. The GPC results (**Figure 3.2** and **Table 3.1**) clearly show that the molecular weight ($\bar{M}_n$) increases in both the sets of copolymers from **P1** to **P3** and **P4** to **P6**. Also, in all the cases the Đ values are very narrow attributing to the successful RAFT polymerization on the surface of the SiNP. It is also to be noted that in all the cases, the obtained $\bar{M}_n$ is quite close to the targeted $\bar{M}_n$ (compare the 5th and 6th columns in **Table 3.1**). We have also performed controlled polymerization reactions to obtain the molecular weight of the polymer chains of the first block before addition of the 2nd monomer to form the block copolymer structure. In each case, the controlled batch is denoted as intermediate (**i**) such as **P1(i)**, **P2(i)** and so on. **Appendix I-Table 1** provides the complete details of the molecular weight distribution of the intermediate polymer chains and the GPC chromatographs of these intermediates are shown in **Appendix I-Figure 3.2**. All the intermediates also show the $\bar{M}_n$ variation and narrow Đ. The degree of polymerization (DP) values of each block, which are indicated in **Table 3.1** (see the numbers in the suffix of the polymer chain in the 2nd column of **Table 3.1**), are calculated from the values obtained from the molecular weight of the block copolymer and the intermediate polymers. The $\bar{M}_n$ values of intermediate polymers (**Appendix I-Table 3.1**) are subtracted from the $\bar{M}_n$ of the block copolymer (**Table 3.1**) to find the DP value of the other polymer chains. A closer look at the DP values and comparison among the various samples clearly indicate the ratio of chain length among two blocks (first block: second block) in both the cases varies approximately as 1:1 in case of **P1** and **P4**, 2:1 for **P2** and **P5** and 3:1 in case of **P3** and **P6** even though in all the cases monomers mole feed ratio was kept as 3:1 (see the experimental section). This means as the molecular weight of the first block increases, the growth of the second block slows down relatively. In other words, the reactivity of the second monomer reduces with the increasing chain length of the first block. This may be due to the increase in the dormant active site with increasing chain length of the first block. It is to be noted that the molecular weight data are in good agreement with the increasing weight loss and higher grafting of polymer from **P1** to **P3** and **P4** to **P6** as seen from TGA studies (**Figure 3.1** and **Table 3.1**). Overall, these results clearly demonstrate the formation of the unique architecture of the block copolymer chain grown on the SiNP surface comprising of nitrogen containing aromatic heterocyclic pendent rings.

Table 3.1. Summary of various physical data of synthesized block copolymer *grafted* SiNP.

Sample name	Sample type[a]	Grafting amount polymer (%)[b]	Polymer grafting density[c]	Targeted $\bar{M}_n$	$\bar{M}_n$[d]	Đ[e]	Size (nm)		Poly dispersity in size[g]
							TEM	DLS[f]	
-	SiNP-CPDB	-	0.97		-	-	48±2	58	0.18
P1	$pNVT_{67}$-*b*-$pNVI_{77}$-*g*-SiNP	2.38	0.02	10,000	13600	1.06	52±3	97	0.09
P2	$pNVT_{70}$-*b*-$pNVI_{140}$-*g*-SiNP	29.26	0.19	20,000	19759	1.03	57±2	119	0.07
P3	$pNVT_{97}$-*b*-$pNVI_{270}$-*g*-SiNP	53.89	0.20	40,000	34622	1.01	61±4	159	0.24
P4	$pNVI_{67}$-*b*-$pNVT_{73}$-*g*-SiNP	6.16	0.06	10,000	13179	1.18	50±3	103	0.39
P5	$pNVI_{75}$-*b*-$pNVT_{146}$-*g*-SiNP	35.26	0.21	20,000	20930	1.15	54±3	118	0.04
P6	$pNVI_{95}$-*b*-$pNVT_{286}$-*g*-SiNP	59.3	0.21	40,000	36073	1.31	62±3	165	0.23

[a] describes the chain sequence of each block and the degree of polymerization for each block included in the suffix which are obtained from the molecular weight measurement, [b] estimated from the TGA analysis and [c] expressed as amount of polymer chains/nm^2 of SiNP, [d] and [e] determined by gel permeation chromatography, and [f, g] obtained from DLS analysis in aqueous dispersion.

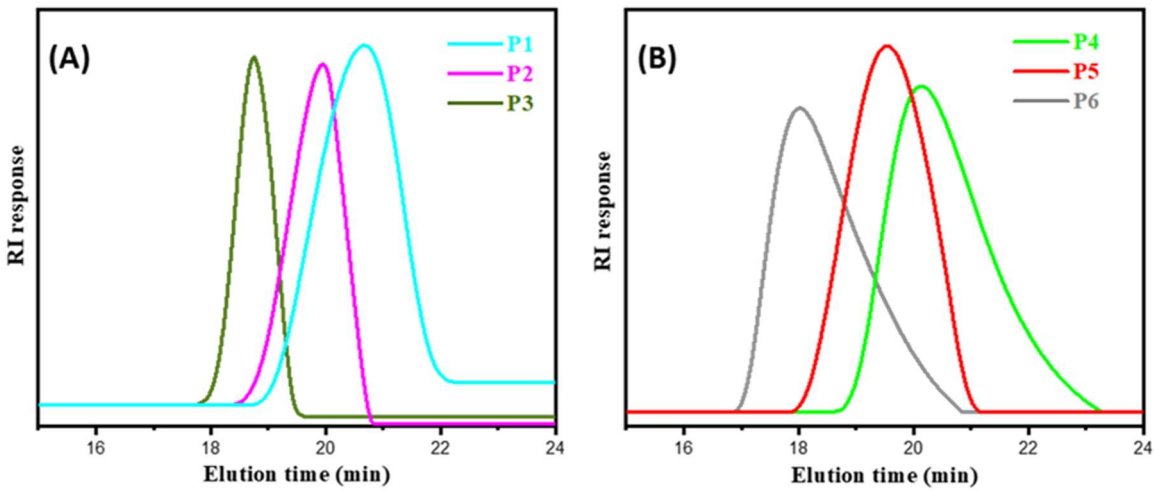

Figure 3.2. GPC traces of polymer chains eluted in DMF/LiBr solvent. Bare polymer chains from the samples were obtained after cleaving the chains from polymer *grafted* SiNPs by using aqueous HF treatment as described in **Appendix I-Scheme 3.1**. **(A) P1-P3** samples refer to pNVT-*b*-pNVI-*g*-SiNPs and **(B) P4-P6** samples are for the pNVI-*b*-pNVT-*g*-SiNPs.

The grafting of block copolymer on SiNP surface with altering block sequence is further confirmed by ^{1}H-NMR and ^{13}C-NMR analysis. NMR data were collected from the bare block copolymer chains obtained after HF treatment (**Appendix I-Scheme 3.1**). The ^{1}H-NMR spectra along with the peak assignments are shown in **Appendix I-Figure 3.3**. The resonance of imidazole protons (c, d, e) are clearly observed in the range of 6.6-7.5 ppm whereas the triazole protons (f, g) being more de-shielded than imidazole protons appeared in the ppm range of 7.6-8.2. The peaks appearing at 1.7-2.3 ppm and 2.8-3.2 ppm correspond to CH_2 and CH protons, respectively of the block copolymer chains which proves the successful polymerization in yielding the block copolymer chains of pNVI-*b*-pNVT and pNVT-*b*-pNVI *grafted* on the SiNP surface. The observed splitting of CH and CH_2 protons of polymer backbone is due to the chain configuration (different chain tacticities) of the block copolymer chains. The amount of pNVI and pNVT *grafted* on SiNP are calculated from ^{1}H-NMR spectra and the ratio is well matched with the DP ratio tabulated in **Table 3.1**. As can be seen from **Appendix I-Figure 3.3** spectral integration of **P3** and **P6** polymers, the ratio of pNVI to pNVT for **P3** is 3:1 and the same is found for pNVT to pNVI (see the integral ratio as highlighted in the **Figure 3.8** by different color). ^{13}C-NMR spectra and the peak assignments are shown in **Appendix I-Figure 3.4** displays all the carbons of the copolymer chains and hence the successful formation of block copolymer structure is proved. IR spectrum of a representative sample **P6** (**Appendix I-Figure 3.5**) shows characteristic peak at 3416 cm^{-1} and 3108 cm^{-1}

which corresponds to non-hydrogen-bonded N-H stretching frequency and C-H (sp^2) stretching frequency, respectively. Peak at 2929 cm^{-1} is observed due to the stretching frequency of C-H (sp^3) bond present in the polymer chain. The peak at 1659 and 1434 cm^{-1} are the characteristic peaks of C=N and C-N bonds, respectively. 1276 cm^{-1} peak represents the characteristic ring N-N bond stretching of NVT.[18]

A distinguishable change in the morphology (both in FESEM and TEM images as shown in **Figure 3.3**) of the BC-*g*-SiNP is observed in comparison to SiNP-CPDB. The later shows smoother surface (**Appendix I-Figure 3.1**) while the former (BC-*g*-SiNP) samples show rough surface and also the agglomeration is observed in the later cases. This phenomenon implies confirmed grafting of polymer chain on the SiNP surface which is well agreement with our earlier recent observations for various kind of polymer *grafted* SiNP.[20,33,54] **Figure 3.3** images clearly show that the SiNP surface when *grafted* with polymer chains of lower molecular weight, the tendency of aggregation is negligible but in case of SiNPs *grafted* with polymer chains of higher molecular weight shows significant tendency to aggregate and show worm like morphology (see the TEM images **P3**, **P5**, **P6**) and this may be due to higher interaction between *grafted* polymer chains. This observation is most prominent in the case of **P3** and **P6** samples those which are having the highest molecular weight polymers among all the samples. The increase in particle size from 48 (±2) nm (**SiNP-CPDB**) to 52(±3) nm (**P1**) to 61 (±4) (**P3**) and similar increase from **P4** to **P6** are clearly visible in FESEM and TEM images (**Figure 3.3**) and also tabulated in **Table 3.1**. These observations also confirm the successful surface grafting of polymer chains on SiNP with variable chain length.

The **P1-P6** particles are inorganic-organic hybrid nanoparticles consisting of inorganic silica cores of same sizes but the outer shell contains polymer chains of different chain lengths. If the outer polymer shell is hydrophilic then the particles should swell in aqueous medium. In order to find this, the particles were subjected to dynamic light scattering (DLS) experiment under aqueous dispersion. The DLS plots are shown in **Appendix I-Figure 3.6** and the particle size and polydispersity are included in the **Table 3.1**. All the particles show two to three-fold increase in size (hydrodynamic diameter) which is directly proportional with increase in the chain length of the *grafted* block copolymer chains. These results provide us an indirect proof of successful grafting of hydrophilic polymer chains of variable chain length on the SiNP surface.

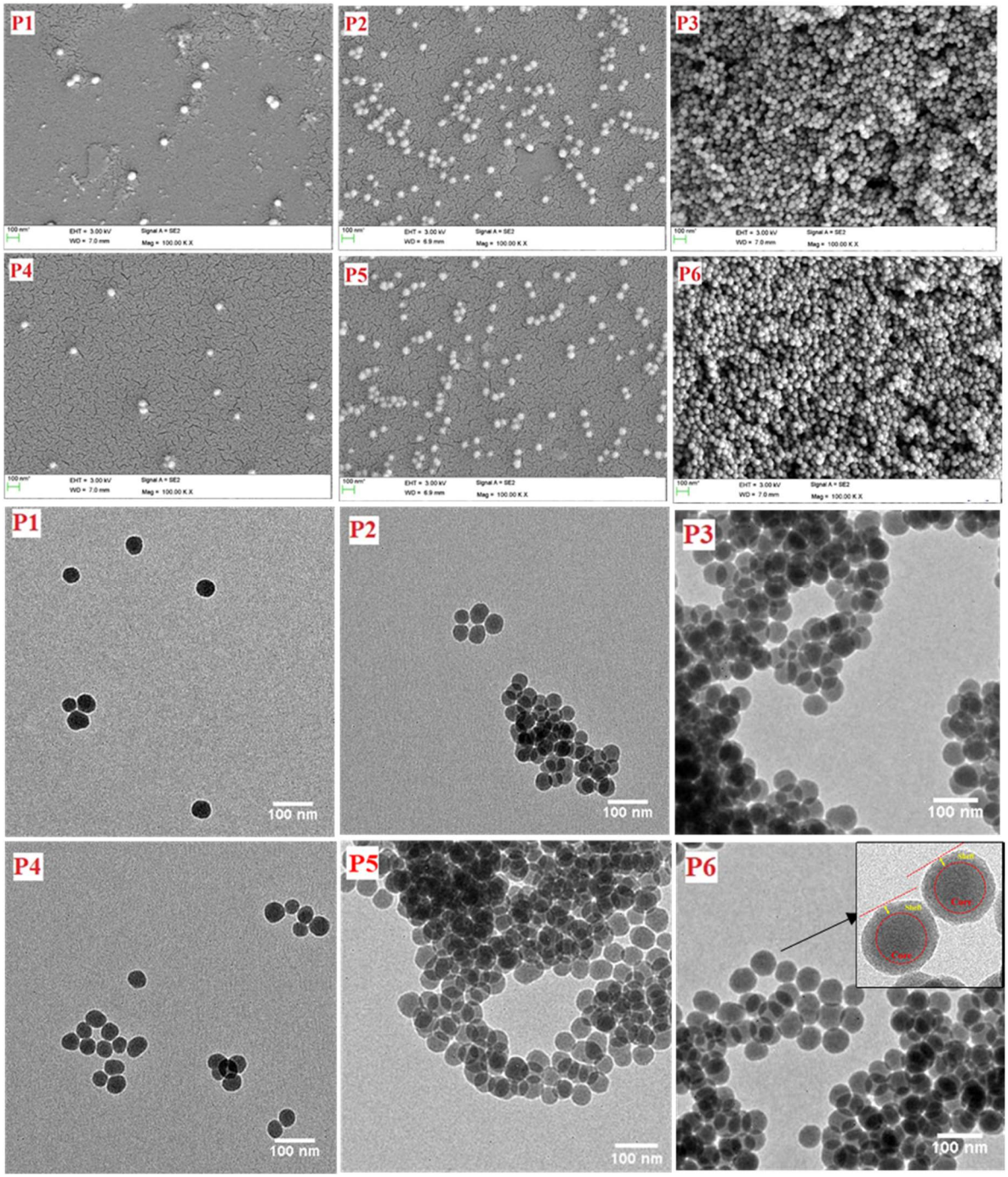

Figure 3.3. FESEM images (top two rows) and TEM images (bottom two rows) of all the block copolymer *grafted* SiNP samples. Inset: a magnified particle to show the core-shell morphology.

We have also calculated the distance (D) between neighbouring *grafted* block copolymer chains and radius of gyration (R_g) of the *grafted* copolymer chains from the grafting density and degree of polymerization, respectively and these values are summarized in the **Appendix I-Table 3.2** along with D/R_g values. D values drastically falls from **P1** to **P2** & **P3** and similarly from **P4** to **P5** & **P6**, attributing the effect of chain length. Also, much lower D

value of **P4** compared to **P1** even though they are having comparable chain length signifies the influence of block copolymer chain sequence. The increasing R_g value with increasing $\bar{M}_n$ is expected. The D/R_g values of all the samples are less than 2 indicating the brush type morphology of the BC-*g*-SiNP samples.[60,61,62] As noted earlier, SiNP forms the core and block copolymer chain forms the shell in the BC-*g*-SiNP. The increasing R_g and decreasing D/R_g values from **P1** to **P3** and **P4** to **P6** attribute the change in the shell thickness with increasing chain length of the block copolymer. Core-shell morphology is also visible from the zoomed TEM image (inset of **Figure 3.3** of **P6**) though the separation between core-shell is not greatly clear-which may be due to agglomeration of the particles as seen in **Figure 3.3** owing to the strong interparticle interaction. It is also to be noted that D/R_g values are not exactly identical for the samples with similar $\bar{M}_n$ values between two sets (**P1-P3** and **P4-P6**) indicating the influence of block copolymer chain sequence.

OPBI/Block copolymer-*g*-SiNP Nanocomposite Membrane

We have prepared nanocomposite membranes by mixing each nanoparticle with two different concentrations (1 wt% and 3 wt %) with OPBI polymer by solution blending process. Then, we have studied thermal stability, proton conductivity, morphology and mechanical strengths of these **OPBI/BC-*g*-SiNP** nanocomposite membranes. Visual observations clearly indicated the formation of homogeneous membrane and FT-IR study of the nanocomposite membrane confirms the interactions between the OPBI and BC-*g*-SiNP. FT-IR spectra of representative nanocomposite membranes along with pristine **OPBI** and **P6** are shown in **Appendix I-Figure 3.7**. In case of nanocomposite samples, the non-hydrogen bonded N-H stretching of OPBI at 3416 cm^{-1} shifted to lower frequency at 3393 cm^{-1} and also becomes broad due to formation of specific interaction between block copolymer chains and OPBI polymer. The self-associated N-H peak at 3147 cm^{-1} is also shifted to higher frequency at 3177 cm^{-1} which can be attributed to the weakening of N-H-N hydrogen bonding of the OPBI chain owing to the interaction with the copolymer chain of the nanofiller. Hence, from the IR studies it is clearly evident that the N-H functionalities of OPBI polymer take part in the interaction with the block copolymer chains consisting of pNVI and pNVT moieties upon blending. Also spectral broadening at 1237 cm^{-1} along with the red shifts of 1276 cm^{-1} and 1434 cm^{-1} peaks to 1290 cm^{-1} and 1442 cm^{-1}, respectively indicate the interaction between OPBI polymer and block copolymer chains. The peak at 1659 cm^{-1} shows substantial broadening and shifting towards lower frequency attributes the presence of a N-H···N type interaction in the nanocomposites.[18]

Thermogravimetric analysis (TGA) plot (**Appendix I-Figure 3.8**) of the nanocomposite membranes shows that the stability decreases with the increasing filler loading and block copolymer chain length. If we just compare the remaining weight % at 700°C, then the order of stability of the composites is **OPBI/P1>OPBI/P2>OPBI/P3** and for the other series it is **OPBI/P4>OPBI/P5>OPBI/P6**. Though the stability of the nanocomposite membranes is little lower than the pristine OPBI but this much stability is sufficient for the use as PEM.

The dynamical mechanical analysis (DMA) was performed for OPBI and all the nanocomposite membranes to find out the effect of nanofiller type and loading on the membrane thermomechanical properties. A huge reinforcement of mechanical strength is observed for all the nanocomposite membranes for all the loadings over the complete temperature range compared to pristine OPBI [**Figure 3.4(A)** and **3.4(B)**]. The reinforcement is more prominent in the glassy state than the rubbery state, which shows different nature of interaction between OPBI and the nanofiller in these two different states. The interactions between the nanofiller and the OPBI is the key factor for high storage modulus values. However, it is to be noted that both the loading and the block copolymer chain sequence show improvement in storage modulus to a similar extent. But most importantly, a huge increment in modulus is observed when the block copolymer chain length ($\bar{M}_n$) increases irrespective of the chain sequence. For example, OPBI/P1(3%) sample storage modulus at 150°C is found to be 4500 MPa however for OPBI/P3(3%) sample this value is ~6500 MPa. This means almost 2000 MPa (about 50%) increase in modulus when $\bar{M}_n$ of *grafted* block copolymer of SiNP increase from 13600 Da (**P1**) to 34622 Da (**P3**). Similar, results are seen in case of composite with **P4** and **P6 [Figure 3.4(B)**]. In several earlier works, we have observed higher T_g of nanocomposite membranes compare to pristine OPBI because of the decrease in the free volume fraction of the polymer in the blend and hence higher temperature is required for the mobility of the free volume segments of the polymer chain[56–58] But in the recent study, all the nanocomposite membranes show nearly similar T_g like OPBI as observed from the loss modulus versus temperature plot in **Figure 3.4**(**C**) and (**D**) and also **Appendix I-Figure 3.9** (tan δ vs temperature plots). This may be explained in terms of very small loading of nanofiller with respect to OPBI and the nature of interaction between them. Since the *grafted* polymer chain and the matrix polymer (OPBI) have many similarities in terms of their functionality (both have a lot of nitrogen containing heterocycles) hence, they are most likely to interact very

strongly resulting almost single-phase material and hence insignificant change in T_g is observed.

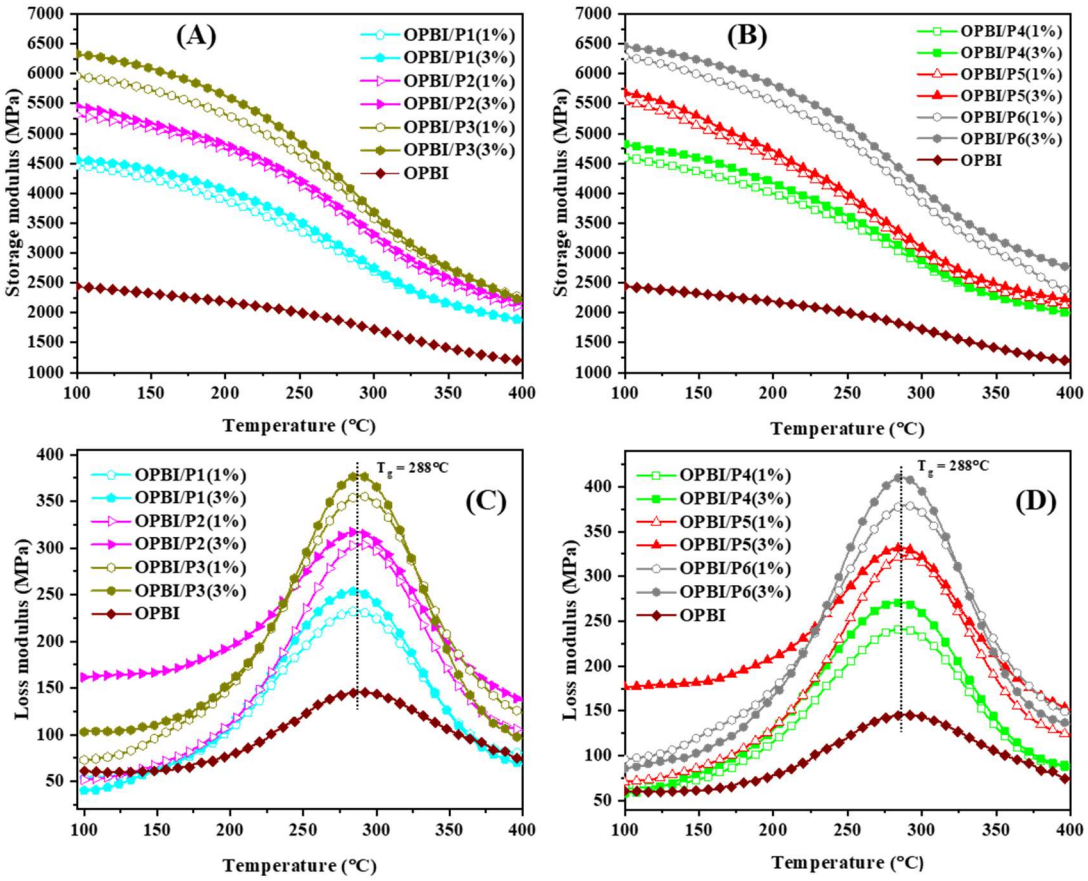

Figure 3.4. Comparison of thermo-mechanical properties: storage modulus versus temperature plots (top panel) and loss modulus vs. temperature plots (bottom panel) for all the nanocomposite membranes with 1 wt % and 3 wt % loading of nanofiller **P1-P6**. T_g values [the peak temperature as shown in (**C**) and (**D**) plots using a dotted vertical line] are also indicated in the figure along with the sample name. tan δ vs temperature plots are shown in **Appendix I-Figure 3.9**.

BC-*g*-SiNP and OPBI which are needed to prepare the nanocomposite membranes do not show any crystalline peaks but on the other hand, the nanocomposite membranes show very sharp crystalline peaks **[Figure 3.5(A)]**. The appearance of the peaks attributes to the formation of crystalline order in the nanocomposite membranes. Similar observations were previously reported by us and other researchers when polymer nanocomposites were prepared made with surface modified SiNPs as nanofiller.[20] In the current cases, we have observed sharp and intense peaks than our previous results where SiNP surface modified with smaller polymer chains of pNVI, indicating higher degree of crystalline order and this may be due to the

presence of block copolymer chain on the surface of SiNP consisting of imidazole and 1,2,4-triazole pendent rings which interacts with OPBI in much greater extent. It is expected that strong interaction between BC-*g*-SiNP with OPBI chain is the driving force for the formation of such crystalline order. We have observed earlier that with the increase in nanofiller loading the ordered structure increases significantly which influences various properties especially proton conductivity significantly.[20] We believe that this high crystallinity can play a significant role for obtaining high proton conductivity values of these nanocomposite membranes which is discussed in the later section of this article.

The morphology of the nanocomposite membranes after cryogenic breaking of the membranes in liquid N_2 is studied using FESEM. Porous features morphology is observed in case of nanocomposite membranes and the intersection shows thick fibrous kind of morphology whereas pristine OPBI is almost feature less [**Figure 3.5 (B)**]. The modified silica nanoparticles are well dispersed and the nanofillers are visible clearly in the images as indicated by circle [**Figure 3.5 (C)** and **(D)**]. The entirely different morphology of nanocomposite than OPBI is responsible for the formation of crystalline character of the former which is seen in PXRD **[Figure 3.5(A)]**. Further, we have taken TEM image of **OPBI/P6** (3 wt%) **[Figure 3.6(A)]**, which clearly shows that the BC-*g*-SiNP is very well dispersed within the OPBI matrix. This is due to the fact that hydrophilic blocks of pNVI and pNVT on the surface of the nano particles are interacting quite well with the OPBI and hence well dispersed in the matrix. The current observation is quite different than our earlier observation where we have observed that the OPBI composite with surface modified SiNP usually results a self-assembled anisotropic morphology but here we do not see such morphology rather we see very well dispersed morphology. This may be due to the strong interaction between similar kind of functionality present both in surface *grafted* chain and OPBI.

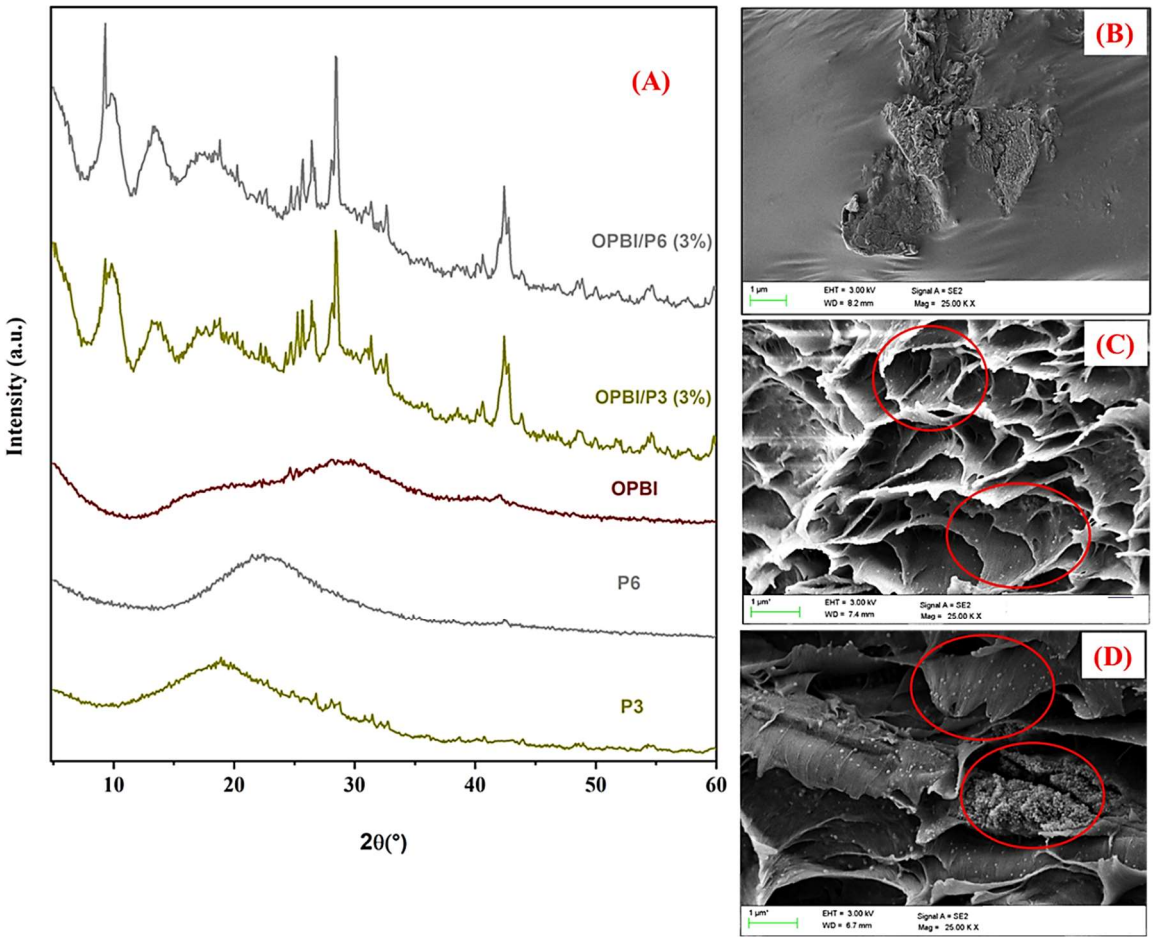

Figure 3.5. (A) PXRD patterns of OPBI, BC-*g*-SiNPs (**P3** and **P6**) and nanocomposite membranes **OPBI/P3** (3%) and **OPBI/P6** (3%) displaying the formation of crystalline ordering in case of nanocomposite membranes. FESEM images of OPBI **(B)**, **OPBI/P6** (1%) **(C)** and **OPBI/P6** (3%) **(D)**.

Acid Loaded Nanocomposite PEM

All the OPBI/BC-*g*-SiNP nanocomposite membranes prepared in this work were converted to proton exchange membrane (PEM) by loading phosphoric acid (PA) into them. The amount of PA loaded on each PEM expressed as number of PA moles/OPBI repeat unit is given in **Appendix I-Table 3.3**. Few important observations must be noted from **Appendix I-Table 3.3** data: (i) no increase in PA loading in nanocomposite in comparison to pristine OPBI, (ii) almost no change in PA loading with increasing nanofiller content and (iii) no effect on PA loading because of increasing chain length ($\overline{M_n}$) of *grafted* chain and also altering chain sequence. Though these observations were quite unexpected as per our previous experience[8,20,54,56-58] but these observations hints a completely new kind of structural interface between nanoparticles and OPBI owing to the strong interactions between them.

The conductivity vs. temperature plots of PA doped pristine OPBI and the nanocomposite PEM are shown in **Figure 3.6(B)** and **Appendix I-Figure 3.10**. In our previous works, we have reported that when OPBI is mixed with 3 wt% of pNVI-*g*-SiNP ($\overline{M_n}$= 7300 Da) to form nanocomposite PEM that showed conductivity 0.15 S cm^{-1} at 180°C.[20] In this work, our aim is to achieve higher proton conductivity by utilizing strategically modified dual hydrophilic block copolymer, consisting of basic imidazole and 1,2,4-triazole functionality, *grafted* on SiNP as potential nanofiller with OPBI polymer. We have achieved 0.278 S cm^{-1} as highest proton conductivity for **OPBI/P6** (3 wt %) at 180°C which is the highest value achieved so far in case of **OPBI/SiNP** nanocomposite-based PEM. The conductivity at 180°C for all the membranes are listed in **Table S3**. All the conductivity data presented in **Figure 3.6(B)**, **Appendix I-Table 3.3** and **Appendix I-Figure 3.10** clearly pointed out three important facts: (1) higher nanofiller loading increases conductivity [for example **OPBI/P3**(1%) sample shows 0.21 S/cm at 180°C which increases to 0.247 S/cm in case of **OPBI/P3**(3%) and so on], (2) a significant increase in conductivity is observed when chain length of the *grafted* copolymer increases [**OPBI** with 3 wt % **P4** loading shows conductivity 0.2 S/cm at 180°C whereas when loaded with 3 wt % **P6** the conductivity increases to 0.278 S/cm at 180°C] and (3) the chain sequence of block copolymer also plays a role though not so significantly - a comparison of data of composites with **P1** to **P3** against **P4** to **P6** reveals that quite clearly. Hence, overall, from the above discussion, it can be said that the surface *grafted* block copolymer chain type, chain length and chain sequence have significant influence in conductivity behaviour of these PEM which may be driven by the nature of interactions between the OPBI and surface *grafted* block copolymer chains.

Few representative membranes were subjected to PA leaching test in order to find out the acid loading capacity of these nanocomposite PEMs. **Figure 3.6(C)** clearly displays less leaching in case of nanocomposite membranes than pristine OPBI. This is because of the basic character of pNVI and pNVT present in nanocomposite membranes which is holding the PA more tightly. It is also noted that less (though not so drastic) leaching of PA with increase in chain length of *grafted* block copolymer chains (**P4** to **P6**) in nanofillers. We believe that the block copolymer of pNVI and pNVT chains on SiNP surface increases the basic nature of the SiNP surface which in turn helps to achieve lower leaching of doped PA than our earlier reported[20] pNVI-*g*-SiNP nanocomposite PEM and hence results in much higher proton conductivity of the nanocomposite PEM studied in this work.

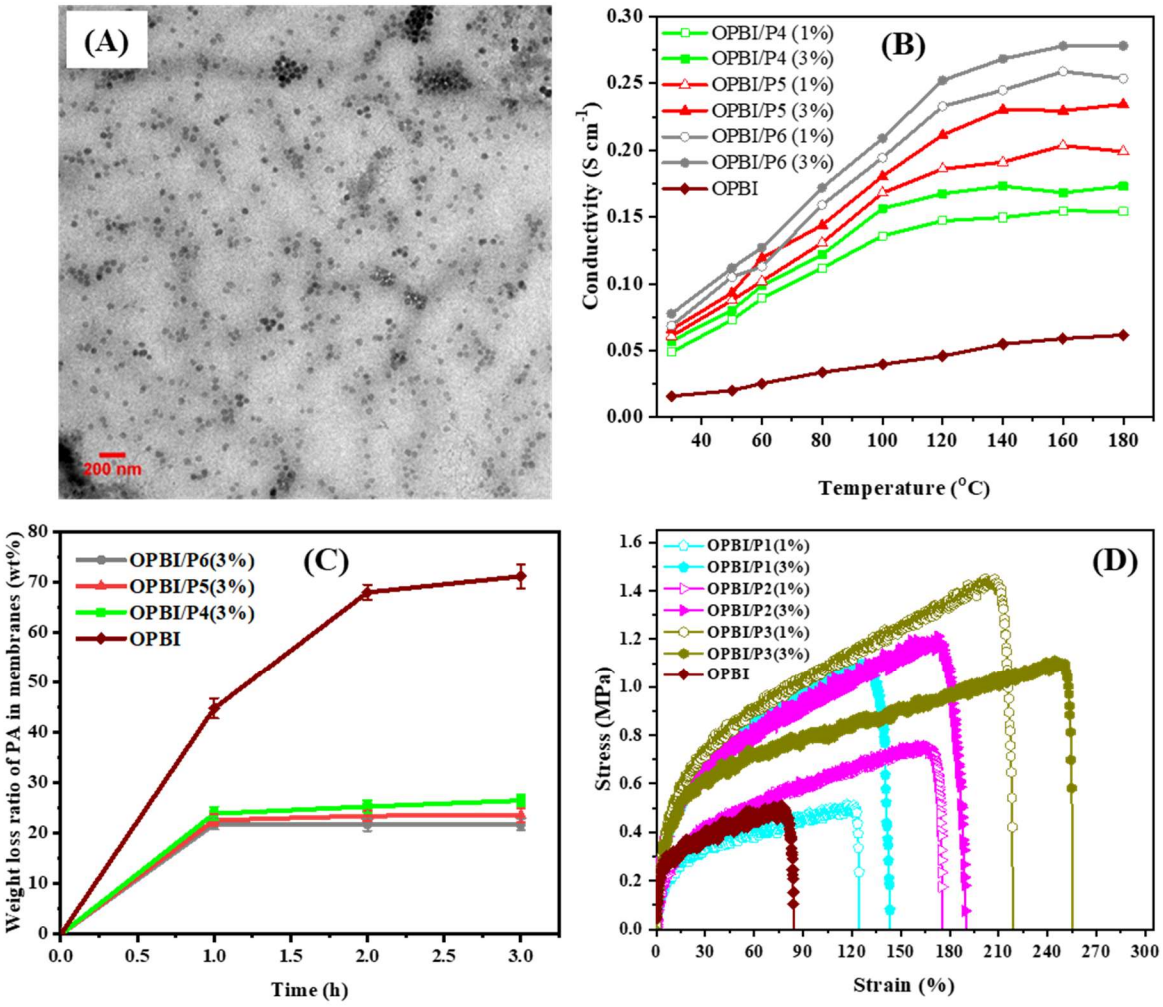

Figure 3.6. (A) TEM image of **OPBI/P6** (3%) nanocomposite membrane. A dilute nanocomposite solution was drop casted on TEM grid for TEM imaging. **(B)** Proton conductivity vs. temperature plot for OPBI and all the nanocomposite membranes with 1 and 3 wt % loading of nanofiller **P4-P6**. **(C)** Leaching study (weight loss ratio vs. time) plot for OPBI and 3 wt % membranes of **P4-P6** with OPBI. **(D)** Stress -strain profiles of PA loaded OPBI and PA loaded nanocomposite membranes of various loadings of **P1-P3.**

We have observed a huge improvement in tensile properties in case of PA loaded nanocomposite membranes when compared to PA loaded pristine OPBI [**Figure 3.6(D)** and **Appendix I-Figure 3.11**]. We have also found increase in tensile strength from 1 to 3 wt % loading in each case. The best result is observed in the case of **P3** and **P6** composite with almost three-fold increase in tensile strength when compared with pristine OPBI. Also, tensile properties increase with the increasing molecular weight of the *grafted* chains. This can be concluded that the nanostructure formation leading to the strengthening of the nanocomposite membranes. Various tensile properties like tensile strength (MPa) and elongation at break (%)

are listed in **Appendix I-Table 3.4**. The data of **Appendix I-Table 3.4** clearly confirms significant reinforcement of mechanical strength in case of nanocomposite PEM.

Conclusion

We have demonstrated here in this chapter, the successful grafting of block copolymer chains on the SiNP surface by using one pot *grafting from* RAFT polymerization technique. The block copolymer contains nitrogen enriched aromatic heterocyclic pendent rings of imidazole and 1,2,4 triazole moiety which resulted in the increase in basic character of the particles. NMR, GPC, TGA, DLS and microscopic studies proved the successful formation of core (silica)-shell (polymer) inorganic-organic hybrid nanomaterial with narrow dispersity. The block copolymer which was grown on the silica nanoparticle surface showed a unique sequential block architecture. The hybrid nanomaterials were mixed with OPBI with varying wt % to form nanocomposite membranes which were tested extensively upon PA doping for proton conduction and mechanical properties. The dangling of N-heterocyclic pendent rings, interacting with phosphoric acid molecules by making it less labile and ensures better proton hopping among the proton conduction channels. Thus, the membranes showed high proton conductivity, mechanical strength and less acid leaching which made the membranes potential candidate for the use in PEM fuel cell. We believe that, this strategically fine-tuned silica surface can provide a new path to develop future nanofiller to improve the properties of polymer nanocomposites.

Reference

(1) Elwan, H. A.; Mamlouk, M.; Scott, K. A Review of Proton Exchange Membranes Based on Protic Ionic Liquid/Polymer Blends for Polymer Electrolyte Membrane Fuel Cells. *J. Power Sources* **2021**, *484*, 229197.

(2) Daud, W. R. W.; Rosli, R. E.; Majlan, E. H.; Hamid, S. A. A.; Mohamed, R.; Husaini, T. PEM Fuel Cell System Control: A Review. *Renew. Energy* **2017**, *113*, 620–638.

(3) Walkowiak-Kulikowska, J.; Wolska, J.; Koroniak, H. Polymers Application in Proton Exchange Membranes for Fuel Cells (PEMFCs). *Phys. Sci. Rev.* **2017**, *2*, 1–34.

(4) Zhang, H.; Shen, P. K. Recent Development of Polymer Electrolyte Membranes for Fuel Cells. *Chem. Rev.* **2012**, *112*, 2780–2832.

(5) Kim, S.-K.; Choi, S.-W.; Jeon, W. S.; Park, J. O.; Ko, T.; Chang, H.; Lee, J.-C. Cross-Linked Benzoxazine–Benzimidazole Copolymer Electrolyte Membranes for Fuel Cells at Elevated Temperature. *Macromolecules* **2012**, *45*, 1438–1446.

(6) Mader, J. A.; Benicewicz, B. C. Sulfonated Polybenzimidazoles for High Temperature

PEM Fuel Cells. *Macromolecules* **2010**, *43*, 6706–6715.

(7) Qingfeng, L.; Hjuler, H. A.; Bjerrum, N. J. Phosphoric Acid Doped Polybenzimidazole Membranes: Physiochemical Characterization and Fuel Cell Applications. *J. Appl. Electrochem.* **2001**, *31*, 773–779.

(8) Koyilapu, R.; Subhadarshini, S.; Singha, S.; Jana, T. An In-Situ RAFT Polymerization Technique for the Preparation of Poly(N-Vinyl Imidazole) Modified Cloisite Nanoclay to Develop Nanocomposite PEM. *Polymer.* **2021**, *212*, 123175.

(9) Annenkov, V. V.; Danilovtseva, E. N.; Tenhu, H.; Aseyev, V.; Hirvonen, S.-P.; Mikhaleva, A. I. Copolymers of 1-Vinylimidazole and (Meth)Acrylic Acid: Synthesis and Polyelectrolyte Properties. *Eur. Polym. J.* **2004**, *40*, 1027–1032.

(10) Beghdadi, S.; Miladi, I. A.; Addis, D.; Romdhane, H. Ben; Bernard, J.; Drockenmuller, E. Synthesis and Polymerization of C-Vinyl- and N-Vinyl-1,2,3-Triazoles. *Polym. Chem.* **2012**, *3*, 1680–1692.

(11) Kizhnyaev, V. N.; Pokatilov, F. A.; Vereshchagin, L. I. Carbochain Polymers with Oxadiazole, Triazole, and Tetrazole Cycles. *Polym. Sci. Ser. C* **2008**, *50*, 1–21.

(12) Yin, K.; Zhang, Z.; Yang, L.; Hirano, S.-I. An Imidazolium-Based Polymerized Ionic Liquid via Novel Synthetic Strategy as Polymer Electrolytes for Lithium Ion Batteries. *J. Power Sources* **2014**, *258*, 150–154.

(13) Unal, H. I.; Erol, O.; Gumus, O. Y. Quaternized-Poly(N-Vinylimidazole)/Montmorillonite Nanocomposite: Synthesis, Characterization and Electrokinetic Properties. *Colloids Surfaces A Physicochem. Eng. Asp.* **2014**, *442*, 132–138.

(14) Bozkurt, A. Proton Conducting Blends of Poly(4-Vinylimidazole) with Phosphoric Acid. *Solid State Ionics* **2001**, *138*, 259–265.

(15) Fodor, C.; Gajewska, B.; Rifaie-Graham, O.; Apebende, E. A.; Pollard, J.; Bruns, N. Laccase-Catalyzed Controlled Radical Polymerization of N-Vinylimidazole. *Polym. Chem.* **2016**, *7*, 6617–6625.

(16) Yao, K.; Wang, Z.; Wang, J.; Wang, S. Biomimetic Material—Poly(N-Vinylimidazole)–Zinc Complex for CO2 Separation. *Chem. Commun.* **2012**, *48*, 1766.

(17) Sen, U.; Bozkurt, A.; Ata, A. Nafion/Poly(1-Vinyl-1,2,4-Triazole) Blends as Proton Conducting Membranes for Polymer Electrolyte Membrane Fuel Cells. *J. Power Sources* **2010**, *195*, 7720–7726.

(18) Hazarika, M.; Jana, T. Proton Exchange Membrane Developed from Novel Blends of Polybenzimidazole and Poly(Vinyl-1,2,4-Triazole). *ACS Appl. Mater. Interfaces* **2012**, *4*, 5256–5265.

(19) Feng, K.; Liu, L.; Tang, B.; Li, N.; Wu, P. Nafion-Initiated ATRP of 1-Vinylimidazole for Preparation of Proton Exchange Membranes. *ACS Appl. Mater. Interfaces* **2016**, *8*,

11516–11525.

(20) Kutcherlapati, S. R.; Koyilapu, R.; Jana, T. Poly(N -Vinyl Imidazole) *Grafted* Silica Nanofillers: Synthesis by RAFT Polymerization and Nanocomposites with Polybenzimidazole. *J. Polym. Sci. Part A Polym. Chem.* **2018**, *56*, 365–375.

(21) Wu, L.; Glebe, U.; Böker, A. Surface-Initiated Controlled Radical Polymerizations from Silica Nanoparticles, Gold Nanocrystals, and Bionanoparticles. *Polym. Chem.* **2015**, *6*, 5143–5184.

(22) Zheng, Y.; Wang, L.; Lu, L.; Wang, Q.; Benicewicz, B. C. PH and Thermal Dual-Responsive Nanoparticles for Controlled Drug Delivery with High Loading Content. *ACS Omega* **2017**, *2*, 3399–3405.

(23) Zheng, C.; Zhou, Y.; Zhang, H. Facile Preparation of Well-Defined Uniform Hydrophilic Hairy Hollow Functional Polymer Micro- and Nanoparticles. *ACS Appl. Polym. Mater.* **2020**, *2*, 220–233.

(24) Tian, J.; Huang, B.; Zhang, W. Precise Self-Assembly and Controlled Catalysis of Thermoresponsive Core–Satellite Multicomponent Hybrid Nanoparticles. *Langmuir* **2018**, *35*, 266–275.

(25) Zhu, T.; Anisur Rahman, M.; C. Benicewicz, B. Synthesis of Well-Defined Polyolefin *Grafted* SiO2 Nanoparticles with Molecular Weight and Graft Density Control. *ACS Macro Lett.* **2020**, *9*, 1255–1260.

(26) Li, M.; Fromel, M.; Ranaweera, D.; Rocha, S.; Boyer, C.; W. Pester, C. SI-PET-RAFT: Surface-Initiated Photoinduced Electron Transfer-Reversible Addition–Fragmentation Chain Transfer Polymerization. *ACS Macro Lett.* **2019**, *8*, 374–380.

(27) Li, Y.; Benicewicz, B. C. Functionalization of Silica Nanoparticles via the Combination of Surface-Initiated RAFT Polymerization and Click Reactions. *Macromolecules* **2008**, *41*, 7986–7992.

(28) Ohno, K.; Ma, Y.; Huang, Y.; Mori, C.; Yahata, Y.; Tsujii, Y.; Maschmeyer, T.; Moraes, J.; Perrier, S. Surface-Initiated Reversible Addition–Fragmentation Chain Transfer (RAFT) Polymerization from Fine Particles Functionalized with Trithiocarbonates. *Macromolecules* **2011**, *44*, 8944–8953.

(29) Chiefari, J.; Chong, Y. K. (Bill); Ercole, F.; Krstina, J.; Jeffery, J.; Le, T. P. T.; Mayadunne, R. T. A.; Meijs, G. F.; Moad, C. L.; Moad, G.; Rizzardo, E.; Thang, S. H. Living Free-Radical Polymerization by Reversible Addition−Fragmentation Chain Transfer: The RAFT Process. *Macromolecules* **1998**, *31*, 5559–5562.

(30) Perrier, S.; Takolpuckdee, P. Macromolecular Design via Reversible Addition-Fragmentation Chain Transfer (RAFT)/Xanthates (MADIX) Polymerization. *J. Polym. Sci. Part A Polym. Chem.* **2005**, *43*, 5347–5393.

(31) Barner-Kowollik, C.; Perrier, S. The Future of Reversible Addition Fragmentation Chain Transfer Polymerization. *J. Polym. Sci. Part A Polym. Chem.* **2008**, *46*, 5715–

5723.

(32) Moad, G.; Rizzardo, E.; Thang, S. H. Living Radical Polymerization by the RAFT Process – A Third Update. *Aust. J. Chem.* **2012**, *65*, 985.

(33) Kutcherlapati, S. N. R.; Koyilapu, R.; Boddu, U. M. R.; Datta, D.; Perali, R. S.; Swamy, M. J.; Jana, T. Glycopolymer-*Grafted* Nanoparticles: Synthesis Using RAFT Polymerization and Binding Study with Lectin. *Macromolecules* **2017**, *50*, 7309–7320.

(34) Fouillet, C. C. J.; Greaves, T. L.; Quinn, J. F.; Davis, T. P.; Adamcik, J.; Sani, M.-A.; Separovic, F.; Drummond, C. J.; Mezzenga, R. Copolyampholytes Produced from RAFT Polymerization of Protic Ionic Liquids. *Macromolecules* **2017**, *50*, 8965–8978.

(35) Mori, H.; Ishikawa, K.; Abiko, Y.; Nakabayashi, K.; Onuma, A.; Morishima, M. Water-Soluble Poly(N-Vinyl-1,2,4-Triazole) Star and Amphiphilic Star Block Copolymers by RAFT Polymerization. *Polymer.* **2013**, *54* (8), 2001–2010.

(36) Nakabayashi, K.; Umeda, A.; Sato, Y.; Mori, H. Synthesis of 1,2,4-Triazolium Salt-Based Polymers and Block Copolymers by RAFT Polymerization: Ion Conductivity and Assembled Structures. *Polymer.* **2016**, *96*, 81–93.

(37) Mirzaei, Y. R.; Twamley, B.; Shreeve, J. M. Syntheses of 1-Alkyl-1,2,4-Triazoles and the Formation of Quaternary 1-Alkyl-4-Polyfluoroalkyl-1,2,4-Triazolium Salts Leading to Ionic Liquids. *J. Org. Chem.* **2002**, *67*, 9340–9345.

(38) Meyer, D.; Strassner, T. 1,2,4-Triazole-Based Tunable Aryl/Alkyl Ionic Liquids. *J. Org. Chem.* **2011**, *76*, 305–308.

(39) De La Hoz, A. T.; Brauer, U. G.; Miller, K. M. Physicochemical and Thermal Properties for a Series of 1-Alkyl-4-Methyl-1,2,4-Triazolium Bis(Trifluoromethylsulfonyl)Imide Ionic Liquids. *J. Phys. Chem. B* **2014**, *118*, 9944–9951.

(40) Daily, L. A.; Miller, K. M. Correlating Structure with Thermal Properties for a Series of 1-Alkyl-4-Methyl-1,2,4-Triazolium Ionic Liquids. *J. Org. Chem.* **2013**, *78*, 4196–4201.

(41) Vestergaard, B.; Bjerrum, N. J.; Petrushina, I.; Hjuler, H. A.; Berg, R. W.; Begtrup, M. Molten Triazolium Chloride Systems as New Aluminum Battery Electrolytes. *J. Electrochem. Soc.* **1993**, *140*, 3108–3113.

(42) Swain, P. K.; Singh, H.; Tewari, S. P. Energetic Ionic Salts Based on Nitrogen-Rich Heterocycles: A Prospective Study. *J. Mol. Liq.* **2010**, *151*, 87–96.

(43) Singh, R. P.; Verma, R. D.; Meshri, D. T.; Shreeve, J. M. Energetic Nitrogen-Rich Salts and Ionic Liquids. *Angew. Chemie Int. Ed.* **2006**, *45*, 3584–3601.

(44) Xue, H.; Gao, Y.; Twamley, B.; Shreeve, J. M. New Energetic Salts Based on Nitrogen-Containing Heterocycles. *Chem. Mater.* **2005**, *17*, 191–198.

(45) Luo, J.; Hu, J.; Saak, W.; Beckhaus, R.; Wittstock, G.; Vankelecom, I. F. J.; Agert, C.; Conrad, O. Protic Ionic Liquid and Ionic Melts Prepared from Methanesulfonic Acid and 1H-1,2,4-Triazole as High Temperature PEMFC Electrolytes. *J. Mater. Chem.*

2011, *21*, 10426–10436.

(46) Zhou, Z.; Liu, R.; Wang, J.; Li, S.; Liu, M.; Brédas, J.-L. Intra- and Intermolecular Proton Transfer in 1 H (2 H)-1,2,3-Triazole Based Systems. *J. Phys. Chem. A* **2006**, *110*, 2322–2324.

(47) Çelik, S. Ü.; Bozkurt, A.; Hosseini, S. S. Alternatives toward Proton Conductive Anhydrous Membranes for Fuel Cells: Heterocyclic Protogenic Solvents Comprising Polymer Electrolytes. *Prog. Polym. Sci.* **2012**, *37*, 1265–1291.

(48) Tian, X.; Wang, S.; Li, J.; Liu, F.; Wang, X.; Chen, H.; Ni, H.; Wang, Z. Composite Membranes Based on Polybenzimidazole and Ionic Liquid Functional Si–O–Si Network for HT-PEMFC Applications. *Int. J. Hydrogen Energy* **2017**, *42*, 21913–21921.

(49) van de Ven, E.; Chairuna, A.; Merle, G.; Benito, S. P.; Borneman, Z.; Nijmeijer, K. Ionic Liquid Doped Polybenzimidazole Membranes for High Temperature Proton Exchange Membrane Fuel Cell Applications. *J. Power Sources* **2013**, *222*, 202–209.

(50) Singha, S.; Koyilapu, R.; Dana, K.; Jana, T. Polybenzimidazole-Clay Nanocomposite Membrane for PEM Fuel Cell: Effect of Organomodifier Structure. *Polymer.* **2019**, *167*, 13–20.

(51) Escorihuela, J.; Sahuquillo, Ó.; García-Bernabé, A.; Giménez, E.; Compañ, V. Phosphoric Acid Doped Polybenzimidazole (PBI)/Zeolitic Imidazolate Framework Composite Membranes with Significantly Enhanced Proton Conductivity under Low Humidity Conditions. *Nanomaterials* **2018**, *8*, 775.

(52) Escorihuela, J.; Narducci, R.; Compañ, V.; Costantino, F. Proton Conductivity of Composite Polyelectrolyte Membranes with Metal-Organic Frameworks for Fuel Cell Applications. *Adv. Mater. Interfaces* **2018**, *6*, 1801146.

(53) Mukhopadhyay, S.; Das, A.; Jana, T.; Das, S. K. Fabricating a MOF Material with Polybenzimidazole into an Efficient Proton Exchange Membrane. *ACS Appl. Energy Mater.* **2020**, *3*, 7964–7977.

(54) Koyilapu, R.; Singha, S.; Kutcherlapati, S. N. R.; Jana, T. Grafting of Vinylimidazolium-Type Poly(Ionic Liquid) on Silica Nanoparticle through RAFT Polymerization for Constructing Nanocomposite Based PEM. *Polymer.* **2020**, *195*, 122458.

(55) Singha, S.; Jana, T. Self-Assembly of Nanofillers in Improving the Performance of Polymer Electrolyte Membrane. *Macromol. Symp.* **2016**, *369*, 49–55.

(56) Ghosh, S.; Maity, S.; Jana, T. Polybenzimidazole/Silica Nanocomposites: Organic-Inorganic Hybrid Membranes for PEM Fuel Cell. *J. Mater. Chem.* **2011**, *21*, 14897.

(57) Maity, S.; Singha, S.; Jana, T. Low Acid Leaching PEM for Fuel Cell Based on Polybenzimidazole Nanocomposites with Protic Ionic Liquid Modified Silica. *Polymer.* **2015**, *66*, 76–85.

(58) Singha, S.; Jana, T. Structure and Properties of Polybenzimidazole/Silica Nanocomposite Electrolyte Membrane: Influence of Organic/Inorganic Interface. *ACS Appl. Mater. Interfaces* **2014**, *6*, 21286–21296.

(59) Singha, S.; Jana, T.; Modestra, J. A.; Naresh Kumar, A.; Mohan, S. V. Highly Efficient Sulfonated Polybenzimidazole as a Proton Exchange Membrane for Microbial Fuel Cells. *J. Power Sources* **2016**, *317*, 143–152.

(60) Uchida, E.; Ikada, Y. Topography of Polymer Chains *Grafted* on a Polymer Surface Underwater. *Macromolecules* **1997**, *30*, 5464–5469.

(61) Zhang, M.; Liu, L.; Zhao, H.; Yang, Y.; Fu, G.; He, B. Double-Responsive Polymer Brushes on the Surface of Colloid Particles. *J. Colloid Interface Sci.* **2006**, *301*, 85–91.

Chapter 4

Grafting of Polymer Brushes on MOF Surface to Achieve Proton-Conducting Membranes

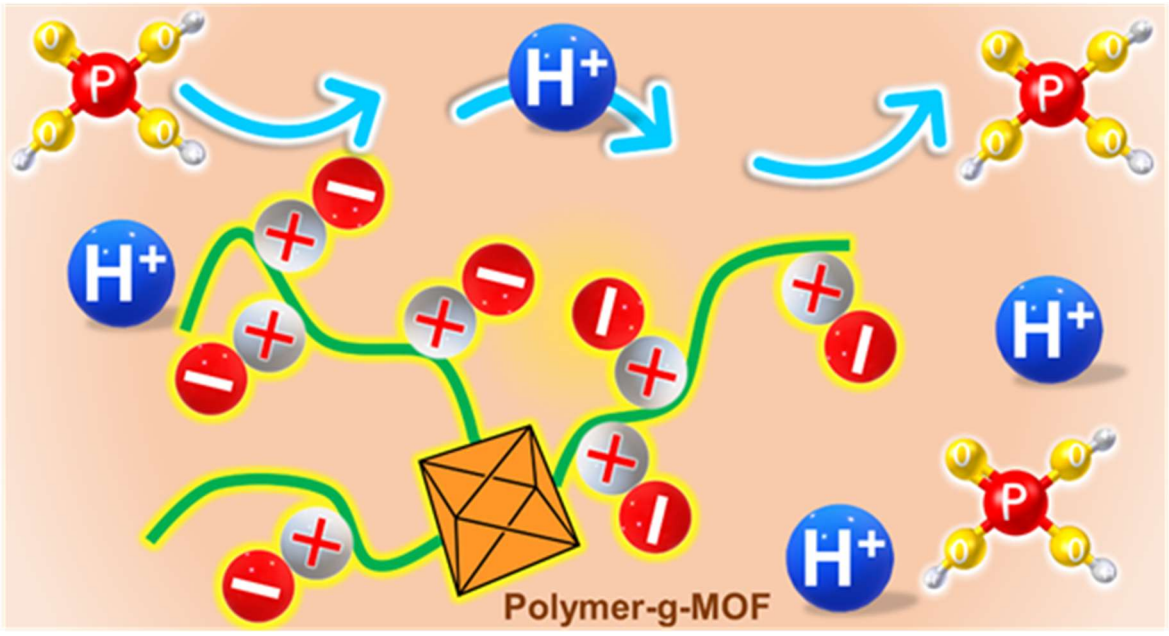

Nilanjan Mukherjee, Anupam Das, Subhabrata Mukhopadhyay, Samar K. Das* and Tushar Jana*. Grafting of Polymer Brushes on MOF Surface to Achieve Proton-Conducting Membranes. *ACS Applied Polymer Materials*. **2024**, *6*, 846-858.

Abstract

In recent years, post synthetic modification (PSM) of a metal organic framework (MOF) has gained immense interests for the synthesis of hybrid materials with improved functionality. However, further improvement in the PSM strategies to make them scalable and synthetically tuneable MOF surface however, can provide the picture-perfect opportunity to create a polymer chain grafted MOF hybrid materials in which polymer chains provide the stability, robustness and desired functional performances and MOF offers interesting physical properties. Towards these goals, in this work we have developed a simple and effective method to functionalize the UiO-66-NH_2 MOF surface by grafting functional polymer brushes using surface-initiated RAFT polymerization. At first, the MOF surface was transformed into a polymerizable surface by attaching a trithiocarbonate based chain transfer agent (CTA) and then, three different sets of polymer brushes consisting of (i) neutral but basic nitrogen functionality (PGM-N), (ii) tri-methyl substituted quaternary ammonium functionality (PGM-C), and (iii) quaternary ammonium along with sulphonate functionality (PGM-Z) were grown on the activated MOF surface, termed as polymer grafted MOF (PGM). The uniqueness of this work has additionally been enhanced by utilizing these synthesized and fully characterized PGMs as nanofiller into the oxypolybenzimidazole (OPBI) membrane matrix to obtain homogeneous mixed matrix membranes (OPBI@PGM) that show a brilliant thermomechanical and tensile properties, exceptional thermal stability; interestingly, these membranes exhibit superior proton conductivity when doped with H_3PO_4 (PA) and minimal acid leaching. Grafting of functional polymer brushes on MOF surface induces strong H-bonding, acid-base interactions with OPBI chains and H_3PO_4 molecules, responsible for such high acid uptake and excellent acid retention and thereby displayed proton conductivity as high as 0.241 S cm^{-1} at 160°C (~ 4-fold increase when compared to OPBI), which is among the highest values reported till date for MOF based proton exchange membrane with excellent mechanical vigour.

Introduction

Metal organic frameworks (MOFs) with ultra-high porosity, inherent crystallinity and very high surface area are emerging materials.[1,2] The applications of MOFs have been demonstrated in diverse fields ranging from gas separation, CO_2 capture,[3–5] to water splitting through water purification[6–9] and from drug delivery to energy applications.[10–13] Recent literature study indicates a growing interest in the field of post synthetic modification (PSM) of MOF materials.[14–19] This modification can be achieved by anchoring functional monolayer on the MOF surface but the efficiency of the modification is limited owing to less number of

active groups of the monolayer and the inability to achieve 100% functionalization using currently available PSM techniques.[15,20–22] However, the number of functional units can be increased substantially by attaching polymer chains on the MOF surface.[23] A few number of reports in the literature demonstrated improvement in various physical properties in the post synthetically modified MOFs when functional polymers are attached to MOFs, or composites are prepared by mixing MOFs and polymers.[14,19,24–26] However, no known PSM for MOF so far addressed the challenges of the non-uniformity in the composites made from MOF and polymer owing to the thermodynamic incompatibility between these two components. In order to resolve this issue, loading or grafting of polymer chains on the surface can be considered to provide better uniformity of the MOF-polymer composite because of the favourable interactions between post synthetically modified MOF-anchored polymer chains and the matrix polymer.

Several attempts have been made to upgrade the properties and improve the interfacial compatibility of UiO-66 based MOF materials by utilizing different strategies.[23,26–29] However, further exploration to develop PSM techniques to functionalize outer crystal structure of MOFs are needed.[22] A proper synthetic strategy and thorough study is missing in the literature to grow precise polymer chains on the outer nano surface of UiO-66 based MOF grafted covalently using reversible addition fragmentation chain-transfer (RAFT) polymerization process under aqueous medium. In the current work, surface-initiated RAFT (SI-RAFT) polymerization is used to grow functional polymer chains on the UiO-66-NH_2 MOF (referred as UiO-66) surface through grafting from approach in the aqueous medium. The obtained hybrids should consist of brush like structures in which polymer chains are like bristles, and are attached to MOF handle. Important to mention that, the availability of the appropriate functionality on the MOF (in this case $-NH_2$ of UiO-NH_2), is crucial to grow polymer chains using SI-RAFT polymerization. The grafted polymer chains are expected to be highly uniform in length as SI-RAFT process enables synthesis of polymer chains with low polydispersity. Next, the different variants of the polymer chain containing MOF were used as nanofillers to synthesize OPBI supported mixed matrix membranes.

To understand the functional behaviour of the PGM hybrids, we have further utilized the PGM hybrids as nanofiller with varying concentrations into the membrane matrix called oxypolybenzimidazole (OPBI) to prepare a series of porous nanofiller containing mixed matrix membranes. Different aspects of their physical properties such as mechanical properties, ability towards proton conduction upon phosphoric acid loading etc were thoroughly investigated. Use of proton exchange membranes (PEMs) are undoubtably a huge leap towards generating energy

using greener sources which are worth mentioning and are necessary part to separate H_2 from the oxidant.[30,31] However, researches are going on to further improve PEM properties using nanocomposite membranes as well.[32] The complex interaction patterns between the UiO-66-NH_2 MOF, the grafted functional polymer brush and the OPBI polymer play crucial role towards the processability, dispersibility and the nanochannel formation ability of the nanofiller in the membrane matrix. These complex interactions may include acid-base interaction, H-bonding, ionic interaction, π-π and non-covalent interactions among the constituents of the mixed matrix membrane. The improved mechanical properties and the nano domain formation in the mixed matrix membrane helped to retain PA molecules which further helped to create a super protonic conductor.

Experimental section

Synthesis of UiO-66-NH_2 (MOF), MOF-BSIPA

We have used a well-known MOF namely UiO-66 NH_2 and modified its surface by covalently attaching a RAFT agent to grow polymer brushes on the MOF surface. To obtain synthetically modified polymer grafted UiO-66-NH_2 (PGM-N, PGM-C, PGM-Z), firstly UiO-66-NH_2 MOF was prepared from $ZrCl_4$ salt and 2-aminoterephthalic acid (BDC-NH_2) using an established synthetic procedure (synthesis procedure is described in details in **Chapter 2**).[15,33] Synthesis, characterization and activation of 2-(((benzylthio)carbonothioyl)thio)propanoic acid (BSIPA), a RAFT agent, are described in the **Chapter 2**. Attachment of activated BSIPA RAFT agent on the surface of UiO-66 NH_2 MOF was achieved by dispersing UiO-66 NH_2 in dry THF solvent by the use of sonication method under N_2 atmosphere and activated BSIPA was added slowly in the dispersion and the product which is UiO-66 NH_2 MOF with covalently attached BSIPA RAFT agent, called as MOF-BSIPA, was separated from the reaction mixture using centrifugation. Detailed synthetic procedure is described in **Chapter 2**.

Synthesis of polymer brush grafted MOF via aqueous SI-RAFT polymerization technique

Poly[2-(dimethylamino)ethyl methacrylate] [pDMAEMA] grafted MOF (PGM-N), poly(2-trimethylammonioethyl methacrylate chloride) [pMETAC] grafted MOF (PGM-C) and poly[3-((2-(methacryloyloxy)ethyl)dimethylammonio)]propane-1-sulfonate [pDMAPS] grafted MOF (PGM-Z) were synthesized in aqueous medium using SI-RAFT grafting-from polymerization approach. In a typical synthetic procedure to grow polymer brush grafted on the UiO-66 NH_2 MOF surface via SI-RAFT polymerization, 150 mg (21.65 µmol) MOF-BSIPA was taken with 5 mL 3:2 (v/v) mixture of water: EtOH in a 25 mL Schlenk tube. 5.89 mg (21.65 µmol) of BSIPA and 1.5 mg of AIBN (8.66 µmol) were also added in the system

with 2-(dimethylamino)ethyl methacrylate (DMAEMA) (calculated amount of monomer added to grow the polymer chains of different molecular weights on the UiO-66 NH_2 MOF surface). The Schlenk tube was sealed with a septum and was subjected to ultra-sonication for 5 minutes and was kept under stirring to make the reaction mixture dispersed evenly. The Schlenk tube was subjected to undergo four freeze-pump-thaw cycles to ensure the complete removal of oxygen and dissolved air from the reaction mixture. The tube was back filled with ultra-high pure N_2 and kept under stirring at 70 °C for 16 h. Upon the completion of 16 h, the RAFT polymerization reaction was quenched using liquid N_2 and was exposed to atmosphere. The quenching with liquid N_2 helps to freeze the active propagating radicals present in the reaction mixture and the exposure to air, terminates the reactive radicals responsible for the propagation of the polymer chain growth. In other cases, the monomer was altered with METAC and DMAPS monomers in order to prepare polymer brushes grafted MOF PGM-C and PGM-Z, respectively. The synthesized polymer brush grafted UiO-66 NH_2 MOF of the three different polymer chains (pDMAEMA, pMETAC and pDMAPS) attached on the UiO-66 NH_2 nano surface was abbreviated as PGM-N (pDMAEMA-g-MOF), PGM-C (pMETAC-g-MOF) and PGM-Z (pDMAPS-g-MOF). The different chain lengths of the polymer brush were represented by '1' and '2' after the abbreviation in each case as PGM-N1, PGM-N2, PGM-C1, PGM-C2, PGM-Z1 and PGM-Z2. The whole process is shown schematically in **Scheme 4.1.**

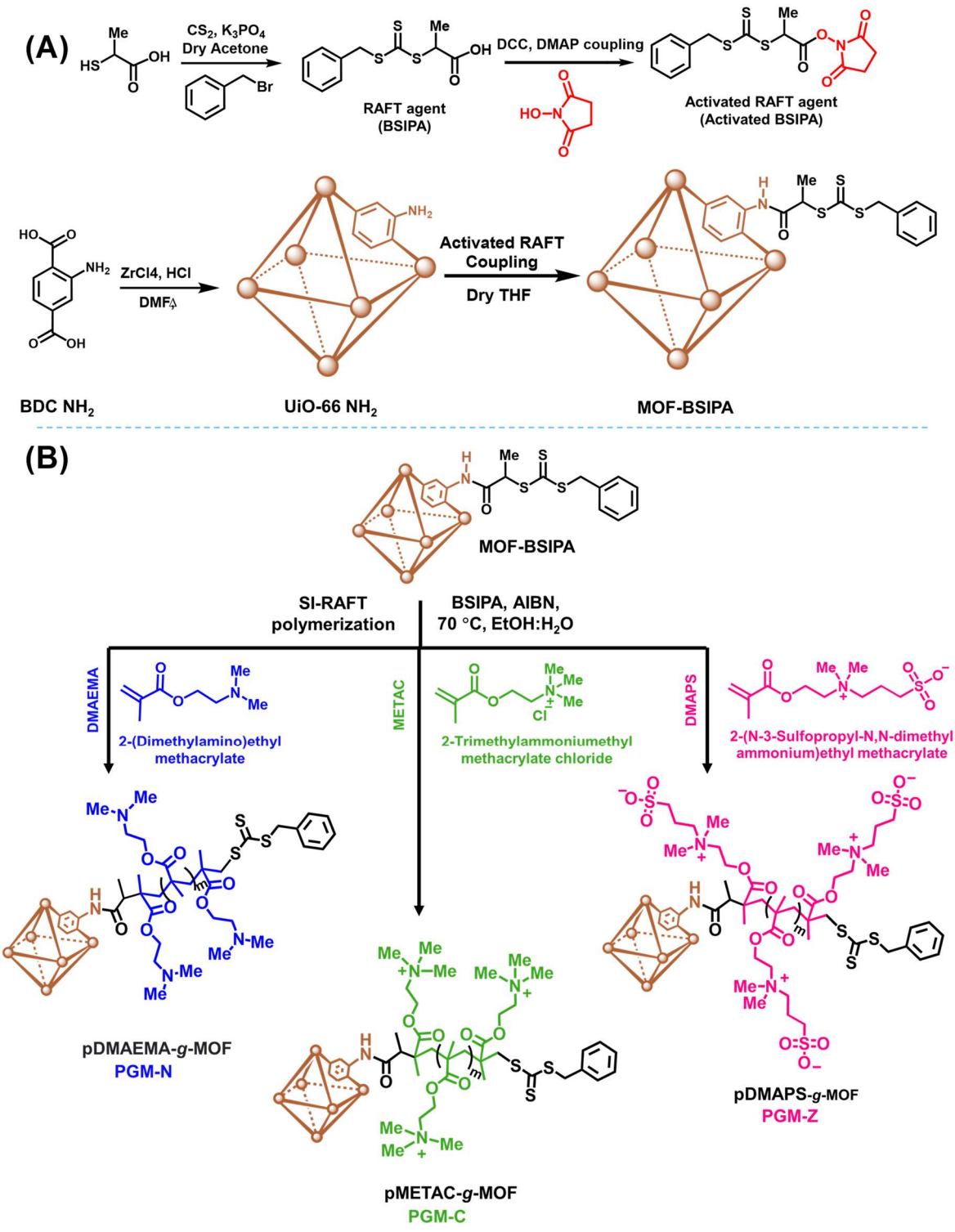

Scheme 4.1. (**A**) Schematic representation of the synthesis of UiO-66 NH_2 MOF, BSIPA RAFT agent and surface functionalization procedure of UiO-66 NH_2 MOF with BSIPA RAFT agent. (**B**) MOF-BSIPA was further used to grow three sets of different polymer brushes on the surface of the MOF using SI-RAFT technique.

The synthesis of OPBI was adapted from the literature, following a modified literature reported procedure[34–36] and is described in detail in **Chapter 2**.

Preparation and characterization of mixed matrix membrane

To prepare mixed matrix membrane (MMM), comprised of OPBI polymer matrix and PGM nanoparticles, solution blending and casting technique were utilized. Firstly, PGM samples (calculated amount) were dispersed in formic acid and were mixed with 2 wt% of OPBI polymer in formic acid solution prepared separately. This results in the final concentration of OPBI polymer to be 1 wt% in the solution. The solution was stirred for 24 h at room temperature to form a homogeneous mixture, which was then poured on to a glass petri dish and allowed for slow evaporation of the solvent at 60 °C. The homogeneously formed MMMs were then peeled off and were dried in a vacuum oven at 100 °C to remove the traces of the solvent molecule and moisture present if any.

All the prepared MMMs were thoroughly characterized and subjected to various studies namely thermal, thermos-mechanical, tensile, microscopic analysis etc. to obtain in depth information about the structural properties and interaction behaviours between PGM and the membrane matrix. Other data obtained from various studies (XRD, TEM etc) supporting the findings of the results are also summarized in the **Appendix II**.

Results and discussion

Choice of monomers and RAFT agent

We have strategically grafted polymer brushes on the MOF surface with three different types of polymer chains which are consisting of (i) neutral charges and tri-substituted basic nitrogen units (pK_b ~ 7.8), (ii) cationic charges in each unit with a tetra substituted quaternized nitrogen and (iii) zwitterionic pair along with a tetra substituted quaternary nitrogen and a very strong sulfonic acidic ($-SO_3H$) group (pK_a ~ -7) (**Scheme 4.1**). The brush structured polymer chains covalently bound on the MOF surface, wraps the MOF surface while partially maintaining the inherent porous structure of the MOF intact, resulting in a porous MOF-polymer hybrid conjugate material. The presence of hydrophilic self-assembled hexa-nuclear Zr_6-oxo core in the UiO-66 makes it suitable to create hydrophilic proton conducting nano-channel. The inherent porosity of the MOF makes it even a better choice. Additionally, the tactically designed charged polymer brushes create loosely bound proton rich environment in proximity to the MOF upon doping with phosphoric acid. The presence of neutral/ cationic/ zwitterionic charged polymer chains effectively contribute to the strong interaction between polymer chains and MOF and thereby creates a loosely bound proton rich environment for

better proton hopping ability upon doping with phosphoric acid (a more detailed discussion is given at the later stage).

The design of the BSIPA RAFT agent is carefully chosen so that the activated carboxylic acid group when attached covalently with the free primary amine groups of UiO-66-NH_2 by forming amide linkage, the phenyl group resides away from the MOF surface. The phenyl methyl group acts as Z group to control the reactivity of the C-S bond while, the free radical leaving group R• remains attached to the MOF nano surface during the RAFT polymerization process (**Scheme 4.1**). Also, there is a methyl group positioned strategically on the -CH position (acting as R group here) adjacent to the trithiocarbonate group to ensure extra stability to the generated free radical species upon dissociation of the C-S bond between trithiocarbonate and the R group (**Scheme 4.1**). Upon SI-RAFT polymerization process the growing polymer chain will reside between the trithiocarbonate group and the R group in our case. Thus, the polymer brush is grown towards the MOF surface and trithiocarbonate group resides away from the MOF surface. This predominantly designed synthetic strategy and the choice of BSIPA RAFT agent allows us to keep the polymer brush which consist of neutral/ cationic/ zwitterionic pendent units close to the MOF core (see **Scheme 4.1**) and will also help not only to provide greater amount of interaction with the adjacent MOF moieties and the membrane matrix but also to incorporate and retain higher amount of phosphoric acid (PA) units into the inherent pores of the MOF core. Thus, the hybrid polymer grafted MOF materials can result in an improvement of the membrane properties when used as nanofiller in the membrane matrix to create an MMM. MMMs are well known in the literature which has been used in a number of applications owing to their unique contributory effects between the polymer matrix and the solid (here polymer grafted porous MOF) nano particles.

Grafting of various types of polymer chains on MOF surface

Figure 4.1(A) shows the thermal degradation patterns of all the polymer grafted MOF materials with varying polymer chain type and length. In all the cases, a gradual decrease in weight % is observed till 200 °C which reflects the hygroscopic nature of the materials and accounts for the adsorbed water molecules. Except this weight loss, all the PGM materials are stable up to ~400 °C while a little premature degradation is observed in case of PGMs with zwitterionic polymer brushes (PGM-Z). The sharp degradation at ~400 °C indicates the breakdown of the polymer brush structure attached covalently on the MOF surface. The degradation increases for each set (neutral/ cationic/ zwitterionic) with the increase in the polymer chain length. Thermal stability of the BSIPA RAFT agent is only up to 200 °C [see

Appendix II-Figure 4.4] which is also reflected in the case of thermal stability of the MOF-BSIPA (BSIPA RAFT agent attached to UiO-66-NH_2). Among the three different types, the polymer brushes containing neutral amine functionality shows a little better thermal stability when compared with the cationic one and the highest thermal degradation is observed in the case of zwitterionic polymer [**Figure 4.1(A)**]. We have achieved a maximum polymer grafting density of 549 mg g^{-1} of MOF in the case of PGM-Z2.

We have also performed gel permeable chromatography (GPC) after treating the polymer grafted MOF samples with the aqueous HF. This procedure has been used by us and others in recent times to detach the surface grafted polymer chains by the action of HF leaching of the framework structure[15,37–39] (see details in the **Chapter 2 Scheme 4.7**). Upon completion of the HF treatment, the solution was kept in a petri dish to dry. The bare polymer chains were extracted with HPLC water, purified and the molecular weight was determined with the help of GPC measurements using HPLC water as eluent [shown in **Figure 4.1(B)**]. All the molecular weights (PGM-N1 to PGM-Z2) have been tabulated in **Table 4.1.** All the synthesized PGM samples show a narrow polydispersity index (Đ) and the molecular weights acquired from the GPC technique are in good agreement with the targeted molecular weight, which suggests that the polymer grafting took place using the SI-RAFT polymerization technique. Design of the RAFT agent plays an important role in controlling the dispersity of the polymer chains.[40,41] But, in order to check the effect of nano surface support towards the growth of the polymer chains, further, controlled experiments were also performed with all the three monomers in absence of MOF-BSIPA under similar conditions in presence of free RAFT agents in order to check the effect of surface grafting on the polymerization process. The polymers were purified upon reaction and characterized using GPC (**Appendix II-Figure 4.2** and **Appendix II-Table 4.1**). The samples were named as Controlled-N, Controlled-C and Controlled-Z for neutral, cationic and zwitterionic polymer samples respectively. The observation illustrates that the relative increment of Đ observed in the case of controlled experiments. The observation suggests that the nano surface plays an important role in order to control the growth of the polymer chains under similar solid support. Also, the unbound polymer chains are getting washed out during the purification process which provides us a synthetic edge to eliminate any amount of unbound polymer chains in the system which results in narrow Đ. Thus, creating an even distribution of polymer brushes as well as providing better control over the growing polymer chains in the system.

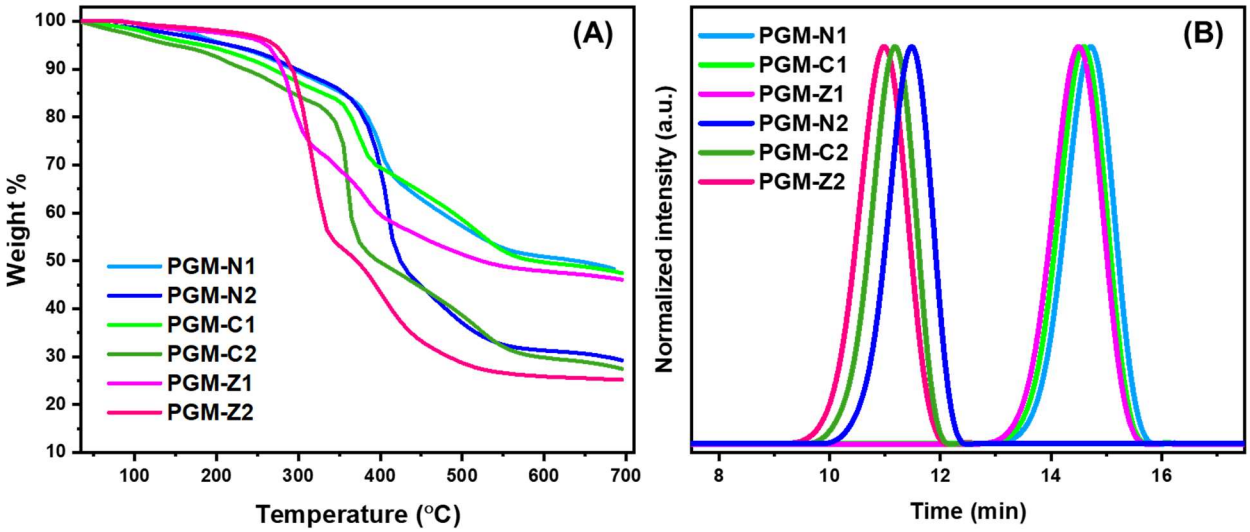

Figure 4.1. (**A**) TGA plot of polymer grafted MOF materials. (**B**) GPC plots for the PGM samples after the detachment of the grafted polymer chains.

Table 4.1. Physical properties of the polymers grafted on the surface functionalized MOFs.

Sample name	Sample type[a]	Remaining weight % at 700 °C (wt%) [b]	Polymer content[c]	$\bar{M}_w$ [d]	$\bar{M}_n$ [e]	Đ [f]
UiO-66-NH_2	-	55.20	-	-	-	-
MOF-BSIPA	UiO-66-NH_2-BSIPA	53.03	39.31	-	-	-
PGM-N1	pDMAEMA$_{59}$(L)-g-MOF	48.31	126.72	9197	9017	1.02
PGM-N2	pDMAEMA$_{130}$(H)-g-MOF	29.21	486.89	20209	19620	1.03
PGM-C1	pMETAC$_{46}$(L)-g-MOF	47.43	143.31	9510	9144	1.04
PGM-C2	pMETAC$_{105}$(H)-g-MOF	27.45	502.08	21616	21192	1.02
PGM-Z1	pDMAPS$_{35}$(L)-g-MOF	46.06	169.15	9667	9207	1.05
PGM-Z2	pDMAPS$_{83}$(H)-g-MOF	25.20	566.28	22911	21614	1.06

[a] sample type describes the chain sequence for each of the copolymer chain and the degree of polymerization for each chain included in the suffix which are obtained from the molecular weight measurements using gel permeation chromatography, [b] estimated from the TGA

analysis (at 600 °C) and [c]polymer content was obtained from the analysis of the TGA curves in Figure 1(A) and expressed as amount (in mg) of polymer chains /g of MOF-BSIPA, [d], [e] and [f] are determined by gel permeation chromatography.

UiO-66-NH_2 MOF, MOF-BSIPA, PGM-N2, PGM-C2 and PGM-Z2 samples were subjected to powder XRD analysis [see **Figure 4.2(A)**] and the patterns are validated against the simulated pattern[33] of UiO-66-NH_2 MOF. The synthesized MOF material and the PGM samples PXRD patterns are matching very well with the simulated patterns suggesting that the integrity of the UiO-66 framework is maintained and the crystal structures of UiO-66 NH_2 are stable during the grafting-from SI-RAFT polymerization process. We have observed a decrease in the intensity of the sharp peaks of PGMs when compared with the pristine MOF and MOF-BSIPA. This can be a result of grafting of polymer chains on the MOF surface. All the materials are found to be stable even after keeping for 6 months at room temperature. Further PXRD analysis was performed on PGM-N1 sample after 6 months and found that the sample can retain crystalline structure as seen from the PXRD pattern (**Appendix II-Figure 4.4**). The PGM-Z samples were also kept under high temperature and 100% humidity condition for 10 days and even then, samples can retain crystalline structure as seen from PXRD pattern (**Appendix II-Figure 4.5**).

Notable similarities are present among the FT-IR spectra of PGM samples and UiO-66 [see **Figure 4.2(B)**]. Stretching frequency at 1565 cm^{-1} is present in all the five samples which corresponds to the presence of C=O bond of the carboxylate group. The stretching of N-H bond is present at 3352 cm^{-1} while in case of PGM-Z2, an intense peak appears at 3420 cm^{-1} which corresponds to the O-H bond stretching due to the presence of sulphonate group on the attached polymer brush. The stretching frequency at 2962 cm^{-1} is present in all the three PGM samples corresponding to C-H stretching frequency and the intensity increases from PGM-N2 to PGM-C2 and appears sharp in the case of PGM-Z2 which implies the presence of additional -methyl group in case of PGM-C2 and a longer alkyl chain in the case of PGM-Z2. In all the PGM samples, stretching frequency at 1721 cm^{-1} is present due to the abundance of methacrylate ester C=O bond, present in the polymer brushes attached at the outer shell of all the PGMs. Two distinct new peaks appear at 1166cm^{-1} and 1034 cm^{-1} in case of PGM-Z2 indicating the presence of -SO_3H group which are absent in all the other samples. The peak position of -SO_3H group is shifted a little due to the presence of intense intra- and inter-molecular H-bonding interactions between quaternary amine group and the strong acid (-SO_3H)

group and strong interaction between the adjacent zwitterionic polymer chains with the unbound amine groups of UiO-66-NH_2.

^{1}H-NMR and ^{13}C-NMR analysis [**Appendix II-Figure 4.6-4.8** and **Figure 4.2(C)]** of the polymer samples, recovered after the aqueous HF treatment of the PGM samples, reveal the grafting of targeted polymer chains on the MOF surface. The peaks are assigned for each sample and the peaks observed corresponding to each sample further confirms the formation of polymer chains using RAFT technique. The data obtained from GPC and NMR studies further provide direct proof towards the applicability of the RAFT polymer grafting technique for nano materials.

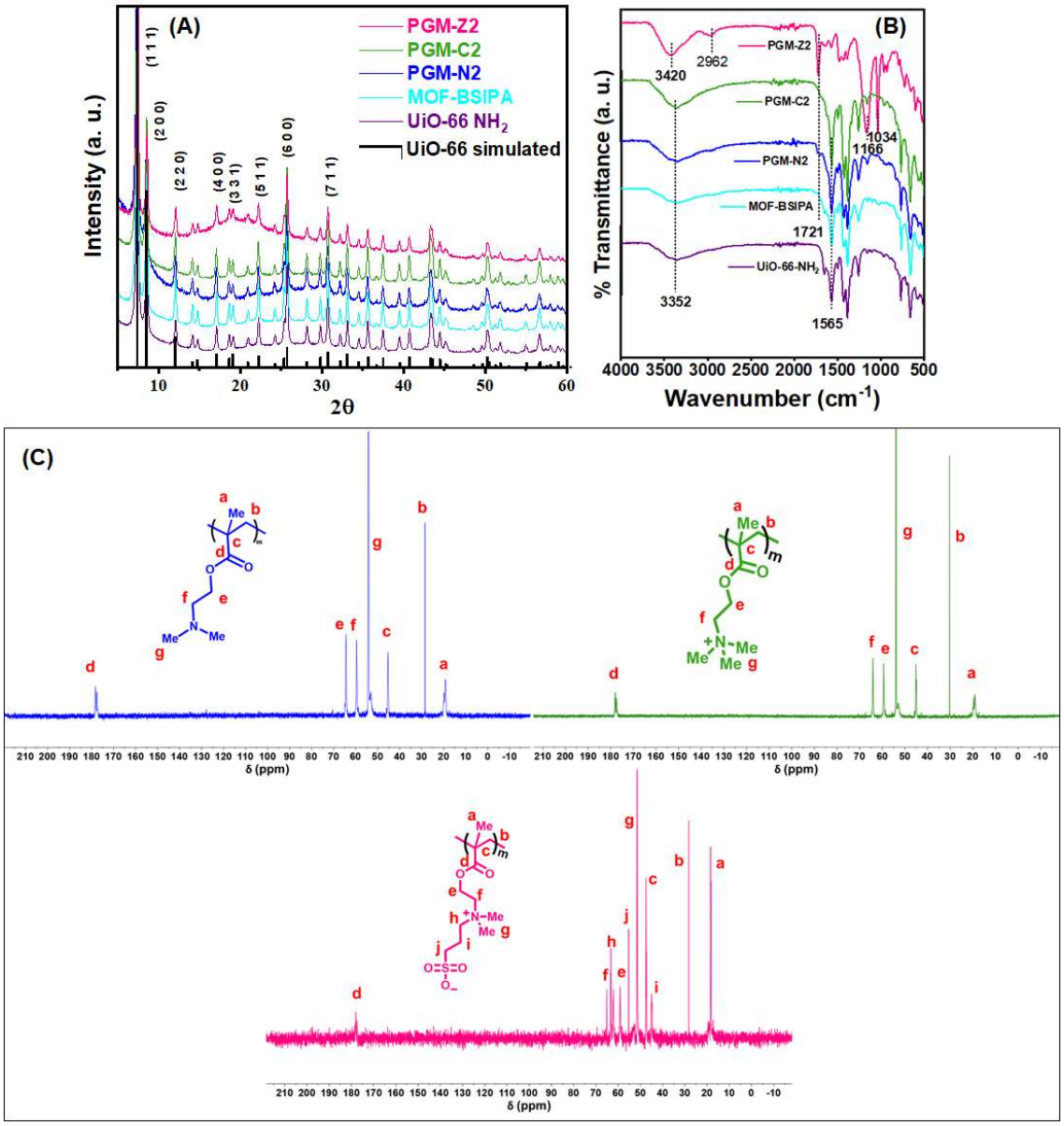

Figure 4.2. (**A**) PXRD plots and (**B**) FT-IR plots of UiO-66-NH_2, MOF-BSIPA and PGM samples along with simulated patterns of UiO-66 MOF sample. (**C**) 13C NMR spectra of the polymer chains detached from PGM-N, PGM-C and PGM-Z.

Detailed morphological analyses [**Figure 4.3** and **Appendix II-Figure 4.9-4.22**] were carried out using FESEM, TEM and EDX techniques. FESEM analysis reveals that the MOF particles are roughly spherical in nature with a diameter of 150-200 nm (**Appendix II-Figure 4.9**). MOF-BSIPA represents a rough surface with little coagulation of the particles whereas the coagulation increases in case of PGM samples which is expected, as the interaction between particles via extensive H-bonding and electrostatic interactions start to dominate upon removal solvent molecules in the dry state of the prepared samples for the microscopic analysis [**Appendix II-Figure 4.9** and **Figure 4.3 (A-F)**]. A visible change in the particle surface is observed as the polymer patches are visible covering the surface of the MOF [**Figure 4.3 (A-F)]**. Similar observations are validated using TEM analysis [**Figure 4.3 (I-J)**]. The polymer patch increases with the increment of the chain length of the grafted polymer chains. In case of PGM-Z1 and PGM-Z2, where the dangling zwitterionic pendent chain is larger in size compared to neutral and cationic moiety in the case of PGM-N and PGM-C materials, the effect is more prominent as observed from FESEM and TEM analysis. In the case of PGM-Z (zwitterionic polymer grafted MOF) samples, the abundance of sulphur could be detected due to the presence of -SO_3H group The EDX data suggests increase in the nitrogen content of the PGM material upon the increment of the chain length. This is a direct consequence of the increase in the self-repeating nitrogen containing monomer unit in the increased polymer chain length. Similarly, the sulphur content found to increase with increasing chain length of the PGM-Z samples. In all the cases, the abundance of the elements (C, N, O, S, Zr) are observed to be evenly dispersed throughout the material surface (**Appendix II-Figure 4.10-4.15**). Similar distributions of the atoms are also validated from TEM-EDX and mapping studies (**Appendix II-Figure 4.16-4.18**). HR-TEM analysis proves the inherent porosity[33,42–44] of the MOF material [**Figure 4.3 (H)**]. The TEM images of PGM samples clearly show the polymer patches on the MOF surface which suggests the successful implication of the integrity of the SI-RAFT process on the MOF surface. Careful observation of the data obtained from TEM analysis suggests that the polymer grafting effects the porosity of the PGM samples as the polymer chains found to cover the porous MOF core (**Appendix II-Figure 4.19**). The observation was further analyzed and proved from the BET studies (discussed in latter section). Upon extensive stability treatment of the PGM samples, PGM-C2 and PDM-Z2 were again analyzed under FESEM and EDX which directly prove that the polymer grafted MOF samples are stable under the harsh conditions (**Appendix II-Figure 4.20-4.22**) suggesting the integrity of the process and the newly synthesized super hybrid materials.

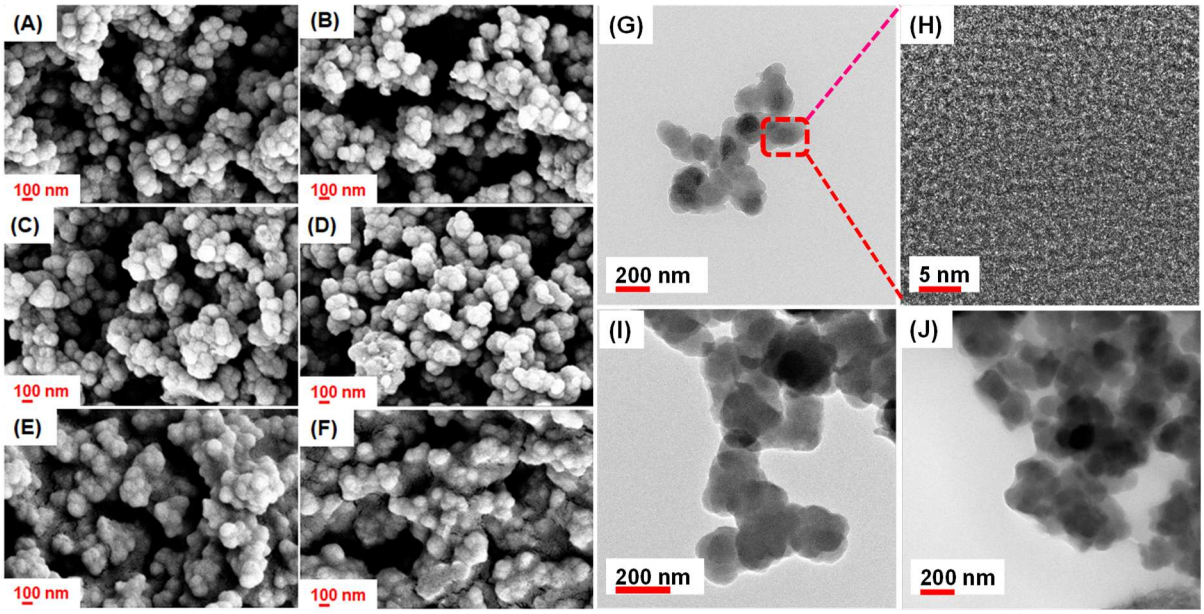

Figure 4.3. FESEM images of polymer grafted MOFs (**A**) PGM-N1, (**B**) PGM-N2, (**C**) PGM-C1, (**D**) PGM-C2, (**E**) PGM-Z1 and (**F**) PGM-Z2. TEM images of (**G**) UiO-66-NH_2, (**H**) high resolution image of UiO-66-NH_2, (**I**) PGM-Z1 and (**J**) PGM-Z2.

BET adsorption analysis was performed in order to get further insight on the successful grafting of polymer brushes on the porous MOF surface [see **Figure 4.4** (**A**)-(**C**) and **Appendix II-Figure 4.23**]. All the PGMs were subjected to vacuum dry at 80 °C for 18 hours in order to remove the air and moisture adsorbed in the inherent pores of the material. All the six samples illustrate the type-I behaviour with rapid rise of the isotherm at around P/P_0 = 0.9−1, which is a typical phenomenon observed in the case of microporous materials. UiO-66-NH_2 shows a surface area of 918 $m^2\ g^{-1}$ (high value considering activation at 80 °C) while, we have observed a decrease in the surface area for PGM samples (PGM-N1 having surface area of 677 $m^2\ g^{-1}$) owing to the grafting of the polymer brush which fills-up the pores present in the MOF. Also, decrease in the surface area with the increase in the chain length of the grafted polymer brush is observed in all the cases (PGM-C1 having surface area of 561 $m^2\ g^{-1}$ while PGM-C2 shows surface area of 222 $m^2\ g^{-1}$). The decrease in the surface area in the case of PGM-C2 (222 $m^2\ g^{-1}$) from PGM-N2 (593 $m^2\ g^{-1}$) considering similar molecular weight of the grafted polymer chains, indicates that the cationic polymer brushes can take up more space. This is due to the presence of an extra methyl group in the cationic unit when compared to the neutral one. More particularly, the special arrangement of the three methyl groups around the cationic nitrogen centre incorporates extra bulkiness like a propeller, when compared with the neutral nitrogen with two methyl groups. Similar observations are observed in the case of

PGM-Z having a much longer alkyl chain with a bulky sulphonate group dangling at the end of each bristle of the grafted polymer brush. The significant decrease in the surface area in the case of PGM-Z1 (90.6 m^2 g^{-1}) and PGM-Z2 (66.6 m^2 g^{-1}) directly imply the consequence of the less availability of the free space due to the impregnation of long polymer bristles inside the pores of the PGM samples.[15] The distribution of pore size data [**Appendix II-Figure 4.23(B)**] also indicates that the abundance of small pores is getting lesser in the PGMs when compared with the pristine UiO-66-NH_2 sample. This observation effect is also found to tally with the increase in the molecular weight of the grafted polymer brush. This data implies that, the grafted polymer chains not only reside on the surface of the MOF but also filling up of the hollow interior which is in well agreement with the observations from the FESEM and TEM analysis shown in earlier section.

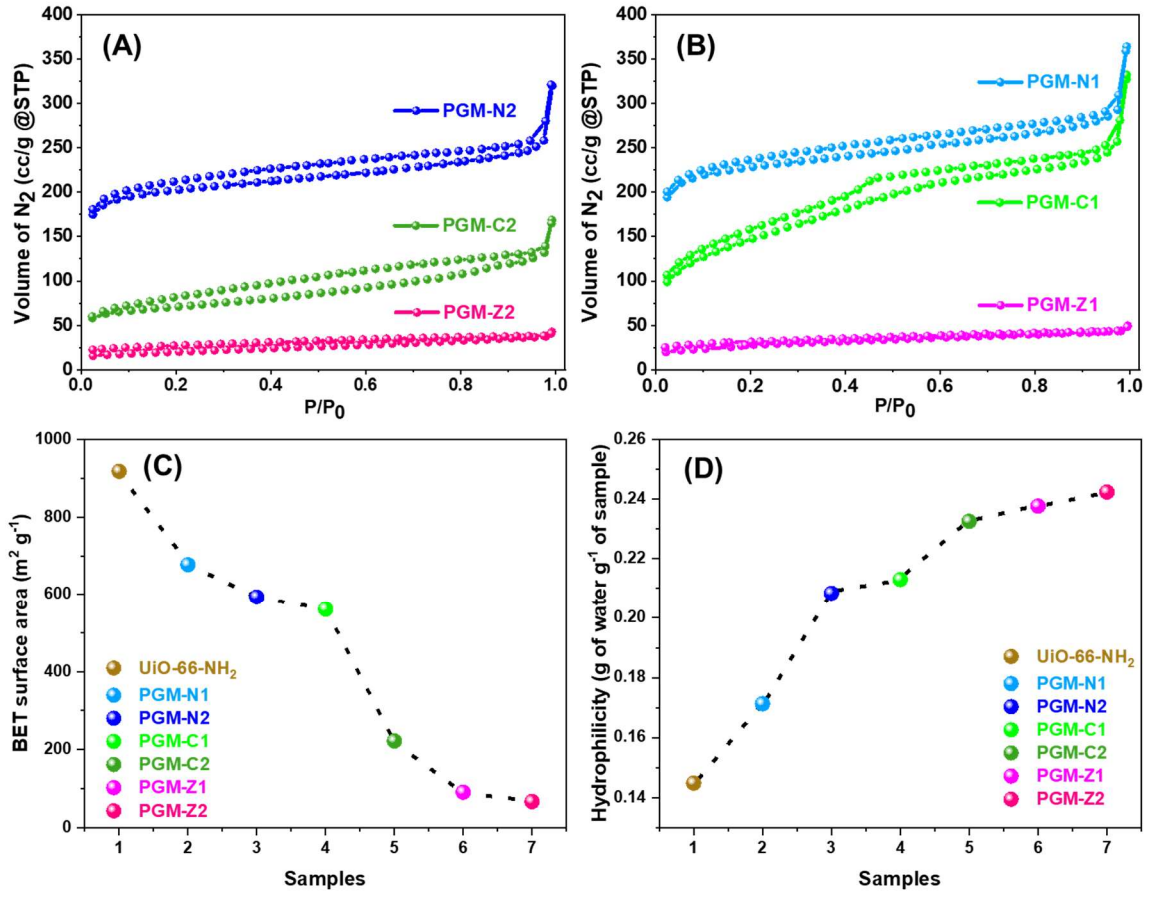

Figure 4.4. BET adsorption desorption isotherm from nitrogen sorption studies of polymer grafted MOFs (**A**) PGM-N1 to PGM-Z1 and (**B**) PGM-N2 to PGM-Z2. (**C**) variation of BET surface area and (**D**) variation of hydrophilicity (derived from DVS studies) for all the PGM samples along with UiO-66-NH_2.

Furthermore, water vapour adsorption and desorption of all the samples were studied using dynamic vapour sorption (DVS) technique and the data are shown in **Figure 4.4(D)** and **Appendix II-Figure 4.24.** In the case of MOF material, the observed hydrophilicity is 0.14 g of water/ g of the MOF material which comes from the free amine groups present in the framework structure along with the highly hygroscopic Zr_6-oxo nodes which are surrounded by carboxylic acid groups from the BDC-NH_2 ligand. DVS analysis shows a clear increase in hydrophilicity upon grafting of polymer chains on the MOF surface. The hydrophilicity increases with the increase in the molecular weight of the grafted polymer brushes. An ascending order of hydrophilic nature is noted while moving from neutral to cationic and again to zwitterionic charged polymer brush grafted MOF. The maximum observed hydrophilicity is obtained for PGM-Z2 (0.24 g of water/g of PGM-Z2) which is nearly double when compared to the pristine MOF. The PGM samples display hysteresis loop which attributes to the fact that, the diffusion of water molecules from the bulk to the surface has a different kinetics. It also implies that, the PGMs possess high affinity towards water molecules not only on the surface but also the water molecules go into the bulk of the material. So, PGMs show a box suction dominated mechanism as the hollow hydrophilic interiors are decorated by hydrophilic polymer brushes. In the case of PGM-Z samples the initial and the final points of the isotherm are well disconnected suggesting that, the sample can hold moisture to a better extent.

The aqueous stability of the PGMs were analyzed by checking Zeta potential values (**Appendix II-Figure 4.25**). The study shows that all the PGM samples are highly dispersed and stable in the aqueous medium. The zeta potential values are positive in the case of PGM-N and PGM-C samples and are negative for PGM-Z samples which is expected in terms of the different charge present at the surface of the nanoparticles with respect to the polymer brushes grafted on the surface. Moreover, the data also suggests that the zeta potential increases a little with higher chain length of the grafted polymer brush. The robustness and the stability of the PGMs were further checked under 100% humid condition with high temperature for a period of 10 days and afterwards analysed using PXRD. The study shows that the framework structure is quite stable under the chosen harsh environments and able to retain its crystalline patterns (**Appendix II-Figure 4.5**).

OPBI@PGM mixed matrix membranes

In order to demonstrate the possible application of the PGM materials in the improvement of proton exchange membrane (PEM) properties, we have utilized PGM samples with higher polymer content to prepare nanocomposite mixed matrix membrane (MMM) by

dispersing PGM sample in OPBI matrix to prepare MMMs containing different weight percentage of PGMs in the matrix (**Scheme 4.2**). We have thus produced MMMs by varying the amount of nanofiller loading of 2.5 wt% and 5 wt % PGM content with respect to the OPBI weight. We have also evaluated the effect of structure of different polymer brushes grafted on the nano MOF surface.

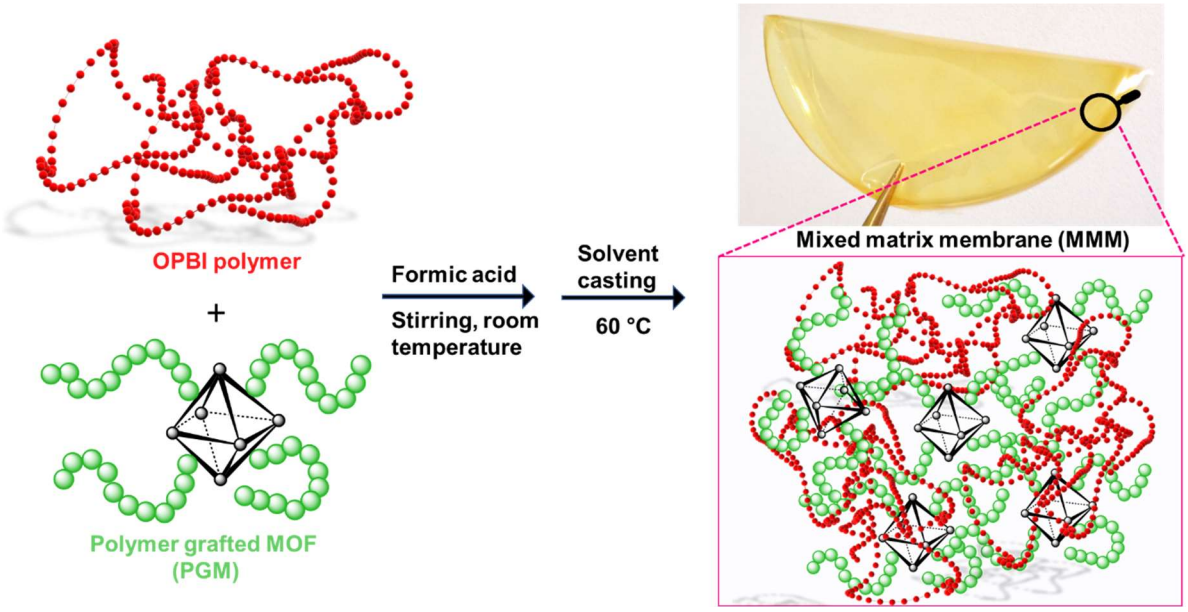

Scheme 4.2. Schematic representation of the fabrication of OPBI@PGM nanocomposite mixed matrix membrane.

Powder XRD analysis of the MMMs indicate the presence of new semicrystalline peaks between 10°-20° of 2θ value which indicates the strong interaction patterns acting between PGM and the membrane matrix (**Appendix II-Figure 4.26**). However, this is to note that the OPBI polymer is amorphous in nature and PGMs contain crystalline MOF. The intensity of the new semicrystalline peaks increases with the increment in the nanofiller loading. From the TEM analysis (**Appendix II-Figure 4.27**) of the MMMs which indicates the dispersion of the PGMs in the membrane matrix are better when we move from neutral to cationic and again to zwitterionic polymer grafted MOF material. The presence of ionically charge reflects in better interaction with the membrane matrix and thus results in better dispersion of the nanofiller. The data indicates the variation in the dispersion abilities of the PGMs with the alternation of the surface charge of the polymer grafted MOFs. The dispersion ability of the nanofiller material in the matrix imposes significant impact on the different

physical as well as mechanical properties (discussed in the later sections) of the MMMs which are in agreement with our recent studies.[34,35]

Thermal stability is one of the most important features in order to design high temperature-PEMs (HT-PEMs). Thus, all the OPBI@PGM membranes along with pristine OPBI membrane were thoroughly checked for thermal stability up to 700 °C [**Figure 4.5 (A)**]. All the MMM samples show initial weight loss around 200 °C which is better than initial weight loss of OPBI. Thermal stability of MMM samples decrease from neutral to cationic and further to zwitterionic polymer brush grafted MOF when used as nanofiller. But the increase in the nanofiller loading from 2.5 wt % to 5 wt % in the MMM increases the thermal stability up to 400 °C indicating the strong interaction pattern between the nanofiller and the membrane matrix which helps to resist the thermal degradation. Above 300 °C thermal stability of the MMMs is observed to decrease a little bit compared the pristine OPBI which can be interpreted with respect to the thermal degradation patterns of the UiO-66-NH_2 framework. After 550 °C, the degradation indicates the breakdown of the main polymer backbone of the OPBI polymer. The data illustrates that all the MMMs show even better stability than pristine OPBI (below 200 °C) and the overall thermal stability is also impressive to be used as HT-PEM.

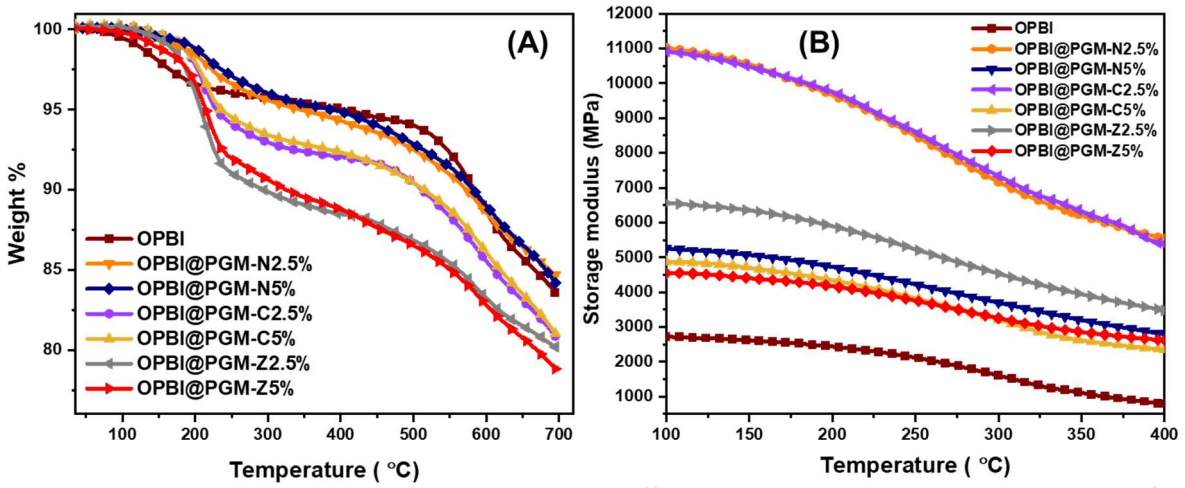

Figure 4.5. (**A**) TGA plot and (**B**) storage modulus *vs* temperature plot of all the OPBI@PGM membranes along with the pristine OPBI membrane.

The dispersibility and the strong interaction pattern between the nanofiller and the membrane matrix have great consequences on the thermo-mechanical behaviour of the nanocomposites. Temperature-dependent storage modulus (E′) plot of OPBI along with all the OPBI@PGM mixed matrix membranes are shown in **Figure 4.5 (B)** (obtained from DMA study). The storage modulus values at 100 °C and 400 °C for all the membranes are tabulated

(Appendix II-Table 4.2). The increment of storage modulus in the case of MMMs are incontestable when compared with the pristine OPBI membrane. The storage modulus (E′) is found to increase significantly at 100 °C for all the OPBI@PGMs with the values 11019, 10913 and 6563 MPa recorded for OPBI@PGM-N2.5%, OPBI@PGM-C2.5% and OPBI@PGM-Z2.5%, respectively. Similarly, a significant increase in storage modulus is observed at 400 °C for all the samples in comparison to pristine OPBI. Two important observations to be noted: firstly, the type of grafted polymer chain on the PGM has a strong influence on the E′ value of MMM and then the increment of E′ value is much more significant at higher temperature, for example, the data (**Appendix II-Table 4.2**) show that the % of increment in E′ value for OPBI@PGM-N2.5% at 100 °C and 400 °C are 305% and 600%, respectively. However, the value decreases as the amount of nanofiller loading increases which originates due to the presence of greater amount of hydrophilic nanofiller loading which makes the membrane more flexible, though the lowest value (OPBI@PGM-Z5%) was 67% higher at 100 °C and 231% higher at 400 °C when compared with the pristine OPBI. The controlling the amount of nanofiller loading must be taken into account in order to obtain best mechanical properties out of the MMMs. The plots of loss modulus (E″) and tan δ against temperature (see **Appendix II-Figure 4.28**) show only one relaxation peak for all the composites and OPBI membrane. The T_g values obtained from tan δ vs temperature plot for all the OPBI@PGM membranes, range between 280- 291 °C whereas the value obtained for OPBI membrane is 321 °C. The little change in the T_g values is observed for the nanocomposites because of the presence of plasticizer effect arising from the hydrophilic and porous nature of the nanofiller.

All the OPBI@PGM membranes along with the pristine OPBI membrane were analyzed for water uptake ability, swelling ratio and phosphoric acid (PA) doping levels, and all the data are tabulated in **Appendix II-Table 4.3**. OPBI polymers tend to absorb moisture and PA molecules inside the membrane matrix, owing to its tendency to form strong H-bonds with the imidazole functionality present in the OPBI structure.[5] Therefore, the membranes often undergo dimensional changes due to excessive swelling upon PA loading which limits their usability as a potential proton conducting membrane material. Hygroscopic nanofiller materials are reported in literature to increase the water uptake ability of the resulting nanocomposite.[24,45] On the other hand, dimensional stability must be maintained at the same time. We have observed slight increase in the water uptake of the MMMs and the value increases with the increase in the nanofiller loading which signify the water absorptivity and the water holding abilities of the PGMs as observed from the DVS studies (discussed in the earlier section). Changes in the swelling ratio in water and PA of the OPBI@PGM membranes are observed,

when compared with the pristine OPBI membrane and there is a clear-cut dependence of the type of PGM nanofillers and the % of nanofillers in the MMMs. PA doping level of OPBI is 15.77 mol/ repeat unit (r.u) while a significant jump in PA doping level is observed for all the MMMs and the effect of neutral, cationic and zwitterionic moiety present in the grafted polymer brush structure are very significant. Best values are obtained with ionic moiety present in the case of OPBI@PGM-C and OPBI@PGM-Z with 5 wt% nanofiller loading. The presence of Zr_6-oxo nodes, free amine functionality presents on the MOF surface and the inherent porosity present in the basic UiO-66-NH_2 also play a noteworthy role in achieving higher PA doping levels.

We have also studied the stress-strain profiles of the PA doped membranes to investigate the dimensional stability of the proton exchange membranes which has always been a serious problem to utilize the membranes further. A huge increase in the tensile strain is observed in the case of the PGM loaded membranes when compared with the pristine OPBI **[Figure 4.6 (A)]**. Incorporation of crystalline materials even in small amounts in the system have proven to improve tensile properties of the membrane in many folds.[46–49] Strong interactions acting between the OPBI matrix, the hydrophilic nanofiller materials and absorbed PA molecules directly contribute to the mechanical and tensile reinforcement of the PA doped membranes which indicates the importance of properly designed nanofiller material for the compatibility with the polymer matrix. Also, the effect of grafted polymer structure of hydrophilic nanofiller is observed from the stress-strain profile. With the increase in the amount of nanofiller loading, the MMMs experience better PA doping levels which plays a great role in the stretchability of the membranes as observed from the less stress values and more strain % values in all the cases. OPBI@PGM-C5% PA doped membrane shows 220% increase in elongation at break value (%) while, with 2.5 wt% nanofiller loading resulted in 200% increment with respect to OPBI membrane **[Figure 4.6 (A)]**.

Proton conductivity (σ) measurements were performed for all the PA doped OPBI@PGM membranes and OPBI membrane at different temperature using a four-electrode set-up, utilizing impedance spectroscopy [**Figure 4.6 (B)**]. The proton conductivity for OPBI is 0.064 S cm^{-1} at 160 °C whereas proton conductivity value for OPBI@PGM-C5% is 0.214 S cm^{-1} at 160°C. The highest proton conductivity value obtained is 0.241 S cm^{-1} at 160 °C in the case of OPBI@PGM-Z5% membrane. A significant increment of proton conductivity (~3.8 fold) is obtained for PA doped OPBI@PGM-Z5% composite membrane when compared to the pristine OPBI polymer. The higher conductivity of the zwitterionic PGM-Z, compared to PGM-N and PGM-C was a result of the $-SO_3H$ groups, which serve as suitable Brønsted acidic

cites, and is present in the polymer chain of PGM-Z. Because of the $-SO_3H$ groups, and the zwitterionic nature of the PGM-Z, it can also form strong H-bonding within the material, which also results to high hydrophilicity. All these factors lead to high observed conductivity of the material compared to its other counterparts. Important to mention that the proton conducting ability of the MMM increases with the nanofiller content in the membrane in all the cases. Careful analysis of the proton conductivity data reveals that the increased proton conductivity is not only due to the high PA uptake (although the main source for labile proton here is PA molecules) but also the presence of strategically designed polymer grafted porous MOF particles as nanofiller, that plays a significant role. Nevertheless, the presence of cationic and zwitterionic pendent groups dangling from the grafted polymer chains creates a stronger ionic environment surrounding the MOF particles containing free amine functionality and Zr_6-oxo nodes.

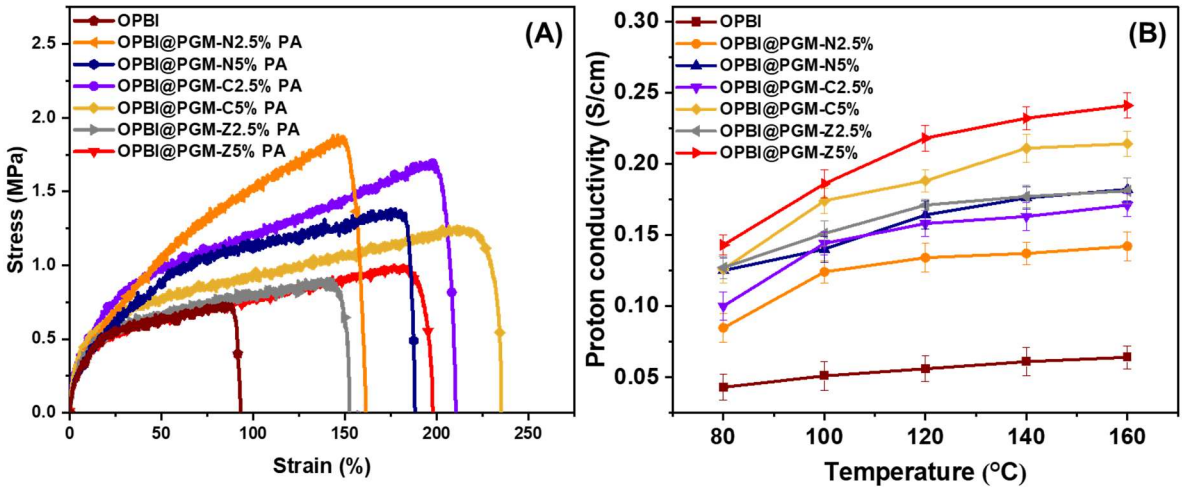

Figure 4.6. (**A**) Stress-strain and (**B**) proton conductivity vs. temperature plots of OPBI and OPBI@PGM membranes.

Appendix II-Figure 4.29 represents the Arrhenius plots of PA doped OPBI@PGM membranes along with the pristine OPBI. The activation energy (E_a) values derived from Arrhenius plots are calculated based on the proton conductivity values observed within the temperature range 80 °C to 160 °C. All the OPBI@PGM membranes and OPBI show activation energy values in the range of ~9-12 kJ/mol. Thus, it could be inferred that, the proton conduction is occurring through Grotthuss proton transport mechanism. Continuous construction and distraction of the extensive H-bonding network between the: (a) functional groups of the OPBI polymer, (b) ionic network of dangling ionic polymer brush grafted on the

porous MOF and (c) absorbed PA molecules, are the key to achieve such high proton conductivity.

In order to utilize the newly developed nanocomposite membranes as PEMs, two most important properties must be examined which are (i) retention of proton conductivity for longer period and (ii) holding of the doped PA molecules by the membrane under high temperature and high humidity conditions. The data shown in **Figure 4.7 (A)** indicate an initial decrease in the proton conductivity for all the samples due to initial leaching of PA molecules from the system but after that all the nanocomposite membranes are retaining the proton conductivity quite well even after 24 hours. In order to study the leaching behaviour, all the membranes were treated under high temperature (100 °C) and high humidity conditions (98% RH) using a home-made set-up adapted from the previous studies.[16,34,36] The weight was measured periodically for all the membranes to obtain the weight loss owing to the PA leaching. The membranes were flooded with continuous boiling water vapour which provides an ideal environment for PA to leach out from the system. **Figure 4.7 (B)** clearly reveals that OPBI membrane can hold only around 56 % of PA after the 1 hour of the leaching treatment and upon completion of 3 hour only 30.7 % of the doped PA molecules are retained in the membrane. Whereas, in the case of MMMs, upon the completion of 3 hour of the treatment, the membranes display better PA holding abilities by retaining on an average around 73% of PA molecules. The strong acid-base, π-π, noncovalent interactions acting between the nanofiller and the matrix polymer along with free amine decorated hollow MOF interior, presence of Zr_6-oxo nodes and presence of grafted ionic polymer brushes provides a quintessential environment which helps to hold the PA molecules in the system.

Further, thermal stability of the MMMs upon PA doping were checked using TGA study. TGA analysis of undoped membranes **[Figure 4.5 (A)]** shows that the nanocomposite membranes have less thermal stability with respect to the pristine OPBI membrane (in the temperature range >200 °C) but the PA doped membranes show thermal stability in a reverse order. The PA doped OPBI@PGM membranes show better stability than the PA doped OPBI membrane in the temperature range of 100 °C – 300 °C **(Appendix II-Figure 4.30)**. This observation implies that the PGM nanofillers are well designed to incorporate and embrace more PA in the membrane matrix efficiently when compared to pristine OPBI, which directly infers with our conclusions obtained from the PA leaching studies. Upon PA doping, a number of new and complicated interaction patterns arise in the matrix which contribute towards better thermal stability of the membranes. In this context it has to be mentioned that, at around 500 °C, the composite membranes lead to a sharp decay in the weight loss with respect to OPBI PA

membrane, which can be attributed to the evaporation and polycondensation of PA molecules present in the composite matrix.

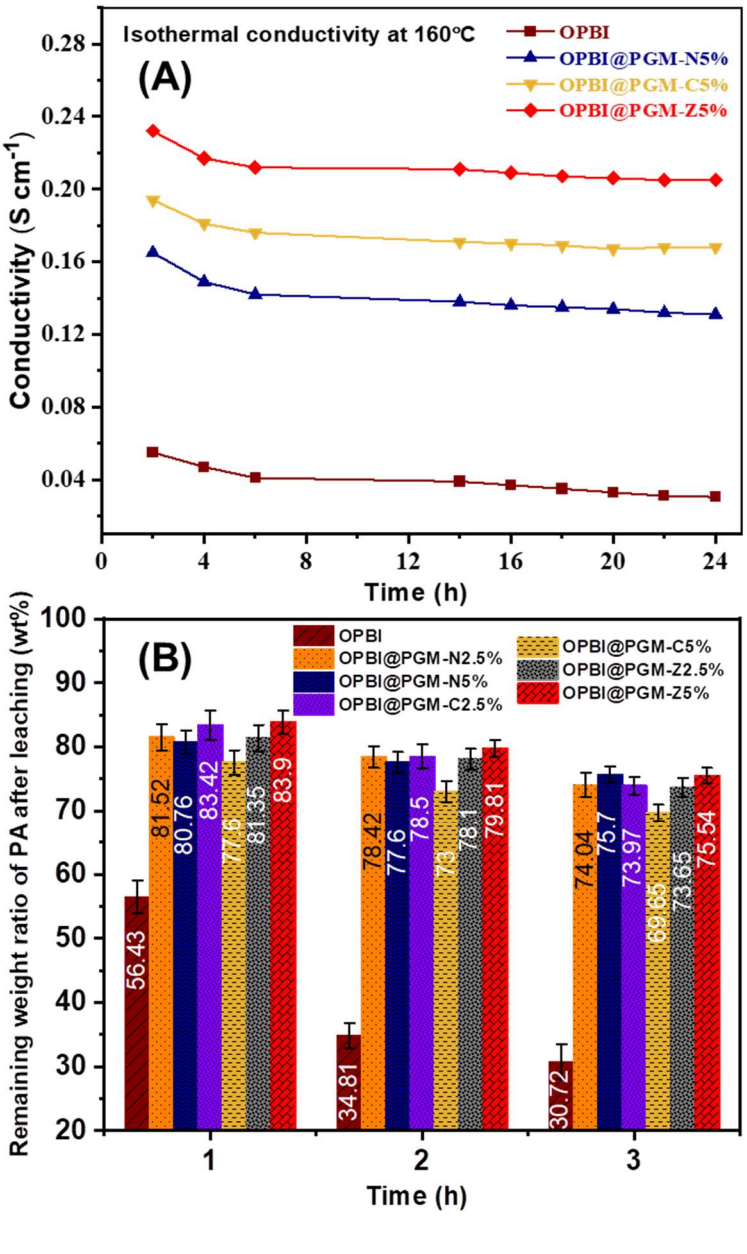

Figure 4.7. (**A**) Isothermal conductivity at 160 °C and (**B**) acid retention studies of PA loaded OPBI@PGM samples.

Conclusion

We have successfully demonstrated a simple but efficient way to attach RAFT agent on the UiO-66-NH_2 (a MOF) surface which opens an enormous amount of possibility towards controlled surface modifications. Further, we have grown ionic polymer brushes of varied chain lengths containing neutral (PGM-N), cationic (PGM-C) and zwitterionic (PGM-Z)

functional groups on the nano MOF surface using SI-RAFT grafting-from approach. Furthermore, mixed matrix membranes (MMMs) of oxypolybenzimidazole (OPBI) and porous nanofiller (PGM) were developed with different amount of nanofiller loading and were characterized methodically. The achievement of high storage modulus value of 11019 MPa at 100 °C in the case of OPBI@PGM-N 2.5% indicates the effect of basic nitrogen content of the neutral polymer brushes towards the complex interaction patterns that have been arisen in the MMM. The ionic functionality present in the grafted polymer brush impacts on the dispersibility of the nanofiller in the membrane matrix and the best results were obtained for OPBI@PGM-Z 5%. We have also proved that, the strong and complex interaction patterns acting between the nanofiller and the membrane matrix in the MMM help to achieve better phosphoric acid (PA) doping levels without compromising on the dimensional stability of the membrane resulting in excellent PA holding capabilities of the MMM, thereby less leaching of PA. Better PA doping levels and the ability to form nano proton migration pathway by virtue of the extensively porous network structure of the framework along with precise grafting of the ionic polymer brushes helped to create super protonic conductors with conductivity as high as 0.241 S cm^{-1} (~ 4 fold increase when compared to pristine OPBI) for OPBI@PGM-Z5% which is among the utmost values reported till date for MOF based PEM systems with excellent mechanical robustness.

References

(1) Zhou, H. C.; Long, J. R.; Yaghi, O. M. Introduction to Metal–Organic Frameworks. *Chem. Rev.* **2012**, *112*, 673–674.

(2) Yuan, S.; Feng, L.; Wang, K.; Pang, J.; Bosch, M.; Lollar, C.; Sun, Y.; Qin, J.; Yang, X.; Zhang, P.; Wang, Q.; Zou, L.; Zhang, Y.; Zhang, L.; Fang, Y.; Li, J.; Zhou, H. Stable Metal–Organic Frameworks: Design, Synthesis, and Applications. *Adv. Mater.* **2018**, *30*, 1704303.

(3) Li, Y. Z.; Wang, G.-D.; Ma, L.-N.; Hou, L.; Wang, Y.-Y.; Zhu, Z. Multiple Functions of Gas Separation and Vapor Adsorption in a New MOF with Open Tubular Channels. *ACS Appl. Mater. Interfaces* **2021**, *13*, 4102–4109.

(4) Qian, Q.; Asinger, P. A.; Lee, M. J.; Han, G.; Mizrahi Rodriguez, K.; Lin, S.; Benedetti, F. M.; Wu, A. X.; Chi, W. S.; Smith, Z. P. MOF-Based Membranes for Gas Separations. *Chem. Rev.* **2020**, *120*, 8161–8266.

(5) Emerson, A. J.; Hawes, C. S.; Marshall, M.; Knowles, G. P.; Chaffee, A. L.; Batten, S. R.; Turner, D. R. High-Connectivity Approach to a Hydrolytically Stable Metal–Organic Framework for CO 2 Capture from Flue Gas. *Chem. Mater.* **2018**, *30*, 6614–6618.

(6) Shekhawat, A.; Samanta, R.; Barman, S. MOF-Derived Porous Fe 3 O 4 /RuO 2 -C Composite for Efficient Alkaline Overall Water Splitting. *ACS Appl. Energy Mater.* **2022**, *5*, 6059–6069.

(7) Zhao, X.; Pattengale, B.; Fan, D.; Zou, Z.; Zhao, Y.; Du, J.; Huang, J.; Xu, C. Mixed-Node Metal–Organic Frameworks as Efficient Electrocatalysts for Oxygen Evolution Reaction. *ACS Energy Lett.* **2018**, *3*, 2520–2526.

(8) Chang, R.; Ma, S.; Guo, X.; Xu, J.; Zhong, C.; Huang, R.; Ma, J. Hierarchically Assembled Graphene Oxide Composite Membrane with Self-Healing and High-Efficiency Water Purification Performance. *ACS Appl. Mater. Interfaces* **2019**, *11*, 46251–46260.

(9) Ahmadijokani, F.; Ahmadipouya, S.; Haris, M. H.; Rezakazemi, M.; Bokhari, A.; Molavi, H.; Ahmadipour, M.; Pung, S.-Y.; Klemeš, J. J.; Aminabhavi, T. M.; Arjmand, M. Magnetic Nitrogen-Rich UiO-66 Metal–Organic Framework: An Efficient Adsorbent for Water Treatment. *ACS Appl. Mater. Interfaces* **2023**, *15*, 30106–30116.

(10) Chen, X.; Tong, R.; Shi, Z.; Yang, B.; Liu, H.; Ding, S.; Wang, X.; Lei, Q.; Wu, J.; Fang, W. MOF Nanoparticles with Encapsulated Autophagy Inhibitor in Controlled Drug Delivery System for Antitumor. *ACS Appl. Mater. Interfaces* **2018**, *10*, 2328–2337.

(11) Lawson, H. D.; Walton, S. P.; Chan, C. Metal–Organic Frameworks for Drug Delivery: A Design Perspective. *ACS Appl. Mater. Interfaces* **2021**, *13*, 7004–7020.

(12) He, B.; Zhang, Q.; Pan, Z.; Li, L.; Li, C.; Ling, Y.; Wang, Z.; Chen, M.; Wang, Z.; Yao, Y.; Li, Q.; Sun, L.; Wang, J.; Wei, L. Freestanding Metal–Organic Frameworks and Their Derivatives: An Emerging Platform for Electrochemical Energy Storage and Conversion. *Chem. Rev.* **2022**, *122*, 10087–10125.

(13) Li, X.-M.; Wang, Y.; Mu, Y.; Liu, J.; Zeng, L.; Lan, Y.-Q. Superprotonic Conductivity of a Functionalized Metal–Organic Framework at Ambient Conditions. *ACS Appl. Mater. Interfaces* **2022**, *14*, 9264–9271.

(14) Basu, O.; Das, A.; Jana, T.; Das, S. K. Design of Flexible Metal–Organic Framework-Based Superprotonic Conductors and Their Fabrication with a Polymer into Proton Exchange Membranes. *ACS Appl. Energy Mater.* **2023**, *6*, 9092–9107.

(15) Mukhopadhyay, S.; Debgupta, J.; Singh, C.; Sarkar, R.; Basu, O.; Das, S. K. Designing UiO-66-Based Superprotonic Conductor with the Highest Metal–Organic Framework Based Proton Conductivity. *ACS Appl. Mater. Interfaces* **2019**, *11*, 13423–13432.

(16) Mukhopadhyay, S.; Das, A.; Jana, T.; Das, S. K. Fabricating a MOF Material with Polybenzimidazole into an Efficient Proton Exchange Membrane. *ACS Appl. Energy Mater.* **2020**, *3*, 7964–7977.

(17) Nguyen, H. L.; Matheu, R.; Diercks, C. S.; Doan, T. L. H.; Nguyen, B. T.; Cordova, K. E. Postsynthetic Metalation of a New Metal–Organic Framework To Improve Methane Working Storage Capacity. *ACS Mater. Lett.* **2022**, *4*, 2375–2380.

(18) Li, F.; Du, M.; Xiao, X.; Xu, Q. Self-Supporting Metal-Organic Framework-Based Nanoarrays for Electrocatalysis. *ACS Nano* **2022**, *16*, 19913–19939.

(19) Kalaj, M.; Cohen, S. M. Postsynthetic Modification: An Enabling Technology for the Advancement of Metal–Organic Frameworks. *ACS Cent. Sci.* **2020**, *6*, 1046–1057.

(20) Zhang, B.; Bai, X.; Wang, S.; Li, L.; Li, X.; Fan, F.; Wang, T.; Zhang, L.; Zhang, X.; Li, Y.; Liu, Y.; Chen, J.; Meng, F.; Fu, Y. Preparation of Superhydrophobic Metal–Organic Framework/Polymer Composites as Stable and Efficient Catalysts. *ACS Appl. Mater. Interfaces* **2021**, *13*, 32175–32183.

(21) Qian, Q.; Chi, W. S.; Han, G.; Smith, Z. P. Impact of Post-Synthetic Modification Routes on Filler Structure and Performance in Metal–Organic Framework-Based Mixed-Matrix Membranes. *Ind. Eng. Chem. Res.* **2020**, *59*, 5432–5438.

(22) Figueroa-Quintero, L.; Villalgordo-Hernández, D.; Delgado-Marín, J. J.; Narciso, J.; Velisoju, V. K.; Castaño, P.; Gascón, J.; Ramos-Fernández, E. V. Post-Synthetic Surface Modification of Metal–Organic Frameworks and Their Potential Applications. *Small Methods* **2023**, *7,* 2201413.

(23) Qian, Q.; Wu, A. X.; Chi, W. S.; Asinger, P. A.; Lin, S.; Hypsher, A.; Smith, Z. P. Mixed-Matrix Membranes Formed from Imide-Functionalized UiO-66-NH 2 for Improved Interfacial Compatibility. *ACS Appl. Mater. Interfaces* **2019**, *11*, 31257–31269.

(24) K, B.; Paul P, A.; Kalarikkal, N.; Stephen, A. M.; G, G. V.; Rouxel, D.; Thomas, S. Effects of Nanofillers on Morphology and Surface Wetting of Microporous Polypropylene Composite Membranes. *Mater. Chem. Phys.* **2021**, *257*, 123742.

(25) Gavinehroudi, R. G.; Mahjoub, A.; Karimi, M.; Sadeghi, S.; Heydari, A.; Mohebali, H.; Ghamami, S. Non -Covalent LDH/MOF Composite Formation: A New Approach in Sustainability for Solvent-Dependent Photocatalytic Aerobic Alcohol Oxidation. *Green Chem.* **2022**, *24*, 6965–6979.

(26) Muldoon, P. F.; Venna, S. R.; Gidley, D. W.; Baker, J. S.; Zhu, L.; Tong, Z.; Xiang, F.; Hopkinson, D. P.; Yi, S.; Sekizkardes, A. K.; Rosi, N. L. Mixed Matrix Membranes from a Microporous Polymer Blend and Nanosized Metal–Organic Frameworks with Exceptional CO 2 /N 2 Separation Performance. *ACS Mater. Lett.* **2020**, *2*, 821–828.

(27) Luz, I.; Toy, L.; Rabie, F.; Lail, M.; Soukri, M. Synthesis of Soluble Metal Organic Framework Composites for Mixed Matrix Membranes. *ACS Appl. Mater. Interfaces* **2019**, *11*, 15638–15645.

(28) Jia, Z.; Dai, X.; Liu, B.; Li, Y.; Bo, C. Poly(Sodium 4-Styrenesulfonate) Brushes-Functionalized UiO-66-NH2 Metal-Organic Framework for High and Selective Adsorption of Dyes. *Colloids Surfaces A Physicochem. Eng. Asp.* **2022**, *639*, 128312.

(29) Abánades Lázaro, I.; Haddad, S.; Sacca, S.; Orellana-Tavra, C.; Fairen-Jimenez, D.; Forgan, R. S. Selective Surface PEGylation of UiO-66 Nanoparticles for Enhanced

Stability, Cell Uptake, and PH-Responsive Drug Delivery. *Chem* **2017**, *2*, 561–578.

(30) Divya, K.; Saraswathi, M. S. A.; Rana, D.; Nagendran, A. Non-Nafion-Based Cation Exchange Membranes for Direct Methanol Fuel Cells. In *Direct Methanol Fuel Cell Technology*; Elsevier, 2020; pp 37–70.

(31) Rana, D.; Matsuura, T.; Zaidi, S. M. J. Research and Development on Polymeric Membranes for Fuel Cells: An Overview. In *Polymer Membranes for Fuel Cells*; Springer US: Boston, MA, 2008; pp 1–20.

(32) Muthumeenal, A.; Saraswathi, M. S. A.; Rana, D.; Nagendran, A. Recent Research Trends in Polymer Nanocomposite Proton Exchange Membranes for Electrochemical Energy Conversion and Storage Devices. In *Membrane Technology*; CRC Press: Boca Raton : Taylor & Francis, 2018., 2018; pp 351–374.

(33) Katz, M. J.; Brown, Z. J.; Colón, Y. J.; Siu, P. W.; Scheidt, K. A.; Snurr, R. Q.; Hupp, J. T.; Farha, O. K. A Facile Synthesis of UiO-66, UiO-67 and Their Derivatives. *Chem. Commun.* **2013**, *49*, 9449.

(34) Mukherjee, N.; Das, A.; Jana, T. Poly(N -Vinyl Triazole- b - N -Vinyl Imidazole) Grafted on MWCNTs as Nanofillers to Improve Proton Conducting Membranes. *ACS Appl. Nano Mater.* **2023**, *6*, 544–557.

(35) Das, A.; Mukherjee, N.; Jana, T. Polymer-Grafted Graphene Oxide/Polybenzimidazole Nanocomposites for Efficient Proton-Conducting Membranes. *ACS Appl. Nano Mater.* **2023**, *6*, 6365–6379.

(36) Mukherjee, N.; Das, A.; Dhara, M.; Jana, T. Surface Initiated RAFT Polymerization to Synthesize N-Heterocyclic Block Copolymer Grafted Silica Nanofillers for Improving PEM Properties. *Polymer.* **2021**, *236*, 124315.

(37) Barcus, K.; Cohen, S. M. Free-Standing Metal–Organic Framework (MOF) Monolayers by Self-Assembly of Polymer-Grafted Nanoparticles. *Chem. Sci.* **2020**, *11*, 8433–8437.

(38) Nagata, S.; Kokado, K.; Sada, K. Metal–Organic Framework Tethering PNIPAM for ON–OFF Controlled Release in Solution. *Chem. Commun.* **2015**, *51*, 8614–8617.

(39) Ploskonka, A. M.; DeCoste, J. B. Tailoring the Adsorption and Reaction Chemistry of the Metal–Organic Frameworks UiO-66, UiO-66-NH 2 , and HKUST-1 via the Incorporation of Molecular Guests. *ACS Appl. Mater. Interfaces* **2017**, *9*, 21579–21585.

(40) Asadi-Eydivand, M.; Brown, T. C.; Bagheri, A. RAFT-Mediated 3D Printing of "Living" Materials with Tailored Hierarchical Porosity. *ACS Appl. Polym. Mater.* **2022**, *4*, 4940–4948.

(41) Tan, J.; Rao, X.; Jiang, D.; Yang, J.; Zeng, Z. One-Stage Photoinitiated RAFT Dispersion Polymerization – Reaction Parameters for Achieving High Particle Size Uniformity. *Polymer.* **2014**, *55*, 2380–2388.

(42) Liu, L.; Zhang, D.; Zhu, Y.; Han, Y. Bulk and Local Structures of Metal–Organic

Frameworks Unravelled by High-Resolution Electron Microscopy. *Commun. Chem.* **2020**, *3*, 99.

(43) Gong, X.; Gnanasekaran, K.; Chen, Z.; Robison, L.; Wasson, M. C.; Bentz, K. C.; Cohen, S. M.; Farha, O. K.; Gianneschi, N. C. Insights into the Structure and Dynamics of Metal–Organic Frameworks via Transmission Electron Microscopy. *J. Am. Chem. Soc.* **2020**, *142*, 17224–17235.

(44) Zheng, A.; Yin, K.; Pan, R.; Zhu, M.; Xiong, Y.; Sun, L. Research Progress on Metal–Organic Frameworks by Advanced Transmission Electron Microscopy. *Nanomaterials* **2023**, *13*, 1742.

(45) Salarizadeh, P.; Javanbakht, M.; Pourmahdian, S. Enhancing the Performance of SPEEK Polymer Electrolyte Membranes Using Functionalized TiO 2 Nanoparticles with Proton Hopping Sites. *RSC Adv.* **2017**, *7*, 8303–8313.

(46) Rana, D.; Lee, C. H.; Cho, K.; Lee, B. H.; Choe, S. Thermal and Mechanical Properties for Binary Blends of Metallocene Polyethylene with Conventional Polyolefins. *J. Appl. Polym. Sci.* **1998**, *69*, 2441–2450.

(47) Rana, D.; Cho, K.; Woo, T.; Lee, B. H.; Choe, S. Blends of Ethylene 1-Octene Copolymer Synthesized by Ziegler-Natta and Metallocene Catalysts. I. Thermal and Mechanical Properties. *J. Appl. Polym. Sci.* **1999**, *74*, 1169–1177.

(48) Rana, D.; Kim, H. L.; Kwag, H.; Rhee, J.; Cho, K.; Woo, T.; Lee, B. H.; Choe, S. Blends of Ethylene 1-Octene Copolymer Synthesized by Ziegler-Natta and Metallocene Catalysts. II. Rheology and Morphological Behaviors. *J. Appl. Polym. Sci.* **2000**, *76*, 1950–1964.

(49) Rana, D.; Kim, H. L.; Kwag, H.; Choe, S. Hybrid Blends of Similar Ethylene 1-Octene Copolymers. *Polymer.* **2000**, *41* (19), 7067–7082.

Chapter 5

Grafting of Poly(vinyl phosphonic acid) to MOF surface by RAFT Polymerization: A Novel Method for the Development of Proton Conducting Materials

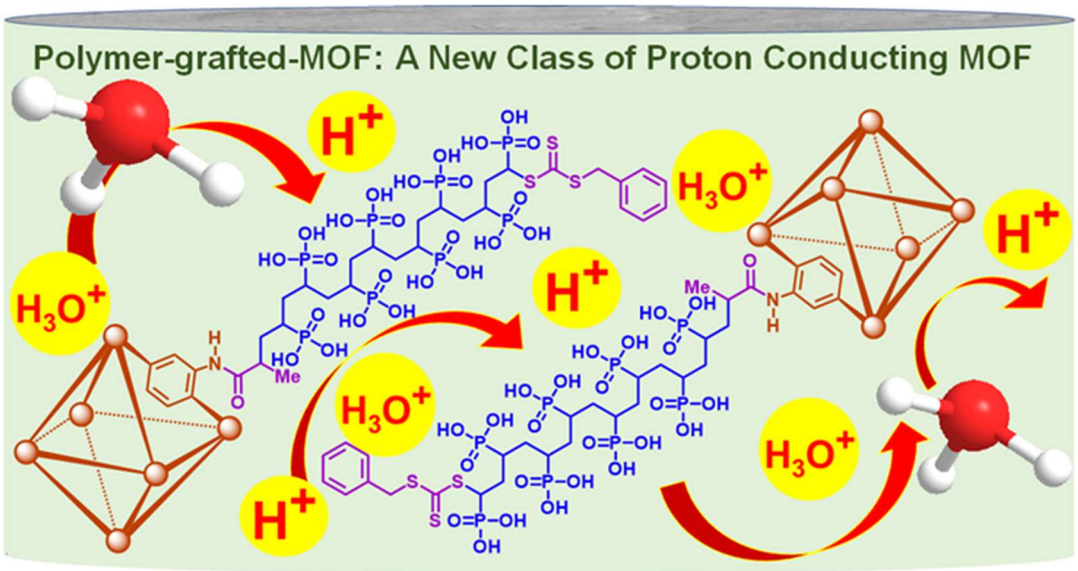

Nilanjan Mukherjee, Olivia Basu, Subhabrata Mukhopadhyay, Samar K. Das* and Tushar Jana*. Grafting of Poly(vinyl phosphonic acid) to MOF surface by RAFT Polymerization: A Novel Method for the Development of Proton Conducting Materials. (*Manuscript to be communicated)*

Abstract

In recent times, metal organic frameworks (MOFs) along with the evolution of different post-synthetic modification (PSM) procedures are being used frequently to design better hybrid materials for numerous applications. However, the combination of polymers with MOF systems (polymer-MOF conjugates) has proven to be an interesting area for improving the stability factors of MOF systems even under harsh environments. Nevertheless, the need for a proper synthetic approach and extensive study limits the designing flexibility of 'MOF-polymer'-based efficient hybrid materials. An efficient surface functionalization technique, without the use of harsh chemicals, simple but scalable with synthetic tuneability and inexpensive, with uniformly of chemically stable grafted polymer chains can provide immense freedom to synthesize functional polymer-grafted MOF materials. In this work, at first, the MOF surface was chemically transformed into a polymerizable surface by trithiocarbonate based chain transfer agent (CTA) namely, RAFT agent. This modified MOF surface was utilized to grow poly vinyl phosphonic acid (PVPA) chains using aqueous surface initiated RAFT polymerization technique with varying chain length and grafting density. Grafting of PVPA polymer chains were confirmed by TGA, GPC, FT-IR, NMR, FESEM, TEM, EDX and mapping studies. The stability of the novel hybrid material under various harsh environments were further analyzed. The applicability of this work was further explored by analysing the newly synthesized PGMs for proton conductivity under varying temperature and relative humidity conditions. Pendent phosphonic acid group containing stable polymer chain grafted on the MOF surface creates strong H-bonding, acid-base, ionic and non-covalent interaction patterns with the neighbouring PGMs and the water molecules which are responsible for such high stability, water sorption ability and also exhibits inherent proton conductivity of 1.26×10^{-2} S cm^{-1} at 80 °C for PGM-L3 sample under 98% relative humidity, and 9.8×10^{-3} S cm^{-1} at 60 °C for PGM-H1 sample under 75% relative humidity, which is amongst the highest values reported so far for MOF based systems.

Introduction

Research on metal organic framework (MOF), a class of porous crystalline framework material with high surface area, is rapidly growing owing to its application in numerous fields including gas separation[1,2], CO_2 capture[3,4], water splitting[5], water purification[6,7], drug delivery[8,9] and energy applications[10–13]. A recent literature review reveals, a growing curiosity in developing post synthetic modification (PSM) approaches of MOF

materials in order to create MOF based hybrid materials with further enhancement in the properties[14–18]. PSM of a MOF can be achieved by attaching small molecules like sultone, anhydride, halogens etc. on the MOF surface which yields a functional monolayer on the MOF surface. Unfortunately, improvement of properties of the resulting MOF hybrid obtained by this method is inadequate because of the limited number of active functionality available on the modified MOF surface owing to the synthetic challenges to achieve 100% functionalization .[7,19–22] Alternatively, amplification of such properties are reported either by impregnation of small molecules in the confined pores or incorporating polymer with the MOF particles to make nanocomposite, and is based on non-covalent interactions between the nanofiller and the polymer matrix.[23–28] However, uneven distribution of the filler (MOF) material in the matrix can encumber the improvement in desired properties. On the other hand, grafting of polymer chains on the MOF surface is found to provide improved homogeneity of the material resulting significant improvement in the properties of MOF hybrid.[29]

In recent times, many research groups have reported polymer-MOF composites with improved compatibility by doing appropriate surface chemistry and enhancing the interfacial interactions between MOF and polymer.[30–32] However, proton conducting behaviour of bare polymer-grafted MOF, without mixing (blending) with another polymer to make composite, has not been explored to a great detail. In this work, we made an effort to study this aspect of polymer-grafted MOF. Here, we have taken UiO-66NH_2 as a model MOF system and our plan is to come up with a simple method to grow different types of polymer chains consisting of ionic functionality on the MOF nano surface which will create a new class functional materials for their use as ion conducting hybrid MOF.

In this work, we have modified the surface of the UiO-66NH_2 MOF by grafting phosphonic acid unit containing polymer chains (PVPA) using SI-RAFT grafting from technique. FT-IR, TGA, NMR, GPC, BET, DVS, FESEM, TEM, EDX and mapping techniques were used to confirm the grafting of PVPA chains on the nano surface.

We have judiciously chosen to graft PVPA chain on the MOF surface as diprotic acid monomer VPA has (i) two acid dissociation constant with values of pKa_1=2 and pKa_2=8, (ii) stable phosphorus atom with +5 oxidation state and (iii) $P^{\delta+}=O^{\delta-}$ units along with -OH functionality. These features of the PVPA chains can enable holding more amount of H^+ ions and water molecules so that nano proton conducting channels may be created in the resulting PGMs. Additionally -PO_3H_2 unit dangling from the polymeric chain has two possible conjugate

base structures and the abundance of each of the microspecies varies with the change in the pH value of the medium. Also, we have calculated the abundance of each of the microspecies under different pH conditions from the predicted acid dissociation constant data available publicly at *Chemicalize.com* & *Marvin* (details are shown in **Appendix III** and **Appendix III-Figure 5.1**). Considering the variation in the abundance of different microspecies, $-PO_3H^-$ is considered to be the dominating species under the humidified conditions while $-PO_3H_2$ is under low pH condition. $-PO_3H^-$ species is considered to be an ideal candidate for the creation of an environment for better proton hopping considering the presence of both, (i) negative charged oxygen dispersed over two oxygen atoms and also (ii) the presence of a dissociable acidic proton attached to oxygen. Thus, the presence of strong acidic protons when interacts with the water molecules of pH=7 in the polymeric chain grafted MOF system, creates a loosely bound H^+ enriched environment which can be beneficial for inherent proton conductivity of the polymer-MOF super hybrid material. The presence of strong and complicated interaction patterns (ionic, acid-base, H-bonding and non-covalent interactions) acting amongst the grafted PVPA polymer chains, hollow MOF interior consisting of free amine functionality and hexanuclear core of Zr_6 metal nodes (consisting of Zr^{+4} species) helps to build a strong interconnected network which can contribute extensively towards the stability of the super hybrid material under harsh thermal and mechanical environment. The grafting of PVPA polymers chains on particularly Zr based UiO-66 NH_2 MOF is very fascinating because the grafted polymer chains tend to wrap up around the hollow interiors of the MOF material which is well anticipated to create hygroscopic proton conducting nano channels by improving the stability of the core framework structure and there by not only creating a protective shield around the MOF core but also populating the neighbourhood with enriched H^+ ions. Thus, tactically designed polymer chains with dangling phosphonic acid units play a crucial role towards the creation of well-organized proton conduction channels to achieve super proton conductivity via simultaneously breaking and making of H-bonds (discussed in latter section).

Materials and Methods

Preparation of polymerizable MOF surface

We have synthesized UiO-66 type MOF (UiO-66-NH_2) and modified the surface chemically with the synthesized RAFT agent (BSIPA) to convert the MOF surface into a polymerizable surface (MOF-BSIPA) using PSM technique. The details of MOF synthesis and modification by RAFT agents are given in **Chapter 2** and **Appendix-III**. The amount of

BSIPA (RAFT agent) attached on the MOF surface was varied to obtain two sets of MOF-BSIPA namely MOF-BSIPA(L) and MOF-BSIPA(H) with low and high RAFT agent attached on the MOF surface, respectively (see **Chapter 2** and **Appendix III** for detailed procedure). RAFT agent attached UiO-66-NH_2 (MOF-BSIPA) was used in aqueous SI-RAFT polymerization in order to grow polymer chains of poly vinyl phosphonic acid (PVPA) on the nano MOF surface (**Scheme 5.1**).

Synthesis of poly(vinyl phosphonic acid) grafted MOF

Poly (vinyl phosphonic acid) grafted MOF (PVPA-g-MOF) materials were prepared using 'grafting from' approach of SI-RAFT polymerization technique in aqueous medium. Two types of polymer PVPA-g-MOF (hereafter called as PGM) were prepared using MOF-BSIPA (L) and MOF-BSIPA (H) and these are named as PGM-L and PGM-H, respectively. The procedure to prepare PGM-L is as follows: 200 mg (21.66 µmol) MOF-BSIPA(L) was taken with 5 mL 3:2 (v/v) mixture of water: EtOH in a 25 mL Schlenk tube. 5.9 mg (21.66 µmol, 1 eq.) of BSIPA and 1.5 mg of AIBN (8.66 µmol, 0.2 eq.) were also added in the Schlenk tube with vinyl phosphonic acid (VPA) (calculated amount of VPA monomer added to grow the polymer chain of PVPA with different molecular weights). The Schlenk tube was sealed with a septum and then sonicated for 5 minutes and further the tube was kept under stirring condition to make the reaction mixture dispersed uniformly. To ensure the complete removal of oxygen and dissolved air from the reaction mixture the Schlenk tube was subjected to undergo four freeze-pump-thaw cycles. The tube was then back filled with ultra-high pure N_2, sealed and kept under stirring at 70°C for 16 h. Upon the completion of 16 h, the active propagating radicals in the RAFT polymerization reaction were frozen by quenching with liquid N_2 and the exposure to air terminates the reactive radicals responsible for the propagation of the active polymer chain growth. Similarly, to grow PVPA polymer chains on the MOF-BSIPA(H) surface to get PGM-H following protocol was followed: 200 mg (69.35 µmol) MOF-BSIPA(H) was taken with 5 mL 3:2 (v/v) mixture of water: EtOH in a 25 mL Schlenk tube. 18.89 mg (69.35 µmol, 1 eq.) of BSIPA and 4.6 mg of AIBN (27.74 µmol, 0.2 eq.) were also added in the Schlenk tube with vinyl phosphonic acid (VPA) (calculated amount of monomer added to grow the PVPA polymer chain with different molecular weights grafted on the MOF surface). Similar reaction procedure was employed in the case of PGM-H sample synthesis as described earlier for the PGM-L samples.

Characterization Methods

All the details characterization procedures which include the detachment procedure of grafted polymer chains from the MOF surface, GPC, NMR, FT-IR, BET studies, powder XRD, FESEM, TEM, EDX and mapping technique along with TGA, DVS, zeta potential and proton conductivity measurement studies are given in **Chapter 2** and **Appendix III**.

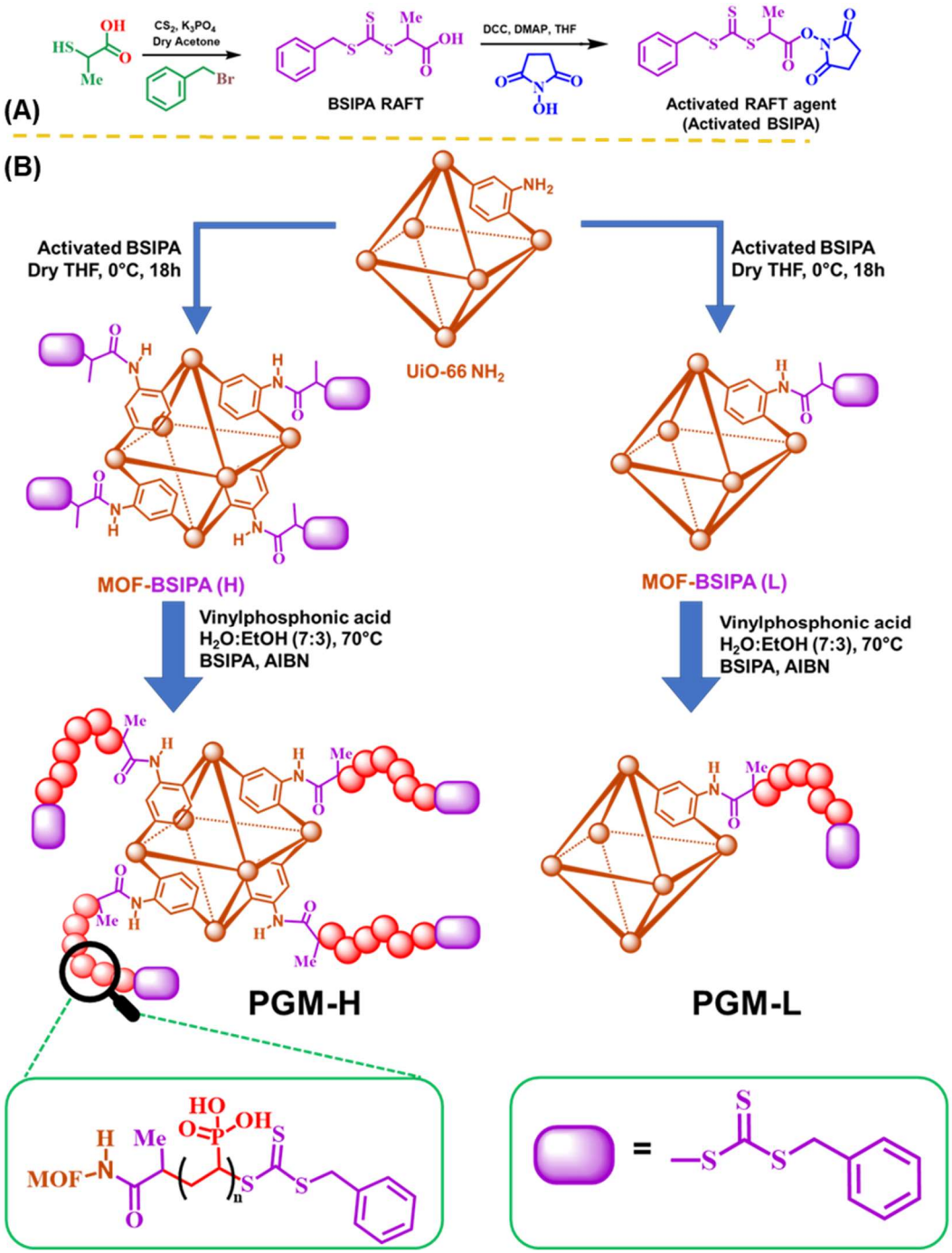

Scheme 5.1. Schematic representation of the synthesis of **(A)** BSIPA RAFT and activation, **(B)** surface functionalization procedure of UiO-66 NH_2 MOF with BSIPA RAFT agent with varying the amount of RAFT agent attached. MOF-BSIPA(H) and MOF-BSIPA(L) was further utilized to graft two different sets (PGM-H and PGM-L) of polymer grafted MOF using aqueous SI-RAFT technique.

Two different sets of PGM namely PGM-L and PGM-H were prepared with varying grafted PVPA chain length as described above. These samples are named as PGM-L1, PGM-L2, PGM-L3, PGM-H1, PGM-H2 where L and H represents lower and higher grafting of polymer chains on MOF surface. The different chain lengths of the polymer brush are represented by '1', '2' and '3' after the abbreviation. The complete process of making these samples are schematically represented in **Scheme 5.1** and physical properties of these samples are tabulated in **Table 5.1**.

Result and Discussion

An interesting fact to note that, here we have altered the polymer grafting density by carefully tuning the amount of trithiocarbonate based RAFT agent grafted on the surface of the nanomaterial by utilizing the available free amine groups on the UiO-66 NH_2 MOF surface. This helps us to get better control over the growth of the PVPA polymer chains during the SI-RAFT aqueous polymerization process. The low polydispersity (Đ) and high uniformity of the polymer grafted surface were possible to achieve by virtue of the RAFT process.

The BSIPA RAFT agent was sensibly designed thus, the activated carboxylic acid group (-COO-NHS) when attached covalently with the free primary amine groups (-NH_2) exist on the UiO-66 NH_2 surface by means of forming amide linkage so that, the phenyl group stays away from the MOF surface and acts as a Z group to control the reactivity of the C-S functionality of the BSIPA while the free radical leaving group R• remains attached to the MOF surface during the RAFT propagation process. Also, the methyl group was positioned strategically on the -CH position (which is a part of the R group here) adjacent to the trithiocarbonate group [-S-C(=S)-S-] to ensure the desired extra stability to the generated free radical species upon dissociation of the C-S bond present between the trithiocarbonate and the R group. Upon SI-RAFT polymerization process the growing polymer chains (PVPA) will reside between the trithiocarbonate group and the R group. Thus, the monomer units are getting attached towards the MOF surface of the active polymer chain keeping the trithiocarbonate group residing away from the MOF surface. This fundamental synthetic design strategy and the choice of RAFT agent (BSIPA) allows us to keep the polymer chains which consist of phosphonic acid pendent units closer to the MOF hollow core which will help not only to provide greater amount of interaction with the adjacent MOF moieties but also to incorporate and retain higher amount of water molecules in the inherent pores of the hollow MOF core.

Thus, the PVPA grafted MOF hybrid materials can result in designing better and improved materials for efficient proton conducting materials.

PGM-1(Li) was prepared by implementing ion exchange technique between the labile protons and Li^+ ions. Briefly, PGM-1 sample was stirred in 0.5 M aqueous LiCl solution for 24 h. upon completion of 24 h the sample [PGM-L1(Li)] was thoroughly washed in order to get rid of excess LiCl salt after ion exchange process. PGM-L1(Li) was particularly interesting as the material can provide better incite about the proton transfer process upon the exchange of labile protons with Li^+ ions.

Figure 5.1(A) illustrates the thermal degradation profiles of all the polymer grafted MOF materials with varying polymer chain grafting amount and chain lengths. In all the cases an initial gradual weight loss is observed till 200 °C which reflects the hygroscopic nature of the materials and accounts for the absorbed water molecules in the hollow framework. All the PGM materials are fairly stable up to ~450 °C while a little premature degradation is observed in case of PGM-H where the grafted polymer chain length is higher. We have observed that the PGM-L samples are showing even higher stability than the UiO-66-NH_2 under high temperature environment (till 450 °C) which contradicts to the fact that upon SI-RAFT polymerization the organic content of the MOF material increases and thus more weight loss is expected from the PGM samples. The anomaly in the TGA pattern can however be explained as the presence of phosphonic moiety in the grafted polymer chains plays a crucial role towards the thermal stability of the PGMs.[33] The presence of stable phosphorus (+5) moiety (acidic in nature) interacts at a greater extent with the available -NH_2 functionality (basic in nature) of the neighbouring framework structure, thus making the framework not only inter-connected in nature by virtue of strong acid-base, ionic, H-bonding and non-covalent interactions but also incorporates crystallinity in the system as observed from the HR-TEM and SAED data (described in the latter section). These interactions and crystallinity make the PGM materials less susceptible towards thermal degradation. Stability of Zr based MOF materials are well reported for better thermal stability even at 500 °C when the Zr nodes are surrounded by phosphonate ligands when compared to carboxylate ligands.[34,35] Furthermore, different systems are also reported where the presence of phosphoric acid doping enhances the thermal degradation of the materials.[36] On the other hand, when the polymer chain grafting density increases and crosses the optimum polymer loading, the presence of high polymer content in the system induces instability in the structure as observed from the weight loss pattern at 350 °C and finally the degradation at ~500 °C which originates from the decomposition of the

backbone structure of the PGM. Therefore, the grafting amount must be optimized in order to synthesize polymer-MOF conjugate with better thermal properties. TGA data of the BSIPA RAFT agent attached UiO-66-NH_2 [see **Figure 5.1(A)**] indicates that the thermal degradation increases with the increase in the BSIPA loading on the MOF surface as the BSIPA RAFT agent degrades above 200 °C. Among the two different types of the polymer grafting variation, we have achieved a maximum polymer grafting density (calculated from the weight loss data of TGA plot) of 336 mg/g of MOF material in the case of PGM-H2.

Gel permeable chromatography (GPC) was performed after chemically treating the polymer grafted MOF samples with HF in H_2O medium. As the grafting of the polymer chains are covalent in nature so, the MOF core needs to be digested in order to detach the grafted polymer chains to be analyzed by GPC technique. This treatment is well known in the literature to free the surface grafted polymer chains by the action of HF digesting the framework structure[20,37–39] (see details in the **Chapter 2** and **Appendix III**). Upon completion of the MOF core digestion treatment with HF, the solution was kept in a Petri dish in order to dry. The bare polymer chains were extracted with HPLC water, purified and then the molecular weights were determined with the help of GPC measurements using HPLC water as eluent [shown in **Figure 5.1(B)**]. All the molecular weights and the polydispersity index (Đ) value (PGM-L1 to PGM-H2) have been tabulated in **Table 5.1.** All the synthesized PGM samples showed a narrow Đ and the molecular weights acquired from the GPC technique are in agreement with the targeted molecular weight, which suggests that the polymer grafting took place using the RAFT polymerization technique.

UiO-66-NH_2, MOF-BSIPA(H), PGM samples were analyzed by powder XRD analyzer [see **Figure 5.1(C)**] and the samples were thoroughly validated against the simulated XRD pattern of the UiO-66 MOF. The synthesized UiO-66-NH_2 MOF material and all the PVPA polymer grafted MOF samples are in well agreement with the simulated crystallinity patterns which suggests that the integrity of the UiO-66 framework was undisturbed and the synthesized UiO-66-NH_2 is stable even after grafting PVPA chains. Upon evaluating the data obtained from PXRD studies, no significant change in the crystalline patterns are observed upon grafting of the RAFT agent on the MOF surface. Whereas, a decrease in the intensity and broadening of the sharp crystalline peaks for the polymer grafted MOF materials are observed and the broadening tend to increase as the polymer content increased. This observation is well justified owing to the fact that the MOF material is highly crystalline but the PVPA polymer shell is amorphous in nature and the insertion of polymer chains inside the inherent pores of the MOF material supresses the crystallinity of the MOF. The crystalline peaks around 2θ

values 8°, 20°, 35° and 55° indicates the presence of highly crystalline MOF core, although the peak positions are found to shift indicating the strong interactions acting between the grafted PVPA polymer chains and the MOF core. Another interesting observation is noticed upon increasing the grafting density of the grafted polymer chains is that the peak at 2θ=8.26° shifted to 8.04° implying that the polymer chains are prone to interact with the MOF core at a higher extent when the polymer chain density is increased resulting an increase in the d-spacing value. The observation was further evaluated from the TEM studies (discussed in the later section). To analyze further in terms of stability, PGM-L3 material is found to be stable in terms of retaining the crystalline nature even after keeping for 6 months at room temperature. Further analysis was performed on PGM-L3 sample after keeping under high temperature and humidity condition for 10 days and the samples were evaluated for EDX analysis and the sample is able to retain its Zr and phosphorus ratio (**Appendix III-Figure 5.2**).

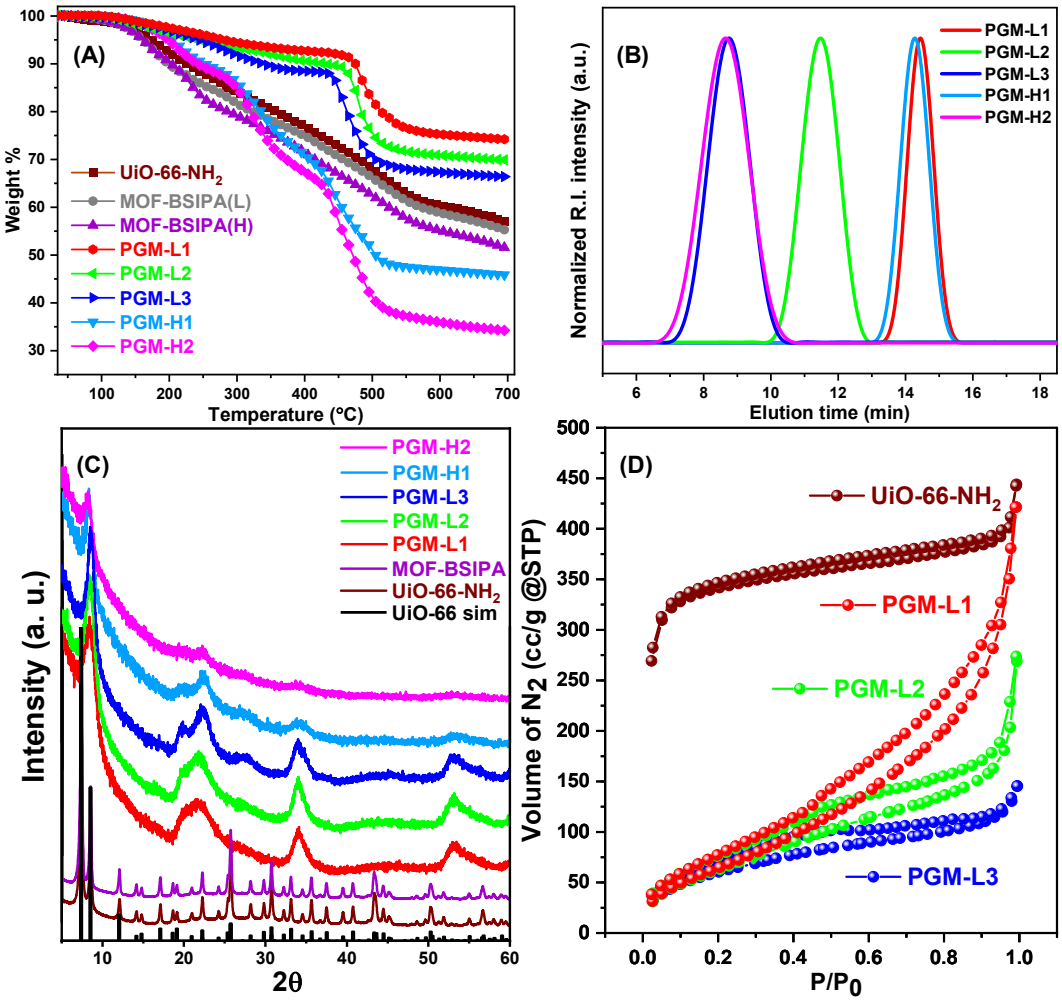

Figure 5.1. TGA plot of surface polymer grafted MOF materials along with the UiO-66-NH_2, MOF-BSIPA(L) and MOF-BSIPA(H) **(A).** GPC plots for the PGM samples after the detachment of the grafted polymer chains from the MOF surface **(B)**. PXRD plot **(C)** and BET isotherm plot **(D)** of polymer grafted MOF samples.

All the samples were further analyzed using FT-IR technique to understand the effect of polymer grafting on the MOF samples. Notable similarities are existing between the PGM samples and the core MOF [see **Appendix III-Figure 5.6** and **Appendix III-Figure 5.7**]. Stretching frequency at 1565 cm^{-1} is present in all the samples which corresponds to the presence of C=O bond of the carboxylate group. The N-H bond stretching vibration is present at 3365 cm^{-1} and an intense peak appears at 3460 cm^{-1} which corresponds to the symmetric O-H bond stretching present due to the presence of unbound water molecules. The broad peak originated in the range 1700-1630 cm^{-1} for all the PGM-L and PGM-H indicates the presence of phosphonic acid. An additional broad peak in the range of 3600-2800 cm-1 corresponds to the presence of phosphonic acid units along with the presence of sp^3 C-H stretching (originating from the PVPA backbone) and the presence of unbound water molecules. The broad FT-IR peak in the range of 3600-2800 cm^{-1} becomes more get intense with the higher grafting of the PVPA polymer chains. To check the stability, the samples were subjected to different harsh environments and are found to be highly stable (see **Appendix III-Figure 5.2**). PGM-L1(Li) and PVPA polymer (without the presence of MOF core) were also analyzed and the peak positions were validated (**Appendix III-Figure 5.7**).

In order to confirm the grafting of the PVPA polymer chains on the UiO-66-NH_2 MOF surface, we have taken dry PGM-L3 as a representative sample, dispersed the sample in D_2O and recorded ^{1}H-NMR, ^{13}C-NMR and ^{31}P-NMR spectra (**Appendix III-Figure 5.3-5.5**). In ^{1}H-NMR spectra peak at 1.1 ppm corresponds to the -CH_3 group present in the RAFT moiety. The NMR signals at 1.75 ppm and 2.5 ppm correspond to the presence of -CH and -CH_2 functionality in the PVPA backbone, respectively. Peak at 2.75 ppm arises due to the presence of -CH group attached to the amide functionality. Peak at 3.8 ppm corresponds to the benzylic protons. The phosphonic acid units containing -OH groups appear at 4.8 ppm and cannot be separated from the peak arises due to the presence of trace amount of H_2O present in the D_2O. The broad peaks arise ~7-8 ppm corresponds to the BDC-NH_2 linker. ^{13}C-NMR data further confirms the grafting of the polymer chain on the MOF surface (**Appendix III-Figure 5.4**). ^{31}P-NMR reveals the presence of two sets of peaks corresponding to the PVPA polymer chain where the first peak along with a shoulder peak appears ~24 ppm originating from the terminal phosphonate groups (neighbouring the trithiocarbonate and the amide linkage respectively) and a broad peak around 30 ppm corresponding to the remaining phosphonic acid units in the grafted polymer chain (**Appendix III-Figure 5.5**).

Strong acid-base and H-bonding interactions have a dominating effect towards the structural aspect of the PVPA-g-MOFs. BET nitrogen adsorption analysis [see **Figure 5.2 (D)** and **Appendix III-Figure 5.8**] of PGM samples were performed to understand the change in the porous nature of the core MOF upon polymer chain grafting. Samples were subjected to vacuum at 80 °C for 18 hours to remove the air and moisture molecules adsorbed in the inherent pores of the material. PGM samples display the type-I behaviour with rapid rise of the isotherm at around P/P_0 value = 0.9−1, a typical phenomenon which is often observed in the case of microporous materials. UiO-66-NH_2 gives a surface area of 1012 $m^2\ g^{-1}$, but we have observed a significant decrease in the surface area values for PGM samples attributing that the grafting of the PVPA polymer chains must have covered the pores present in the pristine MOF material. We have also observed a reduction in the surface area as the chain length of the grafted polymer chain increases as 262, 245 and 217 m^2g^{-1} for PGM-L1, PGM-L2 and PGM-L3, respectively. The PVPA polymer chain contain small dangling cones (~2.7 Å in height) of phosphonic acid unit from the polyvinyl backbone which can easily penetrate the pores of the MOF unit. The decrease in the pore size value from 15.83 Å (UiO-66-NH_2) to 15.28 Å (PGM-L1) and from 15.15 Å (PGM-L2) to 14.96 Å (PGM-L3) supports our conclusion that the grafted polymer chains are not only covering up the surface of the pristine MOF but also filling up the inherent pores of the framework structure and the effect gets prominent as the chain length of the grafted polymer chain increases (**Appendix III-Figure 5.8**). The increase in the number of dangling phosphonic acid units also increases with the higher chain length of the grafted polymer chains and there by increases acid-base, H-bonding, non-covalent interactions by many folds and creates a much-suited environment not only to adsorb water molecules in the newly polymer decorated pores but also to hold the adsorbed water molecules with better efficiency by virtue of H-bonding, ionic and non-covalent interactions. In order to investigate deep into the water sorption and water retention properties of the material, samples were subjected to dynamic vapor sorption studies (**Appendix III-Figure 5.29**). The data indicates that upon the grafting of PVPA polymer chains, the material becomes highly hygroscopic in nature as the water sorption capacity increases to 0.19g of water /g of PGM-L3 while the water sorption value was 0.14g of water/g of UiO-66-NH_2. The enhancement in the water sorption capacity arises due to the presence of highly hygroscopic nature of the grafted PVPA chains. The sorption value further increases for PGM-H samples and the highest value obtained was 0.204g of water/g in case of PGM-H2. The pristine MOF sample has inherent pores, which can be observed from the absence of a substantial hysteresis loop in the adsorption-desorption isotherm. In contrast, the PGM samples showed a considerable large hysteresis loop, which suggests that the

diffusion of water molecules from the bulk to the surface has a different kinetics, and the PGMs have a high affinity towards water molecules not only on the surface but also the water molecules that enter the bulk of the material. Therefore, PGMs exhibit a box-suction-dominated mechanism as the hollow hydrophilic interiors are decorated with hydrophilic polymer chains. In the case of the PGM samples, the initial and final points of the isotherm are disconnected, suggesting that the sample could hold water molecules in the polymer-decorated cavity even after a reduction in the relative humidity to a greater extent. The adsorption isotherm further supports our argument of the highly hygroscopic nature induced in the system upon grafting with phosphonic acid units containing polymer chains.

Detailed morphological investigations [**Figure 5.2(A-D)** and **Appendix III-Figure 5.9-5.28**] of the PGM samples were performed using FESEM, TEM and EDS FESEM analysis confirms that the MOF particles are spheroid in nature with a diameter of 150-200 nm. MOF-BSIPA shows a porous surface with slight agglomeration of the nanoparticles whereas the increased agglomerated morphology is observed with the grafting of the polymer chains and becomes more prominent with increasing polymer chain length. This is expected because of the strong interactions between PVPA-g-MOF particles through H-bonding, acid-base and electrostatic interactions. A noticeable change in the particle surface in case of PGM-L3, PGM-H1 and PGM-H2 samples, is also spotted as the polymer patches are significantly visible where the grafted polymer chains are of high molecular weight or the grafting density of the polymer chains are high. The same observation is also validated from TEM images (**Figure 5.3**). The evidences were further crosschecked with FESEM-EDX and TEM-EDX data (**Appendix III-Figure 5.10-5.18 and Appendix III-Figure 5.23-5.26**) which confirms the phenomenon is predominantly observed because of the presence of the grafted PVPA chains on the surface. This study again confirms directly that the grafting of polymer chains is covalent in nature and are uniformly distributed throughout the material at a molecular level. The elemental mapping data obtained from FESEM and TEM EDX analysis (**Appendix III-Figure 5.10-5.18 and Appendix III-Figure 5.23-5.26**) further confirms the even distribution of the elements throughout the material surface. The EDX data indicates the increase in the phosphorus content of the PGM materials upon the increment of the chain length and the grafting density of the PVPA polymer chains and in the case of PGM-H2 (highest chain length and the highest grafting density of the grafted PVPA chains) sample, the abundance of phosphorus is found to be the highest as per expectation.

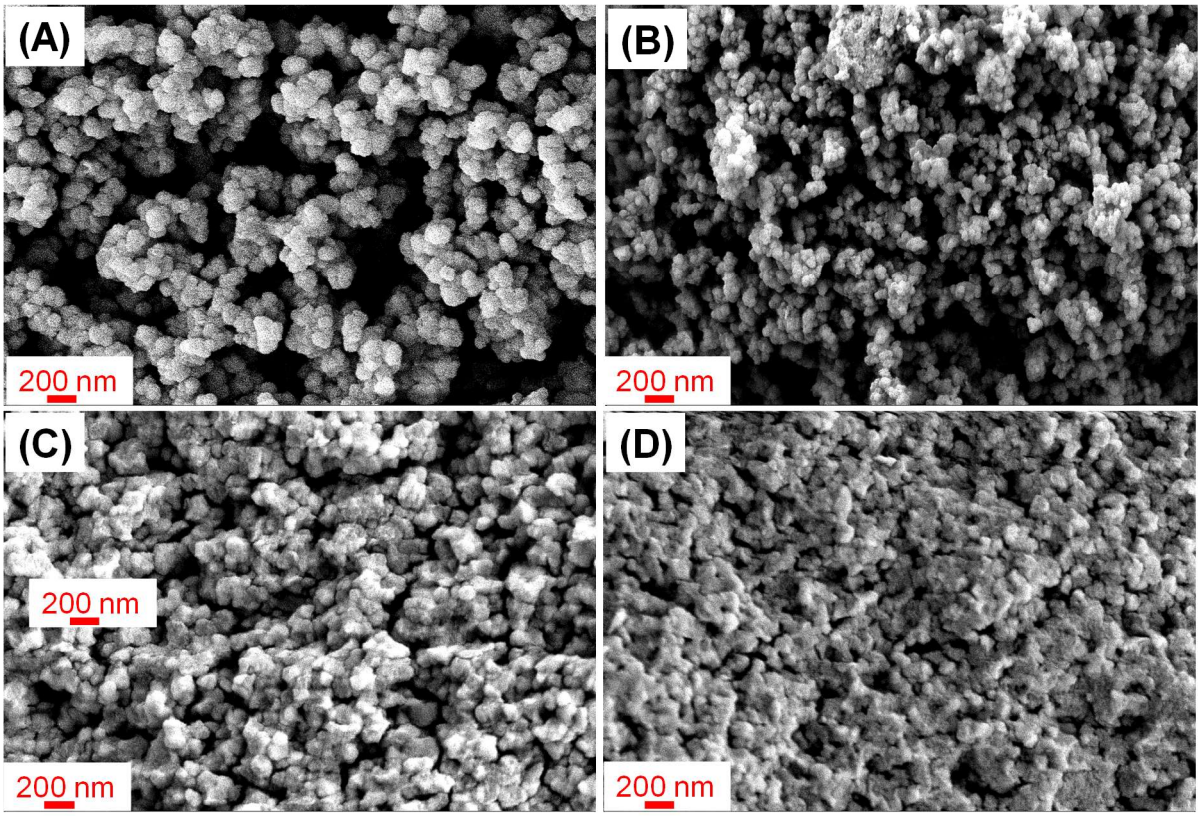

Figure 5.2. FESEM images of polymer grafted MOFs **(A)** PGM-L1, **(B)** PGM-L3, **(C)** PGM-H1, **(D)** PGM-H2.

HR-TEM analysis provides insight about the inherent porosity of the PGM materials. Careful observation of the data obtained from TEM analysis suggests that the grafted polymer chains have an adverse effect on the porosity of the PGM samples in the dry state as the polymer chains are found to cover up the porous core of the MOF. The detailed analysis of the lattice fringe spacing measurements obtained from the HR-TEM images (**Figure 5.3**) illustrates that the spacing between the lattice planes are getting narrower upon the increment of the grafted polymer chain length and the grafting density. This observation suggests that the inherent pores are getting filled up with the grafted polymer chains and are getting closer by means of strong interaction patterns acting between the MOF and the PVPA chains. The observation converges with the data obtained from the BET analysis (discussed in earlier section). Upon extensive stability treatment, the PGM samples were analyzed under FESEM and EDS which directly proves that the grafted polymer chains are highly stable and the PVPA grafted MOF materials are stable under the harsh conditions (**Appendix III-Figure 5.2** and **Appendix III-Figure 5.19**).

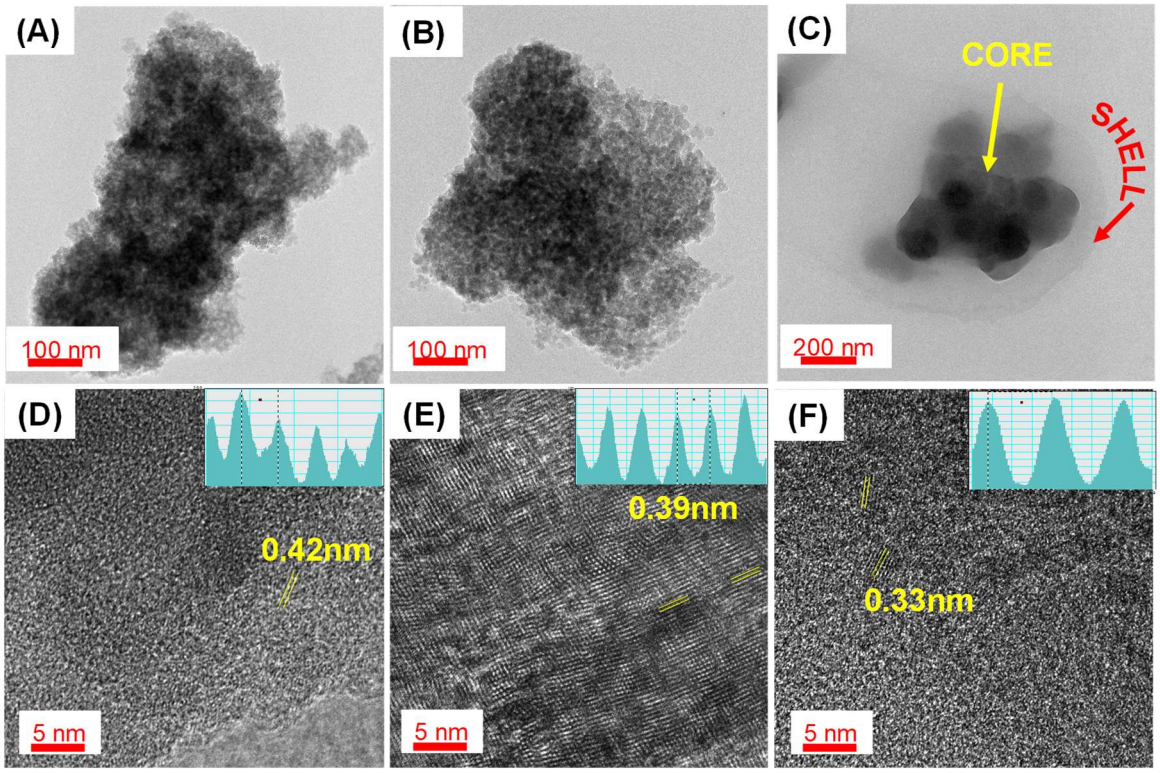

Figure 5.3. TEM images of **(A)** PGM-L3, **(B)** PGM-H1 and **(C)** PGM-H2. **(D)**, **(E)** and **(F)** represent the high-resolution images corresponding to **(A)**, **(B)** and **(C),** respectively.

The aqueous dispersion stability of the PGMs were studied by measuring Zeta potential (**Appendix III-Figure 5.30**). The study shows that all the PGM samples are highly stable under aqueous dispersion condition. The zeta potential values are negative for all the PGM samples which is expected owing to the presence of phosphonic acid units dangling from the grafted PVPA chains on the surface of the nanoparticles under aqueous dispersion condition. The zeta potential values are also listed in the **Table 5.1**. Moreover, the data also suggests that the zeta potential is observed to increase a little with higher chain length of the grafted polymer chains but with increment in the polymer grafting density the reverse trend is observed. For the PGM-L1(Li) a little increase in the zeta potential value is observed (-59.8mV) which directly implies the presence of Li+ ions in the system which enhances the dispersion stability in the aqueous medium.

Table 5.1. Physical properties of the surface functionalized MOF materials.

Sample name	Sample type[a]	Remaining weight % at 700 °C (wt%) [b]	Polymer content[c]	$\bar{M}_w$ [d]	$\bar{M}_n$ [e]	Đ [f]	Zeta potential (mV)[g]
UiO-66-NH_2	-	56.96	-	-	-	-	-20
MOF-BSIPA(L)	UiO-66-NH-BSIPA	55.28	29.5	-	-	-	-7.5
MOF-BSIPA(H)	UiO-66-NH-BSIPA	51.58	94.45	-	-	-	-5.8
PGM-L1	$PVPA_{95}$-*g*-MOF	74.21	-	10373	10270	1.01	-49.6
PGM-L2	$PVPA_{182}$-*g*-MOF	69.91	-	20417	19632	1.04	-57.9
PGM-L3	$PVPA_{268}$-*g*-MOF	66.40	-	30346	28901	1.05	-63.6
PGM-H1	$PVPA_{98}$-*g*-MOF	45.88	110.5	10756	10545	1.02	-22.9
PGM-H2	$PVPA_{272}$-*g*-MOF	34.23	336.4	31169	29405	1.06	-18.4

[a] sample type describes the degree of polymerization for each sample included in the suffix which are obtained from the molecular weight measurements using gel permeation chromatography, [b] estimated from the TGA analysis (at 700 °C) and [c]Polymer content was obtained from the analysis of the TGA curves in **Figure 5.1(A)** and expressed as amount (in mg) of polymer chains /g of MOF-BSIPA, [d], [e] and [f] are determined by gel permeation chromatography, and [g] obtained from Zeta potential analysis in HPLC water**.**

Proton conductivity studies

Taking into consideration the grafting of hygroscopic PVPA polymer chains on the MOF surface and the promising physical properties including high thermal stability, low polydispersity of the grafted polymer chains, considerably high hydrophilicity of the PGM samples, we further studies proton conducting abilities of PGMs under humidified environment at varying temperatures. In order to verify whether the origin of the conductivity is due to the available protons in the polymer grafted MOFs system (Brønsted acid groups) or due to the transportation of other mobile charge carriers, such as electrons and metal ions, we have taken PGM-L1 as a representative sample and exchanged the available protons in the sample with

Li^+ ions, following a procedure from previous literature report. This controlled experiment is expected to provide us with better understanding of the origin of the conductivity.

Proton conductivity was measured using electrochemical impedance spectroscopy (EIS) (details of sample preparation procedure and the methodology are given in **Chapter 2** and **Appendix III**). Nyquist plots were constructed using the real (Z′) and imaginary (Z″) part of the impedance as obtained from the EIS measurements. The samples in the form of pellets were allowed to equilibrate for 30 minutes under a constant temperature and relative humidity condition before taking impedance readings. The PGM pellets were further analyzed after EIS measurements using PXRD, FT-IR, FESEM, TEM, EDX and mapping studies, and no notable changes were observed which directly provides evidence towards the stability of the material under the experimental conditions. Further PGM samples were tested by keeping the samples under high pressure (6 ton) for 1 h and high temperature (80 °C) in 98% relative humidity condition. FT-IR and FESEM data reveals that the samples were highly stable under the above-mentioned conditions which provides a direct proof of the stability of the samples (**Appendix III-Figure 5.7**).

The proton conductivity recorded at 40 °C and 98% RH for PGM-L1 is 3.5×10^{-3} S cm^{-1} whereas for PGM-L3 the conductivity is 7×10^{-3} S cm^{-1}, that is ~2 times increase. The increment in the proton conductivity considering the fact that both the samples were kept under identical conditions is only possible because of the presence of varying molecular weight of the grafted polymer chains which contributes to the proton conduction abilities of the material to a great extent. The proton conductivity value observed for PGM-L3 sample at 80 °C is 1.26×10^{-2} S cm^{-1} which is an 80% increase in the proton conductivity as compared to that in lower temperatures. Nyquist plots obtained from impedance measurements of the samples are provided in **Appendix III-Figure 5.32**. A careful observation of the data sets (**Appendix III-Figure 5.32** and **Figure 5.4**) obtained from various experiments suggests that the presence of strong and complex interaction patterns including H-bonding interactions, acid-base interaction, ionic and non-covalent interactions between the cationic Zr_6 nodes $\{Zr_6O_4(OH)_4\}$, $-NH_2$ groups (Brønsted base), the grafted PVPA chains consisting of dangling phosphonic acid groups (Brønsted acid) and the adsorbed water molecules in the structure create numerous proton enriched nano channels in the matrix leading to the strong proton conduction characteristics.

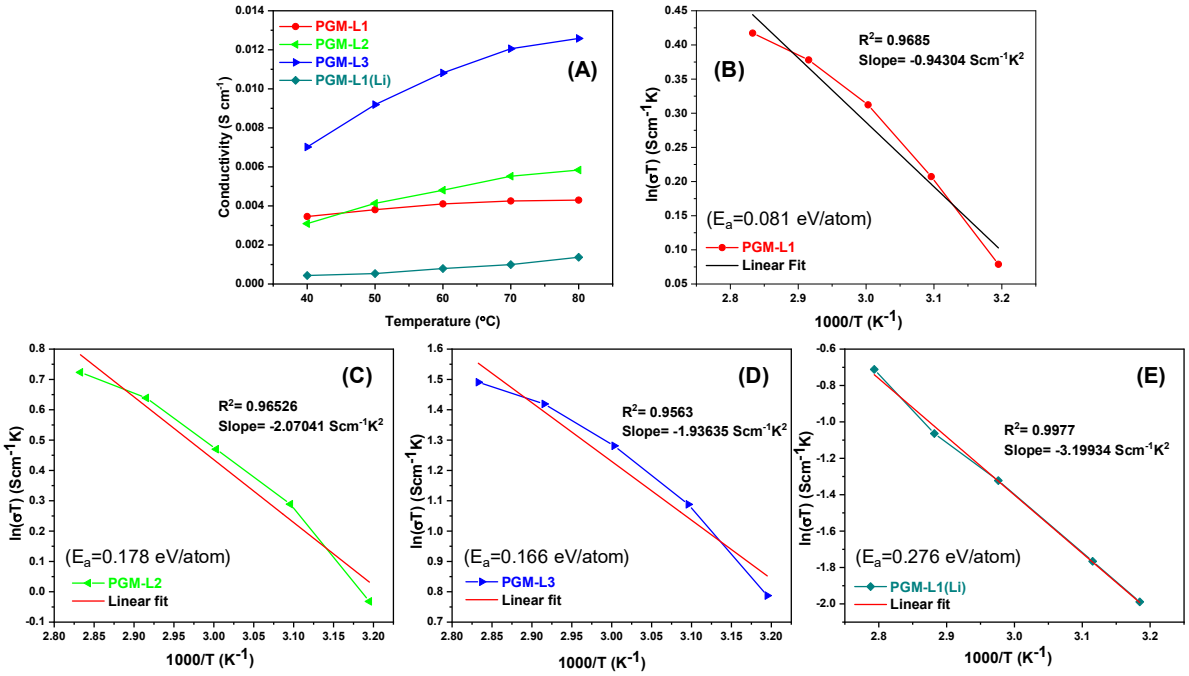

Figure 5.4. (A) Temperature dependent proton conductivity values and **(B-E)** activation energy plot of PGM samples.

The close proximity and the tight packing of the sample particles in a pellet, as evident from the microscopic evaluation of the prepared pellet (**Figure 5.5**) provides an ideal platform for the formation of water channels under humidified condition. The FESEM EDX mapping data further confirms that the pellets are able to hold the structural integrity during the proton conductivity measurements and the distribution of the elements are uniform throughout the system. Moreover, the pellets maintained a stable Zr: P ratio even after the EIS measurements at 80 °C and 98% RH confirming to the fact that the grafting of PVPA polymer chains on the MOFs are stable in nature (**Appendix III-Figure 5.14** and **Appendix III-figure 5.19)**. Thus, the PGM samples were found to be efficient proton conducting solid electrolyte materials.

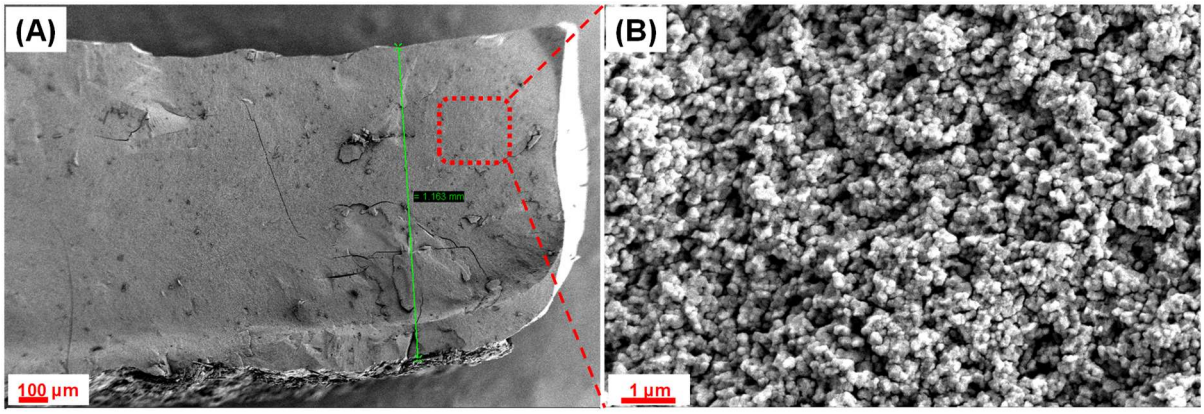

Figure 5.5. FESEM image of PGM-L3 sample after conductivity studies **(A)** in pellet form and **(B)** magnified surface image.

In order to investigate the effect of the replacement of the labile protons from the system, PGM-L1(Li) was studied for its proton conductivity using EIS (**Figure 5.4** and **Appendix III-Figure 5.32**). The data reveals that the Li^+ ion exchange results in a significant loss in proton conducting ability of the solid electrolyte. The highest observed proton conductivity for PGM-L1(Li) is 1.37×10^{-3} at 80 °C and 98% RH, which is pretty low compared to its parent material PGM-L1, and having an activation energy of 0.2756 eV/atom. This data illustrates that the replacement of H^+ ions with Li^+ ions naturally lower the carrier concentration in the material and also disrupts the H-bonded network. And this caused a lowering of the proton conductivity of the material.

For the sake of curiosity and to have a better understanding of the effect of polymer grafting we have chosen PGM-H1 as another example and have studied its proton conductivity (**Figure 5.6**). In this case, due to the presence of a high amount of hygroscopic polymer chain grafted on the MOF particles, the bulk material was difficult to be studied as pellets under high relative humidity of 98%. But upon careful designing of the proton conductivity experiment under low humidity condition, the PGM-H1 sample is able to function as a much better proton conductor (9.8×10^{-3} S cm^{-1}) at mild temperatures (60 °C) and relative humidity (75%) as compared to PGM-L3.

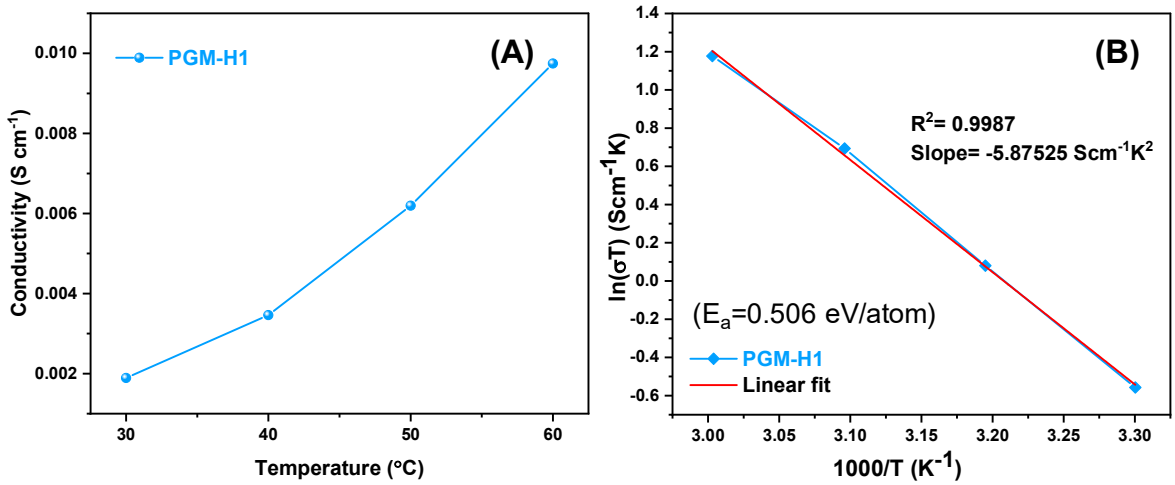

Figure 5.6. (A) Temperature dependent proton conductivity value and **(B)** activation energy plot of PGM-H1 at 75% relative humidity condition.

An evaluation of the various experiments along with the activation energy studies (**Figure 5.4** and **5.6**) suggest that the water assisted proton conductivity of the samples is due to the presence of labile protons in the system and primarily due to the presence of grafted polymer chains containing phosphonic acid moieties. The activation energy (E_a) values [**Figure 5.4 (B-E)**] for PGM-L samples suggest that the proton transport is occurring by continuous

making and breaking of labile H-bonds i.e., Grotthuss mechanism (proton hopping mechanism). **Scheme 5.2** illustrates the proton hopping pathway in the PGM matrix. On the other hand, an anomaly is observed for PGM-H1 as the E_a for the sample is on much higher range (0.5062 eV/atom). The presence of higher amount of polymer chains (considering the ratio of MOF and the grafted polymer chains) in the matrix is well known to introduce vehicular mechanism along with the Grotthuss mechanism, which might be affecting the activation energy parameters of the system. Nevertheless, a sweet balance between the MOF material and the grafted polymer chain is an essential factor in order to achieve high proton conductivity with low activation energy. This work opens up new possibilities and new scopes towards designing and upgradation of solid electrolytes which can enhance the proton conduction efficiently and can withstand the harsh environments of high temperature and relative humidity conditions. Upon evaluation of the proton conductivity and stability data, PGM-L samples have been found to remain better resistant under high humidified condition, whereas the PGM-H sample showed better efficiency of proton conduction even at low temperature and less humid environment.

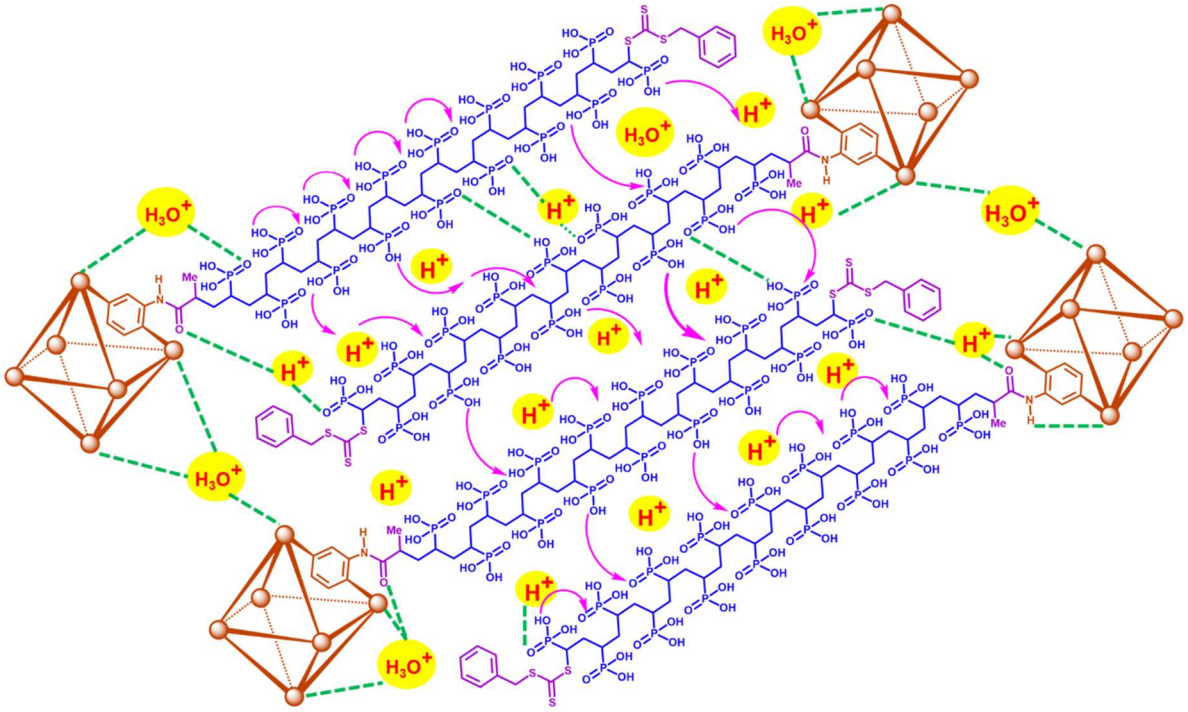

Scheme 5.2. Proton hopping mechanism during the proton conductivity study of PGM samples under humidified condition.

Conclusion

We have successfully designed an efficient method for grafting polymer chains, in the current study PVPA chains, on the MOF surface by the utilization of the available functionality on the MOF surface. We have executed the grafting of polymer chains in an easy, efficient and less hazardous way under aqueous condition using SI-RAFT *grafting from* approach resulting narrow polydispersity and better control over molecular weights of the grafted chains. We have also varied the grafting density of the grafted PVPA polymer chains on the MOF surface (PGM-L and PGM-H) with further variation in the chain length of the attached polymer chains and the grafting was confirmed in terms of FT-IR, NMR, FESEM, TEM, EDX and mapping studies. High thermal stability, strong water affinity and the ability to create labile proton enriched environment in the vicinity of the material by virtue of the presence of the grafted PVPA chains makes PGM particles a potential candidate to conduct protons efficiently under humidified condition. Further investigation on the proton conduction ability of the PGM samples under different temperatures and relative humidity conditions were conducted along with the stability studies of the samples under such conditions. We have achieved proton conductivity of 1.26×10^{-2} S cm^{-1} at 80 °C for PGM-L3 sample under 98% relative humidity and 9.8×10^{-3} S cm^{-1} at 60 °C for PGM-H1 sample under 75% relative humidity which are amongst the premium values reported till date for MOF based systems operating below 100 °C. We have successfully investigated and proved that the origin of the conductivity is because of the presence of the labile protons owing to the presence of dangling phosphonic acid groups of the grafted PVPA chains in the system and the polymer-MOF super hybrid materials (PGMs) are highly stable and can retain their proton conductivity upon long term usage.

Reference

(1) Daglar, H.; Keskin, S. Combining Machine Learning and Molecular Simulations to Unlock Gas Separation Potentials of MOF Membranes and MOF/Polymer MMMs. *ACS Appl. Mater. Interfaces* **2022**, *14*, 32134–32148.

(2) Li, Y.-Z.; Wang, G.-D.; Ma, L.-N.; Hou, L.; Wang, Y.-Y.; Zhu, Z. Multiple Functions of Gas Separation and Vapor Adsorption in a New MOF with Open Tubular Channels. *ACS Appl. Mater. Interfaces* **2021**, *13*, 4102–4109.

(3) Emerson, A. J.; Hawes, C. S.; Marshall, M.; Knowles, G. P.; Chaffee, A. L.; Batten, S. R.; Turner, D. R. High-Connectivity Approach to a Hydrolytically Stable Metal–Organic Framework for CO 2 Capture from Flue Gas. *Chem. Mater.* **2018**, *30*, 6614–6618.

(4) Chen, C.-X.; Wei, Z.-W.; Jiang, J.-J.; Zheng, S.-P.; Wang, H.-P.; Qiu, Q.-F.; Cao, C.-

C.; Fenske, D.; Su, C.-Y. Dynamic Spacer Installation for Multirole Metal–Organic Frameworks: A New Direction toward Multifunctional MOFs Achieving Ultrahigh Methane Storage Working Capacity. *J. Am. Chem. Soc.* **2017**, *139*, 6034–6037.

(5) Shekhawat, A.; Samanta, R.; Barman, S. MOF-Derived Porous Fe 3 O 4 /RuO 2 -C Composite for Efficient Alkaline Overall Water Splitting. *ACS Appl. Energy Mater.* **2022**, *5*, 6059–6069.

(6) Chang, R.; Ma, S.; Guo, X.; Xu, J.; Zhong, C.; Huang, R.; Ma, J. Hierarchically Assembled Graphene Oxide Composite Membrane with Self-Healing and High-Efficiency Water Purification Performance. *ACS Appl. Mater. Interfaces* **2019**, *11*, 46251–46260.

(7) Saleem, H.; Rafique, U.; Davies, R. P. Investigations on Post-Synthetically Modified UiO-66-NH 2 for the Adsorptive Removal of Heavy Metal Ions from Aqueous Solution. *Microporous Mesoporous Mater.* **2016**, *221*, 238–244.

(8) Alves, R. C.; Schulte, Z. M.; Luiz, M. T.; Bento da Silva, P.; Frem, R. C. G.; Rosi, N. L.; Chorilli, M. Breast Cancer Targeting of a Drug Delivery System through Postsynthetic Modification of Curcumin@N 3 -Bio-MOF-100 via Click Chemistry. *Inorg. Chem.* **2021**, *60*, 11739–11744.

(9) Lawson, H. D.; Walton, S. P.; Chan, C. Metal–Organic Frameworks for Drug Delivery: A Design Perspective. *ACS Appl. Mater. Interfaces* **2021**, *13*, 7004–7020.

(10) He, B.; Zhang, Q.; Pan, Z.; Li, L.; Li, C.; Ling, Y.; Wang, Z.; Chen, M.; Wang, Z.; Yao, Y.; Li, Q.; Sun, L.; Wang, J.; Wei, L. Freestanding Metal–Organic Frameworks and Their Derivatives: An Emerging Platform for Electrochemical Energy Storage and Conversion. *Chem. Rev.* **2022**, *122*, 10087–10125.

(11) Somnath; Waris; Ali, A.; Ahmad, M.; Siddiqui, K. A. Bifunctional Self-Penetrating Co(II)-Based 3D MOF for High-Performance Environmental and Energy Storage Applications. *Cryst. Growth Des.* **2022**, *22*, 7374-7394.

(12) Li, X.-M.; Wang, Y.; Mu, Y.; Liu, J.; Zeng, L.; Lan, Y.-Q. Superprotonic Conductivity of a Functionalized Metal–Organic Framework at Ambient Conditions. *ACS Appl. Mater. Interfaces* **2022**, *14*, 9264–9271.

(13) Paul, S.; Choi, S.-J.; Kim, H. J. Enhanced Proton Conductivity of a Zn(II)-Based MOF/Aquivion Composite Membrane for PEMFC Applications. *Energy & Fuels* **2020**, *34*, 10067–10077.

(14) Mukhopadhyay, S.; Das, A.; Jana, T.; Das, S. K. Fabricating a MOF Material with Polybenzimidazole into an Efficient Proton Exchange Membrane. *ACS Appl. Energy Mater.* **2020**, *3*, 7964–7977.

(15) Nguyen, H. L.; Matheu, R.; Diercks, C. S.; Doan, T. L. H.; Nguyen, B. T.; Cordova, K. E. Postsynthetic Metalation of a New Metal–Organic Framework To Improve Methane Working Storage Capacity. *ACS Mater. Lett.* **2022**, *4*, 2375–2380.

(16) Li, F.; Du, M.; Xiao, X.; Xu, Q. Self-Supporting Metal-Organic Framework-Based Nanoarrays for Electrocatalysis. *ACS Nano* **2022**, *16*, 19913–19939.

(17) Cohen, S. M. Postsynthetic Methods for the Functionalization of Metal–Organic Frameworks. *Chem. Rev.* **2012**, *112*, 970–1000.

(18) Ponomareva, V. G.; Kovalenko, K. A.; Chupakhin, A. P.; Dybtsev, D. N.; Shutova, E. S.; Fedin, V. P. Imparting High Proton Conductivity to a Metal–Organic Framework Material by Controlled Acid Impregnation. *J. Am. Chem. Soc.* **2012**, *134*, 15640–15643.

(19) Zhang, B.; Bai, X.; Wang, S.; Li, L.; Li, X.; Fan, F.; Wang, T.; Zhang, L.; Zhang, X.; Li, Y.; Liu, Y.; Chen, J.; Meng, F.; Fu, Y. Preparation of Superhydrophobic Metal–Organic Framework/Polymer Composites as Stable and Efficient Catalysts. *ACS Appl. Mater. Interfaces* **2021**, *13*, 32175–32183.

(20) Mukhopadhyay, S.; Debgupta, J.; Singh, C.; Sarkar, R.; Basu, O.; Das, S. K. Designing UiO-66-Based Superprotonic Conductor with the Highest Metal–Organic Framework Based Proton Conductivity. *ACS Appl. Mater. Interfaces* **2019**, *11*, 13423–13432.

(21) Qian, Q.; Chi, W. S.; Han, G.; Smith, Z. P. Impact of Post-Synthetic Modification Routes on Filler Structure and Performance in Metal–Organic Framework-Based Mixed-Matrix Membranes. *Ind. Eng. Chem. Res.* **2020**, *59*, 5432–5438.

(22) Wang, H.; Zhu, Q.-L.; Zou, R.; Xu, Q. Metal-Organic Frameworks for Energy Applications. *Chem* **2017**, *2*, 52–80.

(23) Gavinehroudi, R. G.; Mahjoub, A.; Karimi, M.; Sadeghi, S.; Heydari, A.; Mohebali, H.; Ghamami, S. Non -Covalent LDH/MOF Composite Formation: A New Approach in Sustainability for Solvent-Dependent Photocatalytic Aerobic Alcohol Oxidation. *Green Chem.* **2022**, *24*, 6965–6979.

(24) Baumann, A. E.; Burns, D. A.; Liu, B.; Thoi, V. S. Metal-Organic Framework Functionalization and Design Strategies for Advanced Electrochemical Energy Storage Devices. *Commun. Chem.* **2019**, *2*, 86.

(25) Qian, Q.; Wu, A. X.; Chi, W. S.; Asinger, P. A.; Lin, S.; Hypsher, A.; Smith, Z. P. Mixed-Matrix Membranes Formed from Imide-Functionalized UiO-66-NH 2 for Improved Interfacial Compatibility. *ACS Appl. Mater. Interfaces* **2019**, *11*, 31257–31269.

(26) Basu, O.; Das, A.; Jana, T.; Das, S. K. Design of Flexible Metal–Organic Framework-Based Superprotonic Conductors and Their Fabrication with a Polymer into Proton Exchange Membranes. *ACS Appl. Energy Mater.* **2023**, *6*, 9092–9107.

(27) Figueroa-Quintero, L.; Villalgordo-Hernández, D.; Delgado-Marín, J. J.; Narciso, J.; Velisoju, V. K.; Castaño, P.; Gascón, J.; Ramos-Fernández, E. V. Post-Synthetic Surface Modification of Metal–Organic Frameworks and Their Potential Applications. *Small Methods* **2023**. https://doi.org/10.1002/smtd.202201413.

(28) Basu, O.; Mukhopadhyay, S.; De, A.; Das, A.; Das, S. K. Tuning the Electrochemical

and Catalytic ORR Performance of C 60 by Its Encapsulation in ZIF-8: A Solid-State Analogue of Dilute Fullerene Solution. *Mater. Chem. Front.* **2021**, *5*, 7654–7665.

(29) Mukherjee, N.; Das, A.; Mukhopadhyay, S.; Das, S. K.; Jana, T. Grafting of Polymer Brushes on MOF Surface to Achieve Proton-Conducting Membranes. *ACS Appl. Polym. Mater.* **2024**, *6*, 846–858.

(30) Shanahan, J.; Kissel, D. S.; Sullivan, E. PANI@UiO-66 and PANI@UiO-66-NH 2 Polymer-MOF Hybrid Composites as Tunable Semiconducting Materials. *ACS Omega* **2020**, *5*, 6395–6404.

(31) Muldoon, P. F.; Venna, S. R.; Gidley, D. W.; Baker, J. S.; Zhu, L.; Tong, Z.; Xiang, F.; Hopkinson, D. P.; Yi, S.; Sekizkardes, A. K.; Rosi, N. L. Mixed Matrix Membranes from a Microporous Polymer Blend and Nanosized Metal–Organic Frameworks with Exceptional CO 2 /N 2 Separation Performance. *ACS Mater. Lett.* **2020**, *2*, 821–828.

(32) Kalaj, M.; Cohen, S. M. Postsynthetic Modification: An Enabling Technology for the Advancement of Metal–Organic Frameworks. *ACS Cent. Sci.* **2020**, *6*, 1046–1057.

(33) Lv, X.; Fang, J.; Xie, J.; Yang, X.; Wang, J. Thermal Stability of Phosphorus-Containing Epoxy Resins by Thermogravimetric Analysis. *Polym. Polym. Compos.* **2018**, *26*, 400–407.

(34) Malfatti, L.; Falcaro, P.; Amenitsch, H.; Caramori, S.; Argazzi, R.; Bignozzi, C. A.; Enzo, S.; Maggini, M.; Innocenzi, P. Mesostructured Self-Assembled Titania Films for Photovoltaic Applications. *Microporous Mesoporous Mater.* **2006**, *88*, 304–311.

(35) Barthelet, K.; Merlier, C.; Serre, C.; Riou-Cavellec, M.; Riou, D.; Férey, G. Microporous Hybrid Compounds: Hydrothermal Synthesis and Characterization of Two Zinciomethylenediphosphonates with 3D Structures, Structure Determination of Their Dehydrated FormsElectronic Supplementary Information (ESI): Final Rietveld Plots for MIL-48. *J. Mater. Chem.* **2002**, *12*, 1132–1137.

(36) Mukherjee, N.; Das, A.; Jana, T. Poly(N -Vinyl Triazole- b - N -Vinyl Imidazole) Grafted on MWCNTs as Nanofillers to Improve Proton Conducting Membranes. *ACS Appl. Nano Mater.* **2023**, *6*, 544–557.

(37) Wang, H.; Mahle, J. J.; Tovar, T. M.; Peterson, G. W.; Hall, M. G.; DeCoste, J. B.; Buchanan, J. H.; Karwacki, C. J. Solid-Phase Detoxification of Chemical Warfare Agents Using Zirconium-Based Metal Organic Frameworks and the Moisture Effects: Analyze via Digestion. *ACS Appl. Mater. Interfaces* **2019**, *11*, 21109–21116.

(38) Ploskonka, A. M.; DeCoste, J. B. Tailoring the Adsorption and Reaction Chemistry of the Metal–Organic Frameworks UiO-66, UiO-66-NH2, and HKUST-1 via the Incorporation of Molecular Guests. *ACS Appl. Mater. Interfaces* **2017**, *9*, 21579–21585.

(39) Nagata, S.; Kokado, K.; Sada, K. Metal–Organic Framework Tethering PNIPAM for ON–OFF Controlled Release in Solution. *Chem. Commun.* **2015**, *51*, 8614–8617.

Chapter 6

Poly(N-vinyl triazole-b-N-vinyl imidazole) *Grafted* on MWCNTs as Nanofillers to Improve Proton Conducting Membranes

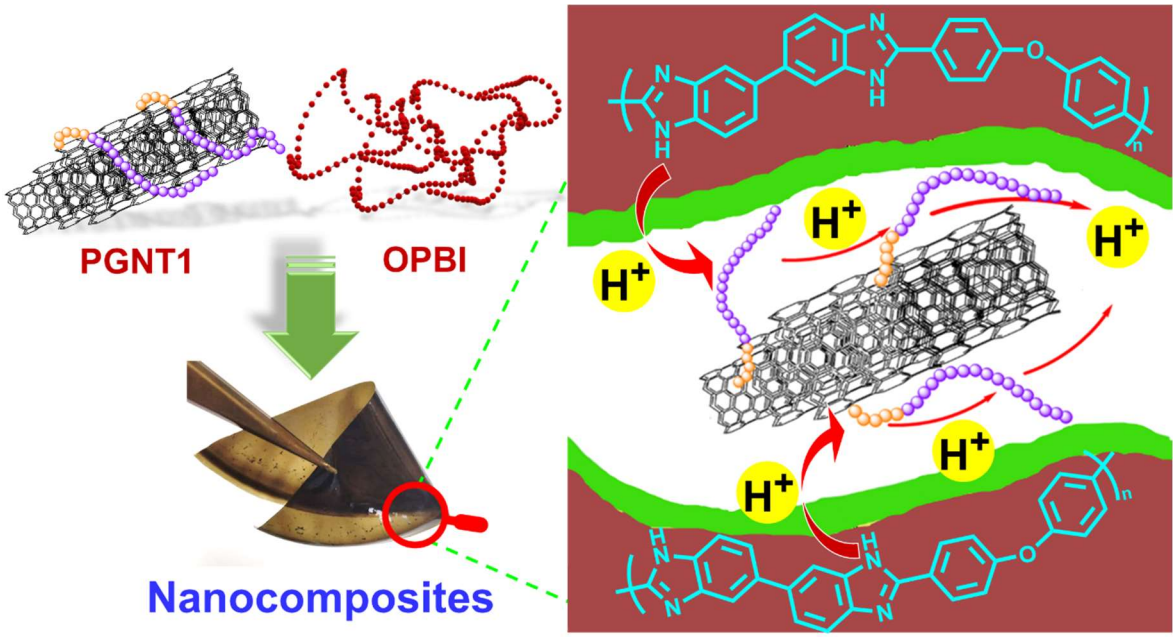

Nilanjan Mukherjee, Anupam Das, and Tushar Jana*. Poly(N-vinyl triazole-b-N-vinyl imidazole) Grafted on MWCNTs as Nanofillers to Improve Proton Conducting Membranes. *ACS Applied Nano Materials*. **2023**, *6*, 544-557.

Abstract

Carbon nanotubes (CNTs) are of particular interest because of their ability to enhance the mechanical strength in the material, however, processing difficulties of CNTs often restrict utilization up to its full potential. To resolve this, in the current study, we have developed a simple and efficient method to functionalize the surface of multiwalled carbon nanotube (MWCNT) with precise functional polymer chains, which were covalently *grafted* on the surface of the MWCNT and delved into an application to demonstrate this material as an efficient nanofiller in developing proton conducting membrane (PEM) from polybenzimidazole (PBI). At first, MWCNT surface was converted to a polymerizable surface by attaching a trithiocarbonate based chain transfer agent (CTA). Then, N-heterocyclic block copolymer namely poly-N-vinyl-1,2,4-triazole-*b*-poly-N-vinyl imidazole (pNVT-*b*-pNVI) was grown from the CTA anchored surface in one-pot surface initiated reversible addition fragmentation chain transfer (SI-RAFT) technique. *Grafting* of block copolymer chain was confirmed by GPC, NMR and TGA studies. To the best of our knowledge, this will be the first report of growing block copolymer structure *grafted* covalently on the surface of the MWCNT. The novelty of the work was further enhanced by incorporating pNVT-*b*-pNVI-*g*-MWCNT as nanofiller into the oxypolybenzimidazole (OPBI) membrane to obtain homogeneous nanocomposite membranes with an excellent thermomechanical and tensile properties, thermal stability, superior proton conduction when doped with phosphoric acid (PA) and the acid (PA) holding capacity. The nanocomposite membrane with 2.5 wt% nanofiller loading displayed a tensile stress of 1.8MPa, strain of 176% at break and exhibited proton conductivity as high as 0.164 S cm^{-1} at 180°C which is a 2.6-fold increment when compared with pristine OPBI membrane. This significant increase in conductivity is attributed to the new proton conducting nano channel pathway generated along the polymer-*g*-MWCNT surface.

Introduction

Carbon nanotubes (CNTs) have attracted immense interest of material scientists due to its versatile chemical characteristics and physical properties in catalysis[1–3], gas adsorption[4], water purification[5,6], electrical and thermal conductivity[7–10] and high mechanical stability,[11,12] since the discovery.[13] However, there is a significant limitation on the usage of CNTs because of the presence of strong van der Waals interaction which makes it insoluble in almost all the solvents and are held together tightly to form bundles and rope like aggregation in solution and also in the polymer matrix.[14–16] This strong aggregating nature restricts their processability and

hampers the performance in nano level.[17,18] To address these problems, different approaches have evolved in literature which include modification with surfactant, polymer absorption, encapsulation of polymer, end group modification of CNT surface for covalent *grafting* of different molecules and polymers.[17,19–21] While investigating, we have observed that covalent functionalization of CNTs with polymer chains or surface modification of CNT with strategically designed *grafted* block copolymer chains can be of great advantage as the design of the polymer structure can enhance the material properties significantly and can be modified to further improve the processability with the target matrix which can significantly improve to meet the requirements for particular applications.

"*Grafting to*" and "*grafting from*" are the major two approaches towards the *grafting* of polymer chains on the surface of a nanomaterials. Only few reports are found in the literature for *grafting* of polymer chain on CNT by emulsion polymerization, ATRP, RAFT processes.[22–25] Herrera *et al*. reported the growth of polymer brush modified single walled CNTs using SI-ATRP approach.[26] Pan *et al.* reported poly(N-isopropylacrylamide) modified MWCNT for better water dispersion using RAFT agent which was created *in situ* using organometallic reaction.[27] Jiang *et al.* used distillation-precipitation-polymerization approach to grow polymer chains covalently attached on the MWCNT surface and used then as nanofiller with Nafion matrix to create low energy barrier proton transport pathway.[15] A number of interesting articles were published in recent years exploring the effect of surface functionalization of CNTs.[28–37]

But, no report is found to grow block copolymer chains on the CNT surface. In a series of studies, we found that surface initiated *grafting from* RAFT polymerization approach allows the *in-situ* formation of the polymer chains on the modified solid surface effectively[38–42] and hence we have chosen this technique in the current work, so that we can control the gradual growth of the block copolymer chain at the molecular level, on the surface of the CNT with better precision and check their properties. Our objective here, is to grow block copolymer consisting of pNVT and pNVI chains on MWCNT in such a way so that pNVI portion of the chain, which has pKa 7.05[40], resides near to the nanotube walls while, the pNVT part which has pKa 2.33 and high hydrolysis stability[43], resides away from the nano walls. This particular arrangement can enhance the formation of proton conducting nanochannel formation as the more basic moiety can hold the protons strongly along the nanotube walls creating a proton enriched nanochannel while the more acidic pNVT part creates loosely bound proton enriched environment which is ideal for long range proton hopping upon protonation using an acidic

environment. The specific architecture is ideal towards formation of better proton conducting materials.

Further, pNVT-*b*-pNVI-*g*-MWCNT was utilized as a nanofiller to prepare oxy-polybenzimidazole (OPBI) based proton exchange membrane (PEM) in order to study the contribution of block copolymer *grafted* MWCNT towards the enhancement of physical properties especially proton conducting behaviour of PEM. To the best of our knowledge, this will be the first ever report to study the effect of block copolymer *grafted* MWCNT as a nanofiller on the properties of PBI based nanocomposite PEM.

EXPERIMENTAL SECTION

The sources of material are given in **Chapter 2**. RAFT agent [3-((((1-phenylethyl)thio)carbonothioyl)thio)propanoic acid] (BEPA) synthesis, characterization and activation of RAFT agent (BEPA-NHS) are described in **Chapter 2.** Also, the preparations of MWCNT-COOH, MWCNT-NH_2 and attachment of BEPA-NHS on the surface of MWCNT-NH_2 to form MWCNT-BEPA are discussed in **Chapter 2** and shown in **Scheme 6.1(A)**.

Synthesis of pNVT-b-pNVI-*g*-MWCNT via SI-RAFT polymerization

In a typical SI-RAFT polymerization in order to grow block copolymer chains on the MWCNT surface, 150 mg (15.4 µmol) MWCNT-BEPA was taken with 4 mL dry DMF in a 25 mL Schlenk tube along with 4.4 mg (15.4 µmol) of BEPA and 0.5 mg of AIBN (3.08 µmol). Calculated amount of N-vinyl-1,2,4-triazole (NVT) was added in the reaction mixture to grow the poly(N-vinyl-1,2,4-triazole) (pNVT) polymer of different chain lengths on the MWCNT surface. The Schlenk tube was sealed with septum and was subjected to sonication for 5 minutes and was kept under rotation to make the reaction mixture evenly dispersed. The Schlenk tube was subjected to 3 freeze-thaw cycles to ensure complete removal of O_2 and dissolved air from the system. The tube was back filled with ultra-high pure N_2 and kept under stirring at 70 °C for 16 h. Upon the completion of 16 h, calculated amount of N-vinyl imidazole (NVI) to grow the poly(N-vinyl imidazole) (pNVI) chain of different chain length and AIBN (3.08µmol) were dissolved in DMF (2 mL) and degassed thoroughly and injected into the polymerization mixture. After injecting, the tube was kept at 75°C for another 16 hours under stirring condition. The reaction was quenched after 32 hours using liquid N_2 and was exposed to air. The whole polymerization process is schematically represented in **Scheme 6.1 (B)**.

We kept the mole ratio of the two monomers (NVT and NVI) as constant at 3:1 in the *grafted* block copolymer on the MWCNT surface where the pNVT is the first block and the second block is pNVI. We purposefully kept the first block pNVT three times larger than the pNVI block. The combination of pNVT and pNVI is very important as pNVI, having 2 N atoms in the heterocyclic ring structure is basic in character which helps to hold the protons tightly. While, the pNVT chains having 3 N atoms on the corresponding ring experiences an enhancement in the acidic character of the ring which helps for protons to hop easily. The ratio was maintained 3:1 purposefully because, we aimed here to grow pNVT (having pKa 2.33) chains away from the MWCNT surface and with greater chain length to create a loosely bound proton rich environment for better proton hopping ability (discussed in details in the result and discussion section). The growth of pNVI (having pKa 7.05) chains were designed to place near the nanotube walls to hold the acid more tightly with the careful design of RAFT agent (discussed in latter section). We have altered the chain length of both pNVT and pNVI by adjusting the NVT and NVI monomer feed in the reaction mixture though the overall relative mole ratio between the NVT and NVI kept constant at 3:1. By following the above procedure three different chain length of the *grafted* block copolymers were prepared and these samples were named as polymer *grafted* nanotubes and abbreviated as PGNT1, PGNT2, PGNT3. Higher the numbers after PGNT indicates higher chain length of the *grafted* block copolymer chain. A parallel set of reactions were conducted where the second monomer was not introduced in the polymerization reaction. The first monomer was allowed to undergo polymerization reaction using the same recipe described above but the reaction was stopped after the completion of 16 h (before the introduction of the second monomer NVI) to isolate the intermediate product which is pNVT-*g*-MWCNT. The intermediates of the corresponding PGNT samples were abbreviated as PGNT1i, PGNT2i and PGNT3i in the manuscript.

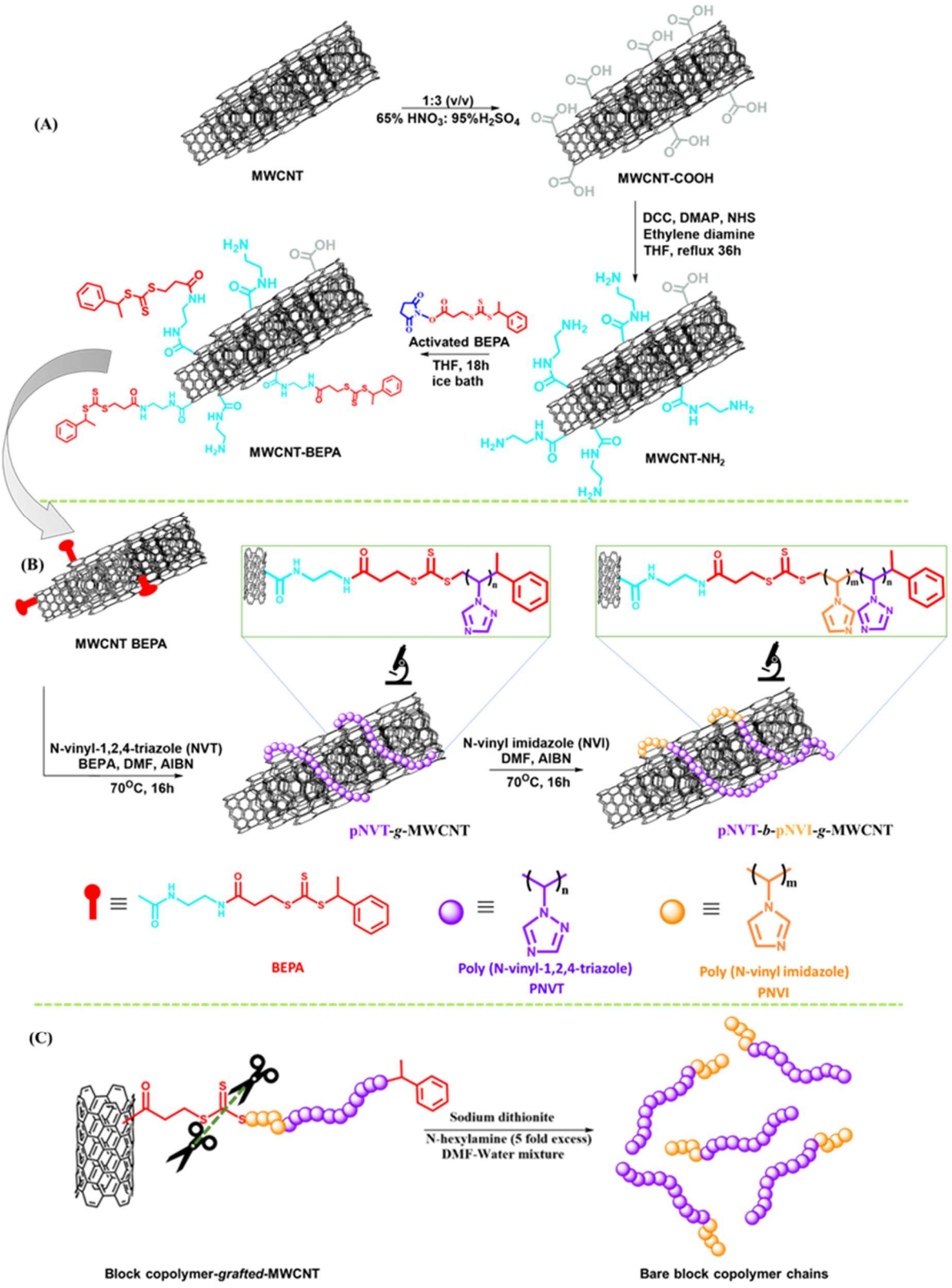

Scheme 6.1. Schematic representation of the surface functionalization of MWCNT by a RAFT agent to make polymerizable surface on MWCNT (**A**) and the growth of the block copolymer consisting of pNVT and pNVI chains on the surface of the MWCNT using SI-RAFT technique (**B**). The schematic representation for the detachment of *grafted* polymer chain from the surface of MWCNT for the GPC study (**C**).

Detachment of polymer chains from the MWCNT surface for molecular weight measurements

Molecular weights (M.W.) and polydispersity index (Đ) of detached polymers, which were obtained after detaching the polymer and block copolymer chains from the MWCNT core by breaking the trithiocarbonate moiety linking between the polymer chains and nanotube walls. The polymer chains for all the samples PGNT1 to PGNT3 including their intermediates which were isolated after growing the first block of the polymer chain (designated with 'i' at the end to signify the intermediate state such as 'PGNT1i'). All the polymer modified nanotubes were subjected to polymer detachment using N-hexyl amine in the presence of sodium dithionite and was purified in order to isolate the bare polymer chains [**Scheme 6.1 (C)**]. The bare polymer chains were dissolved in DMF/LiBr, were injected in gel permeation chromatography (GPC) and molecular weight was measured by using polystyrene standards and eluted in DMF/LiBr as an eluent at a flow rate of 0.4 mL/min at 30 °C on a GPC (Waters 515 HPLC) fitted with Waters 2414 refractive index detector and using Styragel HR 4 DMF column.

The various characterization details of block copolymer *grafted* MWCNT and their composites with OPBI samples are discussed in **Chapter 2** and **Appendix IV**.

RESULT AND DISCUSSION

Grafting of pNVT-b-pNVI on MWCNT surface

Scheme 6.1 (A) illustrated the synthetic strategy to functionalize the MWCNT in order to convert the electronically conducting surface into an insulating surface upon reduction with EDA. Further, the material was treated with activated RAFT agent (BEPA-NHS) to covalently attach BEPA on the surface of the concentric nanotubes which helps in terms of growing block co-polymer chains using *'grafting from'* approach. The design of the RAFT agent and the sequence of the addition of the two monomers are carefully designed. The RAFT agent is designed in such a way that the activated carboxylic acid group when attached covalently with the free amine groups dangling on the MWCNT surface so that the methyl phenyl group resides away from the surface. The synthesis of the BEPA RAFT agent is carried out by reacting thiopropanoic acid ($C_3H_6O_2S$) with carbon disulfide (CS_2) and 1-bromoethylbenzene (C_8H_9Br) in presence of K_3PO_4 (for detailed synthetic procedure see **Chapter 2**) that the ethylbenzene group acts as a R group ensuring the propagation of the growing polymer chain by providing extra stability to the propagating radial while the carboxylic acid part is bound to the nanotube surface acting as Z group to stabilize the radical

species. The stability of the radical R• is important in terms of propagation of the growing polymer chain which is enhanced by the careful placement of a methyl group adjacent to phenyl group of the BEPA RAFT agent. The modification of MWCNT to carboxyl group modified MWCNT (MWCNT-COOH) and then to amine modified MWCNT (MWCNT-NH_2) is already described in details in the earlier section. The attachment of BEPA to the MWCNT surface is discussed in **Chapter 2.** The formation of covalently modified MWCNT surface with BEPA RAFT agent (MWCNT-BEPA) has been proved by microscopic analysis and thermogravimetric analysis (described in details in the following section). ^{1}H NMR data supports the grafting of block copolymer chain on the MWCNT surface and described in detail in **Appendix IV-Figure 6.1**.

Upon RAFT polymerization process, the polymer chain will grow between the trithio carbonate group and methyl phenyl group. When we added the second monomer in the system, the pre- grown polymer chain is extended by the addition of the new monomer units but the incorporation of the new monomer units will be between the trithiocarbonate group and the pre-grown polymer chain attached to the trithiocarbonate group. Thus, the second block is grown towards the core (MWCNT) and not away from it. This particularly designed synthetic strategy allows us to keep the polymer chain which consist of 1,2,4 triazole pendent units away from the core and will help to interact in a great extent with the OPBI further, which makes the polymer modified MWCNTs more suitable to be used as nanofiller.

The thermal degradation patterns of MWCNT, MWCNT-COOH, MWCNT-NH_2 and MWCNT-BEPA shown in **Figure 6.1(A)** suggest that they are highly stable until 600 °C. As the thermal stability of the BEPA RAFT agent is only up to 200 °C [see inset **Figure 6.1(A)**], MWCNT-BEPA thermal stability decreases a little upon RAFT agent BEPA attachment. Though the thermal degradation increases with the increase in the *grafted* polymer content of the polymer *grafted* MWCNT samples (PGNT1, PGNT2, PGNT3), all the materials are pretty stable up to 300 °C [**Figure 6.1(B)**]. The increasing weight loss (**Table 6.1** column 3) as we go from PGNT1 to PGNT3 attributing the *grafting* of longer chain polymers. Also, the calculated polymer content (in mg) per gram of MWCNT tabulated in **Table 6.1** (column 4) clearly increases from PGNT1 to PGNT3 indicating the presence of large size polymer chains. We have achieved a maximum polymer *grafting* density of 549 mg/g of MWCNT in case of PGNT3 (**Table 6.1**).

We have performed gel permeable chromatography (GPC) after chemically treating the polymer *grafted* MWCNT samples with N-hexylamine (5-fold excess) in presence of

sodium dithionite ($Na_2S_2O_4$) in DMF-H_2O medium [**Scheme 6.1 (C)**]. This treatment breaks trithiocarbonate bond[44], linking between the block copolymer chain with the surface of MWCNTs, and releases bare polymer chains in the solution as discussed in the experimental section. The polymer chains were purified by extracting using DMF and the molecular weight was determined with the help of GPC measurements using DMF/LiBr as eluent [shown in **Figure 6.1(C**)]. All the molecular weights (PGNT1-PGNT3) are tabulated in **Table 6.1** and the intermediates (where the reaction was quenched at the first step) are shown in **Appendix IV-Table 6.1**. All the prepared samples show a narrow polydispersity index (Đ) and the molecular weights obtained from the GPC technique are in well agreement with the targeted molecular weight, which suggests that the polymer *grafting* took place using the RAFT polymerization technique. The increase in the molecular weight after addition of the second monomer (NVI) provides direct proof about the successful synthesis of the block copolymer on the surface of MWCNTs. A comparison of $\bar{\mathbf{M}}_n$ values in **Table 6.1** (column 5) and **Appendix IV-Table 6.1** (column 2) clearly display the increase in molecular weights from intermediates, where pNVT is *grafted* on MWCNT, to the final products in which pNVT-*b*-pNVI is *grafted* on MWCNT surface. In addition to that, it is to be noted from degree of polymerization value (which are indicated in the suffix of sample identity in column 2 of **Table 6.1**) clearly indicates the formation of longer chain length of pNVT chains as we increase the NVT feed in the polymerization reaction but pNVI chain length does not alter even though NVI feed increases. This attributes to the fact that the pNVT chain growth is happening in the first step of the polymerization reaction, and in the second step NVI monomer was added in the reaction mixture to grow the block copolymer chains. The growth of the pNVI block is to occur between the trithiocarbonate group and the pre grown pNVT chains, which is getting slightly hampered due to the presence of steric factor arising because of the larger pNVT chains containing pendent heterocyclic triazole rings already present in the polymer structure. Block copolymer grafted MWCNT (BC-*g*-MWCNT) samples are thereby providing a nitrogen rich aromatic heterocyclic ring surrounded environment around multiwalled hollow carbon nanotubes which may be useful for various purposes.

All the PGNT samples along with MWCNT and MWCNT-BEPA were subjected to RAMAN studies using 405 nm leaser. Prominent D band and G band were observed around ~1350cm^{-1} ~1570 cm^{-1} (**Appendix IV-Figure 6.2**). I_D/I_G values obtained for MWCNT, MWCNT-BEPA, PGNT1, PGNT2 and PGNT3 are 0.9, 0.91, 0.86, 0.85 and 0.73 respectively. The data suggests that upon RAFT agent attachment the system incorporates a little amount of

chaos. But the descending trend observed as we move from PGNT1 to PGNT3 suggests no exfoliation however took place during the grafting process of block copolymer chain length via RAFT process. Rather this observation suggests that the grafting of block copolymer chains on the MWCNT surface introduces orderliness in the hybrid system. The lower I_D value also indicates the growth of the polymer chain does not hamper the internal structure of MWCNT and thus provides another proof that the block copolymer has grown on the outer surface of MWCNT via RAFT polymerization technique and integrity of our polymerization method to retain the core structure MWCNT under the described reaction conditions. This phenomenon is reported in the literature for other nanomaterials.[45]

We have further analysed the MWCNT, PGNT1 and PGNT3 utilizing BET surface area analyser [**Appendix IV-Figure 6.3** and **Figure 6.1(D)**]. Pristine MWCNT sample shows a well-defined type-IV like isotherm with nearly vertical and parallel adsorption-desorption branches with an H1 hysteresis loop.[46] The isotherm nature indicates a typical mesoporous material while the H1 hysteresis loop suggests the presence of cylindrical pores in the material. The surface area obtained is 192.36 m^2/g which is an acceptable value as per the literature (170-280 m^2/g) considering the uneven distribution of the multi wall thickness.[47] PGNT1 shows a surface area of 153.62 m^2/g while PGNT3 shows a much lower surface area of 9.61 m^2/g, and display a type-IV isotherm consists of an H2 hysteresis loop. The significant H2 hysteresis loop indicates the presence of ink-bottle pores in the material. The shape of the pore changes from cylindrical to ink-bottle from bare MWCNT to PGNT indicates the incorporation of polymer chains in the hollow interior of the nanotubes. The decrease in the surface area in the case of PGNT samples and significantly low surface area in the case of higher chain length of the *grafted* polymer suggest the filling of mesoporous channels by the polymer chains. The decrease in the surface area is proportional with the increasing order of the *grafted* polymer chains on the MWCNT surface. This data implies that, the *grafted* polymer chains not only reside on the surface but also filling up of the hollow interior of the concentric nanotubes and the amount of insertion increases with the increase in polymer chain length. The similar kind of observation about the filling up of the hollow interior of the MWCNT is also confirmed by TEM analysis as discussed in the following section.

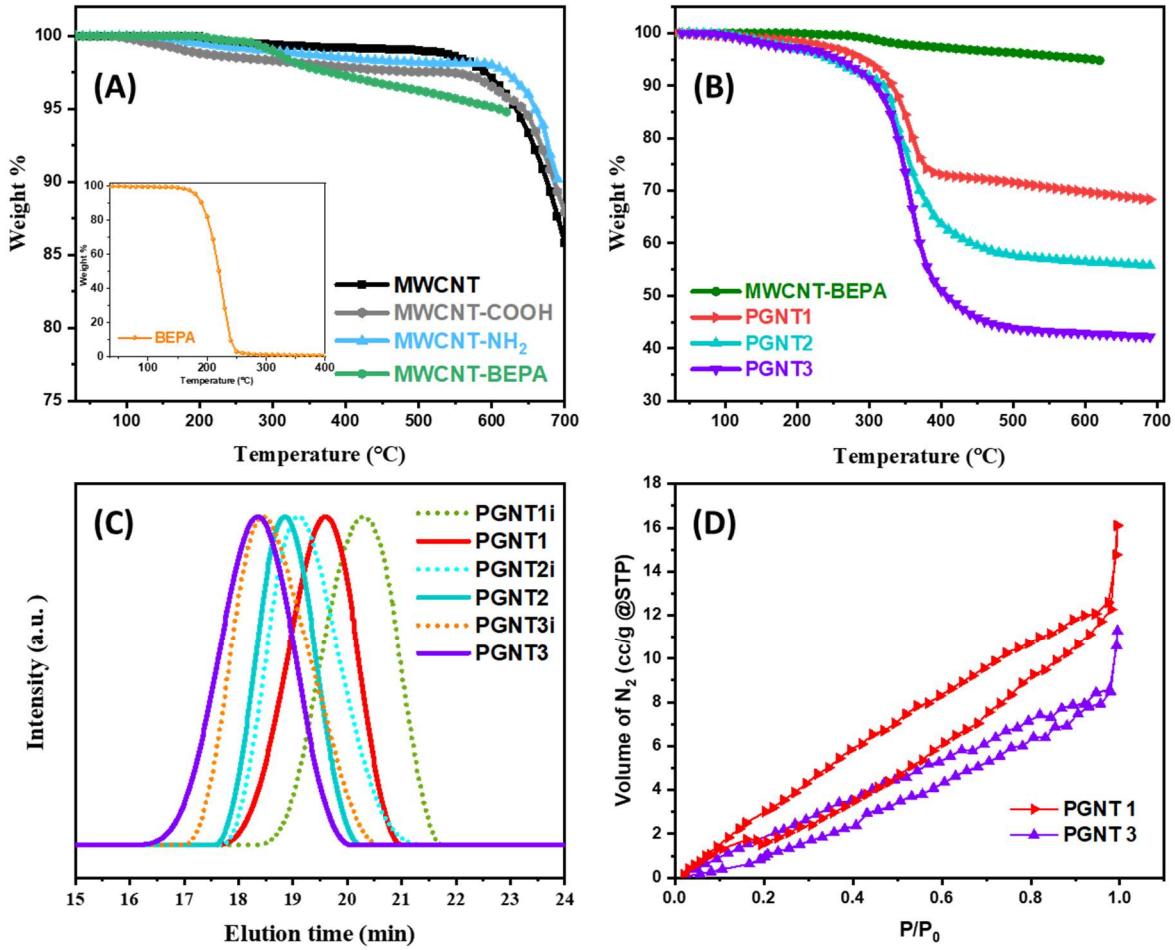

Figure 6.1. TGA of surface functionalized MWCNTs **(A)** and polymer *grafted* MWCNTs **(B).** GPC plots **(C)** for the polymer *grafted* MWCNT samples after the detachment of the polymer and block copolymer chains from the surface of the MWCNT. BET N_2 sorption isotherm of PGNT1 and PGNT3 samples **(D).**

Table 6.1. Physical properties of the surface functionalized MWCNT samples and polymer *grafted* MWCNT samples.

Sample name	Sample type[a]	Remaining weight % at 600 °C (wt%) [b]	Polymer content[c]	$\bar{M}_n$ [d]	Đ [e]	Zeta potential (mV)[f]
MWCNT	-	97.13	-	-	-	-15.9
MWCNT-COOH	-	96.55	-	-	-	-20
MWCNT-NH_2	-	98.02	-	-	-	-8.6
MWCNT-BEPA	-	95.14	29.38	-	-	-4.9
PGNT1	$pNVT_{73}$-*b*-$pNVI_{32}$-*g*-MWCNT	69.82	266	9891	1.07	-9.3
PGNT2	$pNVT_{119}$-*b*-$pNVI_{27}$-*g*-MWCNT	56.52	406	13826	1.05	-5.6
PGNT3	$pNVT_{159}$-*b*-$pNVI_{32}$-*g*-MWCNT	42.86	549	18119	1.08	-3.1

[a] sample type describes the chain sequence for each of the block corresponding the block copolymer chain and the degree of polymerization for each block included in the suffix which are obtained from the molecular weight measurements using gel permeation chromatography, [b] estimated from the TGA analysis (at 600 °C) and [c] polymer content was obtained from the analysis of the TGA curves in **Figure 6.1(A, B)** and expressed as amount (in mg) of *grafted* polymer chains /g of MWCNT-BEPA, [d and e] are determined by gel permeation chromatography, and [f] obtained from zeta potential analysis in appropriate medium [see **Appendix IV-Figure 6.13 (A)**].

Detailed morphological analysis [**Figure 6.2** and **Appendix IV-Figure 6.4-6.11**] using FESEM and TEM provides a clearer picture towards the *grafting* of polymer chains on the MWCNT surface. MWCNT, MWCNT-COOH and MWCNT-NH_2 FESEM morphology show that the nanotubes are tangled and looped together (**Appendix IV-Figure 6.4**) which is also confirmed from TEM analysis of MWCNT [**Figure 6.2(D)**]. Nevertheless, MWCNT-BEPA shows increased aggregating behaviour when compared to pristine MWCNT [**Appendix IV-Figure 6.4(D)** and **Figure 6.2(E)**]. Also, BC-g-MWCNTs show significant

morphological change from the pristine MWCNT and resulted in the agglomerated morphology [**Figure 6.2(A)-(C)**]. BC *grafting* induces polymer patch formation on the nanotube surface which is evidently visible from the FESEM images. The polymer patch formation and aggregation increases with the increased polymer molecular weight of the *grafted* BC as can be seen from the comparison of **Figure 6.2 (A)-(C)**. All the samples were further analysed by FESEM-EDX [**Appendix IV-Figure 6.5-6.9**] which confirms the surface modification with amine, BEPA and block copolymer. A significant increase in the EDX signal has been observed for nitrogen element in case of all PGNT samples compare to MWCNT-NH_2 sample which is another proof by spectroscopic means towards the growth of the BC chains on the MWCNT surface via SI-RAFT technique [**Appendix IV-Figure 6.5-6.9**]. Similarly, the nitrogen content increases with increasing BC chain length as we go from PGNT1 to PGNT3 (see **Appendix IV-Figure 6.7-6.9**). For the shake of curiosity sodium dithionite and N-hexylamine treated PGNT1, denoted as polymer detached nanotubes (PDNT1), was subjected to FESEM, EDX and elemental mapping analysis. The data (summarized in **Appendix IV-Figure 6.10** and **6.11**) clearly indicates a sheer morphological change of the nanotube surface before and after the polymer detachment process. The surface looks smoother than the PGNT1 but the nanofiber structure retains its stability even after treated with sodium dithionite/ N-hexylamine though the polymer chains were separated. Thus, the disconnection approach as shown in **Scheme 6.2 (C)** is effective towards the treatment of this kind of materials. The EDX and mapping data (**Appendix IV-Figure 6.11**) shows that even after washing the PDNT1 for several times with DMF and H_2O-acetone mixture, around 6-7 wt% of sodium and sulfur are still present in the nanotube interior. However, nitrogen content decreased significantly and in fact it became lower than MWCNT-NH_2 (**Appendix IV-Figure 6.5**) indicating complete removal of BC chains which consist large amount of N atoms.

HR-TEM data supports the *grafting* of RAFT agent on the MWCNT surface which is distributed evenly at the microscopic level. Small patches of crystalline patterns arises from the incorporation of RAFT agent which is indicated using red colour circle in the **Figure 6.2 (E)**. These small crystalline patches were completely absent in MWCNT. Upon careful observation of the PGNT samples using TEM technique, it is evident that the surface *grafted* polymer chains are not only residing at the surface but also getting filled up inside the cavity of the hollow tubes [**Figure 6.2(F)**].

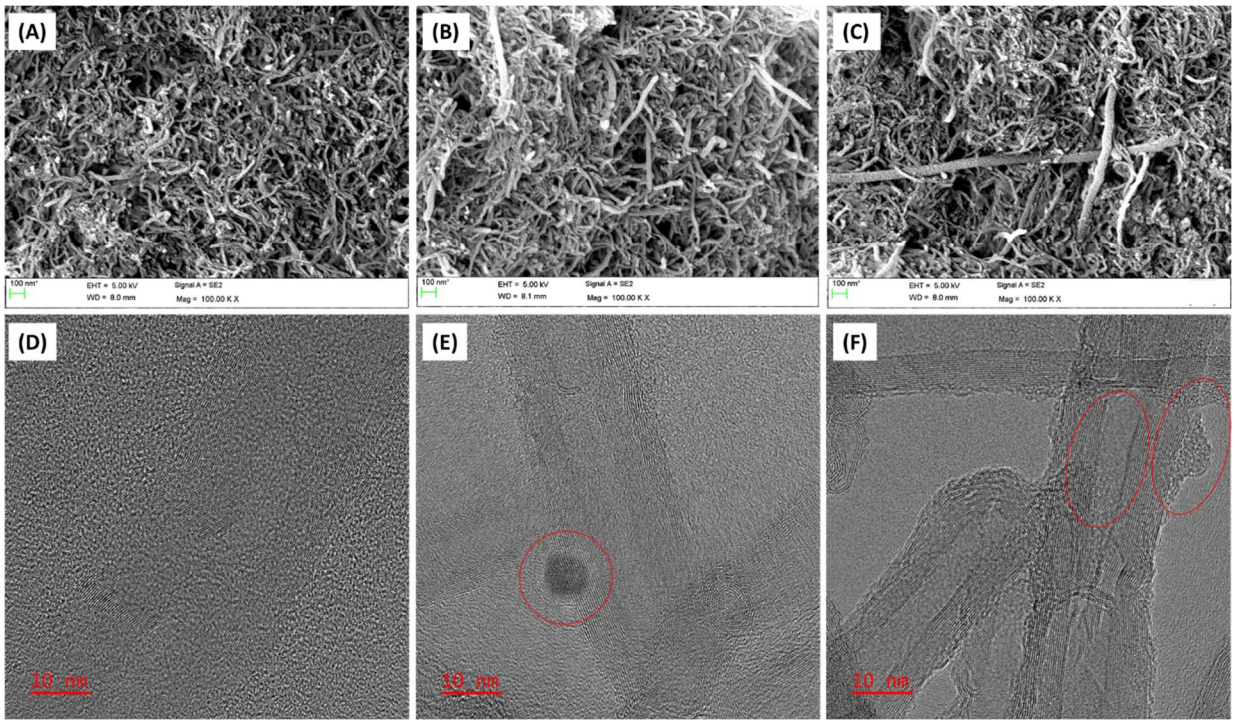

Figure 6.2. FESEM images of block copolymer *grafted* MWCNTs **(A)** PGNT1, **(B)** PGNT2 and **(C)** PGNT3. TEM images of **(D)** unmodified MWCNT, **(E)** MWCNT-BEPA and **(F)** PGNT1.

MWCNT is not much susceptible to water vapour sorption (only ~0.04 g of water/g of MWCNT) as evident from dynamic vapour sorption (DVS) studies (see **Appendix IV-Figure 6.12**). But, water vapour sorption value of PGNT1 and PGNT3 are 0.12 g of water/g and 0.14 g of water/g, respectively. The values suggest that MWCNT is hydrophobic in nature because of the presence of concentric tubes of aromatic graphene sheets while the presence of carboxylic acid groups and epoxide groups on the surface are only responsible for the amount of water uptake. In the case of BC-*g*-MWCNTs the hydrophilicity arises due to the presence of N rich heterocyclic rings. However, the π-π interaction between pendent imidazole and 1,2,4-triazole of the polymer chain in the water dispersion leading to the aggregation of the nanotubes. Zeta potential data (**Table 6.1** last column) for the PGNT samples in aqueous dispersion at ambient temperature suggests that the increase in the polymer chain length is responsible for the aggregation behaviour due to the presence of strong π-π interaction between the polymer chains of the adjacent nanotubes. PGNT1 shows better stability in aqueous dispersion than the other two BC-*g*-MWCNTs [see **Appendix IV-Figure 6.13(A)]**. We have also performed the Zeta potential studies of MWCNT, PGNT1, PGNT2 and PGNT3 in formic acid dispersion in order to check their dispersion ability upon protonation. The values

[**Appendix IV-Figure 6.13(B)**] suggest that the nanotube materials are stable in the formic acid dispersion. The positive zeta potential values suggest that the formation of a positively charged electrostatic layer on the nano surface which helps to create an electrostatic repulsion barrier along the surface of the block copolymer *grafted* nanotubes. With the increase in the chain length, the zeta potential also increases in formic acid dispersion which is opposite from what we have observed in the aqueous dispersion which suggests that the formic acid medium is able to protonate the dangling N heterocyclic pendent of the block copolymer chains successfully. A pictorial observation of the samples both in aqueous and formic acid medium are presented in **Appendix IV-Figure 6.14**. The striking features to be noted that in aqueous and formic acid medium BC-*g*-MWCNT are dispersible, but after 7 days these samples are precipitated in case of aqueous medium but remains in solution even after 7 days in formic acid medium and this is because of high positive zeta potential of the samples due to the formation of positively charged layer owing to the protonation of heterocyclic triazole and imidazole moiety. Thereafter, we believe these BC-*g*-MWCNT can be a good filler for making composites with PBI in acidic medium.

PGNT1@OPBI nanocomposite membranes

In order to explore the possible application of the block copolymer *grafted* MWCNT materials, we have taken PGNT1 as a representative sample and used it as a nanofiller with oxypolybenzimidazole (OPBI) polymer using solvent casting blending technique. We have varied the amount of nanofiller loading and to obtain 1 wt% and 2.5 wt % PGNT1 content (with respect to the OPBI weight) in the resulting nanocomposite. The PGNT1 polymer was dispersed in formic acid and mixed with 2 wt% of OPBI polymer in formic acid solution resulting in the final concentration of OPBI polymer to be 1 wt% in the solution. Finally, the solution was stirred for 24 h at room temperature to form a homogeneous mixture which was then poured on to a glass petri dish and let the solvent evaporated slowly at 60 °C. The formed homogeneous composite membrane was then peeled off and was dried in a vacuum oven at 100 °C to remove the traces of the solvent molecule present. Composite membrane with 2.5 wt% of MWCNT-NH_2 loading was also prepared using the same synthetic protocol as a control. Phosphoric acid (PA) loaded nanocomposite membranes were obtained by dipping the membranes into 85% PA solution for 5 days.

PXRD plots shown in **Figure 6.3 (A)** suggest that both PGNT1 and the pristine OPBI are amorphous in nature. OPBI exhibits a broad peak in the 2θ range of 20° to 30° which attributes to the amorphous halo of the polymer.[38,48,49] MWCNT shows an intense peak at 2θ = 26° and low intensity peak at 43° corresponds to (002), (100) diffraction pattern of a typical

graphite type material, respectively.[50] Upon carboxylic acid modification (MWCNT-COOH), amine modification (MWCNT-NH_2) or RAFT modification (MWCNT-BEPA), the PXRD pattern of the material remain unchanged because these modification does not impose any structural change in the MWCNT (**Figure 6.3A**). PGNT1-PGNT3 (**Figure 6.3A** and **Appendix IV-Figure 6.15**) show similar PXRD patterns which are expected owing to the amorphous nature of the *grafted* BC chains consisting of pendent imidazole and 1,2,4-triazole rings.[51–53] Alternatively, PGNT1-@OPBI membranes which consist of amorphous OPBI and PGNT1 nanofiller exhibited a large number of sharp crystalline peaks in the 2θ range 10°-60°. The observed new crystalline peaks are highlighted with * in the **Figure 6.3 (A)**. Crystalline peak which arises at 2θ=26° and 43° in the nanofiller (PGNT1) material shows splitting and sharpening nature (shown using dotted line and box in the figure) in the case of PGNT1@OPBI sample. The generation of the new crystalline peaks in the composite material arises because of the strong π- π interaction between the PGNT1 nanofiller and the OPBI which can be the result of the self-assembly driven crystalline pattern. Similar observations have been observed in various nanocomposites of PBI where though both the nanofiller and the polymer are amorphous in nature but the final nanocomposite display strong crystalline peaks.[38,49,54–57] These results have been explained as the outcome of self-assembly of nanofiller in the polymer matrix.[38,58]

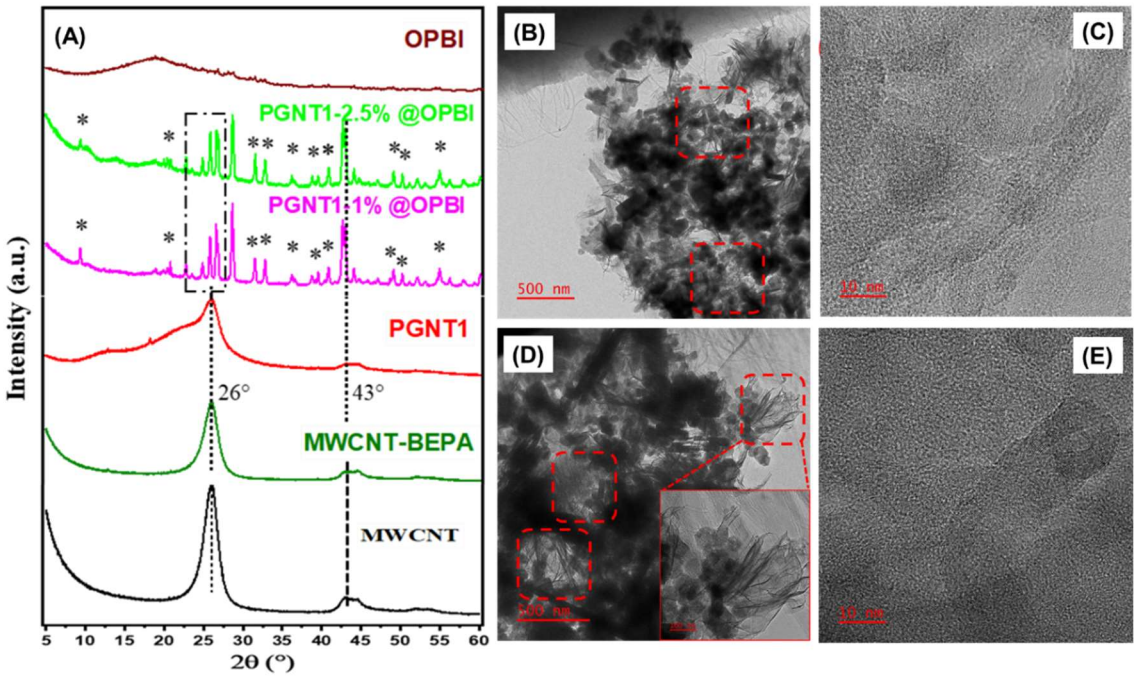

Figure 6.3. (A) PXRD pattern of the MWCNT, MWCNT-BEPA, PGNT1, PGNT1@OPBI nanocomposite and OPBI samples. TEM images (in various magnifications) of **(B, C)** PGNT1-1%@OPBI and **(D, E)** PGNT1-2.5% @OPBI nanocomposite membrane.

TEM images of 1% and 2.5% membrane are represented in **Figure 6.3**. Fibre like network morphology formation can be confirmed for both the nanocomposites for the lower magnification images [**Figure 6.3(B)** and **(D)]** and cluster of the fibres [inset of **Figure 6.3 (D)**] are more prominent in the case of higher filler loading because of the presence of more amount of BC-*g*-MWCNT. **Figure 6.3(C)** and **(E),** are the high-resolution images which provide an insight of the nanofiller dispersion in the nanocomposite membranes. The highly dispersed and well distributed polymer-g-MWCNT fibres in the OPBI are clearly visible from these images. The dispersibility ascends due to the presence of strong H-bonding interaction between the imidazole, 1,2,4-triazole units and the benzimidazole nitrogen which makes the nanofiller inseparable and easy to form nanocomposite. Higher amount of filler loading gives rise to higher amount of aggregation behaviour and increase in the interfacial H-bonding as well as π- π interaction in the polymer matrix. The formation of such fibrillar structure with aggregation of BC-g-MWCNT all over the membrane matrix provides better thermal, mechanical and tensile properties with enhanced chemical stability and improved acid retention properties (discussed in the later section), but increasing the filler loading even higher (> 2.5%) may cause predominant aggregation behaviour in the membrane matrix which may cause mechanical failure. Thus, a fine balance has to be maintained with nanofiller loading to obtain better mechanical properties in the case of composite membranes. We believe the nanofiber assembly and alignment in the membrane matrix helps to rise the new crystalline plane as obtained from the PXRD studies.

We have also analysed the surface of PGNT1-1%@OPBI, PGNT1-2.5%@OPBI, and OPBI samples using atomic force microscopy (AFM) and these studies support our argument regarding the orientation of the nanofiller tubes in the interface of OPBI chains. Even though the PGNT1 nanofiller is distributed evenly in the membrane matrix, the surface roughness in the case of nanocomposite sample increases significantly upon increasing nanofiller loading as can be seen from 3D AFM morphology and height profile [**Figure 6.4 (A)-(D**)] while OPBI membrane showed rather smooth surface (**Appendix IV-Figure 6.16**). Therefore, AFM data provides evidence for the formation of rough fibrillar surface in the PGNT1%@OPBI membranes which is clearly absent in the pristine OPBI. The results provide a direct proof of the successful dispersion of the nanofiller material with the OPBI matrix. The aligned nano-fibrils structure can contribute significantly towards the formation of the proton conducting nanochannels in the membrane matrix. The membrane samples cross-sections were also subjected to FESEM analysis upon cryogenic fracture to investigate the morphology at the

interface of nanofiller (BC-*g*-MWCNT) and OPBI. **Figure 6.4 (E, F)** provide a clear picture of the interface in which thick fibrillar network of nanofiller inside the polymer cavity is evident in both the nanocomposite case and the nanofiller is distributed evenly, and aligned with the polymer matrix (shown with a red circle). However, only pristine OPBI membrane morphology is rather smooth and featureless in cross-sectional FESEM image.[58] It can be stated that the influence of strong π- π interaction between the PGNT1 modified MWCNTs and the PBI polymer is solely responsible for the formation of such thick fibre like network morphology and it can be therefore expected that the nanocomposite samples will have significantly different physical properties than pristine OPBI.

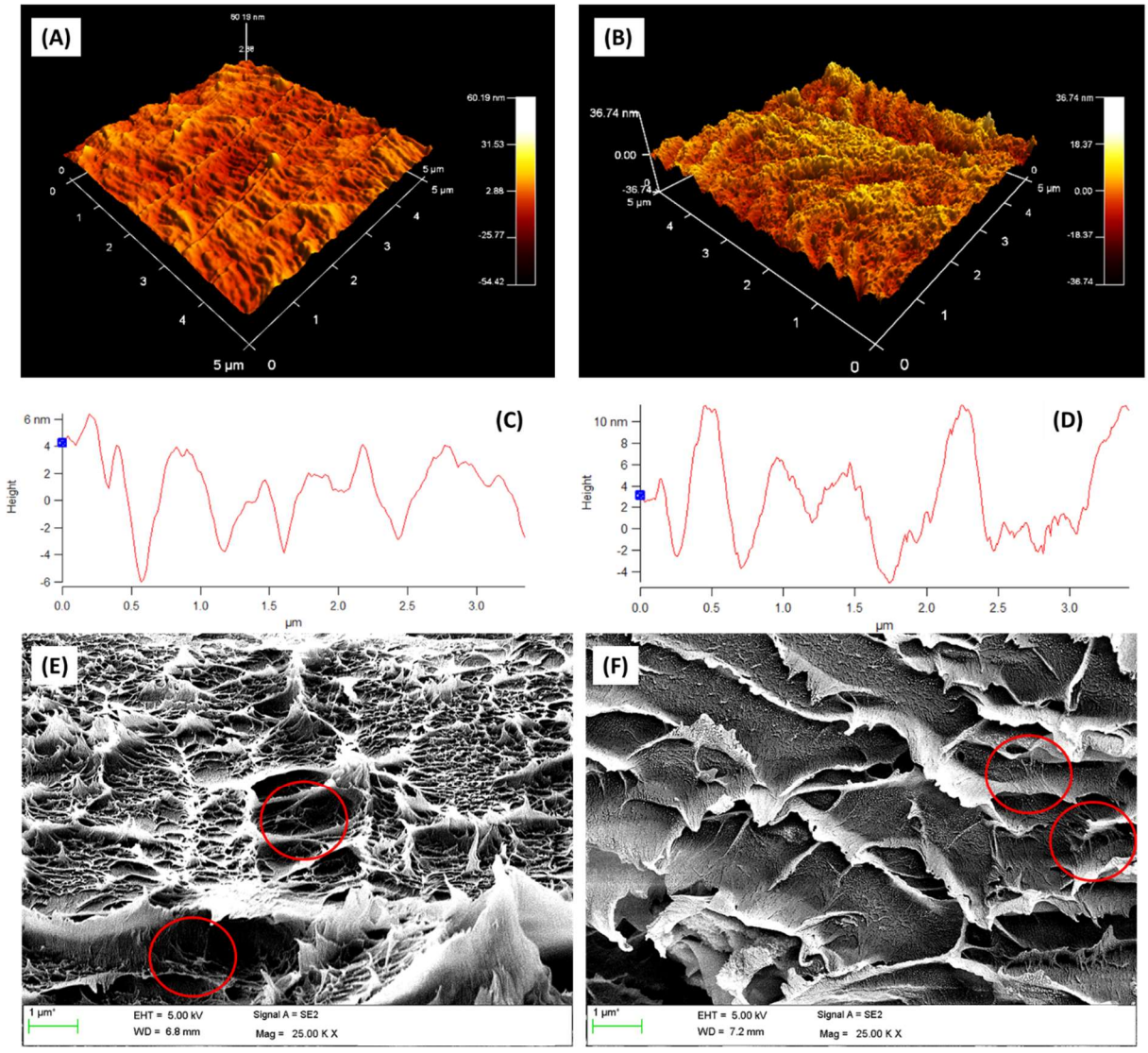

Figure 6.4. AFM 3D images of the surface morphology of **(A)** PGNT1-1%@OPBI, **(B)** PGNT1-2.5%@OPBI. **(C)** and **(D)** represents the height profile of (A) and (B) surface morphology, respectively. FESEM cross-sectional image of **(E)** PGNT1-1%@OPBI, **(F)** PGNT1-2.5%@OPBI. Nanofillers are scattered into the cross-section of composite membranes marked with red circles in the images.

Studies of various physical properties of PGNT1@OPBI composites:

Thermal and mechanical properties:

TGA [**Figure 6.5 (A)**] results shows that OPBI membrane along with the composite membranes are quite stable up to 200°C while a little weight loss is observed due to the bound water molecules and absorbed moisture which arises due to the presence of polymer modified hollow nanofiller material. With the increase in the filler loading the weight loss increment is little bit visible in the temperature range <200 °C. The degradation starts for all the membranes including OPBI and composites >200 °C. All the PGNT1 loaded membranes show better thermal stability above 200 °C with respect to pristine OPBI. With the increase in nanotube content the thermal stability is found to be increased slightly. For all the membranes, thermal degradation was observed after 550 °C which indicates the degradation of polymer main backbone.[38,49]

The dispersion pattern along with the nanofiller content imposes a great effect on the thermo-mechanical properties obtained from DMA study of the nanocomposite membranes. Temperature-dependent storage modulus (E′) plot for OPBI along with all the PGNT1-@OPBI composite membranes shown in **Figure 6.5 (B)**. The storage modulus values at 100 °C and 400 °C for all the membranes are also tabulated in **Table 6.2**. It is observed that, with the increase in PGNT1 loading in the nanocomposite, the storage modulus of the nanocomposite membranes has increased drastically. The storage modulus (E′) increment at 100 °C for 1 wt % nanofiller loading is ~25% higher than the pristine OPBI whereas the value increases drastically to ~184% when the nanofiller content is 2.5%. The storage modulus value for PGNT1-2.5%@OPBI is 160% more than the value possessed by OPBI membrane at 400 °C where as it is only 9% more than OPBI when loading is 1%. Significant difference in the morphology and strong π-π interaction within the nanocomposite matrix with OPBI is the key factor for such high value of E′. The effective increase in the fibrillar network in case of higher filler loading as obtained from FESEM, AFM and TEM studies explain the higher value of E′ obtained for composite with high PGNT1 content. The plots of loss modulus (E″) and tan δ against temperature (**Appendix IV-Figure 6.17**) show only one relaxation peak for all the composites and OPBI membrane. The T_g value obtain from E″ and tan δ vs temperature plots are 288 °C and 308 °C, respectively for all the membranes. No significant change in T_g is observed for the nanocomposites because of two reasons: (i) the nanofiller and membrane matrix both having similar kind of functional groups consist of N-heterocyclic rings, thus, the nanofiller and membrane matrix is expected to interact strongly in a very similar fashion and

(ii) the amount of BC-*g*-MWCNT loading is very less with respect to matrix polymer which contributes insignificantly towards the overall T_g of the composite membranes.

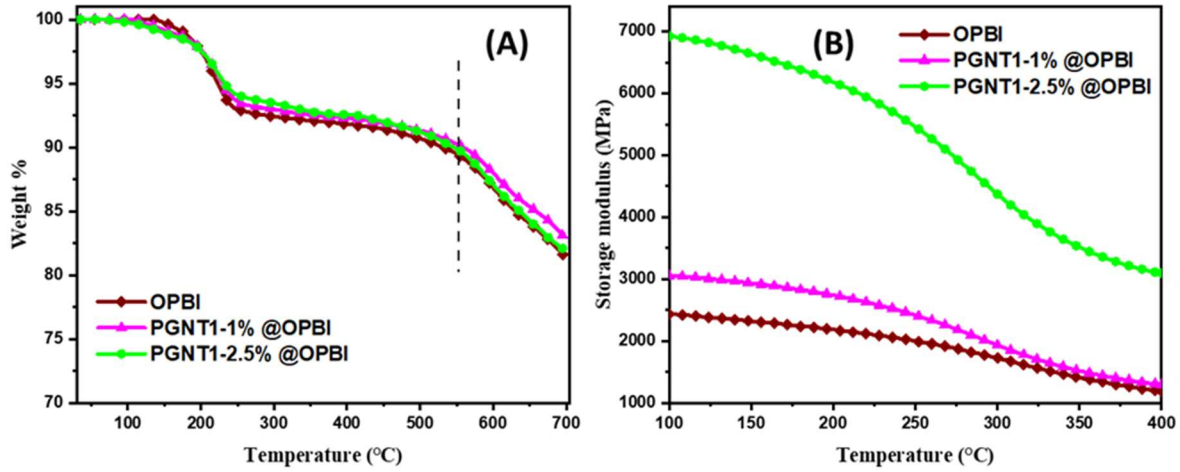

Figure 6.5. (A) TGA and **(B)** storage modulus vs temperature plots of the PGNT1-@OPBI membranes along with the pristine OPBI membrane.

Table 6.2. Temperature dependent storage modulus of the nanocomposites along with OPBI membrane obtained from DMA study.

Sample	**E′ (MPa) at 100°C**	**% of increment at 100°C**	**E′ (MPa) at 400°C**	**% of increment at 400°C**
OPBI	2439	-	1188	-
PGNT1-1% @OPBI	3055	25.30	1298	9.3
PGNT1-2.5% @OPBI	6934	184.3	3097	160.7

Water uptake, swelling ratio and phosphoric acid (PA) loading and proton conductivity:

Water uptake, swelling ratio and PA doping levels were measured for all the PGNT-@OPBI membranes along with the pristine OPBI membrane and the data are tabulated in **Table 6.3** (see **Chapter 2** and **Appendix IV** for detailed experimental procedure). OPBI polymers are prone to absorb PA and the moisture inside the membrane matrix due to its tendency to form H-bonds with the '-N=' moiety present in the polymer structure,[49] therefore, often undergo excessive swelling and dimensional changes upon PA loading which limits their use as a potential proton conducting membrane. We have observed a significantly decreased swelling ratio for all the PGNT-@OPBI membranes in water and PA when compared with the

pristine OPBI membrane. The reason behind this particularly interesting behaviour is attributed to the presence of strong interfacial interactions acting between the pendent imidazole and triazole rings immobilized on the MWCNT nanofiller surface with the OPBI functional groups. The strong interaction hinders water and PA molecules to penetrate into the cavity of polymer chains and hence resists excessive swelling and resulted lower water uptake in the composite membranes in a comparison with OPBI **(Table 6.3).** Our experimental analysis reveals that, the PA doped composite membranes have better dimensional stability when compared with the pristine OPBI. PA doping level for OPBI is observed 15.98 mol/ repeat unit (r.u) which is in agreement with earlier reports while, for PGNT1-1%@OPBI is 18.26 mol/ r.u and for PGNT1-2.5%@OPBI is 17.69 mol/ r.u, respectively which are marginally higher than OPBI. As the composites show higher PA loading and significantly less swelling upon PA loading, the PA doped nanocomposites can be highly useful as efficient PEMs.

Table 6.3. Water uptake, swelling ratio, PA loading data of OPBI and the nanocomposite membranes of PGNT1.[#]

Sample	Water uptake (wt%)	Swelling ratio in water (%)	Swelling ratio in PA (%)	PA doping level (no. of PA mol/OPBI r.u)
OPBI	12.41 (0.63)	4.58 (0.77)	6.30(0.87)	15.98 (0.71)
PGNT1-1% @OPBI	10.61 (0.31)	2.63 (0.41)	2.08(0.61)	18.26 (0.39)
PGNT1-2.5% @OPBI	9.63 (0.28)	2.41 (0.37)	1.64(0.52)	17.69 (0.51)

#Standard deviation of the data are included in the parenthesis.

Figure 6.6 (A) presents the temperature dependent proton conductivity of the PA loaded membranes. The obtained proton conductivity of OPBI membrane is 0.062 S cm^{-1} at 180 °C whereas the observed proton conductivity of PGNT1-1%@OPBI is 0.128 S cm^{-1} at 180°C. On the other hand, highest proton conductivity is observed in case of PGNT1-2.5%@OPBI composite membrane and that is 0.164 S cm^{-1} at 180 °C**.** A significant increase (~2.5 fold) in proton conductivity in case of PA doped PGNT1-2.5%@OPBI composite membrane with respect to the pristine OPBI is observed. In order to compare, we have also taken into account the proton conducting ability of PA doped MWCNT-NH_2-2.5%@OPBI composite membrane and found that this sample shows almost similar proton conductivity

(0.089 S cm^{-1} at 180°C) like OPBI. These all data together indicate that a huge increment in proton conductivity in case of PGNT1@OPBI samples is only achieved because of the presence of block copolymer chains of dangling imidazole and 1,2,4-triazole pendent rings which is *grafted* covalently on the MWCNT surface. The main source for proton conduction in these membrane is PA, thus, higher PA loading usually reflects higher proton conductivity. But this simple proportionality trend does not hold here as PA loading of PGNT1@OPBI samples are not significantly high compare to OPBI and also higher loading samples (PGNT1-2.5%@OPBI) has even lower PA loading than PGNT1-1%@OPBI (**Table 6.3**) but still displays high conductivity. Thus, we believe in case of nanocomposites, the two most important factors: (i) highly basic block copolymer *grafted* chain of the PGNT1 play an important role as the dangling imidazole and 1,2,4-triazole polymer chain increases proton hopping sites and (ii) the presence of new crystalline phases in the case of nanocomposites helps to achieve high proton conducting ability.[38,41,59,60] Thus, PGNT1 loaded membrane resulted more proton conductivity despite of having comparable PA doping level with pristine OPBI. In our earlier reports, we have demonstrated that the presence of crystallinity in the composite enhances the proton conduction of the membrane upon PA doping.[47,49] The most interesting fact here is that neither the nanofiller nor the pristine OPBI is crystalline in nature but the nanocomposite membranes possess a number of sharp crystalline planes observed in the PXRD analysis[38,58] as displayed in **Figure 6.3** which arises from the strong interaction between the nanofiller and the polymer which led to the formation of proton conducting nanochannels responsible for the super protonic conductivity.

Figure 6.6 (B) represents the Arrhenius plots of PA doped pristine OPBI with all the PGNT1-@OPBI membranes. The activation energy (E_a) values, derived from Arrhenius equation are calculated and included within the **Figure 6.6 (B)**. All the samples show activation energy value are in the range of ~7-10 kJ/mol attributing to the fact that the proton conduction is occurring through Grotthuss proton transport mechanism.[61] The E_a values for the composite sample (PGNT1-2.5%@OPBI) is little lower than the pristine OPBI which suggests that the block copolymer *grafted* MWCNT interacts in a greater extent with the OPBI polymer creating a extended network of proton rich environment, which helps in transportation of protons easily. The existence of acid-base dangling proton enriched network of N-heterocyclic rings connected with a polymer backbone attached to the interconnected network of hollow carbon nanotubes providing extensive proton conduction channels for the hopping of protons within the matrix.

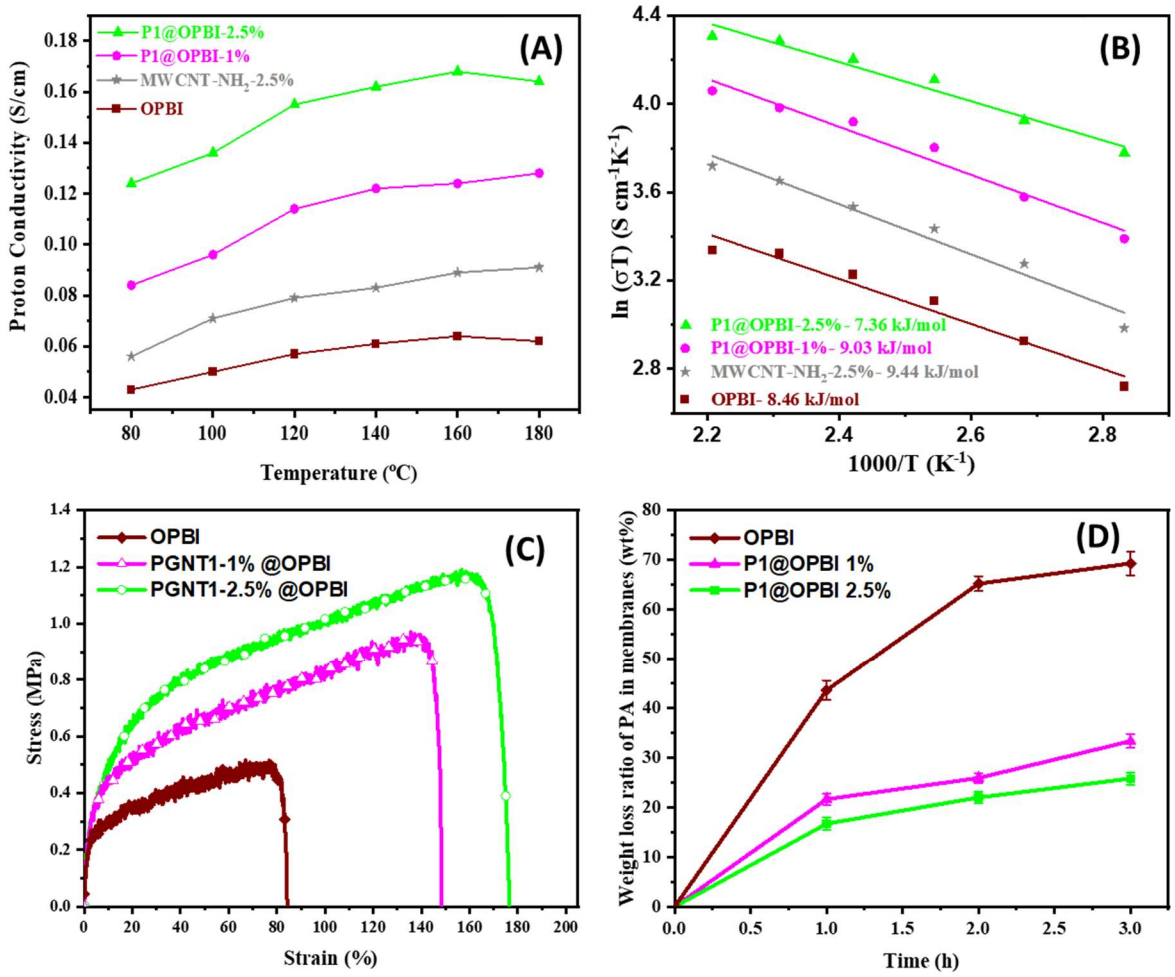

Figure 6.6. (A) proton conductivity and **(B)** Arrhenius plot of PA loaded pristine OPBI and nanocomposite membranes. Calculated activation energy from the plots are shown in the figure. **(C)** Stress-strain plot and **(D)** acid leaching plots at the PA loaded OPBI and PGNT1@OPBI nanocomposite membranes.

We have also studied the stress-strain profiles [**Figure 6.6 (C)**] of the PA doped membranes to investigate the dimensional stability of the proton exchange membranes which has always been a serious problem for utilization of the membranes in the fuel cell. A huge increase in the tensile strength is observed in the case of the nanocomposite membranes when compared with the pristine OPBI. The interfacial interaction presents between the OPBI matrix and the nanofiller directly contributes to the mechanical and tensile reinforcement of the membranes. The nanocomposite membrane with 1 wt% nanofiller loading shows 76% (from 84% of OPBI to 148.2% in case of 1 wt% nanocomposite) increase in elongation at break value while with 2.5 wt% nanofiller loading resulted 110% increment with respect to OPBI membrane **[Figure 6.6 (C)]**. With the increase in PGNT1 loading, both the stress (MPa) and strain (%) values observed to be increased simultaneously. The tensile strength value of OPBI,

1 wt% and 2.5wt% nanocomposite membrane are 0.49 MPa, 0.95 MPa and 1.18 MPa, respectively suggesting a huge mechanical reinforcement in nanocomposite samples. The altered morphology of the nanocomposites evident from the FESEM, TEM and AFM images (shown in earlier section) are responsible for such huge reinforcement in the tensile properties.

In order to utilize the nanocomposite membranes as PEM, the PA leaching from membrane under high temperature and high humidity conditions should be minimum. Though PBI based membranes have become quite popular as PEM but, acid leaching is a serious drawback and as a result proton conductivity of the membrane diminishes under these conditions. To verify the leaching probability and holding ability, our nanocomposite membranes were subjected to leaching studies under high temperature and high humidity conditions using a home-made set-up (see **Chapter 2** and **Appendix IV**)[38,53,58] The results shown in **Figure 6.6 (D)** clearly state that OPBI membrane loses around 43 % of PA after the 1st hour of the leaching treatment and at the completion of the 3rd hour total acid leaching observed was ~69.3 %. In the case of composite membranes, upon the completion of 1st hour the weight loss of 21 % and 17 % were observed for 1 wt% and 2.5 wt% membranes, respectively and after 3 hours total leaching increased very little to 33.33% and 25.79% for 1wt% and 2.5wt%, respectively. The strong acid-base interactions present between the nanofiller owing to the presence of pNVT and pNVI chains enable the holding of PA in the membrane more tightly. The basic nature of dangling imidazole, 1,2,4-triazole rings along with the strong interfacial interaction with the benzimidazole units plays an important role in holding the PA in the cavity which is reflected in the temperature dependent proton conductivity measurements too.

We have also checked the thermal stability of the PA doped membranes and this study validates the results obtained from acid leaching studies. We have observed less thermal stability of the nanocomposite membranes with respect to the pristine OPBI membrane in the temperature range 100-200 °C [**Figure 6.5 (A)**] but the PA doped membranes show reverse order (**Appendix IV-Figure 6.18**). The PA doped PGNT1@OPBI membranes are bit more stable than the PA doped OPBI membrane in the given temperature range of 100 °C – 300 °C (see **Appendix IV-Figure 6.18**) which is the operating temperature for PEM. This observation suggests that the nanofiller is holding more PA molecules in the membrane effectively than OPBI, which is in agreement with leaching data shown in **Figure 6.6**.

CONCLUSION

Our current work demonstrates, a simple but highly effective strategy to modify the MWCNT surface by *grafting* functional polymer chain with high control over surface

functionalization. In, a one-pot SI-RAFT "*grafting from*" approach was used to covalently grow block copolymer chains consisting of pNVT and pNVI on the surface of the MWCNT with controlled molecular weight to obtain pNVT-*b*-pNVI-*g*-MWCNT. These samples have been thoroughly characterized by several techniques to prove the attachment and various physical parameter. The main objective here, is to create the proton conduction nanochannels into the polymer *grafted* MWCNT surface. The prepared block copolymer *grafted* MWCNT (BC-*g*-MWCNT) was further utilized as a nanofiller to fabricate an efficient PBI based PEMs and was characterized thoroughly. Nanocomposite membranes with two different amounts of nanofiller loading (1 wt% and 2.5 wt %) were prepared to check the effect of the polymer modified MWCNTs towards proton conduction and the other various physical and mechanical properties of the membranes. The newly generated crystalline phases in the nanocomposite membrane are not only responsible for superior proton conductivity but also for high acid retention at elevated temperature (160 °C – 180 °C). The basic N-heterocyclic rings from the *grafted* polymer chain units which are dangling allowed to form strong H-bonding interaction with PA which is responsible for high acid uptake and superior PA retention. The BC-*g*-MWCNT loaded membranes remains mechanically stable and highly flexible even after the proton conductivity measurements which was performed at 180 °C. So far, block copolymer *grafted* MWCNTs have never been explored in literature to be used as potential nanofiller materials for improving PEM properties, and to the best of our knowledge this will be the first report on such materials.

Reference

(1) Kang, S.; Jeong, Y. K.; Mhin, S.; Ryu, J. H.; Ali, G.; Lee, K.; Akbar, M.; Chung, K. Y.; Han, H.; Kim, K. M. Pulsed Laser Confinement of Single Atomic Catalysts on Carbon Nanotube Matrix for Enhanced Oxygen Evolution Reaction. *ACS Nano* **2021**, *15*, 4416–4428.

(2) Yan, Y.; Miao, J.; Yang, Z.; Xiao, F.-X.; Yang, H. Bin; Liu, B.; Yang, Y. Carbon Nanotube Catalysts: Recent Advances in Synthesis, Characterization and Applications. *Chem. Soc. Rev.* **2015**, *44*, 3295–3346.

(3) Yang, P.; Devasenathipathy, R.; Xu, W.; Wang, Z.; Chen, D.-H.; Zhang, X.; Fan, Y.; Chen, W. Pt 1 (CeO 2) 0.5 Nanoparticles Supported on Multiwalled Carbon Nanotubes for Methanol Electro-Oxidation. *ACS Appl. Nano Mater.* **2021**, *4*, 10584–10591.

(4) Yang, Y.; Narayanan Nair, A. K.; Sun, S. Adsorption and Diffusion of Carbon Dioxide, Methane, and Their Mixture in Carbon Nanotubes in the Presence of Water. *J. Phys. Chem. C* **2020**, *124*, 16478–16487.

(5) Lee, B.; Baek, Y.; Lee, M.; Jeong, D. H.; Lee, H. H.; Yoon, J.; Kim, Y. H. A Carbon

Nanotube Wall Membrane for Water Treatment. *Nat. Commun.* **2015**, *6*, 7109.

(6) Ihsanullah. Carbon Nanotube Membranes for Water Purification: Developments, Challenges, and Prospects for the Future. *Sep. Purif. Technol.* **2019**, *209*, 307–337.

(7) Wang, Q.; Dai, J.; Li, W.; Wei, Z.; Jiang, J. The Effects of CNT Alignment on Electrical Conductivity and Mechanical Properties of SWNT/Epoxy Nanocomposites. *Compos. Sci. Technol.* **2008**, *68*, 1644–1648.

(8) Mora, A.; Verma, P.; Kumar, S. Electrical Conductivity of CNT/Polymer Composites: 3D Printing, Measurements and Modeling. *Compos. Part B Eng.* **2020**, *183*, 107600.

(9) Wang, Y.; Yang, C.; Xin, Z.; Luo, Y.; Wang, B.; Feng, X.; Mao, Z.; Sui, X. Poly(Lactic Acid)/Carbon Nanotube Composites with Enhanced Electrical Conductivity via a Two-Step Dispersion Strategy. *Compos. Commun.* **2022**, 101087.

(10) Wei, Q.; Gao, M.-R.; Li, Y.; Zhang, D.; Wu, S.; Chen, Z.; Sun, Y. Directionally Assembled MoS 2 with Significantly Expanded Interlayer Spacing: A Superior Anode Material for High-Rate Lithium-Ion Batteries. *Mater. Chem. Front.* **2018**, *2*, 1441–1448.

(11) Zhan, H.; Chen, Y. W.; Shi, Q. Q.; Zhang, Y.; Mo, R. W.; Wang, J. N. Highly Aligned and Densified Carbon Nanotube Films with Superior Thermal Conductivity and Mechanical Strength. *Carbon N. Y.* **2022**, *186*, 205–214.

(12) Li, Y.; Li, M.; Pang, M.; Feng, S.; Zhang, J.; Zhang, C. Effects of Multi-Walled Carbon Nanotube Structures on the Electrical and Mechanical Properties of Silicone Rubber Filled with Multi-Walled Carbon Nanotubes. *J. Mater. Chem. C* **2015**, *3*, 5573–5579.

(13) Iijima, S. Helical Microtubules of Graphitic Carbon. *Nature* **1991**, *354*, 56–58.

(14) Sakellariou, G.; Priftis, D.; Baskaran, D. Surface-Initiated Polymerization from Carbon Nanotubes: Strategies and Perspectives. *Chem. Soc. Rev.* **2013**, *42*, 677–704.

(15) He, G.; Zhao, J.; Hu, S.; Li, L.; Li, Z.; Li, Y.; Li, Z.; Wu, H.; Yang, X.; Jiang, Z. Functionalized Carbon Nanotube via Distillation Precipitation Polymerization and Its Application in Nafion-Based Composite Membranes. *ACS Appl. Mater. Interfaces* **2014**, *6*, 15291–15301.

(16) Pramanik, C.; Gissinger, J. R.; Kumar, S.; Heinz, H. Carbon Nanotube Dispersion in Solvents and Polymer Solutions: Mechanisms, Assembly, and Preferences. *ACS Nano* **2017**, *11*, 12805–12816.

(17) Karousis, N.; Tagmatarchis, N.; Tasis, D. Current Progress on the Chemical Modification of Carbon Nanotubes. *Chem. Rev.* **2010**, *110*, 5366–5397.

(18) Gorityala, B. K.; Ma, J.; Wang, X.; Chen, P.; Liu, X.-W. Carbohydrate Functionalized Carbon Nanotubes and Their Applications. *Chem. Soc. Rev.* **2010**, *39*, 2925.

(19) Georgakilas, V.; Kordatos, K.; Prato, M.; Guldi, D. M.; Holzinger, M.; Hirsch, A. Organic Functionalization of Carbon Nanotubes. *J. Am. Chem. Soc.* **2002**, *124*, 760–761.

(20) Khabashesku, V. N.; Billups, W. E.; Margrave, J. L. Fluorination of Single-Wall Carbon Nanotubes and Subsequent Derivatization Reactions. *Acc. Chem. Res.* **2002**, *35*, 1087–1095.

(21) Cheng, C. C.; Wang, Y. S.; Chen, J. K.; Lee, D. J. Supramolecular Electrospun Nanofibers with High Conductivity at Ultra-Low Carbon Nanotube Content. *J. Mater. Chem. C* **2016**, *4*, 5207–5213.

(22) Khan, M. U.; Gomes, V. G.; Altarawneh, I. S. Synthesizing Polystyrene/Carbon Nanotube Composites by Emulsion Polymerization with Non-Covalent and Covalent Functionalization. *Carbon N. Y.* **2010**, *48*, 2925–2933.

(23) Hong, C. Y.; You, Y. Z.; Pan, C. Y. Functionalized Multi-Walled Carbon Nanotubes with Poly(N-(2-Hydroxypropyl)Methacrylamide) by RAFT Polymerization. *J. Polym. Sci. Part A Polym. Chem.* **2006**, *44*, 2419–2427.

(24) Xu, G.; Wu, W.-T.; Wang, Y.; Pang, W.; Zhu, Q.; Wang, P. Functionalized Carbon Nanotubes with Polystyrene- Block -Poly (N -Isopropylacrylamide) by in Situ RAFT Polymerization. *Nanotechnology* **2007**, *18*, 145606.

(25) Pei, X.; Hao, J.; Liu, W. Preparation and Characterization of Carbon Nanotubes−Polymer/Ag Hybrid Nanocomposites via Surface RAFT Polymerization. *J. Phys. Chem. C* **2007**, *111*, 2947–2952.

(26) Qin, S.; Qin, D.; Ford, W. T.; Resasco, D. E.; Herrera, J. E. Polymer Brushes on Single-Walled Carbon Nanotubes by Atom Transfer Radical Polymerization of n -Butyl Methacrylate. *J. Am. Chem. Soc.* **2004**, *126*, 170–176.

(27) Hong, C.-Y.; You, Y.-Z.; Pan, C.-Y. Synthesis of Water-Soluble Multiwalled Carbon Nanotubes with Grafted Temperature-Responsive Shells by Surface RAFT Polymerization. *Chem. Mater.* **2005**, *17*, 2247–2254.

(28) Kohls, A.; Maurer Ditty, M.; Dehghandehnavi, F.; Zheng, S.-Y. Vertically Aligned Carbon Nanotubes as a Unique Material for Biomedical Applications. *ACS Appl. Mater. Interfaces* **2022**, *14*, 6287–6306.

(29) Ngoma, M. M.; Mathaba, M.; Moothi, K. Effect of Carbon Nanotubes Loading and Pressure on the Performance of a Polyethersulfone (PES)/Carbon Nanotubes (CNT) Membrane. *Sci. Rep.* **2021**, *11*, 23805.

(30) Gholami, S.; Llacuna, J. L.; Vatanpour, V.; Dehqan, A.; Paziresh, S.; Cortina, J. L. Impact of a New Functionalization of Multiwalled Carbon Nanotubes on Antifouling and Permeability of PVDF Nanocomposite Membranes for Dye Wastewater Treatment. *Chemosphere* **2022**, *294*, 133699.

(31) Amin, M.; Abdullah, B. M.; Rowley-Neale, S. J.; Wylie, S.; Slate, A. J.; Banks, C. E.; Whitehead, K. A. Diamine Oxidase-Conjugated Multiwalled Carbon Nanotubes to Facilitate Electrode Surface Homogeneity. *Sensors* **2022**, *22*, 675.

(32) Tromm Steffen, T.; César Fontana, L.; Hammer, P.; Becker, D. Amine Functionalization

of Carbon Nanotubes with Solid Urea Using Different Plasma Treatments. *Appl. Surf. Sci.* **2022**, *583*, 152493.

(33) Thakur, P.; Mannuthodikayil, J.; Kalita, G.; Mandal, K.; Narayanan, T. N. Correction: In Situ Surface Modification of Bulk or Nano Materials by Cytochrome- c for Active Hydrogen Evolution Catalysis. *Mater. Chem. Front.* **2021**, *5*, 2470–2470.

(34) Zhao, C.; Wang, X.; Chen, X.; Liu, Y.; Xie, Y.; Xu, H. Covalent Interactions between Carbon Nanotubes and P3HT by Thiol–Ene Click Chemistry towards Improved Thermoelectric Performance. *Mater. Chem. Front.* **2020**, *4*, 1174–1181.

(35) Mosnáčková, K.; Mrlík, M.; Mičušík, M.; Kleinová, A.; Sasinková, V.; Popelka, A.; Opálková Šišková, A.; Kasák, P.; Dworak, C. L.; Mosnáček, J. Light-Responsive Hybrids Based on Carbon Nanotubes with Covalently Attached PHEMA-g-PCL Brushes. *Macromolecules* **2021**, *54*, 2412–2426.

(36) Contreras-Torres, F. F.; Salas-Treviño, D.; Soto-Domínguez, A.; De Jesús García-Rivas, G. Carbon Nanotubes in Tumor-Targeted Chemotherapeutic Formulations: A Review of Opportunities and Challenges. *ACS Appl. Nano Mater.* **2022**, *5*, 8649–8679.

(37) Lavagna, L.; Bartoli, M.; Suarez-Riera, D.; Cagliero, D.; Musso, S.; Pavese, M. Oxidation of Carbon Nanotubes for Improving the Mechanical and Electrical Properties of Oil-Well Cement-Based Composites. *ACS Appl. Nano Mater.* **2022**, *5*, 6671–6678.

(38) Mukherjee, N.; Das, A.; Dhara, M.; Jana, T. Surface Initiated RAFT Polymerization to Synthesize N-Heterocyclic Block Copolymer Grafted Silica Nanofillers for Improving PEM Properties. *Polymer.* **2021**, *236*, 124315.

(39) Dhara, M.; Rudra, S.; Mukherjee, N.; Jana, T. Hollow Polymer Nanocapsules with Ferrocenyl Copolymer Shell. *Polym. Chem.* **2021**, *12*, 3976-3991.

(40) Koyilapu, R.; Subhadarshini, S.; Singha, S.; Jana, T. An In-Situ RAFT Polymerization Technique for the Preparation of Poly(N-Vinyl Imidazole) Modified Cloisite Nanoclay to Develop Nanocomposite PEM. *Polymer.* **2021**, *212*, 123175.

(41) Kutcherlapati, S. R.; Koyilapu, R.; Jana, T. Poly(N-Vinyl Imidazole) Grafted Silica Nanofillers: Synthesis by RAFT Polymerization and Nanocomposites with Polybenzimidazole. *J. Polym. Sci. Part A Polym. Chem.* **2018**, *56*, 365–375.

(42) Raju Kutcherlapati, S. N.; Yeole, N.; Gadi, M. R.; Perali, R. S.; Jana, T. RAFT Mediated One-Pot Synthesis of Glycopolymer Particles with Tunable Core–Shell Morphology. *Polym. Chem.* **2017**, *8*, 1371–1380.

(43) Fink, J. K. Triazole Polymers. In *High Performance Polymers*; Elsevier, 2014; pp 221–240.

(44) Li, C.; Wang, C.; Ji, Z.; Jiang, N.; Lin, W.; Li, D. Synthesis of Thiol-Terminated Thermoresponsive Polymers and Their Enhancement Effect on Optical Limiting Property of Gold Nanoparticles. *Eur. Polym. J.* **2019**, *113*, 404–410.

(45) Cai, N.; Hou, D.; Shen, L.; Luo, X.; Xue, Y.; Yu, F. Functionalization of Graphene with Hyperbranched Polyglycerol for Stable Aqueous Dispersion. *Funct. Mater. Lett.* **2015**, *8*, 1550068.

(46) Hazra, B.; Wood, D. A.; Mani, D.; Singh, P. K.; Singh, A. K. Organic and Inorganic Porosity, and Controls of Hydrocarbon Storage in Shales; 2019; pp 107–138.

(47) Singha, S.; Jana, T. Effect of Composition on the Properties of PEM Based on Polybenzimidazole and Poly(Vinylidene Fluoride) Blends. *Polymer.* **2014**, *55*, 594–601.

(48) Sana, B.; Jana, T. Polybenzimidazole Composite with Acidic Surfactant like Molecules: A Unique Approach to Develop PEM for Fuel Cell. *Eur. Polym. J.* **2016**, *84*, 421–434.

(49) Singha, S.; Jana, T. Structure and Properties of Polybenzimidazole/Silica Nanocomposite Electrolyte Membrane: Influence of Organic/Inorganic Interface. *ACS Appl. Mater. Interfaces* **2014**, *6*, 21286–21296.

(50) Haque, M. A.; Sulong, A. B.; Shyuan, L. K.; Majlan, E. H.; Husaini, T.; Rosli, R. E. Synthesis of Polymer/MWCNT Nanocomposite Catalyst Supporting Materials for High-Temperature PEM Fuel Cells. *Int. J. Hydrogen Energy* **2021**, *46*, 4339–4353.

(51) Shurygina, I. A.; Prozorova, G. F.; Trukhan, I. S.; Korzhova, S. A.; Fadeeva, T. V.; Pozdnyakov, A. S.; Dremina, N. N.; Emel'yanov, A. I.; Kuznetsova, N. P.; Shurygin, M. G. NonToxic Silver/Poly-1-Vinyl-1,2,4-Triazole Nanocomposite Materials with Antibacterial Activity. *Nanomaterials* **2020**, *10*, 1477.

(52) Sabaa, M. W.; Mohamed, N. A.; Mohamed, R. R.; Khalil, N. M.; Abd El Latif, S. M. Synthesis, Characterization and Antimicrobial Activity of Poly (N-Vinyl Imidazole) Grafted Carboxymethyl Chitosan. *Carbohydr. Polym.* **2010**, *79*, 998–1005.

(53) Kutcherlapati, S. R.; Koyilapu, R.; Jana, T. Poly(N -Vinyl Imidazole) Grafted Silica Nanofillers: Synthesis by RAFT Polymerization and Nanocomposites with Polybenzimidazole. *J. Polym. Sci. Part A Polym. Chem.* **2018**, *56*, 365–375.

(54) Singha, S.; Koyilapu, R.; Dana, K.; Jana, T. Polybenzimidazole-Clay Nanocomposite Membrane for PEM Fuel Cell: Effect of Organomodifier Structure. *Polymer.* **2019**, *167*, 13–20.

(55) Maity, S.; Singha, S.; Jana, T. Low Acid Leaching PEM for Fuel Cell Based on Polybenzimidazole Nanocomposites with Protic Ionic Liquid Modified Silica. *Polymer.* **2015**, *66*, 76–85.

(56) Ghosh, S.; Maity, S.; Jana, T. Polybenzimidazole/Silica Nanocomposites: Organic-Inorganic Hybrid Membranes for PEM Fuel Cell. *J. Mater. Chem.* **2011**, *21*, 14897.

(57) Singha, S.; Jana, T. Self-Assembly of Nanofillers in Improving the Performance of Polymer Electrolyte Membrane. *Macromol. Symp.* **2016**, *369*, 49–55.

(58) Mukhopadhyay, S.; Das, A.; Jana, T.; Das, S. K. Fabricating a MOF Material with Polybenzimidazole into an Efficient Proton Exchange Membrane. *ACS Appl. Energy*

Mater. **2020**, *3*, 7964–7977.

(59) Jankowska, I. A.; Pogorzelec-Glaser, K.; Ławniczak, P.; Matczak, M.; Pankiewicz, R. New Liquid-Free Proton Conductive Nanocomposite Based on Imidazole-Functionalized Cellulose Nanofibers. *Cellulose* **2021**, *28*, 843–854.

(60) Satheesh Kumar, B.; Sana, B.; Mathew, D.; Unnikrishnan, G.; Jana, T.; Santhosh Kumar, K. S. Polybenzimidazole-Nanocomposite Membranes: Enhanced Proton Conductivity with Low Content of Amine-Functionalized Nanoparticles. *Polymer.* **2018**, *145*, 434–446.

(61) Ghosh, S.; Sannigrahi, A.; Maity, S.; Jana, T. Role of Clays Structures on the Polybenzimidazole Nanocomposites: Potential Membranes for the Use in Polymer Electrolyte Membrane Fuel Cell. *J. Phys. Chem. C* **2011**, *115*, 11474–11483.

Chapter 7

Poly (N-Vinyl Imidazole) Grafted MWCNT Supported Pd Nanoparticle: An Efficient Catalyst for Suzuki-Mayura Coupling Reaction

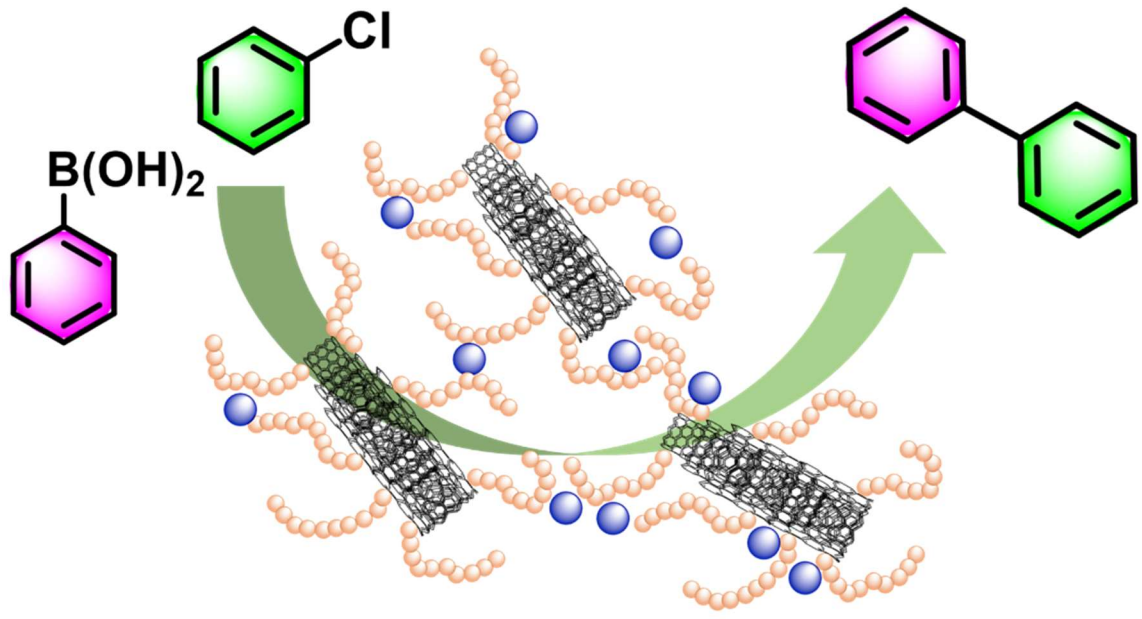

Nilanjan Mukherjee and Tushar Jana*. Poly (N-Vinyl Imidazole) Grafted MWCNT Supported Pd Nanoparticle: An Efficient Catalyst for Suzuki-Mayura Coupling Reaction. (*Manuscript to be communicated*)

Abstract

Palladium catalysts are well known for their role in Suzuki-Miyaura cross coupling reactions between an aryl halide and an aryl boronic acid to generate coupled aryl and poly cyclic systems by means of formation of a new C-C bond. C-C bond formation between two aryl compounds is particularly interesting as this is not only the key step in the synthetic procedures of a number of organic chemicals and natural products but also useful in a number of industrial applications. On the other hand, Pd is costly. Heterogeneous Pd catalysts are preferred over homogeneous catalysts due to their facile reusability and compatibility with flow systems. Another preferred route for cross-coupling reactions involves reusable palladium nanoparticles that promote these reactions in organic solvents or in water. Multi walled carbon nanotubes on the other hand are well known for their stability, durability and hollow interior design. Furthermore, covalently grafting of the MWCNT surface with strategically designed functional polymer chains can however provide a stable and reducing environment to coordinate Pd^{2+} ions on the surface of the nanotubes. The dangling imidazole rings of poly (N-vinyl imidazole) (pNVI) chains help in the formation of Pd nanoparticle on the polymer grafted MWCNT walls in the absence of any external reducing agent. Microscopic studies along with the EDX data provided concrete evidence towards the formation of Pd nanoparticles. The synthesized polymer grafted MWCNT supported Pd nanoparticles (Pd@PGNT1) were taken into account to thoroughly investigate the catalytic properties in Suzuki-Miyaura coupling reaction. The reaction conditions were investigated and optimizes. The solvent scope, utilization of mild basic conditions were checked thoroughly and the substrate scope was also examined by incorporating different functional group containing aryl bromide and aryl boronic acid in the reaction medium as substrate. The efficiency of the catalyst was also validated for 1 gm scale reaction in EtOH solvent with K_2CO_3 as base at 80 °C in the presence of as low as 1 mg of the Pd@PGNT1 catalyst which contains only 12.65 mass % of Pd was able to produce 99% yields.

Introduction

Carbon nanotube (CNT) is particularly interesting among carbon based materials because of the unique chemical and physical properties.[1] Hollow interior along with the stacked concentric tube structure makes multiwalled carbon nanotubes (MWCNTs) of particularly interesting material. CNT based materials are particularly used in a number of applicative fields such as gas adsorption[2], water purification[3,4], catalysis[5–7] and better mechanical robustness,[8,9] since its discovery. Although, the presence of strong van der Waals

forces acting among the concentric tubes often initiates agglomeration nature in the material to result in the formation of tightly tangled loop structures which hinders the processability of the material.[10–12] The strong interaction patterns (van der Waals, π-π and non-covalent interaction) are often reported in literature to hamper the performance of the material in the nano level.[13,14] A number of different approaches are reported in the literature to overcome these issues by physically or chemically modifying the CNT surface with surfactants, polymer absorption and encapsulation. Chemical treatments to introduce new functionalities and alteration of the existing functional groups of the nanotubes are also known in the literature. Furthermore, covalent *grafting* on the hollow nanotube surface with different small molecules and functional polymer chains which are also known to enhance the properties of the nanotube material many folds.[13,15–18] Upon further investigation it is been found that the covalently functionalization of the nanotubes with functional polymer chains particularly the surface modification with *grafted* homo polymer or block copolymer chains can enhance the properties of the pristine CNT material efficiently and also holds an opportunity in terms of modifying the material further more to improve the desired properties and the processability.

"*Grafting to*", "*grafting from*" and "*grafting through*" are considered to be the major approaches in order to *graft* the polymer chains on the nanomaterial surface. Also, few reports are there in the literature where emulsion polymerization, ATRP and RAFT processes were used to *graft* polymer chains on CNT.[18–22] Herrera *et al*. reported the use of SI-ATRP process on single walled CNTs to grow polymer brush structures.[23] Pan *et al.* focused on the better aqueous dispersibility of the MWCNTs by carefully using organometallic reactions to synthesize RAFT agent *in situ* to grow poly(N-isopropylacrylamide) chains on the MWCNT.[24] A few interesting literatures were published recently reporting the effects of surface functionalization of the carbon nanotubes.[25–34]

We have reported recently, the growth of block copolymer chains *grafted* on the CNT surface using surface initiated RAFT *grafting from* approach.[18] We have observed that surface initiated *grafting from* RAFT polymerization approach provides us opportunity to grow different polymer chains on the RAFT agent attached nano surface efficiently.[35–39] Thus, here we have preferred SI-RAFT technique in the work to grow poly (N-vinyl imidazole) chains on MWCNT surface with better precision and to investigate into the effect of the grafted polymer chains on the properties of the material. We have chosen to grow pNVI chains on the MWCNT surface because of the presence of dangling N-heterocyclic chains which are basic in nature (pKa 7.05[37]). The grown polymer chains reside on the nanotube surface thus providing an

opportunity to grow metal nanoparticles on the polymer grafted MWCNT support. Here the basic nature and the easy coordinating ability of the imidazole rings with the metal ions like Pd^{2+} opens up a new possibility to design polymer grafted MWCNT supported transition metal catalyst for organic catalytic reactions.[40–42] Our idea is to utilize the basic character of the imidazole rings and the effect of cluster polymer chains on hollow nanotube to synthesize Pd nanoparticles without the need for external reducing agents. This particular arrangement of pNVI chains on the nanotube surface can enhance the reducing properties leading to the formation of metal nano particles. Heterogeneous Pd catalysts are well preferred over the homogeneous one due to their reusability and compatibility with the flow systems considering the high cost of Pd catalysts. Another preferred route for cross-coupling reactions involves reusable palladium nanoparticles which promotes the reaction in different organic and aqueous mediums. The catalytic activity increases as the size of particles decreases. Thus, the catalyst needs to be recovered and regenerated and then can be reused after the reaction in order to preserve the precious metal catalyst. Thus, the design of the heterogeneous catalyst is much tricky in terms of reusability and durability.

In order to examine the catalytic properties of MWCNT bound, polymer supported metal nanoparticles, we have utilized pNVI-*g*-MWCNT to use grow Pd nanoparticles and the synthesized material was characterized by means of spectroscopic and microscopic studies. Further we have used the material in Suzuki-Miyaura coupling reaction to synthesize coupled aryl and polycyclic systems.

EXPERIMENTAL SECTION

The sources of the materials which were used in the project are provided in **Chapter 2**. Synthesis and characterization procedure of BEPA RAFT agent [3-((((1-phenylethyl)thio)carbonothioyl)thio)propanoic acid] along with the activation of BEPA (BEPA-NHS) are discussed in **Chapter 2.** The preparations of MWCNT-COOH, MWCNT-NH_2 and attachment of BEPA-NHS on MWCNT-NH_2 surface in order to synthesize MWCNT-BEPA are discussed in **Chapter 2**.

Synthesis of pNVI-*g*-MWCNT via SI-RAFT polymerization

In a characteristic SI-RAFT polymerization reaction to grow poly-N-vinyl imidazole (pNVI) chains on the MWCNT surface, 100 mg (10.27 µmol) MWCNT-BEPA was taken with 3 mL dry DMF in a 25 mL *Schlenk tube* with 2.9 mg (10.27 µmol) of BEPA RAFT agent and 0.3 mg of AIBN initiator (2.05 µmol). Calculated amount of N-vinyl-imidazole (NVI) was

taken in the reaction mixture in order to grow the poly(N-vinyl-imidazole) (pNVI) polymer chains of different chain lengths, grafted on the MWCNT surface. The *Schlenk tube* was sealed with septum and was subjected to sonication for 5-6 minutes and was kept under stirring to make the reaction mixture consistently dispersed. The Schlenk tube was subjected to 3 freeze-pump-thaw cycles to ensure the complete removal of O_2 and dissolved air from the system. The *Schlenk tube* was back filled with ultra-high pure N_2 and kept under stirring at 70 °C for 16 h. Upon the completion of 16 h, the reaction was quenched using liquid N_2 and was exposed to air. The whole polymerization process is schematically represented in **Scheme 7.1 (A)**.

We purposefully chosen to grow polymer chains with dangling imidazole rings which is very important as pNVI chains, having 2 N atoms in each heterocyclic ring structure which are basic in character and are reported in literature to bind with positively charged atoms or protons in the system. The growth of pNVI (having pKa 7.05) chains were controlled to synthesize pNVI-g-MWCNT (PGNT) samples with varying molecular weight of the grafted pNVI chains which can interact strongly with Pd^{2+} ions and to further reduce the metal ion without the need of an external reducing agent to form Pd nanoparticles. The above synthesis procedure was followed to synthesize three different chain lengths of the *grafted* polymer chains and these samples were named as polymer *grafted* nanotubes and abbreviated as PGNT1, PGNT2, PGNT3. Higher the numbers after PGNT indicates higher chain length of the *grafted* polymer chain.

Polymer detachment procedure was employed in order to detach the grafted polymer chains from the MWCNT surface using ammonolysis process (Discussed in **Chapter 6** and **Appendix IV**).

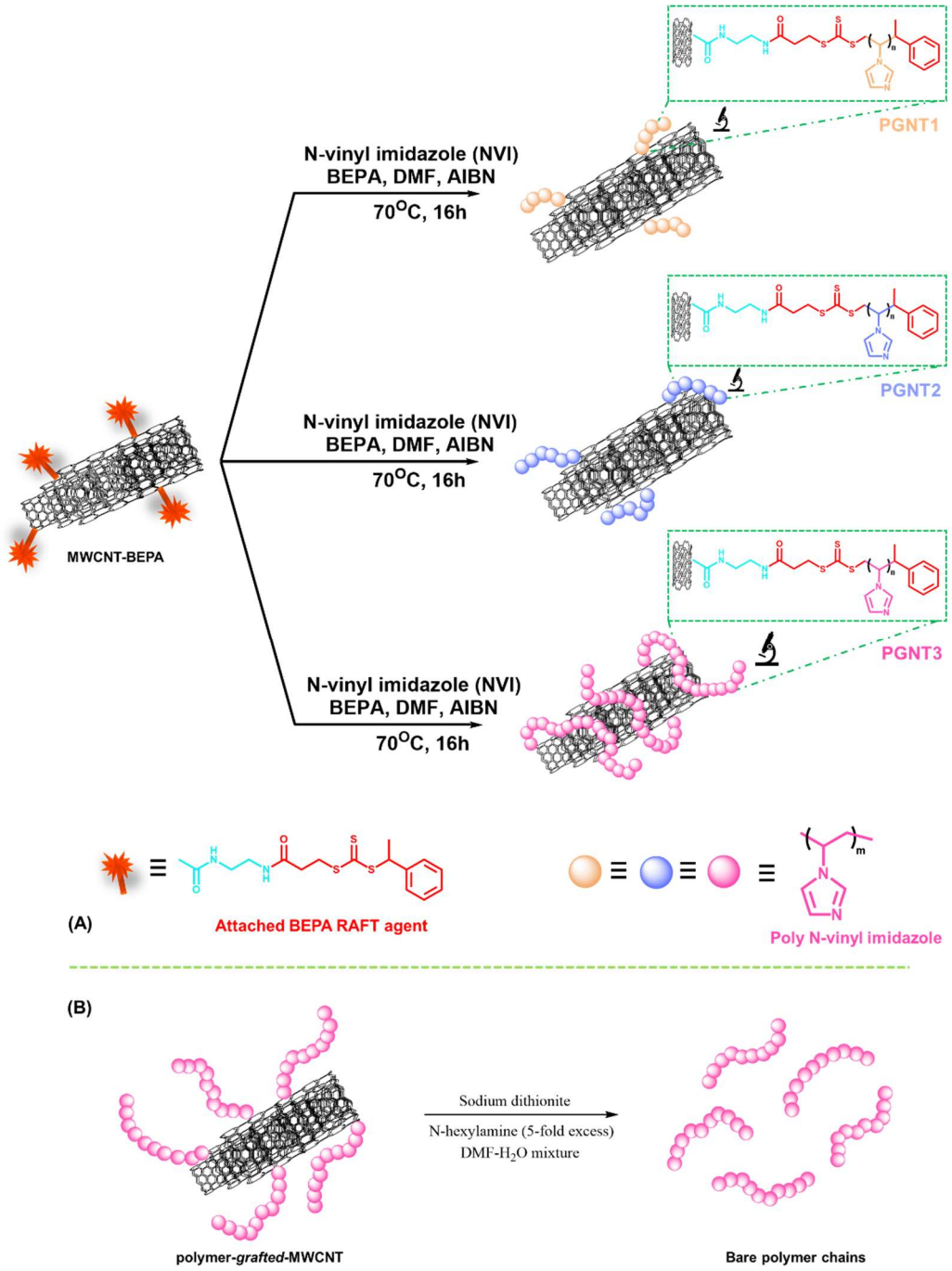

Scheme 7.1. Schematic representation of the growth of the polymer consisting of pNVI chains on the surface of the MWCNT using SI-RAFT technique **(A)** and the schematic representation for the detachment of grafted polymer chain from the surface of MWCNT for the GPC study **(B).**

In order to check the binding abilities and the ability to reduce metal ions in absence of an external reducing agent (NaBH4 or LiAlH4 or NaH), PGNT1 was taken as a model system and further studies were performed.

Synthesis of Pd@PGNT1

Scheme 7.2 represents the schematic representation towards the synthesis procedure of the Pd@PGNT1. 70 mg of PGNT1 was taken in a dry 50 mL round bottom flask with 20 mL dry THF and purged with dry N_2 gas for 15 minutes. The flask was subjected to ultra-sonication for 10 minutes followed by stirring under N_2 gas. 70 mg of $PdCl_2$ was added to the flask and reflux condenser was set under N_2 atmosphere. The reaction mixture was refluxed under nitrogen atmosphere for 5 h and allowed to cool slowly. The resulted mixture (yellow solution with black MWCNT dispersion) was subjected to centrifugation at 13000 rpm for 15 min in order to get rid of the unreacted supernatant liquid containing $PdCl_2$ dispersed in THF. The collected black solid was redispersed in dry THF and centrifuged in order to get rid of the unbound Pd species. The process was repeated 3 times followed by a final washing with dry Acetone to washout any impurities from the system. The collected Pd@PGNT1 material was dried under vacuum at 60 °C to get black powdered material which was subjected to further analysis.

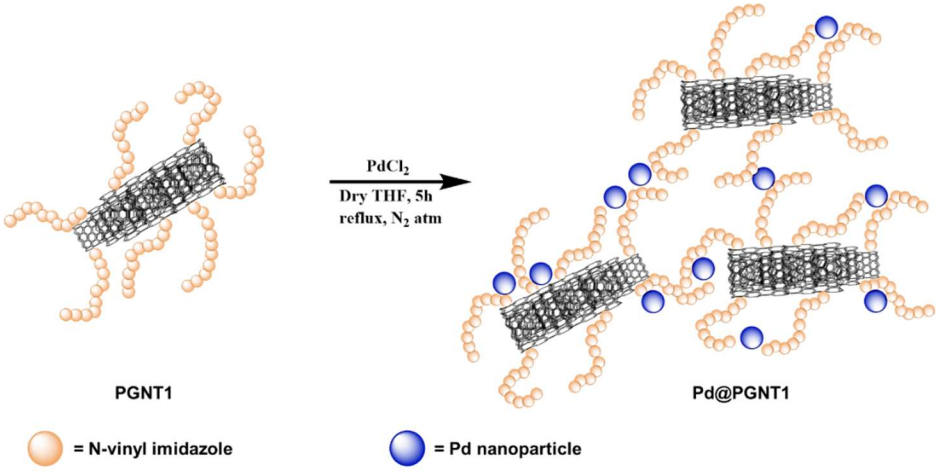

Scheme 7.2. Schematic representation of the synthesis procedure to produce Pd nano particle loaded PGNT1 (Pd@PGNT1).

Result and discussion

Grafting of pNVI on MWCNT surface

Appendix V-Scheme 7.1 shows the synthetic pathway to modify the nanotube to change the electronically conducting surface into an insulating one after reduction with ethylene diamine. The material was then treated with activated RAFT agent (BEPA-NHS) to attach BEPA RAFT agent on the concentric nanotube surface which helps to grow polymer

chains using *'grafting from'* approach. The synthetic procedure was reported by our group elsewhere.[18] The structure of the RAFT agent is designed in such a way so that the activated carboxylic acid group side when attached covalently with the -NH_2 groups, dangling on the MWCNT surface, the methyl phenyl group of the BSPA resides away from the surface. The synthesis of the BEPA RAFT agent is carried out by reacting thiopropanoic acid ($C_3H_6O_2S$) with carbon disulfide (CS_2) and 1-bromoethylbenzene (C_8H_9Br) in presence of K_3PO_4 (for detailed synthetic procedure see **Chapter 2**)[18] that the ethylbenzene group acts as a R group which ensures the propagation of the growing polymer chain (living polymer chain) by providing extra stability to the propagating radial species while the carboxylic acid part is bound to the MWCNT surface acting as Z group in order to stabilize the radical species. The stability of the radical R• is important in terms of propagation of the living polymer chain which is enhanced by the careful placement of a methyl group adjacent to phenyl group of the BEPA. The modification of MWCNT to carboxyl group modified MWCNT (MWCNT-COOH) and then to amine modified MWCNT (MWCNT-NH_2) is already described in details with the attachment process of BEPA on the MWCNT surface in **Chapter 2.** The formation of BEPA RAFT agent modified MWCNT surface has been proved by microscopic analysis and thermogravimetric analysis (described in details in the later section). ^{1}H NMR data supports the *grafting* of pNVI chains on the MWCNT surface and described in detail in the **Appendix V-Figure 7.1**.

The thermal degradation shapes of MWCNT, MWCNT-COOH, MWCNT-NH_2 and MWCNT-BEPA shown in **Figure 7.1 (A)** suggest their high thermal stability until 600 °C. MWCNT-BEPA thermal stability decreases a little upon RAFT agent BEPA attachment owing to the fact that BEPA RAFT agent shows sharp degradation ~200°C **[**see **Figure 6.1 (A)]**. The thermal degradation is observed to increase with the increment in the molecular weight of the *grafted* polymer chains of the polymer *grafted* MWCNT samples (PGNT1, PGNT2, PGNT3) considering the grafting amount of the RAFT agent is same for all the samples, all the materials are quite stable till 300 °C [**Figure 7.1(A)**]. The high thermal stability can be interpreted in terms of strong interaction patterns (π-π, H-bonding, non-covalent interaction) acting between the MWCNT hollow fibres and N-heterocyclic imidazole rings. The increase in the weight loss pattern (**Table 7.1** column 3) as we move from PGNT1 to PGNT3 indicates the *grafting* of longer polymer chains. Also, the calculated polymer content (in mg) per gram of MWCNT are tabulated in **Table 7.1** (column 4) clearly rises from PGNT1 to PGNT3 which indicates the presence of larger size pNVI polymer chains. We have achieved a maximum polymer *grafting*

density of 501 mg/g of MWCNT in the case of PGNT3 (**Table 7.1**). On the other hand, less thermal stability and early degradation pattern is observed for Pd@PGNT1 sample. The less thermal stability can be corelated with the coordination of imidazole rings with the $PdCl_2$ which then reduces the Pd^{2+} ions into Pd nano particles. The strong interactions acting between dangling imidazole rings and Pd nano particles reduces the inter nanotube interactions which results in reduction of the thermal stability of the material compared to the pristine PGNT1.

We have performed gel permeable chromatography (GPC) after detaching the grafted polymer chains upon chemically treating the polymer *grafted* MWCNT samples with N-hexylamine (5-fold excess) in the presence of sodium dithionite ($Na_2S_2O_4$) in DMF-H_2O medium [**Scheme 7.1 (B)**]. This treatment breaks trithiocarbonate bond[18,43], which is present between the polymer chain and the surface of MWCNTs. The process releases bare polymer chains in the solution which were purified by extraction using DMF and the molecular weights were determined by GPC measurements using DMF/LiBr as eluent [shown in **Figure 7.1 (B)**]. All the molecular weights (PGNT1-PGNT3) are represented in **Table 7.1**. The PGNT samples display narrow polydispersity index (Đ) and the molecular weights as obtained from the GPC measurements are in glowing agreement with the targeted molecular weight, which suggests that the *grafting* of the polymer chain was obtained using the RAFT polymerization technique. A comparison of $\bar{\mathbf{M}}_n$ values in **Table 7.1** (column 5) clearly display the increase in molecular weights from PGNT1 to PGNT2 and PGNT3. In addition to that, it is to be noted that, the degree of polymerization value (which are indicated in the suffix of sample identity in column 2 of **Table 7.1**) clearly indicates the formation of longer chain length upon the increment in the monomer feed ratio. PGNT samples are thus provides a basic, nitrogen rich, aromatic heterocyclic ring surrounded neighbourhood around the multiwalled hollow carbon nanotube core which may be useful for a number of purposes.

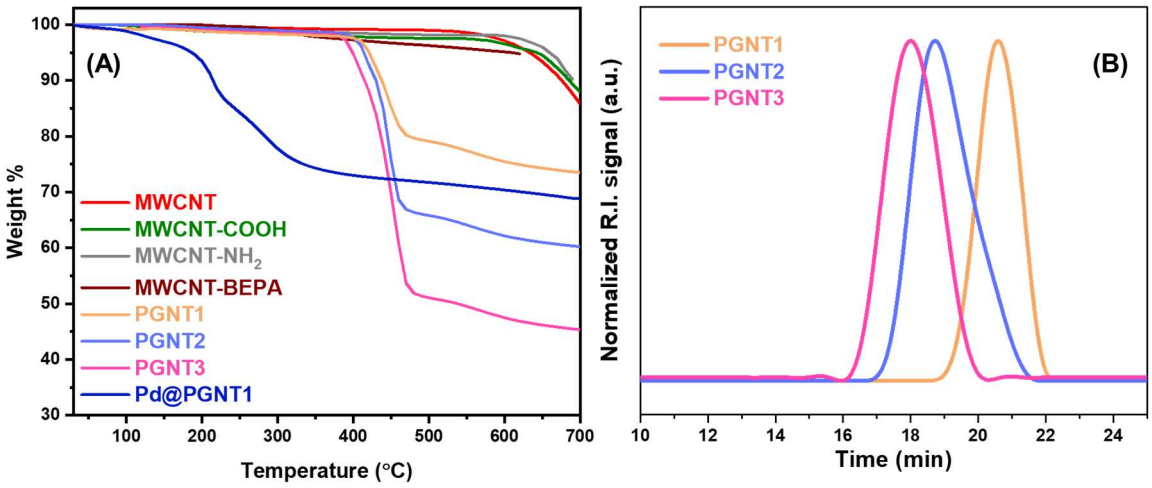

Figure 7.1. TGA of surface functionalized MWCNTs and polymer *grafted* MWCNTs **(A).** GPC plots **(B)** for the polymer *grafted* MWCNT samples after the detachment of the polymer chains from the surface of the MWCNT.

Table 7.1. Physical properties of the MWCNT samples upon surface functionalization and polymer *grafting*.

Sample name	Sample type[a]	Remaining weight % at 600 °C (wt%)[b]	Polymer content[c]	$\bar{M}_n$[d]	Đ[e]	Zeta potential (mV)[f]
MWCNT	-	97.13	-	-	-	-15.9
MWCNT-COOH	-	96.55	-	-	-	-20
MWCNT-NH_2	-	98.02	-	-	-	-8.6
MWCNT-BEPA	-	95.14	29.4	-	-	-4.9
PGNT1	$pNVI_{56}$-*g*-MWCNT	75.47	207	9891	1.07	-12.9
PGNT2	$pNVI_{153}$-*g*-MWCNT	62.17	347	13826	1.05	-6.1
PGNT3	$pNVI_{214}$-*g*-MWCNT	47.51	501	18119	1.08	-2.9
Pd@PGNT1	Pd attached PGNT1	68.89	87.19	-	-	-12.2

[a] sample type describes the chain sequence for each of the block corresponding the block copolymer chain and the degree of polymerization for each block included in the suffix which are obtained from the molecular weight measurements using gel permeation chromatography, [b] estimated from the TGA analysis (at 600 °C) and [c] polymer content was obtained from the analysis of the TGA curves in **Figure 7.1 (A)** and expressed as amount (in mg) of *grafted* polymer chains /g of MWCNT-BEPA but, for Pd@PGNT1 the value represents the Pd content and was calculated with respect to PGNT1, [d and e] are determined by gel permeation chromatography, and [f] obtained from zeta potential analysis in aqueous medium (see **Appendix V-Figure 7.XX)**.

PXRD plots illustrated in **Figure 7.2** suggest that MWCNT, MWCNT-BEPA and PGNT1 are amorphous in nature. Although, MWCNT represents an intense peak at 2θ = 26° and a low intensity peak at 43° which corresponds to diffraction pattern of a typical graphite type material (002), (100), respectively.[44] Upon carboxylic acid modification (MWCNT-COOH), amine modification (MWCNT-NH_2) or RAFT modification (MWCNT-BEPA), the PXRD patterns of the material remain unaffected because these chemical modifications does not enforce any structural change in the basic structure as reported earlier.[18] PGNT1 (**Figure 7.2**) shows a broad amorphous peak at 2θ value between 20-30° owing to the fact that pendent imidazole rings are amorphous in nature.[18,45,46] A small broadening is also observed below 2θ = 10° for PGNT1, Pd@PGNT1 and Pd@PGNT1 AR. Alternatively, Pd@PGNT1 which consist of amorphous PGNT1 and crystalline Pd nanoparticles exhibited a number of sharp crystalline. The peak at 2θ = 40.5° and 46.8° corresponds to the (1 1 1) and (2 0 0) diffraction pattern of face centred cubic (fcc) Pd, respectively.[47] This confirms the presence of Pd nanoparticles in the Pd@PGNT1 in high purity and high crystallinity (according to **JCPDS No. 05-0681**). The X-ray crystallite size as calculated from Scherrer equation is 22.13 nm which is in well agreement with the size observed using TEM studies (discussed in later section). A number of new peaks were observed in the Pd@PGNT1 material which arises because of the presence of strong interaction patterns acting between the PGNT1, nanotubes and the pNVI along with the Pd nanoparticles. The observation can be the result of the self-assembly driven crystalline pattern. Similar kind of observations have been reported in different polymer modified nanofiller systems where the interaction patterns between the amorphous nanomaterial and the polymer chains gives rise to strong crystalline peaks upon PXRD analysis.[35,48–52] The presence of crystalline nature was further evaluated using SAED

patterns as observed from TEM studies. The SAED pattern reflects the presence of Pd nanoparticle in the system (**Appendix V-Figure 7.11)**.

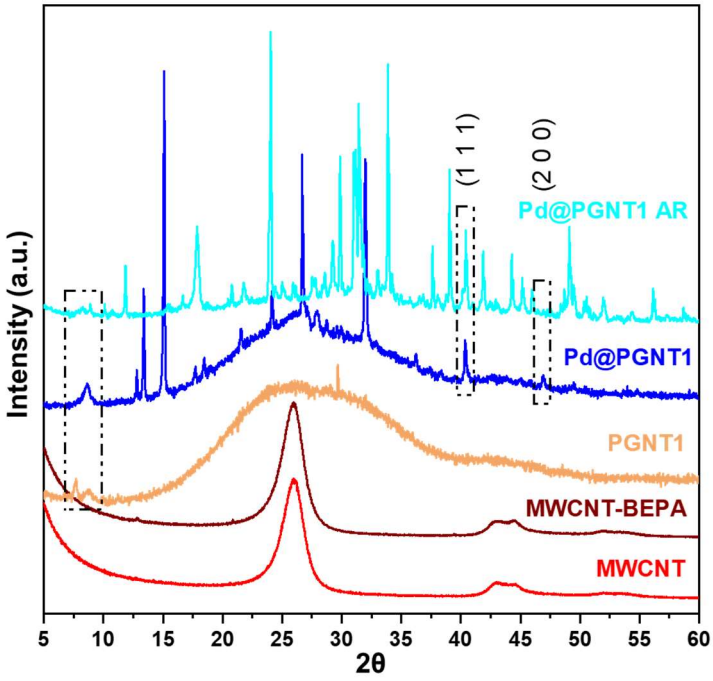

Figure 7.2. PXRD patterns of MWCNT, MWCNT-BEPA, PGNT1 along with Pd@PGNT1 and Pd@PGNT1 AR (here AR represents the sample was taken into account for catalytic reaction studies and represents the PXRD patterns after reaction).

The detailed morphological pictures [**Figure 7.3** and **Appendix V-Figure 7.2-7.7**] using FESEM and EDX studies provide significant evidence towards the successful *grafting* of polymer chains on the MWCNT surface. MWCNT and MWCNT-BEPA FESEM images show that the carbon nanotubes are tangled together (**Appendix V-Figure 7.2**). Nevertheless, MWCNT-BEPA shows increased aggregating behaviour when compared to unmodified MWCNT [**Appendix V-Figure 7.2 (A** and **B)**]. pNVI-g-MWCNTs show significant change in the morphology from the pristine MWCNT and give rise to highly clustered morphology. The *grafting* of polymer chains induces polymer patch formation on the MWCNT nano surface and is clearly visible from the FESEM data. The tendency to form polymer patch and the increase in the agglomeration behaviour increases with the increase in the polymer molecular weight of the *grafted* polymer chain which can be seen from the comparison of **Figure 7.3 (A)-(D)**. All the samples were further analysed by FESEM-EDX [**Appendix V-Figure 7.5-7.7**] which confirms the successful surface alteration with BEPA and polymer. A substantial increment in the EDX signal was observed for nitrogen in the case of PGNT2 material when compared to PGNT1 sample and is another proof towards the growth of the pNVI chains on the nanotube

surface by spectroscopic means [**Appendix V-Figure 7.6-7.7**]. The surface of the nanofibers are observed to be stable even after the polymerization process showing the integrity of the SI-RAFT process. Alternatively, upon Pd nanoparticle formation on the PGNT1 surface, formation of small nodes are visible under the FESEM and the surface morphology changes drastically. Further we have analyzed the sample using FESEM EDS instrument which reflected the presence of Pd on the surface of the Pd@PGNT1. Mapping studies confirms the even distribution of the elements along with Pd and the Pd is only observed on the pNVI-g-MWCNT surface exclusively which further supports our argument that the Pd nanoparticle formation is supported by the grafted pNVI chains only. Which was also evident from the TEM studies (discussed in the later section).

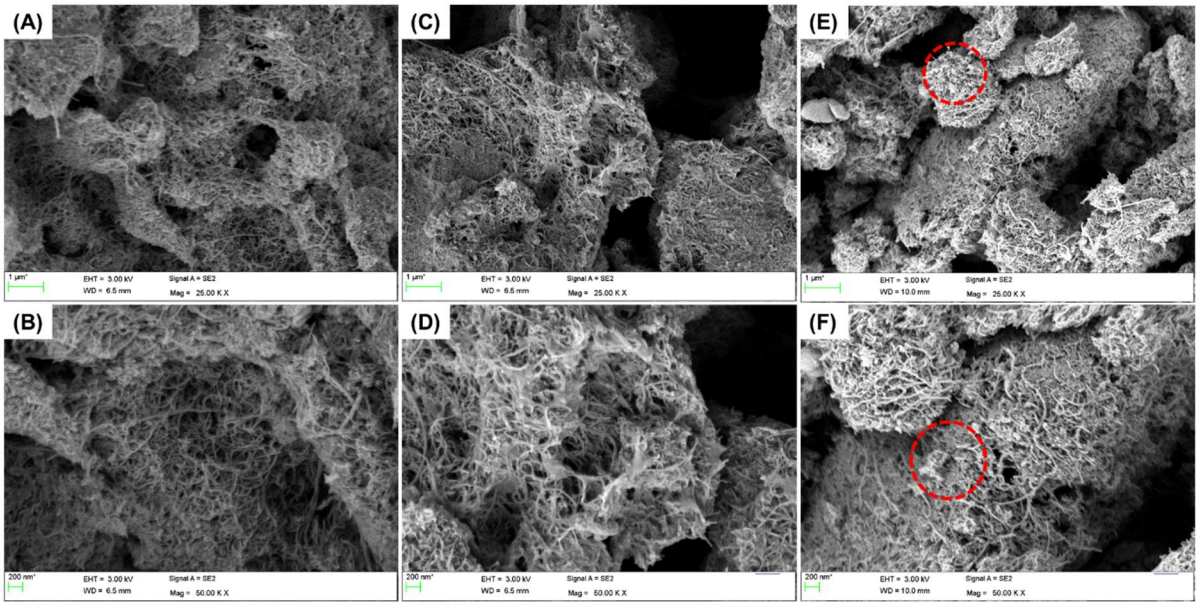

Figure 7.3. FESEM images of pNVI polymer *grafted* MWCNTs **(A, B)** PGNT1, **(C, D)** PGNT3 and **(E, F)** Pd@PGNT1 with different magnification. The red dotted circle represents the formation of small nodes upon Pd nanoparticle formation.

TEM data suggests that the *grafting of* pNVI polymer chains create a morphological change as evident from **Figure 7.4 (A and B)** where the MWCNT can be seen as a clear stacking of hollow concentric tubes but in the case of PGNT1 the polymer grafting is clearly evident. Furthermore, Pd@PGNT1 illustrates the presence of dark crystalline particles on the polymer grafted MWCNT walls. Although the presence of BEPA raft agent creates slightly dark patches on the nanotube walls as observed from the previous studies reported by our group. Further analysis using HR-TEM and EDX confirms that, the presence of dark spots reflects the presence of sulphur originating from BSPA RAFT agent and not due to Pd (**Appendix V-Figure 7.9-7.12**). But, in the case of Pd@PGNT1 the black spots are highly

crystalline and indicates the presence of heavier element which was studied using TEM EDX technique and confirms the presence of Pd nanoparticles of ~20 nm size (**Figure 7.4** and **Appendix V-Figure 7.11**). The presence of *grafted* polymer chains are also visible in the case of Pd@PGNT1. SAED pattern further implies the presence of Pd and the crystalline nature (**Appendix V-Figure 7.11**). Aliquots were obtained during the Pd nanoparticle synthesis procedure to and examined under TEM (**Appendix V-Figure 7.10**). The data reveals the incomplete formation of Pd nanoparticle on the MWCNT surface but upon the completion of the total reaction procedure the spherical Pd nanoparticles were observed.

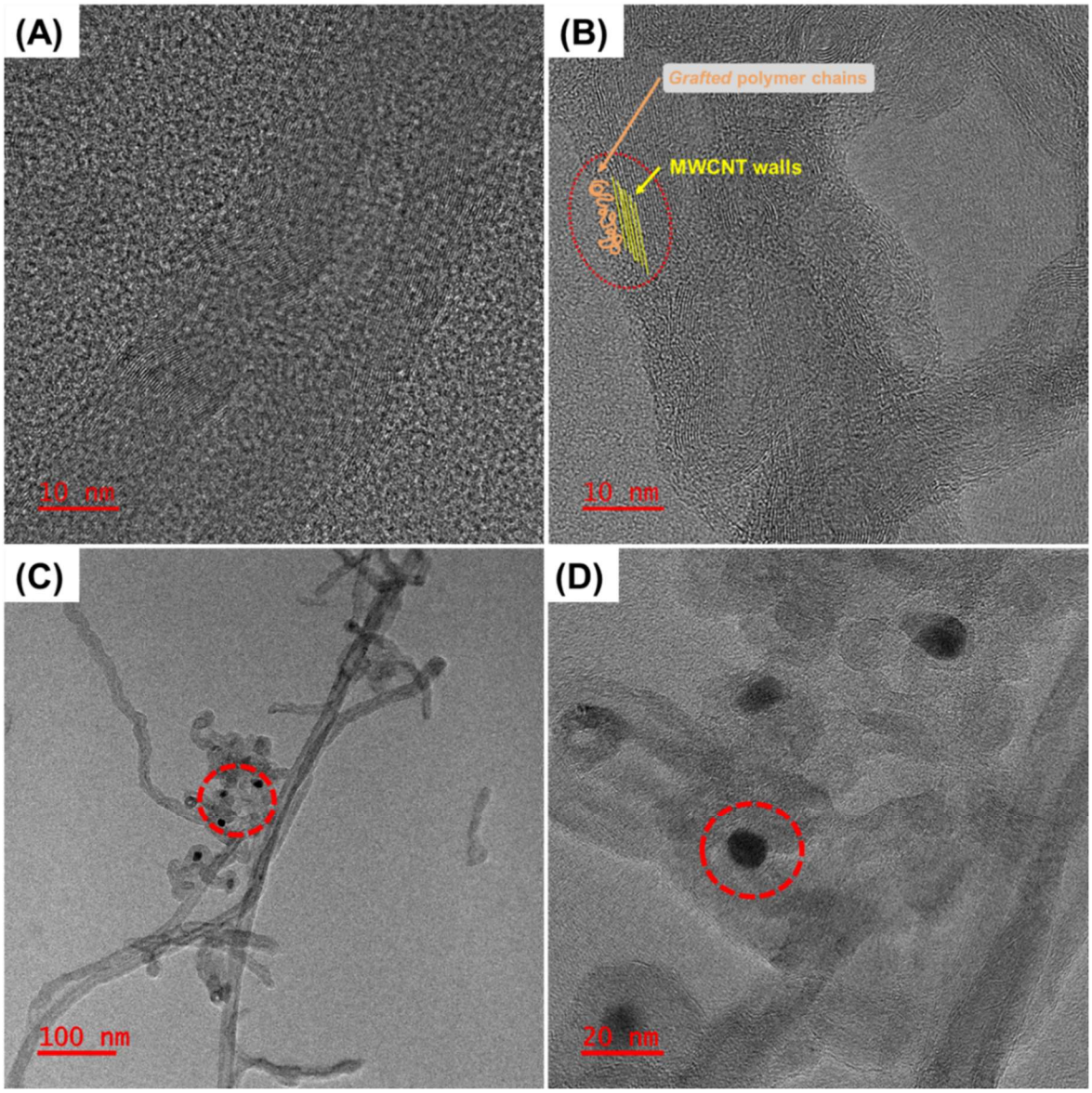

Figure 7.4. TEM images of MWCNT **(A),** PGNT1 **(B). (C)** and **(D)** represents the TEM image of Pd@PGNT1 in different magnification. The red dotted circle represents Pd nanoparticles.

Pd@PGNT1 as a catalyst towards the Suzuki-Miyaura coupling reaction

As a probable application of pNVI polymer *grafted* nanotube supported Pd nanoparticle, we have considered Pd@PGNT1 as a heterogeneous catalyst and have used it in Suzuki-Miyaura (SM) coupling reaction between an aryl halide and an aryl boronic acid to generate coupled aryl and poly cyclic systems. The reaction conditions were investigated and optimizes. The solvent scope and the utilization of mild basic conditions were checked thoroughly towards the SM coupling reaction. The substrate scope was examined by incorporating different functional group containing aryl bromide and aryl boronic acid in the reaction medium as substrate. NMR analysis for the structural confirmation of the products synthesized towards checking the substrate scope are represented in **Appendix V.**

SM coupling reaction procedure

In a typical SM reaction aryl bromide (1mmol, 1eq.), aryl boronic acid (1mmol, 1eq.), base (2 eq.), Pd catalyst (amount was varied in order to optimize the reaction procedure) were taken in a 25 mL sealed tube with 3 mL of solvent (a wide range of polar and nonpolar solvents were checked to optimize the reaction procedure). The reaction mixture was subjected to stirring using a magnetic bead in a preheated oil bath at 80 °C for 1-2 h. The reaction was stopped after the predetermined time and subjected to workup using water and ethyl acetate. The ethyl acetate layer was further washed with brine solution and concentrated using a rotary evaporator. The concentrated solution was purified using column chromatography.

Optimization of SM reaction conditions

The reaction of iodo benzene with phenyl boronic acid in the presence of Pd catalyst were examined in different solvent medium and also in the presence of different bases in different temperatures (**Scheme 7.3**). The variation of solvent medium used are tabulated in Table 1. The reaction produced better yield in the presence of THF, dioxane, MeOH and EtOH solvent (see Table 2). The yield was compromised in the presence of water. The variation of base used in the reaction was varied with KOH, NaOH, K_2CO_3, K_3PO_4 in different temperature conditions (see Table 3). The observation suggested the use of mild basic condition incorporated with K_2CO_3 and K_3PO_4 is adequate to carry out SM reaction in EtOH condition and the yield decreases with lowering of the temperature. The yield observed at room temperature with K_2CO_3 and EtOH condition is 30%.

The optimization studies of base, solvent and temperature suggests that mild basic condition of K_2CO_3 with EtOH as solvent at 80 °C is sufficient to carry out the reaction and this condition is followed for our current investigation.

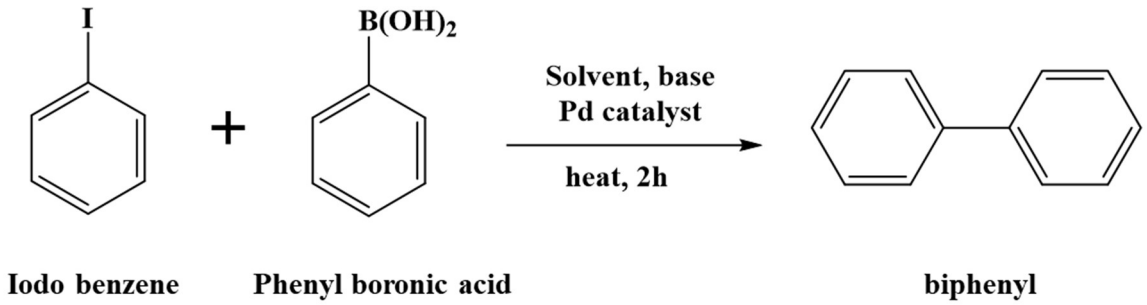

Iodo benzene **Phenyl boronic acid** **biphenyl**

Scheme 7.3. The general reaction procedure of SM reaction between an aryl halide (iodo benzene) and an aryl boronic acid (phenyl boronic acid) in the presence of a base, solvent and a Pd catalyst.

Table 7.2. The variation of yield % in presence of different bases and solvents for SM reaction between iodo benzene and phenyl boronic acid.

Entry	Base	Solvent	Yield%
1	K_2CO_3	DMF	30-40
2	K_2CO_3	THF	88
3	K_2CO_3	Dioxane	99
4	K_2CO_3	EtOH: H_2O (1:1)	20
5	K_2CO_3	MeOH	95
6	K_2CO_3	EtOH	99
7	NaOH	EtOH	99

Table 7.3. The variation of yield % in different solvent conditions at different temperature for SM reaction between iodo benzene and phenyl boronic acid.

Entry	Solvent	Base	Temp	Yield%
1	EtOH	KOH	Reflux	99
2	EtOH	KOH	80	99
3	EtOH	NaOH	Reflux	99
4	EtOH	NaOH	80	99
5	EtOH	K_2CO_3	80	99
6	EtOH	K_2CO_3	70	94
7	EtOH	K_2CO_3	RT	30
8	EtOH	K_3PO_4	80	95

RT represents room temperature.

Optimization of catalyst concentration in SM reaction

Upon optimization of the optimum reaction condition for the SM coupling reaction the amount of Pd@PGNT1 was varied in order to check the performance of the synthesized catalyst. The amount was reduced to 1 mg of Pd@PGNT1 for a 1 gm scale reaction. The yield obtained is 99% considering the reaction between iodo benzene and phenyl boronic acid in presence of K_2CO_3 at 80 °C in ethanol. TEM EDX analysis of Pd@PGNT1 suggested the presence of 12.65 mass % of Pd in the material. Thus 1 mg of Pd@PGNT1 contains 0.127 mg (1.189 µmol) of Pd. The high presence of MWCNT support provides a stable backbone towards the high catalytic activity of the material. We have also investigated the reusability of the catalyst and performed SM coupling reaction between iodo benzene and phenyl boronic acid in 1 gm scale. The catalyst was separated from the reaction mixture using ethanol solvent and the same catalyst was subjected to 5 consecutive reactions and provided excellent yield. The catalyst obtained after 5 consecutive reactions were washed thoroughly and subjected to TEM analysis (**Appendix V-Figure 7.12**). Pd@PGNT1 was observed to retain the structural integrity while an increase in the agglomeration nature is observed as evident from the TEM studies. Which indicates the robustness of the synthesized material. Substrate scope for the reaction was investigated using 1 mg Pd@PGNT1 for ~200mg scale reaction.

Investigation of substrate scope

The substrate scope for the reaction was explored upon varying the aryl group and substituted aryl groups of the boronic acid and aryl halides. The reaction was carried out using different substitutions of the halide group (-Cl, -Br, -I) to understand the effect of different halide groups in the case of yield % of the SM reaction. The yield % was observed to be increased with the better leaving nature of the halide group (see **Table 7.4**). Thus, better yield obtained for iodo and bromo substituents.

Table 7.4. The effect of different halide groups towards the yield % of SM reaction between aryl halide and phenyl boronic acid.

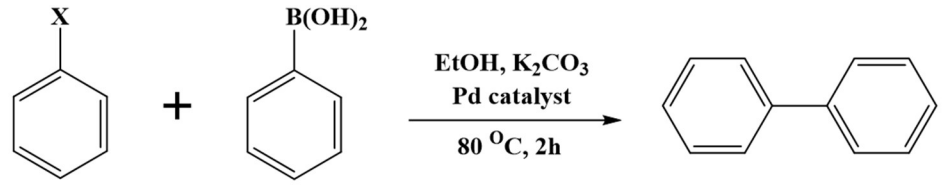

aryl halide Phenyl boronic acid biphenyl

Entry	X	Yield %	Product[a]
1	Chloro	93	1
2	Bromo	98	1
3	iodo	99	1

[a] The numbers in the product column represents the product code which is used to differentiate between the products formed in each case.

Substrate scope of the reaction were further checked by altering the substituents of the aryl boronic acid in the optimal conditions (see **Table 7.5**). The reaction was performed under the influence of electron donating and withdrawing groups and the products were obtained in quantitative yields in most of the cases. Although the yields were observed to be a little less in case of strong electron withdrawing group (-F, -CHO) present in the aryl boronic acid. But the unsubstituted naphthyl moiety with the boronic acid functionality produced high yields in SM reaction with phenyl iodide.

Table 7.5. Yield % of products (substituted biphenyl) for different substituted aryl boronic acids in the SM reaction.

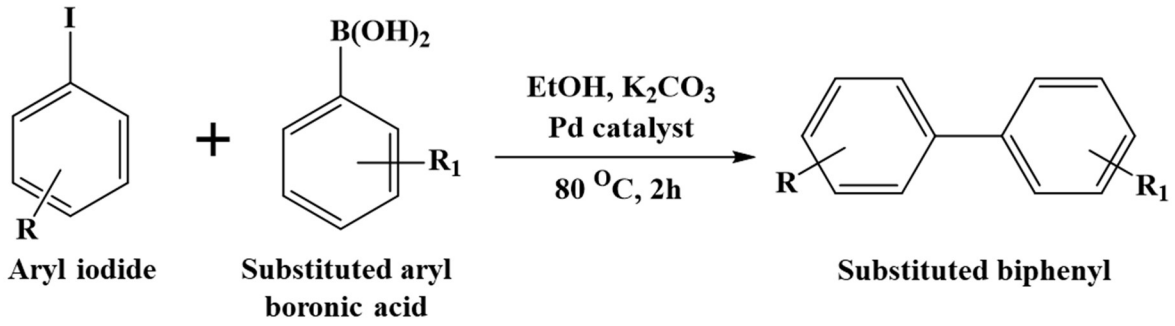

Entry	R	R_1	Yield %	Product[c]
1[a]	o –Me	H	94	2
2[a]	m –Me	H	98	3
3[a]	p –Me	H	99	4
4	H	p –F	35	5
5[b]	H	1 –nap BA	94	6
6[b]	H	2 –nap BA	96	7

[a] The aryl bromide derivative were used here is instead of aryl iodide. [b] In case of 6th and 7th entry, the second column (R) represents the aryl boronic acid name where as in all the other cases the second column represents the substituent of the phenyl boronic acid. [c] The numbers in the product column represents the product code which is used to differentiate between the products formed in each case.

The variation of the aryl group of the phenyl halide was examined with a variety of aryl group substituted boronic acids under optimized reaction conditions. The results are tabulated in **Table 7.6**. Better yields of the products were obtained in each case. The data suggests that the reaction is well controlled and provides better yields even in the presence of polycyclic aryl systems in both the halide and boronic acid part.

Table 7.6. Yield % of products for different substituted aryl boronic acids with 9-bromo phenanthrene in the SM reaction.

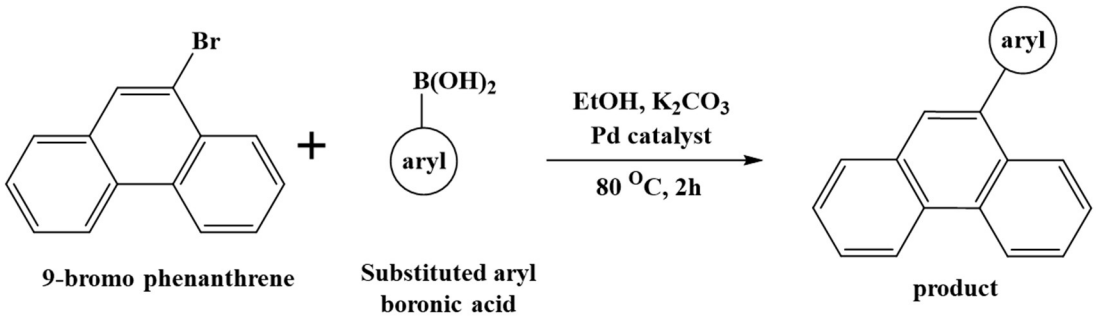

Entry	Aryl	Yield	Product[a]
1	1 –nap	96	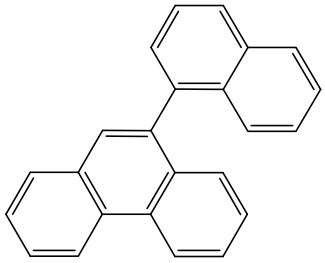 8
2	2 –nap	98	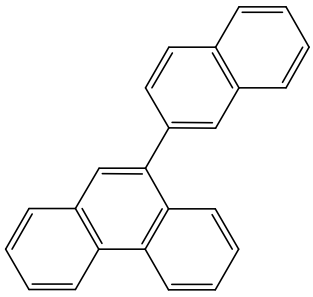 9

[a] The numbers in the product column represents the product code which is used to differentiate between the products formed in each case.

Conclusion

Our work validates, a simple and highly efficient approach for the covalent *grafting* of polymer chains on the nanotube surface by utilizing *grafting from* SI-RAFT technique. The growth of the polymer chains on the nano surface was highly controlled and with narrow Đ. All the samples were thoroughly characterized by numerous techniques and various physical

parameters to confirm the surface *grafting*. Our main objective here, is to create dangling imidazole ring enriched reducing environment around the MWCNT surface in order to reduce the Pd^{2+} ions to synthesize Pd nanoparticles on the polymer *grafted* MWCNT surface which was validated in terms of microscopic studies. TEM EDX data confirms the presence of 12.65 mass% of Pd in the Pd@PGNT1 material. The material was further checked for its catalytic activities in Suzuki-Miyaura coupling reaction. The product yield was checked in terms of varying different parameters of the reaction condition including temperature, solvent, base, etc. The efficiency of the catalyst as well as substrate scope were further evaluated confirming the high efficiency of the catalyst. The reusability as well as the stability of the catalyst upon Suzuki-Miyaura reaction was examined and found to be the catalyst is stable under the reaction conditions.

Reference

(1) Iijima, S. Helical Microtubules of Graphitic Carbon. *Nature* **1991**, *354*, 56–58.

(2) Yang, Y.; Narayanan Nair, A. K.; Sun, S. Adsorption and Diffusion of Carbon Dioxide, Methane, and Their Mixture in Carbon Nanotubes in the Presence of Water. *J. Phys. Chem. C* **2020**, *124*, 16478–16487.

(3) Lee, B.; Baek, Y.; Lee, M.; Jeong, D. H.; Lee, H. H.; Yoon, J.; Kim, Y. H. A Carbon Nanotube Wall Membrane for Water Treatment. *Nat. Commun.* **2015**, *6*, 7109.

(4) Ihsanullah. Carbon Nanotube Membranes for Water Purification: Developments, Challenges, and Prospects for the Future. *Sep. Purif. Technol.* **2019**, *209*, 307–337.

(5) Kang, S.; Jeong, Y. K.; Mhin, S.; Ryu, J. H.; Ali, G.; Lee, K.; Akbar, M.; Chung, K. Y.; Han, H.; Kim, K. M. Pulsed Laser Confinement of Single Atomic Catalysts on Carbon Nanotube Matrix for Enhanced Oxygen Evolution Reaction. *ACS Nano* **2021**, *15*, 4416–4428.

(6) Yan, Y.; Miao, J.; Yang, Z.; Xiao, F.-X.; Yang, H. Bin; Liu, B.; Yang, Y. Carbon Nanotube Catalysts: Recent Advances in Synthesis, Characterization and Applications. *Chem. Soc. Rev.* **2015**, *44*, 3295–3346.

(7) Yang, P.; Devasenathipathy, R.; Xu, W.; Wang, Z.; Chen, D.-H.; Zhang, X.; Fan, Y.; Chen, W. Pt 1 (CeO 2) 0.5 Nanoparticles Supported on Multiwalled Carbon Nanotubes for Methanol Electro-Oxidation. *ACS Appl. Nano Mater.* **2021**, *4*, 10584–10591.

(8) Zhan, H.; Chen, Y. W.; Shi, Q. Q.; Zhang, Y.; Mo, R. W.; Wang, J. N. Highly Aligned and Densified Carbon Nanotube Films with Superior Thermal Conductivity and Mechanical Strength. *Carbon N. Y.* **2022**, *186*, 205–214.

(9) Li, Y.; Li, M.; Pang, M.; Feng, S.; Zhang, J.; Zhang, C. Effects of Multi-Walled Carbon Nanotube Structures on the Electrical and Mechanical Properties of Silicone Rubber

Filled with Multi-Walled Carbon Nanotubes. *J. Mater. Chem. C* **2015**, *3*, 5573–5579.

(10) Sakellariou, G.; Priftis, D.; Baskaran, D. Surface-Initiated Polymerization from Carbon Nanotubes: Strategies and Perspectives. *Chem. Soc. Rev.* **2013**, *42*, 677–704.

(11) He, G.; Zhao, J.; Hu, S.; Li, L.; Li, Z.; Li, Y.; Li, Z.; Wu, H.; Yang, X.; Jiang, Z. Functionalized Carbon Nanotube via Distillation Precipitation Polymerization and Its Application in Nafion-Based Composite Membranes. *ACS Appl. Mater. Interfaces* **2014**, *6*, 15291–15301.

(12) Pramanik, C.; Gissinger, J. R.; Kumar, S.; Heinz, H. Carbon Nanotube Dispersion in Solvents and Polymer Solutions: Mechanisms, Assembly, and Preferences. *ACS Nano* **2017**, *11*, 12805–12816.

(13) Karousis, N.; Tagmatarchis, N.; Tasis, D. Current Progress on the Chemical Modification of Carbon Nanotubes. *Chem. Rev.* **2010**, *110*, 5366–5397.

(14) Gorityala, B. K.; Ma, J.; Wang, X.; Chen, P.; Liu, X.-W. Carbohydrate Functionalized Carbon Nanotubes and Their Applications. *Chem. Soc. Rev.* **2010**, *39*, 2925.

(15) Georgakilas, V.; Kordatos, K.; Prato, M.; Guldi, D. M.; Holzinger, M.; Hirsch, A. Organic Functionalization of Carbon Nanotubes. *J. Am. Chem. Soc.* **2002**, *124*, 760–761.

(16) Khabashesku, V. N.; Billups, W. E.; Margrave, J. L. Fluorination of Single-Wall Carbon Nanotubes and Subsequent Derivatization Reactions. *Acc. Chem. Res.* **2002**, *35*, 1087–1095.

(17) Cheng, C.-C.; Wang, Y.-S.; Chen, J.-K.; Lee, D.-J. Supramolecular Electrospun Nanofibers with High Conductivity at Ultra-Low Carbon Nanotube Content. *J. Mater. Chem. C* **2016**, *4*, 5207–5213.

(18) Mukherjee, N.; Das, A.; Jana, T. Poly(N -Vinyl Triazole- b - N -Vinyl Imidazole) Grafted on MWCNTs as Nanofillers to Improve Proton Conducting Membranes. *ACS Appl. Nano Mater.* **2022**. https://doi.org/10.1021/acsanm.2c04603.

(19) Khan, M. U.; Gomes, V. G.; Altarawneh, I. S. Synthesizing Polystyrene/Carbon Nanotube Composites by Emulsion Polymerization with Non-Covalent and Covalent Functionalization. *Carbon N. Y.* **2010**, *48*, 2925–2933.

(20) Hong, C.-Y.; You, Y.-Z.; Pan, C.-Y. Functionalized Multi-Walled Carbon Nanotubes with Poly(N-(2-Hydroxypropyl)Methacrylamide) by RAFT Polymerization. *J. Polym. Sci. Part A Polym. Chem.* **2006**, *44*, 2419–2427.

(21) Xu, G.; Wu, W.-T.; Wang, Y.; Pang, W.; Zhu, Q.; Wang, P. Functionalized Carbon Nanotubes with Polystyrene- Block -Poly (N -Isopropylacrylamide) by in Situ RAFT Polymerization. *Nanotechnology* **2007**, *18*, 145606.

(22) Pei, X.; Hao, J.; Liu, W. Preparation and Characterization of Carbon Nanotubes−Polymer/Ag Hybrid Nanocomposites via Surface RAFT Polymerization. *J.*

Phys. Chem. C **2007**, *111*, 2947–2952.

(23) Qin, S.; Qin, D.; Ford, W. T.; Resasco, D. E.; Herrera, J. E. Polymer Brushes on Single-Walled Carbon Nanotubes by Atom Transfer Radical Polymerization of n -Butyl Methacrylate. *J. Am. Chem. Soc.* **2004**, *126*, 170–176.

(24) Hong, C.-Y.; You, Y.-Z.; Pan, C.-Y. Synthesis of Water-Soluble Multiwalled Carbon Nanotubes with Grafted Temperature-Responsive Shells by Surface RAFT Polymerization. *Chem. Mater.* **2005**, *17*, 2247–2254.

(25) Kohls, A.; Maurer Ditty, M.; Dehghandehnavi, F.; Zheng, S.-Y. Vertically Aligned Carbon Nanotubes as a Unique Material for Biomedical Applications. *ACS Appl. Mater. Interfaces* **2022**, *14*, 6287–6306.

(26) Ngoma, M. M.; Mathaba, M.; Moothi, K. Effect of Carbon Nanotubes Loading and Pressure on the Performance of a Polyethersulfone (PES)/Carbon Nanotubes (CNT) Membrane. *Sci. Rep.* **2021**, *11*, 23805.

(27) Gholami, S.; Llacuna, J. L.; Vatanpour, V.; Dehqan, A.; Paziresh, S.; Cortina, J. L. Impact of a New Functionalization of Multiwalled Carbon Nanotubes on Antifouling and Permeability of PVDF Nanocomposite Membranes for Dye Wastewater Treatment. *Chemosphere* **2022**, *294*, 133699.

(28) Amin, M.; Abdullah, B. M.; Rowley-Neale, S. J.; Wylie, S.; Slate, A. J.; Banks, C. E.; Whitehead, K. A. Diamine Oxidase-Conjugated Multiwalled Carbon Nanotubes to Facilitate Electrode Surface Homogeneity. *Sensors* **2022**, *22*, 675.

(29) Tromm Steffen, T.; César Fontana, L.; Hammer, P.; Becker, D. Amine Functionalization of Carbon Nanotubes with Solid Urea Using Different Plasma Treatments. *Appl. Surf. Sci.* **2022**, *583*, 152493.

(30) Thakur, P.; Mannuthodikayil, J.; Kalita, G.; Mandal, K.; Narayanan, T. N. Correction: In Situ Surface Modification of Bulk or Nano Materials by Cytochrome- c for Active Hydrogen Evolution Catalysis. *Mater. Chem. Front.* **2021**, *5*, 2470–2470.

(31) Zhao, C.; Wang, X.; Chen, X.; Liu, Y.; Xie, Y.; Xu, H. Covalent Interactions between Carbon Nanotubes and P3HT by Thiol–Ene Click Chemistry towards Improved Thermoelectric Performance. *Mater. Chem. Front.* **2020**, *4*, 1174–1181.

(32) Mosnáčková, K.; Mrlík, M.; Mičušík, M.; Kleinová, A.; Sasinková, V.; Popelka, A.; Opálková Šišková, A.; Kasák, P.; Dworak, C. L.; Mosnáček, J. Light-Responsive Hybrids Based on Carbon Nanotubes with Covalently Attached PHEMA- g -PCL Brushes. *Macromolecules* **2021**, *54*, 2412–2426.

(33) Contreras-Torres, F. F.; Salas-Treviño, D.; Soto-Domínguez, A.; De Jesús García-Rivas, G. Carbon Nanotubes in Tumor-Targeted Chemotherapeutic Formulations: A Review of Opportunities and Challenges. *ACS Appl. Nano Mater.* **2022**, *5*, 8649–8679.

(34) Lavagna, L.; Bartoli, M.; Suarez-Riera, D.; Cagliero, D.; Musso, S.; Pavese, M. Oxidation of Carbon Nanotubes for Improving the Mechanical and Electrical Properties

of Oil-Well Cement-Based Composites. *ACS Appl. Nano Mater.* **2022**, *5*, 6671–6678.

(35) Mukherjee, N.; Das, A.; Dhara, M.; Jana, T. Surface Initiated RAFT Polymerization to Synthesize N-Heterocyclic Block Copolymer Grafted Silica Nanofillers for Improving PEM Properties. *Polymer.* **2021**, *236*, 124315.

(36) Dhara, M.; Rudra, S.; Mukherjee, N.; Jana, T. Hollow Polymer Nanocapsules with a Ferrocenyl Copolymer Shell. *Polym. Chem.* **2021**, *12*, 3976–3991.

(37) Koyilapu, R.; Subhadarshini, S.; Singha, S.; Jana, T. An In-Situ RAFT Polymerization Technique for the Preparation of Poly(N-Vinyl Imidazole) Modified Cloisite Nanoclay to Develop Nanocomposite PEM. *Polymer.* **2021**, *212*, 123175.

(38) Kutcherlapati, S. R.; Koyilapu, R.; Jana, T. Poly(N -Vinyl Imidazole) Grafted Silica Nanofillers: Synthesis by RAFT Polymerization and Nanocomposites with Polybenzimidazole. *J. Polym. Sci. Part A Polym. Chem.* **2018**, *56*, 365–375.

(39) Raju Kutcherlapati, S. N.; Yeole, N.; Gadi, M. R.; Perali, R. S.; Jana, T. RAFT Mediated One-Pot Synthesis of Glycopolymer Particles with Tunable Core–Shell Morphology. *Polym. Chem.* **2017**, *8*, 1371–1380.

(40) Pekel, N.; Güven, O. Investigation of Complex Formation between Poly(N-Vinyl Imidazole) and Various Metal Ions Using the Molar Ratio Method. *Colloid Polym. Sci.* **1999**, *277*, 570–573.

(41) Pathreeker, S.; Hosein, I. D. Vinylimidazole-Based Polymer Electrolytes with Superior Conductivity and Promising Electrochemical Performance for Calcium Batteries. *ACS Appl. Polym. Mater.* **2022**, *4*, 6803–6811.

(42) Jääskeläinen, S.; Koshevoy, I. O.; Suvanto, S.; Ryhänen, T.; Hirva, P. Vinylimidazole Coordination Modes to Pt and Au Metal Centers. *New J. Chem.* **2020**, *44*, 12762–12770.

(43) Li, C.; Wang, C.; Ji, Z.; Jiang, N.; Lin, W.; Li, D. Synthesis of Thiol-Terminated Thermoresponsive Polymers and Their Enhancement Effect on Optical Limiting Property of Gold Nanoparticles. *Eur. Polym. J.* **2019**, *113*, 404–410.

(44) Haque, M. A.; Sulong, A. B.; Shyuan, L. K.; Majlan, E. H.; Husaini, T.; Rosli, R. E. Synthesis of Polymer/MWCNT Nanocomposite Catalyst Supporting Materials for High-Temperature PEM Fuel Cells. *Int. J. Hydrogen Energy* **2021**, *46*, 4339–4353.

(45) Sabaa, M. W.; Mohamed, N. A.; Mohamed, R. R.; Khalil, N. M.; Abd El Latif, S. M. Synthesis, Characterization and Antimicrobial Activity of Poly (N-Vinyl Imidazole) Grafted Carboxymethyl Chitosan. *Carbohydr. Polym.* **2010**, *79*, 998–1005.

(46) Kutcherlapati, S. R.; Koyilapu, R.; Jana, T. Poly(N -Vinyl Imidazole) Grafted Silica Nanofillers: Synthesis by RAFT Polymerization and Nanocomposites with Polybenzimidazole. *J. Polym. Sci. Part A Polym. Chem.* **2018**, *56*, 365–375.

(47) Yu, Y.; Zhao, Y.; Huang, T.; Liu, H. Shape-Controlled Synthesis of Palladium Nanocrystals by Microwave Irradiation. *Pure Appl. Chem.* **2009**, *81*, 2377–2385.

(48) Singha, S.; Jana, T. Structure and Properties of Polybenzimidazole/Silica Nanocomposite Electrolyte Membrane: Influence of Organic/Inorganic Interface. *ACS Appl. Mater. Interfaces* **2014**, *6*, 21286–21296.

(49) Singha, S.; Koyilapu, R.; Dana, K.; Jana, T. Polybenzimidazole-Clay Nanocomposite Membrane for PEM Fuel Cell: Effect of Organomodifier Structure. *Polymer.* **2019**, *167*, 13–20.

(50) Maity, S.; Singha, S.; Jana, T. Low Acid Leaching PEM for Fuel Cell Based on Polybenzimidazole Nanocomposites with Protic Ionic Liquid Modified Silica. *Polymer.* **2015**, *66*, 76–85.

(51) Ghosh, S.; Maity, S.; Jana, T. Polybenzimidazole/Silica Nanocomposites: Organic-Inorganic Hybrid Membranes for PEM Fuel Cell. *J. Mater. Chem.* **2011**, *21*, 14897.

(52) Singha, S.; Jana, T. Self-Assembly of Nanofillers in Improving the Performance of Polymer Electrolyte Membrane. *Macromol. Symp.* **2016**, *369*, 49–55.

Chapter 8

Summary and Conclusion

Summary

The thesis entitled "Polymer *grafted* Nanomaterials: Synthesis via RAFT Polymerization and the Applications" illustrates the synthesis procedure and the characterization techniques to synthesize and chemically modify SiNP UiO-66 NH_2 MOF and MWCNT nano surface in order to graft different RAFT agents attached covalently on the surface of the nanomaterials. This thesis also describes the SI-RAFT techniques used to grow homo polymer, block copolymer and polymeric brushes on the nano surface in aqueous and non-aqueous medium which can further be detached using the described different polymer detachment techniques to isolate the grafted polymer chains in order to characterize them. The use of polymer grafted SiNP, MOF and MWCNT materials as nanofiller to prepare flexible, stable and robust MMMs were also described thoroughly. Different techniques in order to estimate the stability of the nanomaterials and the inherent and matrix supported proton conductivity were illustrated in detail. The complete thesis comprises of five working chapters along with the introduction and material, synthesis and method chapter. A brief description about the out come corresponds to each chapter is mention below.

Chapter 1

Chapter 1 illustrates the brief history of CRP, RAFT technique and advantages of smart nanomaterials. Also, the SI-RAFT technique on the nano material surface (SiNP, MOF and CNT) was discussed in detail in order to synthesize the smart nano surface for the use in different applicative fields. Furthermore, the benefits of fuel cells and its classifications, PEMFC and its working principle along with the need for the improvement of PEM material were described. Different techniques for the synthesis of MMMs using a properly designed nanofiller material with PBI polymer were also described in order to enhance the efficiency of the PEM material. This chapter also explains the benefits of the heterogeneous catalyst for industrial and commercial purpose. The requirement for better and efficient catalyst for Suzuki-Miyaura coupling is explained in detail. In brief this chapter provides ephemeral understanding of the background and the history of the working chapters (***Chapter 3-7***)

Chapter 2

This chapter comprises of all the materials utilized for the whole thesis work, as well as details on the synthesis of precursor materials and the different instrumentation methods used for the synthesis and characterization of all of the compounds listed in the thesis.

Chapter 3: Block Copolymer *Grafted* Silica Nanoparticles: Designer Nanofiller for Improving Proton Exchange Membrane Properties

Surface functionalized silica nanoparticles (SiNP) have gained massive attention as an efficient nanofiller in improving the properties of the proton exchange membrane (PEM) but, a lot more can be done on the SiNP surface to prepare smart nanofiller for the further improvement in the PEM performance. Strategic surface functionalization of SiNP surface can enhance the properties of nanocomposite PEM in the matrix. Here, we report about the development of the block copolymer *grafted* SiNP (BC-*g*-SiNP) as functional nanofiller which was further blended with oxypolybenzimidazole (OPBI) polymer to prepare nanocomposite based PEM. Block copolymer chains which comprise of poly (N-Vinyl imidazole) (pNVI) and poly (N-Vinyl-1,2,4-triazole) (pNVT) were grown on the polymerizable SiNP surface using *grafting-from* RAFT polymerization in one pot process. Two series of BC-*g*-SiNP namely pNVI-*b*-pNVT-*g*-SiNP and pNVT-*b*-pNVI-*g*-SiNP were synthesized by altering the polymer chain grafting sequence. In addition to that chain length of each block was changed to obtain a series of BC-*g*-SiNP to understand the effect of the chain sequence and the chain length on the properties of the nanofiller and their influence in altering the PEM properties. The block copolymer structure, the chain sequence and the chain length were confirmed by means of NMR and GPC analysis of the cleaved copolymer chains. The BC-*g*-SiNP exhibits core-shell morphology where the thickness of the shell alters as the chain length and the sequence of the grafted chain start to vary. OPBI/BC-*g*-SiNP a hybrid nanocomposite membrane, having different wt% of nanofillers were loaded with phosphoric acid (PA) to produce PEM. The nanocomposite PEM showed very high thermal, mechanical and chemical stabilities along with the proton conductivity as high as 0.278 S cm^{-1} at 180°C in case of **OPBI/P6(3%)**. A very clear-cut dependence of the PEM properties was observed on the architecture of the **BC-*g*-SiNP** such as chain length, chain sequence and so on.

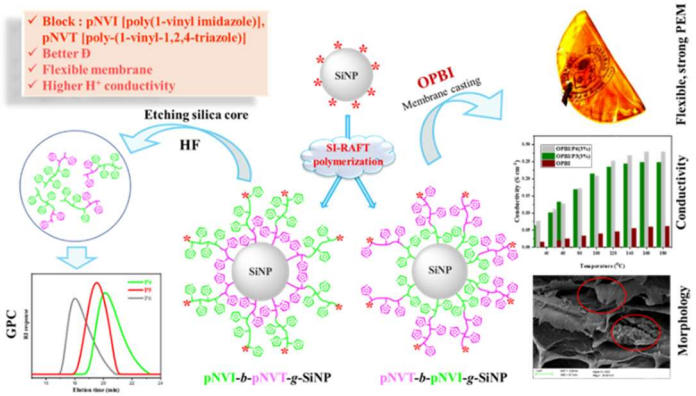

Chapter 4: Grafting of Polymer Brushes on MOF Surface to Achieve Proton-Conducting Membranes

In recent years, metal organic framework (MOF) and its post synthetic modification (PSM) procedures have gained an immense interest in order to synthesize a better hybrid material for their applications in their respective fields. Polymer-MOF conjugates were proved to incorporate better stability of the MOF materials even in harsh conditions. Nevertheless, the absence of proper synthetic strategy and extensive study limits the full potential of designing a MOF based better hybrid material. Proper surface functionalization technique (inexpensive, scalable with synthetically tuneable) with functional polymer chains (physically and chemically stable) however, can provide the picture-perfect opportunity to create a polymer chain *grafted* MOF material with polymer chains comprising the shell attached covalently on the MOF core in order to enhance the properties and the applicability of a MOF material in a larger extent which also opens up an enormous scope towards designing of a metal organic framework based organic inorganic super hybrid material. In order to provide a better incite into the surface chemistry and the limitations faced during the surface functionalization approach, we have developed a simple and effective method to functionalize the MOF surface precisely with functional polymer brushes which were grown covalently step by step using

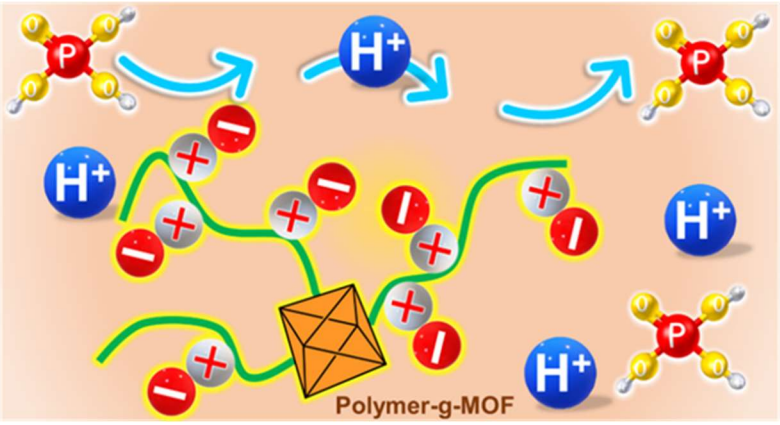

grafting from SI-RAFT technique. At first, the MOF surface was transformed into a polymerizable surface by the attachment of a trithiocarbonate based chain transfer agent (CTA). Then, three different sets of polymer brushes were grown which comprised of neutral but basic nitrogen functionality (PGM-N), tri methyl substituted quaternary ammonium functionality (PGM-C) and quaternary ammonium along with sulphonate functionality (PGM-Z) on the nano MOF surface using SI-RAFT technique. *Grafting* of polymer brushes were confirmed by GPC, FT-IR, NMR, TGA, FESEM, TEM, EDX and Mapping studies. The stability of the novel super hybrid material under various harsh environments were further analyzed using PXRD, TEM, FESEM, EDX and Mapping studies. The uniqueness of this work was additionally enhanced by using the synthesized PGMs as nanofiller into the oxypolybenzimidazole (OPBI) membrane matrix to get homogeneous

mixed matrix membranes with a brilliant thermomechanical and tensile properties, well thermal stability, superior proton conductivity when doped with H_3PO_4 (PA) and PA holding capabilities. Neutral, cationic and zwitterionic functional group containing polymer brush *grafted* on the MOF surface forms strong H-bonding, acid-base interaction with OPBI chains and H_3PO_4 molecules which is responsible for such high acid uptake, progressive PA retention and also displayed proton conductivity as high as 0.241 S cm^{-1} at 160°C (~ 4 fold increase when compared to OPBI) which is among the supreme values reported till date for MOF based PEM systems with excellent mechanical vigour.

Chapter 5: Grafting of Poly(vinyl phosphonic acid) to MOF surface by RAFT Polymerization: A Novel Method for the Development of Proton Conducting Materials

In recent times, metal organic frameworks (MOFs) along with the evolution of different post-synthetic modification (PSM) procedures are being used frequently to design better hybrid materials for numerous applications. However, the combination of polymers with MOF systems (polymer-MOF conjugates) has proven to be an interesting area for improving the stability factors of MOF systems even under harsh environments. Nevertheless, the need for a proper synthetic approach and extensive study limits the designing flexibility of 'MOF-polymer'-based efficient hybrid materials. An efficient surface functionalization technique, without the use of harsh chemicals, simple but scalable with synthetic tuneability and inexpensive, with uniformly of chemically stable grafted polymer chains can provide immense freedom to synthesize functional polymer-grafted MOF materials. In this work, at first, the MOF surface was chemically transformed into a polymerizable surface by trithiocarbonate based chain transfer agent (CTA) namely, RAFT agent. This modified MOF surface was utilized to grow poly vinyl phosphonic acid (PVPA) chains using aqueous surface initiated RAFT polymerization technique with varying chain length and grafting density. Grafting of PVPA polymer chains were confirmed by TGA, GPC, FT-IR, NMR, FESEM, TEM, EDX and mapping studies. The stability of the novel hybrid material under various harsh environments were further analyzed. The applicability of this work was further explored by analysing the newly synthesized PGMs for proton

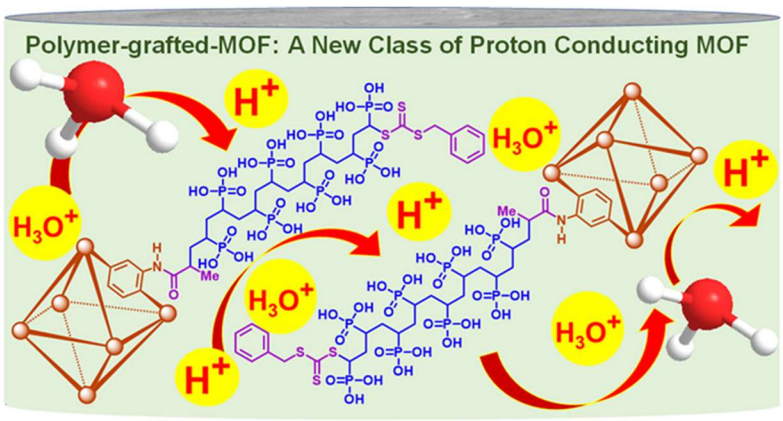

conductivity under varying temperature and relative humidity conditions. Pendent phosphonic acid group containing stable polymer chain grafted on the MOF surface creates strong H-bonding, acid-base, ionic and non-covalent interaction patterns with the neighbouring PGMs and the water molecules which are responsible for such high stability, water sorption ability and also exhibits inherent proton conductivity of 1.26×10^{-2} S cm^{-1} at 80 °C for PGM-L3 sample under 98% relative humidity, and 9.8×10^{-3} S cm^{-1} at 60 °C for PGM-H1 sample under 75% relative humidity, which is amongst the highest values reported so far for MOF based systems.

Chapter 6: Poly(N-vinyl triazole-b-N-vinyl imidazole) *Grafted* on MWCNTs as Nanofillers to Improve Proton Conducting Membranes

Carbon nanotubes (CNTs) are of particular interest because of their ability to enhance the mechanical strength in the material, however, processing difficulties of CNTs often restrict utilization up to its full potential. To resolve this, in the current study, we have developed a simple and efficient method to functionalize the surface of multiwalled carbon nanotube (MWCNT) with precise functional polymer chains, which were covalently *grafted* on the surface of the MWCNT and delved into an application to demonstrate this material as an efficient nanofiller in developing proton conducting membrane (PEM) from polybenzimidazole (PBI). At first, MWCNT surface was converted to a polymerizable surface by attaching a trithiocarbonate based chain transfer agent (CTA). Then, N-heterocyclic block copolymer namely poly-N-vinyl-1,2,4-triazole-*b*-poly-N-vinyl imidazole (pNVT-*b*-pNVI) was grown from the CTA anchored surface in one-pot surface initiated reversible addition fragmentation chain transfer (SI-RAFT) technique. *Grafting* of block copolymer chain was confirmed by GPC, NMR and TGA studies. To the best of our knowledge, this will be the first report of growing block copolymer structure *grafted* covalently on the surface of the MWCNT. The novelty of the work was further enhanced by incorporating pNVT-*b*-pNVI-*g*-MWCNT as nanofiller into the oxypolybenzimidazole (OPBI) membrane to obtain homogeneous

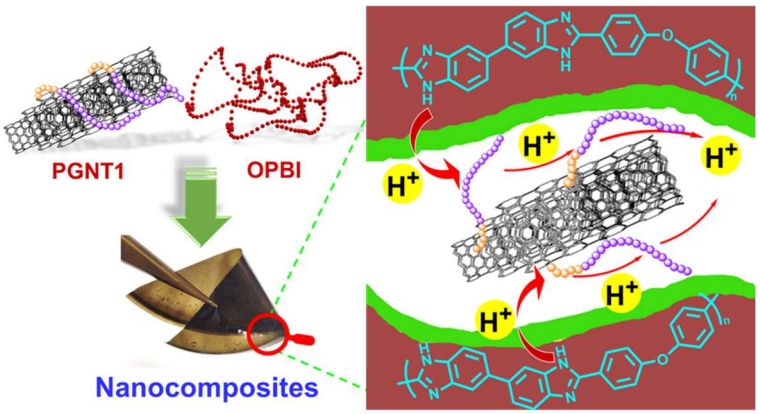

nanocomposite membranes with an excellent thermomechanical and tensile properties, thermal stability, superior proton conduction when doped with phosphoric acid (PA) and the acid (PA) holding capacity. The nanocomposite membrane with

2.5 wt% nanofiller loading displayed a tensile stress of 1.8MPa, strain of 176% at break and exhibited proton conductivity as high as 0.164 S cm^{-1} at 180°C which is a 2.6-fold increment when compared with pristine OPBI membrane. This significant increase in conductivity is attributed to the new proton conducting nano channel pathway generated along the polymer-*g*-MWCNT surface.

Chapter 7: Poly (N-Vinyl Imidazole) *Grafted* MWCNT Supported Pd Nanoparticle: An Efficient Catalyst for Suzuki-Mayura Coupling Reaction

Pd catalysts are well known for their role in Suzuki-Miyaura cross coupling reactions between an aryl halide and an aryl boronic acid to generate coupled aryl and poly cyclic systems by means of formation of a new C-C bond. C-C bond formation between two aryl compounds is particularly interesting as this is not only the key step in the synthetic procedures of a number of organic chemicals and natural products but also useful in a number of industrial applications. On the other hand, Pd is costly. Heterogeneous Pd catalysts are preferred over homogeneous catalysts due to their facile reusability and compatibility with flow systems. Another preferred route for cross-coupling reactions involves reusable palladium nanoparticles that promote these reactions in organic solvents or in water. Multi walled carbon nanotubes on the other hand are well known for their stability, durability and hollow interior design. Furthermore, covalently grafting of the MWCNT surface with strategically designed functional polymer chains can however provide a stable and reducing environment to coordinate Pd^{2+} ions on the surface of the nanotubes. The dangling imidazole rings of poly (N-vinyl imidazole) (pNVI) chains help in the formation of Pd nanoparticle on the polymer grafted MWCNT walls in the absence of any external reducing agent. Microscopic studies along with the EDX data provided concrete evidence towards the formation of Pd nanoparticles. The synthesized polymer grafted MWCNT supported Pd nanoparticles (Pd@PGNT1) were taken into account to thoroughly investigate the catalytic properties in Suzuki-Miyaura coupling reaction. The reaction conditions were investigated and optimizes. The solvent scope, utilization of mild basic conditions were checked thoroughly and the substrate scope was also examined by incorporating different functional group containing aryl bromide and aryl boronic acid in the reaction medium as substrate. The efficiency of the catalyst was also

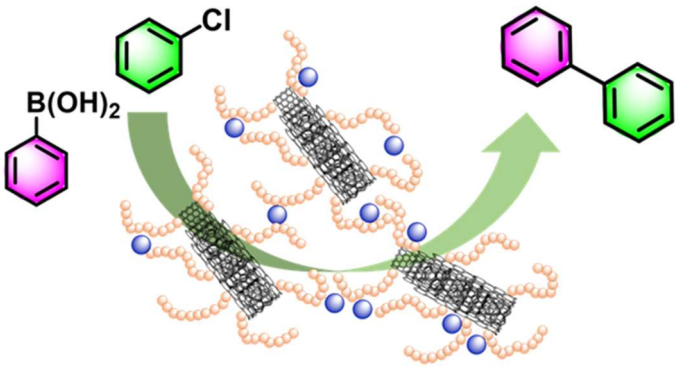

validated for 1 gm scale reaction in EtOH solvent with K_2CO_3 as base at 80 °C in the presence of as low as 1 mg of the Pd@PGNT1 catalyst which contains only 12.65 mass % of Pd was able to produce 99% yields.

Chapter 8

This particular chapter illustrates the summery and conclusions corresponds to all the previous chapters of this thesis.

Conclusion

The following concluding remarks can be drawn from the studies of "**Polymer *grafted* Nanomaterials: Synthesis via RAFT Polymerization and the Applications**"

1. An effective method was established in order to grow monodispersed SiNP of ~50nm size.
2. Successful *grafting* of two series of BC-*g*-SiNP namely pNVI-*b*-pNVT-*g*-SiNP and pNVT-*b*-pNVI-*g*-SiNP were synthesized by altering the polymer chain *grafting* sequence with core-shell morphology.
3. *Grafted* polymer and block copolymer chains were detached from the SiNP surface using HF treatment in order to have better insight of the SI-RAFT technique used.
4. Successful preparation of composite membranes of OPBI polymer and the BC-*g*-SiNP nanofiller and further testing of the nano composite membrane shows excellent mechanical and thermal properties.
5. Proton conductivity of 0.278 S cm^{-1} at 180 °C in case of OPBI/P6(3%) nanocomposite membrane was achieved with very less leaching of PA which is among the supreme values reported till date.
6. Successful transformation of MOF surface into a polymerizable surface by the attachment of a trithiocarbonate based RAFT agent (BSIPA).
7. Successful *grafting* of three different sets of polymer brushes were grown comprised of neutral but basic nitrogen functionality (PGM-N), tri methyl substituted quaternary ammonium functionality (PGM-C) and quaternary ammonium along with sulphonate functionality (PGM-Z) on the nano MOF surface using SI-RAFT technique.
8. Homogeneous mixed matrix membranes were prepared with a brilliant thermomechanical and tensile properties, well thermal stability, superior proton conductivity when doped with H_3PO_4 (PA) and PA holding capabilities.

9. Highest proton conductivity achieved for OPBI@Z5% was 0.241 S cm^{-1} at 160°C (~ 4-fold increase when compared to pristine OPBI) which is among the supreme values reported till date.
10. We have successfully executed the *grafting* of PVPA polymer chains in an easy, efficient and less hazardous way under aqueous condition using SI-RAFT *grafting from* approach with narrow polydispersity and better control over molecular weights. We have also varied the *grafting* density of the *grafted* polymer chains on the MOF surface (PGM-L and PGM-H) with further variation in the chain length of the attached polymer chains.
11. We have achieved proton conductivity of 1.26×10^{-2} S cm^{-1} at 80 °C for PGM-L3 sample under 98% relative humidity and 9.8×10^{-3} S cm^{-1} at 60 °C for PGM-H1 sample under 75% relative humidity which are amongst the premium values reported till date for MOF based systems, operating below 100 °C.
12. We have successfully investigated and proved that, the source of the conductivity is because of the presence of the labile protons in the system and the polymer-MOF super hybrid materials (PGMs) are highly stable and can retain their proton conductivity upon long term usage.
13. Block copolymer chains consisting of pNVT and pNVI successfully *grafted* on the MWCNT surface with excellent control over molecular weights to obtain pNVT-*b*-pNVI-*g*-MWCNT.
14. The prepared block copolymer *grafted* MWCNT (BC-*g*-MWCNT) was further utilized as a nanofiller to fabricate an efficient PBI based PEMs.
15. So far, block copolymer grafted MWCNTs have never been explored in literature to be used as potential nanofiller materials for improving PEM properties, and to the best of our knowledge this will be the first report on such materials.
16. Pd nanoparticles were efficiently grown on the polymer *grafted* MWCNT surface and thoroughly tested for catalytic properties of the material under Suzuki-Miyaura coupling reaction conditions.

Scope of future work

The investigation and the findings of this thesis addressed some of the problems associated with the surface grafting approach on different nano surface and thus, opens up new possibilities in terms of growing polymer brushes or block copolymer chains on the nano material surface. This thesis also provides a concrete background in terms of the development of MMMs with not only excellent mechanical properties and proton conducting abilities but also for different applicative fields.

1. Chapter 3 demonstrates successful grafting of block copolymer chains of pNVI and pNVT moiety with core-shell morphology. Efforts should be made in order to partially and completely convert the grafted block copolymer chains with quaternization with varying alkyl chains and further investigate their antimicrobial activity.
2. Efforts should be made in order to leach out the silica from the polymer grafted SiNP in the membrane matrix. This methodology can create monodispersed pores inside the membrane matrix. Further more the pores will be pre decorated with the functional polymer or block copolymer chains for efficient PEM properties.
3. Different organic polymer particles can also be taken into account to grow functional polymer brush structure for different applications.
4. A number of different membrane matrix other that PBI can be employed to develop new class of MMMs.
5. Fuel cell testing of the MMMs can be performed in order to have further understanding of the nanofiller and membrane matrix interactions.
6. Efforts should be made to investigate the doping of the MMMs in different organic/ inorganic acid conditions in order to have better understanding and choice of the dopant acid for these particular MMM type.
7. Investigations can be performed in order to grow Pd nanoparticles inside the polymer grafted MOF material where the unique pore structure of the MOF material can be used to selectively transform organic molecules and potential stability can be achieved from the polymer decorated MOF structure. The material can also be investigated for flow chemistry.

Appendix I

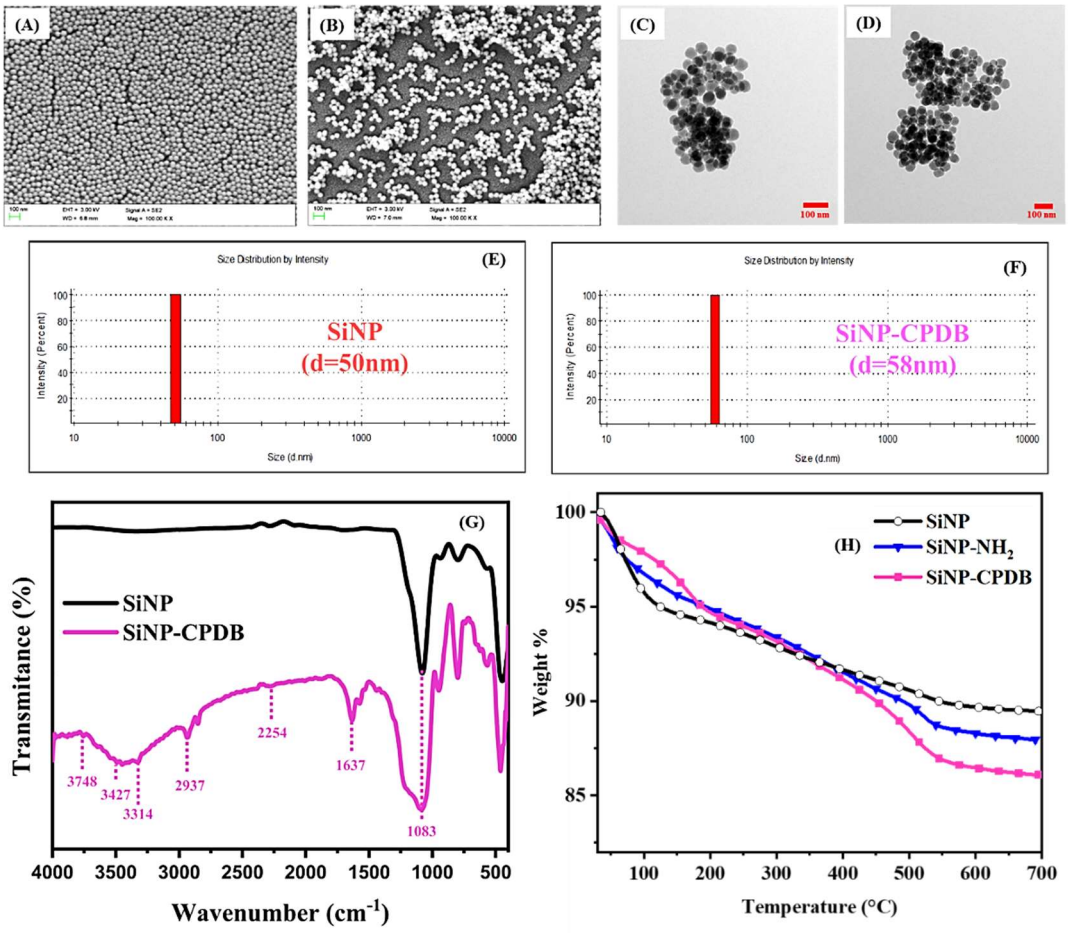

Appendix I-Figure 3.1. FESEM (**A** & **B**) and TEM (**C** & **D**) images of SiNP and SiNP-CPDB, respectively. (**E**) and (**F**) are the DLS plots for SiNP and SiNP-CPDB, respectively. (**G**) comparison of FT-IR spectra of SiNP & SiNP-CPDB. (**H**) TGA of SiNP, SiNP-NH_2 and SiNP-CPDB to calculate CPDB grafting density of SiNP surface.

Appendix I-Table 3.1. Summary of molecular weight ($\overline{M_n}$) and Đ of bare polymer chains after cleaving the polymer from pNVI-g-SiNP [P1(i)-P3(i)] and pNVT-g-SiNP [P4(i)-P6(i)]. All the data obtained from the controlled reactions of P1to P6 are mentioned as intermediates (i).

Sample identity	$\overline{M_n}$	Đ
P1(i)	7199	1.03
P2(i)	13129	1.06
P3(i)	25444	1.24
P4(i)	6907	1.01
P5(i)	13903	1.07
P6(i)	27155	1.31

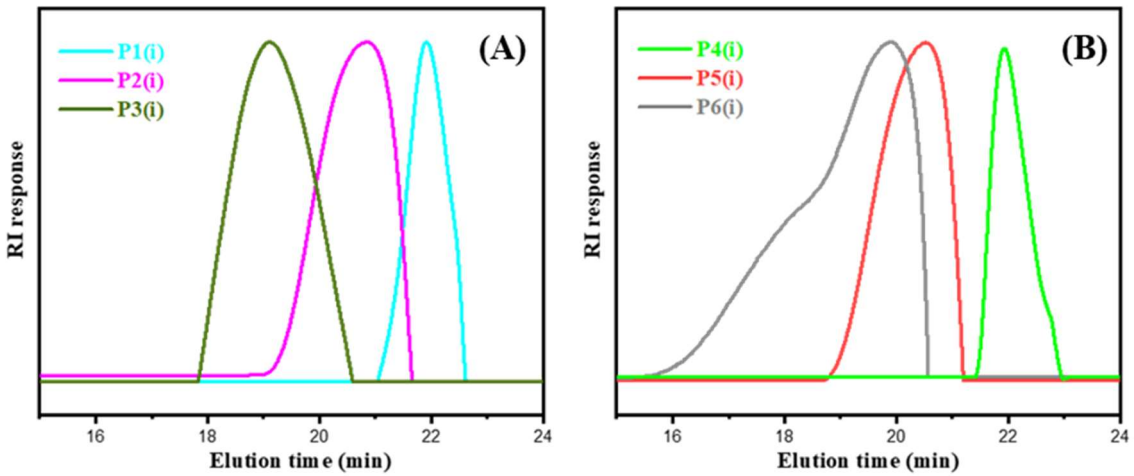

Appendix I-Figure 3.2. GPC traces of bare polymer chains eluted in DMF/LiBr solvent. Bare polymer chains of **pNVI** (**A**) and **pNVT** (**B**) chains were obtained after cleaving the chains from polymer grafted SiNPs by using aqueous HF treatment.

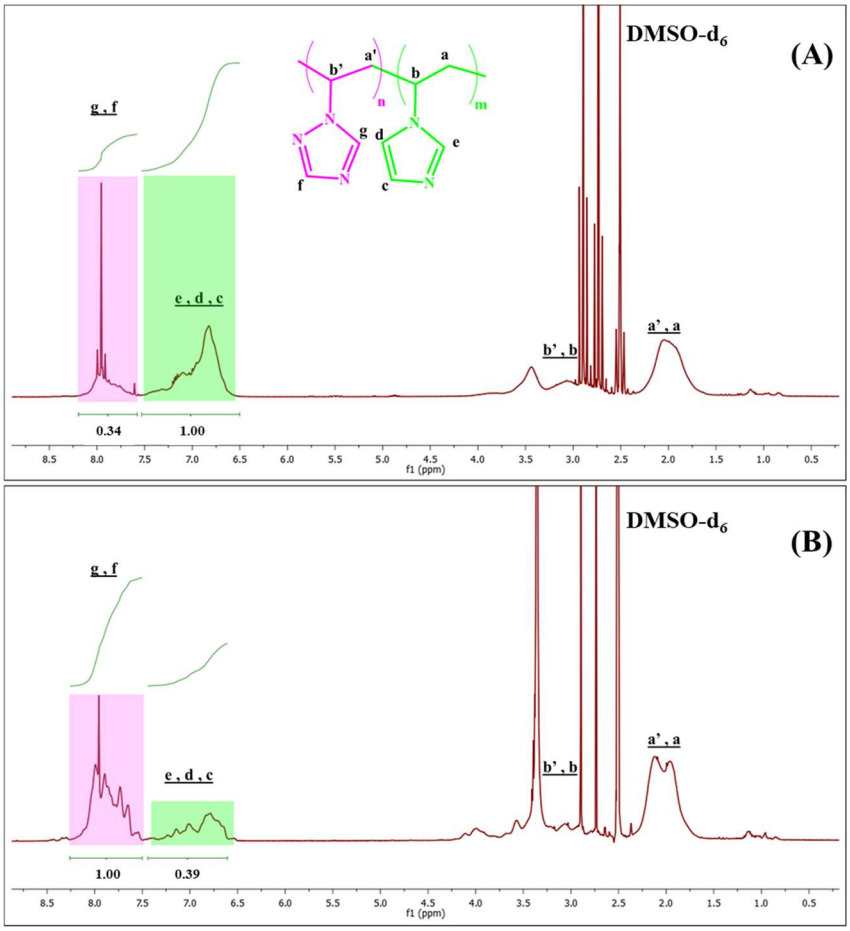

Appendix I-Figure 3.3. ^{1}H-NMR spectra of **(A)** pNVT-*b*-pNVI-*g*-SiNP (**P3**) and **(B)** pNVI-*b*-pNVT-*g*-SiNP (**P6**) samples after removal of SiNP core using HF treatment to obtain bare polymers.

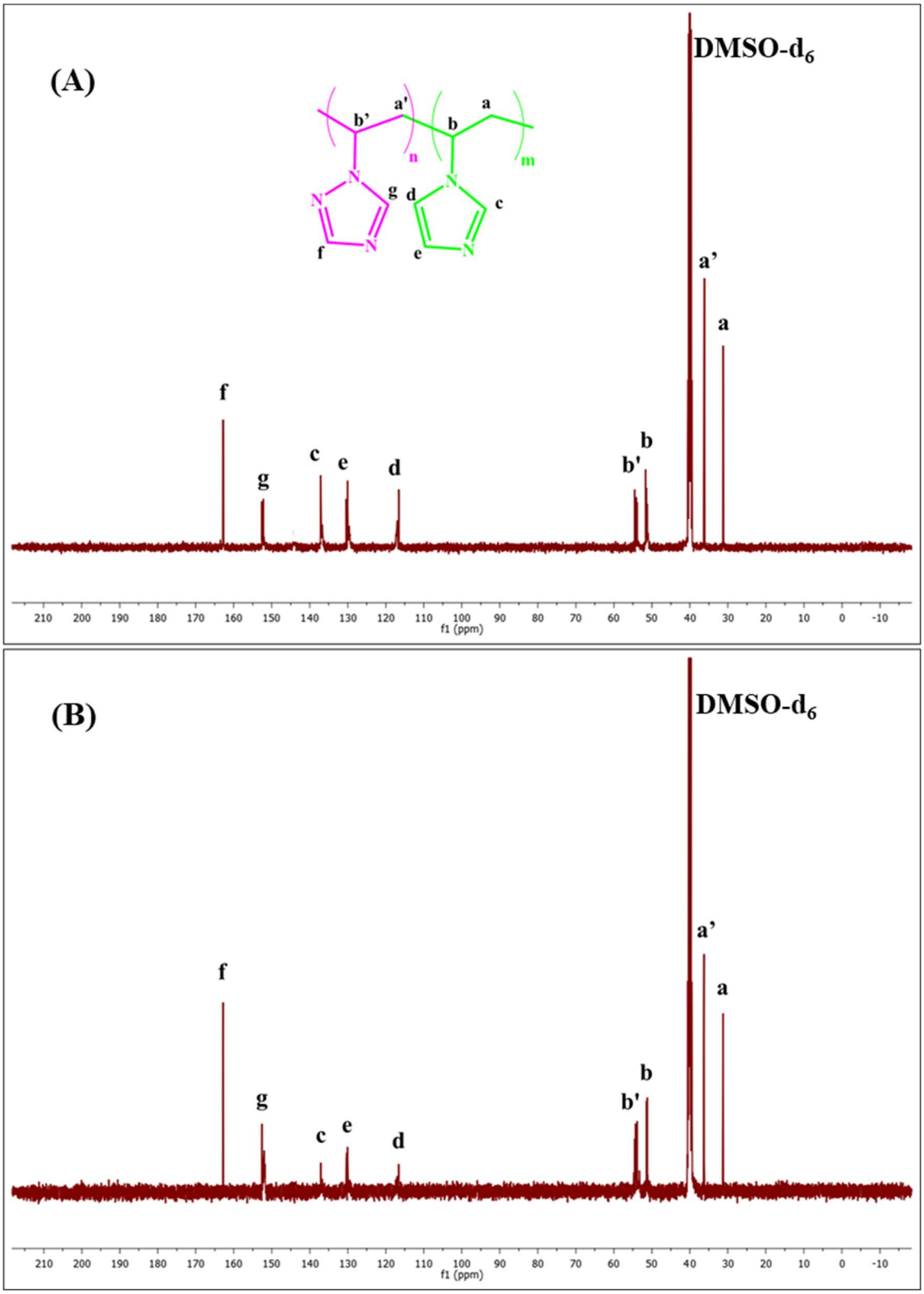

Appendix I-Figure 3.4. ^{13}C NMR spectra of **(A)** pNVT-*b*-pNVI-*g*-SiNP (**P3**) and **(B)** ^{13}C NMR spectra of pNVI-*b*-pNVT-*g*-SiNP (**P6**) after HF treatment.

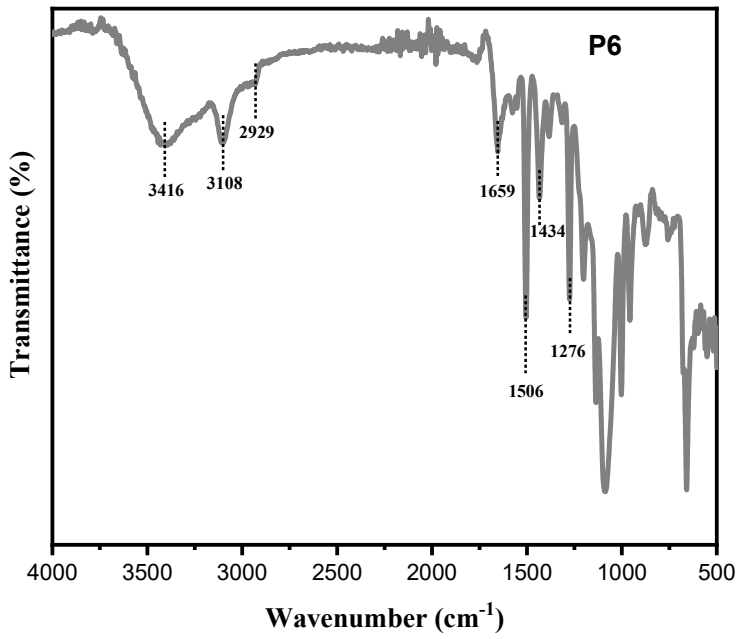

Appendix I-Figure 3.5. FT-IR spectrum of **P6** (pNVI-*b*-pNVT-*g*-SiNP).

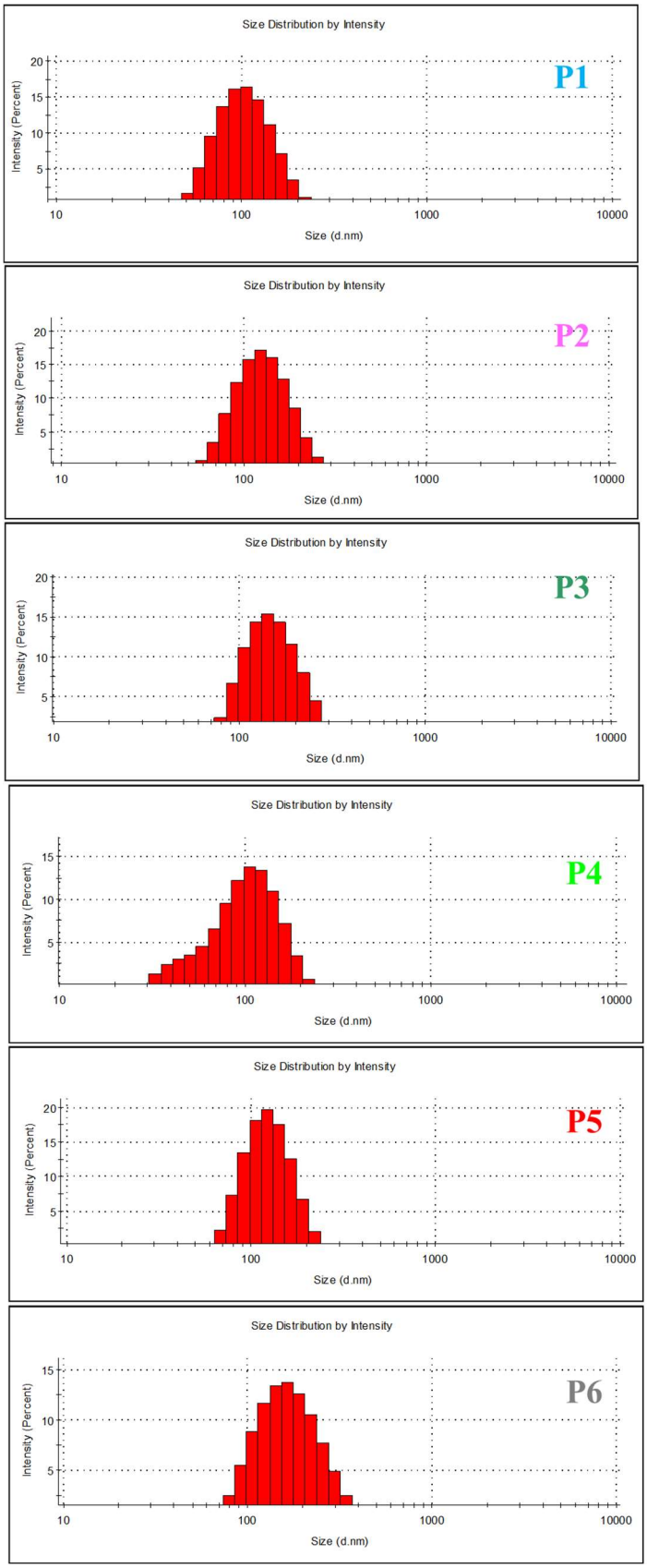

Appendix I-Figure 3.6. DLS plots of block copolymer *grafted* SiNP samples dispersed in aqueous medium.

Appendix I-Table 3.2. Distance (D) between the *grafted* chains, Radius of gyration (R_g) and the ratio of D to R_g (D/R_g) values of all the BC-*g*-SiNP samples.

Sample	D(nm)[a]	R_g (nm)[b]	D/R_g
P1	7.07	6	1.2
P2	2.29	7.25	0.32
P3	2.24	9.6	0.23
P4	4.08	6	0.68
P5	2.18	7.4	0.29
P6	2.18	9.8	0.22

[a] Calculated from $D=\sigma^{-1/2}$,[1,2] where σ is the grafting density and [b] calculated from $R_g= 0.5\ N^{0.5}$.[1, 2] Where N is the degree of polymerization of the block copolymer.

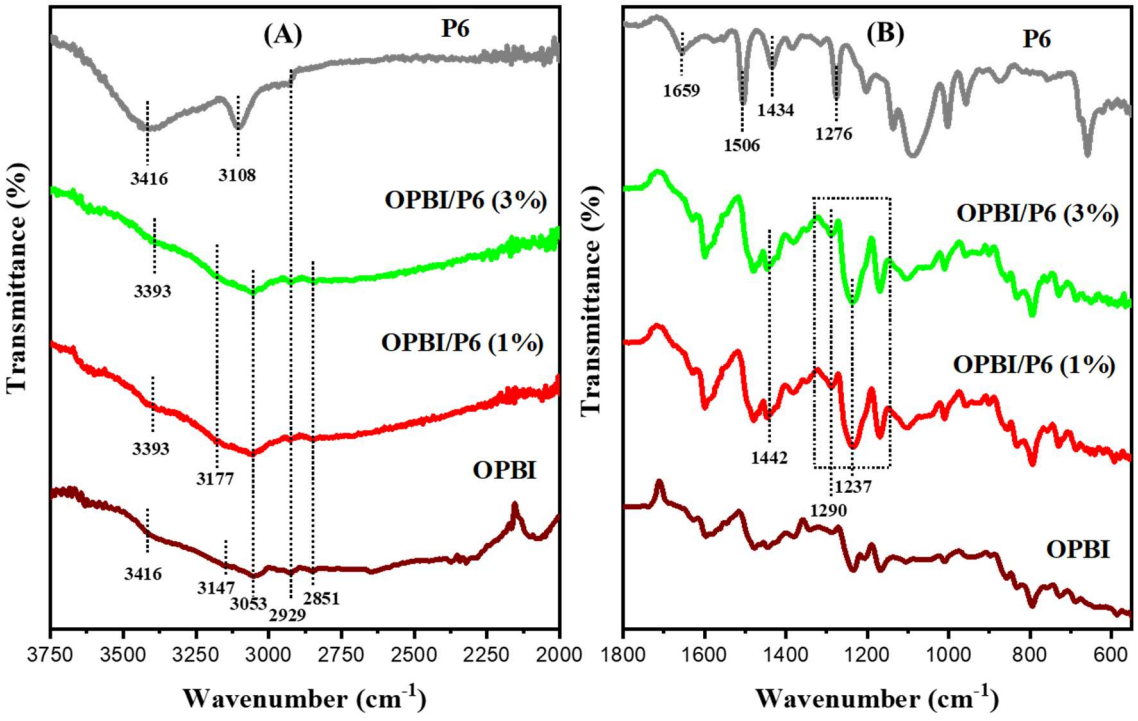

Appendix I-Figure 3.7. FT-IR spectra of **P6**, **OPBI/P6** (3%), **OPBI/P6** (1%), **OPBI** are shown in (**A**) 3750-2000cm^{-1} and (**B**) 1800-550cm^{-1} range.

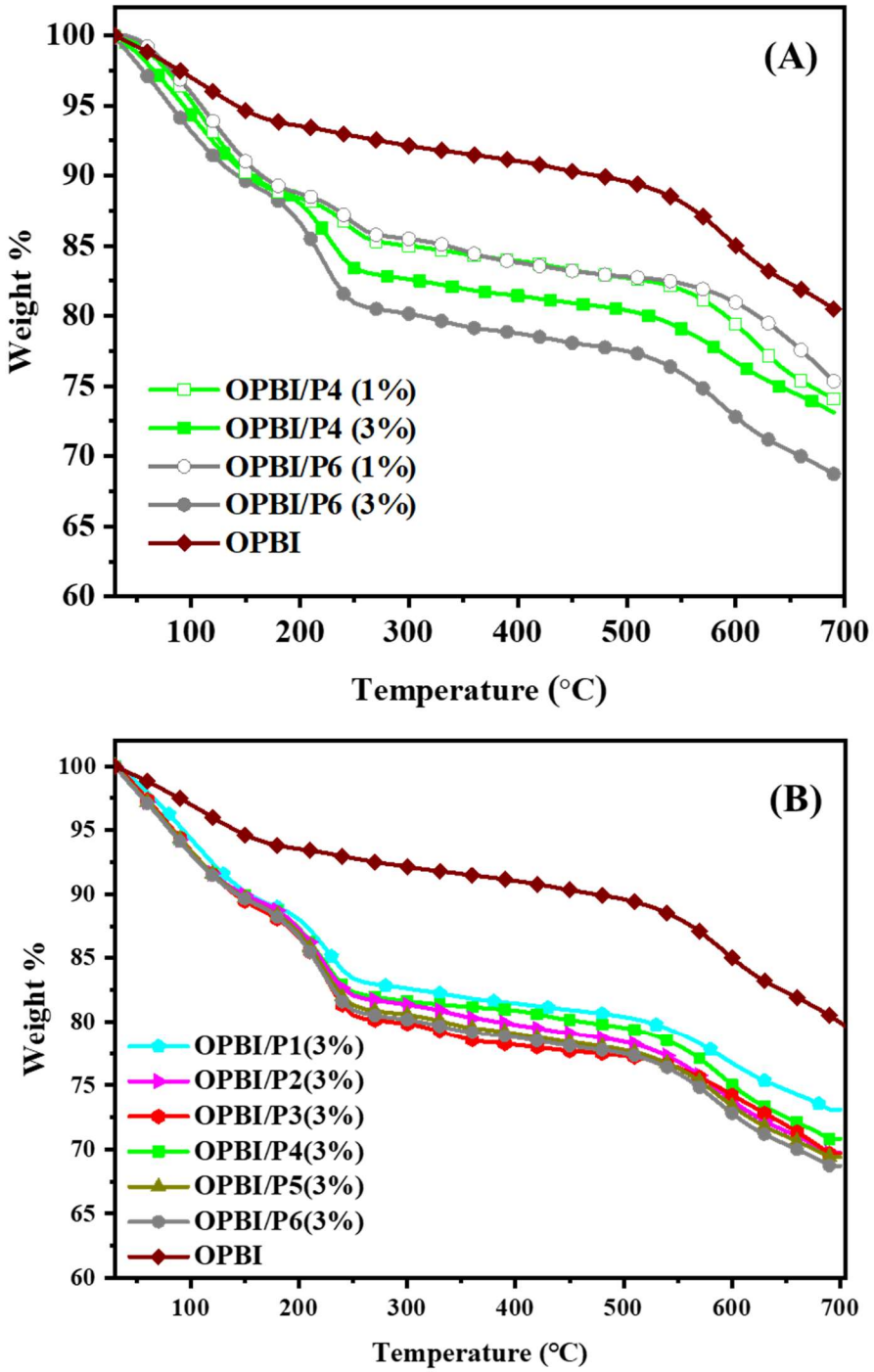

Appendix I-Figure 3.8. TGA plots of OPBI/BC-*g*-SiNP nanocomposites along with OPBI: Effect of nanofiller loading (**A**) and nanofiller type (**B**).

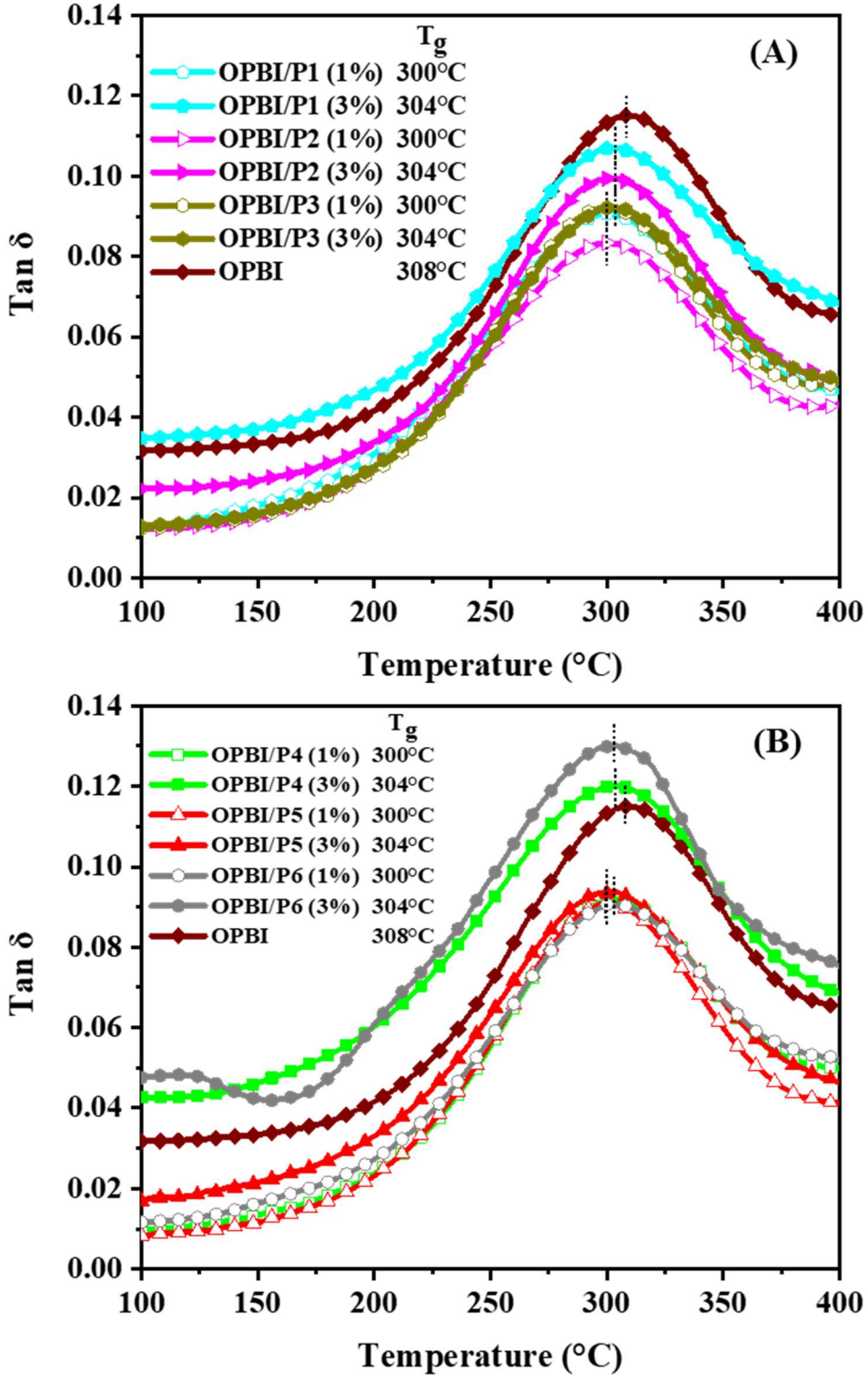

Appendix I-Figure 3.9. Tan delta vs. temperature plot for all the nanocomposite membranes: (**A**) **OPBI/P1-P3** and (**B**) **OPBI/P4-P6**.

Appendix I-Table 3.3. PA loading and conductivity values at 180°C for all the nanocomposite PEM.

Sample identity	PA loading[#] (no. of PA moles/OPBI repeat unit)	Conductivity at 180°C ($S\ cm^{-1}$)
OPBI	13.18 (±1.48)	0.061
OPBI/P1 (1%)	12.98 (±1.51)	0.129
OPBI/P1 (3%)	12.92 (±1.40)	0.148
OPBI/P2 (1%)	12.72 (±1.29)	0.153
OPBI/P2 (3%)	12.49 (±1.22)	0.184
OPBI/P3(1%)	12.82 (±0.87)	0.209
OPBI/P3 (3%)	12.36 (±0.46)	0.247
OPBI/P4 (1%)	13.02 (±1.40)	0.154
OPBI/P4 (3%)	12.96 (±1.34)	0.173
OPBI/P5 (1%)	12.89 (±0.92)	0.199
OPBI/P5 (3%)	12.55 (±0.73)	0.234
OPBI/P6 (1%)	12.81 (±0.67)	0.253
OPBI/P6 (3%)	12.35 (±0.38)	0.278

Standard deviation in the measurements are given in the parenthesis.

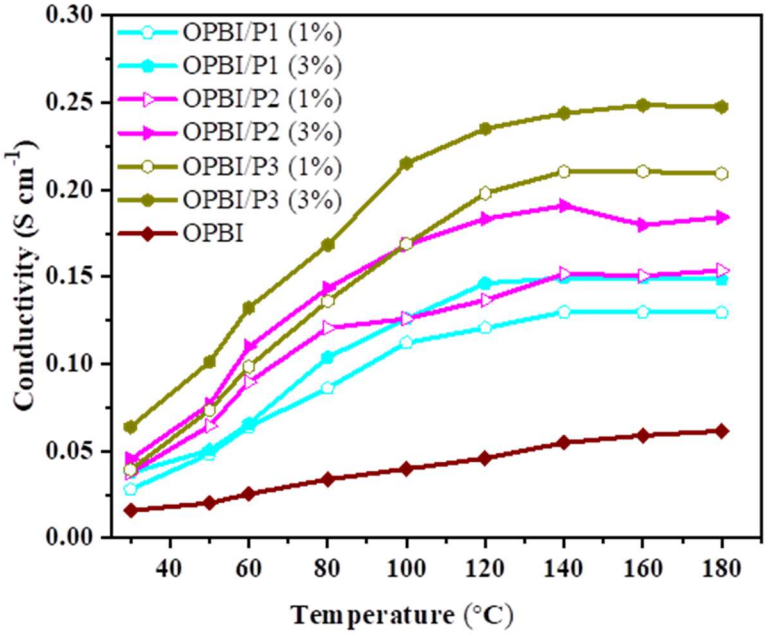

Appendix I-Figure 3.10. Proton conductivity vs. temperature plot for **OPBI** and all the nanocomposite membranes with 1 and 3 wt % loading of nanofiller **P1-P3**.

Appendix I-Table 3.4. Summary of various tensile properties for all the nanocomposite membranes.

Sample identity	Tensile strength (MPa)	Elongation at break (%)	Sample identity	Tensile strength (MPa)	Elongation at break (%)
OPBI/P1(1%)	0.5	120	OPBI/P4(1%)	0.67	124
OPBI/P1(3%)	1.1	131	OPBI/P4(3%)	0.89	134
OPBI/P2(1%)	0.75	167	OPBI/P5(1%)	0.74	174
OPBI/P2(3%)	1.2	171	OPBI/P5(3%)	0.83	181
OPBI/P3(1%)	1.4	207	OPBI/P6(1%)	0.93	211
OPBI/P3(3%)	1.1	250	OPBI/P6(3%)	1.1	249

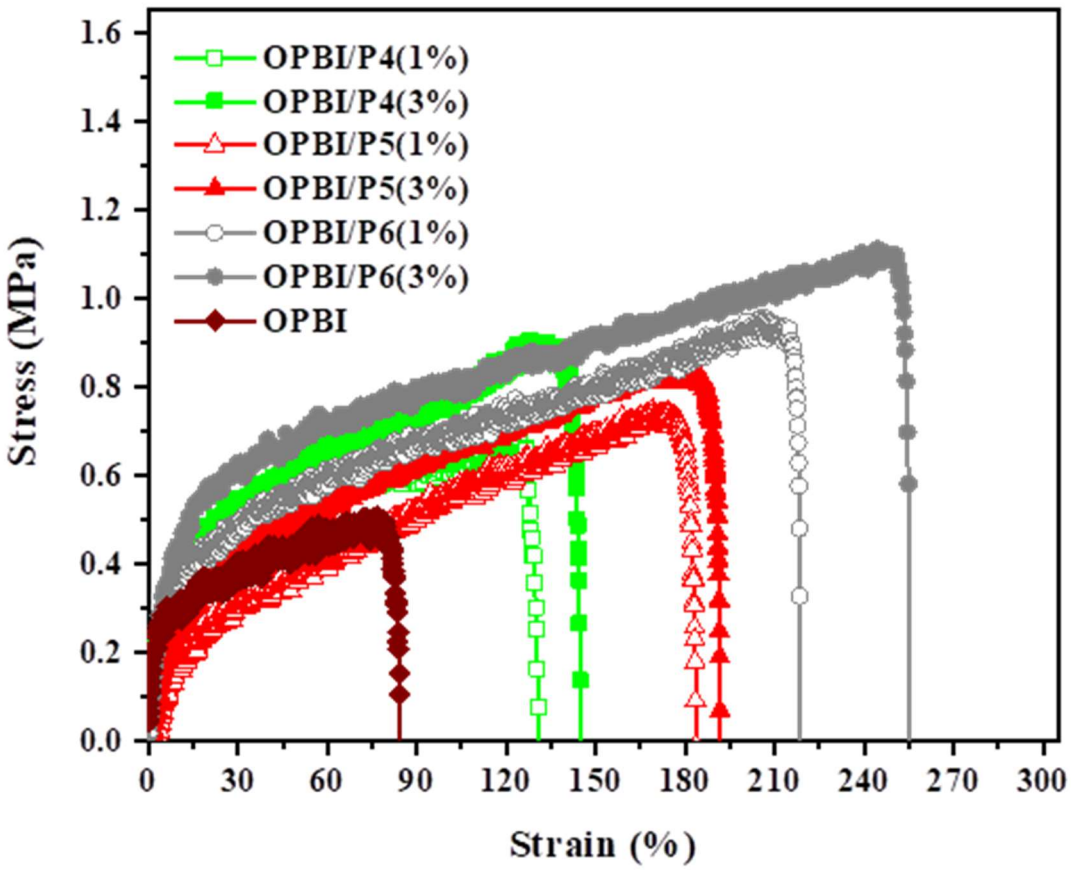

Appendix I-Figure 3.11. Stress-strain profiles of PA loaded **OPBI** and PA loaded nanocomposite membranes of **P4-P6** with various loading.

References

(1) Uchida, E.; Ikada, Y. Topography of Polymer Chains Grafted on a Polymer Surface Underwater. *Macromolecules* **1997**, *30*, 5464–5469.

(2) Zhang, M.; Liu, L.; Zhao, H.; Yang, Y.; Fu, G.; He, B. Double-Responsive Polymer Brushes on the Surface of Colloid Particles. *J. Colloid Interface Sci.* **2006**, *301*, 85–91.

Appendix II

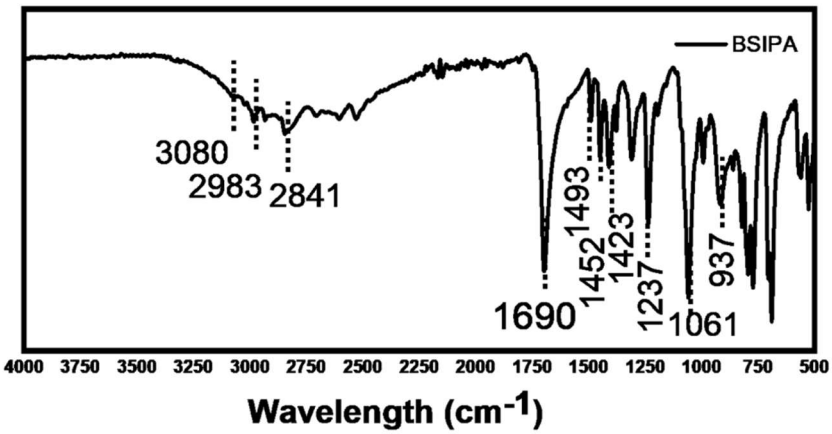

Appendix II-Figure 4.1 FT-IR spectrum of BSIPA.

Molecular weight (M. W.) determination of polymer chains detached from the MOF surface

Molecular weights (M.W.) and polydispersity index (Đ) of detached polymers, which were obtained after detaching the polymer brushes from the MOF core was achieved by using aqueous HF acid solution which helps to break down the framework structure. Detailed synthetic procedure is described in **Chapter 2**.

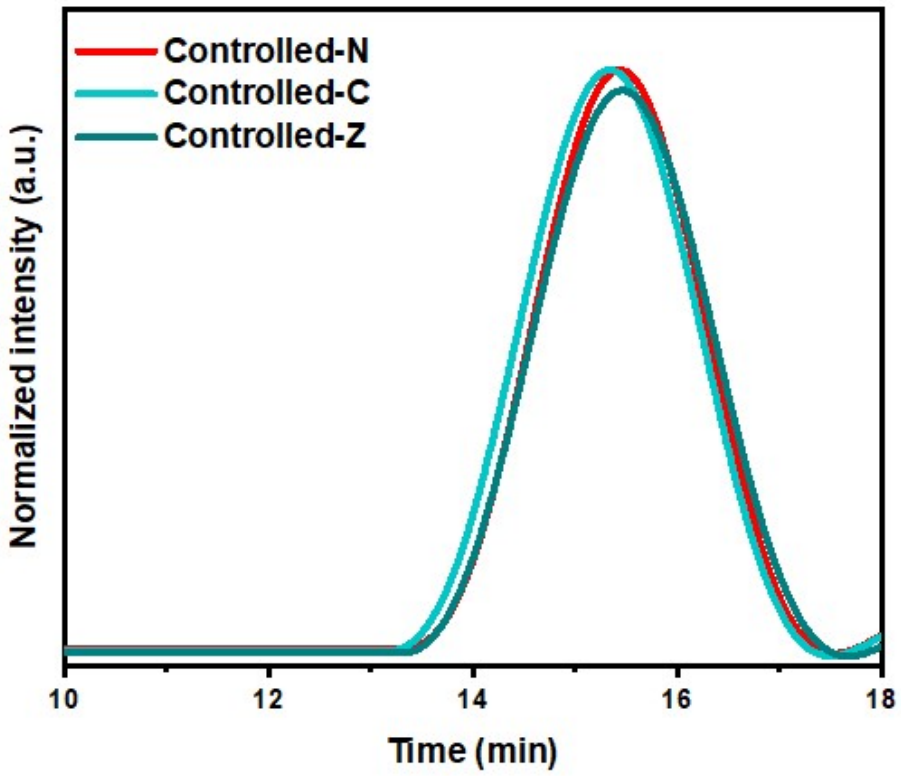

Appendix II-Figure 4.2. GPC plots of the polymer chains obtained from the controlled experiments in absence of MOF-BSIPA.

Appendix II-Table 4.1. Details of the molecular weight distribution of neutral, cationic and zwitterionic controlled samples.

Samples	$\bar{M}_w$	$\bar{M}_n$	Đ
Controlled-N	9690	8320	1.16
Controlled-C	9811	8636	1.14
Controlled-Z	9657	8557	1.14

TGA studies

Thermal study of UiO-66 NH_2, MOF-BSIPA, RAFT agent (BSIPA), along with the PGM samples, OPBI and all OPBI@PGM dried membranes and its PA doped membranes were carried out between the temperature range from 35 °C to 700 °C with a heating rate of 10°C / min under nitrogen gas flow of 0.4-0.6 mL/min.

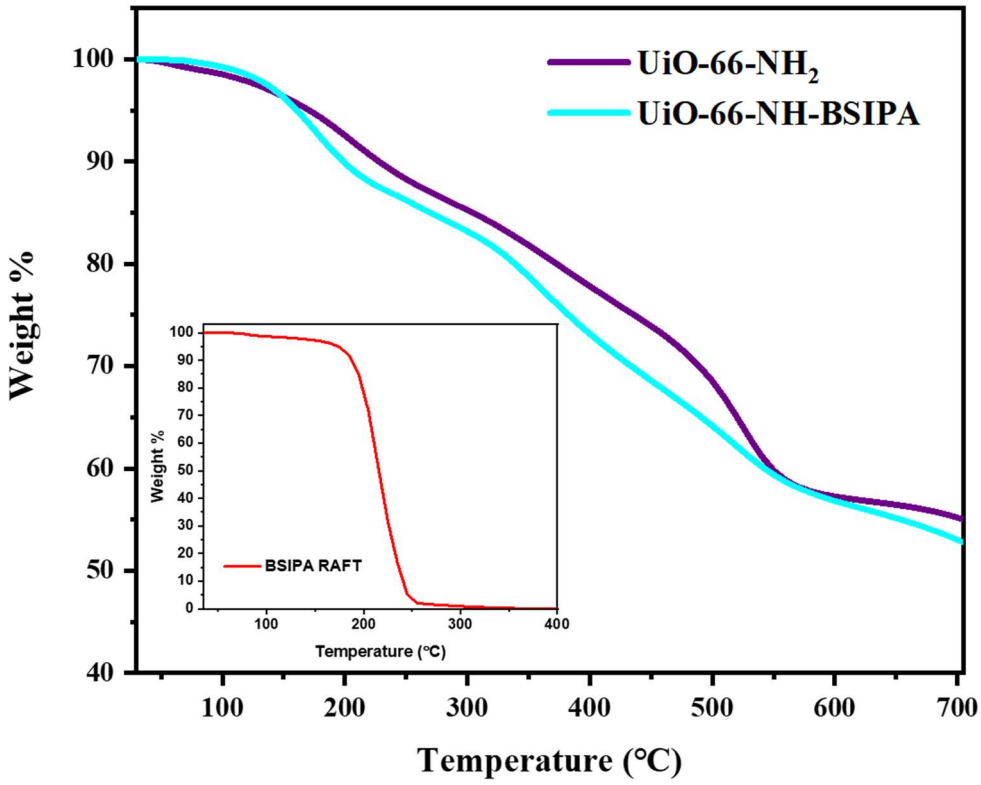

Appendix II-Figure 4.3. TGA of UiO-66 NH_2, MOF-BSIPA and BSIPA RAFT agent (in the inset).

Powder X-ray study (PXRD)

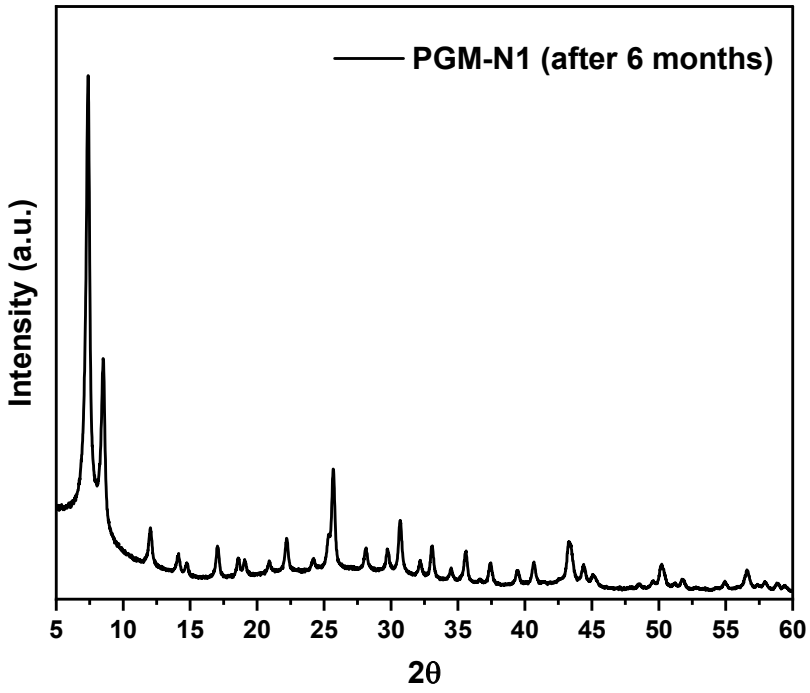

Appendix II-Figure 4.4. PXRD pattern of PGM-N1 sample after keeping the sample at room temperature for 6 months.

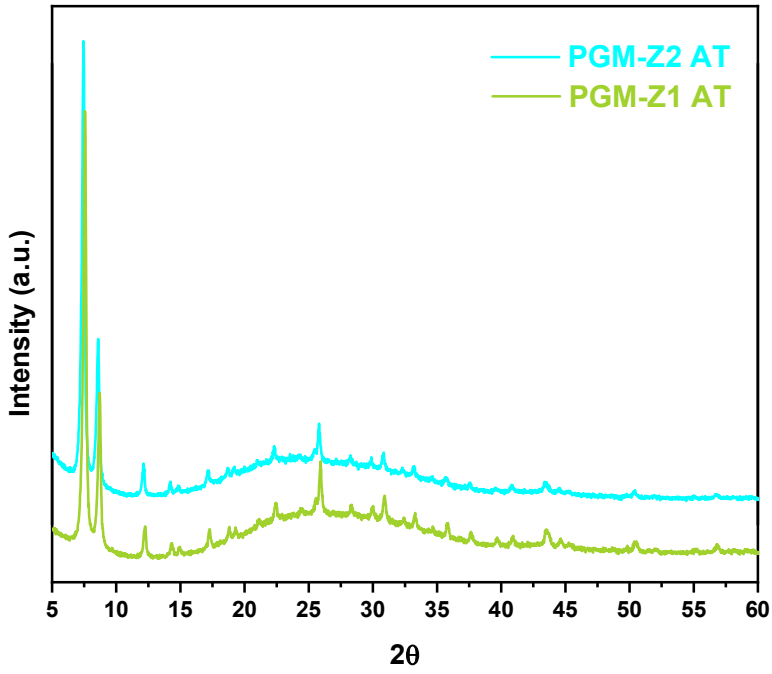

Appendix II-Figure 4.5. PXRD pattern of PGM-Z1 and PGM-Z2 sample after the sample at 80 °C under 100% humidity condition for 10 days (here AT represents after treatment).

NMR analysis of detached polymer brush from PGM

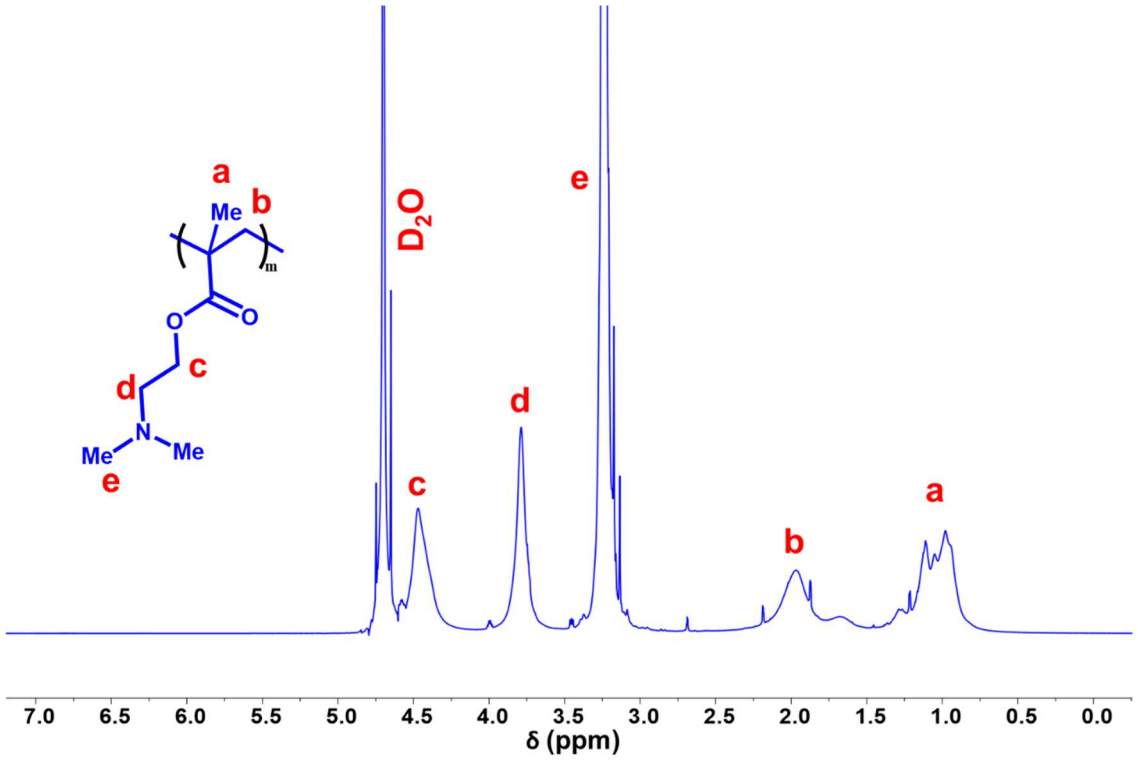

Appendix II-Figure 4.6. ^{1}H NMR **(A)** spectra of the detached polymer from PGM-N.

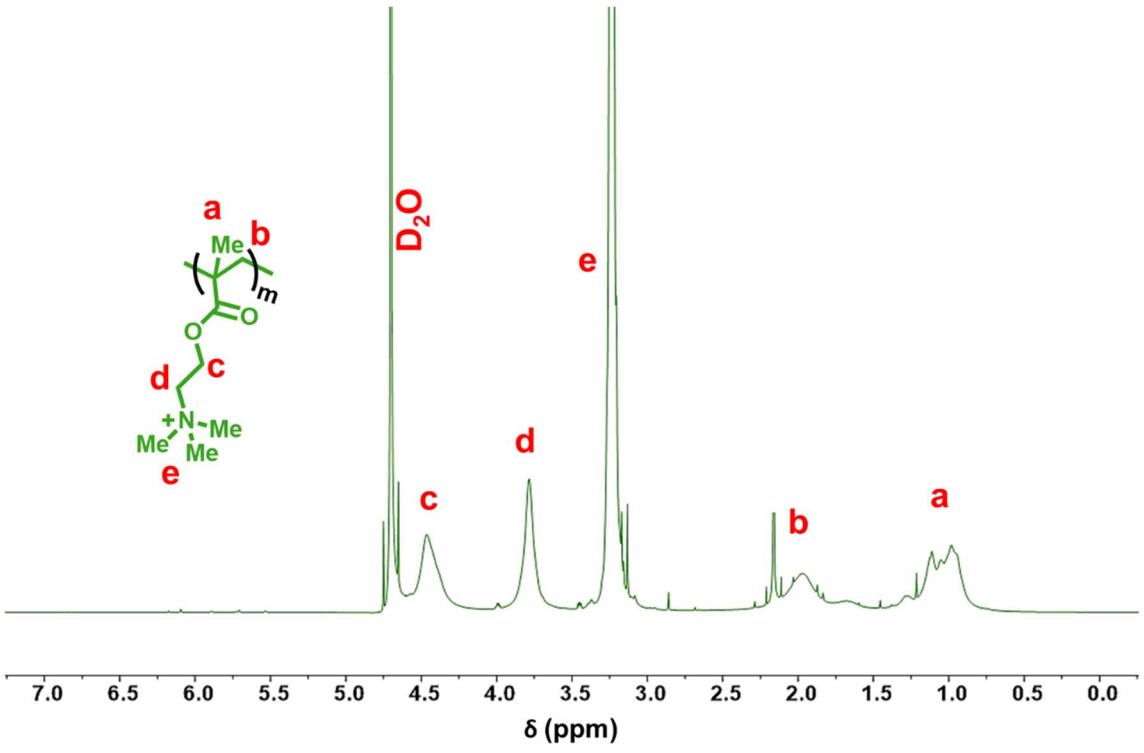

Appendix II-Figure 4.7. ^{1}H NMR **(A)** spectra of the detached polymer from PGM-C.

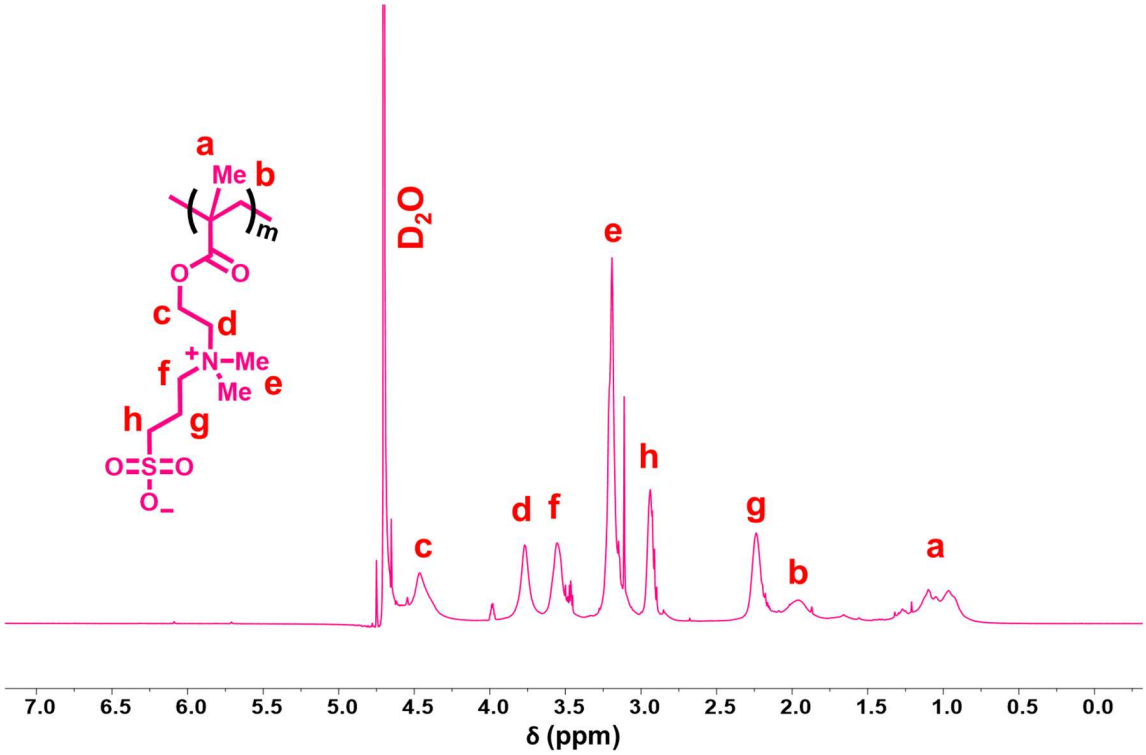

Appendix II-Figure 4.8. ^{1}H NMR **(A)** spectra of the detached polymer from PGM-Z.

Morphology study

Field Emission Scanning Electron Microscopy (FESEM)

The morphology of UiO-66 NH_2, MOF-BSIPA, PGM-N, PGM-C, PGM-Z and all the OPBI@PGM composite membranes were evaluated by using a field emission scanning electron microscope (FESEM) (Model: Zeiss Merlin Compact). The powder samples were dispersed in dry ethanol by using sonication and drop casted on a clean piece of glass slide. The slides were dried at 70 °C overnight to remove solvent traces from the sample cavity and gold coated before analysis. The FESEM cross section morphology of the membrane samples were done by breaking the membranes in liquid nitrogen medium. Samples were gold coated before imaging in FESEM.

Transmission electron microscopy (TEM)

The MOF and PGM powder samples were prepared by placing a drop of the sample dispersed in ethanol on the carbon coated side of the copper grid (200 mesh) and dried in an oven overnight. The composite samples were prepared by placing a drop of formic acid dispersed OPBI@PGM solution on carbon coated side of the copper grids (200 mesh).

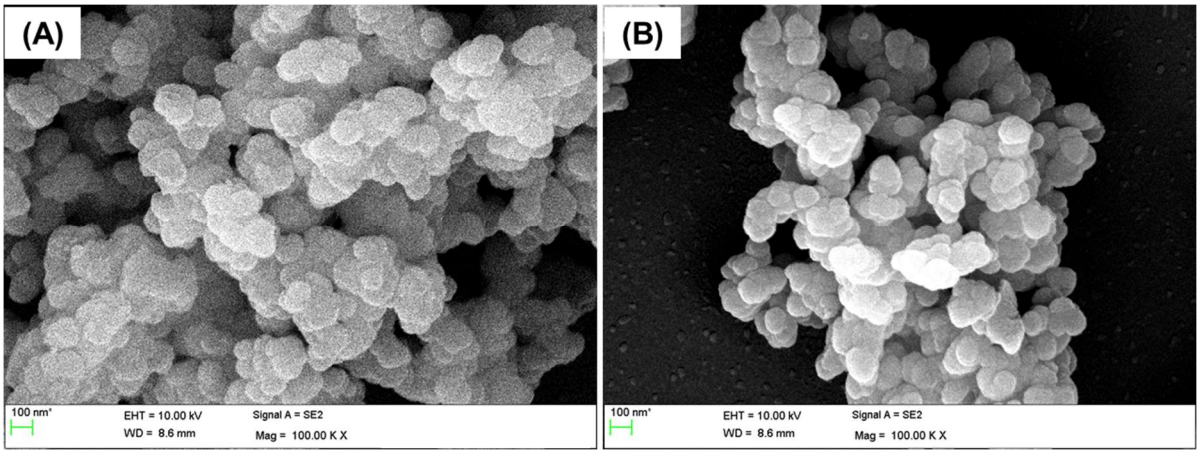

Appendix II-Figure 4.9. FESEM image of **(A)** UiO-66 NH_2 and **(B)** MOF-BSIPA.

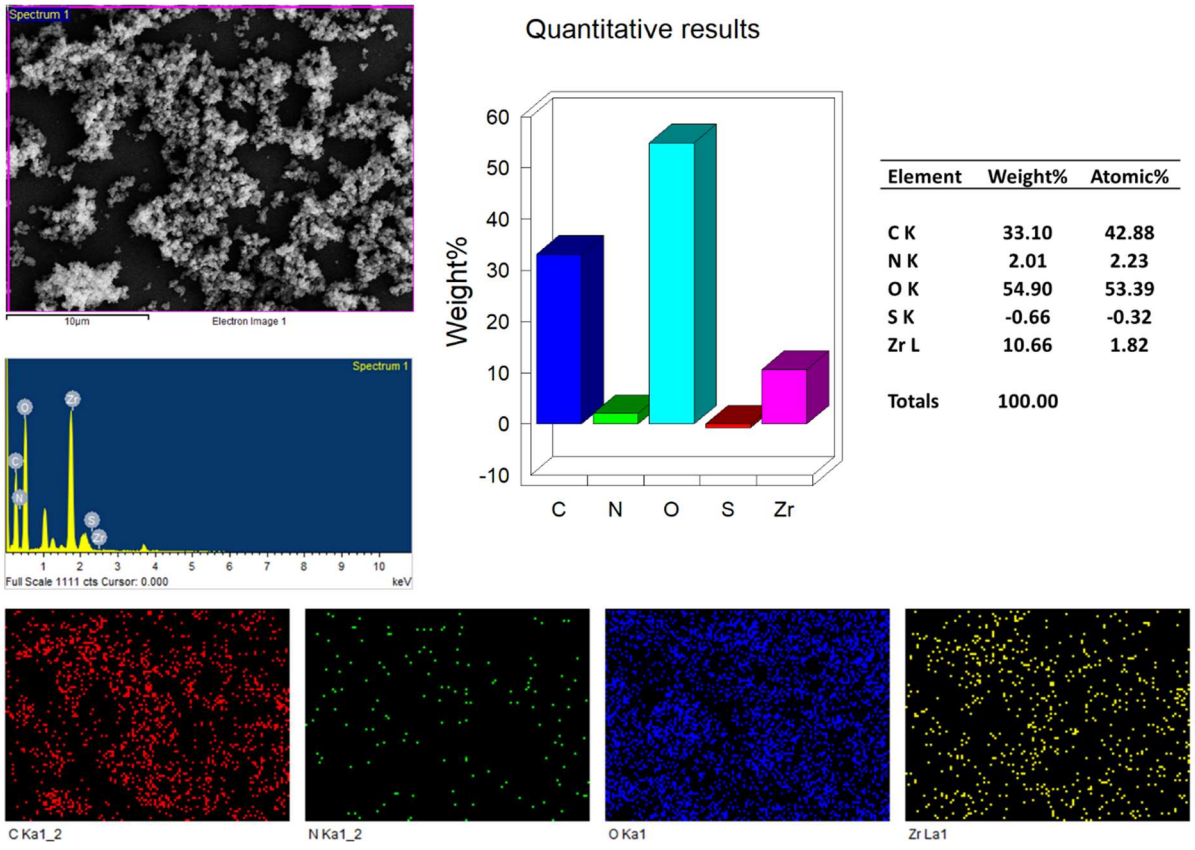

Appendix II-Figure 4.10. FESEM and EDX data of PGM-N1 with elemental mapping.

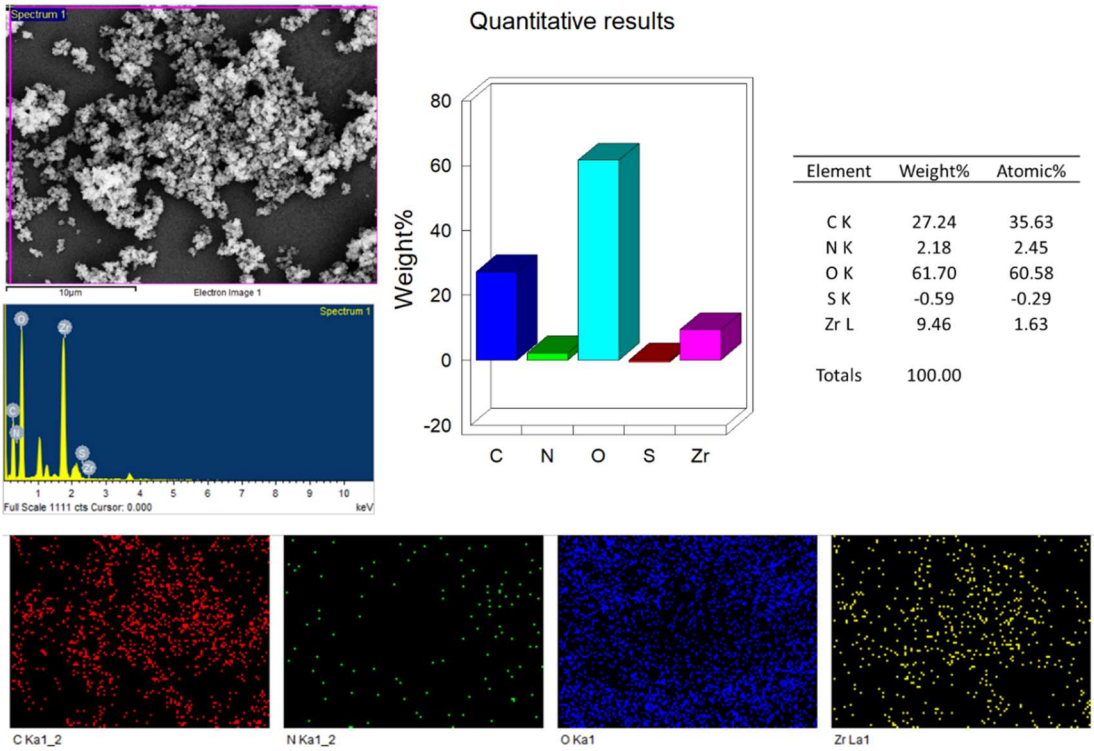

Appendix II-Figure 4.11. FESEM and EDX data of PGM-N2 with elemental mapping.

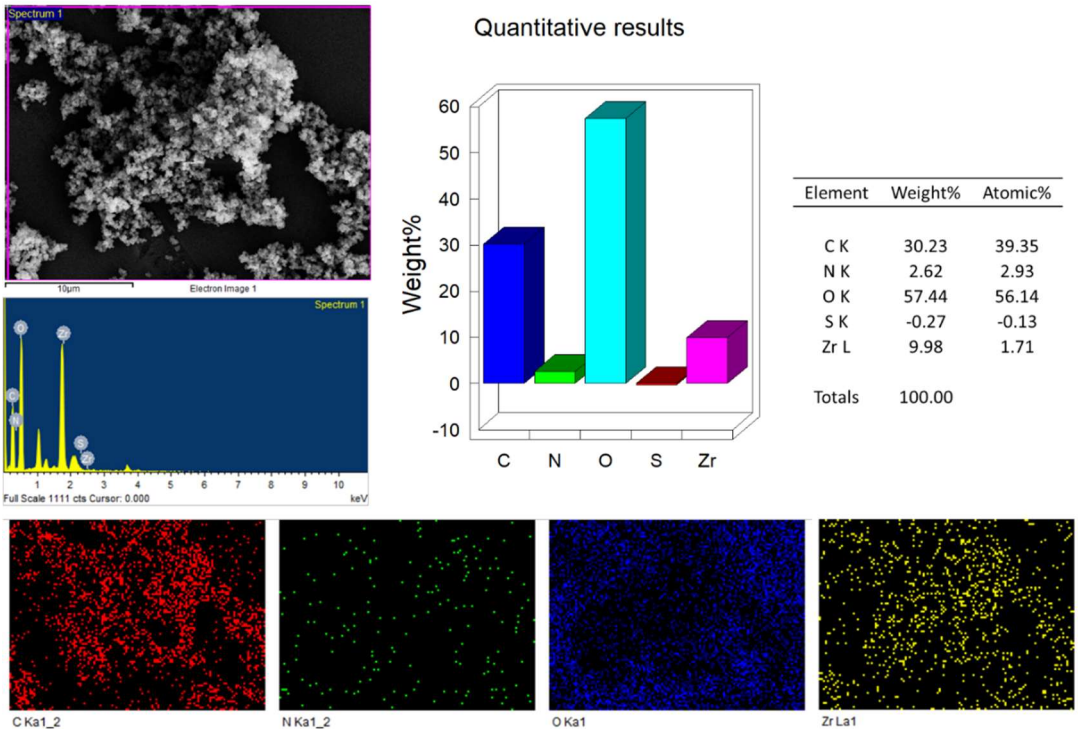

Appendix II-Figure 4.12. FESEM and EDX data of PGM-C1 with elemental mapping.

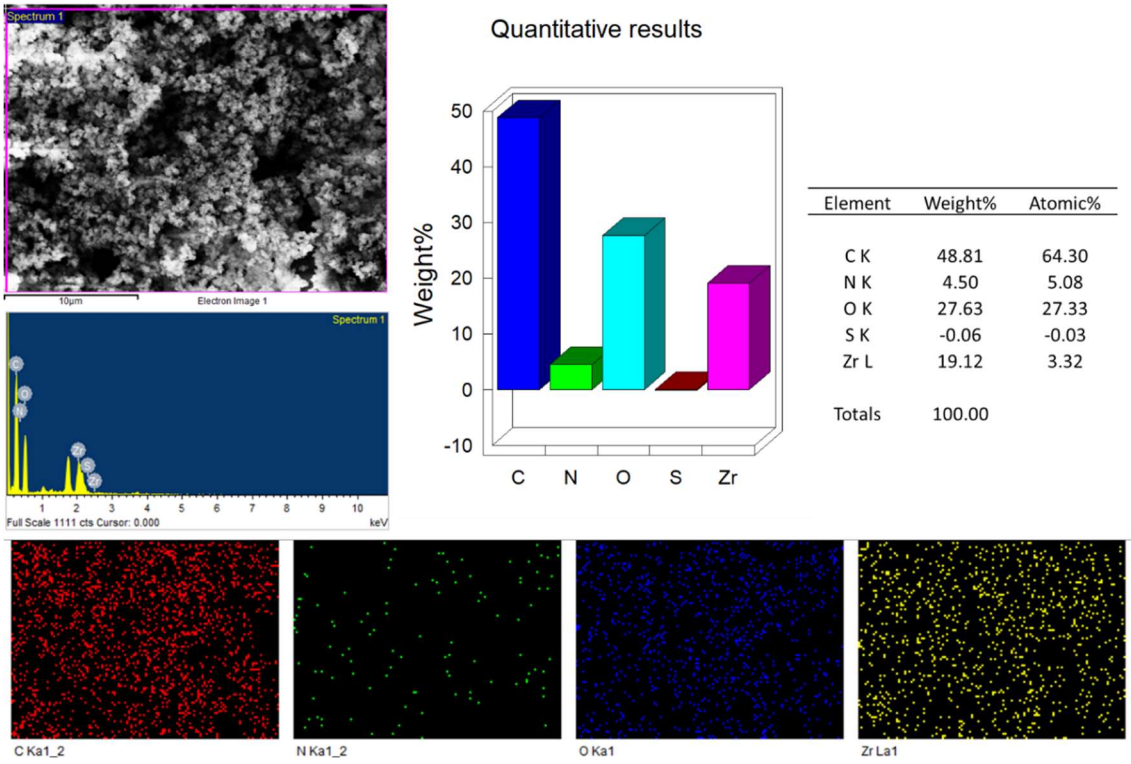

Appendix II-Figure 4.13. FESEM and EDX data of PGM-C2 with elemental mapping.

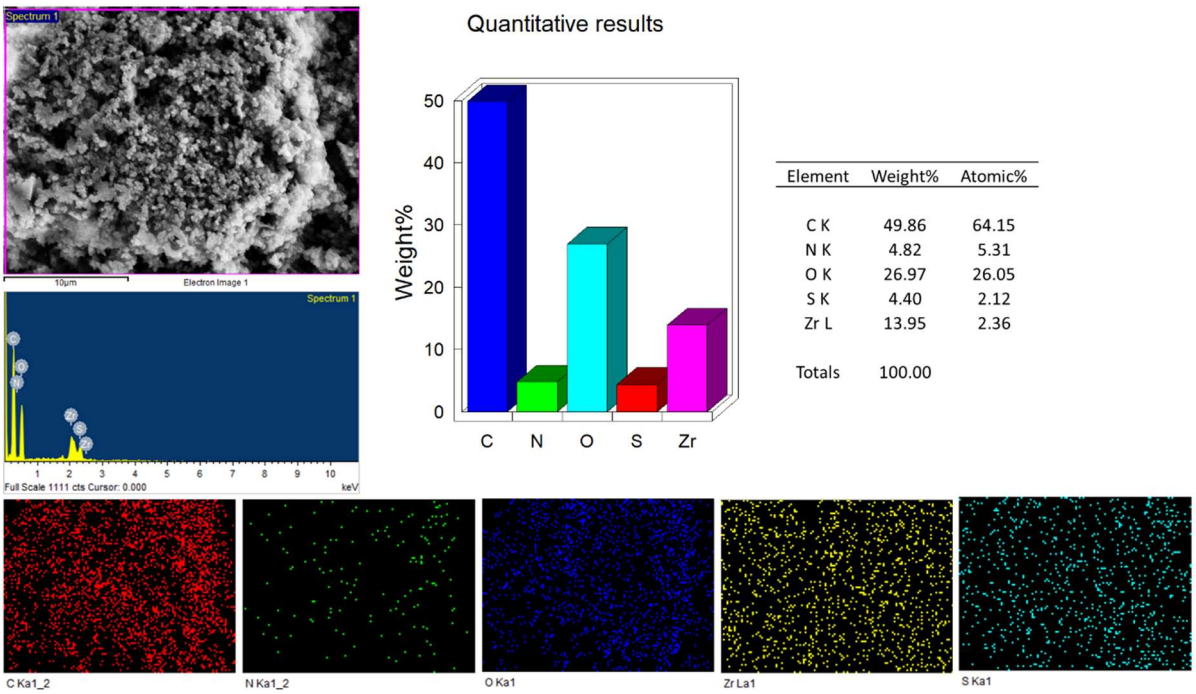

Appendix II-Figure 4.14 FESEM and EDX data of PGM-Z1 with elemental mapping.

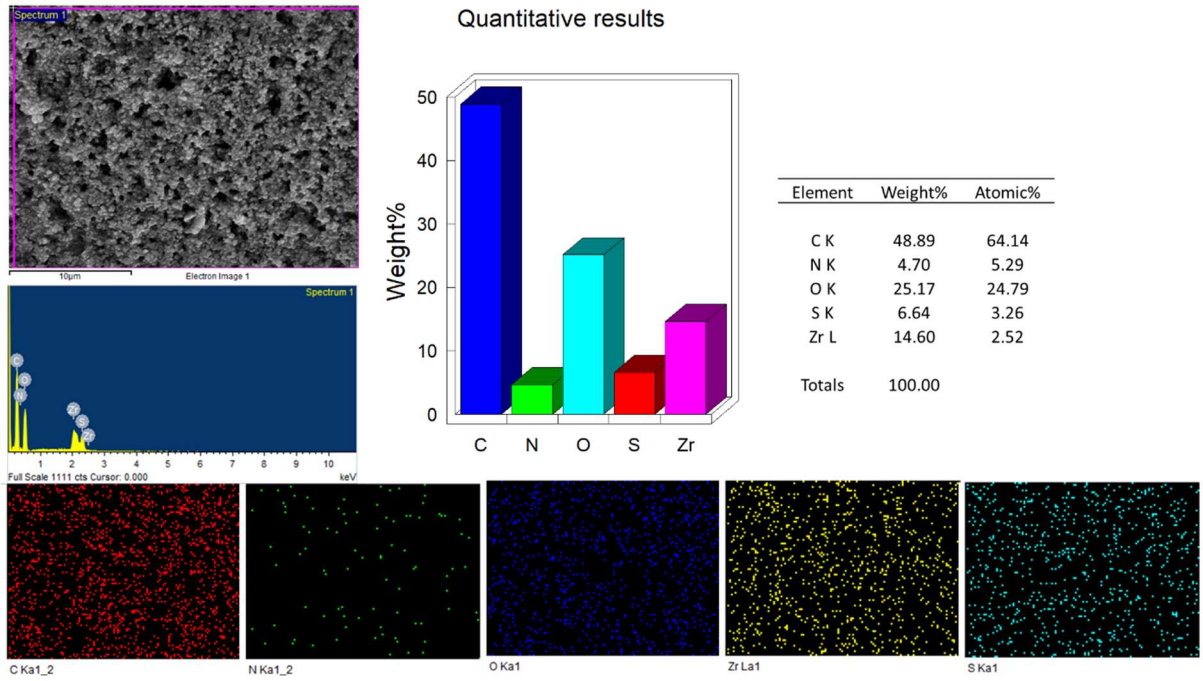

Appendix II-Figure 4.15. FESEM and EDX data of PGM-Z2 with elemental mapping.

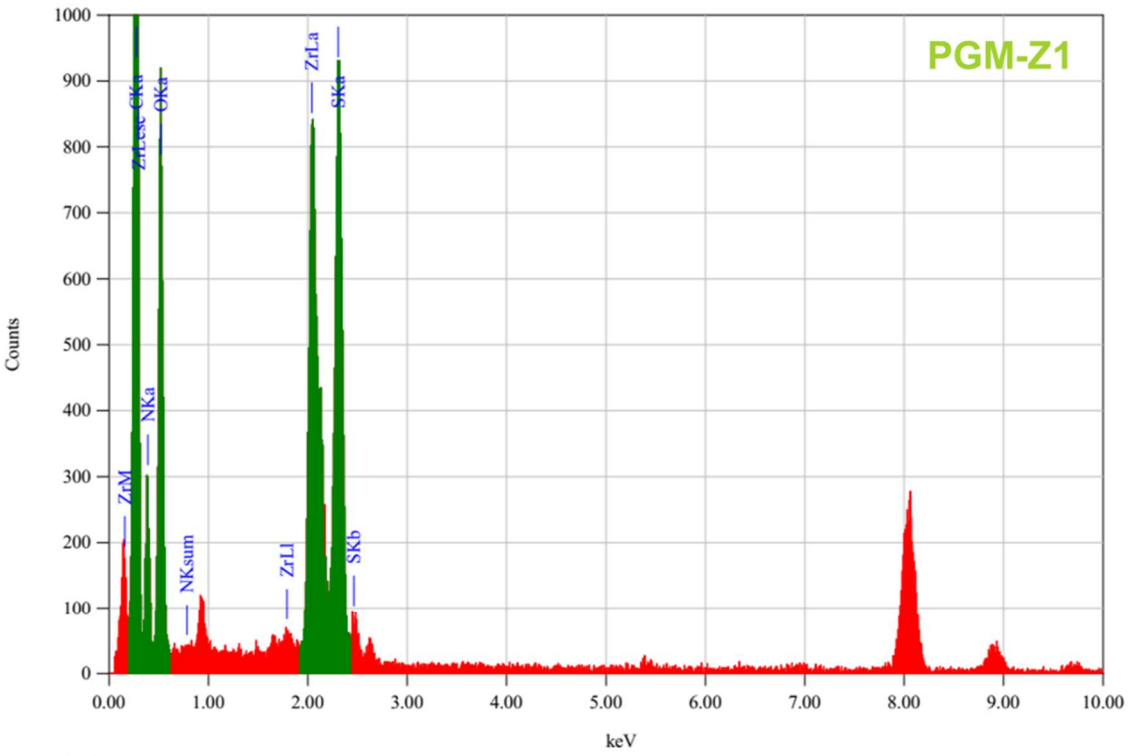

Acquisition Parameter

Acc. Voltage	:	20.0 kV	Probe Current	:	7.47500 nA
Real Time	:	300.00 sec	Dead Time	:	1 %
Live Time	:	295.55 sec	Counting Rate	:	255 Counts/sec
Preset	:	Real Time 300 sec			
Energy Range	:	0 - 40 keV	PHA Mode	:	T4

ZAF Method Standardless Quantitative Analysis

Fitting Coefficient : 0.2269

Element	(keV)	Mass%	Sigma	Atom%	Compound	Mass%	Cation	K
C K	0.277	13.87	0.13	49.82				11.6708
N K	0.392	0.02	0.00	0.07				0.1939
O K	0.525	1.16	0.03	3.13				5.6689
S K	2.307	7.79	0.17	10.49				5.8850
Zr L	2.042	77.15	1.71	36.49				76.5813
Total		100.00		100.00				

Appendix II-Figure 4.16. TEM EDX data of PGM-Z1.

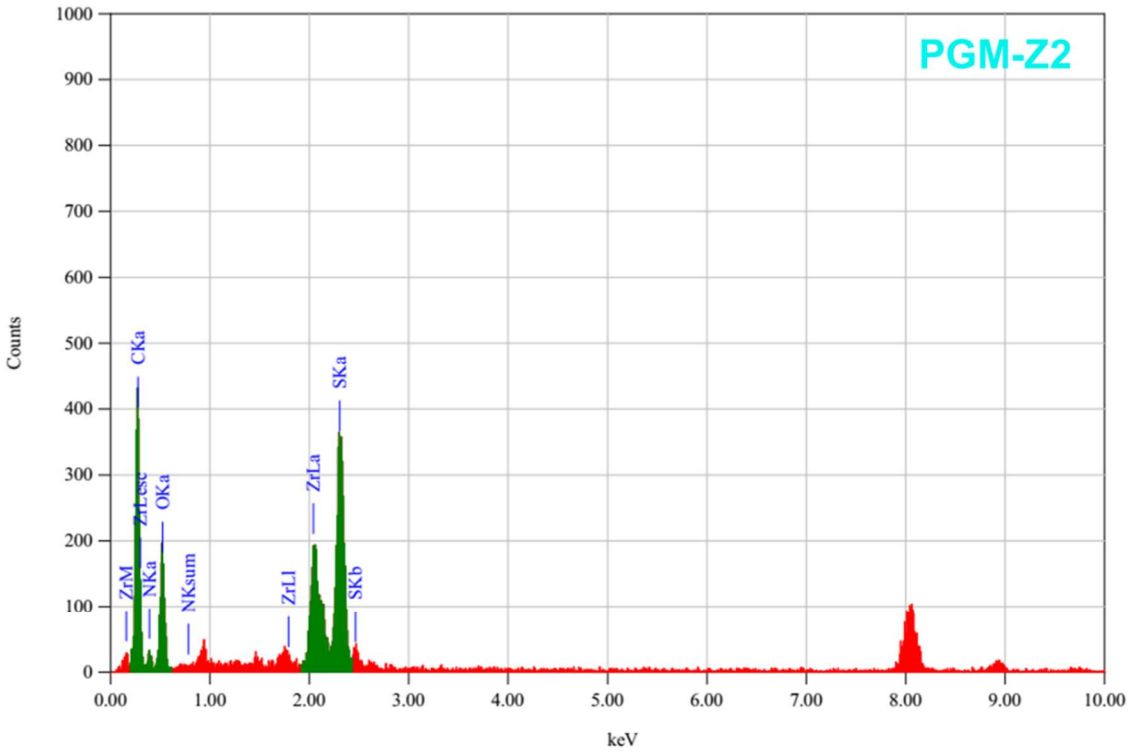

Acquisition Parameter

Acc. Voltage :	20.0 kV	Probe Current :	7.47500 nA
Real Time :	300.00 sec	Dead Time :	0 %
Live Time :	297.80 sec	Counting Rate :	95 Counts/sec
Preset :	Real Time 300 sec		
Energy Range :	0 - 40 keV	PHA Mode :	T4

ZAF Method Standardless Quantitative Analysis
Fitting Coefficient : 0.2200

Element	(keV)	Mass%	Sigma	Atom%	Compound	Mass%	Cation	K
C K	0.277	11.50	0.27	42.26				8.9289
N K	0.392	0.01	0.00	0.03				0.0943
O K	0.525	1.10	0.06	3.02				5.5566
S K	2.307	13.92	0.50	19.16				11.0017
Zr L	2.042	73.47	3.63	35.53				74.4185
Total		100.00		100.00				

Appendix II-Figure 4.17. TEM EDX data of PGM-Z2.

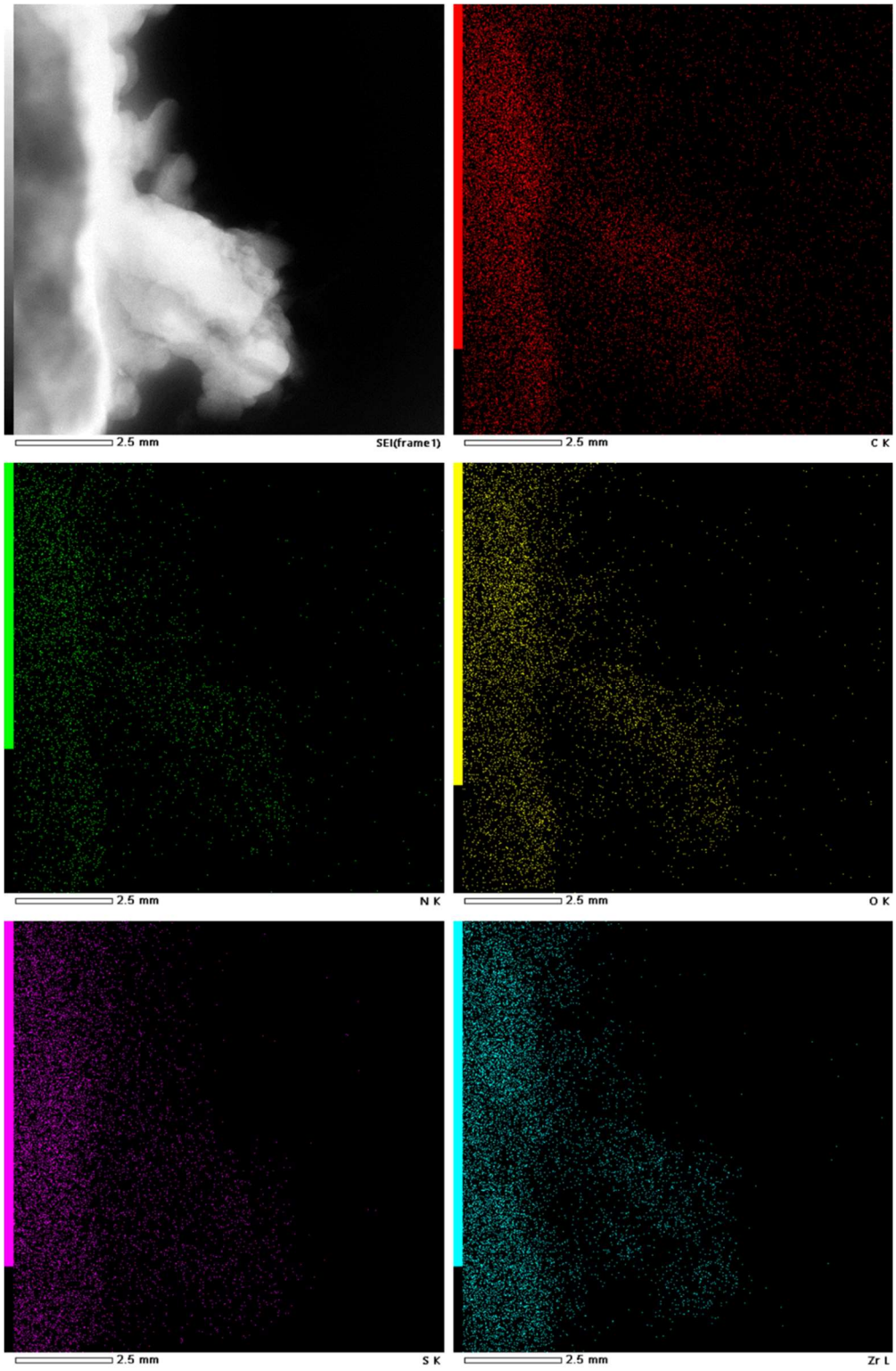

Appendix II-Figure 4.18. Elemental mapping of PGM-Z2 using TEM-EDX analysis. The distribution of C, N, O, S and Zr throughout the image prove the successful polymer grafting on the MOF surface.

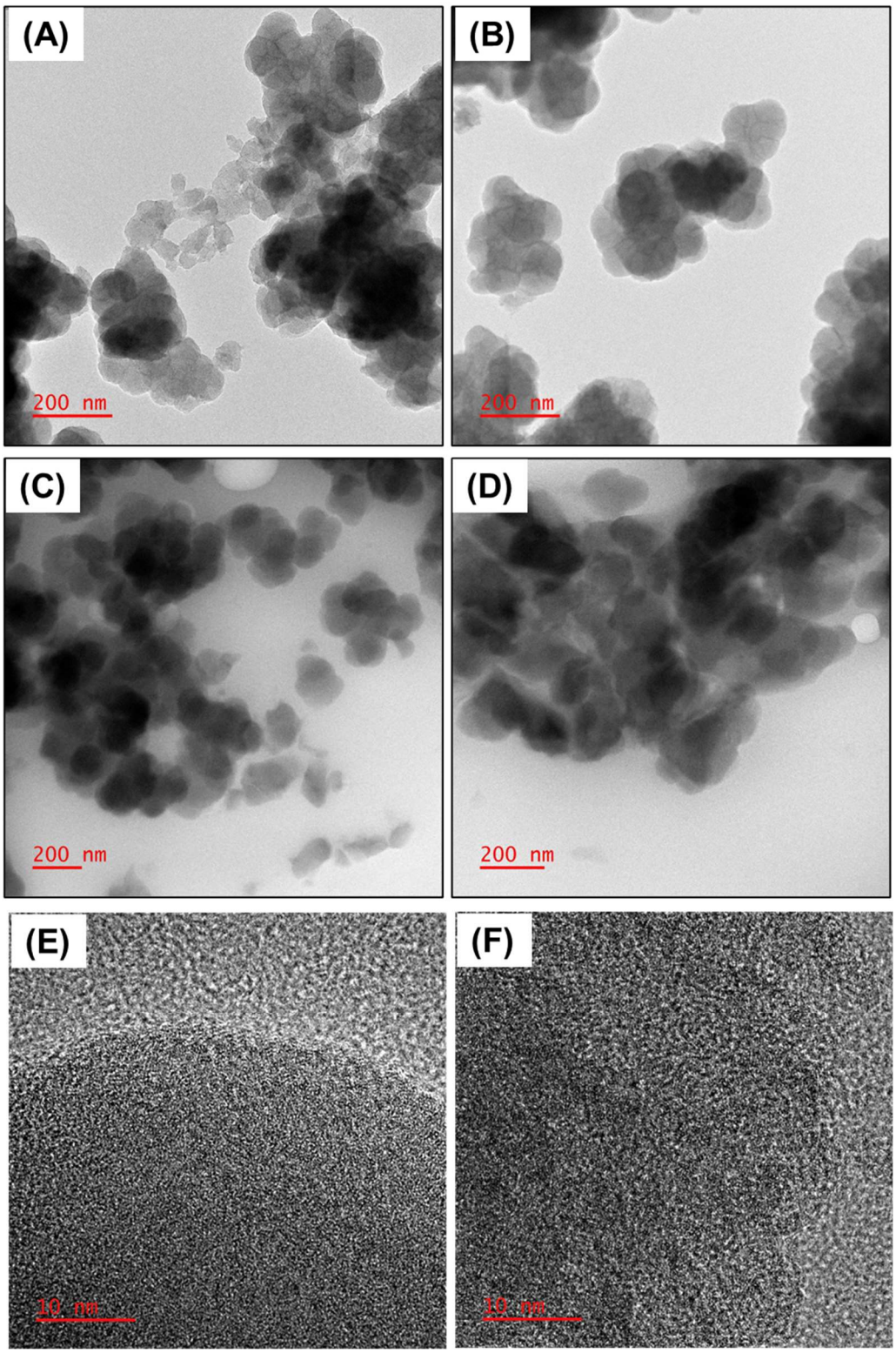

Appendix II-Figure 4.19. TEM images of the **(A)** PGM-N1, **(B)** PGM-C1, **(C)** PGM-N2 and **(D)** PGM-C2. **(E)** and **(F)** are the high-resolution images of PGM-N1 and PGM-C1, respectively representing the porous nature and pore alignments of the MOF samples upon polymer grafting.

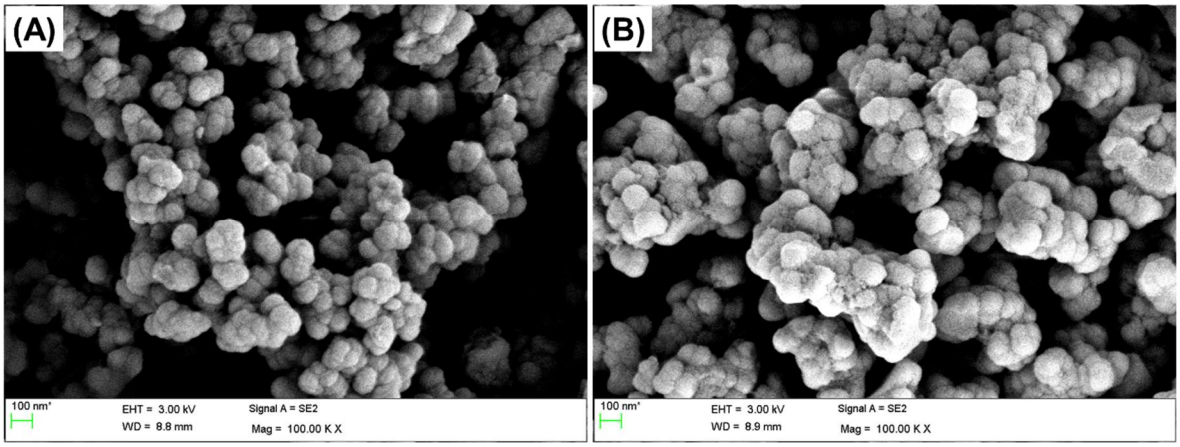

Appendix II-Figure 4.20. FESEM images (A) of PGM-N2 and (B) of PGM-Z2 after keeping the samples at 80 °C in presence of 100% humidity for 10 days.

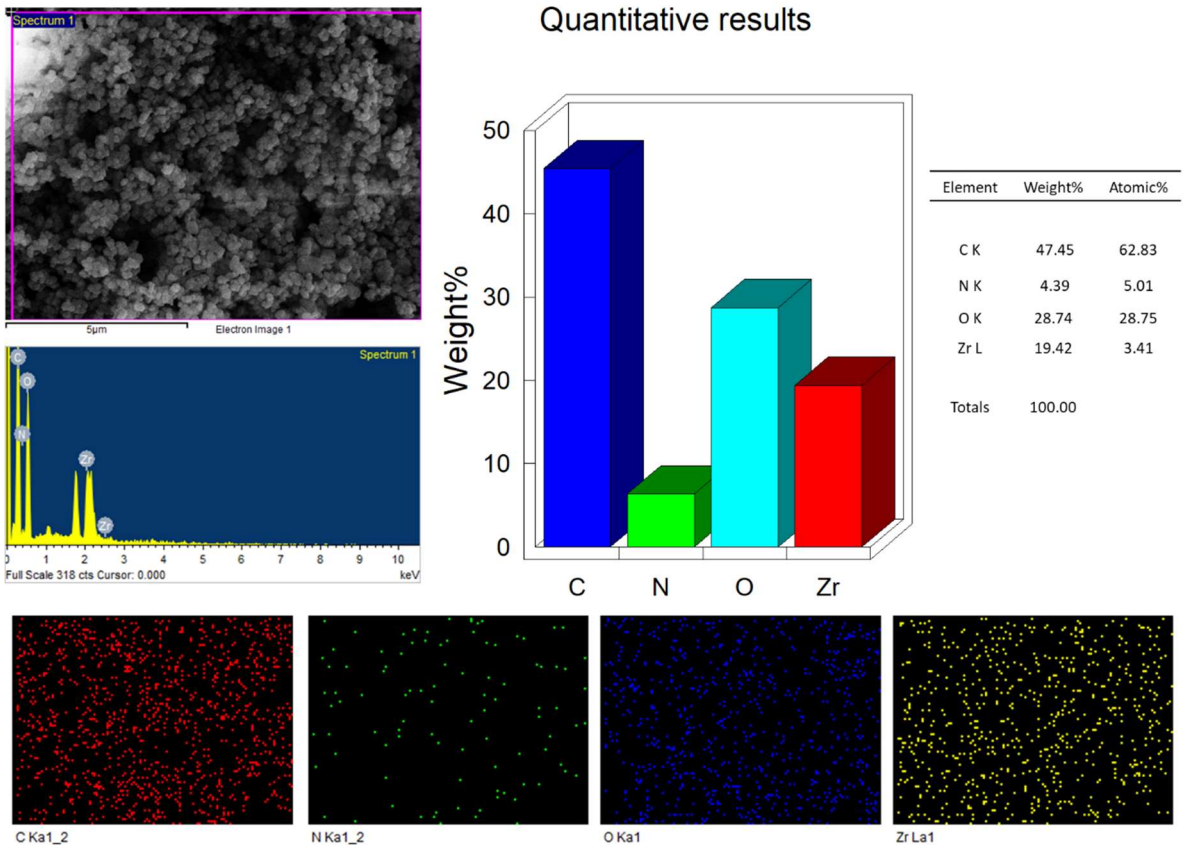

Appendix II-Figure 4.21. FESEM and EDX data of PGM-C2 with elemental mapping after keeping the samples at 80 °C in presence of 100% humidity for 10 days.

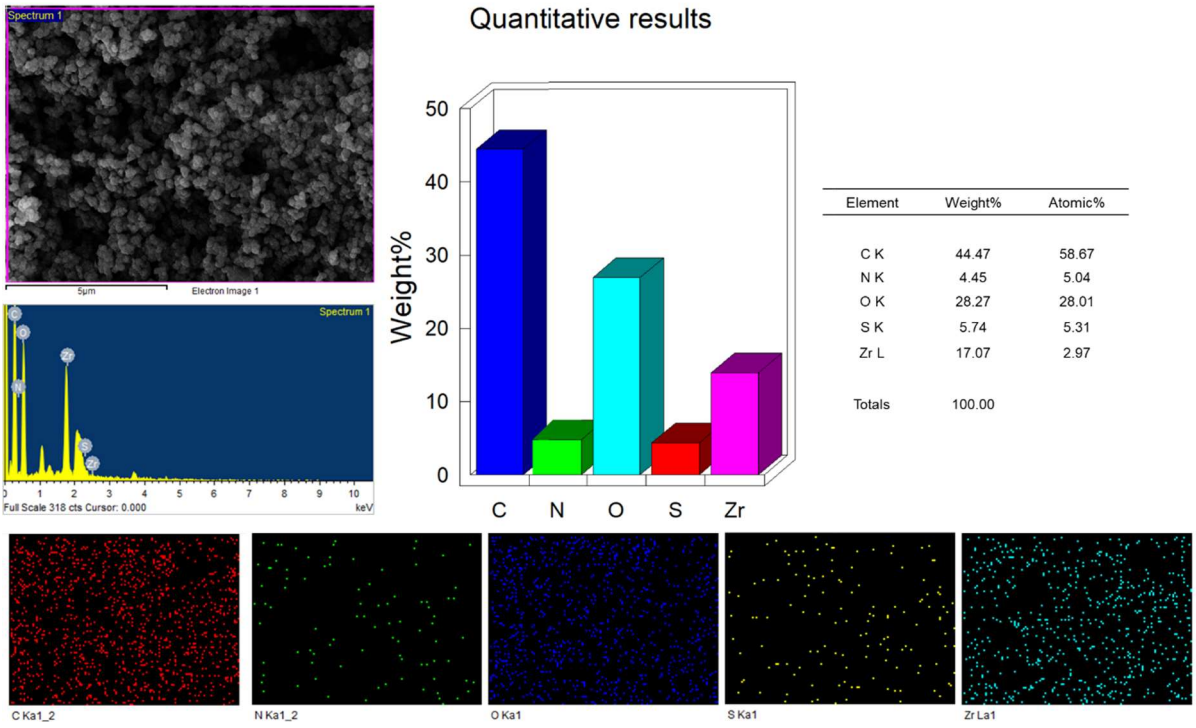

Appendix II-Figure 4.22. FESEM and EDX data of PGM-Z2 with elemental mapping after keeping the samples at 80 °C in presence of 100% humidity for 10 days.

BET isotherm analysis

The samples were activated and degassed at 100 °C under vacuum for 18 h prior to N_2 sorption analysis.

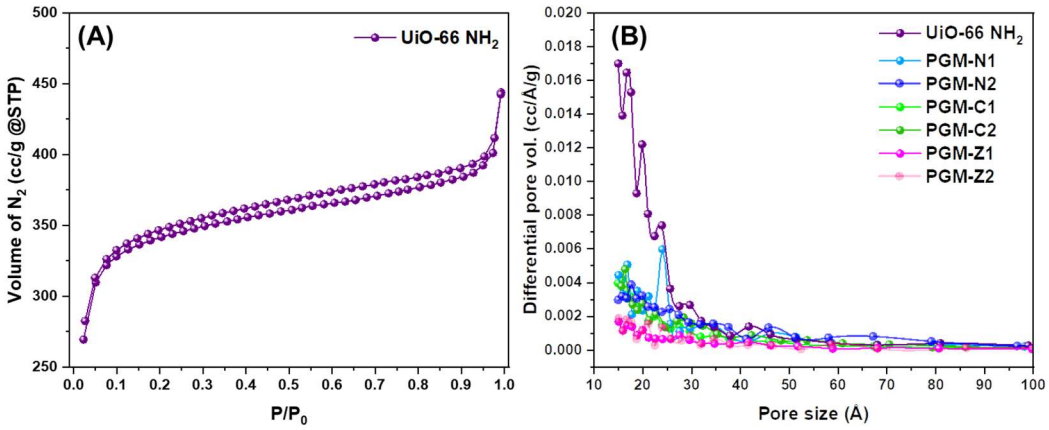

Appendix II-Figure 4.23. (A) BET isotherm of UiO-66 NH_2 and **(B)** pore size distribution of PGMs along with UiO-66 NH_2.

Dynamic vapor sorption study (DVS)

The dynamic vapor sorption (DVS) was measured for UiO-66 NH_2, PGM-N1, PGM-N2, PGM-C1, PGM-C2, PGM-Z1, PGM-Z2 with dry powder samples.

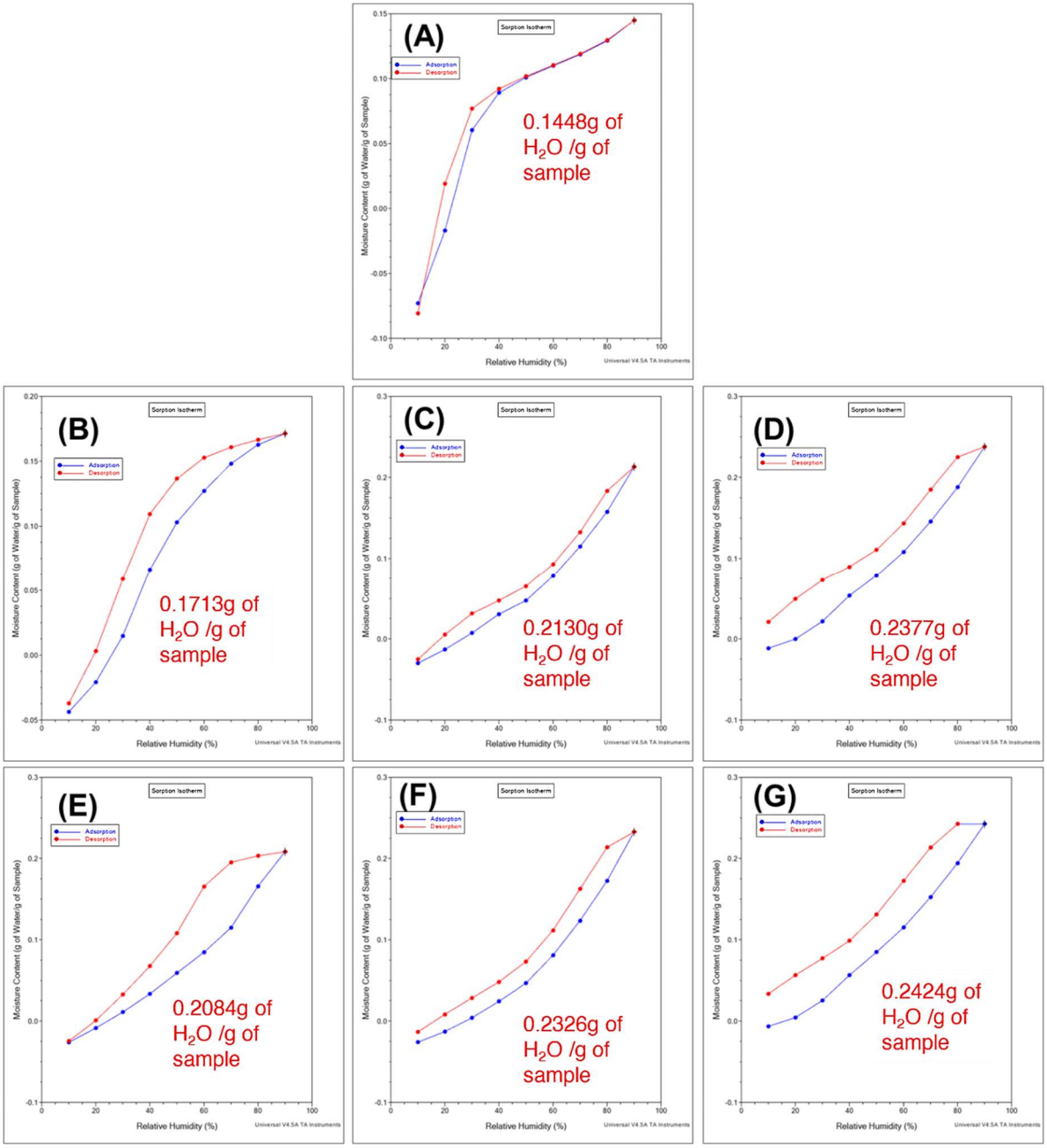

Appendix II-Figure 4.24. DVS adsorption-desorption isotherm of **(A)** UiO-66 NH_2, **(B)** PGM-N1, **(C)** PGM-C1, **(D)** PGM-Z1, **(E)** PGM-N2, **(F)** PGM-C2 and **(G)** PGM-Z2.

Zeta potential study

Zeta potential for all the nanoparticles were dispersed in milliQ water and sonicated for 5 minutes before the measurements were taken.

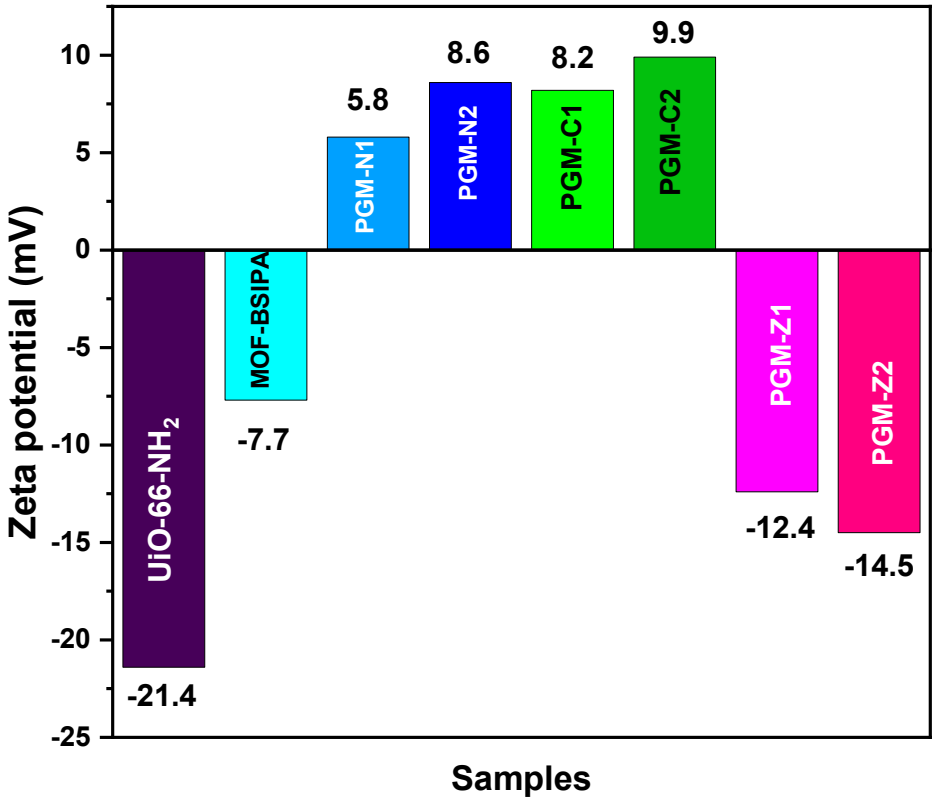

Appendix II-Figure 4.25. Zeta potential of all the PGM samples along with UiO-66 NH_2 and MOF-BSIPA in MiliQ water.

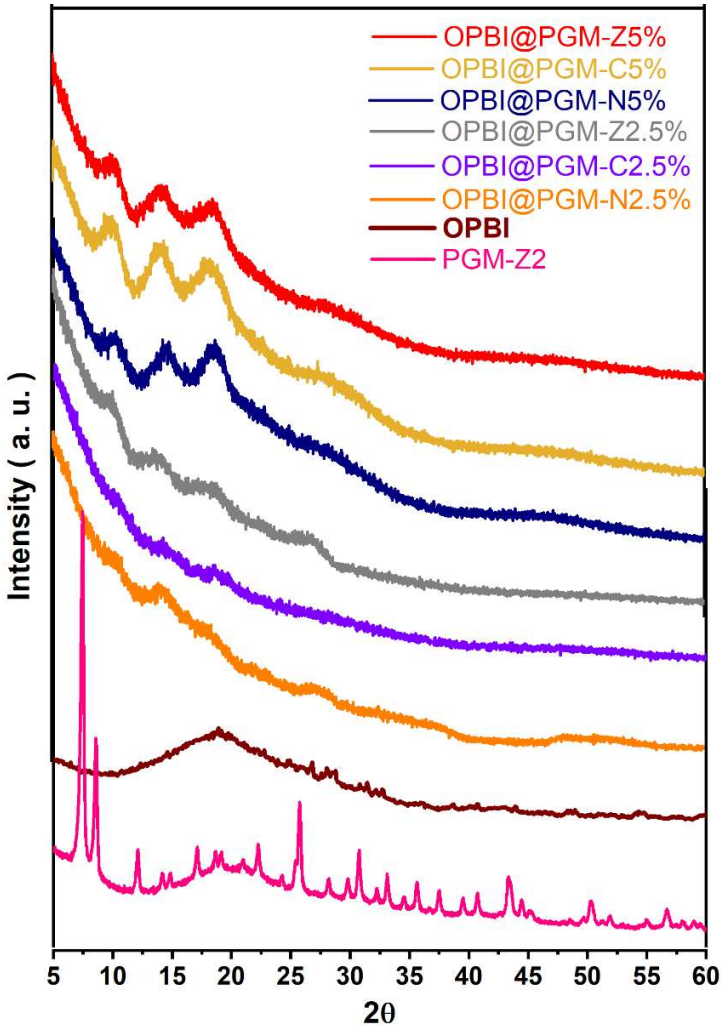

Appendix II-Figure 4.26. PXRD data of all the OPBI@PGM MMMs along with PGM-Z2 and OPBI polymer.

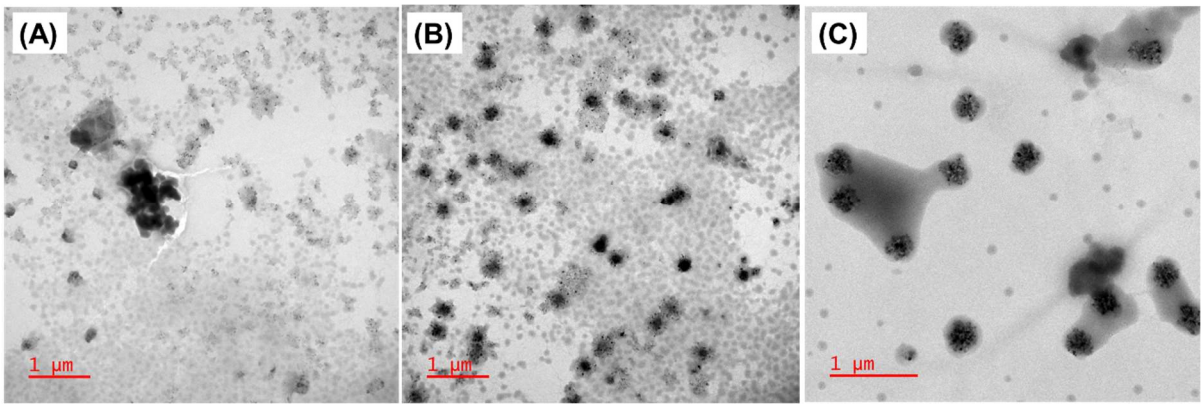

Appendix II-Figure 4.27. TEM images of (A) OPBI@PGM-N5%, (B) OPBI@PGM-C5% and (C) OPBI@PGM-Z5% represents the dispersion of PGMs in the MMM.

Mechanical study

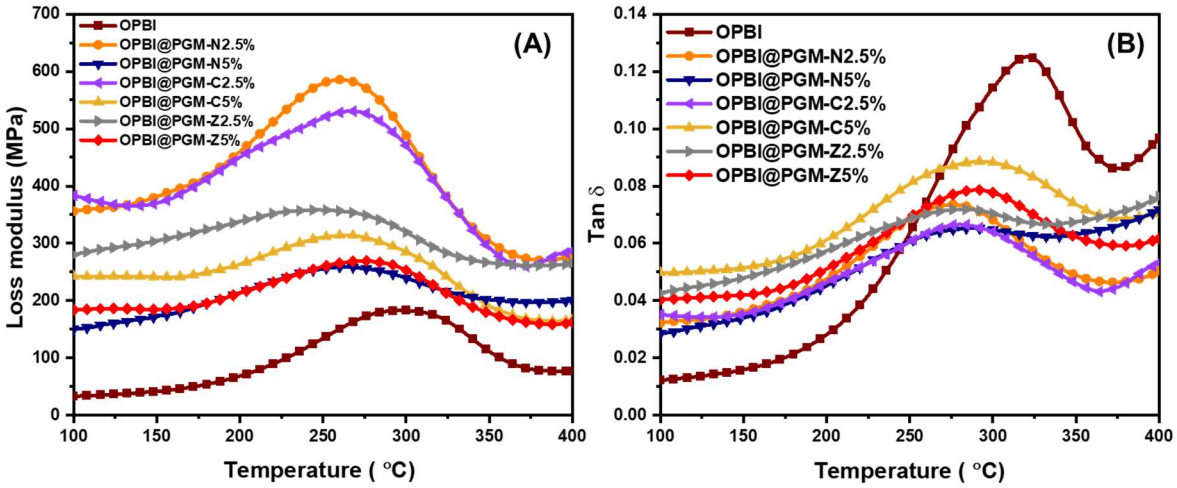

Appendix II-Figure 4.28. (A) Loss modulus and **(B)** tan δ plots of all the OPBI@PGM membranes of different filler loading along with pristine OPBI.

Appendix II-Table 4.2. Temperature dependent storage modulus of the nanocomposites along with OPBI membrane obtained from DMA study

Sample	E′ (MPa) at 100°C	% of increment	E′ (MPa) at 400°C	% of increment
OPBI	2719	-	791	-
OPBI@PGM-N2.5%	11019	305	5537	600
OPBI@PGM-N5%	5258	93	2796	253
OPBI@PGM-C2.5%	10913	301	5383	580
OPBI@PGM-C5%	4877	79	2353	197
OPBI@PGM-Z2.5%	6563	141	3482	340
OPBI@PGM-Z5%	4552	67	2619	231

Appendix II-Table 4.3. Water uptake, swelling ratio, PA loading data of OPBI and the nanocomposite membranes.

Sample	Water uptake (wt%)	Swelling ratio in water (%)	Swelling ratio in PA (%)	PA doping level (no. of PA mol/OPBI r.u)
OPBI	11.87 wt%	4.37 (0.73)	5.89 %	15.77 (0.72)
OPBI@PGM-N2.5%	11.11 wt%	1.07 (0.32)	2.10 %	18.67 (0.41)
OPBI@PGM-N5%	12.41 wt%	0.72 (0.28)	1.76 %	20.88 (0.46)
OPBI@PGM-C2.5%	12.11 wt%	3.77 (0.41)	5.92 %	21.36 (0.51)
OPBI@PGM-C5%	15.34 wt%	3.17 (0.34)	5.60 %	25.85 (0.49)
OPBI@PGM-Z2.5%	13.87 wt%	5.32 (0.45)	5.27 %	21.31 (0.51)
OPBI@PGM-Z5%	16.54 wt%	4.74 (0.42)	4.18 %	24.98 (0.53)

#Standard deviation of the data are included in the parenthesis.

Proton conductivity

The conductivities of the membranes were measured from room temperature to 160 °C at intervals of 20 °C. However, proton conductivity data is shown for 80 °C to 160 °C only considering the application of the membranes at high temperature range only. At every temperature jump, the sample was kept for 30 minutes to attain isothermal equilibrium and then measurements were recorded. The conductivities of the membranes were calculated from the following equation:

$$\sigma = \frac{D}{RBL} \qquad (2)$$

Where, D is the distance between the electrodes (here it is 0.5 cm), B is the thickness of the membrane, L is the width of the membrane and R is the bulk resistance obtained from the Nyquist plot.

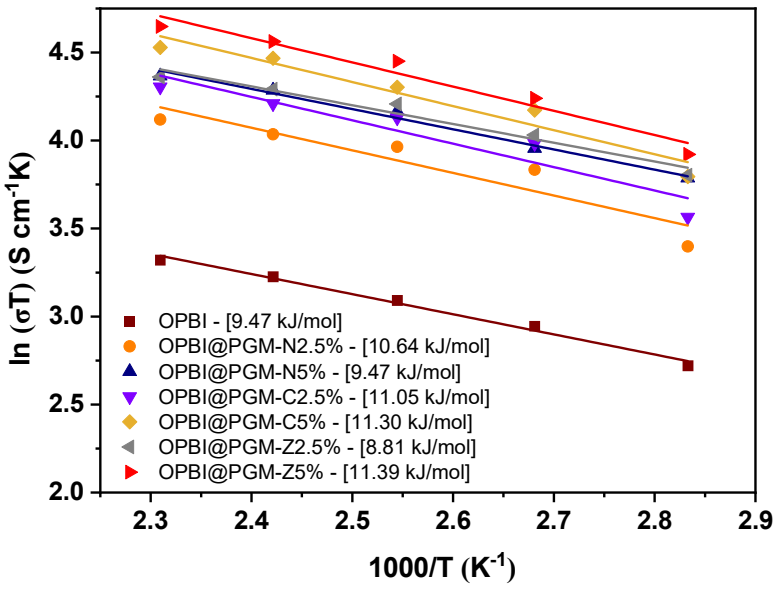

Appendix II-Figure 4.29. Arrhenius plot of OPBI and OPBI@PGM membranes.

Acid retention test

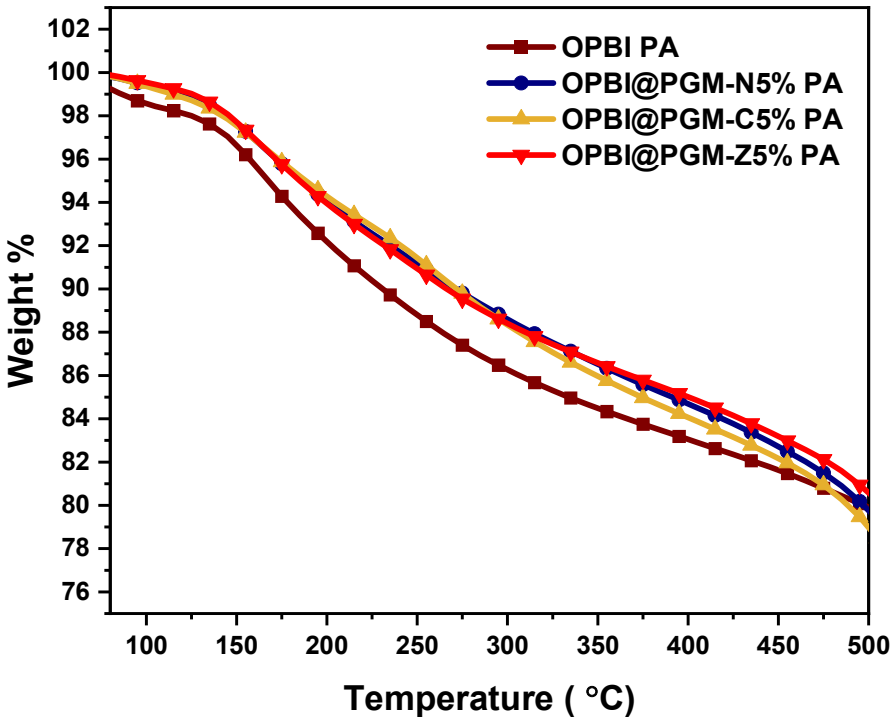

Appendix II-Figure 4.30. TGA plot of the OPBI and OPBI@PGM nanocomposite membranes after PA doping.

Appendix III

Attachment of activated BSIPA on UiO-66-NH_2 surface (MOF-BSIPA)

Attachment of BSIPA RAFT agent on the surface of UiO-66-NH_2 was achieved by utilizing the free amine functionality present on the MOF surface arising from the BDC-NH_2 linker. UiO-66-NH_2 (300 mg) in 200 mL dry THF under N_2 atmosphere and activated BSIPA (30mg) in dry THF was added in the dispersion slowly and was allowed to stir under dark condition for 18 hours at room temperature. After completion of 18 hours covalently attached BSIPA RAFT agent on the surface of UiO-66-NH_2 [MOF-BSIPA(L)] was separated from the reaction mixture using centrifugation at 13000 rpm for 10 minutes. Followed by re-dispersion of the collected material in dry THF and dry acetone was added before centrifuged again to separate from the dispersion. The step was repeated thrice with a final re-dispersion and washing with dry acetone to separate all the unbound RAFT agents from the MOF. The MOF-BSIPA was dried under vacuum at 50°C for 24 hours before any further characterization. In a similar reaction condition, the amount of activated BSIPA RAFT agent was increased to 100mg keeping the rest of the reaction recipe unaltered. The same purification process was followed in order to obtain covalently attached BSIPA-RAFT agent weight higher amount on the surface of UiO-66-NH_2 and this sample is labelled as MOF-BSIPA(H).

Abundance of microspecies under different pH conditions

pK_a calculations were based on the theoretical prediction of partial charge distribution among the atoms in the molecule. Microspecies distribution was obtained from *Chemicalize.com* & *Marvin* software and is deduced using the given formula (2) and (3) for the general reaction (1).

$$HA \leftrightarrow H^+ + A^- \ldots\ldots\ldots\ldots\ldots\ldots (1)$$

$$K_a = \frac{[A^-][H^+]}{[HA]} \qquad \ldots\ldots\ldots\ldots\ldots\ldots (2)$$

$$pK_a = -log_{10}\, K_a = pH + log_{10}(\frac{[HA]}{[A^-]}) \ldots\ldots\ldots\ldots\ldots\ldots (3)$$

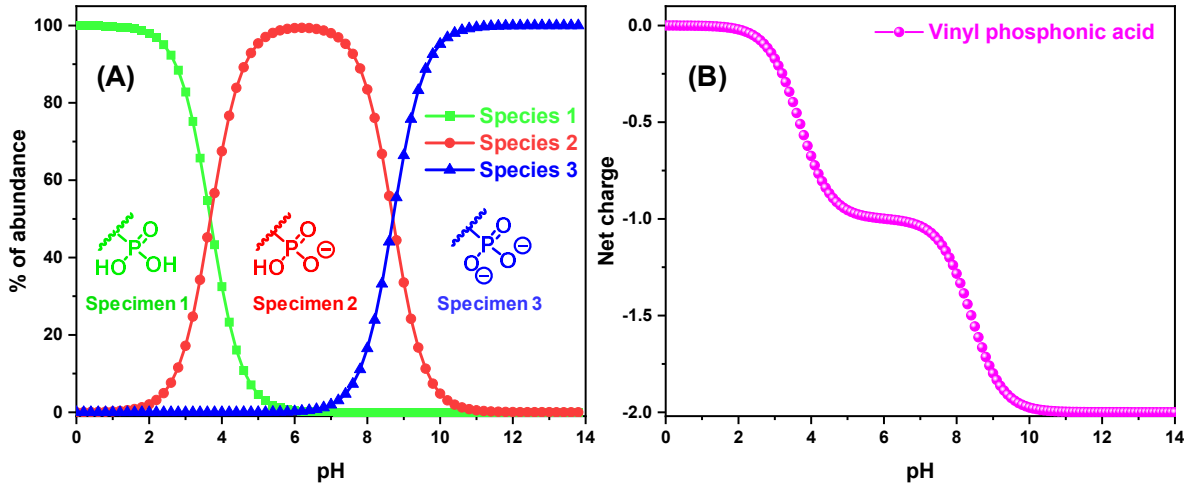

Appendix III-Figure 5.1. (**A**) % of abundance of microspecies vs pH plot and (**B**) net charge vs pH plot of VPA monomer.

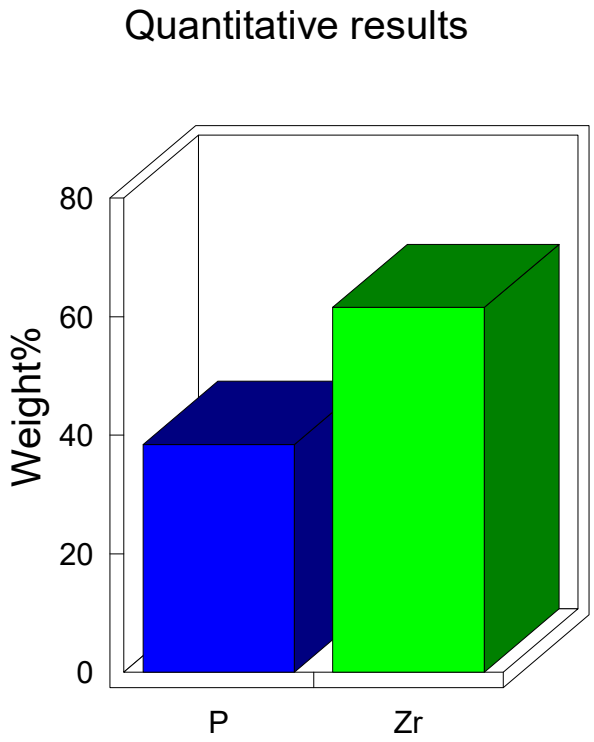

Element	Weight%	Atomic%
P K	38.46	64.79
Zr L	61.54	35.21
Totals	100.00	

Appendix III-Figure 5.2. FESEM EDX data of PGM-L3 after keeping the sample for 10 days at 80°C under 100% humidified condition.

NMR analysis of PVPA polymer grafted MOF

The polymer grafted MOF (PGM-L3) were dried in an oven and dissolved in D_2O in order to analyze using Brucker 500 MHz Spectro meter. The collected data was analyzed using MestReNova software.

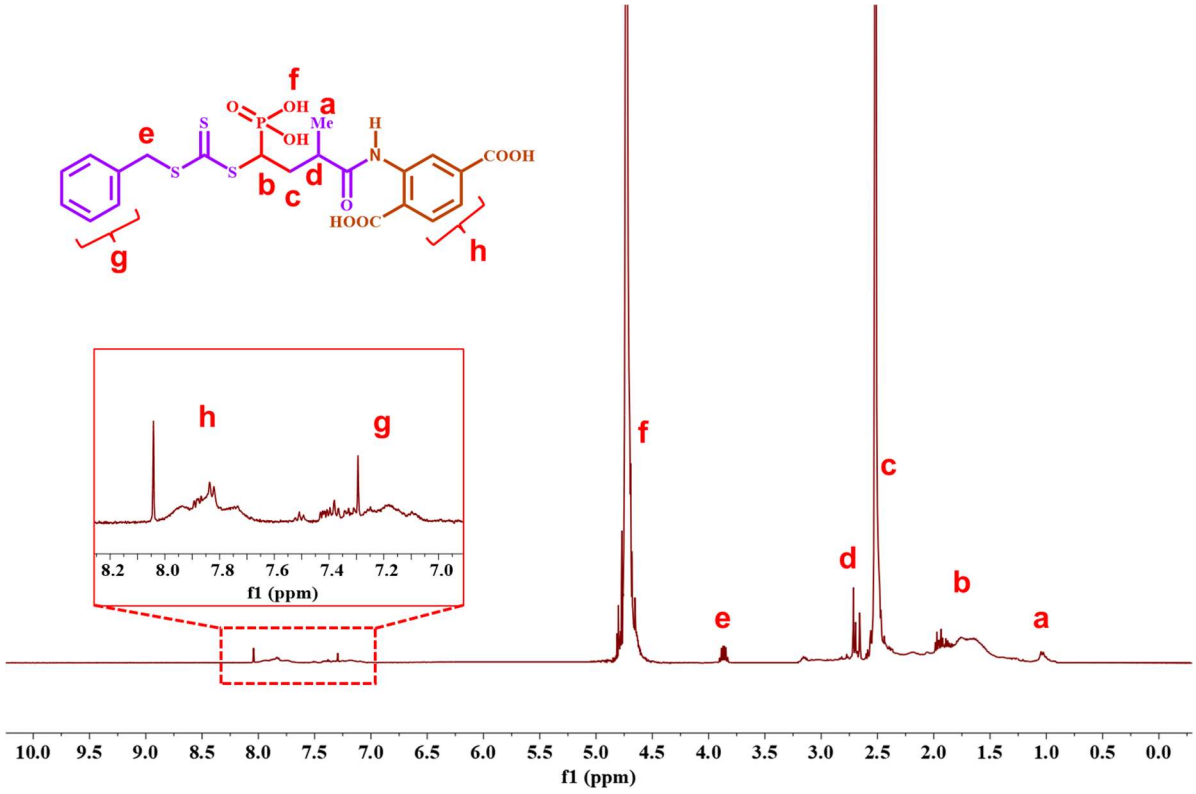

Appendix III-Figure 5.3. ^{1}H NMR spectrum of PVPA polymer chain grafted MOF (PGM-L3).

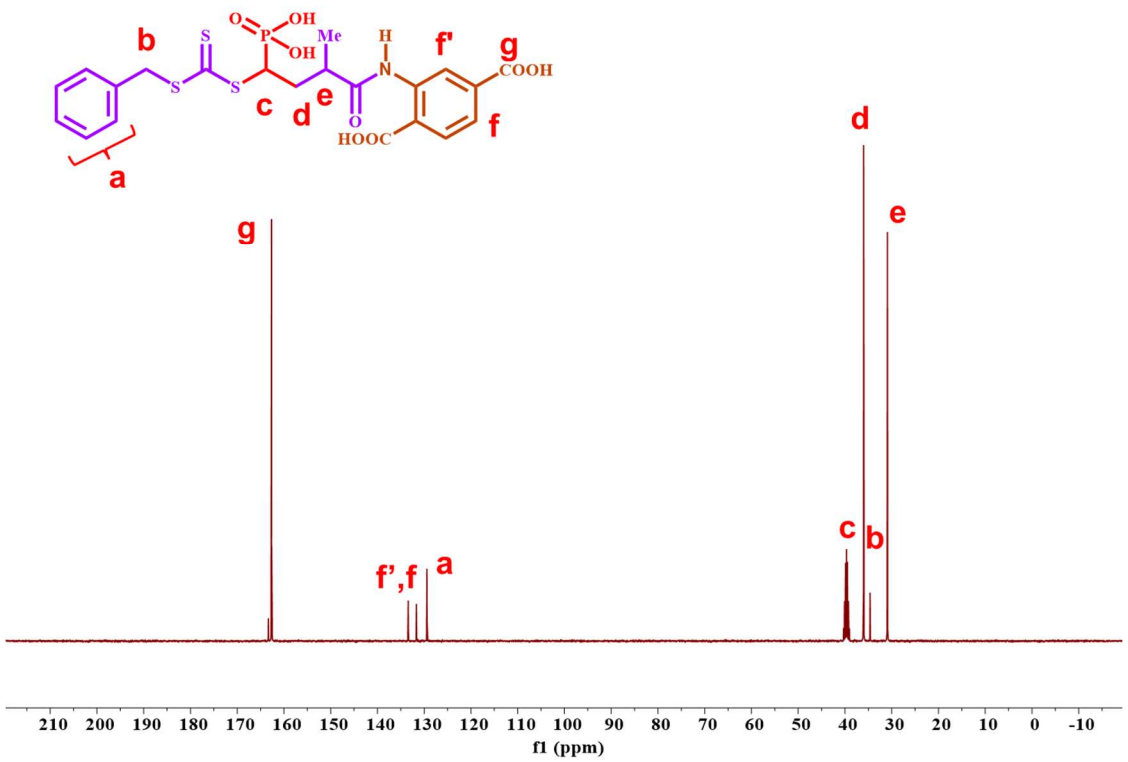

Appendix III-Figure 5.4. ^{13}C NMR spectrum of PVPA polymer chain *grafted* MOF (PGM-L3).

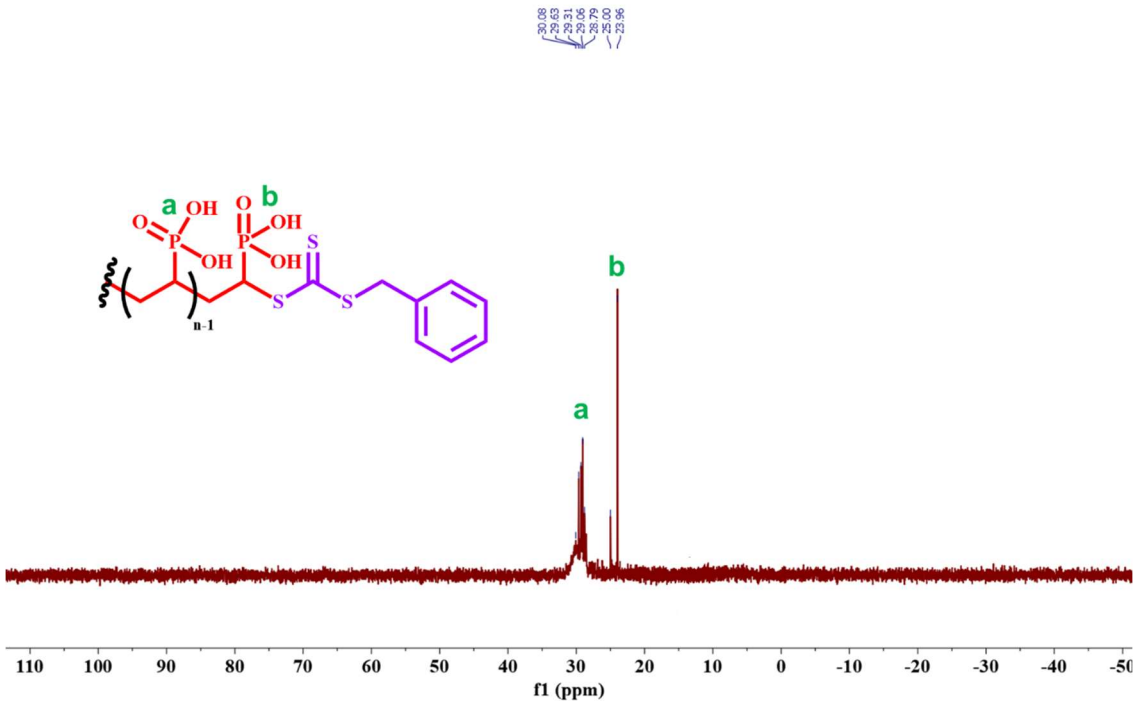

Appendix III-Figure 5.5. ^{31}P NMR spectrum of PVPA polymer chain grafted MOF (PGM-L3).

Detachment of polymer chains from the MOF surface in order to measure the molecular weight (M. W.) of the grafted polymer chain

Molecular weights (M.W.) and polydispersity index (Đ) of detached polymers were obtained after detaching the polymer chains from the MOF core by treating the PGM samples in aqueous HF acid solution which helps to break down the framework structure (Scheme S2). The PGM samples were subjected to dilute HF solution in PTFE vials. Upon digestion the solid residue was removed using centrifugation technique and the supernatant was further purified to obtain bare polymer chains. The bare polymer chains which were detached from the MOF surface were dissolved in HPLC water and the molecular weight was determined by Gel permeation chromatography (GPC) technique using PEG/ PEO as standards and eluted in HPLC water at a flow rate of 0.5 mL/min at 30°C on a GPC (Waters 515 HPLC) fitted with Waters 2414 refractive index detector and using Ultrahydrogel 250 Water column.

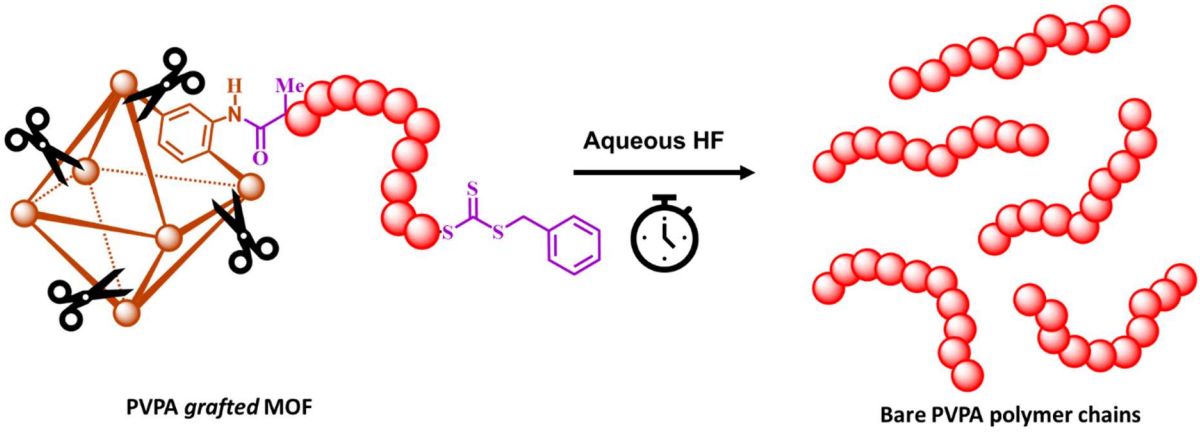

Appendix III-Scheme 5.1. The schematic representation for the detachment of grafted polymer chains from the surface of polymer-*g*-MOF.

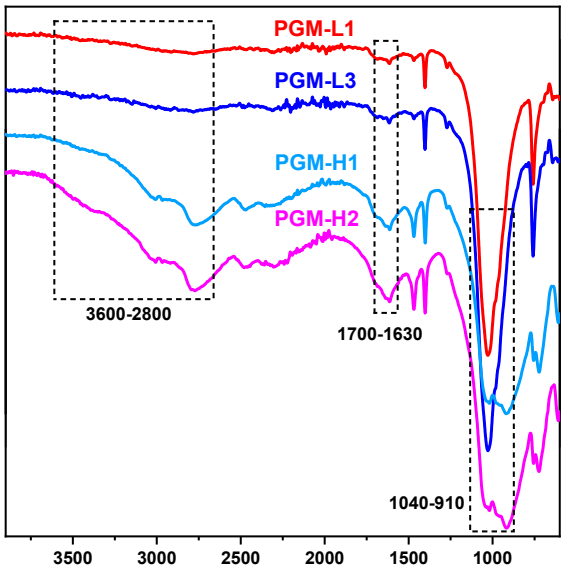

Appendix III-Figure 5.6. FT-IR plots of PGM-L and PGM-H samples.

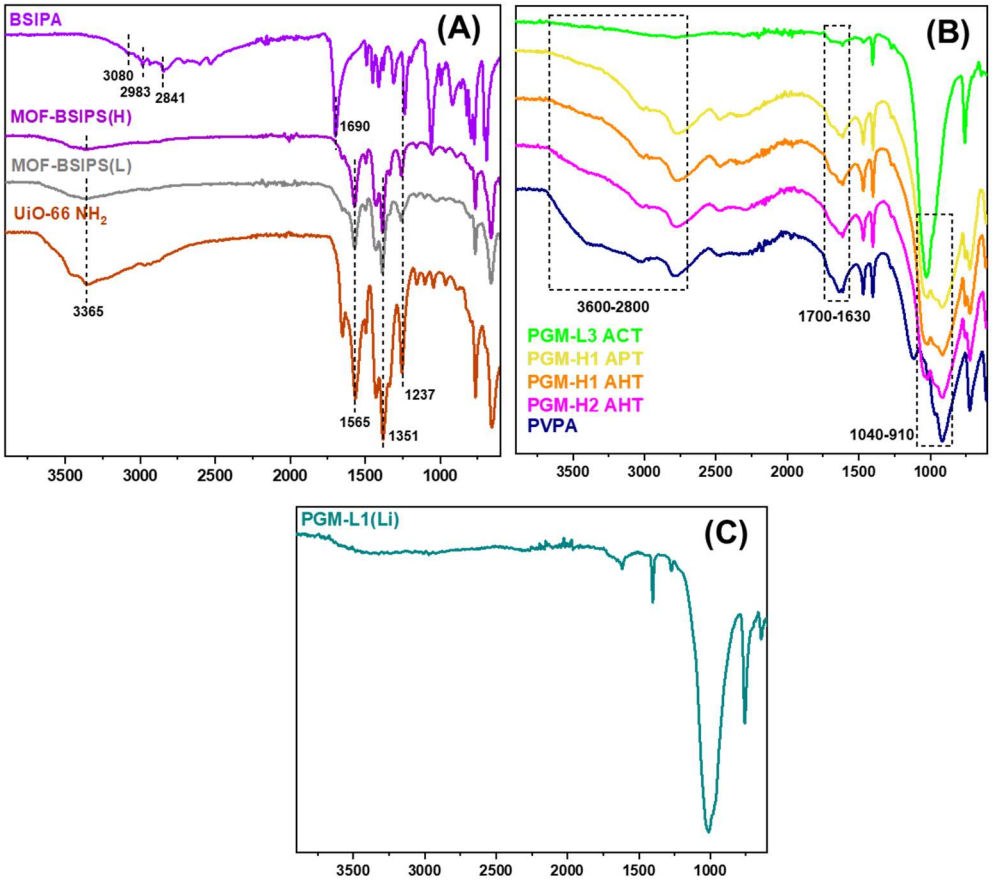

Appendix III-Figure 5.7. FT-IR spectra of BSIPA, MOF-BSIPA(H), MOF-BSIPA(L), UiO-66 NH_2 **(A)** and PGM-L3, PGM-H1, PGM-H2 and PVPA polymer **(B)**. The term ACT, APT and AHT represents 'after conductivity treatment', 'after high pressure treatment' and 'after humidity treatment' respectively. FT-IR spectra of PGM-L1(Li) **(C).**

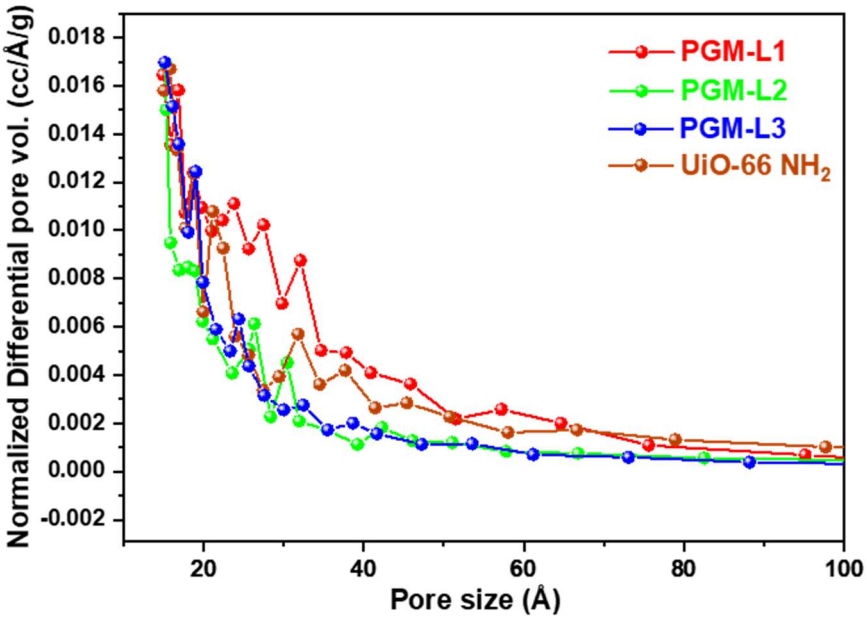

Appendix III-Figure 5.8. Pore size distribution plot of PGM-Ls along with UiO-66-NH_2.

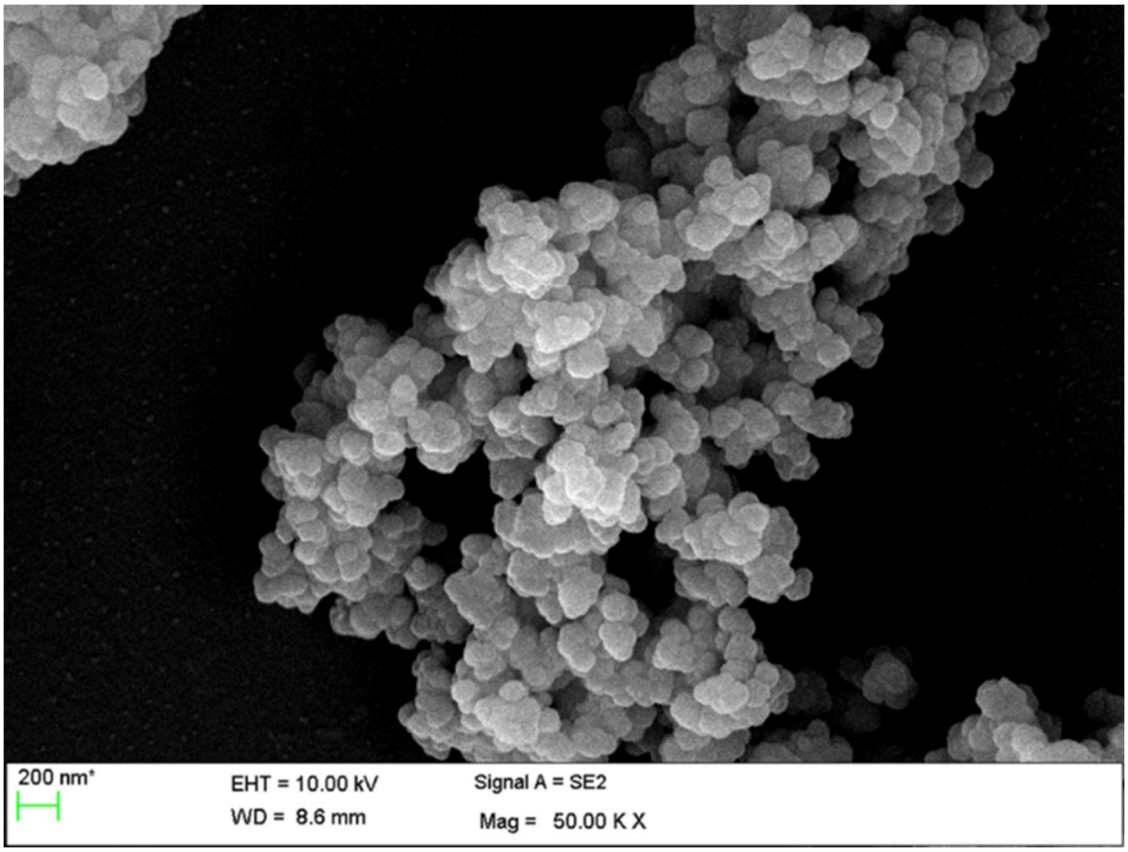

Appendix III-Figure 5.9. FESEM image of MOF-BSIPA(H).

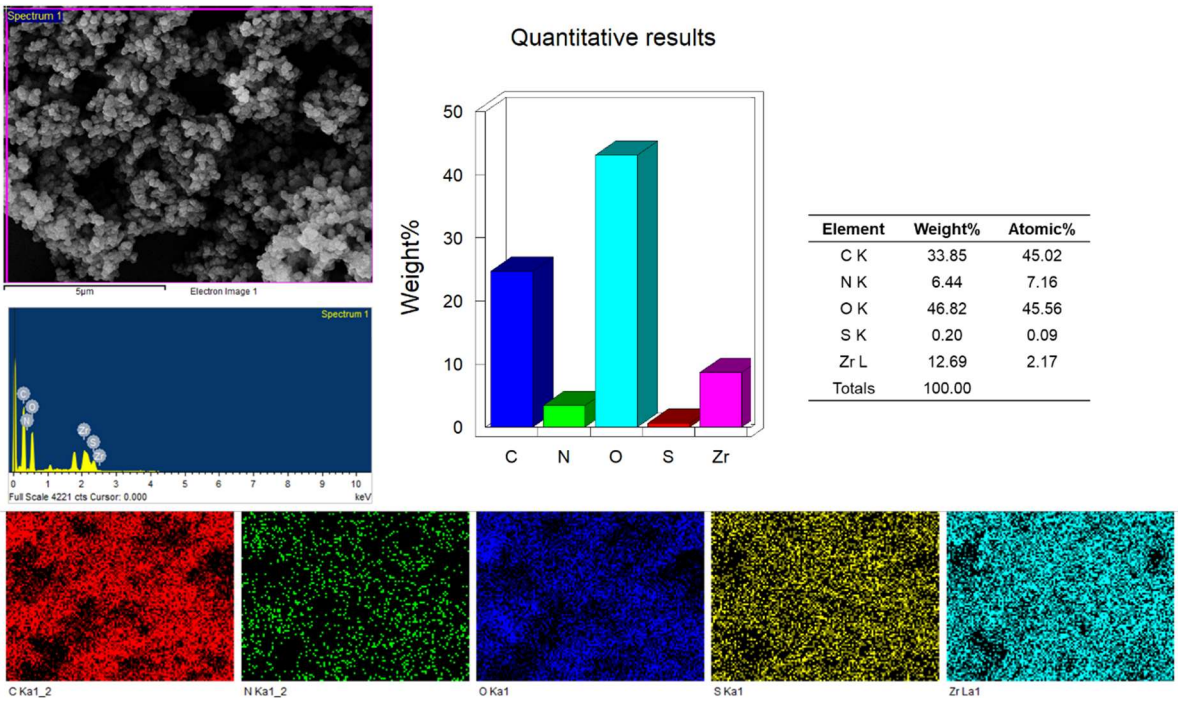

Appendix III-Figure 5.10. FESEM and EDX data of MOF-BSIPA(L) with elemental mapping.

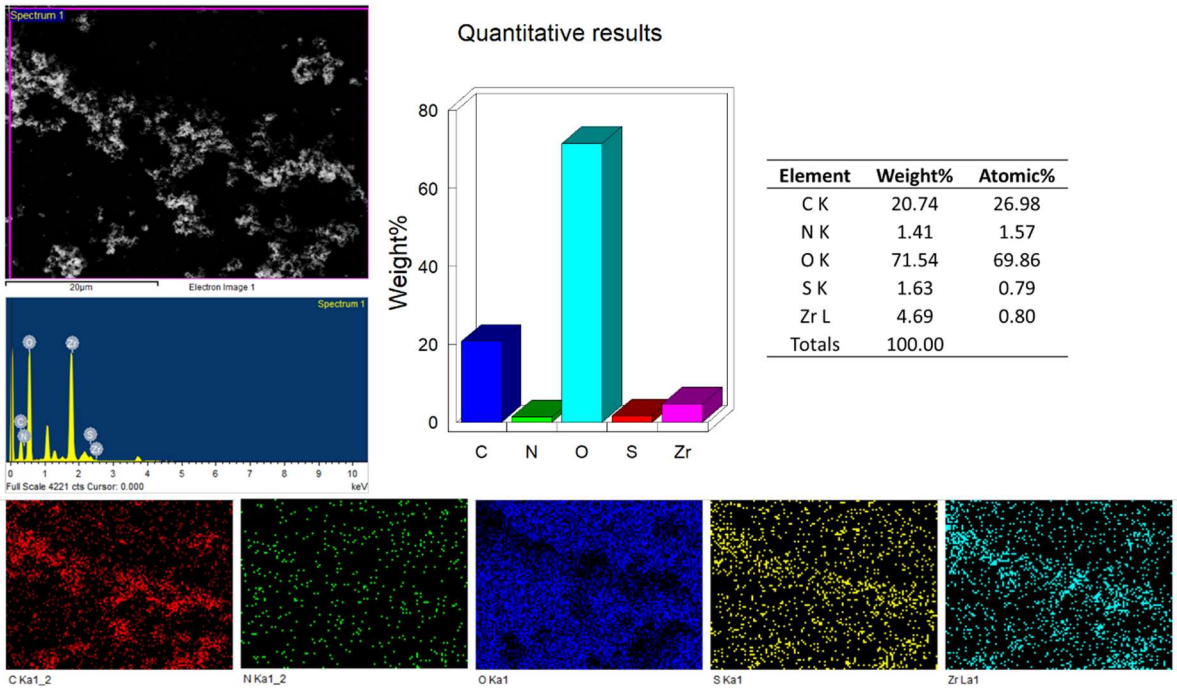

Appendix III-Figure 5.11. FESEM and EDX data of MOF-BSIPA(H) with elemental mapping.

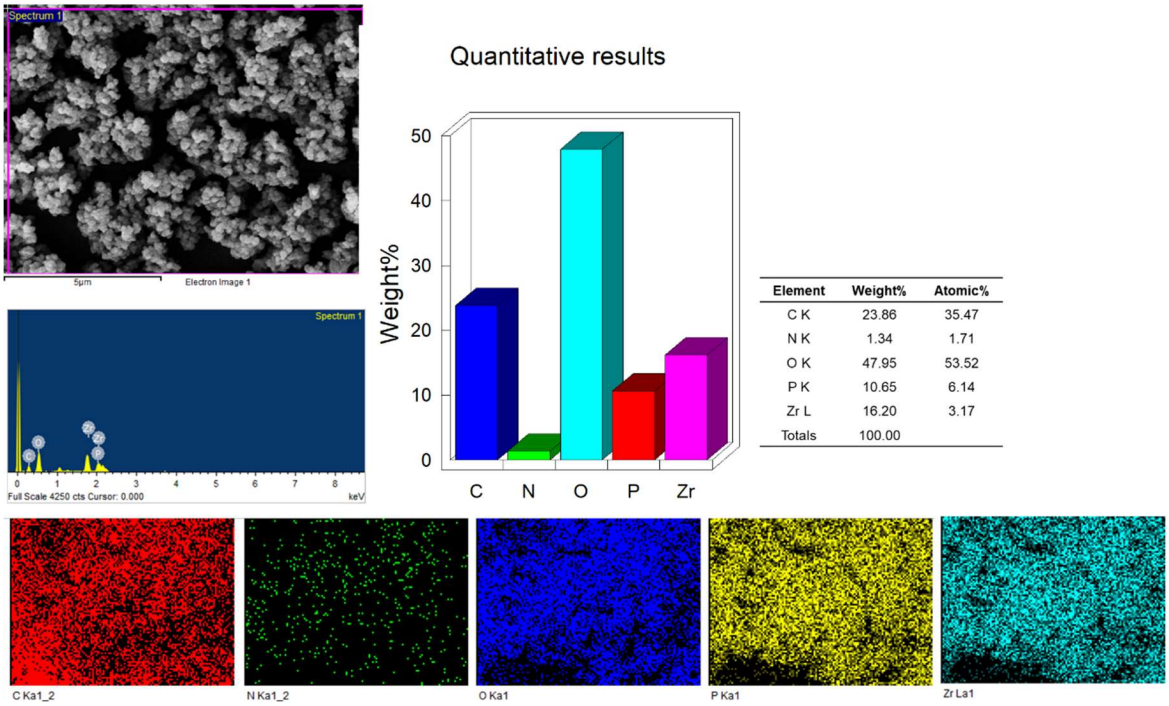

Appendix III-Figure 5.12. FESEM and EDX data of PGM-L1 with elemental mapping.

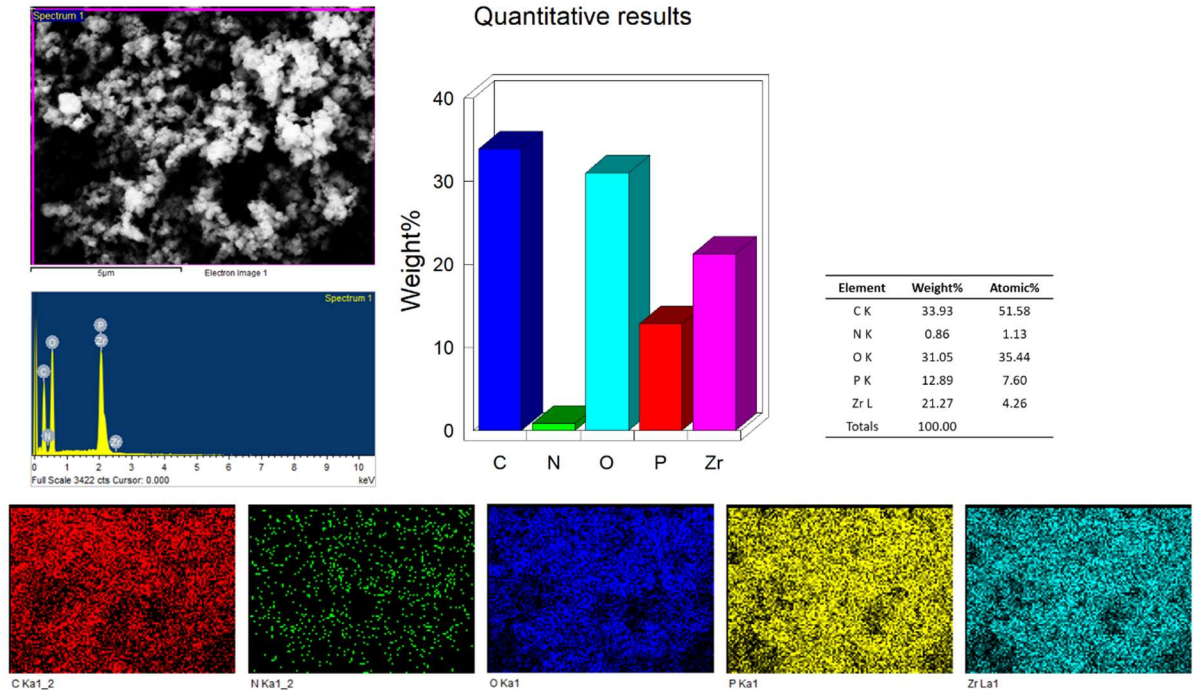

Appendix III-Figure 5.13. FESEM and EDX data of PGM-L2 with elemental mapping.

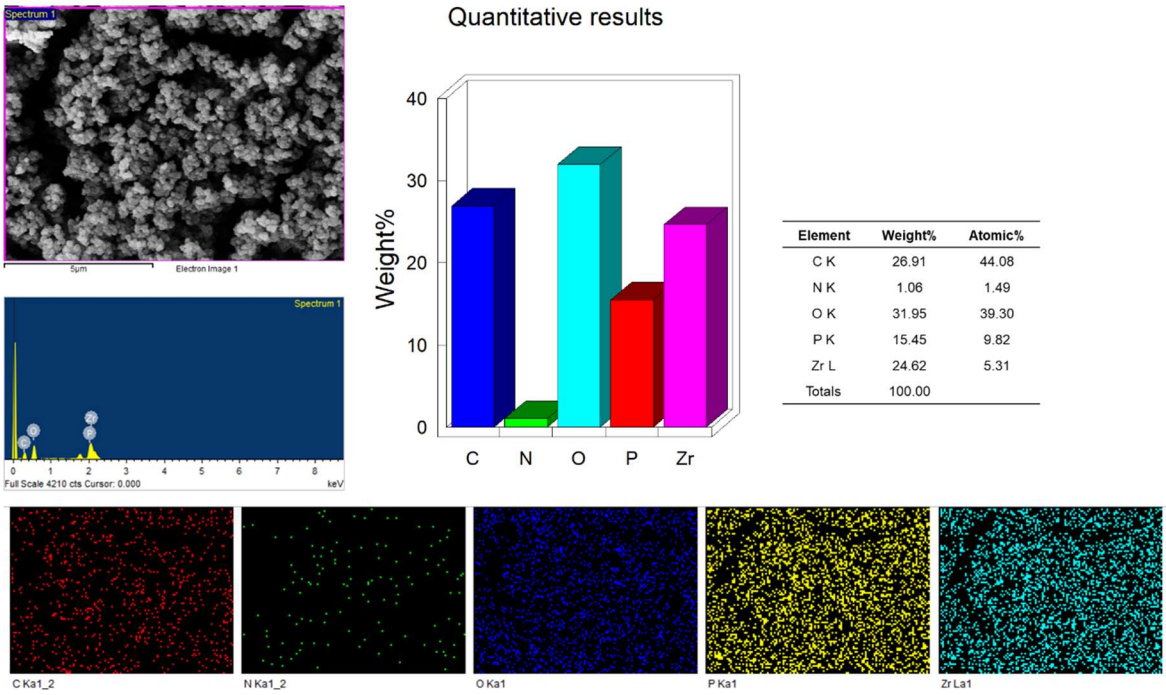

Appendix III-Figure 5.14. FESEM and EDX data of PGM-L3 with elemental mapping.

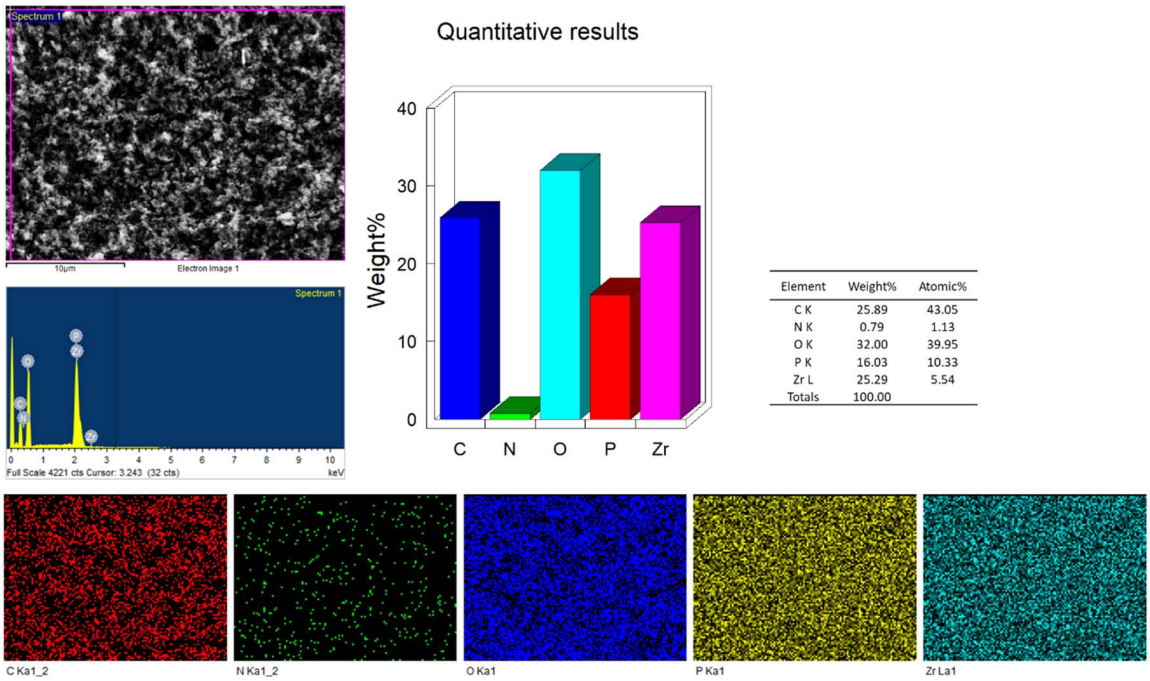

Appendix III-Figure 5.15. FESEM and EDX data of PGM-H1 with elemental mapping.

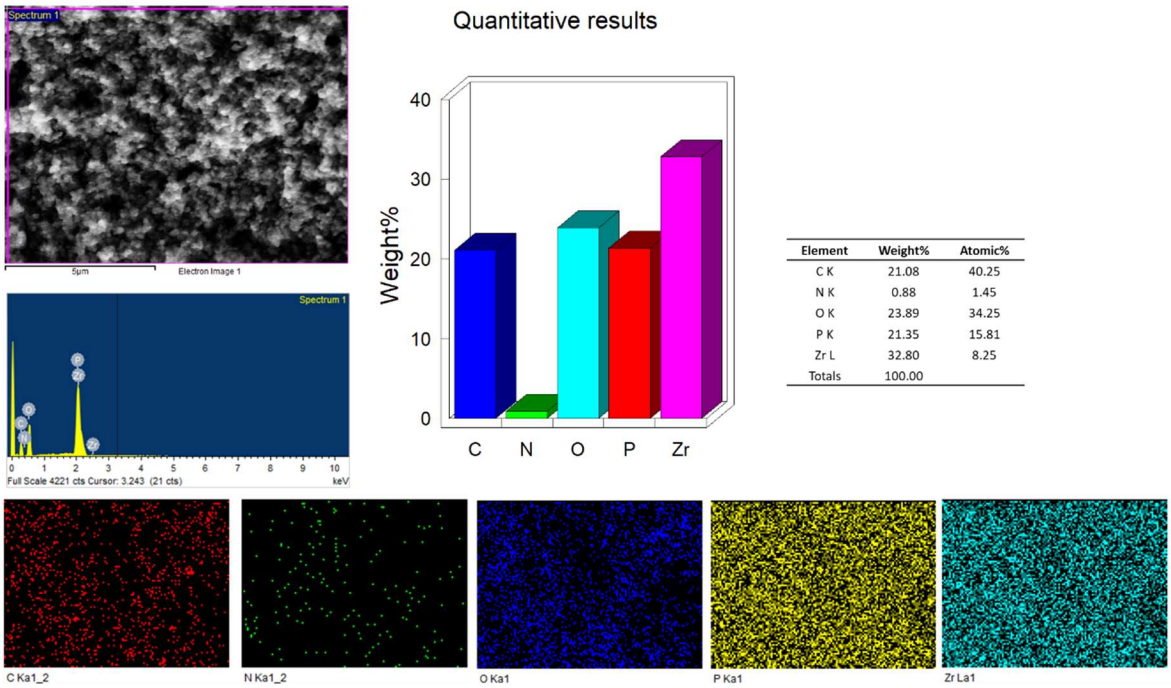

Element	Weight%	Atomic%
C K	21.08	40.25
N K	0.88	1.45
O K	23.89	34.25
P K	21.35	15.81
Zr L	32.80	8.25
Totals	100.00	

Appendix III-Figure 5.16. FESEM and EDX data of PGM-H2 with elemental mapping.

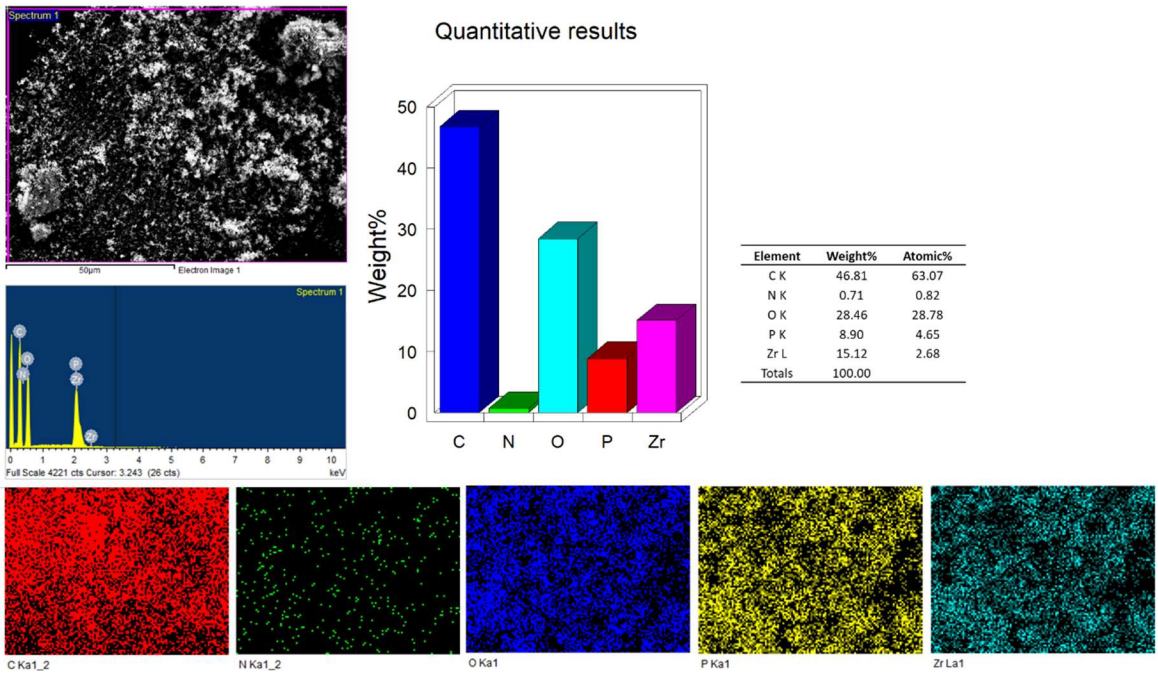

Element	Weight%	Atomic%
C K	46.81	63.07
N K	0.71	0.82
O K	28.46	28.78
P K	8.90	4.65
Zr L	15.12	2.68
Totals	100.00	

Appendix III-Figure 5.17. FESEM and EDX data of PGM-L1(Li) with elemental mapping.

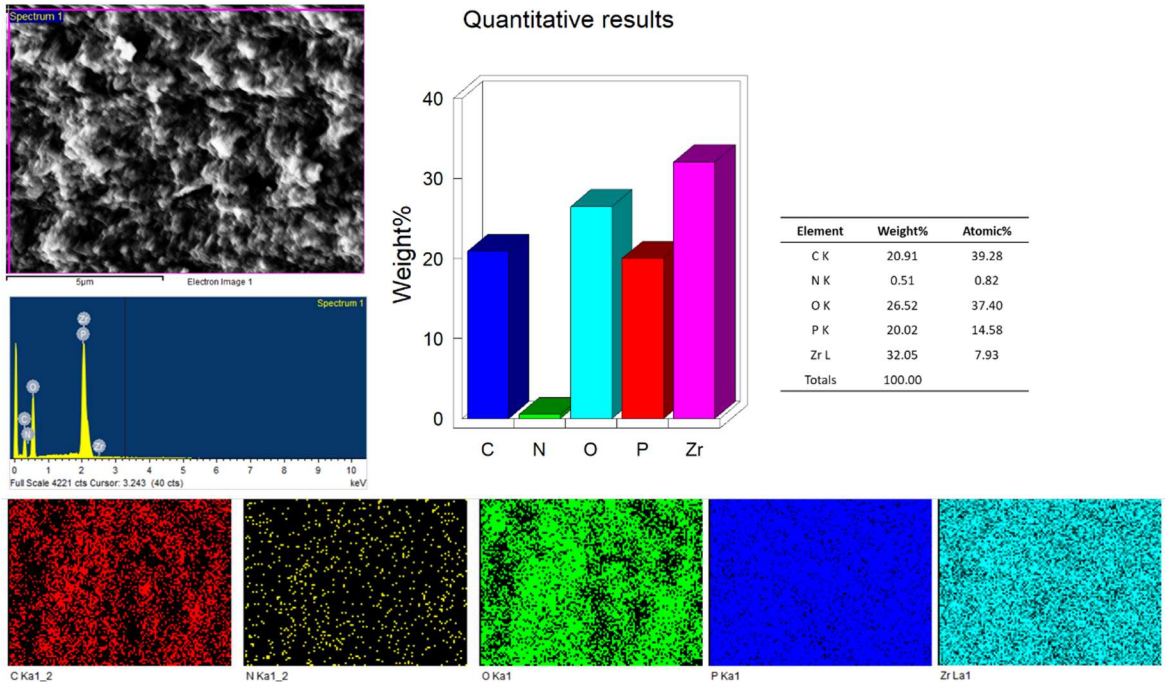

Appendix III-Figure 5.18. FESEM and EDX data of PGM-H1 with elemental mapping after proton conductivity study.

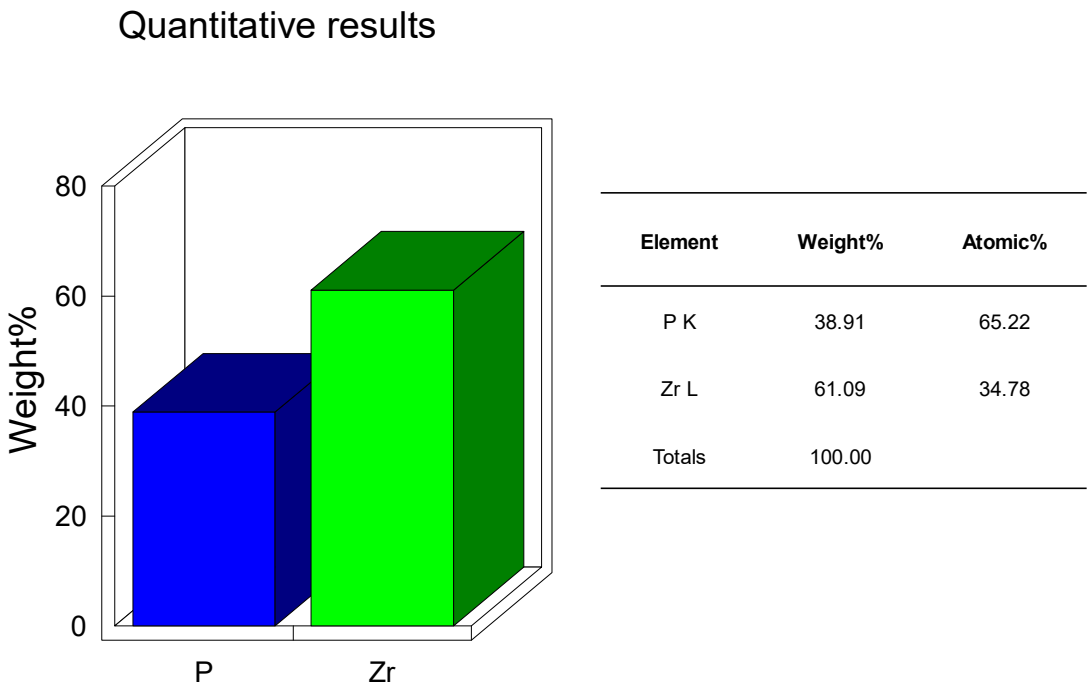

Appendix III-Figure 5.19. FESEM EDX data of PGM-L3 after proton conductivity study.

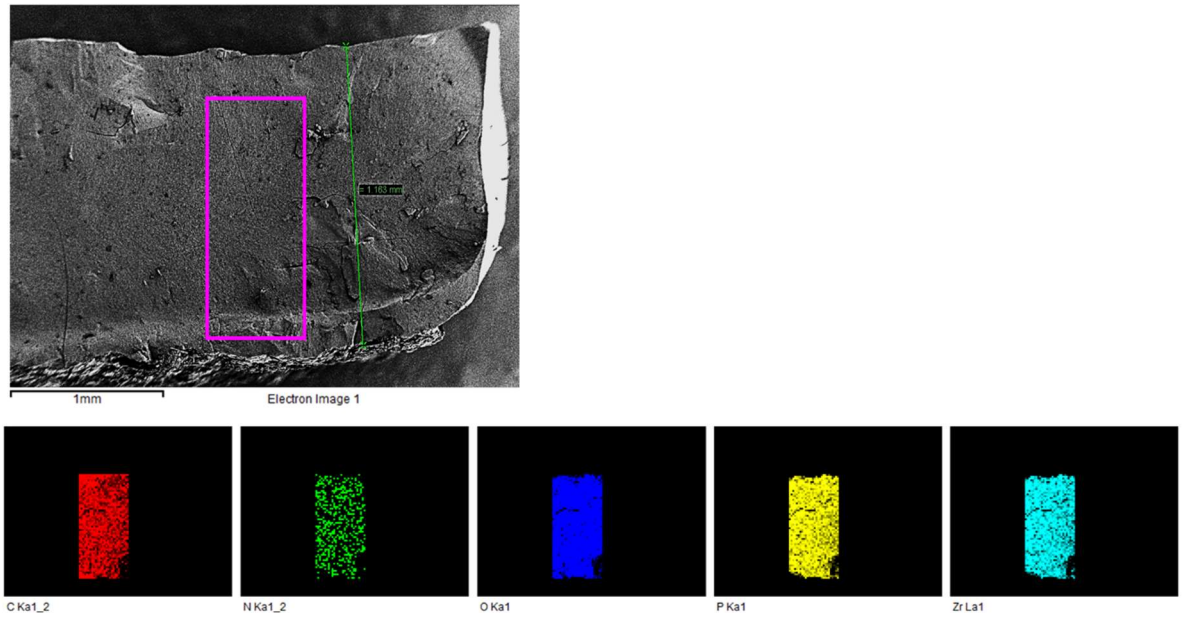

Appendix III-Figure 5.20. FESEM and EDX elemental mapping data of PGM-L3 pellet after the proton conductivity measurement.

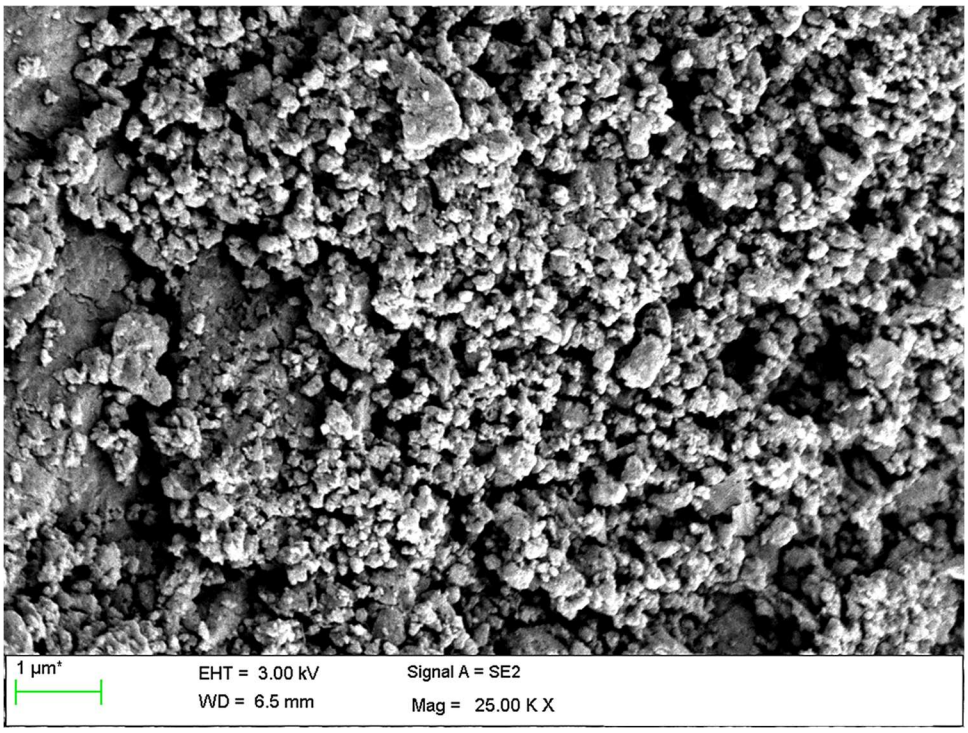

Appendix III-Figure 5.21. FESEM images PGM-L3 pellet upon grinding after proton conductivity study.

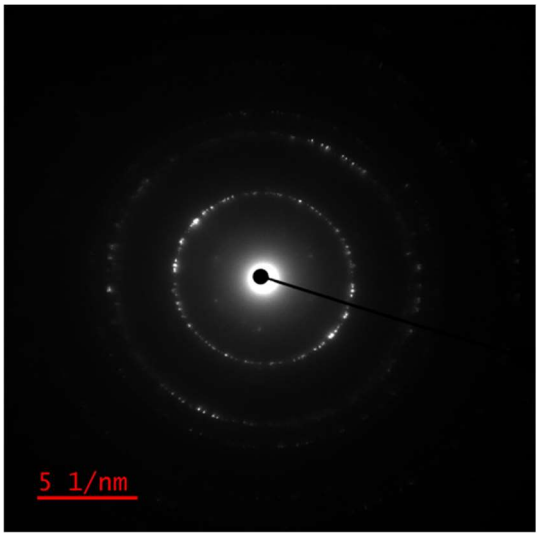

Appendix III-Figure 5.22. SAED pattern of PGM-L3.

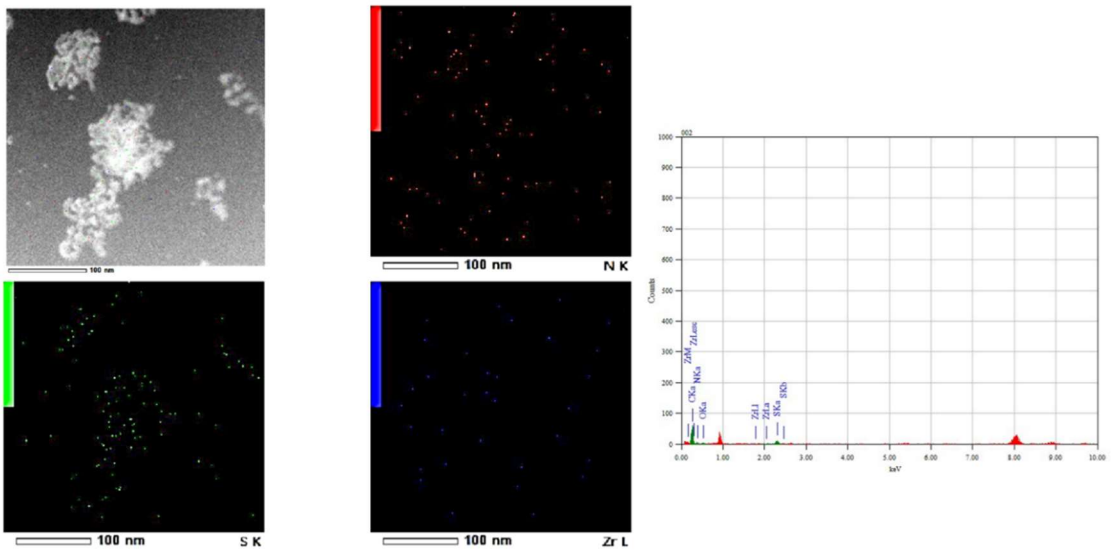

Acquisition Parameter

Acc. Voltage	:	200.0 kV	Probe Current	:	7.47500 nA
Real Time	:	30.15 sec	Dead Time	:	0 %
Live Time	:	30.00 sec	Counting Rate	:	96 Counts/sec
Preset	:	Live Time 30 sec			
Energy Range	:	0 - 40 keV	PHA Mode	:	T3

ZAF Method Standardless Quantitative Analysis
Fitting Coefficient : 0.6660

Element	(keV)	Mass%	Sigma	Atom%	Compound	Mass%	Cation	K
C K	0.277	73.27	4.85	90.08				23.3104
N K	0.392	0.89	0.24	0.93				0.3396
O K	0.525	5.39	2.50	4.98				2.0014
S K	2.307	2.34	0.59	1.08				5.1028
Zr L	2.042	18.11	24.83	2.93				69.2458
Total		100.00		100.00				

Appendix III-Figure 5.23. TEM and EDX data of MOF-BSIPA(H) with elemental mapping.

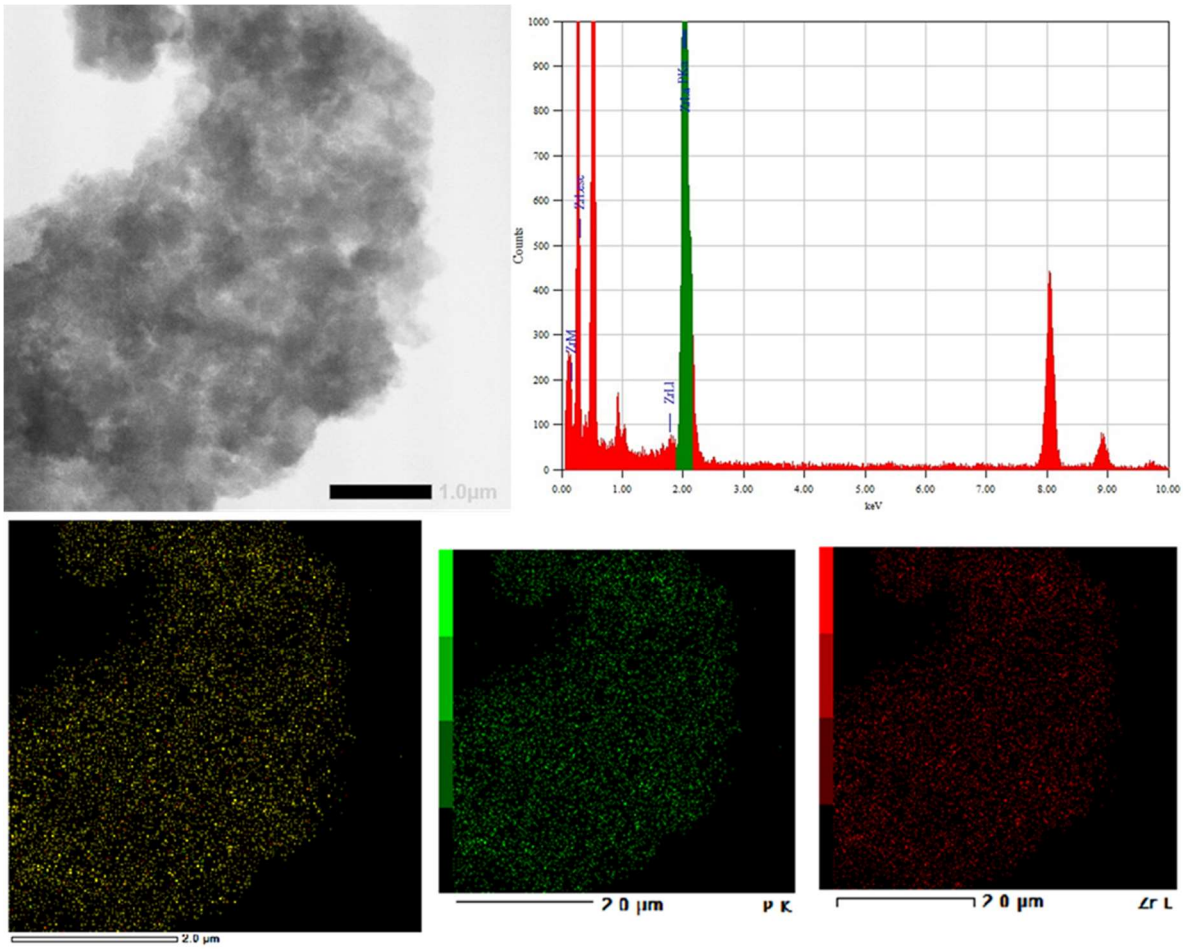

Acquisition Parameter

Acc. Voltage	:	200.0 kV	Probe Current	:	7.47500 nA
Real Time	:	149.39 sec	Dead Time	:	2 %
Live Time	:	144.92 sec	Counting Rate	:	613 Counts/sec
Preset	:	Real Time 300 sec			
Energy Range	:	0 - 40 keV	PHA Mode	:	T4

ZAF Method Standardless Quantitative Analysis
Fitting Coefficient : 0.7554

Element	(keV)	Mass%	Sigma	Atom%	Compound	Mass%	Cation	K
P K	2.013	3.40	0.06	9.40				8.5723
Zr L	2.042	96.60	2.27	90.60				91.4277
Total		100.00		100.00				

Appendix III-Figure 5.24. TEM and EDX data of PGM-L1 with elemental mapping.

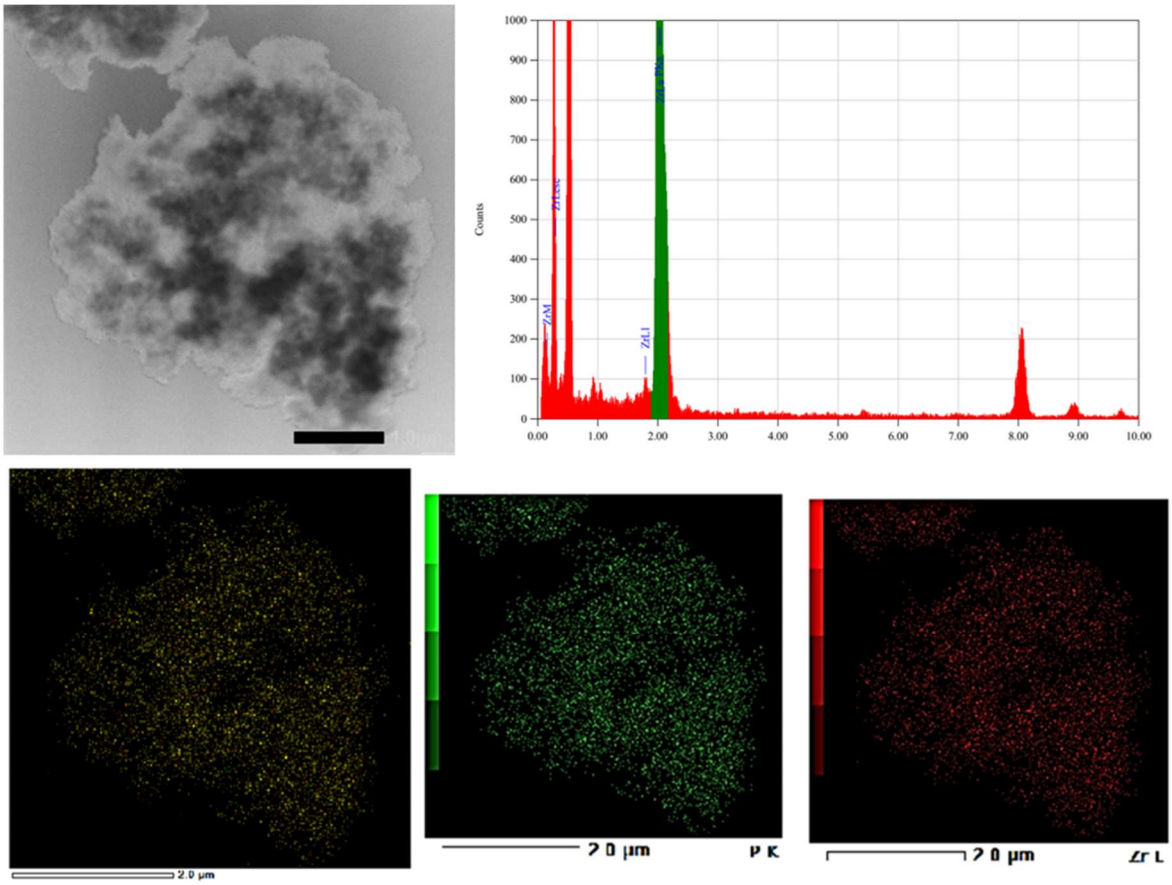

Acquisition Parameter

Acc. Voltage	:	200.0 kV	Probe Current	:	7.47500 nA
Real Time	:	300.00 sec	Dead Time	:	1 %
Live Time	:	294.96 sec	Counting Rate	:	332 Counts/sec
Preset	:	Real Time 300 sec			
Energy Range	:	0 - 40 keV	PHA Mode	:	T4

ZAF Method Standardless Quantitative Analysis
Fitting Coefficient : 0.6814

Element	(keV)	Mass%	Sigma	Atom%	Compound	Mass%	Cation	K
P K	2.013	3.51	0.06	9.68				8.8281
Zr L	2.042	96.49	2.03	90.32				91.1719
Total		100.00		100.00				

Appendix III-Figure 5.25. TEM and EDX data of PGM-L3 with elemental mapping.

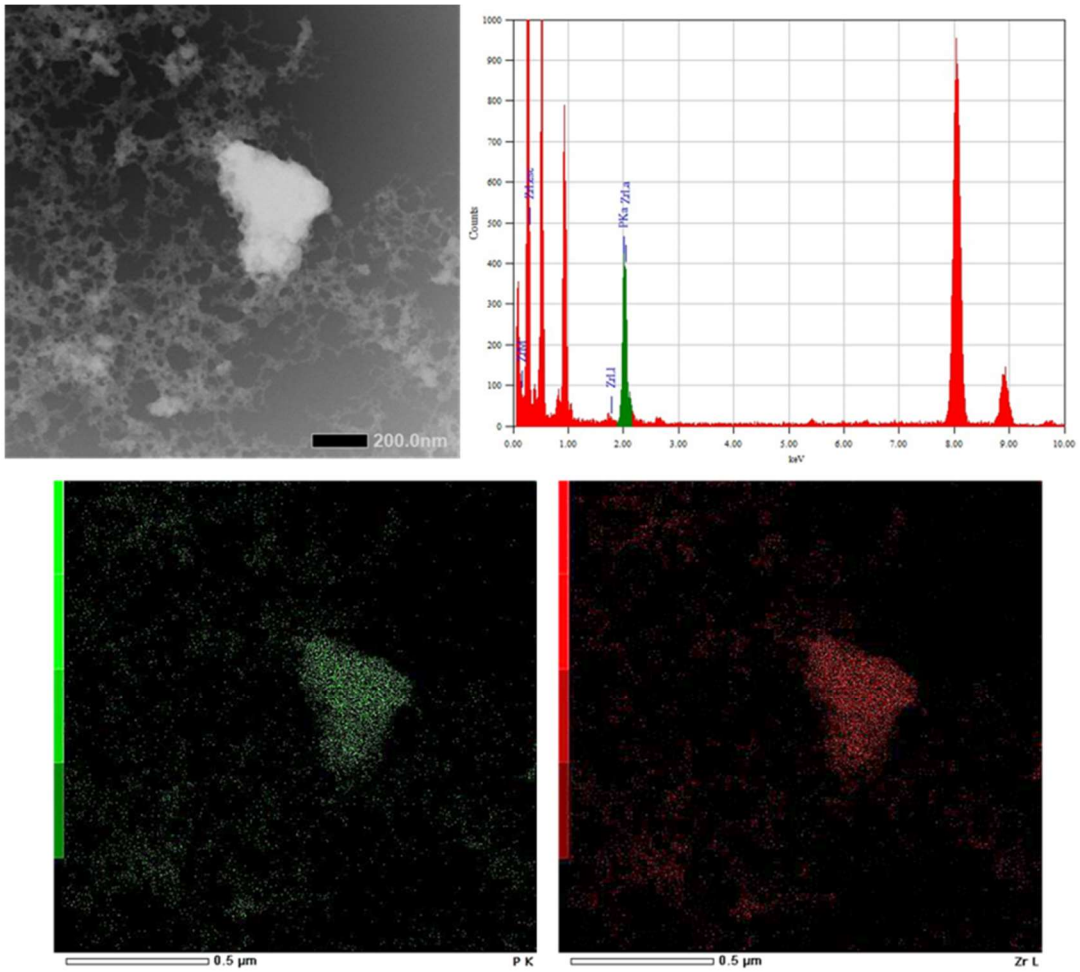

Acquisition Parameter

Acc. Voltage	:	200.0 kV	Probe Current	:	7.47500 nA
Real Time	:	300.00 sec	Dead Time	:	1 %
Live Time	:	295.48 sec	Counting Rate	:	215 Counts/sec
Preset	:	Real Time 300 sec			
Energy Range	:	0 - 40 keV	PHA Mode	:	T4

ZAF Method Standardless Quantitative Analysis

Fitting Coefficient : 0.9396

Element	(keV)	Mass%	Sigma	Atom%	Compound	Mass%	Cation	K
P K	2.013	11.75	0.44	28.17				26.1446
Zr L	2.042	88.25	10.19	71.83				73.8554
Total		100.00		100.00				

Appendix III-Figure 5.26. TEM EDS data of PGM-H2 with elemental mapping.

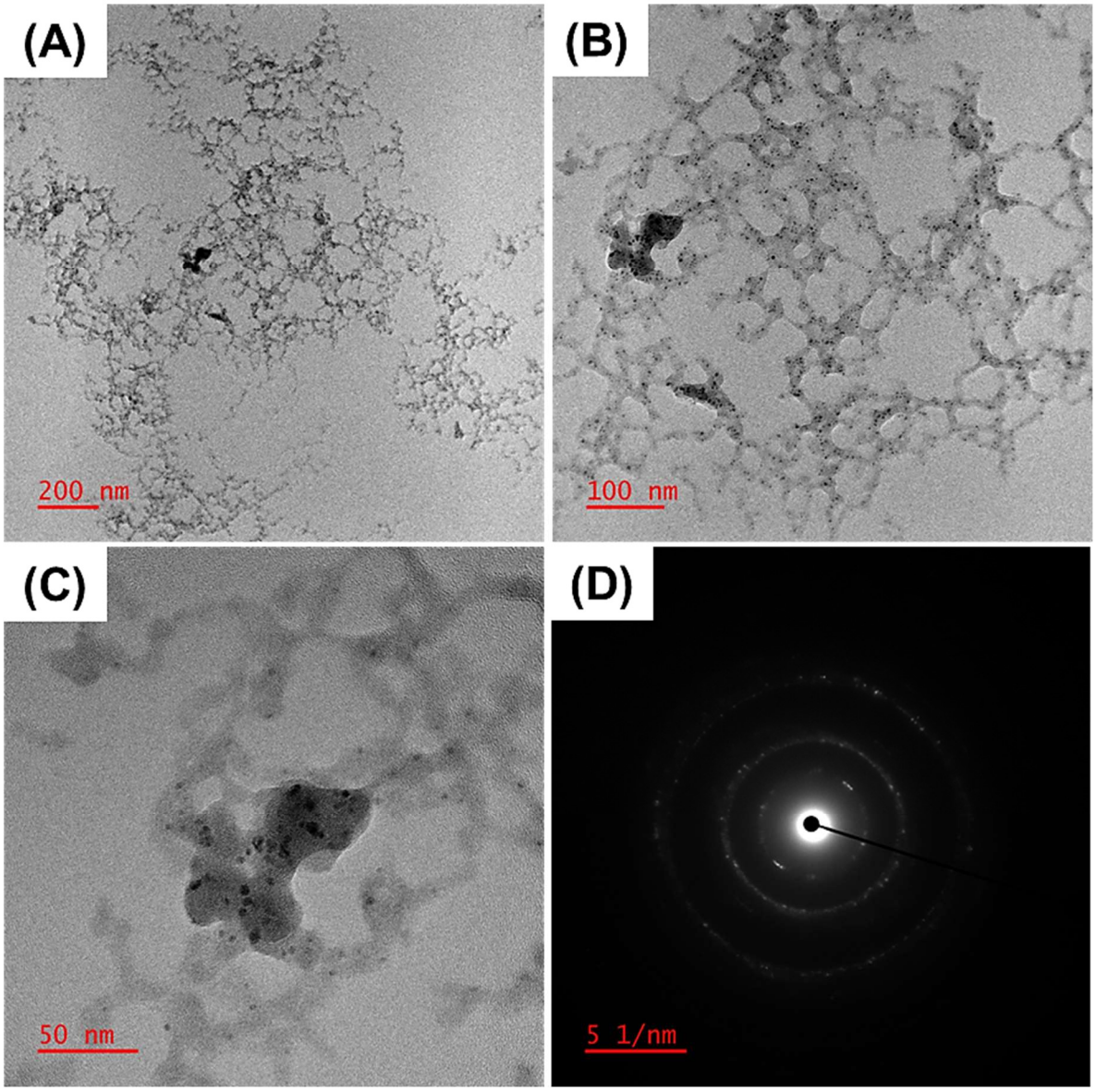

Appendix III-Figure 5.27. TEM images of PGM-H2 **(A-C)** at different magnification and **(D)** SAED data representing the crystallinity of the material.

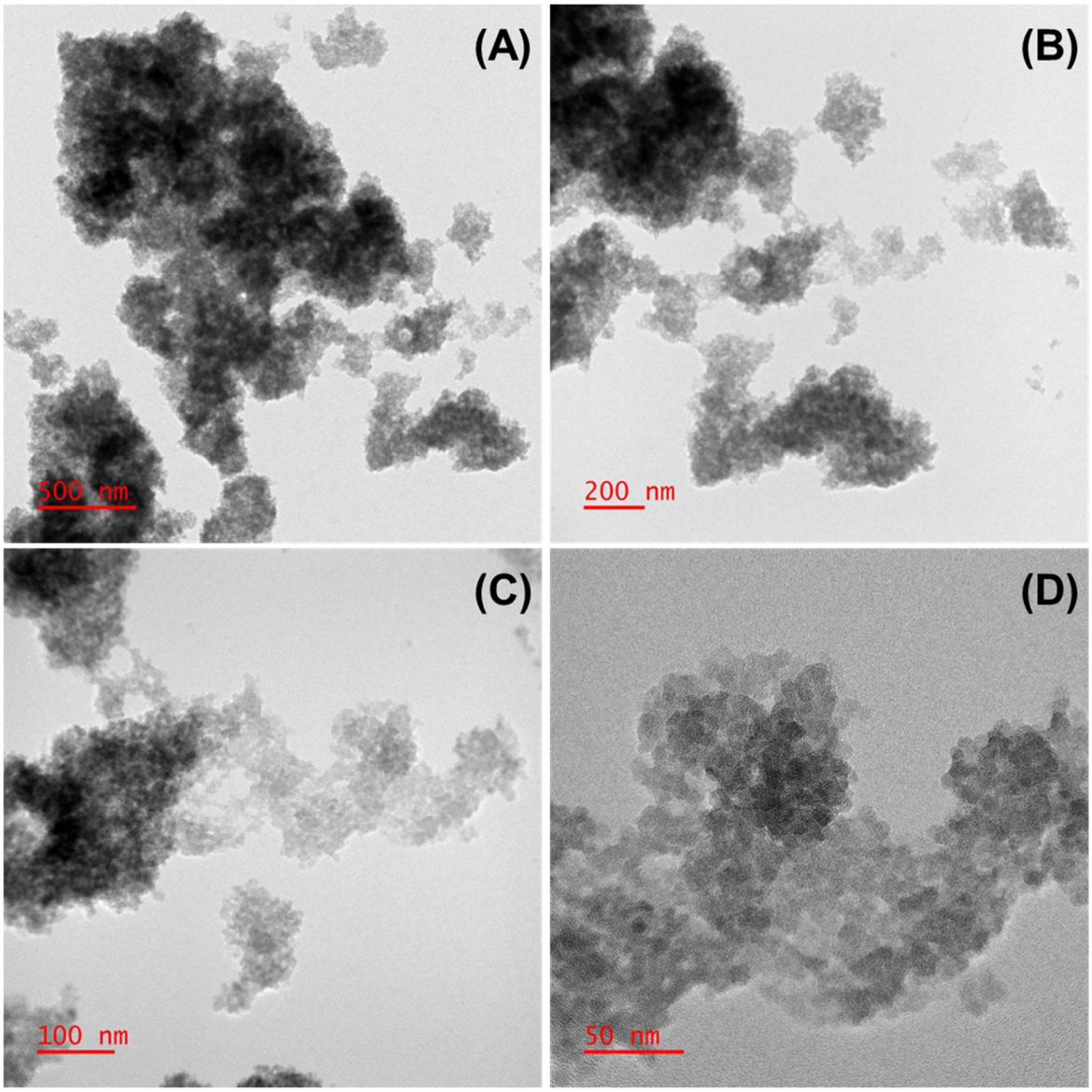

Appendix III-Figure 5.28. TEM image of PGM-L3 at different magnification **(A-D)** after keeping the sample for proton conductivity study.

Dynamic vapor sorption study (DVS)

The dynamic vapor sorption (DVS) was measured for UiO-66 NH_2, PGM-L1, PGM-L3, PGM-H1, PGM-H2 with dry powder samples.

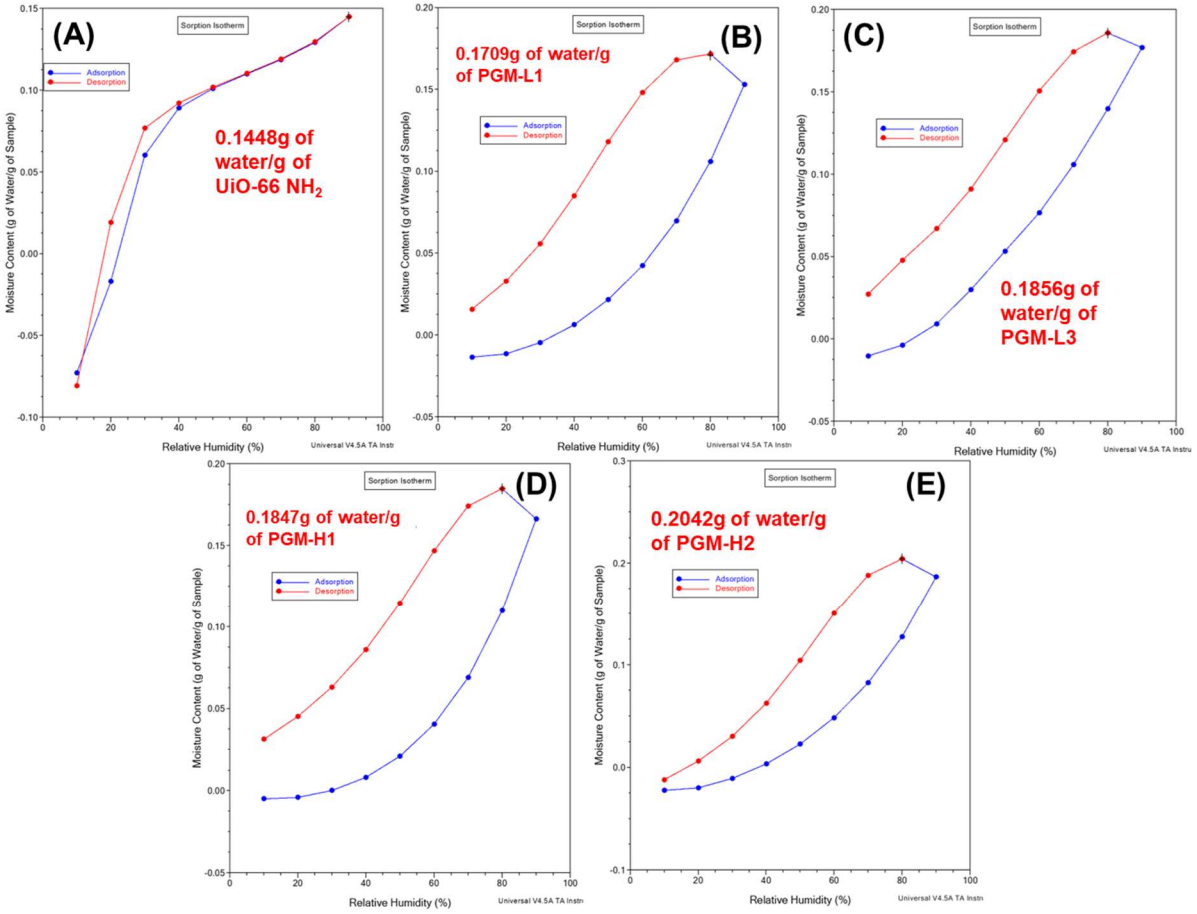

Appendix III-Figure 5.29. DVS adsorption-desorption isotherm of **(A)** UiO-66- NH_2, **(B)** PGM-L1, **(C)** PGM-L3, **(D)** PGM-H1, **(E)** PGM-H2.

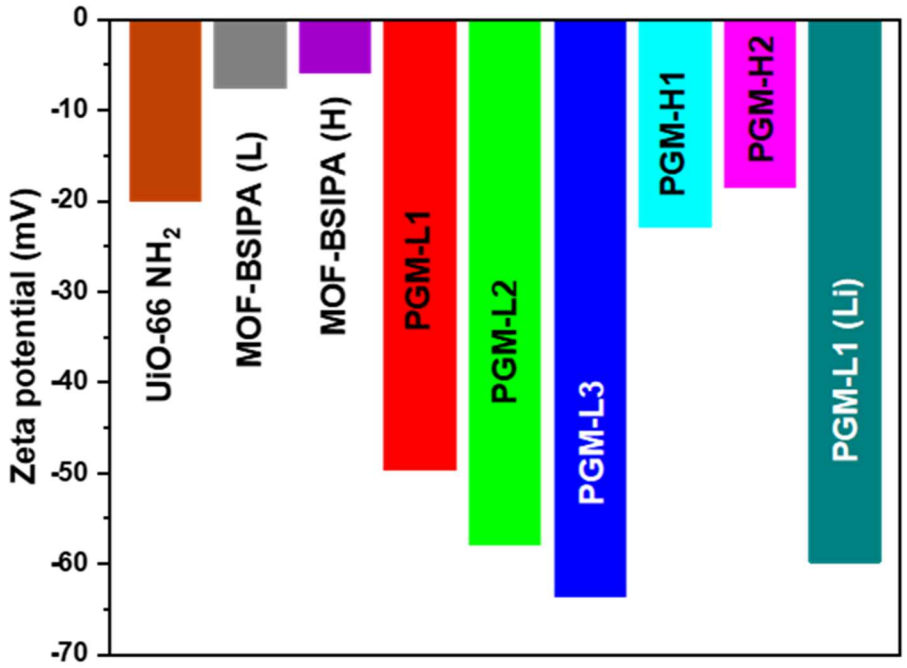

Appendix III-Figure 5.30. Zeta potential of all the PGM samples along with UiO-66-NH_2 and MOF-BSIPA in HPLC water.

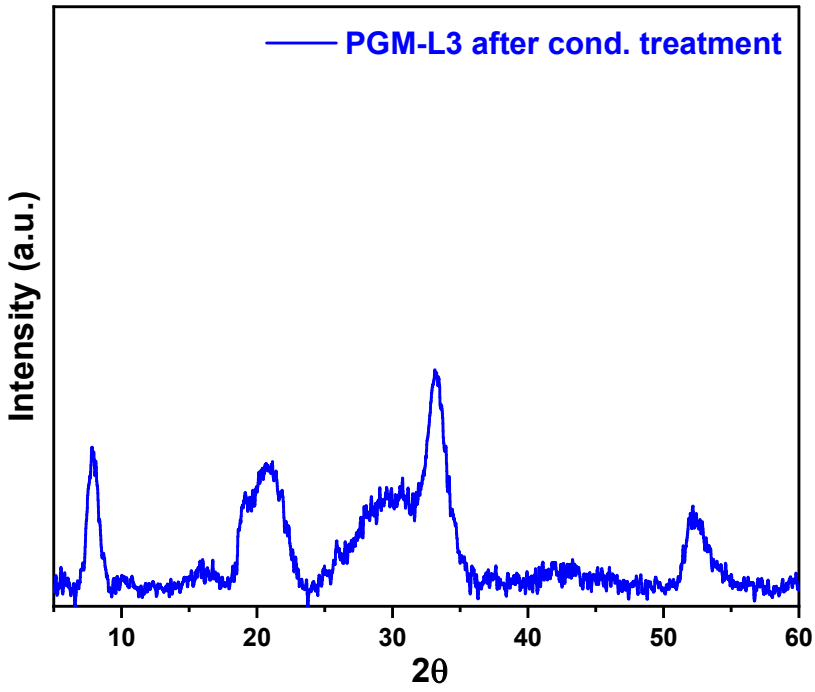

Appendix III-Figure 5.31. PXRD pattern of PGM-L3 sample after proton conductivity measurement.

Sample preparation and methodology of the proton conductivity measurements

Impedance measurements were performed using a 2-electrode setup in parallel plate mode. A similar protocol for sample preparation and experimental setup were followed for all the samples as reported earlier. The MOF (approximately 400 mg) was powdered and pelletized as a sandwich between two carbon wafers, using a custom-made pellet maker die, using a hydraulic pressure of 2 tons for 2 minutes. After the pellets were prepared, they were checked for any cracks or breakage. The thickness of the pellets was then measured carefully using a screw gauze. To determine the thickness of each pellet, three readings from screw gauze were averaged to minimize the manual error. The use of pellet maker die ensures that all the pellets have identical diameter. As the same pellet-maker die and same electrodes were used for all the samples, thus equal surface area of contact between the sample and the electrodes should be achieved. PGM-L1, PGML2, PGM-L3, PGM-H1 and PGM-L1(Li) pellets were then placed between the two electrodes such that, the carbon wafers of the pellet were in contact with each of the stainless-steel plates of the two electrodes. This electrode setup was then placed in a double-walled incubating chamber maintaining the required humidity and temperature. The inner chamber of the incubator maintains the required temperature by circulating hot air. And the humidity is maintained by a separate flow of water vapor inside this chamber. The impedance spectra were recorded at the open circuit potential for each sample, using a sinusoidal signal of amplitude 5 mV. The frequency was swept from 1 MHz to 1 Hz. Before any measurement at a given temperature and relative humidity (RH), the sample pellet was kept for two hours to equilibrate.

The two-electrode set up kept inside incubator impedance measurements were carried out between a temperature range from 30°C to 80 °C and relative humidity between 75% - 98%.

Proton conductivity measurement under various temperature

Proton conductivity by two probe electrochemical impedance spectroscopy (EIS) was conducted using an Ametek (PARSTAT MC) electrochemical workstation operated with VersaStudio software between a frequency range from 1 Hz to 100 KHz. The conductivities of the pellets were calculated from the following equation:

Conductance **(L) = (1/R) = σ** × **(A/d)** ……. Eqn (4)

Thus, conductivity (**σ**) = (L) × **d/A** = (1/**R**) × (**d/A**) …….. Eqn (5)

Where **R** is resistance of sample; σ is conductivity of the sample; **d** = thickness of pellet. **A** = area of cross section of pellet = 1.32665 cm^2.

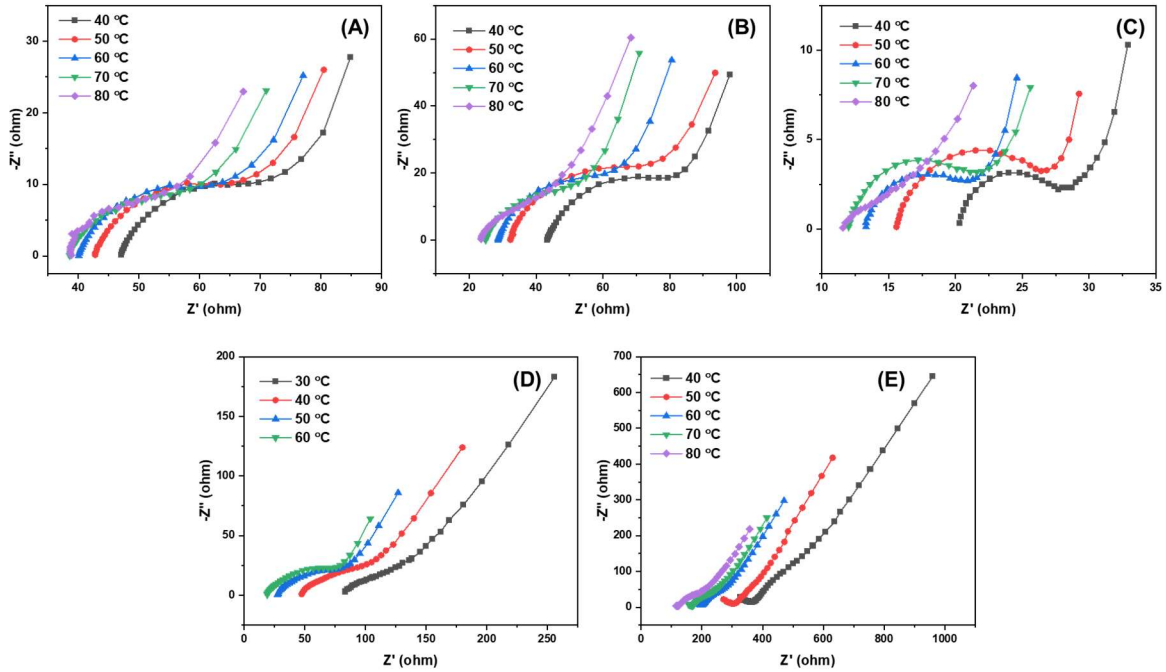

Appendix III-Figure 5.32. Nyquist plot of impedance spectra of PGM-L1 **(A)**, PGM-L2 **(B),** PGM-L3 **(C)**, PGM-H1 **(D)** and PGM-L1(Li) **(E).**

Equivalent circuit diagram

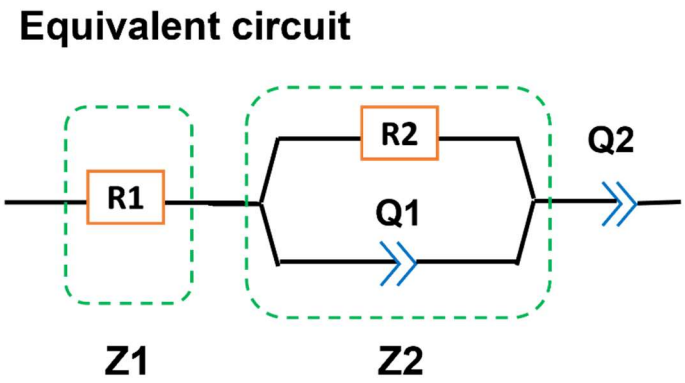

Impedance data were fitted to the most suitable equivalent circuit mentioned above with the help of EC-Lab software. The equivalent circuit is composed of three major components connected to each other in series. The pellet impedance (Z1), impedance at the electrode-electrolyte junction/interface (Z2) and a constant phase element (Q2) are connected in series. The constant phase element (Q2) accounts for the linear low frequency region of the Nyquist plot of impedance spectrum. Z1 is due to the resistance (R1). But, Z2 consists of a resistance (R2) and a constant phase element (Q1) connected in parallel mode. Here R1 accounts for the bulk resistance of the pellet, which is the resistance faced during proton conduction through the polymer chain grafted MOF units. And R2 represents the charge transfer resistance existing between the electrodes and the pellet electrolyte. Here, it should be noted that, charge transfer resistance R2 is not associated with the conductivity of the electrolyte. Instead R1 is the crucial factor which quantifies the resistance of the bulk material. R2 depends on the (a) inter-grain resistance, (b) resistance created between the carbon paper and sample particles (b) resistance existing between electrode surface and carbon paper of pellet. The bulk resistance of the electrolyte i.e., R1, depends on (a) intrinsic conductivity of the pelletized sample (b) thickness of the pellet and (c) area of cross section of the pellet. Thus, to determine the proton conductivity of the pelletized sample from the R1 value both of the other two factors (i.e., area of cross section and thickness of pellet) should be taken as unity.

Determination of activation energy

Activation energies (E_a) for proton conductivity of all the samples were calculated from the Arrhenius plot constructed between ln(σT) and 1000/T.

From Arrhenius equation, $\boldsymbol{\sigma T = \sigma_0 \times \exp(-E_a/RT)}$

σ = proton conductivity of the sample

T = Temperature in Kelvin

$\mathbf{E_a}$ = Activation energy of proton conduction

R= Ideal gas constant

Arrhenius equation can be restructured as $\boldsymbol{\ln(\sigma T) = \ln\sigma_0 - (Ea/RT)}$

Or, $\boldsymbol{\ln(\sigma T) = \ln\sigma_0 + \{-E_a/(1000\times R)\ (1000/T)\}}$

From the plot between **ln(σT)** and **1000/T**, the slope of the straight line = $\boldsymbol{- E_a/1000\times R}$

Appendix IV

NMR studies of PGNT3 sample

PGNT3 was dispersed in DMSO-d6 and sampled for ^{1}H-NMR studies. The spectra was also analyzed using MestReNova software and fitted in order to isolate the compound peaks and solvent peaks. DMSO-d6 solvent peak and H_2O peak are observed at 3.3 and 2.5 ppm respectively. 1,2,4-triazole pendent ring was observed at ~8ppm and imidazole protons appear at ~7ppm. The intensity of the triazole ring protons were observed to be much higher when compared to imidazole ring protons owing to the fact that the triazole units consisting the block copolymer chains are much higher in number with respect to imidazole units. Peak ~1ppm is also observed which appears due to the presence of free amine functionality on the surface of MWCNT upon modification with EDA.

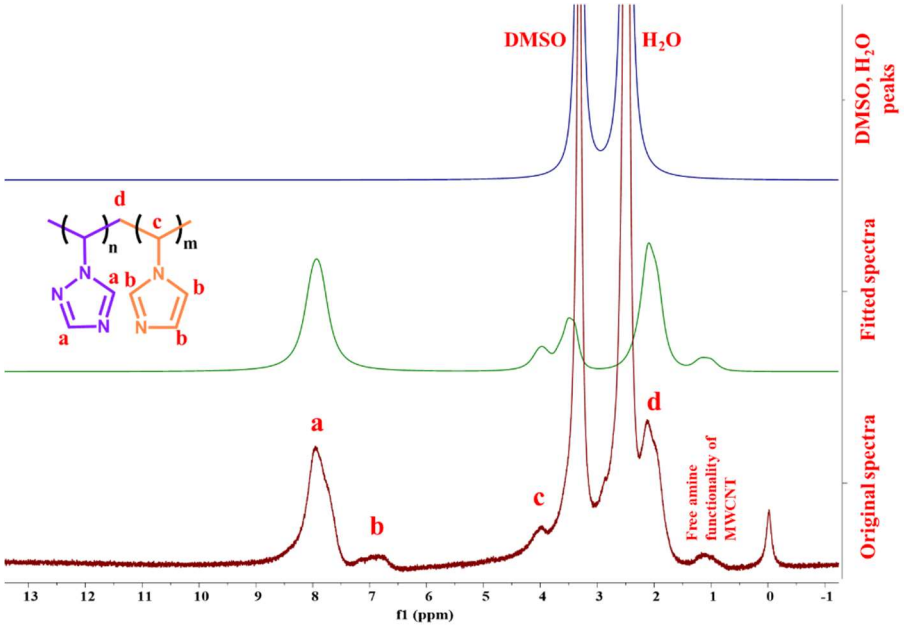

Appendix IV-Figure 6.1. ^{1}H NMR spectra along with the fitted spectra and solvent peak isolation of PGNT3 in DMSO-d6.

Inherent viscosity of OPBI used

The inherent viscosity (I.V.) of the poly (4,4'-diphenyl-5,5'-bibenzimidazole) (**OPBI**) polymer was measured at 30 °C in water bath with the help of Cannon (model F725) Ubbelohde capillary dilution viscometer and the I.V. values were calculated from the flow time data. A solution of **OPBI** in H_2SO_4 was used for the viscosity measurement. The concentration of the **OPBI** solution in H_2SO_4 is 0.2 g/dL. The obtained I.V. value of the synthesised **OPBI** is 2.1 dL/g.

Detachment of polymer chains from the MWCNT surface for molecular weight measurements

Appendix IV-Table 6.1. Summary of the molecular weights ($\bar{M}_n$), ($\bar{M}_w$) and Đ of bare polymer chains after cleaving the polymer from PNVT-*g*-MWCNT [**PGNT1i-PGNT3i**]. All of these data were obtained from the controlled reactions of **PGT1** to **PGNT3** are mentioned as intermediates (**i**).

Sample name	$\bar{M}_n$	$\bar{M}_W$	Đ
PGNT1i	6916	7399	1.07
PGNT2i	11281	12167	1.08
PGNT3i	15136	16614	1.09

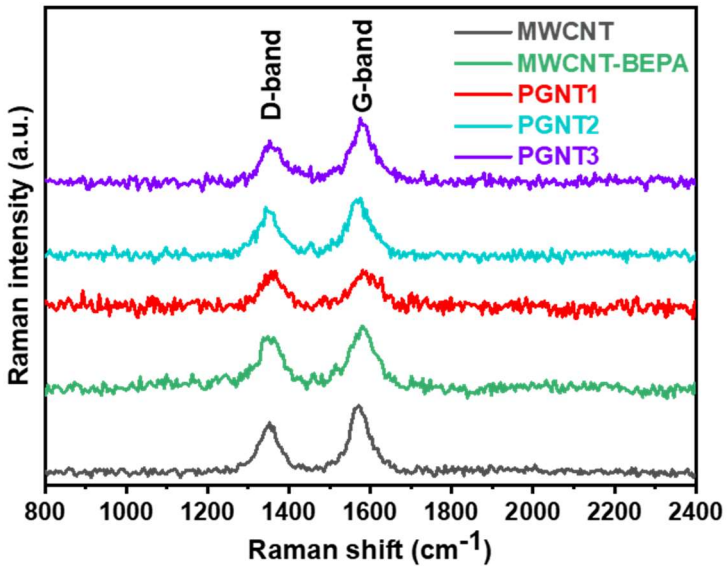

Appendix IV-Figure 6.2. RAMAN spectra of MWCNT, MWCNT-BEPA, PGNT1, PGNT2 And PGNT3 samples.

BET isotherm analysis for N_2 adsorption

MWCNT and polymer-*g*-MWCNT samples were activated and degassed at 100 °C under vacuum for 24 h prior to N_2 sorption analysis. The temperature for adsorption measurements (77 K) was controlled by using the refrigerated bath of liquid nitrogen.

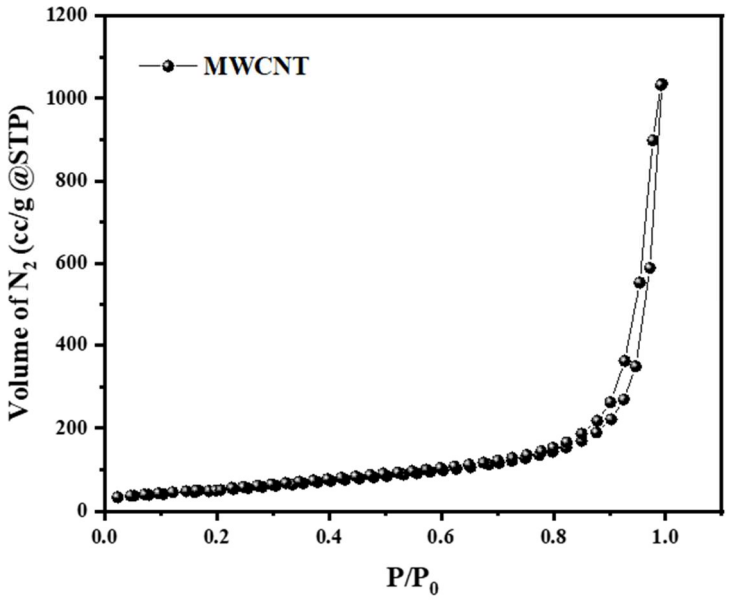

Appendix IV-Figure 6.3. BET isotherm of MWCNT.

Morphology study

Field Emission Scanning Electron Microscopy (FESEM)

The morphology of MWCNT, MWCNT-COOH, MWCNT-NH_2, MWCNT-BEPA, PGNT1, PGNT2, PGNT3 and all the PGNT1-@OPBI composite membranes were evaluated by using powder samples which were dispersed in dry ethanol by using sonication and drop casted on a clean piece of glass slide. The slides were dried at 70 °C overnight to remove the solvent traces from the sample cavity and were gold coated before analysis. The FESEM cross section morphology of the membrane samples were done by breaking the membranes in liquid nitrogen medium. Samples were gold coated before imaging in FESEM.

Transmission electron microscopy (TEM)

The MWCNT and polymer modified MWCNT powder samples were prepared by placing a drop of the sample dispersed in ethanol on the carbon coated side of the copper grid (200 mesh) and were dried overnight in an oven. The composite samples were prepared by placing a drop of formic acid dispersed PGNT1-1% @OPBI and PGNT1-2.5% @OPBI solution on carbon coated side of the copper grids (200 mesh).

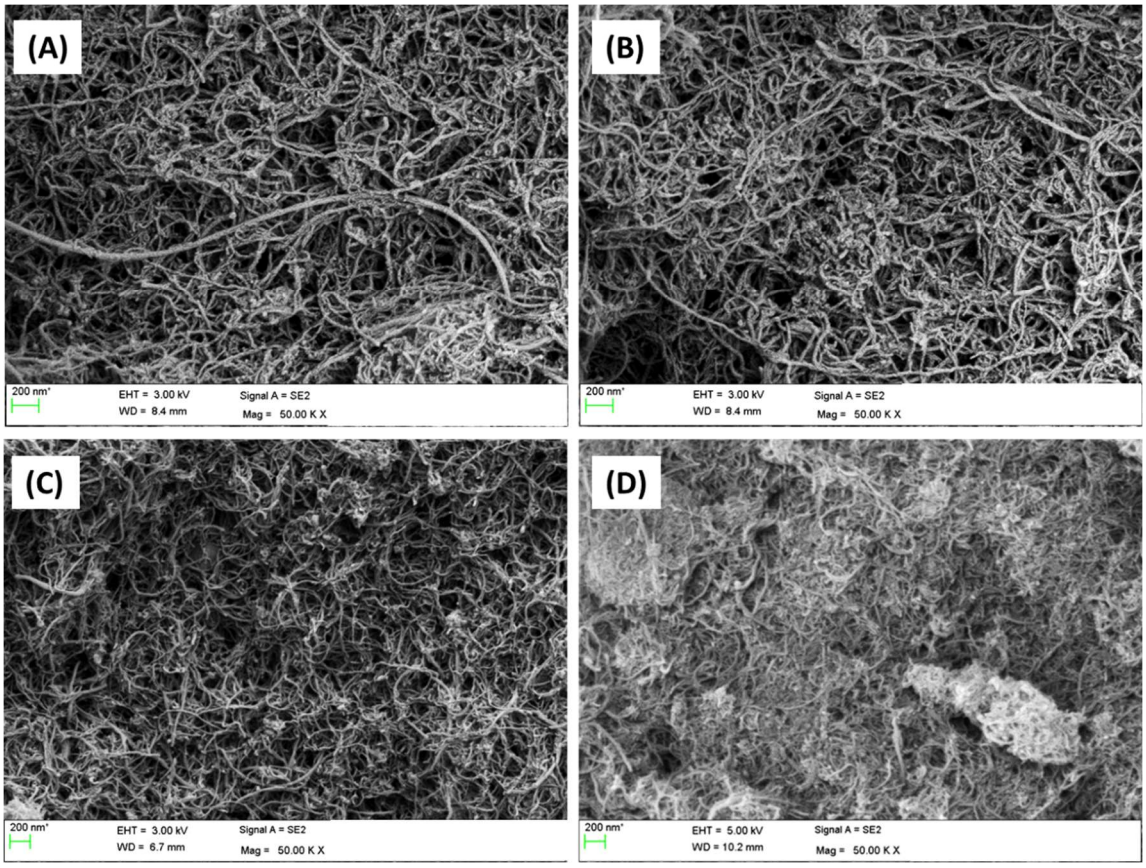

Appendix IV-Figure 6.4. (A) FESEM image of **MWCNT**, **(B) MWCNT-COOH**, **(C) MWCNT-NH_2**, **(D) MWCNT-BEPA**.

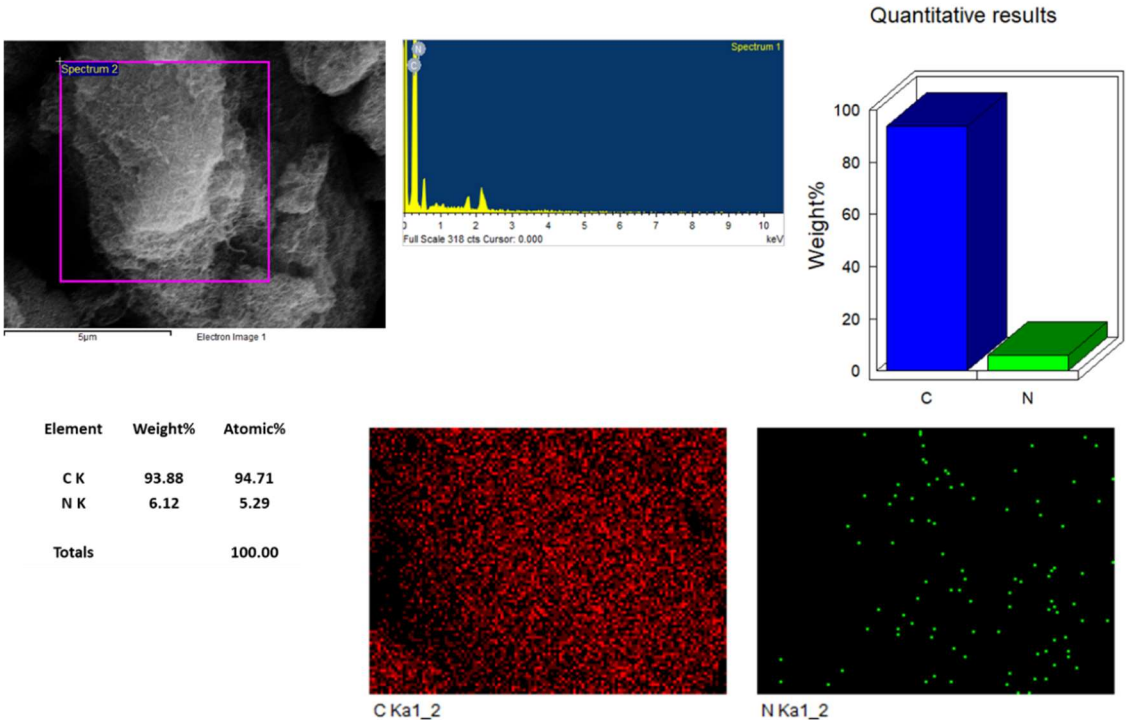

Appendix IV-Figure 6.5. Elemental mapping of MWCNT-NH_2 using FESEM and EDX analysis.

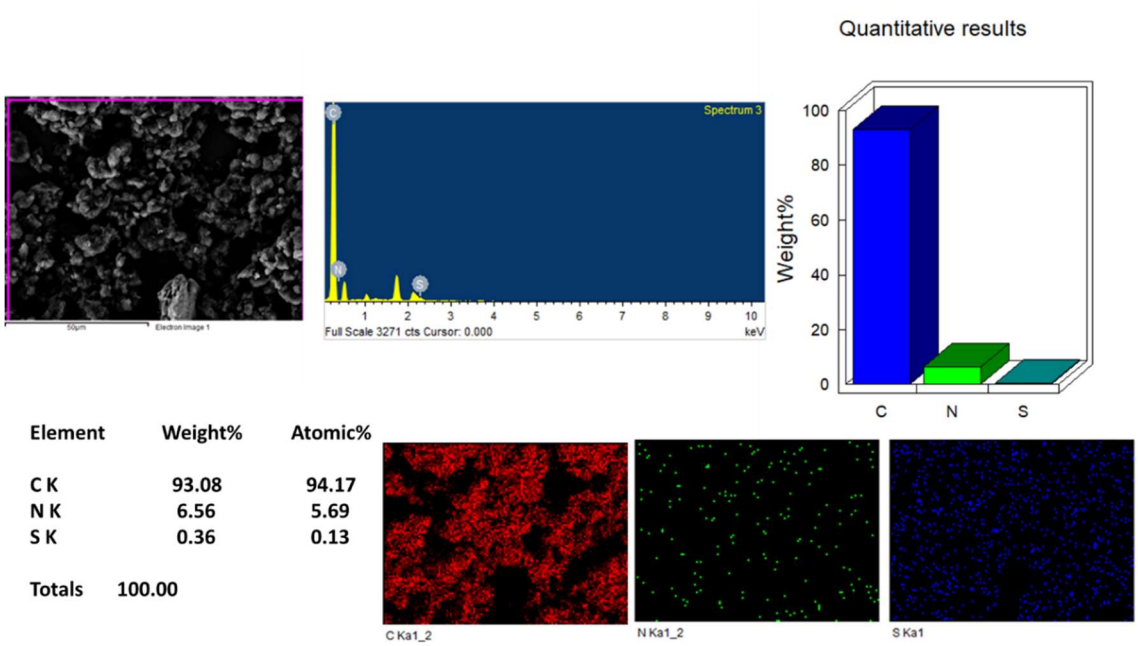

Appendix IV-Figure 6.6. Elemental mapping of MWCNT-BEPA using FESEM and EDX analysis. The distribution of N and S throughout the image prove the successful BEPA grafting on MWCNT.

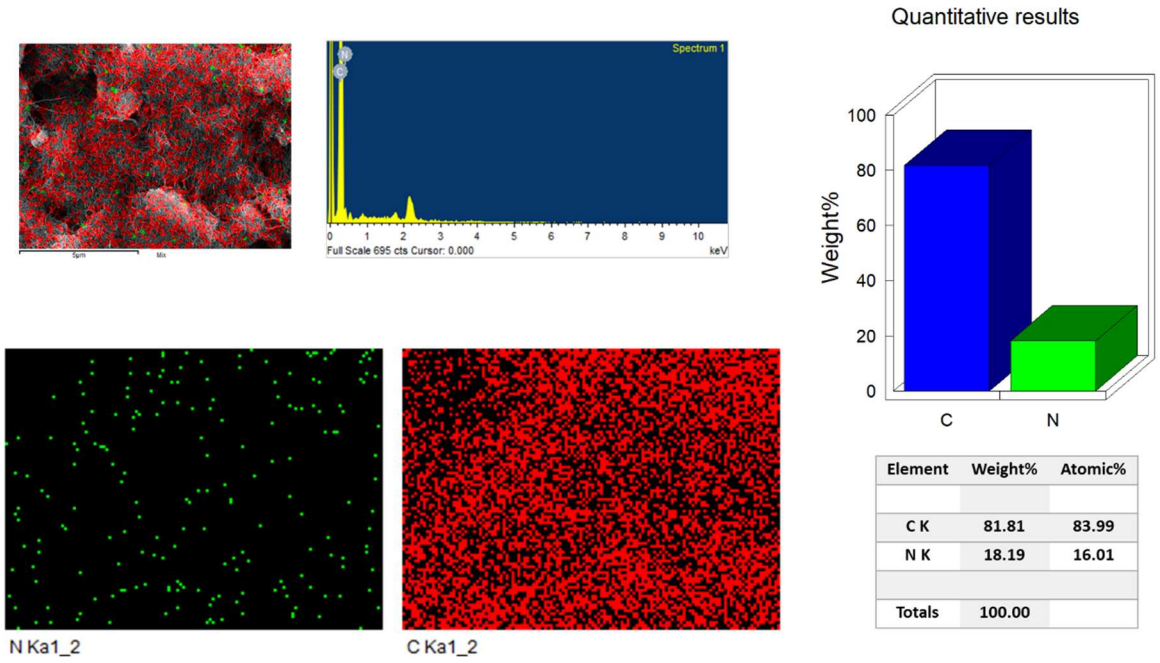

Appendix IV-Figure 6.7. Elemental mapping of PGNT1 using FESEM and EDX analysis.

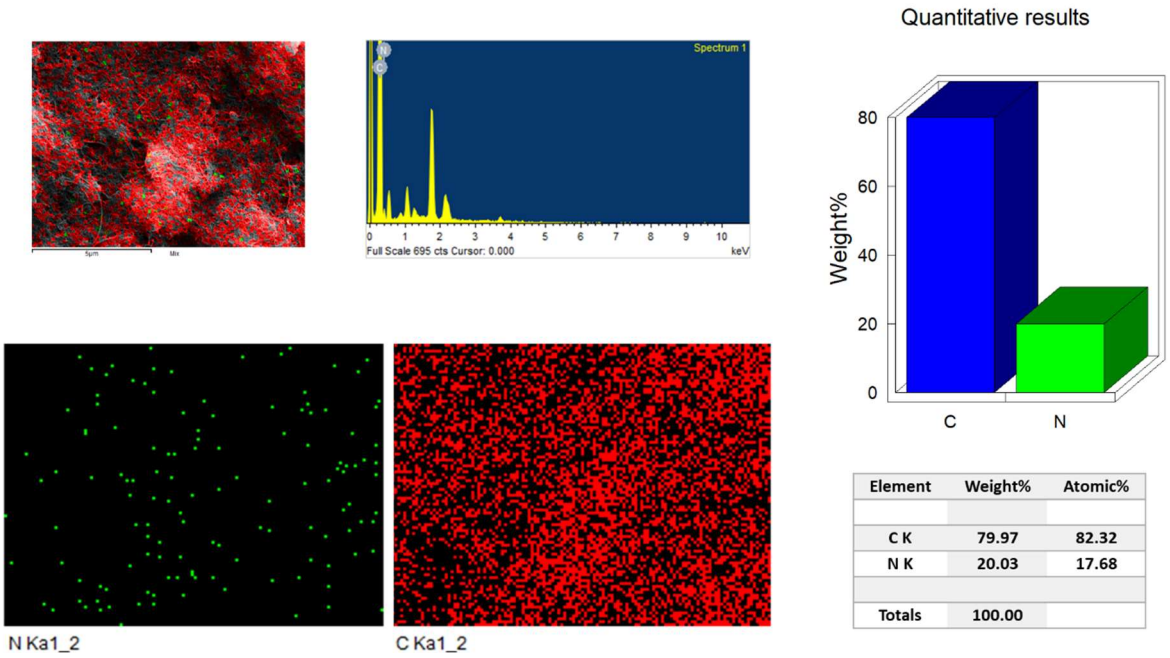

Element	Weight%	Atomic%
C K	79.97	82.32
N K	20.03	17.68
Totals	100.00	

Appendix IV-Figure 6.8. Elemental mapping of PGNT2 using FESEM and EDX analysis.

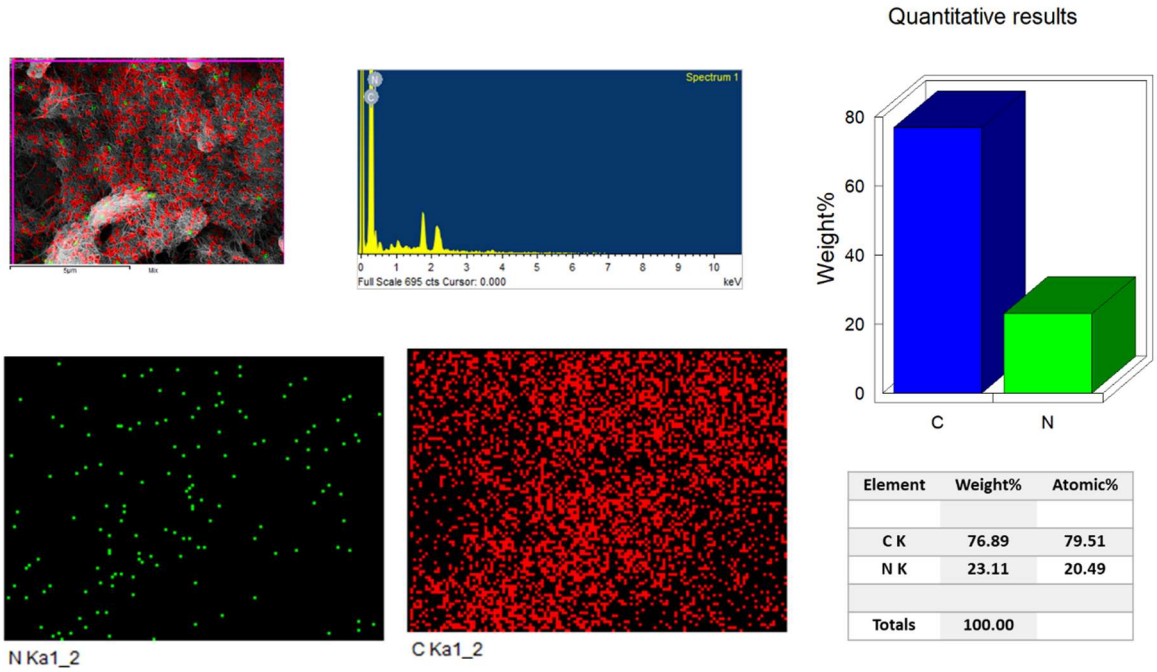

Element	Weight%	Atomic%
C K	76.89	79.51
N K	23.11	20.49
Totals	100.00	

Appendix IV-Figure 6.9. Elemental mapping of PGNT3 using FESEM and EDX analysis.

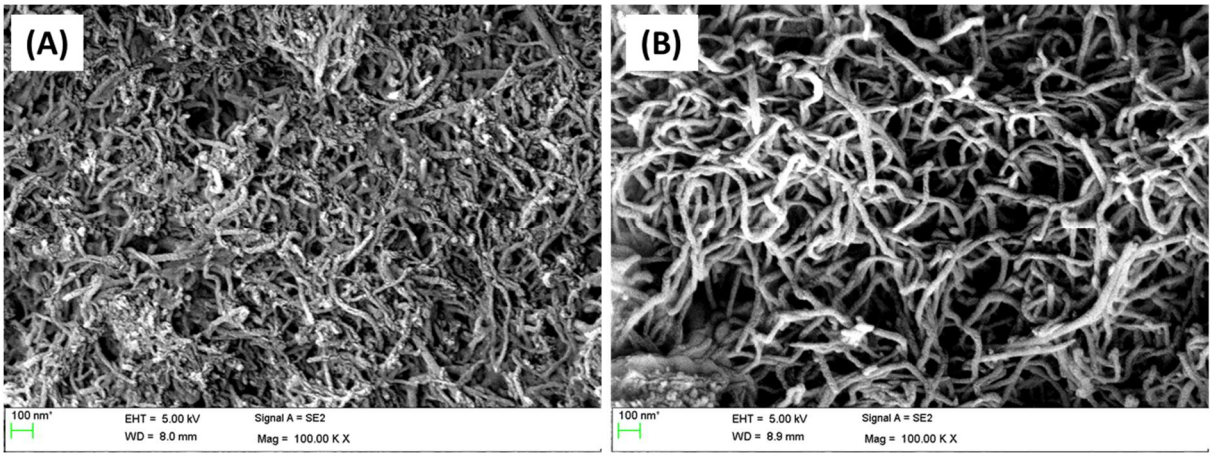

Appendix IV-Figure 6.10. FESEM image of (A) before polymer detachment treatment of PGNT1, (B) after the detachment treatment for PGNT1 (PDNT1).

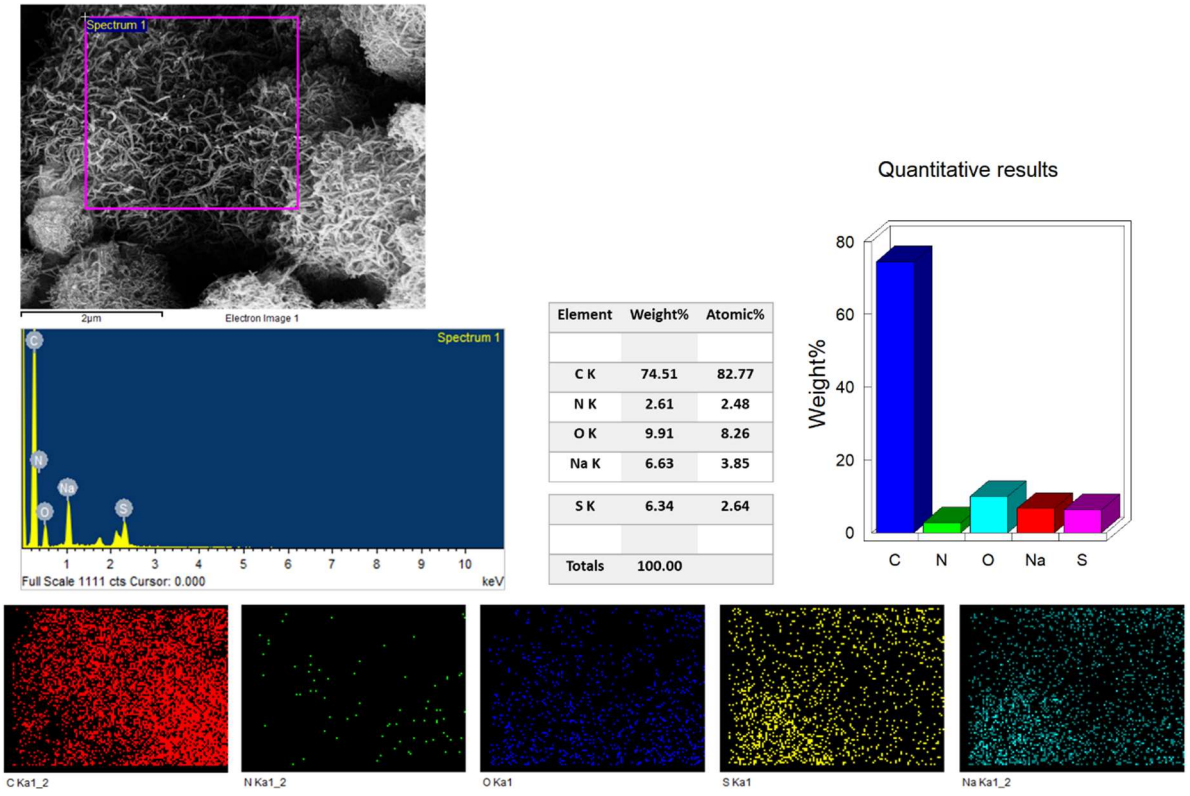

Appendix IV-Figure 6.11. FESEM-EDX data of the polymer detached MWCNT sample of PGNT1 (PDNT1) with elemental mapping.

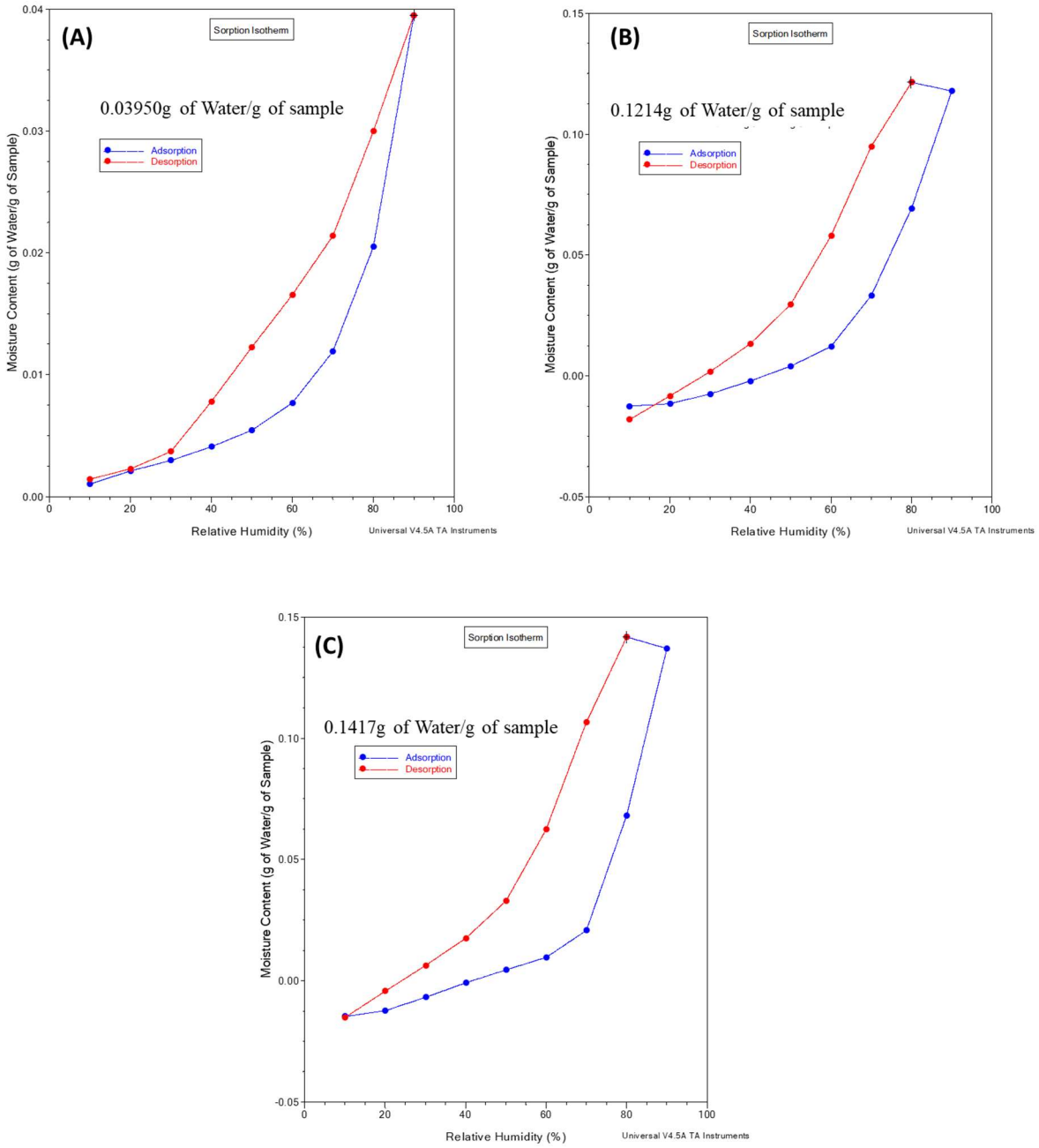

Appendix IV-Figure 6.12. DVS adsorption-desorption isotherm of **(A)** MWCNT**, (B)** PGNT1 and **(C)** PGNT3.

Zeta potential study

All the nanoparticles were dispersed in two different solvents namely milliQ water and 98 % formic acid solution and were sonicated for 5 minutes and the measurements were taken. The zeta potential measurement in 98% formic acid is important in order to get a well dispersed, homogeneous nanocomposite membrane with OPBI. In the presence of strong acidic solution, BC-*g*-MWCNTs having imidazole and 1,2,4-triazole pendent rings get protonated because of their pKa values. The protonated chains form an ionic bilayer which helps to remain dispersed in the solution. The increase in the polymer chain length of the grafted polymer chains help to form the bilayer easily and provides extra dispersion stability. Thus the BC-g-MWCNTs with higher polymer chain lengths proved to have high zeta potential. In order to check the practical aspect of our experiment, upon completion of the zeta potential measurements, the solutions were kept at room temperature in a sealed condition and were undisturbed for 7 days. Thereafter, we have checked their dispersion stability in the medium which were in well agreement with our data obtained from zeta potential studies.

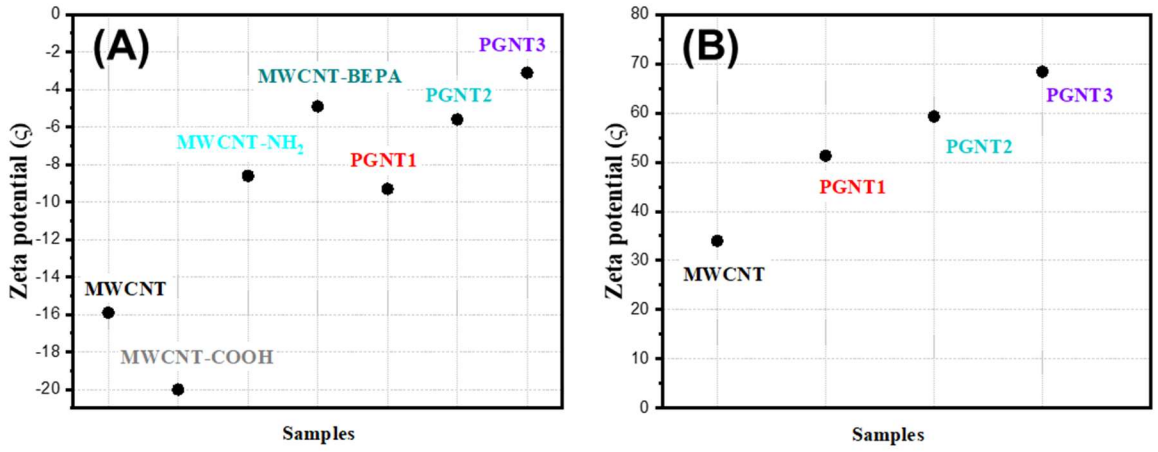

Appendix IV-Figure 6.13. Zeta potential of polymer modified MWCNTs in MiliQ water **(A),** Zeta potential of polymer modified MWCNTs in formic acid **(B).**

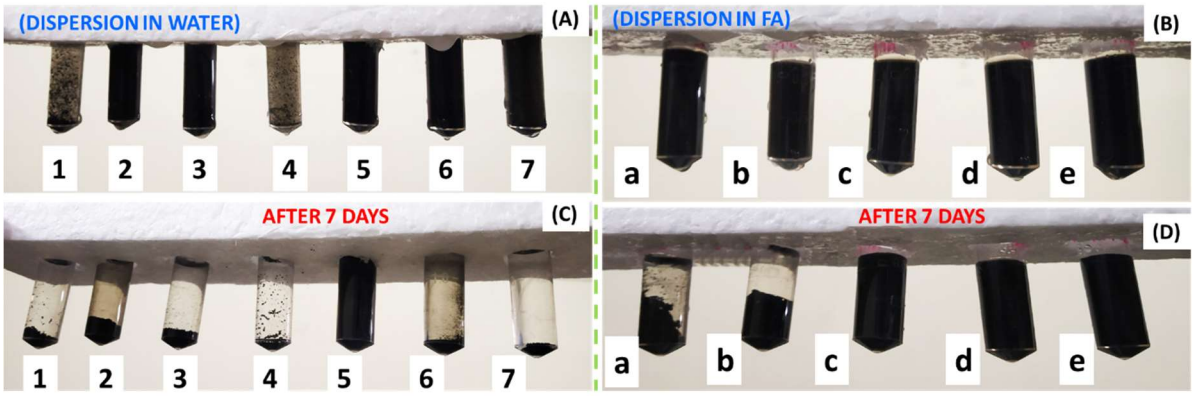

Appendix IV-Figure 6.14. (A) Dispersion of MWCNT materials in milliQ water and **(B)** dispersion of MWCNT material in formic acid. **(C)** dispersed MWCNT materials (in water) after 7 days and **(D)** dispersed MWCNT materials (in formic acid) after 7 days. The Eppendorf tubes [shown in (A) and (C)] labelled numerically with **1-7** represents MWCNT, MWCNT-COOH, MWCNT-NH_2, MWCNT-BEPA, PGNT1, PGNT2 and PGNT3, respectively. The Eppendorf tubes [shown in (B) and (D)] labelled alphabetically with **a-e** represents MWCNT, MWCNT-BEPA, PGNT1, PGNT2 and PGNT3, respectively

X-ray study (PXRD)

The powder x-ray diffraction patterns of MWCNT, MWCNT-BEPA, PGNT1, PGNT2, PGNT3, OPBI, its dry composite membranes were collected.

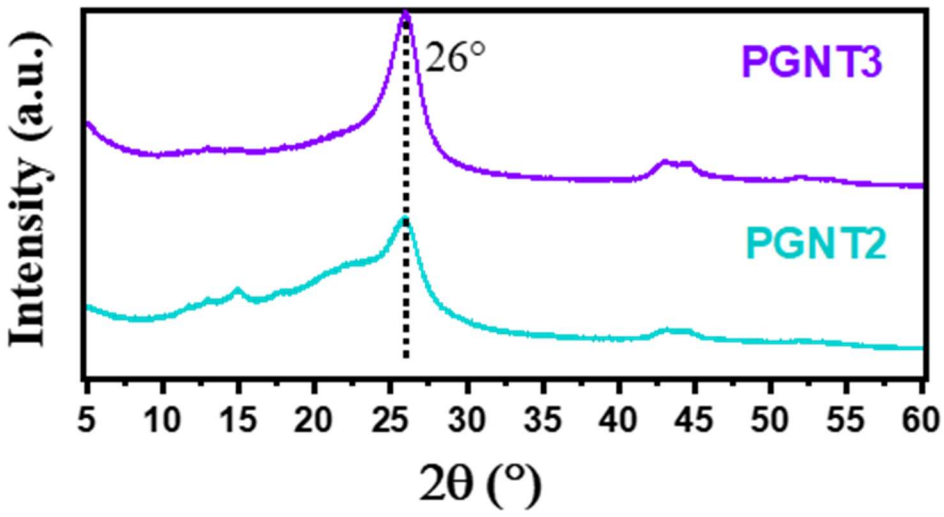

Appendix IV-Figure 6.15. PXRD pattern of PGNT2 and PGNT3**.**

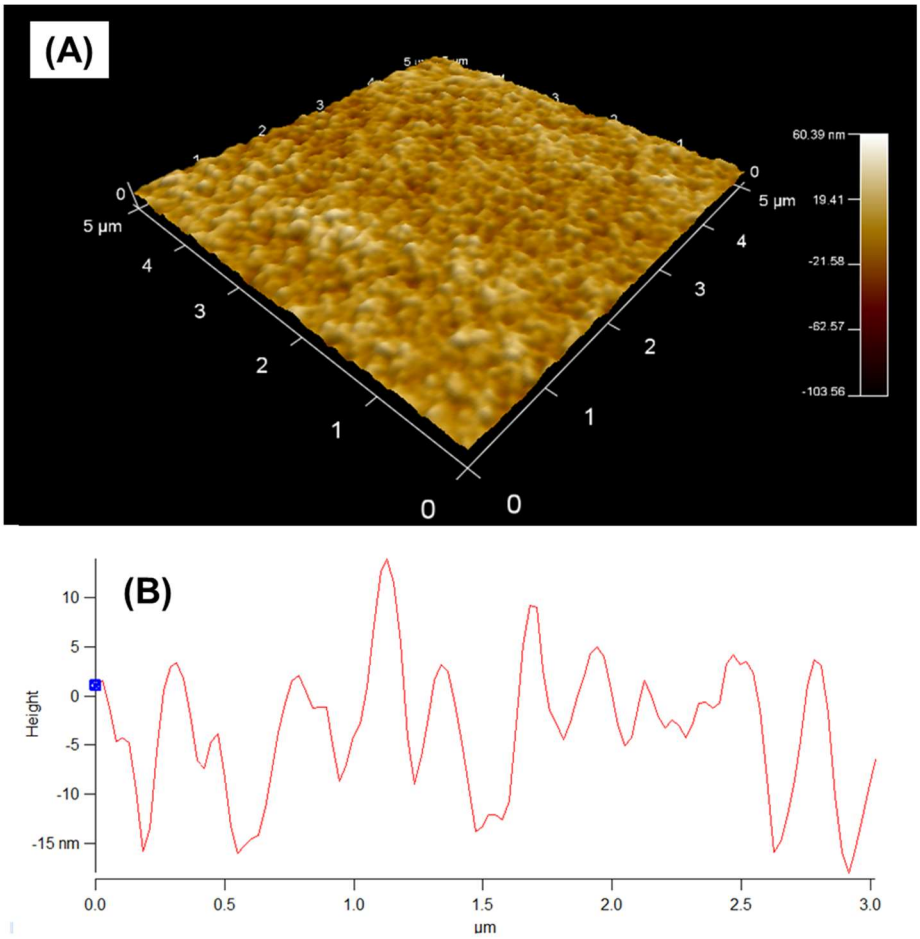

Appendix IV-Figure 6.16. AFM 3D surface morphology image of OPBI membrane (**A**) and (**B**) represents the hight image along a straight line of the membrane morphology.

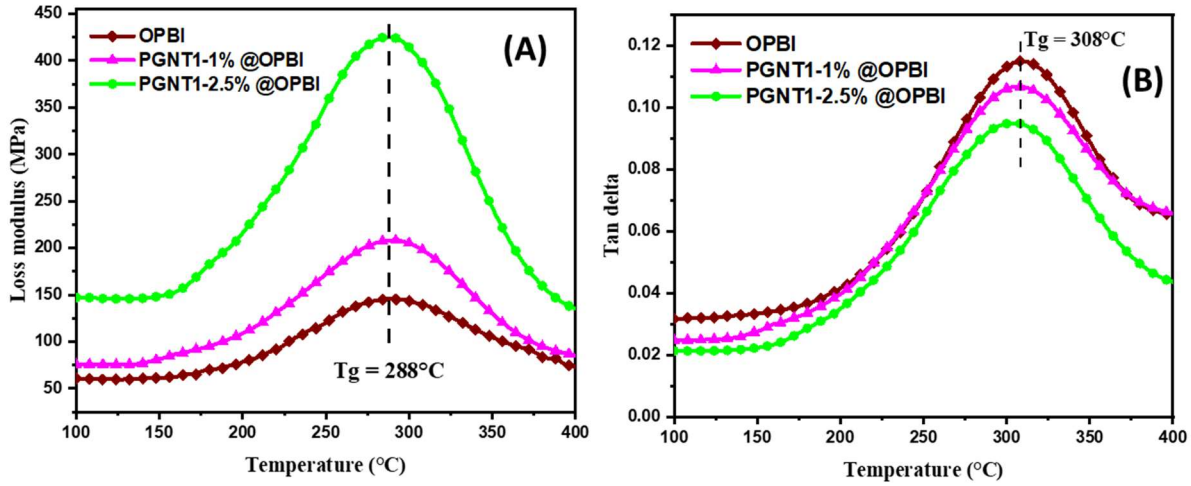

Appendix IV-Figure 6.17. (A) Loss modulus and **(B)** tan δ plots of all the PGNT1-@OPBI membranes of different filler loading along with the pristine OPBI. The T_g values are mentioned in the graph.

Acid retention test

The acid leaching test was performed for the membrane of **OPBI** and PGNT-@OPBI membranes according to the previous reports and described in detail in **Chapter 2**.[1, 2]

TGA plot of the OPBI and PGNT1@OPBI nanocomposite membranes after PA doping.

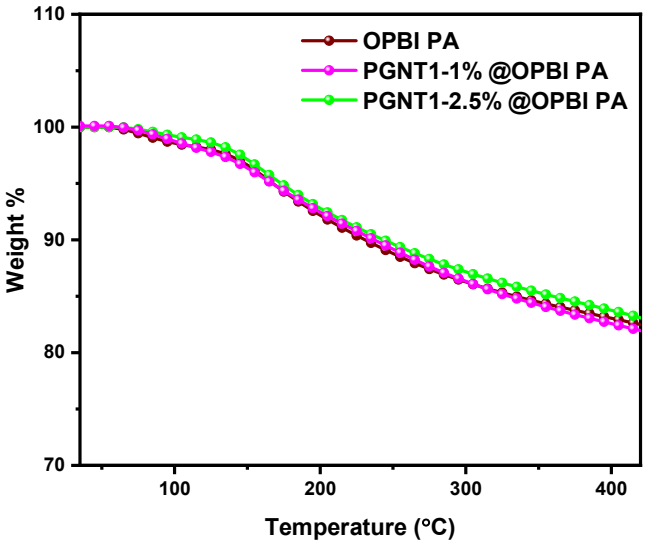

Appendix IV-Figure 6.18. TGA plot of the OPBI and PGNT1@OPBI nanocomposite membranes after PA doping.

References

(1) Mukherjee, N.; Das, A.; Dhara, M.; Jana, T. Surface Initiated RAFT Polymerization to Synthesize N-Heterocyclic Block Copolymer Grafted Silica Nanofillers for Improving PEM Properties. *Polymer.* **2021**, *236*, 124315.

(2) Mukhopadhyay, S.; Das, A.; Jana, T.; Das, S. K. Fabricating a MOF Material with Polybenzimidazole into an Efficient Proton Exchange Membrane. *ACS Appl. Energy Mater.* **2020**, *3*, 7964–7977.

Appendix V

NMR studies of PGNT3 sample

Detached polymer chains from the surface of PGNT3 was dispersed in DMSO-d6 and sampled for 1H-NMR studies using a Brucker 500 MHz instrument. The spectra was also analyzed using MestReNova software and fitted in order to isolate the compound peaks and solvent peaks. DMSO-d6 solvent peak and H_2O peak are observed at 3.3 and 2.5 ppm respectively. Traces of DMF was also observed at 2.75 ppm. Imidazole protons appear at 6.5-7.25 ppm.

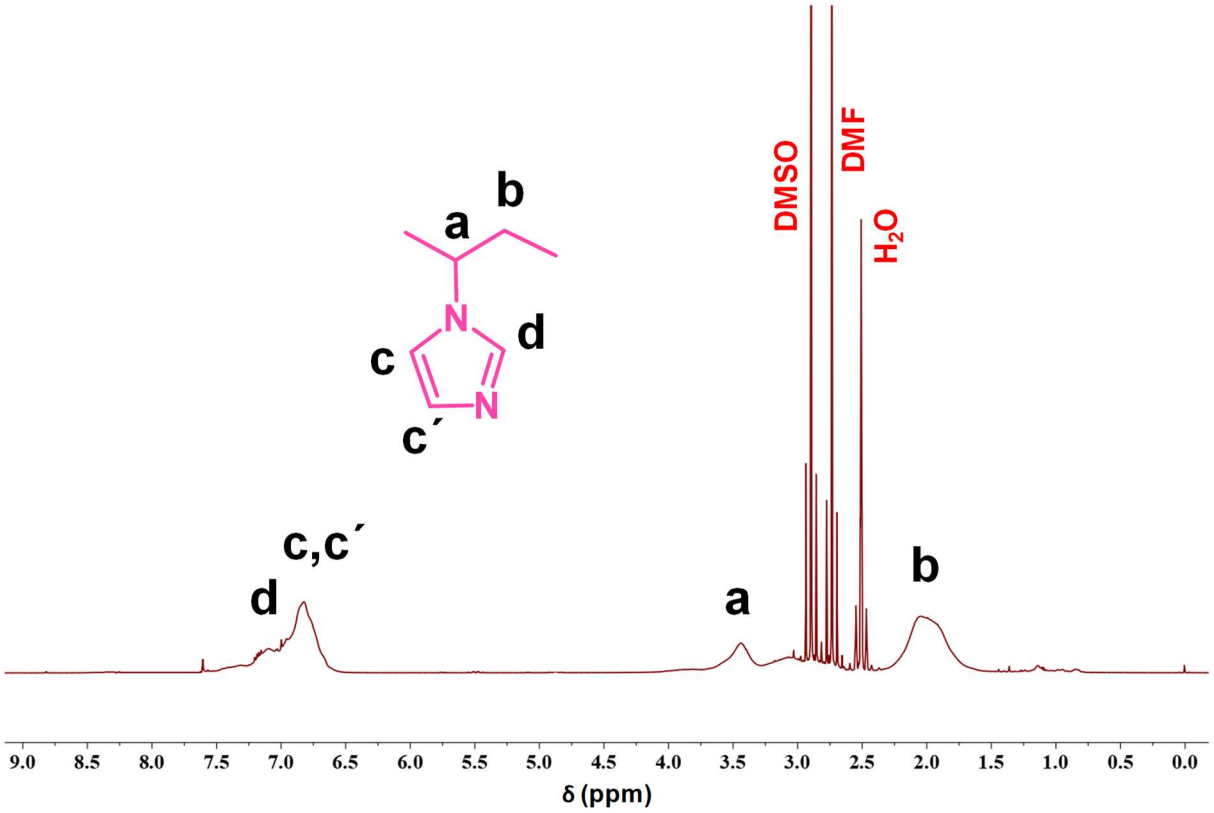

Appendix V-Figure 7.1. ^{1}H NMR spectra in DMSO-d6 of the detached polymer chains (pNVI) upon the polymer detachment procedure was performed on PGNT3.

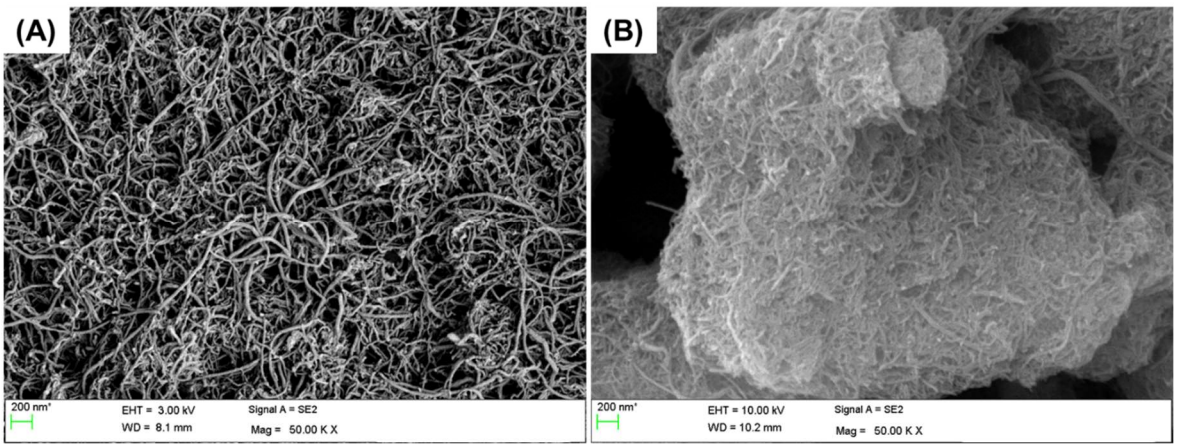

Appendix V-Figure 7.2. (A) FESEM image of MWCNT, **(B)** MWCNT-BEPA.

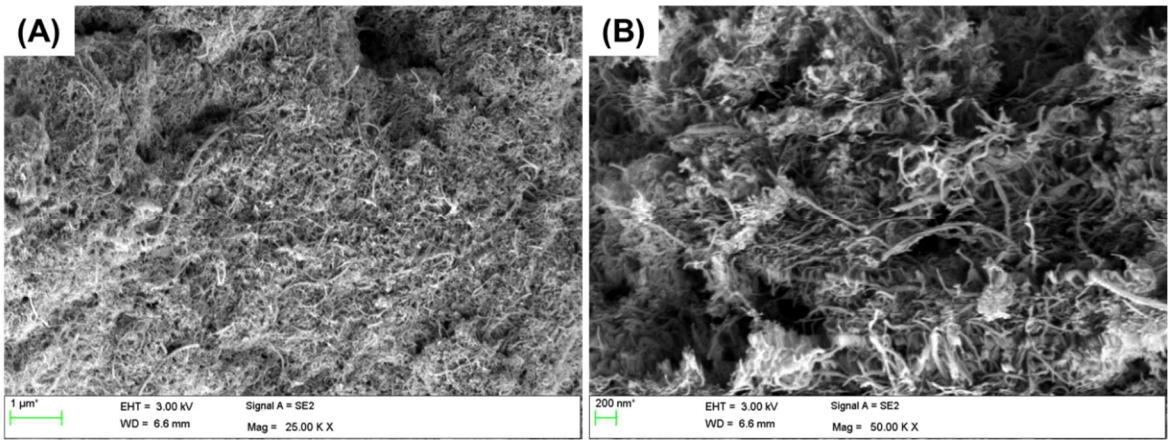

Appendix V-Figure 7.3. FESEM image of **(A)** and **(B)** PGNT2 with different magnification.

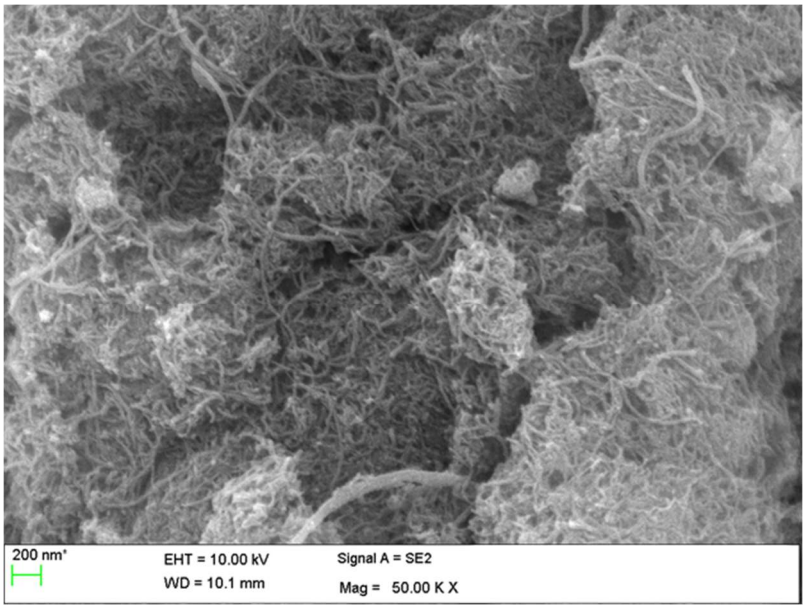

Appendix V-Figure 7.4. FESEM image of recovered Pd@PGNT1 after SM coupling reaction.

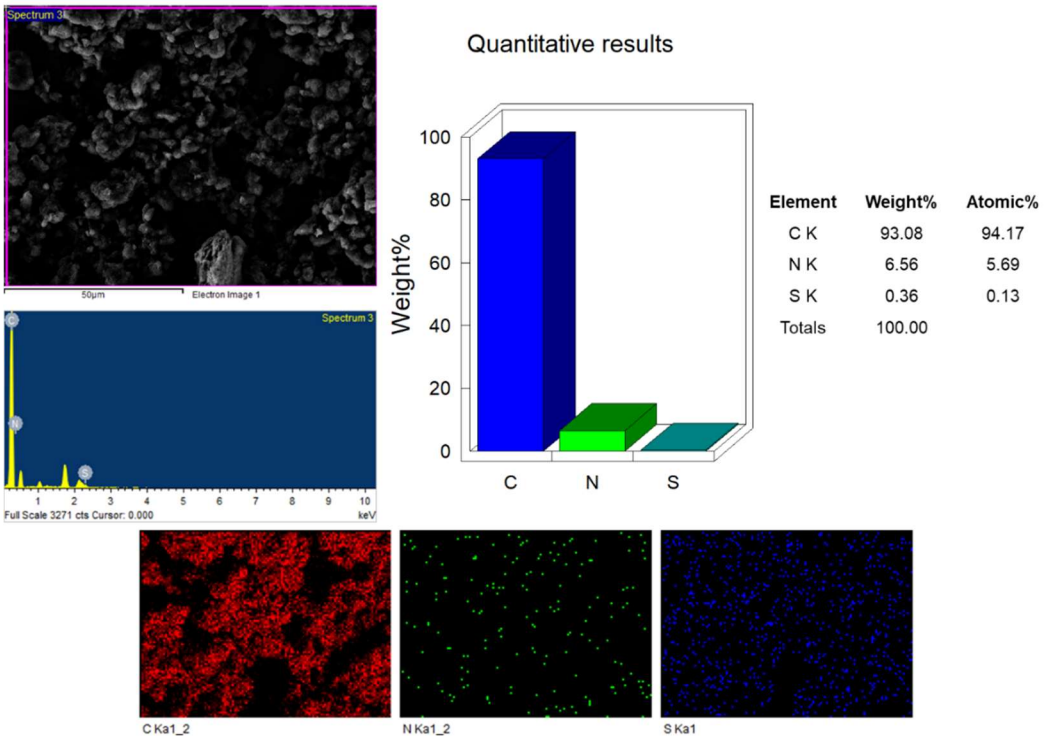

Appendix V-Figure 7.5. Elemental mapping data of MWCNT-BEPA using FESEM and EDX analysis. The distribution of N and S throughout the image prove the successful BEPA grafting on MWCNT.

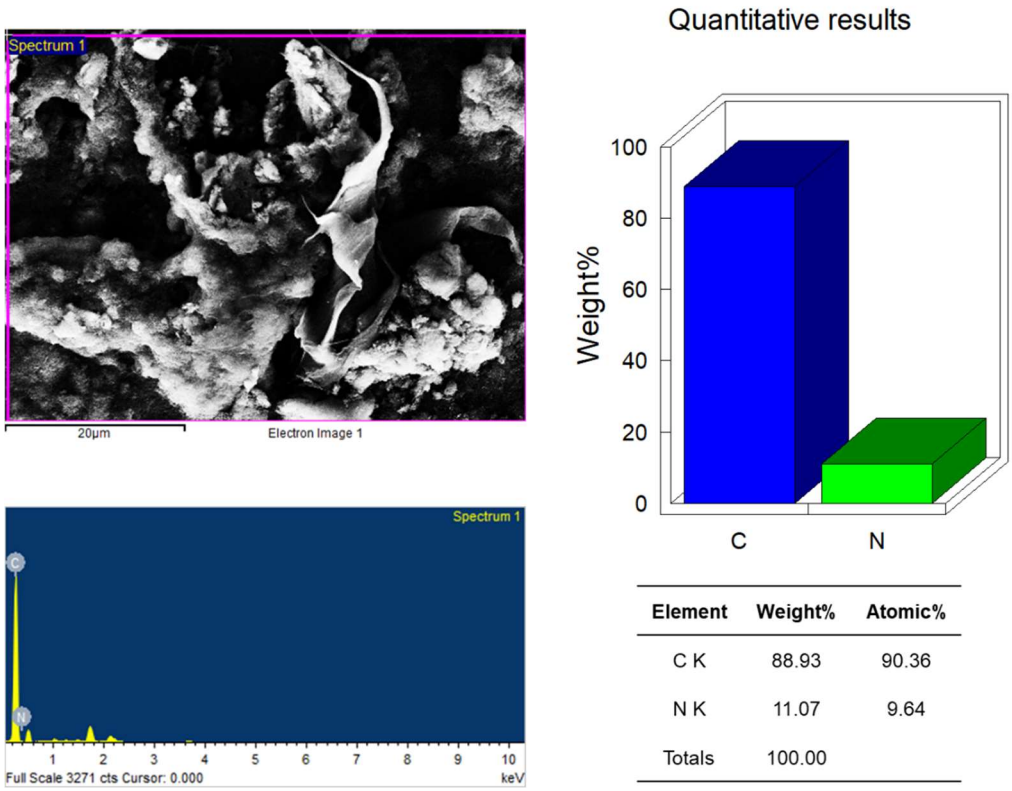

Appendix V-Figure 7.6. FESEM and EDX analysis of PGNT1.

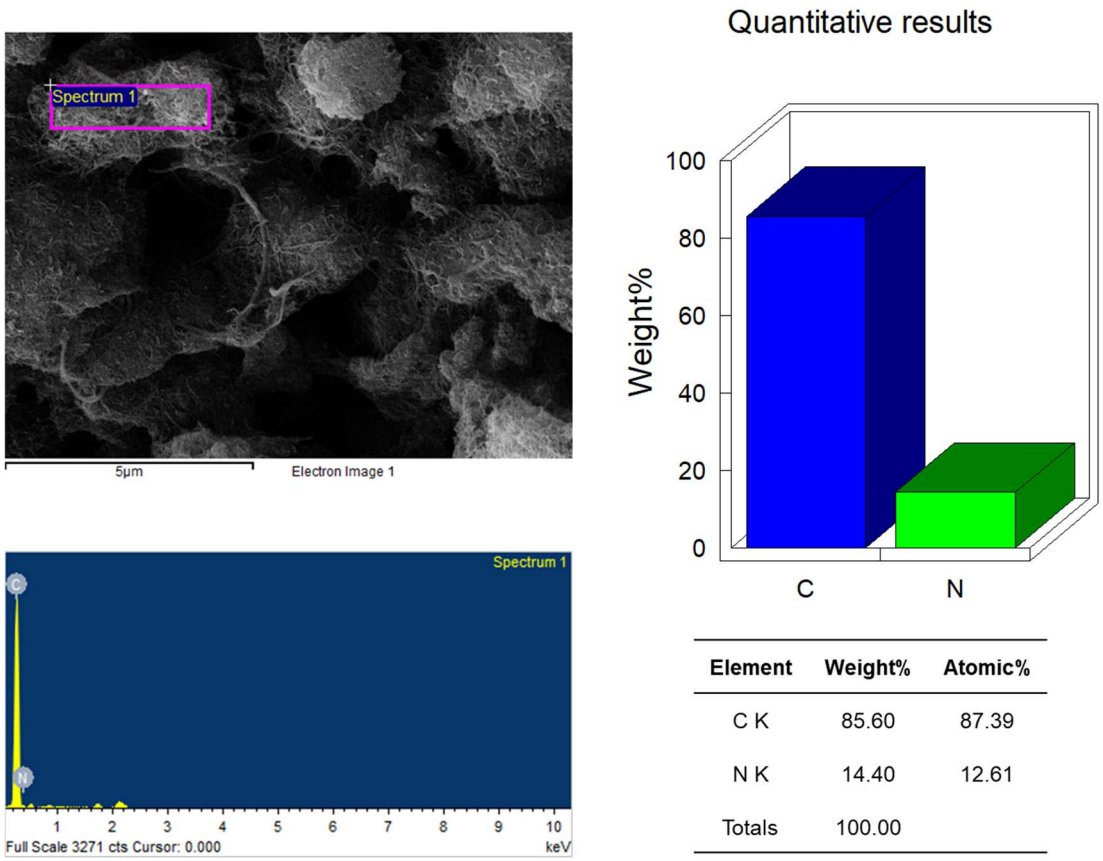

Element	Weight%	Atomic%
C K	85.60	87.39
N K	14.40	12.61
Totals	100.00	

Appendix V-Figure 7.7. FESEM and EDX analysis of PGNT2.

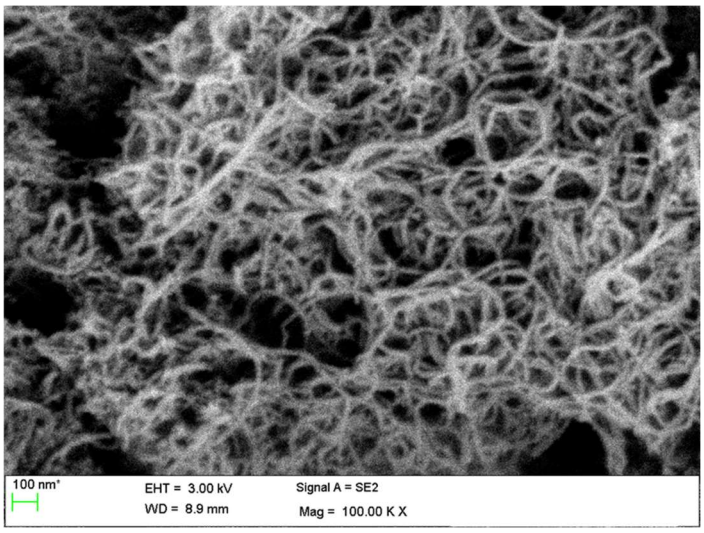

Appendix V-Figure 7.8. FESEM image of PGNT3 after the polymer detachment treatment.

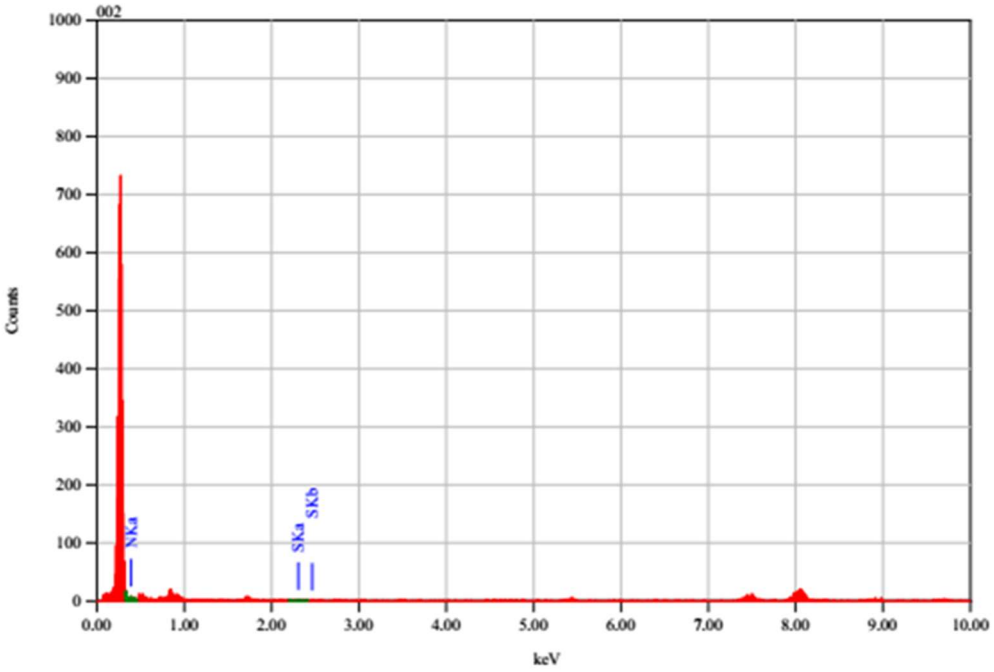

Acquisition Parameter

Acc. Voltage	:	200.0 kV	Probe Current	:	7.47500 nA
Real Time	:	30.20 sec	Dead Time	:	0 %
Live Time	:	30.00 sec	Counting Rate	:	217 Counts/sec
Preset	:	Live Time 30 sec			
Energy Range	:	0 - 40 keV	PHA Mode	:	T3

ZAF Method Standardless Quantitative Analysis

Fitting Coefficient : 0.9997

Element	(keV)	Mass%	Sigma	Atom%	Compound	Mass%	Cation	K
N K	0.392	90.74	37.36	95.73				49.8251
S K	2.307	9.26	215.17	4.27				50.1749
Total		100.00		100.00				

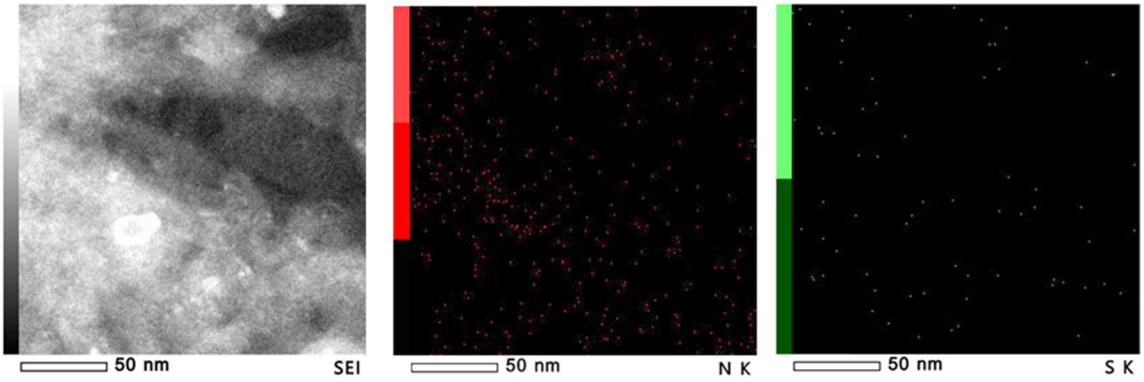

Appendix V-Figure 7.9. TEM EDX and mapping data of MWCNT-BEPA.

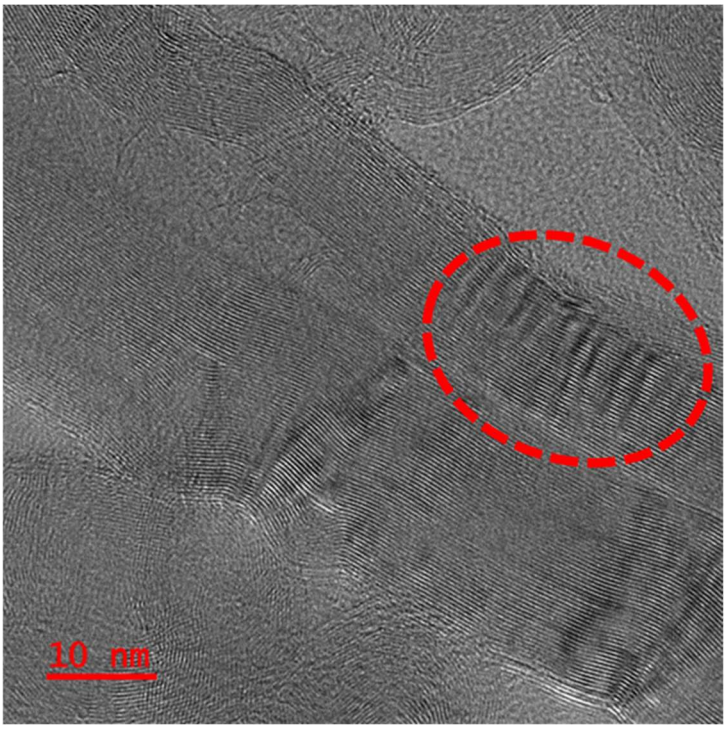

Appendix V-Figure 7.10. TEM image of Pd@PGNT1 isolated intermediate from the Pd nanoparticle formation reaction. Red dotted circle indicated the initiation of Pd nanoparticle formation.

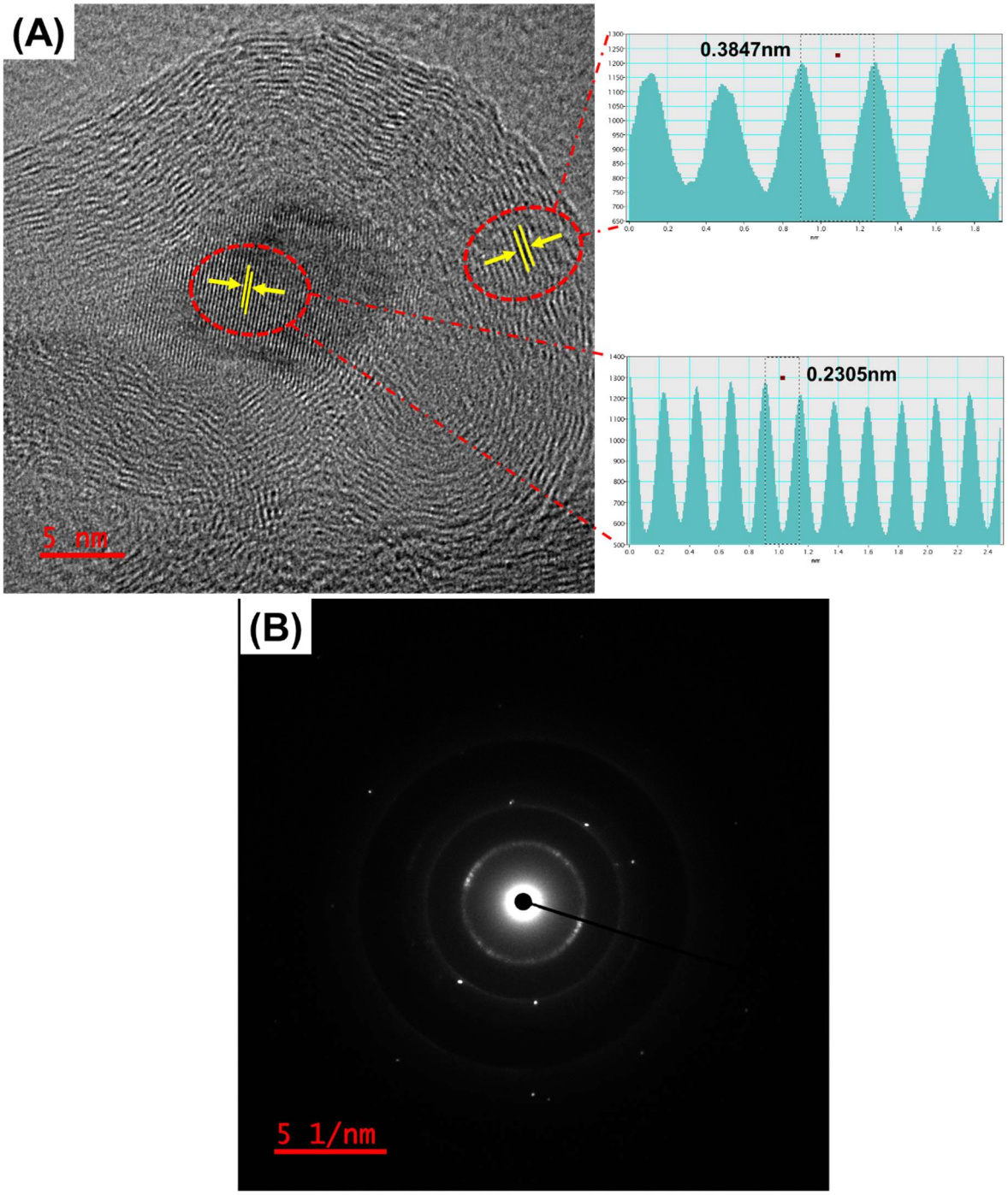

Appendix V-Figure 7.11. TEM image of Pd@PGNT1 with the lattice fringe **(A)** and SAED pattern of Pd@PGNT1 **(B).**

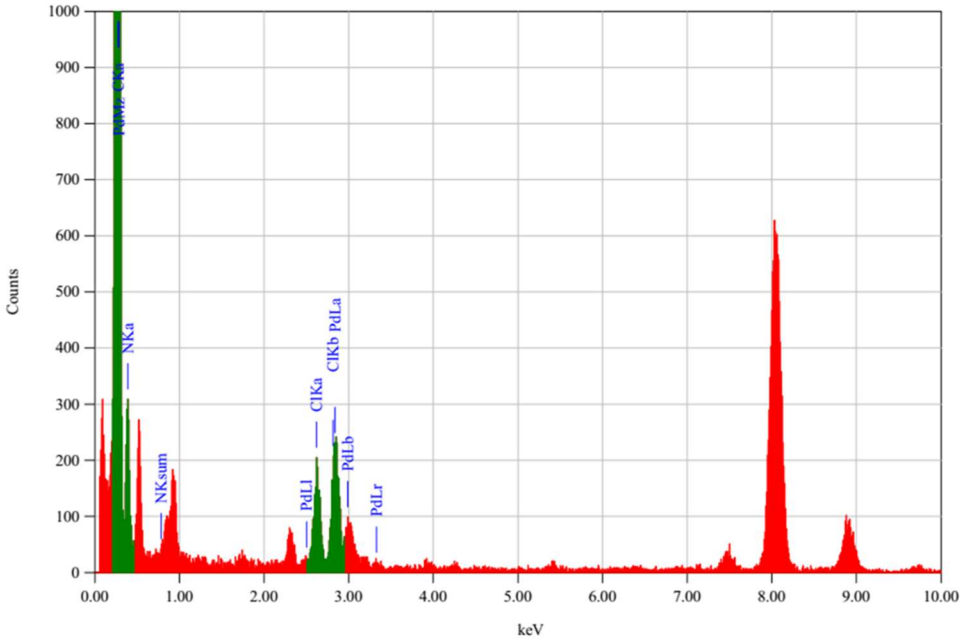

Acquisition Parameter

Acc. Voltage	:	200.0 kV	Probe Current	:	7.47500 nA
Real Time	:	300.00 sec	Dead Time	:	1 %
Live Time	:	295.20 sec	Counting Rate	:	285 Counts/sec
Preset	:	Real Time 300 sec			
Energy Range	:	0 - 40 keV	PHA Mode	:	T4

ZAF Method Standardless Quantitative Analysis
Fitting Coefficient : 0.3500

Element	(keV)	Mass%	Sigma	Atom%	Compound	Mass%	Cation	K
C K	0.277	82.25	0.47	93.42				72.7803
N K	0.392	5.09	0.17	4.95				0.5318
Cl K*	2.621	0.01	0.00	0.01				0.0298
Pd L*	2.838	12.65	0.47	1.62				26.6582
Total		100.00		100.00				

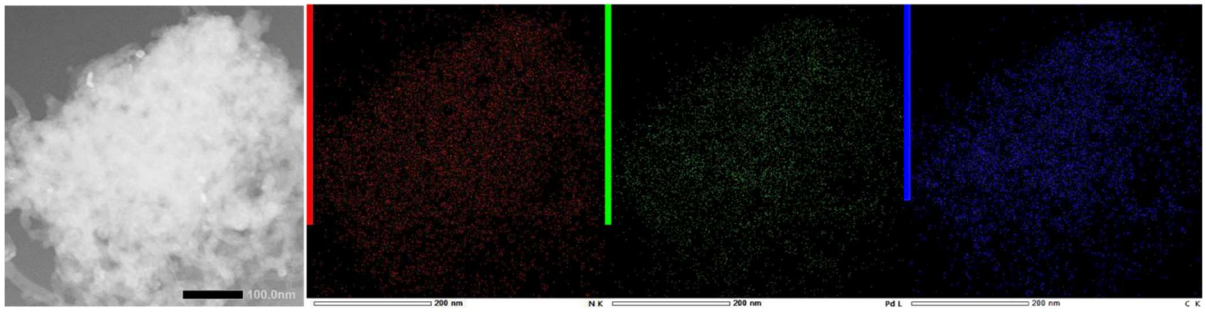

Appendix V-Figure 7.12. TEM EDX and mapping data of Pd@PGNT1.

Zeta potential study

Zeta potential for all the samples were measured using a Horiba Scientific nano partica nano particle analyzer SZ-100 instrument. All the nanoparticles were dispersed in milliQ water and were sonicated for 5 minutes and the measurements were taken.

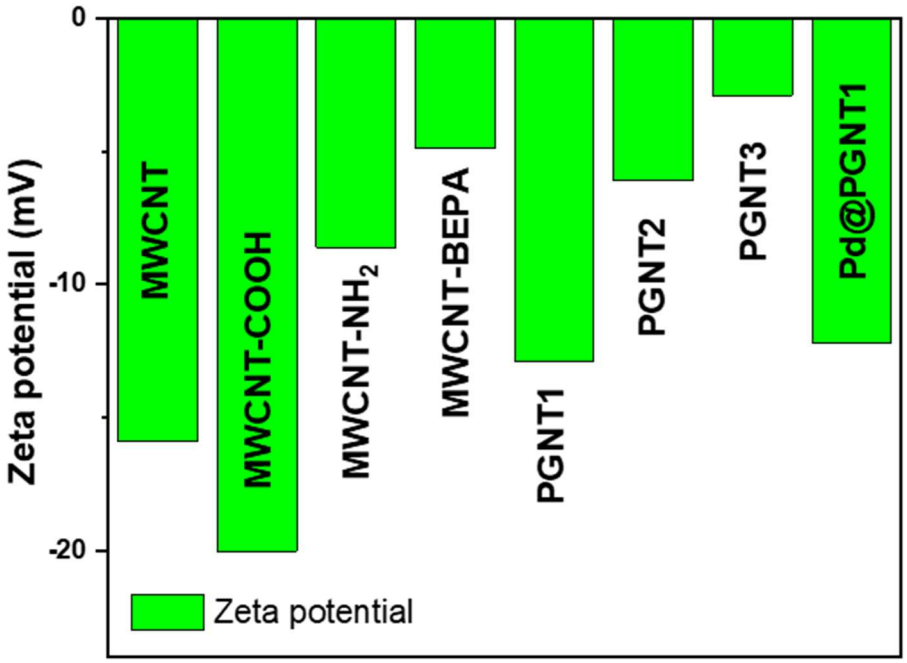

Appendix V-Figure 7.13. Zeta potential of polymer modified MWCNTs in MiliQ water.

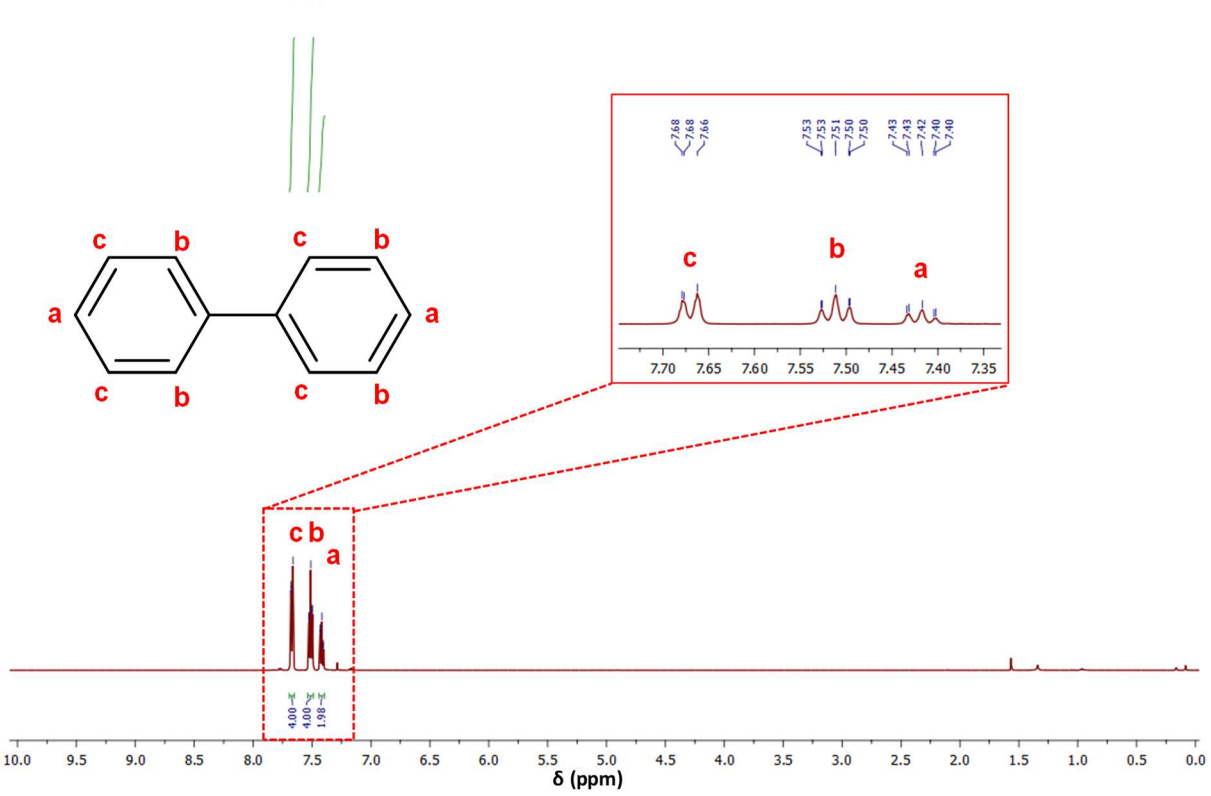

Appendix V-Figure 7.14. ^{1}H data of compound **1**

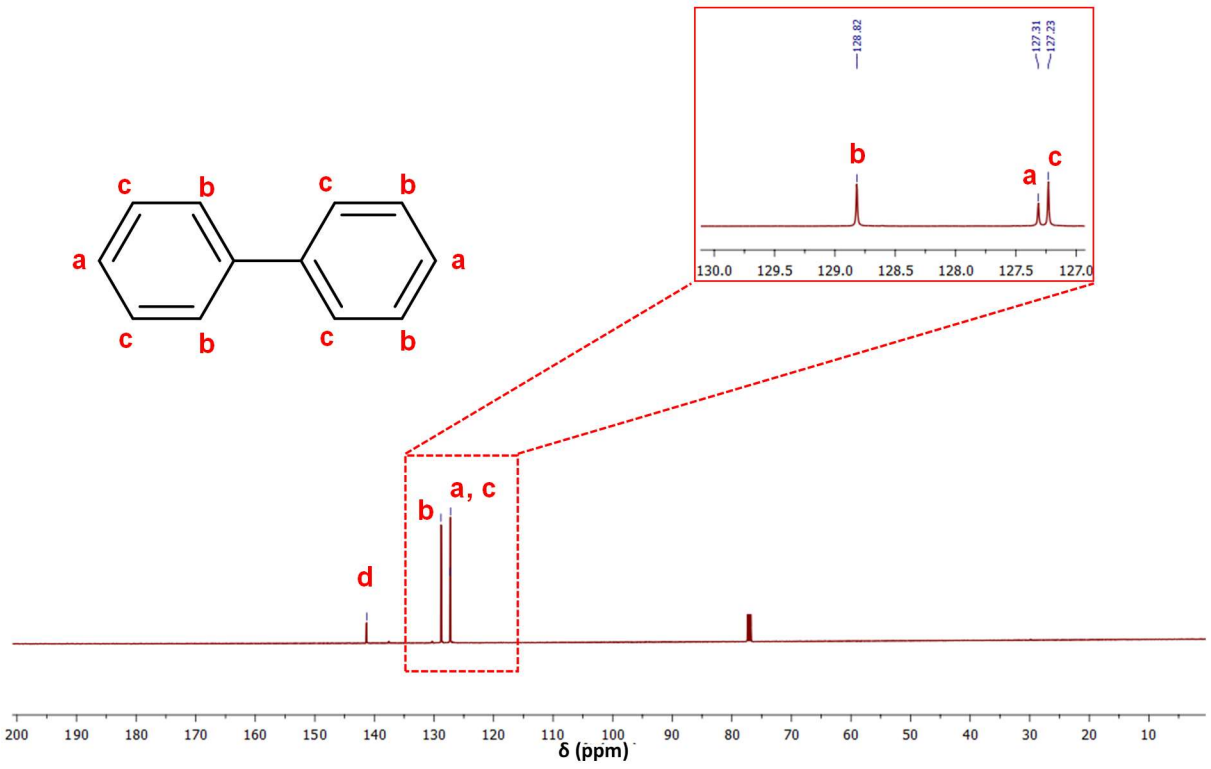

Appendix V-Figure 7.15. ^{13}C data of compound **1**

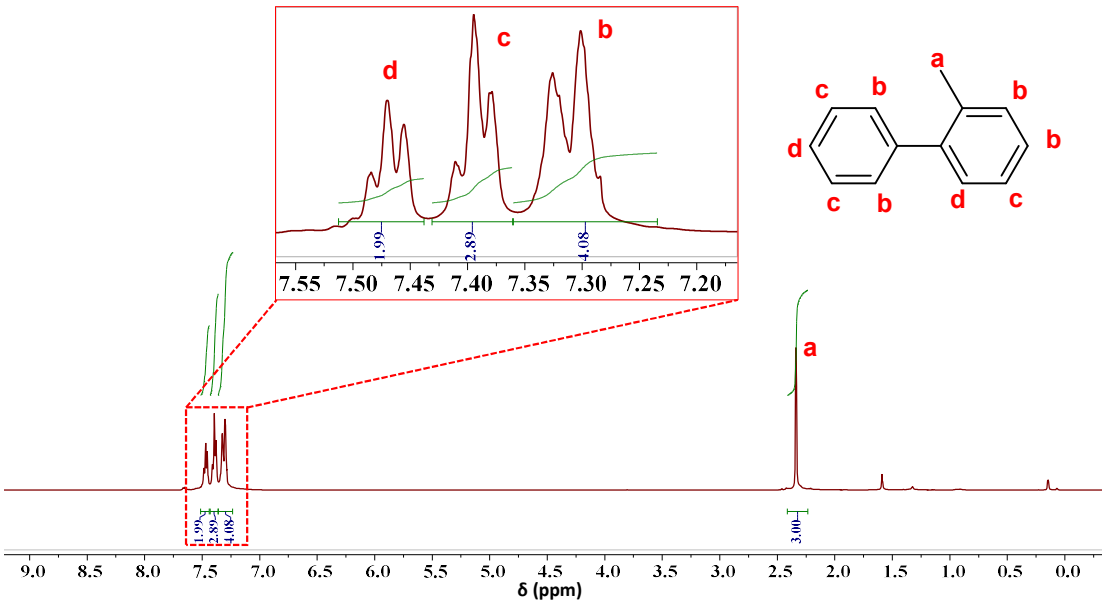

Appendix V-Figure 7.16. ^{1}H NMR of compound **2.**

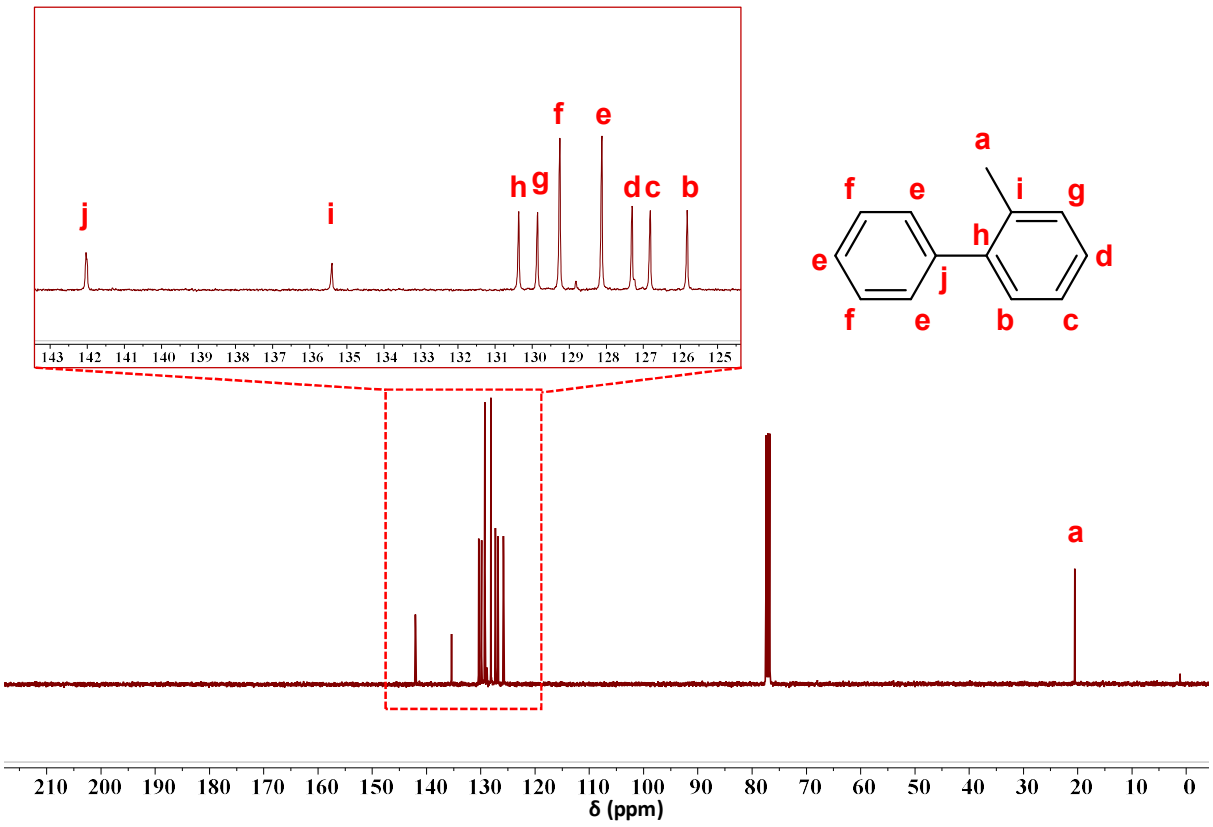

Appendix V-Figure 7.17. ^{13}C NMR of compound **2.**

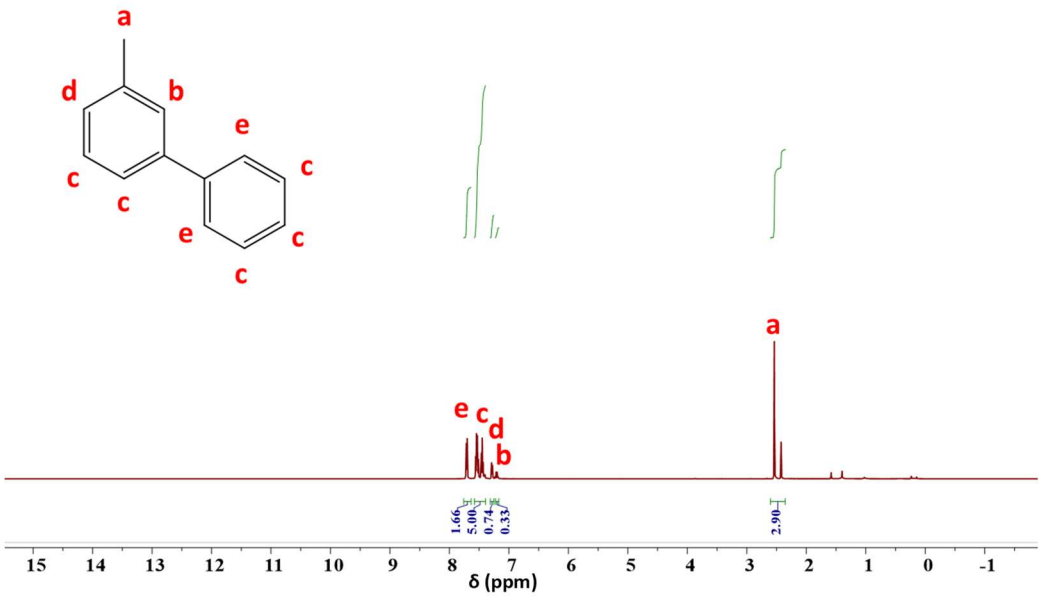

Appendix V-Figure 7.18. ^{1}H NMR of compound **3.**

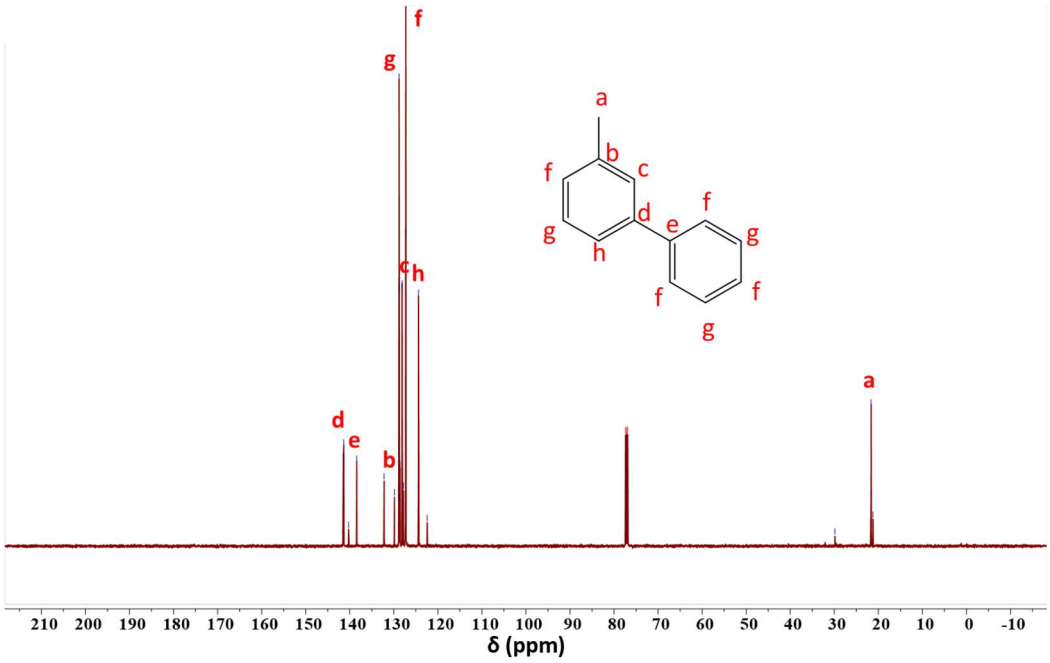

Appendix V-Figure 7.19. ^{13}C NMR of compound **3.**

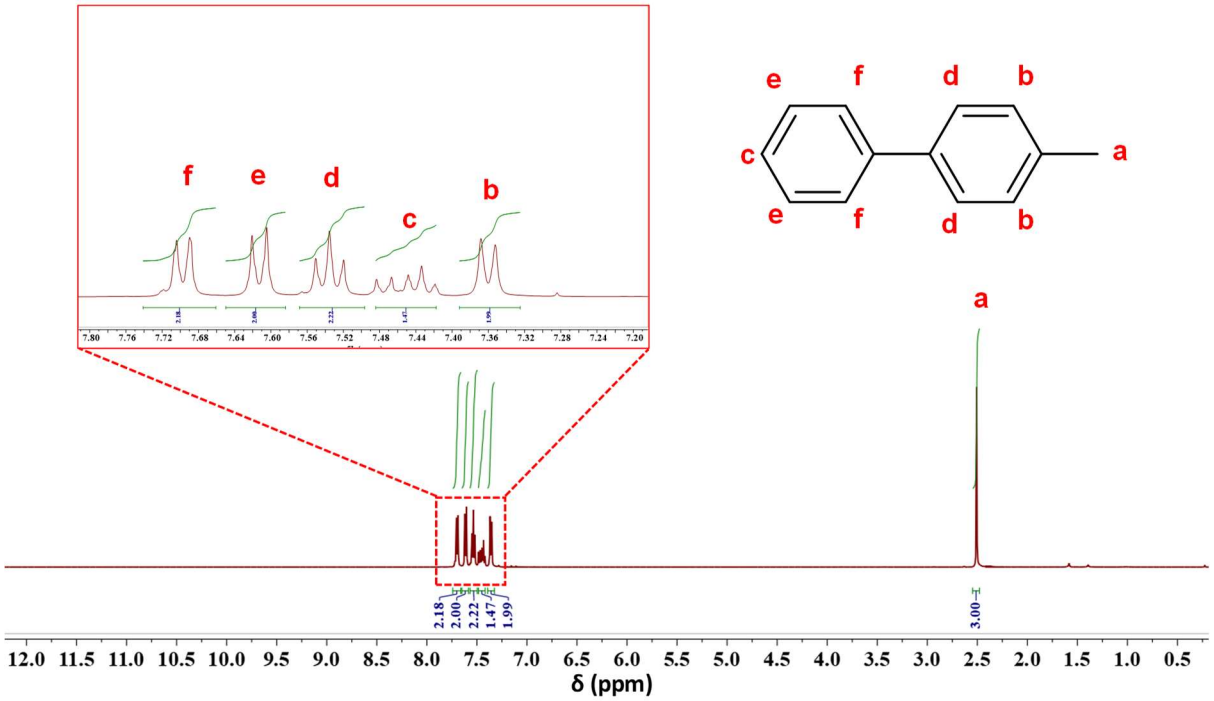

Appendix V-Figure 7.20. ^{1}H NMR of compound **4.**

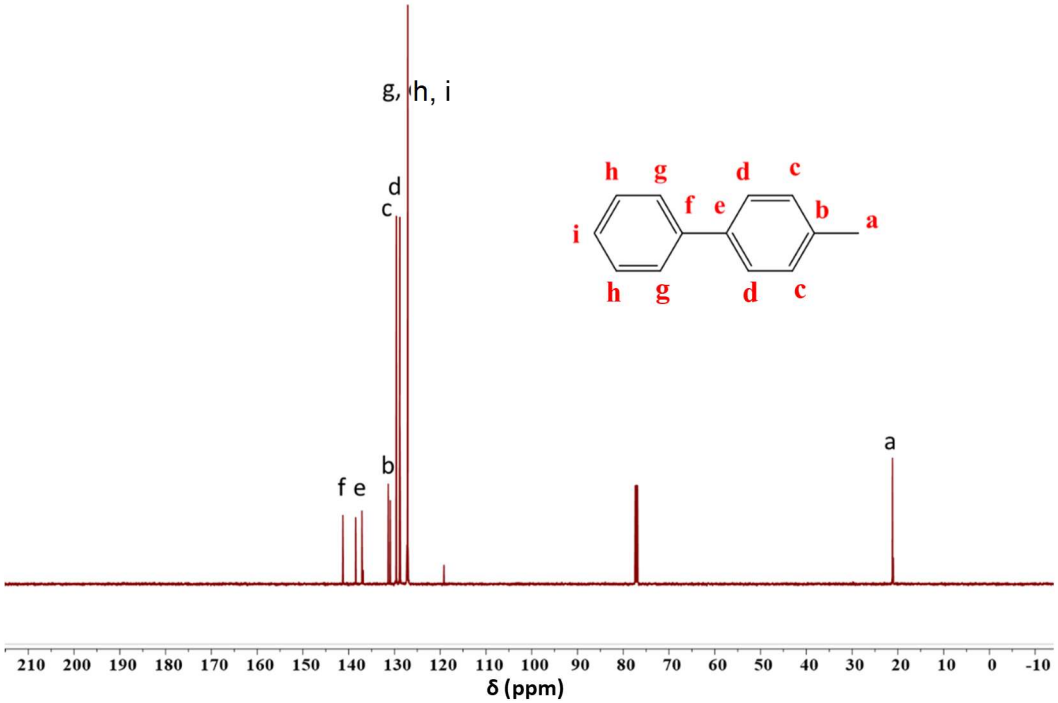

Appendix V-Figure 7.21. ^{13}C NMR of compound **4.**

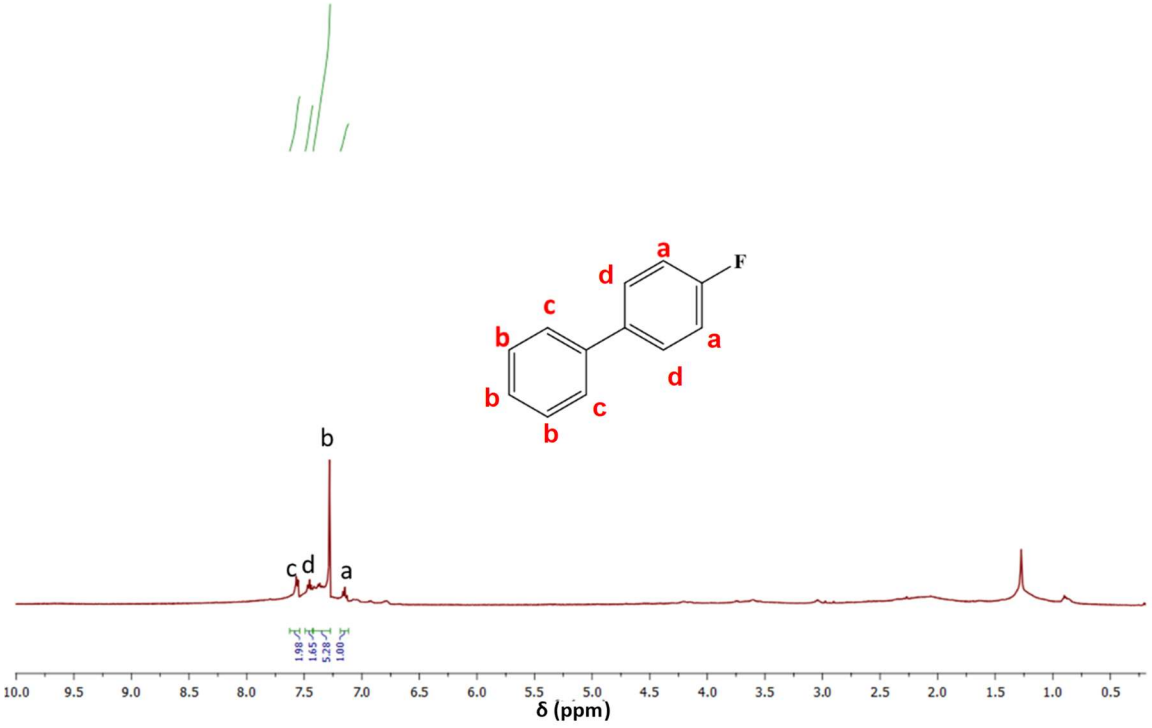

Appendix V-Figure 7.22. ^{1}H NMR of compound **5.**

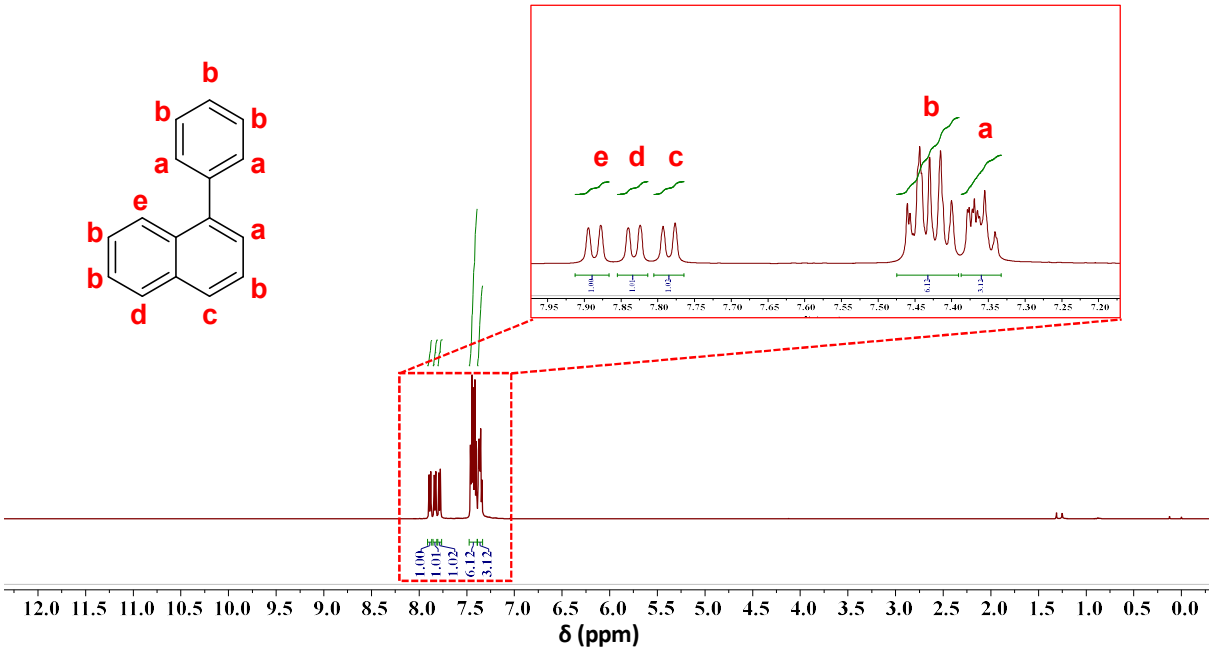

Appendix V-Figure 7.23. ^{1}H NMR of compound **6.**

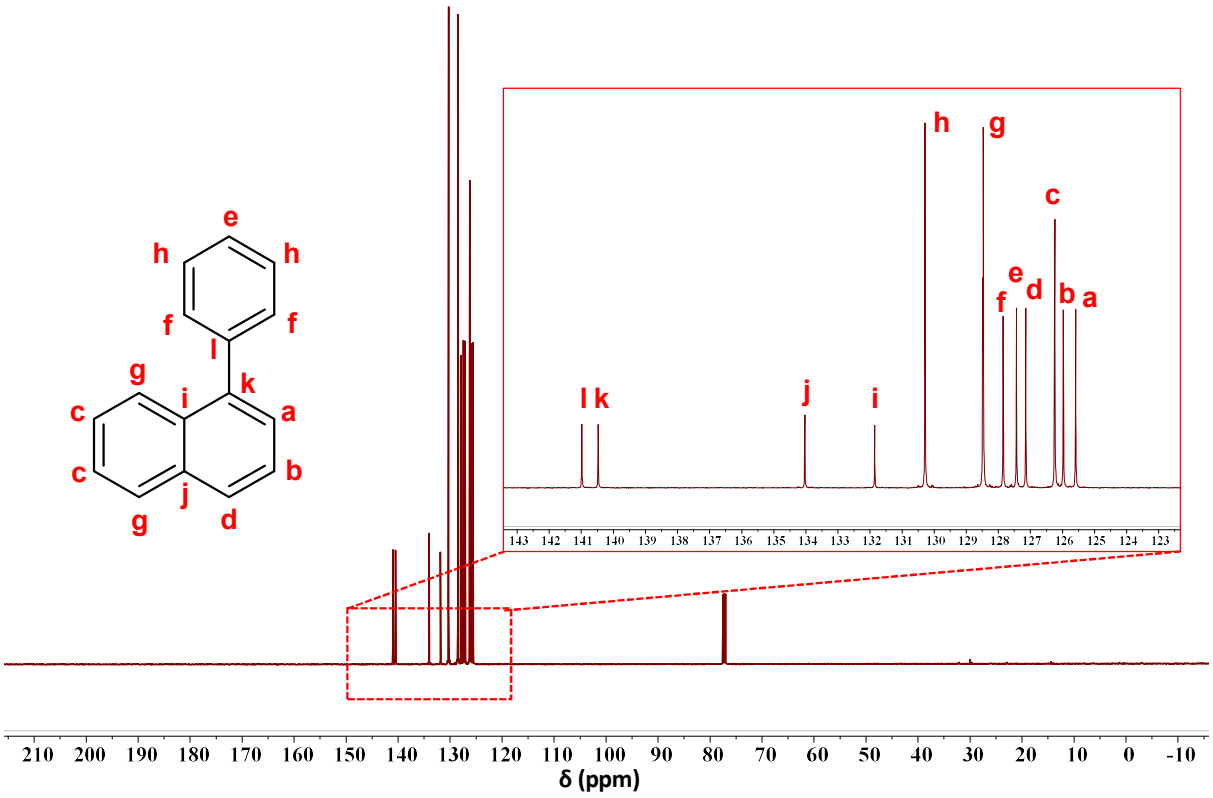

Appendix V-Figure 7.24. ^{13}C NMR of compound **6.**

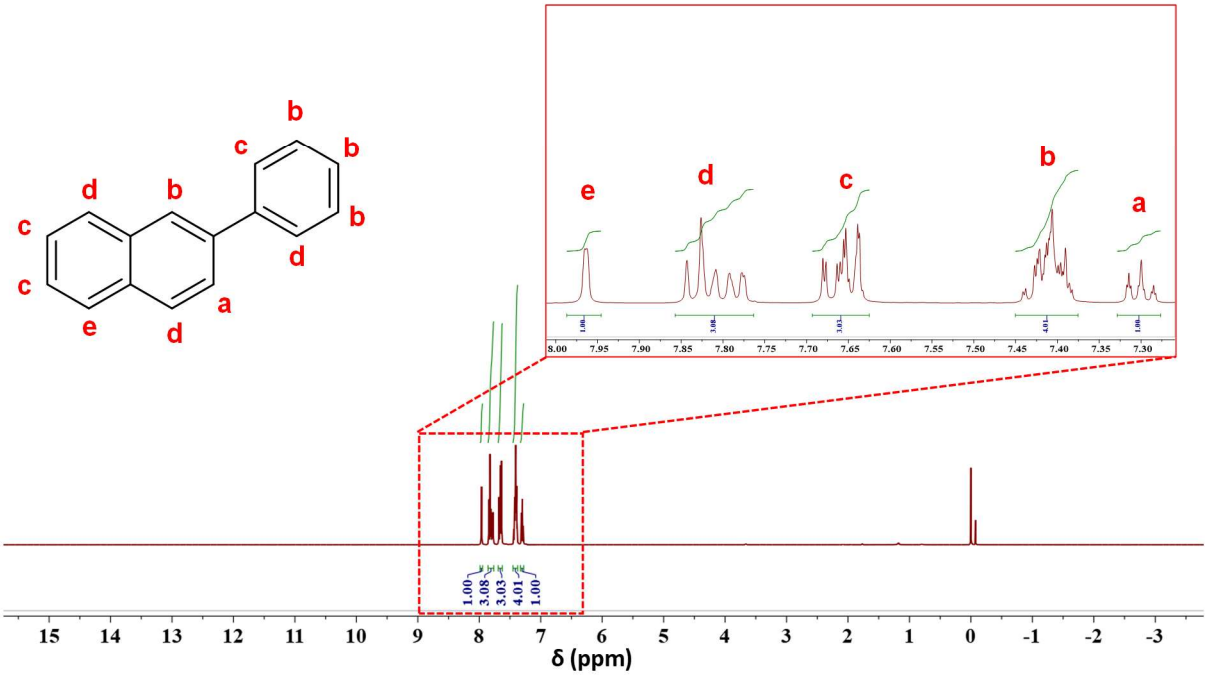

Appendix V-Figure 7.25. ^{1}H NMR of compound **7.**

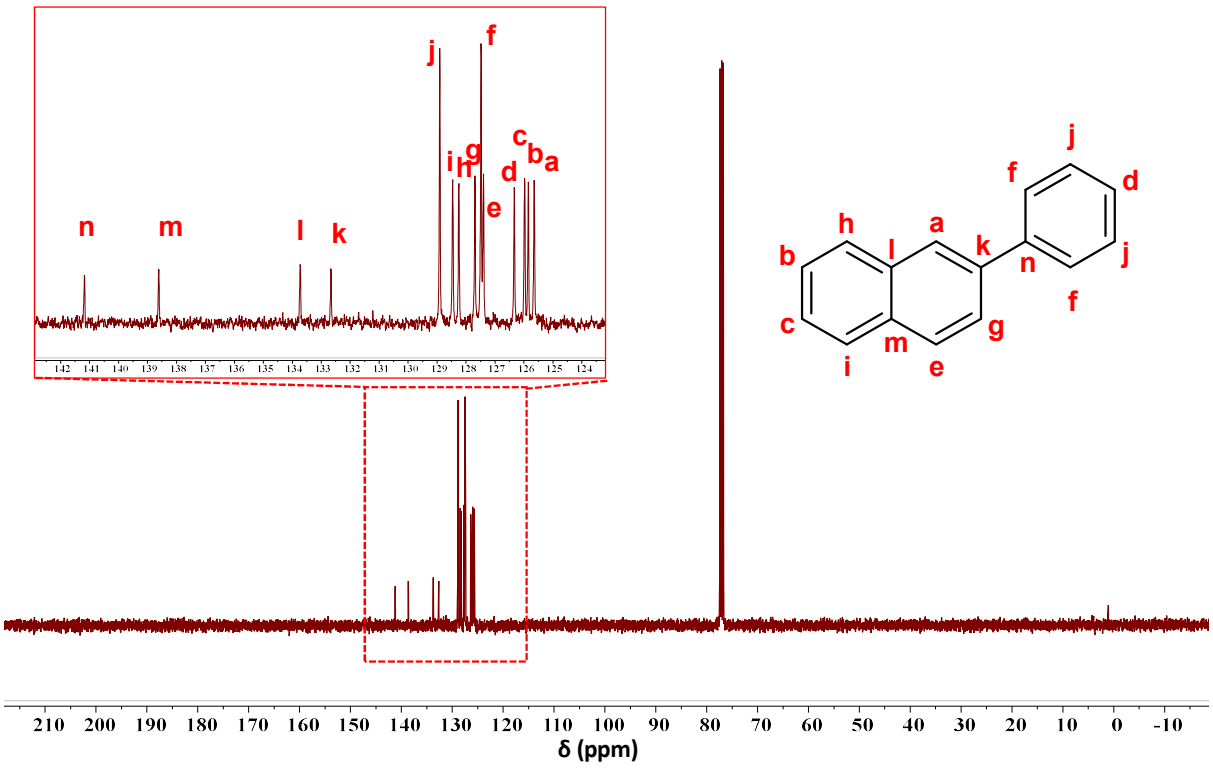

Appendix V-Figure 7.26. ^{13}C NMR of compound **7.**

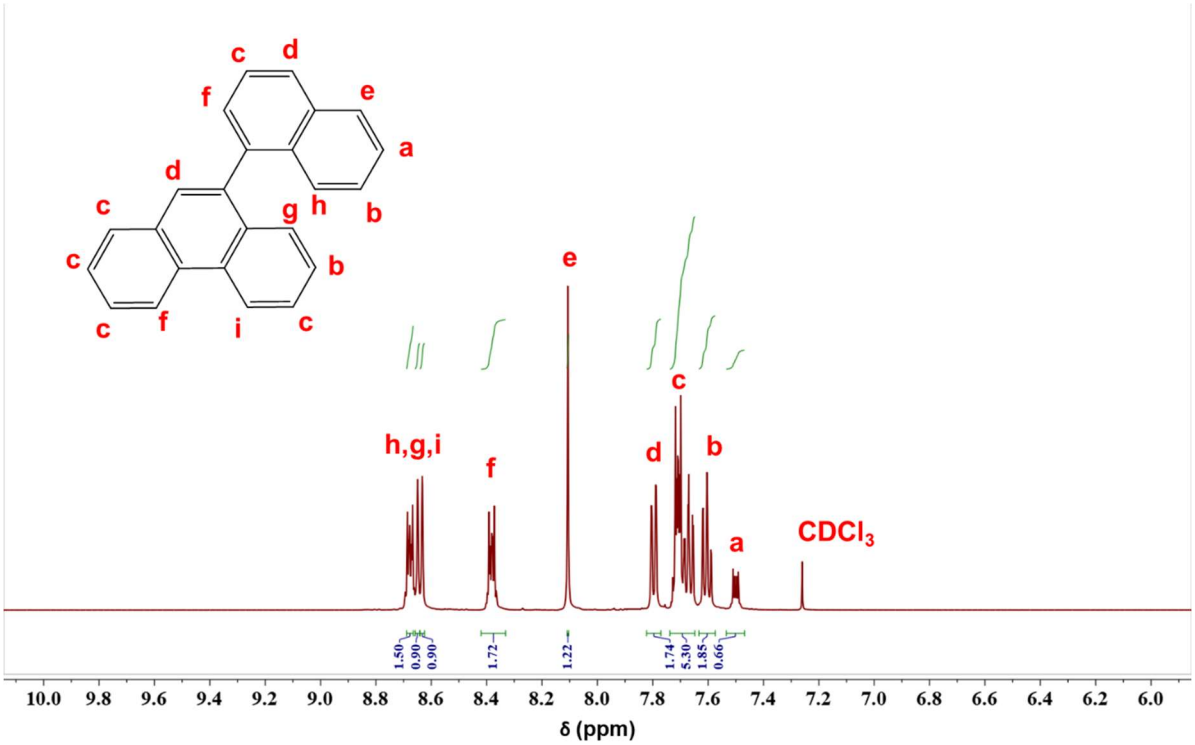

Appendix V-Figure 7.27. ^{1}H NMR of compound **8.**

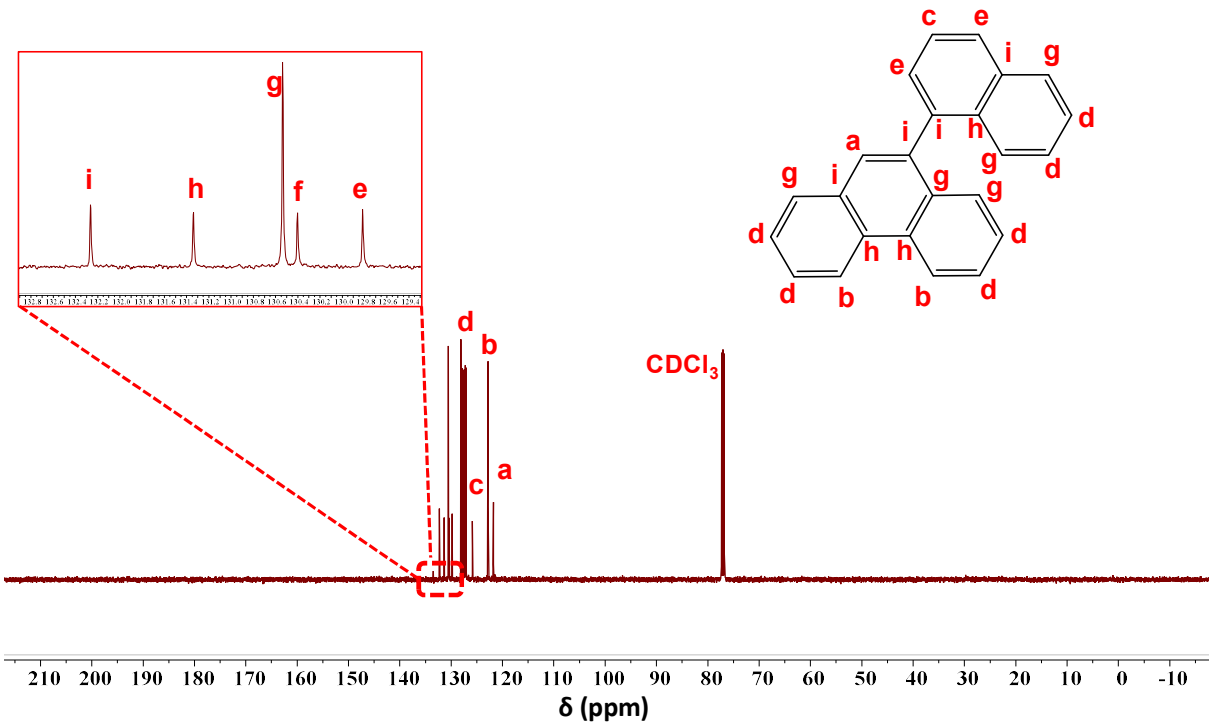

Appendix V-Figure 7.28. ^{13}C NMR of compound **8.**

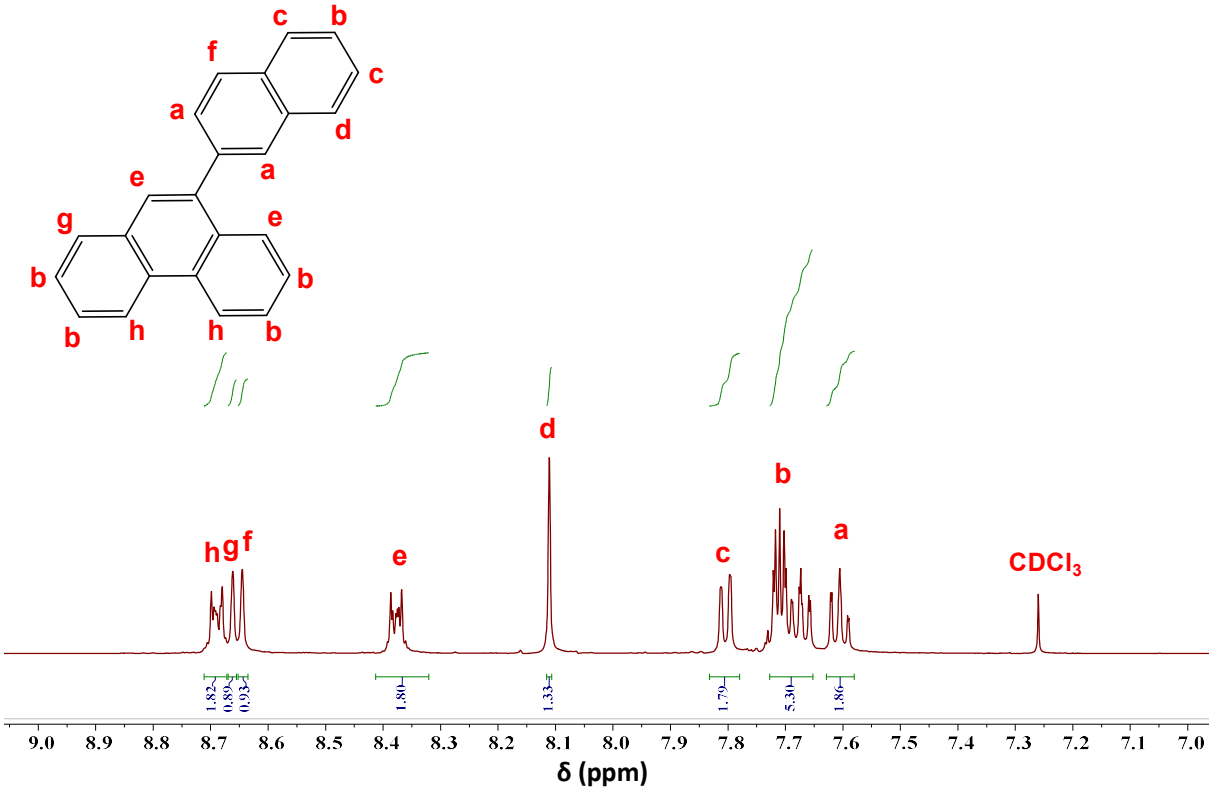

Appendix V-Figure 7.29. ^{1}H NMR of compound **9.**

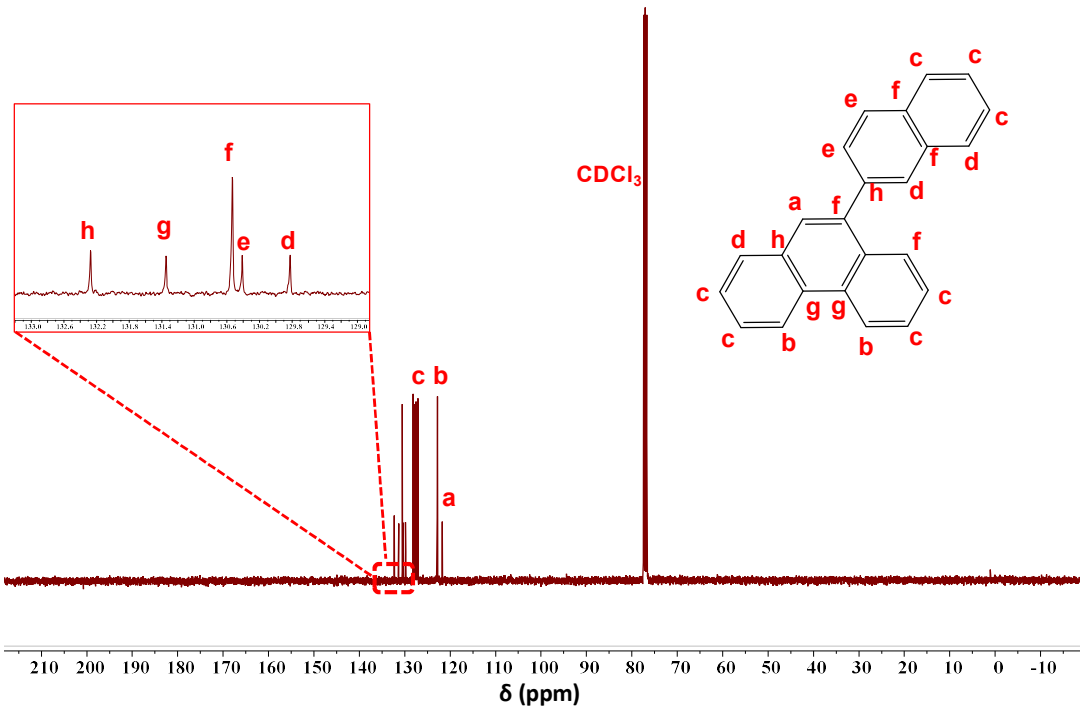

Appendix V-Figure 7.30. ^{13}C NMR of compound **9.**

Publications and Presentations

List of Publications and Presentations

Thesis Chapter Publications:

1. **Nilanjan Mukherjee**, Anupam Das, Moumita Dhara and Tushar Jana*. Surface initiated RAFT polymerization to synthesize N-heterocyclic block copolymer grafted silica nanofillers for improving PEM properties. *Polymer*, **2021**, *236*, 124315. (Chapter 3)
2. **Nilanjan Mukherjee**, Anupam Das, Subhabrata Mukhopadhyay, Samar K. Das*, and Tushar Jana*. Grafting of Polymer Brushes on the UiO-66 MOF for the Development of Super Proton Conducting Mixed Matrix Membranes. *ACS Applied Polymer Materials*, **2024**, *6*, 846-858. (Chapter 4)
3. **Nilanjan Mukherjee**, Olivia Basu, Subhabrata Mukhopadhyay, Samar K. Das*, and Tushar Jana*. Grafting of Poly(vinyl phosphonic acid) to MOF surface by RAFT Polymerization: A Novel Method for the Development of Proton Conducting Materials. (To be Communicated) (Chapter 5)
4. **Nilanjan Mukherjee**, Anupam Das, Tushar Jana*. Poly(N-vinyl triazole-b-N-vinyl imidazole) *Grafted* on MWCNTs as Nanofillers to Improve Proton Conducting Membranes. *ACS Applied Nano Materials*, **2023**, *6*, 544-557. (Chapter 6)
5. **Nilanjan Mukherjee**, Tushar Jana*. Poly (N-Vinyl Imidazole) *Grafted* MWCNT Supported Pd Nanoparticle: An Efficient Catalyst for Suzuki-Mayura Coupling Reaction. (To be Communicated) (Chapter 7)

Other Publications:

1. Anupam Das, **Nilanjan Mukherjee**, Ritu Saraswat, and Tushar Jana*. Multicationic Anion-Exchange Membranes from Pyridine-Bridged Polybenzimidazole and Polymer-Ionic-Liquid-Grafted Graphene Oxide. ACS Applied Energy Materials, 2024, 7, 285-301.
2. Anupam Das, **Nilanjan Mukherjee** and Tushar Jana*. Polymer Grafted Graphene Oxide/Polybenzimidazole Nanocomposites for Efficient Proton Conducting Membranes. ACS Applied Nano Materials, 2023, 6, 6365-6379.
3. Moumita Dhara, Somdatta Rudra, **Nilanjan Mukherjee** and Tushar Jana*. Hollow polymer nanocapsules with a ferrocenyl copolymer shell. Polymer Chemistry, 2021, 12, 3976–3991.

CONFERENCE ATTAINED:

1. Received BEST POSTER award on 'Tailor-made poly (N-vinyl triazole-b-N-vinyl imidazole) grafted MWCNT: Nanofiller for Proton Conducting Membranes' at the 16th International Conference on Polymer Science and Technology of SPSI MACRO 2022 organized by IISER Pune & CSIR-NCL Pune, November 2022.
2. ORAL presentation on 'Effect of Surface Functionalization of Multiwalled Carbon Nanotubes (MWCNTs) towards Block Copolymer grafting via SI-RAFT Technique: A Novel Nanofiller in PEM application' at the 13th International e-Conference of Advancements in Polymer Materials (APM) 2022 organized by CIPET Chennai, India.
3. Participated at the 9th International e-Conference of 9th Asian network of natural unnatural materials international conference (ANNUM-9) 2022 organized by the Department of Chemistry, University of Delhi, India.
4. ORAL presentation on 'Hydrophilic block copolymer grafted silica nanoparticles: A designer nanofiller' at the 18th annual in-house symposium of ChemFest 2021 organized by School of Chemistry, University of Hyderabad, March 2021
5. POSTER presentation on 'RAFT-mediated grafting of diblock copolymers on the silica nanoparticle surface' at 16th annual in-house symposium of ChemFest 2019 organized by School of Chemistry, University of Hyderabad, February 2019
6. POSTER presentation on 'Participated and Presented Poster entitled 'Synthesis of pNVI-b-pNVTgSINP / pNVT-b-pNVI-g-SINP via RAFT polymerization and used as Nanofillers with OPBI' at the 15th International Conference on Polymer Science and Technology of SPSI MACRO 2018 organized by IISER Pune & CSIR-NCL Pune, December 2018
7. Participated at the Symposium on Frontiers in Nanoscience and Technology organized by Centre for Nanotechnology, University of Delhi, April 2018.
8. Participated at the Workshop on Development of Binders and Plasticizers for Energetic Applications organized by ACRHEM, University of Delhi, December 2017.

Polymer grafted Nanomaterials: Synthesis via RAFT Polymerization and the Applications

by Nilanjan Mukherjee

Prof. TUSHAR JANA
School of Chemistry
University of Hyderabad
HYDERABAD-500 046. INDIA.

Librarian
Indira Gandhi Memorial Library
UNIVERSITY OF HYDERABAD
Central University P.O.
HYDERABAD-500 046.

Submission date: 25-Jan-2024 10:27AM (UTC+0530)
Submission ID: 2277989422
File name: Thesis_file_for_plagiarism_check_Nilanjan_Mukherjee_16CHPH18.pdf (6.31M)
Word count: 48154
Character count: 257836

Polymer grafted Nanomaterials: Synthesis via RAFT Polymerization and the Applications

ORIGINALITY REPORT

56%	10%	54%	7%
SIMILARITY INDEX	INTERNET SOURCES	PUBLICATIONS	STUDENT PAPERS

PRIMARY SOURCES

1	Nilanjan Mukherjee, Anupam Das, Subhabrata Mukhopadhyay, Samar K. Das, Tushar Jana. "Grafting of Polymer Brushes on MOF Surface to Achieve Proton-Conducting Membranes", ACS Applied Polymer Materials, 2023 Publication	18%
2	Nilanjan Mukherjee, Anupam Das, Tushar Jana. " Poly(-vinyl triazole- - -vinyl imidazole) on MWCNTs as Nanofillers to Improve Proton Conducting Membranes ", ACS Applied Nano Materials, 2022 Publication	18%
3	Nilanjan Mukherjee, Anupam Das, Moumita Dhara, Tushar Jana. "Surface initiated RAFT polymerization to synthesize N-Heterocyclic block copolymer grafted silica nanofillers for improving PEM properties", Polymer, 2021 Publication	12%

Prof. TUSHAR JANA
School of Chemistry
University of Hyderabad
HYDERABAD-500 046. INDIA.

4	Submitted to University of Hyderabad, Hyderabad Student Paper	3%
5	www.researchgate.net Internet Source	1%
6	Nilanjan Mukherjee, Anupam Das, Moumita Dhara, Tushar Jana. "Surface initiated RAFT polymerization to synthesize N-heterocyclic block copolymer grafted silica nanofillers for improving PEM properties", Polymer, 2021 Publication	1%
7	docs9.chomikuj.pl Internet Source	<1%
8	www.rsc.org Internet Source	<1%
9	Satyanarayana Raju Kutcherlapati, Rambabu Koyilapu, Tushar Jana. " Poly(-vinyl imidazole) grafted silica nanofillers: Synthesis by RAFT polymerization and nanocomposites with polybenzimidazole ", Journal of Polymer Science Part A: Polymer Chemistry, 2018 Publication	<1%
10	Submitted to University of East London Student Paper	<1%
11	Justin O. Zoppe, Nariye Cavusoglu Ataman, Piotr Mocny, Jian Wang, John Moraes, Harm-	<1%

Prof. TUSHAR JANA
School of Chemistry
University of Hyderabad
HYDERABAD-500 046. INDIA.

	Anton Klok. "Surface-Initiated Controlled Radical Polymerization: State-of-the-Art, Opportunities, and Challenges in Surface and Interface Engineering with Polymer Brushes", Chemical Reviews, 2017 Publication	
12	dspace.uohyd.ac.in Internet Source	<1 %
13	discovery.ucl.ac.uk Internet Source	<1 %
14	Submitted to National Chung Hsing University Student Paper	<1 %
15	www.ncbi.nlm.nih.gov Internet Source	<1 %
16	Anupam Das, Nilanjan Mukherjee, Tushar Jana. "Polymer-Grafted Graphene Oxide/Polybenzimidazole Nanocomposites for Efficient Proton-Conducting Membranes", ACS Applied Nano Materials, 2023 Publication	<1 %
17	Mathias Destarac. "On the Critical Role of RAFT Agent Design in Reversible Addition-Fragmentation Chain Transfer (RAFT) Polymerization", Polymer Reviews, 2011 Publication	<1 %
18	Subhabrata Mukhopadhyay, Anupam Das, Tushar Jana, Samar K. Das. "Fabricating a	<1 %

	MOF Material with Polybenzimidazole into an Efficient Proton Exchange Membrane", ACS Applied Energy Materials, 2020 Publication	
19	nozdr.ru Internet Source	<1 %
20	Lewis, David E.. "Advanced Organic Chemistry", Oxford University Press Publication	<1 %
21	www.mdpi.com Internet Source	<1 %
22	d-nb.info Internet Source	<1 %
23	"Hairy Nanoparticles", Wiley, 2023 Publication	<1 %
24	brevets-patents.ic.gc.ca Internet Source	<1 %
25	Guillermo A. Ludueña, Thomas D. Kühne, Daniel Sebastiani. "Mixed Grotthuss and Vehicle Transport Mechanism in Proton Conducting Polymers from Ab initio Molecular Dynamics Simulations", Chemistry of Materials, 2011 Publication	<1 %
26	S. N. Raju Kutcherlapati, Rambabu Koyilapu, Uma Maheswara Rao Boddu, Debparna Datta	<1 %

et al. "Glycopolymer-Grafted Nanoparticles: Synthesis Using RAFT Polymerization and Binding Study with Lectin", Macromolecules, 2017
Publication

27	iopscience.iop.org Internet Source	<1 %
28	Submitted to K12 Incorporated Student Paper	<1 %
29	Martino Rimoldi, Ashlee J. Howarth, Matthew R. DeStefano, Lu Lin, Subhadip Goswami, Peng Li, Joseph T. Hupp, Omar K. Farha. "Catalytic Zirconium/Hafnium-Based Metal–Organic Frameworks", ACS Catalysis, 2016 Publication	<1 %
30	Krzysztof Matyjaszewski. "Atom Transfer Radical Polymerization (ATRP): Current Status and Future Perspectives", Macromolecules, 2012 Publication	<1 %
31	Subhabrata Mukhopadhyay, Joyashish Debgupta, Chandani Singh, Rudraditya Sarkar, Olivia Basu, Samar K. Das. "Designing UiO-66-Based Superprotonic Conductor with the Highest Metal–Organic Framework Based Proton Conductivity", ACS Applied Materials & Interfaces, 2019 Publication	<1 %

32	libstore.ugent.be Internet Source	<1 %
33	Somdatta Rudra, Moumita Dhara, Mithun Chakraborty, Tushar Jana. " Fluorinated Polymer Brush- Silica Nanoparticles: Robust and Durable Self-Cleaning Coating Materials ", ACS Applied Polymer Materials, 2023 Publication	<1 %
34	scholarcommons.sc.edu Internet Source	<1 %
35	Tian, S.H.. "Preparation and properties of novel sulfonated poly(phthalazinone ether ketone) based PEM for PEM fuel cell application", Journal of Power Sources, 20060714 Publication	<1 %
36	fenix.tecnico.ulisboa.pt Internet Source	<1 %
37	Aroosa Javed, Paulina Palafox Gonzalez, Venkataraman Thangadurai. "A Critical Review of Electrolytes for Advanced Low- and High-Temperature Polymer Electrolyte Membrane Fuel Cells", ACS Applied Materials & Interfaces, 2023 Publication	<1 %
38	Arindam Sannigrahi, Sandip Ghosh, Joseph Lalnuntluanga, Tushar Jana. "How the	<1 %

monomer concentration of polymerization influences various properties of polybenzimidazole: A case study with poly(4,4′-diphenylether-5,5′-bibenzimidazole)", Journal of Applied Polymer Science, 2009
Publication

---

39 Zehra Ural Bayrak, Nevin Celik. "Determining the Effects of Operating Conditions on Current Density of a PEMFC by Using Taguchi Method and ANOVA", Arabian Journal for Science and Engineering, 2023 — <1 %
Publication

---

40 eprints.whiterose.ac.uk — <1 %
Internet Source

---

41 patentimages.storage.googleapis.com — <1 %
Internet Source

---

42 patents.patsnap.com — <1 %
Internet Source

---

43 Anupam Das, Mousumi Hazarika, Balakondareddy Sana, Tushar Jana. "Nanoporous Covalent Organic Framework and Polybenzimidazole Composites for Proton Exchange Membranes", ACS Applied Nano Materials, 2023 — <1 %
Publication

---

44 Submitted to Indian Institute of Technology, Madras — <1 %
Student Paper

45	Submitted to Monash University Student Paper	<1 %
46	patents.google.com Internet Source	<1 %
47	research-repository.griffith.edu.au Internet Source	<1 %
48	Gann, John P., and Mingdi Yan. "A Versatile Method for Grafting Polymers on Nanoparticles", Langmuir, 2008. Publication	<1 %
49	Pan, G.. "An efficient approach to obtaining water-compatible and stimuli-responsive molecularly imprinted polymers by the facile surface-grafting of functional polymer brushes via RAFT polymerization", Biosensors and Bioelectronics, 20101115 Publication	<1 %
50	purehost.bath.ac.uk Internet Source	<1 %
51	worldwidescience.org Internet Source	<1 %
52	Shuqin Xiao, Rong Zeng, Lie Chen, Yiwang Chen. "Novel proton exchange membranes with dimensional stability and permeability resistance based on sulfonate	<1 %

polynorbornenes", Journal of Polymer Engineering, 2013
Publication

53	onlinelibrary.wiley.com Internet Source	<1 %
54	uspto.report Internet Source	<1 %
55	Submitted to Jyväskyla University Student Paper	<1 %
56	link.springer.com Internet Source	<1 %
57	pubs.rsc.org Internet Source	<1 %
58	riunet.upv.es Internet Source	<1 %
59	Submitted to Jawaharlal Nehru Technological University Student Paper	<1 %
60	Submitted to Boston University Student Paper	<1 %
61	Lepakshi Barbora. "Synthesis and Ex-situ Characterization of Nafion/TiO_2 Composite Membranes for Direct Ethanol Fuel Cell", Macromolecular Symposia, 02/2009 Publication	<1 %

62	Rambabu Koyilapu, Shuvra Singha, S.N.Raju Kutcherlapati, Tushar Jana. "Grafting of vinylimidazolium-type poly(ionic liquid) on silica nanoparticle through RAFT polymerization for constructing nanocomposite based PEM", Polymer, 2020 Publication	<1 %
63	patents.justia.com Internet Source	<1 %

Exclude quotes	On	Exclude matches	< 14 words
Exclude bibliography	On		

Polymer 236 (2021) 124315

Contents lists available at ScienceDirect

Polymer

journal homepage: www.elsevier.com/locate/polymer

Surface initiated RAFT polymerization to synthesize N-heterocyclic block copolymer *grafted* silica nanofillers for improving PEM properties

Nilanjan Mukherjee, Anupam Das, Moumita Dhara, Tushar Jana *

School of Chemistry, University of Hyderabad, Hyderabad, 500046, India

ARTICLE INFO

Keywords:
RAFT Polymerization
Silica nanoparticle
Block copolymer
Proton exchange membrane (PEM)
Polymer nanocomposite

ABSTRACT

Surface functionalization of silica nanoparticles (SiNP) has gained attention as an efficient methodology in improving the properties of the proton exchange membrane (PEM). Here, we report the development of block copolymer *grafted* SiNP (BC-*g*-SiNP) as functional nanofiller which was further blended with oxy-polybenzimidazole (OPBI) to prepare nanocomposite-based PEM. Block copolymer chains consisting of poly (N-Vinyl imidazole) (pNVI) and poly (N-Vinyl-1,2,4-triazole) (pNVT) were grown on the SiNP surface using *grafting-from* RAFT polymerization in one pot process. Two series of BC-*g*-SiNP namely pNVI-*b*-pNVT-*g*-SiNP and pNVT-*b*-pNVI-*g*-SiNP were synthesized by altering the polymer chain grafting sequence. A series of BC-*g*-SiNP was developed by varying chain length of each block to understand the effect of the chain sequence and length on the properties of nanofiller and their influence in altering the PEM properties. The block copolymer structure, chain sequence and chain length were confirmed by means of NMR and GPC analysis of the cleaved copolymer chains. The BC-*g*-SiNP exhibited core-shell morphology and thickness of the shell altered as the chain length and sequence of the grafted chains tuned. Phosphoric acid (PA) loaded OPBI/BC-*g*-SiNP nanocomposite PEM showed very high thermal, mechanical and chemical stabilities along with the proton conductivity as high as 0.278 S cm^{-1} at 180 °C in case of OPBI/P6(3%). A very clear-cut dependence of the PEM properties was observed on the architecture of the BC-*g*-SiNP such as chain length and sequence.

1. Introduction

Development of efficient polymer electrolyte membrane (PEM) for the use in fuel cell in order to meet the increasing demand of the non-conventional energy sources has become subject of immense interests among polymer chemists [1–3]. Majority of the well-researched PEMs encounter a number of serious problems which includes decrease in conductivity at higher temperature, low mechanical strength, weaker thermal and chemical stabilities, low phosphoric acid (PA) loading and high leaching of PA. Though polybenzimidazole (PBI) based PEM has stability in high temperature condition and fairly good acid retention properties but further improvement of the acid retention will definitely be a right step towards enhancing the proton conducting ability for longer duration at higher temperature [4–7]. Several studies showed that nitrogen containing heterocyclic compounds can play an effective role in alleviating the concerns raised above owing to stable basic heterocyclic rings and ability to form strong interactions with PEM forming polymers [8–11]. It has also been reported widely that polymers consisting of N-heterocycles can efficiently execute the acid-base complexes with the complementary molecules/polymers and hence, resulted efficient materials for the use in various fields [12–16].

Polymers containing imidazole and triazole rings are mostly being used to prepare blend materials [17–19] but, it has also been observed that polymerization of imidazole and triazole ring containing monomers are a bit tricky in terms of controlling the polymerization process. The polymerization of N-vinylic monomers containing heterocyclic rings such as N-vinyl imidazole, N-vinyl triazole are challenging as propagating N-vinyl radicals present in the polymerization media are highly reactive and unstable owing to the absence of resonance stabilization and hence propagating radicals are responsible not only for chain transfer but also for chain termination event [20]. Therefore, it is an important task to get control over the polymerization of these N-vinylic monomers.

Over the last few years, the combination of the surface initiated polymerization and the controlled polymerization techniques have become a very useful tool to design the surface functionality with the desired properties [21–26]. Among such approaches the surface initiated reversible addition-fragmentation chain-transfer (SI-RAFT)

* Corresponding author.
E-mail addresses: tusharjana@uohyd.ac.in, tjscuoh@gmail.com (T. Jana).

https://doi.org/10.1016/j.polymer.2021.124315
Received 20 July 2021; Received in revised form 8 October 2021; Accepted 30 October 2021
Available online 31 October 2021
0032-3861/

ACS APPLIED POLYMER MATERIALS

pubs.acs.org/acsapm Article

Grafting of Polymer Brushes on MOF Surface to Achieve Proton-Conducting Membranes

Nilanjan Mukherjee, Anupam Das, Subhabrata Mukhopadhyay, Samar K. Das,* and Tushar Jana*

Cite This: *ACS Appl. Polym. Mater.* 2024, 6, 846−858 Read Online

ACCESS | Metrics & More | Article Recommendations | Supporting Information

ABSTRACT: In recent years, postsynthetic modification (PSM) of a metal−organic framework (MOF) has gained immense interest for the synthesis of hybrid materials with improved functionality. However, further improvement in the PSM strategies to make them scalable and yield a synthetically tunable MOF surface can create polymer chain-grafted MOF hybrid materials in which polymer chains provide the stability, robustness, and desired functional performances and MOF offers interesting physical properties. Toward these goals, in this work we have developed a simple and effective method to functionalize the UiO-66-NH_2 MOF surface by grafting functional polymer brushes using surface-initiated reversible addition−fragmentation chain-transfer (RAFT) polymerization. At first, the MOF surface was transformed into a polymerizable surface by attaching a trithiocarbonate-based chain-transfer agent (CTA) and then, three different sets of polymer brushes consisting of (i) a neutral but basic nitrogen functionality (PGM-N), (ii) a trimethyl-substituted quaternary ammonium functionality (PGM-C), and (iii) a quaternary ammonium along with sulfonate functionality (PGM-Z) were grown on the activated MOF surface. The uniqueness of this work has additionally been enhanced by utilizing these synthesized PGMs as nanofillers into the oxypolybenzimidazole (OPBI) membrane matrix to obtain homogeneous mixed matrix membranes (OPBI@PGM) that show brilliant thermomechanical and tensile properties and exceptional thermal stability. Interestingly, these membranes exhibit superior proton conductivity when doped with H_3PO_4 (PA) and minimal acid leaching. Grafting of functional polymer brushes on the MOF surface induces strong H-bonding and acid−base interactions with OPBI chains and H_3PO_4 molecules, which are responsible for such high acid uptake and excellent acid retention, thereby displaying a proton conductivity as high as 0.241 S cm^{-1} at 160 °C (~4-fold increase when compared to OPBI), which is among the highest values reported till date for an MOF-based proton exchange membrane with excellent mechanical vigor.

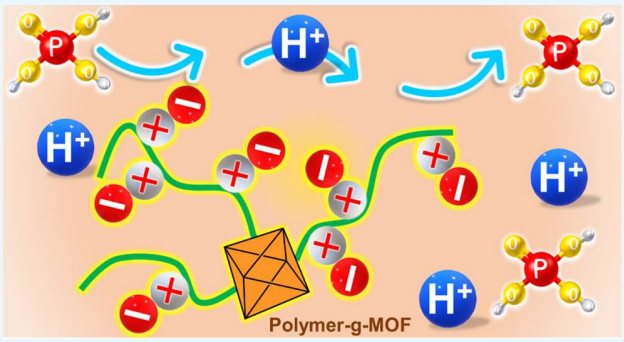

KEYWORDS: *proton exchange membrane, metal−organic framework, grafted polymer brushes, RAFT polymerization, polybenzimidazole*

INTRODUCTION

Metal−organic frameworks (MOFs) with ultrahigh porosity, inherent crystallinity, and a very high surface area are emerging materials.[1,2] The applications of MOFs have been demonstrated in diverse fields ranging from gas separation and CO_2 capture,[3−5] to water splitting through water purification,[6−9] and from drug delivery to energy applications.[10−13] A recent literature study indicates a growing interest in the field of postsynthetic modification (PSM) of MOF materials.[14−19] This modification can be achieved by anchoring a functional monolayer on the MOF surface, but the efficiency of the modification is limited owing to less number of active groups of the monolayer and the inability to achieve 100% functionalization using currently available PSM techniques.[15,20−22] However, the number of functional units can be increased substantially by attaching polymer chains on the MOF surface.[23] A few reports in the literature demonstrated improvement in various physical properties in the postsynthetically modified MOFs when functional polymers are attached to MOFs, or when composites are prepared by mixing MOFs and polymers.[14,19,24−26] However, no known PSM for MOF so far has addressed the challenges of the nonuniformity in the composites made from MOF and polymer owing to the thermodynamic incompatibility between these two components. In order to resolve this issue, loading or grafting of polymer chains on the surface can be considered to provide better uniformity of the MOF-polymer composite because of the favorable interactions between the postsynthetically

Received: October 11, 2023
Revised: November 10, 2023
Accepted: December 6, 2023
Published: December 19, 2023

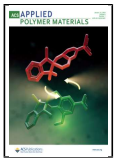

ACS APPLIED NANO MATERIALS

www.acsanm.org Article

Poly(*N*-vinyl triazole-*b*-*N*-vinyl imidazole) *Grafted* on MWCNTs as Nanofillers to Improve Proton Conducting Membranes

Nilanjan Mukherjee, Anupam Das, and Tushar Jana*

Cite This: *ACS Appl. Nano Mater.* 2023, 6, 544−557 Read Online

ACCESS | Metrics & More | Article Recommendations | Supporting Information

ABSTRACT: Carbon nanotubes (CNTs) are of particular interest because of their ability to enhance the mechanical strength in the material; however, processing difficulties of CNTs often restrict utilization up to its full potential. To resolve this, in the current study, we have developed a simple and efficient method to functionalize the surface of a multiwalled carbon nanotube (MWCNT) with precise functional polymer chains, which were covalently *grafted* on the surface of the MWCNT, and delved into an application to demonstrate this material as an efficient nanofiller in developing a proton conducting membrane (PEM) from polybenzimidazole (PBI). At first, the MWCNT surface was converted to a polymerizable surface by attaching a trithiocarbonate based chain transfer agent (CTA). Then, a N-heterocyclic block copolymer, namely poly-*N*-vinyl-1,2,4-triazole-*b*-poly-*N*-vinyl imidazole (pNVT-*b*-pNVI), was grown from the CTA anchored surface with a one-pot surface initiated reversible addition−fragmentation chain transfer (SI-RAFT) technique. *Grafting* of block copolymer chain was confirmed by GPC, NMR, TGA, TEM, FESEM, and EDX studies. To the best of our knowledge, this will be the first report of a growing block copolymer structure *grafted* covalently on the surface of the MWCNT. The novelty of the work was further enhanced by incorporating pNVT-*b*-pNVI-*g*-MWCNT as a nanofiller into the oxypolybenzimidazole (OPBI) membrane to obtain homogeneous nanocomposite membranes with excellent thermomechanical and tensile properties, thermal stability, superior proton conduction when doped with phosphoric acid (PA), and PA holding capacity. The nanocomposite membrane with 2.5 wt % nanofiller loading displayed a tensile stress of 1.8 MPa and a strain of 176% at break. The basic N-heterocyclic rings dangling from the block copolymer chains *grafted* on the MWCNT surface allowed formation of strong H-bonding, acid−base interaction with PA, which is responsible for high acid uptake and superior PA retention, and also exhibited proton conductivity as high as 0.164 S cm^{-1} at 180 °C, which is a 2.6-fold increment when compared with a pristine OPBI membrane. This significant increase in conductivity is attributed to the proton conducting nanochannel pathway generated along the polymer-*g*-MWCNT surface.

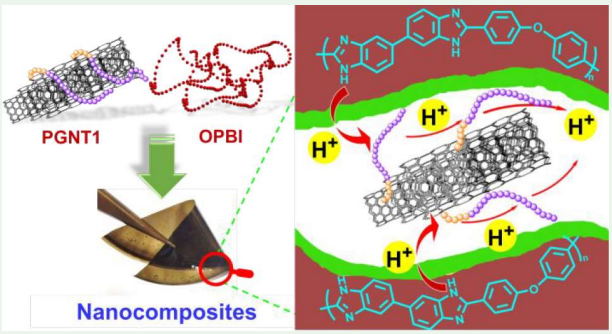

KEYWORDS: *Block copolymer, RAFT polymerization, Multiwalled carbon nanotube, polybenzimidazole, proton exchange membrane*

INTRODUCTION

Carbon nanotubes (CNTs) have attracted immense interest of material scientists due to its versatile chemical characteristics and physical properties in catalysis,[1−3] gas adsorption,[4] water purification,[5,6] electrical and thermal conductivity,[7−10] and high mechanical stability,[11,12] since their discovery.[13] However, there is a significant limitation on the usage of CNTs because of the presence of strong van der Waals interaction which makes them insoluble in almost all the solvents, and they are held together tightly to form bundles and rope like aggregation in solution and also in the polymer matrix.[14−16] This strong aggregating nature restricts their processability and hampers the performance at the nano level.[17,18] To address these problems, different approaches have evolved in literature which include modification with surfactant, polymer absorption, encapsulation of polymer, and end group modification of CNT surface for covalent *grafting* of different molecules and polymers.[17,19−21] While investigating, we have observed that covalent functionalization of CNTs with polymer chains or surface modification of CNT with strategically designed *grafted* block copolymer chains can be of great advantage as the design of the polymer structure can enhance the material properties significantly and can be modified to further improve the processability with the target matrix which can significantly improve to meet the requirements for particular applications.

"*Grafting to*" and "*grafting from*" are the major two approaches toward the *grafting* of polymer chains on the

Received: October 25, 2022
Accepted: December 2, 2022
Published: December 19, 2022

https://doi.org/10.1021/acsanm.2c04603
ACS Appl. Nano Mater. 2023, 6, 544−557